Springer Series on Chemical Sensors and Biosensors 15

Series Editor: Gerald Urban

Claus-Dieter Kohl
Thorsten Wagner *Editors*

Gas Sensing Fundamentals

Springer

15

Springer Series on Chemical Sensors and Biosensors

Methods and Applications

Series Editor: G. Urban

For further volumes:
http://www.springer.com/series/5346

Springer Series on Chemical Sensors and Biosensors

Series Editor: G. Urban

Recently Published and Forthcoming Volumes

Gas Sensing Fundamentals
Volume Editors: C.-D. Kohl, T. Wagner
Vol. 15, 2014

Applications of Nanomaterials in Sensors and Diagnostics
Volume Editor: A. Tuantranont
Vol. 14, 2013

Autonomous Sensor Networks: Collective Sensing Strategies for Analytical Purposes
Volume Editor: D. Filippini
Vol. 13, 2013

Designing Receptors for the Next Generation of Biosensors
Volume Editors: S.A. Piletsky, M.J. Whitcombe
Vol. 12, 2013

Solid State Gas Sensors – Industrial Application
Volume Editors: M. Fleischer, M. Lehmann
Vol. 11, 2012

Optical Nano- and Microsystems for Bioanalytics
Volume Editors: W. Fritzsche, J. Popp
Vol. 10, 2012

Mathematical Modeling of Biosensors
An Introduction for Chemists and Mathematicians
Volume Authors: R. Baronas, F. Ivanauskas, J. Kulys
Vol. 9, 2010

Optical Guided-wave Chemical and Biosensors II
Volume Editors: M. Zourob, A. Lakhtakia
Vol. 8, 2010

Optical Guided-wave Chemical and Biosensors I
Volume Editors: M. Zourob, A. Lakhtakia
Vol. 7, 2010

Hydrogel Sensors and Actuators
Volume Editors: Gerlach G., Arndt K. -F.
Vol. 6, 2009

Piezoelectric Sensors
Volume Editors: Steinem C., Janshoff A.
Vol. 5, 2006

Surface Plasmon Resonance Based Sensors
Volume Editor: Homola J.
Vol. 4, 2006

Frontiers in Chemical Sensors
Novel Principles and Techniques
Volume Editors: Orellana G., Moreno-Bondi M. C.
Vol. 3, 2005

Ultrathin Electrochemical Chemo- and Biosensors
Technology and Performance
Volume Editor: Mirsky V. M.
Vol. 2, 2004

Optical Sensors
Industrial, Environmental and Diagnostic Applications
Volume Editors: Narayanaswamy R., Wolfbeis O. S.
Vol. 1, 2003

Gas Sensing Fundamentals

Volume Editors:
Claus-Dieter Kohl
Thorsten Wagner

With contributions by

F.L. Dickert · N. Donato · M. Eickhoff · H. Fritze · A. Helwig ·
P. Kirchner · P.J. Martin · A. Mujahid · G. Müller · S. Paul ·
M. Penza · P. Reimann · S. Reisert · D. Richter · S. Russ ·
T. Sauerwald · S. Schütz · A. Schütze · M.J. Schöning · J. Teubert ·
M. Tiemann · T. Wagner · B. Weißbecker · J.T.W. Yeow

Springer

Editors
Claus-Dieter Kohl
Institut für Angewandte Physik
Justus-Liebig-Universität
Gießen
Germany

Thorsten Wagner
Naturwissenschaftliche Fakultät
Department Chemie
Universität Paderborn
Paderborn
Germany

ISSN 1612-7617
ISBN 978-3-642-54518-4 ISBN 978-3-642-54519-1 (eBook)
DOI 10.1007/978-3-642-54519-1
Springer Heidelberg New York Dordrecht London

Library of Congress Control Number: 2014947339

© Springer-Verlag Berlin Heidelberg 2014
This work is subject to copyright. All rights are reserved by the Publisher, whether the whole or part of the material is concerned, specifically the rights of translation, reprinting, reuse of illustrations, recitation, broadcasting, reproduction on microfilms or in any other physical way, and transmission or information storage and retrieval, electronic adaptation, computer software, or by similar or dissimilar methodology now known or hereafter developed. Exempted from this legal reservation are brief excerpts in connection with reviews or scholarly analysis or material supplied specifically for the purpose of being entered and executed on a computer system, for exclusive use by the purchaser of the work. Duplication of this publication or parts thereof is permitted only under the provisions of the Copyright Law of the Publisher's location, in its current version, and permission for use must always be obtained from Springer. Permissions for use may be obtained through RightsLink at the Copyright Clearance Center. Violations are liable to prosecution under the respective Copyright Law.
The use of general descriptive names, registered names, trademarks, service marks, etc. in this publication does not imply, even in the absence of a specific statement, that such names are exempt from the relevant protective laws and regulations and therefore free for general use.
While the advice and information in this book are believed to be true and accurate at the date of publication, neither the authors nor the editors nor the publisher can accept any legal responsibility for any errors or omissions that may be made. The publisher makes no warranty, express or implied, with respect to the material contained herein.

Printed on acid-free paper

Springer is part of Springer Science+Business Media (www.springer.com)

Series Editor

Prof. Dr. Gerald Urban

IMTEK - Laboratory for Sensors
Institute for Microsystems Engineering
Albert-Ludwigs-University
Georges-Köhler-Allee 103
79110 Freiburg
Germany
urban@imtek.de

Aims and Scope

Chemical sensors and biosensors are becoming more and more indispensable tools in life science, medicine, chemistry and biotechnology. The series covers exciting sensor-related aspects of chemistry, biochemistry, thin film and interface techniques, physics, including opto-electronics, measurement sciences and signal processing. The single volumes of the series focus on selected topics and will be edited by selected volume editors. The *Springer Series on Chemical Sensors and Biosensors* aims to publish state-of-the-art articles that can serve as invaluable tools for both practitioners and researchers active in this highly interdisciplinary field. The carefully edited collection of papers in each volume will give continuous inspiration for new research and will point to existing new trends and brand new applications.

Preface

This volume addresses several fundamental gas sensing concepts which have gained increased interest during the last years. Various basic sensor principles, including micro-gravimetric sensors, semiconducting and nanotube sensors, calorimetric sensors and optical sensors, are covered. Also recent developments on the related sensitive layers are discussed. These include new properties due to nanostructuring in well-known metal oxide layers, an in-depth insight into the interesting chemistry and signal generation of copper oxide in percolating sensors as well as a variety of applications of functional polymers possible due to proper imprinting.

Many of the recent developments are driven by current application requirements. Extension to higher operating temperatures necessitates new material developments and it may be no surprise that also a new sensor mechanism (for In_2O_3) became evident as a side-product. A workgroup of the DGM (German Material Science Association) focuses on high temperature sensor physics and chemistry.

But also in the low temperature regime stability is an important issue. There are new approaches to improve signal reproducibility. On the material side carbon nanotubes allow for cheap and reliable sensors for integrated devices which will benefit from the highly stable nature of the carbon nanotubes. Potential applications cover the field of environmental monitoring, healthcare, or integrated devices. However, for rough industrial surroundings oxide-based sensors are more promising. Mimicking insect olfactory systems utilizing semiconducting sensors combines the “evolutionary experience” with the reliability and long-term ruggedness of the technical system. Another approach introduces optical readout technique of space charge for inorganic and organic semiconductor sensor to avoid electrical contacts to the sensing material. Such devices are currently (2014) under development within a project funded by the European Union. They also open prospects to sensors for chemically aggressive environments without contact corrosion problems.

On the system side the concept of virtual multisensors has proven to be advantageous. This general concept, which in principle is not limited to semiconductor sensors, is based on the adjustment of several optimized operating conditions which are applied sequentially to only one physical sensing element. The so generated virtual sensing elements combined with refined data algorithms meet the necessary specificity and selectivity for reliable hazard detection.

There is also the necessity to pick the proper transducer technique. Calorimetric sensors offer a versatile transducer concept not only for sensing of explosives, but also in biology and medical applications. Even the concept of imprinted layers can be transferred to them. However, a lot of boundary conditions apply to implement them into a process, e.g. in biology, medicine, or food industry. A contribution deals with a common problem of such applications, to provide an aseptic surrounding.

The concept of percolation is most of us known from current transport in very thin metal films. There exists a characteristic dose (deposition rate multiplied by the time span) and then a sudden irreversible steep conductance increase occurs. This concept has been successfully transferred to chemically reactive gas sensor layers able to act as dosimeters. By cyclic operation those layers can also be used for quasi-continuous monitoring.

For many larger molecules with low vapor pressure and correspondingly stronger tendency to enrich on surfaces with geometrically and chemically optimized surface sites the concept of imprinted layers realized on bulk and surface acoustic wave substrates is a flexible technique. Marked progress has been made in specificity and sensitivity of single sensor systems as well as in sensor arrays.

So we hope that you will be inspired by this book to new thoughts in your own work and the editors like to thank all authors of this volume for their engagement and the quality of their contributions.

Gießen, Germany Claus-Dieter Kohl
Paderborn, Germany Thorsten Wagner

Contents

High-Temperature Gas Sensors

Denny Richter and Holger Fritze

Abstract High-temperature processes in the field of, e.g., energy conversion or chemical technologies require sophisticated process monitoring and control to ensure high-efficiency, low pollutant emissions, and safe operation. These objectives can only be achieved by in-situ control of the processes. The increasing combustion of biofuels, organic waste, wood, etc., tightens the demand for process control even more. Properties to be monitored include temperature, gas composition, pressure, torque, mechanical integrity, and state of functional components. In this chapter, an overview about current gas sensor principles for operation temperatures above 500°C is given. Thereby, the related range of measurement, the selectivity, the sensitivity, the response time, and the long-term stability are presented along with application examples. Since the selection of sensor materials plays a crucial role at high temperatures, material aspects are an essential part of the chapter. The discussion of solid-state sensor principles includes potentiometric, amperometric, resistive, and resonant sensors.

Keywords Defect chemistry, Gas sensors, High-temperature materials, Resonant sensors, Sensor principles

Contents

D. Richter and H. Fritze (✉)
Clausthal University of Technology, Goslar, Germany
e-mail: denny.richter@tu-clausthal.de; holger.fritze@tu-clausthal.de

C.-D. Kohl and T. Wagner (eds.), *Gas Sensing Fundamentals*,
Springer Series on Chemical Sensors and Biosensors (2014) 15: 1–46
DOI 10.1007/5346_2013_56,

1 Introduction

High- and medium-temperature processes related to energy conversion, industrial production, and transportation cause about 85% of the anthropogenic CO_2 emissions and are, therefore, the main source for the accumulation of CO_2 in the atmosphere. As a consequence, improved processes with respect to efficiency, system durability, and emission of pollutants have to be developed. In this context, the general quest for renewable energy and high energy efficiency requires new and improved monitoring technologies. The increasing combustion of biofuels, organic waste, wood, etc., tightens the demands for process control even more since the composition of these primary energy sources varies. Properties to be monitored above about 500°C include temperature, gas composition, pressure, torque, and mechanical integrity of the systems. Further, sensors improve the operational safety of high-temperature systems which also becomes increasingly important.

Gas sensors for harsh environments are not generally available. Except for oxygen and nitric oxide sensors, current systems often exhibit insufficient stability, selectivity, and sensitivity. Oxygen sensors to control the combustion process in stroke engines are one of the few successful examples. They are found in virtually all modern gasoline engines. In concert with three-way catalysts, the emissions of hydrocarbons and nitrous gases are decreased significantly. While the monitoring of combustion processes in cars is quite common today, many other high-temperature processes are controlled without any feedback using characteristics provided by the manufacturer. As a consequence, such systems are rarely adapted to changes in the operating environment. Even if sophisticated process monitoring is realized in large-scale processes of power plants and chemical reactors, it is often not used to actively control the processes. Further, common ex-situ monitoring prevents an effective process control due to the distance between sensor and the actual process site. Long response times and falsified signals are the consequence. Hence, appropriate sensor principles and stable materials are required to install the sensors in high-temperature area.

The following chapter provides an overview about current gas sensor principles for operational temperatures of above 500°C. Thereby, the related range of measurement, the selectivity, the sensitivity, the response time, and the long-term stability are presented along with application examples. Since the selection of sensing materials plays a crucial role at high temperatures, material aspects are an essential part of the chapter. The following solid-state sensor principles are discussed:

- Potentiometric sensors
- Amperometric sensors
- Resistive sensors
- Resonant sensors

It is, however, not intended to give a very broad overview as done, e.g., in [1] for applications, [2] for amperometric sensors, or [3] for solid-state sensors.

Together with amperometric and mixed potential sensors, potentiometric sensors belong to the group of electrochemical sensors. They were first developed for low operational temperatures and are widely used as gas sensors in safety applications to detect a wide range of pollutants with a high sensitivity. Commonly applied electrolytes such as liquids or polymers are inappropriate for high-temperature application. In order to increase the operational temperature of such sensors, solid electrolytes have to be applied. The related sensor principles and materials are discussed in Sects. 2 and 3. Mixed potential sensors are not included. Here, the reader is referred to publications such as [4–7].

Upon application of thin films, resistive sensors offer, in general, gas sensing with short response times at the expense of reduced accuracy and the necessity of calibration. These aspects are given in Sect. 4.

Many sensor principles remain at the conceptual stage largely because of material limitations at high temperatures. Until about 1995, resonant piezoelectric sensors were such an example. They provide a variety of advantages including the option to monitor mechanical properties (sensor film mass, gas adsorption) and high sensitivity (highly precise frequency determination). However, material instabilities and high electromechanical losses prevented its application above 500°C. New piezoelectric crystals overcome those problems. These materials and the related high-temperature sensor principles are presented in Sect. 5.

Despite offering high gas selectivity, the application of optical gas sensors at high temperatures is restricted by the requirement of long-term stable optical windows and high system costs. These sensors are not discussed in this chapter since their basic operational principles do not differ significantly from room-temperature optical sensors. Related publications include [8, 9].

Table 1 Time constants for oxygen diffusion in TiO_2 and MgO for different sensor element thicknesses and temperatures

Dimension	1 mm	50 nm	50 nm
Temperature	1,000°C	1,000°C	1,350°C
	Equilibration time (s)		
TiO_2	2×10^{10}	60	0.6
MgO_2	1.2×10^{19}	3×10^{7}	10^{5}

1.1 Physical Principles and Temperature Ranges

Solid-state gas sensors operate based on the interaction of gas particles with surfaces and adjacent volumes. Commonly, the electrochemical potential, the resistivity, the density, and/or the optical properties are altered upon gas exposure. Gas adsorption processes relevant for high-temperature operation must show higher binding energies than the thermal energy kT. Temperatures of 1,000°C correspond to an energy of about 0.1 eV which is higher or in the same order of magnitude as typical physisorption energies. In other words, comparatively weak van der Waals forces are not able to bind the gases to the surface. The maximum binding energies of, e.g., H_2, H_2O, or CH_4 are lower than the value mentioned above. The heat of chemisorption on metals (O on Pt: 0.7 eV; H_2 on Cr: 0.5 eV [10]) or on oxides (H_2 on Cr_2O_3: 3.2 eV [11]) is bigger than the thermal energy at 1,000°C. Therefore, these covalent, metallic, or ionic bonds change the surface chemistry and impact the electrical conductivity and surface mass loading. With increasing temperature, surface reactions become increasingly important. For example, they modify the surface conduction by accumulation of electrons in the conduction band. Finally, bulk reactions occur at high temperatures which modify the bulk conductivity and density.

At sufficiently high temperatures the response time of sensors might depend solely on the formation of bulk defects. Here, the transport kinetics of the relevant species and the dimension of the sensor are crucial. Taking the oxygen stoichiometry-dependent electronic conductivity as example, the equilibration is determined by the oxygen diffusion and the thickness of the sensor element. The time constants might be estimated according to $t = x^2/(4D)$ where x and D are the dimension of the active sensor material and the diffusion coefficient, respectively. The time constants for 1 mm and 50 nm thick sensor elements are estimated at 1,000°C and 1,350°C using diffusion data for oxygen in TiO_2 and MgO [12]. In Table 1 it is clearly shown that quick responses can be achieved by thin films and/or high transport coefficients. The latter might require sufficiently high temperatures.

2 Potentiometric Gas Sensors

Potentiometric gas sensors determine the difference in the activity of gas species in two compartments separated by a solid electrolyte. Thereby, the activity a_i can be approximated by the related partial pressure p_i. Commonly, the reference pressure p^0 is chosen to be 1 bar with $a_i = p_i/p^0$. The oxygen activity, for example, describes

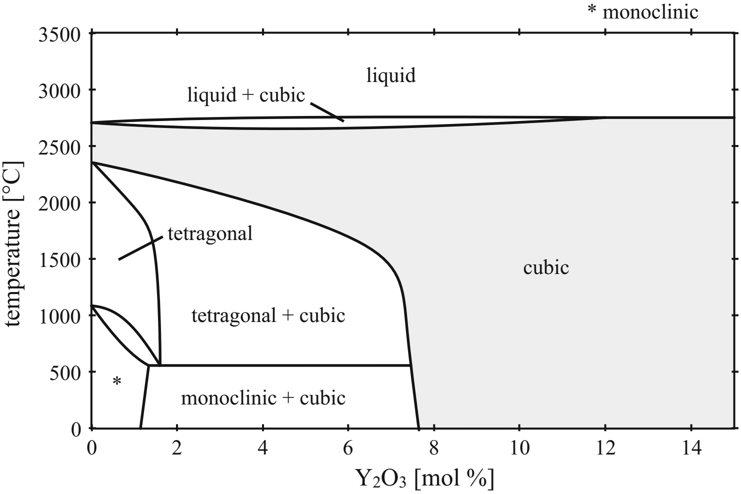

Fig. 1 Yttrium-zirconia phase diagram in the zirconia-rich region [14, 140]

the part of oxygen in a gas mixture or in vacuum that governs the interaction with metals or metal oxides.

2.1 Electrolytes

The electrolyte must be an ion conductor for the species of interest while being mechanically and chemically stable at elevated temperatures. Simultaneously, the electronic conduction must be low. In the following, oxygen sensors are chosen for exemplification. Today, the most suited electrolyte for these sensors is doped zirconia. Pure zirconia exhibits very poor mechanical stability and thermal shock resistance due to significant volume changes occurring during phase transformations between the monoclinic and the tetragonal phase. Adding oxides like MgO, CaO, Y_2O_3, and CeO_2 stabilizes the cubic phase and shifts the phase transition to temperatures out of the intended application range [13]. Figure 1 shows the ZrO_2-rich part of the ZrO_2–Y_2O_3 phase diagram [14]. It becomes clearly obvious that doping levels above about 8 mol% Y_2O_3 stabilizes the cubic phase. The material commonly tolerates thermal cycling as strong as occurring in exhaust pipes of combustion engines.

Besides suppressing the phase transformation, the incorporation of, e.g., yttrium into the zirconia lattice increases the oxygen vacancy concentration in the electrolyte. The replacement of Zr^{4+} by Y^{3+} results in the formation of oxygen vacancies $V_O^{\bullet\bullet}$ according to:

$$\mathrm{O_O} + 2\mathrm{Zr_{Zr}} + \mathrm{Y_2O_3} \rightarrow 2\mathrm{Y}'_{\mathrm{Zr}} + V_{\mathrm{O}}^{\bullet\bullet} + 2\mathrm{ZrO_2} \qquad (1)$$

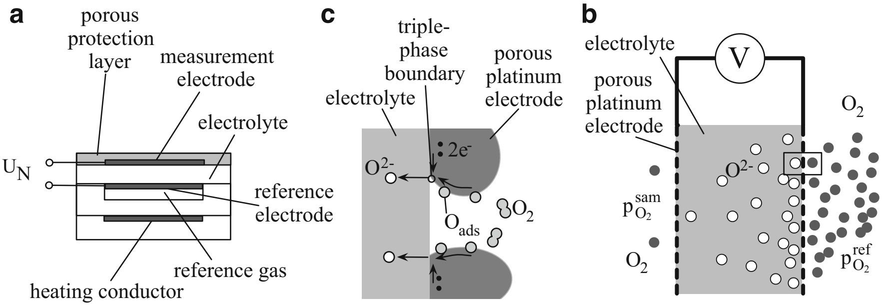

Fig. 2 Scheme of a planar-type potentiometric oxygen sensor (**a**), triple-phase boundary (**b**), and gradient of the oxygen ion concentration (**c**)

Thereby, the Kröger–Vink notation is used [15]. The vacancies support the ionic conductivity which is independent of the oxygen partial pressure p_{O_2} and thermally activated at temperatures above 600°C [3, 16]. Increasing yttria concentrations lower the ionic conductivity due to defect interactions. As a consequence, the ionic conductivity decreases above about 9 mol% Y_2O_3 [17]. Although materials with higher ionic conductivity are available, yttrium-stabilized zirconia (YSZ) is commonly used due to its superior suppression of electronic conductivity, high mechanical, and chemical stability as well as its comparably low manufacturing cost [18]. The impact of interfaces in these electrochemical sensors is discussed, e.g., in [19].

The melting point of zirconia is 1,855°C. Therefore, the electrolyte tolerates very high temperatures even if the operation cannot be guaranteed temporarily. Without the application of an external current, i.e., in case of sensor applications, the reduction of the electrolyte is a minor concern since the equilibrium p_{O_2} for the decomposition $ZrO_2 \leftrightarrow Zr + O_2$ is about 10^{-34} bar at 1,000°C [20].

2.2 Operation Principle

Potentiometric sensors consist of a high-temperature stable electrolyte, porous electrodes, and a reference gas compartment as seen in Fig. 2a. Typical dimensions of the sensor head are in the order of a few millimeters.

An additional heater might be required to ensure sufficiently high ionic conductivity of the electrolyte. YSZ is, for example, operated at temperatures above about 500°C. For oxygen sensors, a platinum electrode is usually applied due to its ability to act as a catalyst for oxygen reduction.

The transport of oxygen involves several steps. First, it is adsorbed and dissociated into atomic oxygen:

$$1/2O_2(\mathrm{ads}) \leftrightarrow O(\mathrm{ads}) \tag{2}$$

Oxygen diffused to the triple-phase boundary (TPB) between electrode, YSZ, and the gas of interest is reduced by an electron transfer from the electrode to oxygen. Subsequently, the oxygen ions are incorporated into the lattice as indicated in Fig. 2b:

$$\mathrm{O(ads)} + V_{\mathrm{O}}^{\bullet\bullet} + 2\mathrm{e}' \leftrightarrow \mathrm{O}_{\mathrm{O}}^{\times} \tag{3}$$

Highly porous electrodes ensure appropriate conditions which include short diffusion paths and large effective TPB lengths.

A gradient of the oxygen ion concentration inside the electrolyte as visualized in Fig. 2c forces the diffusion of oxygen ions to the oxygen poor side producing an electromotive potential which is proportional to the logarithm of the oxygen ion concentration $[\mathrm{O}^{2-}]$ ratio at the sample and reference gas side:

$$\Delta U_N = \frac{RT}{2F}\mathrm{In}\left(\frac{[\mathrm{O}^{2-}]^{\mathrm{ref}}}{[\mathrm{O}^{2-}]^{\mathrm{sam}}}\right) \tag{4}$$

Considering the equilibrium according to Eq. (2), the well known Nernst potential results as a function of the p_{O_2}'s in the sample and reference gas:

$$\Delta U_N = \frac{RT}{4F}\mathrm{In}\left(\frac{p_{\mathrm{O}_2}^{\mathrm{ref}}}{p_{\mathrm{O}_2}^{\mathrm{sam}}}\right) \tag{5}$$

The potential must be measured by a high-impedance voltmeter to ensure virtually open circuit conditions. Provided that the reference oxygen partial pressure $p_{\mathrm{O}_2}^{\mathrm{ref}}$ on one side of the cell and the temperature T are known, the oxygen partial pressure of interest $p_{\mathrm{O}_2}^{\mathrm{sam}}$ can be calculated. Commonly, ambient air is used as reference gas since it exhibits a constant oxygen concentration. Further, the temperature can be controlled precisely. Above that, only physical constants determine the potential. Therefore, the method is, in principle, free of calibration.

Further, it must be noted that p_{O_2} changes from, e.g., 10^{-20} to 10^{-19} bar and from 10^{-1} to 1 bar result in the same voltage change. Consequently, the inherent physical principle of the sensor is well suited to monitor moderate and very low p_{O_2}'s. Besides the Nernst potential, the temperature influences the response time of the sensor due to its impact on ion mobility. In order to achieve a stable signal and a quick response, most solid electrolyte-based sensors are actively heated. The response of the sensor is in the order of only 10–100 ms since a bulk effect is used. The lower value can be achieved at 900°C for sensor setups without protective housings.

2.3 *Application Limits and Measurement Errors*

Under extreme conditions, e.g., at very high operating temperatures or very low p_{O_2}'s, measurement errors might be caused by [21, 22].

2.3.1 Partial Electronic Conduction of the Electrolyte

Enhanced n- or p-type electronic conductivity at very high temperatures and extreme p_{O_2}'s cause an ohmic drop. In other words, electrons or holes contribute significantly to the total conductivity and lower the Nernst voltage [23]. At low p_{O_2}'s, n-type conduction dominates [24] due to the formation of free electrons:

$$O_O \leftrightarrow \frac{1}{2}O_2(\text{gas}) + V_O^{\bullet\bullet} + 2e' \tag{6}$$

Using the law of mass action $p_{O_2} \sim [V_o^{\bullet\bullet}]^{-2} n^{-4}$ and the neutrality condition $[V_o^{\bullet\bullet}] \sim n$, the electron concentration n is found to be:

$$n \sim p_{O_2}^{-1/6} \tag{7}$$

A similar calculation can be done for high p_{O_2}'s which leads to the formation of holes $h^{\bullet}$. They are compensated by zirconium interstitials:

$$O_2(\text{gas}) + Zr_{Zr} \leftrightarrow V_{Zr}^{''''} + 4h^{\bullet} + ZrO_2 \tag{8}$$

For the hole concentration p follows with $p_{O_2} \sim [V'''']p^4$ and $[V''''] \sim p$:

$$p \sim p_{o_2}^{1/5} \tag{9}$$

Using, e.g., the data from [16, 23, 25], the conductivity of the charge carriers can be calculated as function of p_{O_2} and temperature. The resulting Kröger–Vink diagram is shown in Fig. 3. It becomes clearly obvious that the p_{O_2}-independent ionic conductivity σ_o dominates in a wide p_{O_2} range. Taking an operation temperature of 1,100°C as example, the ionic conductivity equals the n-type electronic conductivity σ_e at about 10^{-27} bar. If a measurement error of 1%, i.e., an electronic contribution of 1%, is tolerable, the minimum p_{O_2} is about 10^{-15} bar. The p-type electronic conductivity σ_h impacts the total conductivity σ_{tot} above about 10 bar which is of minor practical relevance. At 700°C, the p_{O_2}-independent range is significantly larger. As a consequence, the sensor should be operated at sufficiently low temperatures to exclude electronic contributions. Temperatures below about 500°C result in instabilities due to the low ionic conductivity and a large response time. Therefore, the range from 600°C to 800°C is regarded as optimum [21]. If higher

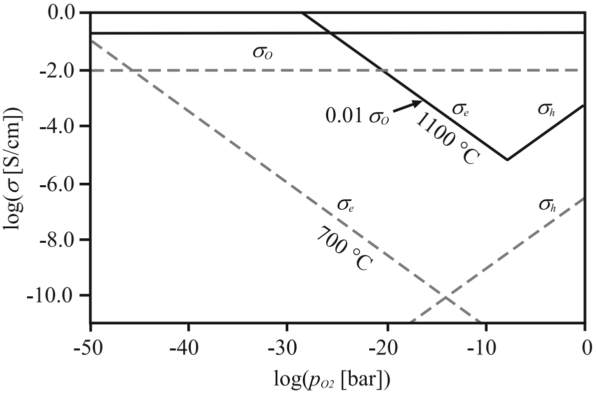

Fig. 3 Electron, hole, and ion conductivity of YSZ as a function of oxygen partial pressure and temperature is calculated using data from [16, 23, 25]

operating temperatures are required, corrections can be made provided that the temperature and p_{O_2} dependence of the electronic contributions are known:

$$\Delta U = \frac{\sigma_{\text{tot}} - \sigma_{\text{e}}}{\sigma_{\text{tot}}} \Delta U_N \tag{10}$$

The latter properties have to be determined once for the actual electrolyte material. This experimental effort prior to the application of the sensors is justified for special applications.

2.3.2 Alteration of the Sample Gas Composition

The ionic current through the electrolyte and the corresponding oxygen injection into the sample gas alters its composition. The effect increases with temperature and depends significantly on the absolute amount of oxygen in the sample gas. Under unfavorable conditions such as slowly flowing gases in thin tubes, the relative amount of inserted oxygen is high. The effect can generally be neglected for buffered gases such as H_2/H_2O mixtures, large volumes, or high p_{O_2}'s. The same applies for operation temperatures below about 700°C where the ionic current is extremely small.

2.3.3 Polarization of the Electrodes by the Ionic Current

The oxygen transport through the electrolyte might polarize the electrode [26]. The strength of this effect depends on the type of sample gas, too. At the same p_{O_2}, the effect of an Ar/O_2 mixture is much higher than of buffer gas mixtures like CO/CO_2 [27]. If required, the problem can be canceled largely by application of zirconia tip electrodes at the sample gas side.

Further error sources include:

2.3.4 Temperature Fluctuations at the Electrodes

The Nernst equation can be applied provided that the temperature is known and identical at both electrodes. However, temperature fluctuations falsify the output voltage. A temperature gradient between the sample and reference gas electrode of already 1 K results in a voltage difference of 0.3 mV [28]. The value corresponds to an error of $\Delta p_{O_2}/p_{O_2} = 1.3\%$ at 800°C. At 700°C, the effect could cause an additional potential about 0.5 mV for $\Delta T = 1\,\mathrm{K}$. The related measurement error of several percent depends on the p_{O_2} [27, 29]. In particular, environments with large temperature gradients may cause a temperature difference much larger than 1 K and, therefore, significant errors. Accurate temperature measurements are required to minimize this error. In order to establish a reliable thermal contact, it is recommended to connect the thermocouple directly with one electrode of the electrochemical cell [21].

2.3.5 Insufficient Supply of the Reference Gas

The maintenance of a well-defined reference p_{O_2} requires a gas supply of known composition and total pressure. Only in damp environments, the oxygen concentration might be altered in the range of several percent and must be considered for the given application [27]. Provided that the composition is known by, e.g., the use of air, the measurement of the total pressure has to be only performed. Further, a reference gas circulation might be required.

2.3.6 Unwanted Catalytic Reactions at the Electrodes

Potentiometric oxygen sensors offer low cross-sensitivities to other gases due to the exclusive transport of oxygen ions. Deviations from this behavior are caused by electrode reactions. Gases like CO or hydrocarbons react potentially at the catalytically active platinum electrodes and influence the equilibrium concentration of oxygen in the vicinity of the triple-phase boundary [30]. Further, contaminations of the sensor surface should be avoided since they may locally affect the Nernst potential due to unpredictable catalytic reactions. In many applications those low cross-sensitivities are seen as an advantage. In contrast, the high selectivity prevents a readily application of oxygen-conducting electrolytes to other gas species. The most obvious approach, i.e., the application of ion conductors for other ions than oxygen, is very limited since there are only a few electrolytes offering low electronic conductivity.

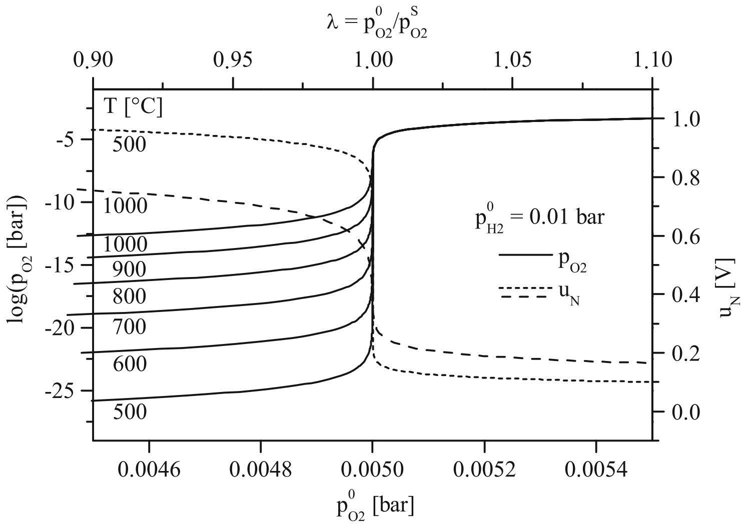

Fig. 4 Calculated Nernst voltage and oxygen partial pressure of a potentiometric oxygen sensor (see text)

2.4 *Application Examples*

In this section two examples, i.e., a conventional λ-probe and the precise p_{O_2} control in a wide range, are presented.

2.4.1 λ-Probe

The most prominent electrochemical solid-state sensor is by far the YSZ-based λ-probe. Introduced in 1976 by Bosch GmbH, it is now applied in almost all modern gasoline cars. In order to minimize the output of unburned hydrocarbons, carbon monoxide, and nitrogen oxides, most cars are equipped with a three-way catalyst. The catalyst enhances the oxidation of carbon monoxide and hydrocarbons while nitrogen oxides are simultaneously reduced to N_2. To enable a high conversion rate with minimal output of pollutants, stoichiometric combustion is anticipated. In other words, the air to fuel ratio of the exhaust λ has to be close to the equilibrium between fuel and oxygen, the so-called lambda point at $\lambda = 1$. Already small deviations to the lean side ($\lambda > 1$) result in a steep increase in NO_x emissions because of an insufficient amount of CO in the exhaust to ensure a reduction of NO_x to N_2.

Figure 4 shows the temperature dependencies of the p_{O_2} and the Nernst potential for the equilibrium $H_2 + 1/2O_2 \leftrightarrow H_2O$. The calculation is done for gas mixtures containing a variable amount of oxygen $p^0_{O_2}$ and a constant amount of hydrogen $p^0_{H_2}$ using thermodynamic data from [31]. The λ-value results from the quotient of the available and the stoichiometric amount of oxygen, i.e., from $\lambda = p^{0}_{O_2}/p^{S}_{O_2}$ with $p^{5}_{O_2} = p^{O}_{H_2}/2$. The reference pressure is $p^{\text{ref}}_{O_2} = 0.2$ bar. Details of a similar calculation are given in [32]. At $\lambda = 1$, a change in p_{O_2} by several orders of magnitude is observed leading to a significant voltage jump. Despite the impact of the temperature on the behavior at fuel-rich combustion ($\lambda < 1$), closed-loop controls to maintain $\lambda = 1$ operate robust with respect to temperature changes and other influences.

The first generation of λ-probes used a thimble-shaped design and were only passively heated by the exhaust gas, resulting in long warm-up periods. Advanced devices include active heating elements and improved overall-stability and reliability of the sensor systems. But even heating elements result in warm-up time of several minutes leading to strong emissions during the start phase of the engine. To circumvent this problem, planar λ-probes have been developed. The design is based on laminated planar ceramic sheets, thick-film electrodes, and integrated heating elements (see Fig. 2a) which reduces the heat capacity and, thereby, the warm-up time of the sensor. In addition, the power consumption and weight of the sensor are significantly lower in comparison to conventional thimble-shaped lambda probes. Finally, the related manufacturing processes enable cost-effective and scalable production of large volumes.

Due to the shallow slope for $\lambda > 1$, it is difficult to determine the exact air to fuel ratio during lean combustion. The latter is advantageous due to its fuel efficiency and requires more elaborated concepts as described in Sect. 3.

2.4.2 Wide-Range Oxygen Partial Pressure Control

Further applications include the p_{O_2} control for scientific experiments such as the determination of the surface tension and the viscosity of molten samples using electromagnetic levitation [33]. The approach is based on the examination of the decay of mechanical oscillations of levitated spheres. Therefore, the samples are extremely sensitive to the state of the surface and, in particular, to the formation of oxide scales. As a consequence, the p_{O_2} must not only be measured but also controlled. The range of interest depends on the material system and spans from about 10^{-6} bar for copper to, e.g., 10^{-18} bar for silicon.

The p_{O_2} control is based on a potentiometric sensor and a YSZ-based oxygen ion pump. The latter adjusts the amount of oxygen inserted in or removed from the sample volume. Elaborated control algorithms enable precise measurement and control of the p_{O_2} at elevated temperatures within 0.2 to 10^{-20} bar. The system achieves an uncertainty of $\Delta \log(p_{O_2}[\text{bar}]) < 0.02$ and response times between 5 and 90 s over the entire p_{O_2} range shown in Fig. 5 [32].

Finally, it must be underlined that the p_{O_2} in buffer gases depends strongly on temperature. As a consequence, the p_{O_2} must be corrected if the temperature of the sample differs from the operating temperature of the oxygen sensor. Even for nominally pure inert gases like argon, residual hydrocarbons cause flawed readouts

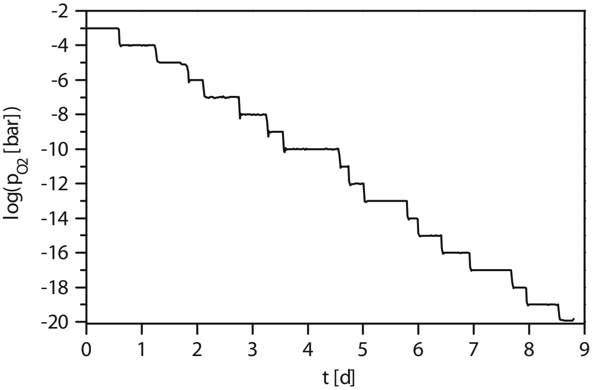

Fig. 5 Stepwise adjustment of the p_{O_2} between 10^{-3} bar and 10^{-20} bar at 600°C [32]

below about 10^{-7} bar. The exact value depends on the amount of reactive impurities and the temperature as described in detail in [32].

3 Amperometric Gas Sensors

Potentiometric sensors are well suited to control processes in the vicinity of $\lambda = 1$ where the Nernst potential changes strongly. To reduce the fuel consumption of cars, new concepts such as lean-burn engines ($\lambda > 1$) with gasoline direct injection are introduced in the market [2, 34, 35]. In these environments, the weak p_{O_2} dependence of the sensor signal and high requirements on the temperature control prevent a precise measurement of the oxygen content in the exhaust gas using this type of sensor. To solve this problem, limiting-current-type sensors with a strong and nearly linear concentration dependence were developed at the beginning of the 1980s.

3.1 Operation Principle

Limiting-current-type or amperometric sensors convert an oxygen flow through a diffusion barrier into an electrical current. They consist of a diffusion barrier and a YSZ-based oxygen ion pump that are arranged in series as shown in Fig. 6. The barrier is a porous medium whose pore structure determines the gas transport. The design of the oxygen ion pump corresponds, in principle, to a potentiometric cell. Instead of measuring the potential, an oxygen flow from the cathode to the anode is forced by application of a voltage [36].

The oxygen flow density through the diffusion barrier follows from the effective diffusion coefficient D inside the barrier, the length of the barrier L, and the oxygen concentration difference over the barrier $\mathrm{co}_2 = \Delta p_{O_2}/kT$:

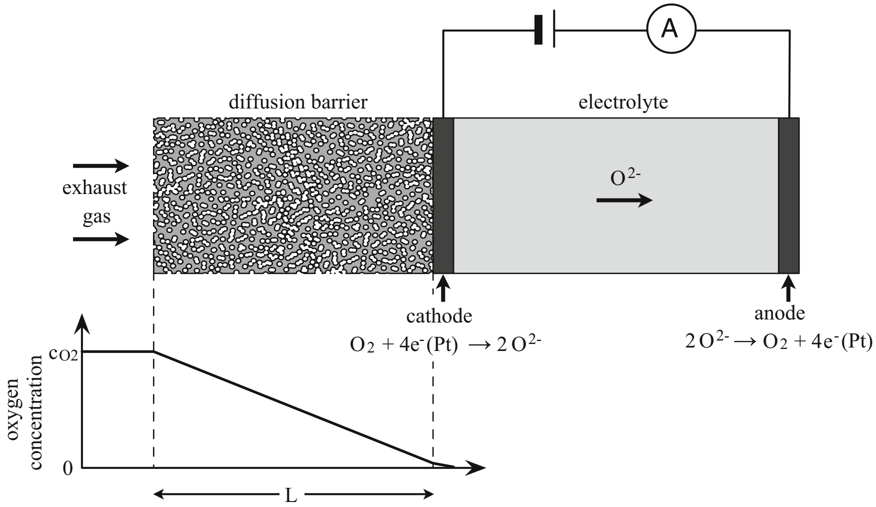

Fig. 6 Scheme of an amperometric oxygen sensor

$$j_{O_2} = -\frac{D}{kT}\frac{\Delta p_{O_2}}{L} \tag{11}$$

If the diffusion barrier is designed properly, the oxygen pump causes a very low p_{O_2} in the vicinity of the cathode. For relatively high p_{O_2}'s in the sample gas as occurring in lean-burning engines, the p_{O_2} gradient over the diffusion barrier and, thereby, the amount of oxygen diffusing through the diffusion barrier depend solely on the p_{O_2} in the sample gas:

$$\Delta p_{O_2} = p_{O_2}^{\text{sam}} - p_{O_2}^{\text{cathode}} \approx p_{O_2}^{\text{sam}} \tag{12}$$

Finally, the electrode reactions at the cathode and anode convert the oxygen flow in an electrical current:

$$I_L = 4\text{eA}j_{O_2} = -\frac{4\text{e}D}{kT}\frac{A}{L}p_{o_2}^{\text{sam}} \tag{13}$$

Thereby, A denotes the cross-sectional area of the diffusion barrier. Consequently, the limitation of the oxygen flow by the diffusion barrier results in an electrical current I_L which is a measure of the p_{O_2} in the sample gas. However appropriate operational conditions must be ensured. They become obvious while discussing the operation limits of such sensors.

The current can only be measured properly, if the rate of the reaction at the electrodes and the current flow are determined by diffusion and all oxygen diffusing to the electrode reacts with the electrode [36]. Further, convection must be suppressed.

Table 2 Pressure and temperature dependence of the current for bulk and Knudsen diffusion

	Bulk diffusion	Knudsen diffusion
	I_{lim}	I_{lim}
Pressure dependence	const	p
Temperature dependence	$T^{0.75}$	$T^{-0.5}$

Thus, the operation range of liming current sensors must be adjusted to the given application by the design of the diffusion barrier. In general, two types of diffusion account to the transport of the gas through the barrier, bulk diffusion D_{B}, and Knudsen diffusion D_{K}. The latter applies if the dimension of the transport path is smaller or equal to the mean free path of the gas particles. Consequently, the contribution of both types to the total diffusion depends on the porosity of the barrier. In barriers with very fine pores, Knudsen diffusion dominates the behavior, whereas in barriers with larger pores or only one larger diffusion channel, bulk diffusion governs the diffusion process. Both types exhibit different pressure and temperature dependencies [12]:

$$D_{\mathrm{B}} = D_0 \frac{T^{1.75}}{p} \text{ and } D_{\mathrm{K}} = \frac{1}{3}\sqrt{\frac{8RT}{\pi M}}d \tag{14}$$

Here, D_0, p, R, M, and d denote a gas-type-dependent constant, the total pressure, the universal gas constant, the mass of the molecule of interest, and the pore diameter, respectively. The pressure and temperature dependencies of the current resulting from Eq. (13) are listed in Table 2. It becomes clearly obvious that a careful design and long-term stability of the pore size and distribution governs the applicability and the reliability of amperometric sensors.

3.2 Application Limits and Measurement Errors

3.2.1 Pump Voltage

The characteristic curve of an amperometric sensor which is operated at $\lambda > 1$ exhibits three distinct ranges as shown in Fig. 7a. Low pump voltages cause small currents which are not limited by the diffusion barrier. Here, the resistance of the electrolyte governs the current. At medium voltages the diffusion barrier limits the current which results in a plateau. High voltages cause low $p_{\mathrm{O_2}}$'s behind the diffusion barrier. Thus, gases such as H_2O and CO_2 might be decomposed at the cathode. Thereby, additional oxygen is provided which falsifies the signal [37]. Very high pump voltages in concert with low $p_{\mathrm{O_2}}$'s in the sample gas might even lead to a decomposition of the electrolyte. At 800°C the reduction of H_2O and ZrO_2 occurs at 10^{-17} bar and 10^{-42} bar, respectively [20].

Consequently, the pump must be operated at medium voltages from about 0.4–0.8 V (gray bar in Fig. 7a) which is above the limiting-current threshold in the $p_{\mathrm{O_2}}$ range of interest and below the decomposition voltage. Usually the pump

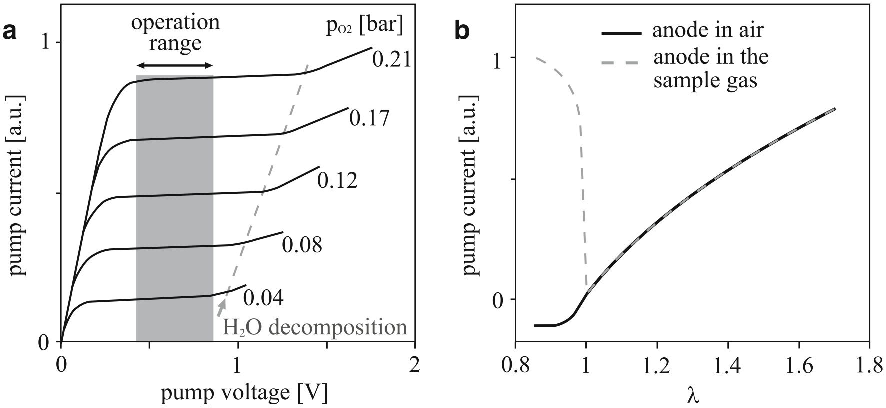

Fig. 7 U/I characteristics of an amperometric oxygen sensor at different oxygen concentrations (**a**) and pump current of such a sensor as a function of the air to fuel ratio λ (**b**) [2, 35, 141, 142]

voltage U_P is adjusted between 0.5 and 0.6 V [2]. The nearly linear dependence of the measured current from the oxygen content as shown in Fig. 7b for $\lambda > 1$ makes this type of sensor suitable for lean combustion control.

3.2.2 Oxygen Partial Pressure Range

As long as the sensor is operated at relatively high p_{O_2}'s, i.e., at $\lambda > 1$, it is of less importance if the gas on the anode is air or the sample gas. For $\lambda < 1$ two different cases must be regarded.

Air at the Anode

The p_{O_2} difference between cathode and anode causes an internal Nernst potential of about 0.8 V (see Fig. 4). The pump voltage $U_P \approx 0.5$–0.8 V and, consequently, the current reverse their signs. The solid curve in Fig. 7b reflects the behavior. Already below $\lambda = 0.95$, the curve becomes flat which causes a lower detection limit in the order of ppm [38].

Sample Gas at the Anode

Here, the pump direction remains unchanged which results in ambiguous signals. The dashed curve in Fig. 7b shows that two λ values correspond to a given current. Even if the engine management enables to decide whether λ is smaller or larger than 1, the measurement would be inaccurate due to the shallow slope for $\lambda < 0.95$.

For sensors solely operating in lean atmospheres, the anode can be exposed to the sample gas which simplifies the sensor setup. If values lower than $\lambda = 1$ have to be detected, the anode has to be kept at high p_{O_2}'s using, e.g., air. However, more

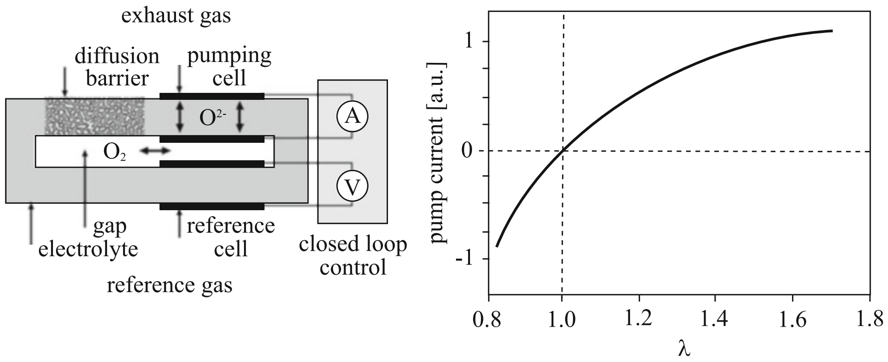

Fig. 8 Schematic cross section of a two-cell limiting-current oxygen sensor (**a**) and its characteristics (**b**) [2, 35, 40]

elaborate approaches are chosen in practice as explained while presenting the application examples.

In summary, amperometric sensors are developed for high p_{O_2}'s showing a minimum accessible p_{O_2} in the order of ppm. While measuring high p_{O_2}'s, their advantages include selectivity to oxygen, no need for a reference gas, and very good resolution. In the past, their major disadvantage had been a limited long-term stability due to aging of the diffusion barrier. Nowadays, technological improvements and reproducible production processes ensure stable diffusion barriers which result in a lifetime of 15 years or in a mileage of 250,000 km [39]. In addition, such devices require calibration and alter the oxygen concentration in the gas of interest.

3.3 Application Examples

For many modern cars, wide-range oxygen sensors operating under lean as well as rich burning conditions are demanded. The related application example is a two-cell design incorporating a pumping and a sensing cell which extends the detection range of amperometric sensors to low p_{O_2}'s. The second example chosen here is an amperometric NO_x sensor.

3.3.1 Wide-Range Oxygen Sensor

The general sensor setup is shown in Fig. 8. It consists of a reference and a pumping cell which are separated by a gap of up to 50 µm [2]. A porous diffusion barrier limits the transport of the sample gas into the gap.

The reference cell is operated as a conventional potentiometric sensor and measures the λ value inside the gap using air as reference. A closed-loop control adjusts the current of the pumping cell so as to maintain a constant value of $\lambda = 1$ in the gap. At high p_{O_2}'s in the sample gas, oxygen diffuses into the gap and must be pumped out. Correspondingly, a reverse current must be applied in case of low p_{O_2}'s. The pumping current is measured and used to evaluate the λ value in the sample gas.

As visualized in Fig. 8b, although not linear, the pumping current increases with the lambda value from $\lambda = 0.8$ to 1.7. Quick response times of this type of sensor enable to use them for single cylinder balancing [2, 40]. Using a pumped reference, it is even possible to omit the necessity of an external reference gas [35]. Disadvantages of the two-cell design are increased manufacturing costs due to additional layers and need for more sophisticated data acquisition units, which is today mostly realized by an application-specific integrated circuit (ASIC).

3.3.2 Amperometric NO_x Sensor

Although the ion transport in YSZ is limited to oxygen, the sensor approach can also be applied to measure other gases like NO_x. Its detection is demanded for cars equipped with lean-burn engines [40]. Due to the operation of the engines at $\lambda > 1$, there is no effective conversion of NO_x by the three-way catalyst. To circumvent this problem, these cars are equipped with a trap to store NO_x during lean burning [41]. In order to regenerate the trap when saturated, the engine has to be operated under rich conditions periodically. Since the interval between two regenerations depends on numerous parameters including the degradation state of the storage, a NO_x sensor is required at the outlet of the NO_x trap and used to initiate the regeneration process as soon as the NO_x content in the exhaust gas increases.

The amperometric NO_x sensor is based on the catalytic reduction of, e.g., NO at the measurement electrode:

$$2NO \rightarrow N_2 + O_2 \tag{15}$$

Subsequently, the formed oxygen is removed by the pump. The resulting current is an indicator for the amount of NO in the exhaust gas. Since the latter might contain a large amount of free oxygen, which would contribute to the pump current, this oxygen has to be removed in advance by an auxiliary pump. Further, the use of highly selective catalytic electrode materials is crucial for a proper operation of the sensor. In order to detect NO in the range of several ten ppm, the O_2/NO ratio has to be reduced from, e.g., 10^3 in the exhaust gas to 10^{-3} at the measurement electrode. A setup of two subsequently arranged cells as shown in Fig. 9 fulfills this requirement. In the auxiliary cell, the free oxygen is removed using an oxygen-selective electrode, which often consists of a platinum/gold alloy [42]. In the second cell, the remaining NO dissociates at the measurement electrode, which may consist of rhodium [43]. The current in the auxiliary pumping cell reflects, of course, the oxygen content in the exhaust gas. The voltages at the electrodes have to be chosen in such a way that NO_x is not reduced at the auxiliary electrode, but sufficient amounts of oxygen are removed. Since the reduction of NO starts at 0.5 V, the auxiliary and the measurement electrodes are commonly operated at 0.3 and 0.55 V, respectively.

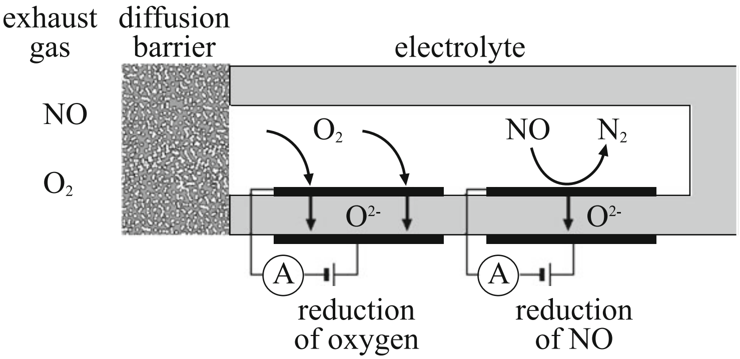

Fig. 9 Schematic cross section of an amperometric NO sensor [35, 40, 44]

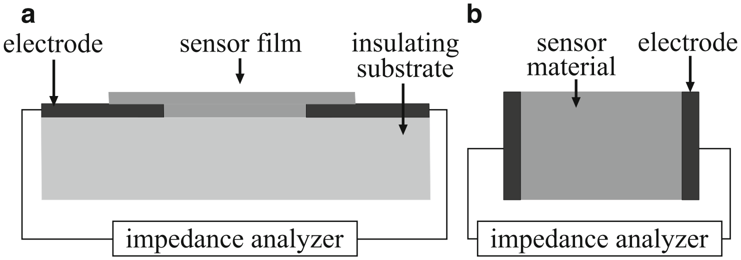

Fig. 10 Thin-film (**a**) and bulk-resistive sensor (**b**)

The principle may also be applied to measure other gases, if materials with selective catalytic activity for the target gas are available [44].

4 Resistive Sensors

The de- or adsorption of gas species changes the electrical resistivity of metal oxides. The related changes in charge carrier density affect predominantly the sensor signal, i.e., the resistivity. Metal oxides are commonly used as thin-film or bulk resistor as shown in Fig. 10. The dimensions of the sensor elements can be reduced below one millimeter.

4.1 Operation Principle

The response of resistive sensors is determined by several charge transport mechanisms taking place at different positions of the device as illustrated in Fig. 11. Besides surface and bulk contributions, the grain boundaries and, potentially, the electrical contacts determine the total resistivity. In general, the environmental

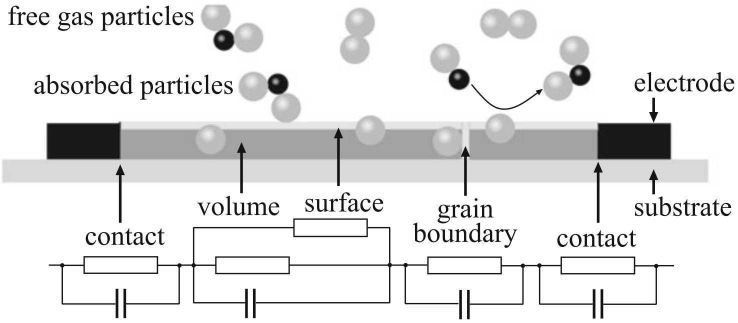

Fig. 11 Scheme of the contributions to the total resistivity and corresponding equivalent circuit

conditions impact those contributions in a different manner. Data evaluation is often done using the elements of the corresponding equivalent circuit. Parallel arrangements of resistor and capacitance reflect the resistance and the permittivity or space charge of each contribution, respectively. Surface capacitances are often very low and can be ignored. In case of diffusion processes other elements such as Warburg impedances [45] might be required to describe the behavior properly.

Two basic mechanisms apply which are described using oxygen sensors for exemplification.

4.1.1 Modification of the Sensor Material Stoichiometry by Partial Reduction

Low p_{O_2}'s result in the formation of oxygen vacancies which is, for example, accompanied by the generation of mobile electrons in order to maintain the charge neutrality. Due to their high mobility, electrons increase the conductivity in general much stronger than mobile oxygen ions. The reduction according to Eq. (6) is such an example. However, materials tending to be reduced at higher p_{O_2}'s than zirconia should be applied. The relationship between conductivity and p_{O_2} is in general given by:

$$\sigma = \text{const}\; p_{O_2}^{\kappa} \tag{16}$$

Thereby, the exponent κ depends on the actual compensation mechanism. Typical values are $-1/4$, $-1/5$, etc. In case of high p_{O_2}'s defect, electrons can be formed which results in positive exponents.

Common sensor materials include semiconductors such as titania [46, 47], gallium oxide [48–51], tin oxide [1, 6, 52–55], and mixed ionic-electronic conductors such as ceria [56], praseodymium-doped ceria [57], and $SrTi_{1-x}Fe_xO_{3-\delta}$ solid solutions [58–62]. In any case, the range of operation and the sensitivity may be influenced by doping and the size of the crystallites [63, 64]. Specific examples are given below.

4.1.2 Formation of Depletion Layers

The adsorption of gas species may result in the depletion or accumulation of charge carriers in the vicinity of the surface or of the grain boundaries. The charge causes a localized bending of conduction and valence band in semiconducting materials and, therefore, strong changes of the conductivity. Since the thickness of such space charge layers is in the order of a few nanometers, appropriate geometrical arrangements such as thin films or interconnected grains are demanded to make the effect usable. The conductivity in the grain boundaries can be several orders of magnitude higher than in the bulk. Therefore, nanocrystalline materials are one preferred option for such sensors.

4.2 Application Limits and Measurement Errors

The limitations and the accuracy of resistive sensors result from:

4.2.1 Reduction and Evaporation of the Active Sensor Material

The reduction of metal oxides can be a serious issue in harsh environments. Depending on the p_{O_2} of interest, sensor materials such as TiO_2, CeO_2, SnO_2, and $SrTiO_3$ can be applied. As TiO_2 is a quite stable material, it can be applied at fairly low p_{O_2}'s. The definite limits given by the total reduction can be found in Richardson-Ellingham diagrams as function of temperature and p_{O_2} [20]. Further, the formation of volatile (sub-)oxides might limit the lifetime of sensors. For example, gallium tends in general to evaporate [65].

4.2.2 Temperature Dependence of the Resistivity

The temperature dependence of the resistivity is commonly governed by a thermally activated process and, therefore, strong. In extreme cases, the influence of the temperature on the measured resistance is more pronounced than the impact of the gas concentration of interest. Consequently, the control or at least the accurate knowledge of the sensor temperature is required. As for potentiometric sensors, the temperature can be determined by thermocouples and used in concert with the resistivity to determine the gas composition. Material systems showing a temperature-independent resistivity are very rare.

4.2.3 Cross-Sensitivities to Other Species

Cross-sensitivities are usually observed. For example, oxide-based sensor materials may be reduced by any redox process caused by gases such as H_2, CO, or NO_x. Consequently, the measurement provides information about all those gas species involved. In order to minimize cross-sensitivities and to cancel out deviations arising from sensor preparation, these transducers have to be calibrated. In many cases, sensor arrays with different sensor materials are applied in order to achieve the required selectivity. Alternatively, the cross-sensitivity can be reduced by temperature cycling [66, 67], application of macroporous layers [68], and catalytic filtering [69].

4.2.4 Space Charge Effects at the Electrode–Oxide Interface

Those space charges may alter the overall conductivity when acquired by simple data acquisition approaches like dc-conductivity measurements. In general, ac-conductivity measurements solve the problem at the expense of more elaborated data acquisition units. Accurate data evaluation may require the knowledge of the impedance in a wide frequency range.

4.2.5 Aging of the Sensor Material

The sensor material and, in particular, its surface undergoes aging effects under harsh environments. Consequently, accurate measurements require frequent recalibration and, therefore, the recurring presence of atmospheres with well-known compositions or the application of reference sensors.

4.2.6 Contamination of the Sensor Surface

Further, the contamination of the sensor surface by foreign materials may alter the response. Even partial covering of the active sensor area impacts the overall resistivity and falsifies, e.g., the local p_{O_2} by catalytic reactions.

The thermal shock resistance of thin-film sensors is in general sufficient. Appropriate ceramic substrates like alumina, magnesia, or mullite are available, too. Further, the stability of the electrodes might limit the sensor operation. Platinum electrodes form, e.g., volatile suboxides which impacts the applicability of very thin films significantly [70].

Surface effects are preferred if a quick response is required. Consequently, thin and/or porous films are commonly applied in order to enhance surface effects. Time constants in the sub-millisecond range are feasible. A quick resistivity response is, e.g., found for porous fine-grained $SrTiO_3$ films [71]. If the impedance spectroscopy has to be applied for data acquisition, the sampling rate is drastically reduced and, at best circumstances, only a few samples per second can be achieved.

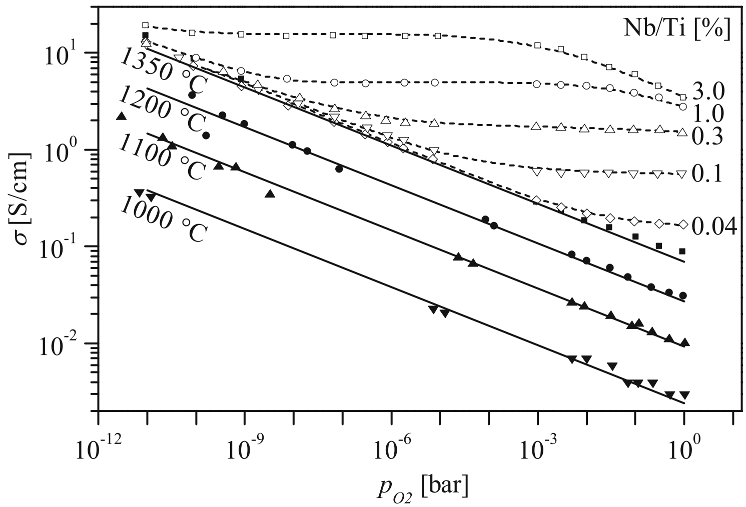

Fig. 12 Conductivity of TiO_2 as function of p_{O_2}. Data of nominally pure TiO_2 at different temperatures (*solid lines*) and of Nb-doped TiO_2 at 1,350°C (*dashed lines*) taken from [72, 143]

The absolute change of the resistivity for a given change of, e.g., $\Delta \log(p_{O_2}[\text{bar}]) = 1$ depends on the p_{O_2} itself. Therefore, the property cannot be measured with the same accuracy in the entire p_{O_2} range.

4.3 Application Examples

The development of resistive sensors aims at sufficiently short response times to monitor, e.g., the exhaust gas of single cylinders in stroke engines. Therefore, these sensor concepts are based commonly on thin films. Further technological demands include stable and temperature-independent signals as well as significant sensor responses in the p_{O_2} range from about 10^{-5} bar to 1 bar as required for lean combustion engines. For exemplification two oxygen sensors, i.e., a resistive TiO_2 sensor and a temperature-compensated $SrTiO_3$–$SrFeO_3$ solid solution-based sensor, are chosen.

4.3.1 TiO_2-Based Oxygen Sensor

Nominally undoped TiO_2 exhibits a nearly $p_{O_2}^{-1/5}$ dependence of the conductivity as visualized by the straight solid lines in Fig. 12. The property is strongly temperature-dependent. However, the lines for different temperatures are parallel which indicates a p_{O_2}-independent activation energy of the conductivity in the p_{O_2} range shown here. At high p_{O_2}'s, a slight deviation from the $p_{O_2}^{-1/5}$ dependence is found. For the nominally undoped material, the observation becomes obvious if the plot is enlarged in the p_{O_2} range from 10^{-2} bar to 1 bar. The effect depends on the impurity concentration of the actual material. Slight intentional doping makes the effect even more clear since it results in stronger deviations from the $p_{\mathrm{O}_2}^{-1/5}$ dependence as visualized by the dashed line for 0.04% Nb on Ti sites at 1,350°C. Reliable sensor operation using nominally undoped $\mathrm{TiO_2}$ would require precise control of the impurity concentrations in large batches which increases the production costs. In contrast, intentional doping results in well-defined, i.e., impurity independent, conductivities as shown for higher Nb concentrations in Fig. 12. Further, the doping causes a change in slope. A dopant concentration of 3% Nb on Ti sites results in a $p_{\mathrm{O}_2}^{-1/4}$ dependence of the conductivity at p_{O_2}'s of technical interest above about 10^{-4} bar. Simultaneously, a plateau at intermediate p_{O_2}'s is formed. The conductivity and the extent of the plateau increase with increasing Nb concentration.

The underlying defect chemistry is described in detail, e.g., in [72, 73] and can be summarized as follows.

Nominally Undoped $\mathrm{TiO_2}$

With decreasing p_{O_2} oxygen leaves the lattice and fourfold charged titanium interstitials $\mathrm{Ti}_i^{\bullet\bullet\bullet\bullet}$ are formed. They are compensated by electrons according to:

$$\mathrm{Ti_{Ti}} + 2\mathrm{O_O} \leftrightarrow \mathrm{O_2(gas)} + \mathrm{Ti}_i^{\bullet\bullet\bullet\bullet} + 4\mathrm{e}' \tag{17}$$

For the electron concentration follows $n \sim p_{\mathrm{O}_2}^{-1/5}$ if the law of mass action $n \sim \left[\mathrm{Ti}_i''''\right]^{-1/4} p_{\mathrm{O}_2}^{-1/4}$ and the neutrality condition $\left[\mathrm{Ti}_i''''\right] \sim n$ are considered. Assuming a concentration-independent electron mobility, the experimentally determined relation between σ and p_{O_2} is found. Other mechanisms such as electronic compensation of oxygen vacancies according to Eq. (6) or the formation of threefold charged titanium interstitials $\left[\mathrm{Ti}_i''''\right]$ result in different relations, i.e., $\sigma \sim p_{\mathrm{O}_2}^{-1/6}$ and $\sigma \sim p_{\mathrm{O}_2}^{-1/4}$, respectively.

Nb-Doped $\mathrm{TiO_2}$

The doping process results in the incorporation of $\mathrm{Nb_2O_3}$ which can be compensated by titanium vacancies:

$$2\mathrm{Nb_2O_5} \rightarrow 4\mathrm{Nb}^{\bullet}_{\mathrm{Ti}} + 10\mathrm{O_O} + V''''_{\mathrm{Ti}} \tag{18}$$

The occurrence of a compensation mechanism via oxygen interstitials is unlikely since the oxygen sublattice is closely packed. Alternatively, $4\mathrm{Nb}^{\bullet}_{\mathrm{Ti}}$ is compensated electronically:

$$2\mathrm{Nb_2O_5} \rightarrow 4\mathrm{Nb}^{\bullet}_{\mathrm{Ti}} + 80\mathrm{O_O} + \mathrm{O_2(gas)} + 4\mathrm{e}' \tag{19}$$

Both mechanisms are correlated by a redox equilibrium which follows from the subtraction of Eqs. (19) and (18):

$$\mathrm{O_2(gas)} + 4\mathrm{e}' \leftrightarrow 2\mathrm{O_O} + V''''_{\mathrm{Ti}} \tag{20}$$

The equilibrium tends to the formation of V''''_{Ti} at high $p_{\mathrm{O_2}}$'s. In other words, ionic compensation according to Eq. (18) dominates in this case. The electron concentration follows from the mass action law related to Eq. (20):

$$n \sim [V''''_{\mathrm{Ti}}]^{1/4} p_{\mathrm{O_2}}^{-1/4} \tag{21}$$

Subsequently, the $p_{\mathrm{O_2}}$ dependence of the conductivity must be discussed in three ranges using the neutrality condition:

$$\left[\mathrm{Nb}^{\bullet}_{\mathrm{Ti}}\right] = n + 4\left[V''''_{\mathrm{Ti}}\right] \tag{22}$$

At high $p_{\mathrm{O_2}}$'s, the ionic compensation dominates and the neutrality condition simplifies to $\left[\mathrm{Nb}^{\bullet}_{\mathrm{Ti}}\right] = 4\left[V''''_{\mathrm{Ti}}\right]$. For a given dopant concentration $n \sim p_{\mathrm{O_2}}^{-1/4}$ follows from Eq. (21). Assuming again $p_{\mathrm{O_2}}$-independent electron mobility, the experimentally determined conductivity is described properly. At intermediate $p_{\mathrm{O_2}}$'s, electronic compensation dominates and the electron concentration is fixed by $\left[\mathrm{Nb}^{\bullet}_{\mathrm{Ti}}\right] = n$. Thus, a $p_{\mathrm{O_2}}$-independent conductivity is found which scales with the dopant concentration. At low $p_{\mathrm{O_2}}$'s, the reduction according to Eq. (17) results in $n \gg \left[\mathrm{Nb}^{\bullet}_{\mathrm{Ti}}\right]$ and the situation corresponds to that of the nominally undoped material with $n \sim P_{\mathrm{o_2}}^{-1/5}$.

4.3.2 Temperature-Compensated Oxygen Sensor

The second example chosen here is $\mathrm{SrTiO_3}$–$\mathrm{SrFeO_3}$ solid solutions (STF). They can be described by $\mathrm{SrTi}_{1\text{-}x}\mathrm{Fe}_x\mathrm{O}_{3\text{-}x/2\text{-}\delta}$ and exhibit a pseudo-perovskitic structure $\mathrm{ABO_3}$ in the entire composition range $0 \leq x \leq 1$ [61]. $\mathrm{SrTiO_3}$ shows a bigger band gap than $\mathrm{SrFeO_3}$ and, accordingly, a lower conductivity. The situation is visualized in Fig. 13. Further, the conductivity exhibits nearly the typical V-type shape formed by branches with $\kappa = -1/4$ and +1/4 (see Eq. (16)) for n- and p-type conduction at intermediate and high $p_{\mathrm{O_2}}$'s, respectively. The slope changes to $\kappa = -1/6$ at low $p_{\mathrm{O_2}}$'s. The same behavior is found for other perovskites such as $\mathrm{BaTiO_3}$ [74, 75].

The temperature dependence of the conductivity of STF appears to be unusual. While the conductivity of $\mathrm{SrTiO_3}$ increases with temperature in the experimentally accessible $p_{\mathrm{O_2}}$ range from about 10^{-20} bar to 1 bar, $\mathrm{SrFeO_3}$ shows a decreasing conductivity above about 10^{-8} bar. Even more interesting from the application

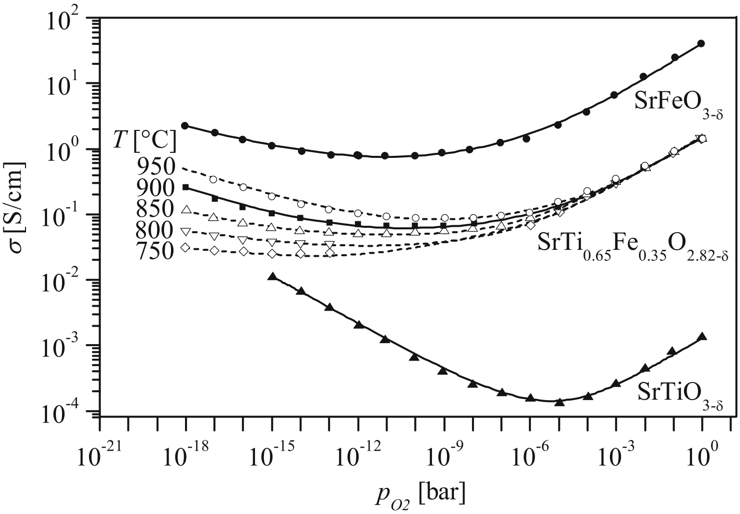

Fig. 13 Conductivity of STF as function of p_{O_2}. Data for different compositions at 900°C (*solid lines*) and temperature dependence for $SrTi_{0.65}Fe_{0.36}O_{2.82-\delta}$ (*dashed lines*) [58, 60, 144]

point of view is the temperature-independent conductivity of the solid solution $SrTi_{0.65}Fe_{0.35}O_{2.82-\delta}$ (STF35) at temperatures from about 750–950°C when operated at p_{O_2}'s above 10^{-5} bar [60, 76]. Figure 13 visualizes the fact for the optimized composition. It should be noted that p-type conduction dominates in this p_{O_2} range.

STF is an inherently oxygen-deficient system with partial occupancy of the oxygen sublattice to compensate Fe^{3+} on the B site which hosts commonly fourfold charged ions. Two Fe^{3+} correspond to one structural oxygen vacancy as considered in the constitutional formula given above [77]. Further, the end members of the system $SrTiO_3$ and $SrFeO_3$ are not suited to interpolate the conductivity for intermediate compositions. Anion Frenkel disorder with the formation of $V_O^{\bullet\bullet}$ and O_i'' at the structural oxygen vacancies is accepted to be the dominating defect mechanism [78, 79]. Considering the related neutrality condition $2\left[V_O^{\bullet\bullet}\right] + p = 2\left[O_i''\right] + n$ and the defect equilibria for the electron–hole generation $\mathrm{np} = \mathrm{const}$, the anion Frenkel disorder $V_O^{\bullet\bullet} O_i'' = \mathrm{const}$, and the reduction/oxidation $1/2O_2 + V_O^{\bullet\bullet} \leftrightarrow \mathrm{Oo} + 2h^{\bullet}$, the band-gap energy can be extracted as a function of the Fe concentration x in STF. Its value decreases with increasing x due to Fe^{4+}/Fe^{3+} redox states which form an additional band in the vicinity of the O 2p valence band edge [60, 62].

In order to understand the temperature independence of the p-type conductivity above 10^{-5} bar, the hole concentration p and mobility μ must be regarded and used to calculate the expression $d\sigma/dT$ which is proportional to $dp/dT + d\mu/dT$. The hole concentration depends on the band gap energy E_G and the enthalpy ΔH_R of the above-mentioned reduction/oxidation [60]:

$$p \sim \exp\left(-\frac{2E_{\mathrm{G}} - \Delta H_{\mathrm{R}}}{2kT}\right) \tag{23}$$

Since $2E_{\mathrm{G}} > \Delta H_{\mathrm{R}}$, a decreasing band gap energy weakens the positive temperature-dependence $dp/dT > 0$. In contrast, the hole mobility decreases with temperature, i.e., $d\mu/dT < 0$. Obviously, STF35 contains the appropriate amount of Fe to fulfill the condition $0 = dp/dT + d\mu/dT$ in the above-mentioned temperature and p_{O_2} range.

5 Resonant Sensors

Resonant piezoelectric gas sensors convert the change of mechanical or electrical properties of a gas-sensitive layer into a resonance frequency shift. Thereby, the sensor properties are mainly governed by the ability of the sensor film to absorb gas molecules selectively. At low temperatures, these gravimetric sensors are often applied as biosensors, e.g., for the selective detection of enzymes or antibodies using specially designed receptors. The approach allows the detection of mass changes which corresponds to the adsorption of submonolayers.

The application of metal oxide films enables high-temperature operation provided that the piezoelectric transducers and the electrodes are sufficiently stable. Piezoelectric crystals suited for room-temperature application have to be replaced by appropriate alternatives. Therefore, this section is focused on high-temperature piezoelectric crystals, the operation principles of resonant sensors, and application examples.

5.1 High-Temperature Piezoelectric Crystals

Resonant piezoelectric devices operated at lower temperatures are based commonly on α-quartz (SiO_2) or lithium niobate ($LiNbO_3$). However, their operation temperature is limited by the intrinsic material properties to about 500°C. High-temperature applications are feasible by applying materials that retain their piezoelectric properties up to higher temperatures. The operational temperature limits are outlined in this section and summarized in Table 3.

Polycrystalline materials such as lead zirconate titanate can be generally excluded from further discussions due to their low Curie temperature and strong damping caused by grain boundaries.

Quartz exhibits a phase transformation at 573°C. Therefore, this temperature is the ultimate application limit. Although the piezoelectric coupling constant is more or less constant up to 450°C, resonators show strongly decreasing Q factors above 300°C due to an increased structural disorder [80]. $LiNbO_3$ and $LiTaO_3$ are primarily used for filters. These crystals are commercially available as large wafers making them suitable for mass production. The composition of commonly grown

Table 3 Piezoelectric single crystals and their maximum operation temperatures

Material	Temperature limit (°C)	Remark	Reference
$LiNbO_3$	300	Decomposition	[83, 84]
α-quartz	573	Phase transformation	[80]
$AlPO_4$	583	Phase transformation	[84, 134, 135]
$GaPO_4$	933	Phase transformation	[93, 94, 104]
AlN	1,000	Oxidation	[92, 136, 137]
$La_3Ga_5SiO_{14}$	1,470	Melting point	[96, 97]
$YCa_4O(BO_3)_3$	≈1,500	Melting point	[98, 138, 139]

congruent $LiNbO_3$ and $LiTaO_3$ is 48.38 mol% Li_2O [81] and 49.0 mol% Li_2O [82], respectively. The nonstoichiometric lithium niobate decomposes at 300°C [83–86]. Only short-term stability at higher temperatures of several days to several hours at 400°C and 450°C, respectively, is observed [87]. Similar temperature ranges for decomposition apply to lithium tantalate. In addition, lithium tantalate shows a comparably low (stoichiometry-dependent) Curie temperature between 520°C and 690°C [82]. However, stoichiometric lithium niobate is expected to show improved high-temperature stability. These crystals are, e.g., manufactured from congruent $LiNbO_3$ wafers whose lithium content is increased by vapor transport equilibration (VTE) [88, 89]. Stoichiometric $LiNbO_3$ resonators operated in the thickness mode show a satisfactorily resonance behavior up to at least 900°C [90]. At 750°C the resonators were successfully operated for several days. However, the long-term stability needs to be confirmed. Another material showing promising piezoelectric properties at high temperatures but suffering from commercial availability of high-quality crystals is aluminum nitride (AlN) [91, 92].

Gallium phosphate, langasite (and its isomorphs), and oxyborates are promising candidates for high-temperature applications. They enable operation temperatures above 500°C. The ultimate temperature limits are given by the phase transformation or the melting point at 970°C [93–95], 1,470°C [96, 97], and about 1,500°C [98], respectively.

Gallium orthophosphate ($GaPO_4$) was already synthesized in 1956 [99]. The increased stability at higher temperatures in comparison to quartz was already mentioned at this time, but extensive studies related to the piezoelectric properties were not performed before the end of the 1980s [100, 101] due to the lack of sufficiently large crystals. Since then, extensive investigation of $GaPO_4$ with respect to bulk acoustic wave applications at high temperature is done [102, 103]. Up to about 700°C, these resonators show very low losses. Above this temperature, a small decrease of the Q factor induced by an increasing structural disorder takes place [104]. However, productivity and yield of growing $GaPO_4$ single crystals is rather low. Extremely anisotropic growth rates, twinning, and the incorporation of OH groups in the crystals are observed [105–108]. Due to these difficulties, the availability of $GaPO_4$ is limited which prevents its large-scale application.

Currently, the most common piezoelectric material for high-temperature applications is langasite ($La_3Ga_5SiO_{14}$), which belong to the family of CGG-type crystals (named after $Ca_3Ga_2Ge_4O_{14}$, the first synthesized material of this group) or

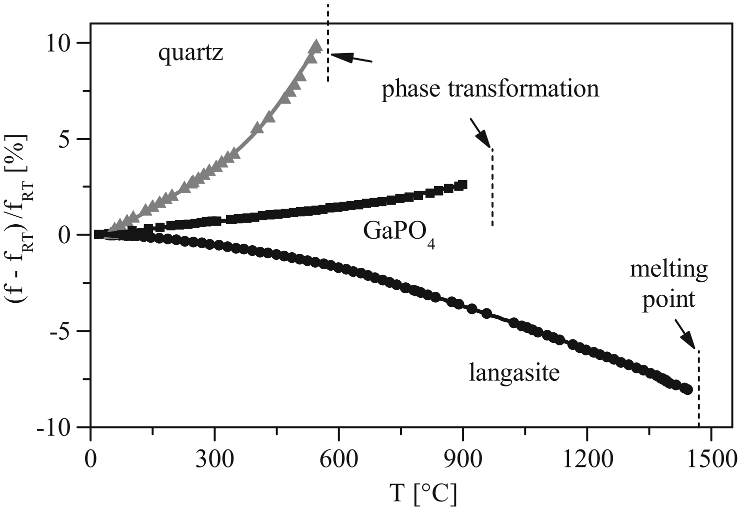

Fig. 14 The relative change of the resonance frequency as a function of the temperature for langasite, quartz, and gallium orthophosphate and their maximal operation temperature [121]

simply the langasite family. $Ca_3Ga_2Ge_4O_{14}$ was first grown in 1979 in Russia with langasite itself following in 1980 [109]. The materials were intended to be used as band-pass filters and *Q* switches for laser systems. In the early 1990s, the field of application was extended to surface acoustic wave and later in this decade to high-temperature applications. Until today, more than one hundred homeotype components of this material class were synthesized. Large high-quality crystals can be grown using conventional Czochralski technique. These materials exhibit a higher piezoelectric coupling and an improved high-temperature stability in comparison to quartz. There is no phase transition up to the melting point, which is between 1,100°C for $Na_2CaGe_6O_{14}$ and about 1,500°C for $La_3Ta_{0.5}Ga_{5.5}O_{14}$. Langasite-type crystals do not show pyroelectricity and ferroelectricity and, therefore, there is no Curie temperature limiting the temperature range. Langasite itself is the most studied and best-known material of the CGG-type crystals and suitable for bulk and surface acoustic wave applications. Its complete set of material data (piezoelectric coefficients, stiffness, etc.) is available up to 900°C [110, 111]. Although langasite may be excited piezoelectrically up to temperatures close to the melting point of 1,470°C as visualized in Fig. 14, some factors limit its practical use at extremely high temperatures. Viscoelastic losses impact the resonance behavior to some extent below 650°C. Conductivity-related losses dominate the behavior above that temperature [112]. As a consequence, the *Q* factor of a 5 MHz langasite bulk acoustic wave resonator decreases from 10^4 at room temperature to about 150 at 1,000°C. A detailed discussion of the losses and the related defect chemistry is given in [110].

Currently, $Ca_3TaGa_3Si_2O_{14}$ (CTGS) and $Ca_3NbGa_3Si_2O_{14}$ (CNGS) are actively investigated members of the langasite family. For a given temperature, these materials show lower conductivities than langasite resulting in *Q* factors of about

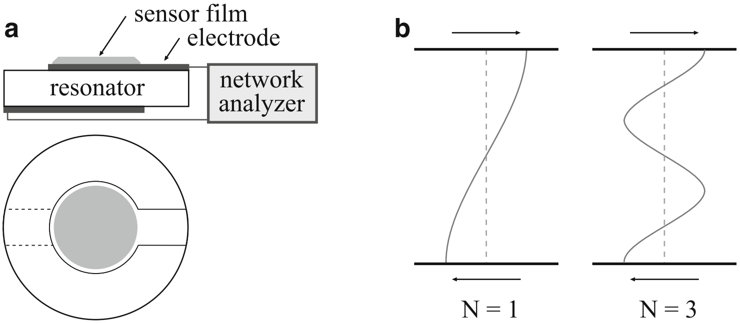

Fig. 15 Scheme of a BAW resonator with a gas-sensitive film (**a**) and displacement profiles for the fundamental mode ($N = 1$) and the first overtone ($N = 3$) (**b**)

4,000 at 850°C [113]. The application of these materials requires, however, information about the stability in harsh environments. Further, the availability of large crystals is limited.

Recently, oxyborate single crystals ($ReCa_4O(BO_3)_3$, Re; rare earth element) were grown. They do not show phase transformations up to their melting point at about 1,500°C. Most remarkably, these crystals exhibit very low conductivity, for example, 5×10^{-7} S/m at 800°C [98, 113, 114] which is about one and three orders of magnitude lower than that for $GaPO_4$ and langasite, respectively. As a consequence, the loss is very low which results in resonant devices with exceptionally high Q factors even at 900°C. Currently, a maximum operation temperature of 1,000°C is reported for $GdCa_4O(BO_3)_3$. Above that temperature the electrodes used so far degraded [114].

5.2 Operation Principles

Two operation principles for resonant sensors are of practical relevance, i.e., bulk acoustic wave (BAW) and surface acoustic wave (SAW) resonators.

5.2.1 Bulk Acoustic Wave Resonators

BAW resonators consist of a piezoelectric plate coated with electrodes on both sides as shown in Fig. 15a. By applying a voltage to the electrodes, the acoustic wave is excited in the volume of the crystal. Mostly, these resonators are operated in the thickness shear mode (TSM), where the movement takes place in the plane of the resonator device. As a consequence, these resonators do not produce compressive waves in the surrounding atmosphere, which reduces the impact of pressure changes.

The resonance frequency of the plate depends on the wave velocity of the shear wave in the piezoelectric material v_{tr} and the thickness of the resonator d_{res}:

$$f^{[N]} = N \frac{v_{\mathrm{tr}}}{2d_{\mathrm{res}}} \tag{24}$$

The factor N is the overtone number, where only positive odd integers ($N = 1, 3, 5, \ldots$) fulfill the boundary conditions. The displacements inside a TSM resonator are shown in Fig. 15b for the fundamental mode ($N = 1$) and the first overtone ($N = 3$).

The resonance frequency of a TSM resonator can be altered by, e.g., a mass uptake or gas composition-dependent stoichiometry changes of thin films already deposited onto the resonators. The latter enables gas sensing provided that the properties of the film are known. The correlation of mass load and frequency shift was first discussed by Sauerbrey in 1959 and described by the eponymous equation. The frequency shift Δf induced by a mass load Δm per area A follows from [115]:

$$\Delta f = -\frac{f}{d_{\mathrm{res}}\rho_{\mathrm{res}}} \frac{\Delta m}{A} \tag{25}$$

Here, ρ_{res} represents the density of the resonator material. This relation is applicable for homogeneous films up to a mass uptake of 2% with respect to the related resonator mass $m_{\mathrm{res}} = A d_{\mathrm{res}} \rho_{\mathrm{res}}$ [116]. Thereby, the mass sensitivity of a resonator can be defined by $S_{\mathrm{res}} = -A\Delta f / \Delta m$. Inhomogeneous mass loads require the consideration of a mass sensitivity distribution S. For a TSM resonator, the property can be approximated by a radially symmetric Gaussian function having its maximum S_{max} at the center of the electrode at $r = 0$ [117]:

$$S(r) = S_{\mathrm{max}} \mathrm{e}^{-wr^2} \tag{26}$$

The relative sensitivity $S_{\mathrm{el}}/S_{\mathrm{max}}$ at the electrode radius r_{el} is a nearly constant value, e.g., $S_{\mathrm{el}}/S_{\mathrm{max}} = 0.08$ [117], and can be used to calculate the width of the Gaussian distribution w as a function of r_{el}:

$$w = -\ln(S_{\mathrm{el}}/S_{\mathrm{max}})/r_{\mathrm{el}}^2 \tag{27}$$

The overall mass sensitivity follows from the mass sensitivity distribution:

$$S_{\mathrm{res}} = \frac{1}{\pi r_{\mathrm{el}}^2} \int_0^{r_{\mathrm{el}}} S(r) 2\pi r \, dr \tag{28}$$

Finally, the frequency shift for inhomogeneous but radially symmetric mass loads $m(r)$ results from:

$$\Delta f = \frac{1}{\pi_{\mathrm{el}}^2} \int_0^{r_{\mathrm{el}}} S(r) m(r) 2\pi r \, dr \tag{29}$$

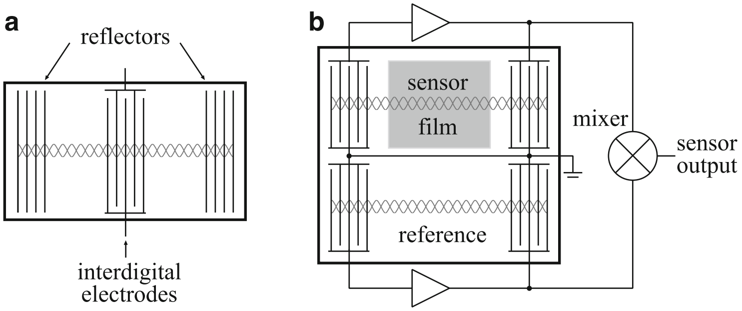

Fig. 16 One-port SAW resonator (**a**) and SAW device with two delay lines (**b**)

In order to describe the resonance behavior in detail, the electrical response of a piezoelectric resonator has to be calculated based on constitutive equations, namely, linear piezoelectric equations, Newton's equation of motion, and Maxwell's equations as presented in [118–120]. At high temperatures, a complete analytical solution of the physical model reflecting all types of material-related losses is required. The approach is described in [121].

5.2.2 Surface Acoustic Wave Resonators

This type of resonant sensor makes use of the influence of an analyte on the change of the wave velocity or attenuation of waves propagating at the surface. Their excitation is realized using planar interdigital electrodes deposited on one surface of a piezoelectric substrate. The characteristic frequency of such devices is governed by the material and crystal cut-dependent velocity of the acoustic wave υ_{saw} and the pitch p of the interdigital fingers [122]:

$$fc = \frac{v_{\mathrm{saw}}}{p} \tag{30}$$

In general, two operational modes, i.e., resonators and delay lines, are used. As visualized in Fig. 16a, resonators consist of one central interdigital structure to excite the acoustic waves and two reflectors to increase the Q factor. At the resonance frequency, a standing wave is induced, which can be measured using a network analyzer or even wirelessly. Resonators are often applied if the properties of the resonator material itself are influenced by the physical quantity of interest, e.g., temperature or mechanical stress. The setup of delay lines is shown in Fig. 16b. They consist of two interdigital structures, where one acts as transmitter and the other acts as receiver for the acoustic wave. The travel time or the attenuation of the acoustic wave between transmitter and receiver is evaluated. Delay lines based chemical sensors comprise gas-sensitive films between both electrode structures. In order to compensate unwanted influences on the signal, a reference delay line

Table 4 Mass sensitivity of 5 MHz y-cut langasite, gallium phosphate, and quartz BAW resonators [121]

	S_{res} (cm^2 Hz/μg)		
T (°C)	Langasite	$GaPO_4$	Quartz
20	32.4	55.7	47.7
600	32.1	56.5	–
800	31.8	56.8	–
1,000	31.4	–	–

without the sensor film is often used. An advantage of delay line sensors compared to resonators is the option to add tagging structures on the delay line. They enable the distinction of different sensors which is advantageous for wireless operation.

The frequency and other acoustic parameters of SAW resonators can be easily adjusted by changing the finger layout. Design and operation of SAW devices are described in detail, e.g., in [86].

The operation frequency of BAW resonators ranges typically from 1 to 20 MHz. In contrast, the frequencies of SAW devices start at about 50 MHz and can reach values of several GHz. In view of high-temperature applications, BAW resonators are, however, simpler and more robust. Here, thick-film techniques can be used to deposit sensor films and electrodes leading to devices which are operational even above 1,000°C. The moderate operation frequency leads to comparatively cheap data acquisition units and robust setups for wired sensors. The lower sensitivity in comparison to SAW devices is compensated by a better signal to noise ratio. Further, the Q factor of BAW devices is significantly higher than that of SAW-based sensors.

The main advantage of SAW devices is the sufficiently high frequency to enable wireless interrogation. Due to the impact of the electrodes on the acoustic wave, their thickness is restricted to 200 nm which limits the operation temperature. Even platinum-based thin-film electrodes and capping layers do not ensure long-term stability above, e.g., 650°C [123]. Higher operational temperatures were achieved at the expense of very limited durability. For example, in 1998 a langasite-based SAW device was operated for a short period of time at 1,000°C [124]. More recently, long-term and cycling tests indicated stable performance of SAW devices with co-deposited $Pt/Rh/ZrO_2$ thin-film electrodes up to 850°C [125]. Finally, the data acquisition equipment, the packaging, and the signal lines have to meet high requirements further increasing the sensor costs.

The mass sensitivity of resonant sensors is extremely high. Even BAW sensors enable the detection of mass changes equivalent to the adsorption of oxygen submonolayers or to stoichiometry changes of oxides [126]. The mass sensitivities listed in Table 4 are calculated from material data and determined experimentally as described in [121].

The response time of resonant sensors is in general determined by the data acquisition technique. If oscillator units are used, a time constant in the order of several milliseconds is expected. Network analysis enable, under best circumstances, a few samples per second.

5.3 Application Limits and Measurement Errors

Besides the thermal stability of the resonator materials, the operation limits of resonant sensors include:

5.3.1 Temperature Dependence of the Resonance Frequency

As seen in Fig. 14, langasite resonators exhibit a large temperature-dependence of the frequency which must be seen in the context of mass load-dependent frequency shifts of the resonators expected to be in the order of tens of Hz. Given the temperature coefficient of a 5 MHz langasite resonator of about 200 Hz/K at 600°C, fluctuations of only 0.1 K overwhelm the signal of interest. Consequently, temperature effects have to be drastically minimized by the application of either compensation methods or temperature-compensated crystal cuts. The latter limit the operation temperature to a narrow range. Nevertheless, they are highly attractive for commercial applications if the operation temperature fluctuations are limited to a narrow range.

Compensation methods might use external temperature probes to determine the temperature-compensated frequency by solving a linear approximation of the resonance frequency in the vicinity of T_0 for the temperature-independent term:

$$f_0^{[N]}(m, ..) = f^{[N]}(T, m, ..) - c^{[N]}(T - T_0) \tag{31}$$

Here, $f^{[N]}$, $c^{[N]}$, T, and T_0 are the measured frequency, the temperature coefficient, and the measured and nominal operation temperature, respectively. Since very accurate temperature measurements are required, difficulties come up with external temperature probes even if they are installed close to the piezoelectric devices. In case of gas sensors, reactions catalyzed by, e.g., platinum electrodes or by sensor films may cause local temperature fluctuations. Alternatively, the simultaneous measurement of different overtones can be used for compensation. The frequency of the fundamental mode and the first overtone can be expressed by Eq. (31) and used to calculate a temperature-independent frequency:

$$f_{\mathrm{TC}}(m, ..) = f_0^{[1]}(m, ..) - \frac{c^{[1]}}{c^{[3]}} f_0^{[3]}(m, ..) = f^{[1]}(T, m, ..) - \frac{c^{[1]}}{c^{[3]}} f^{[3]}(T, m, ..) \tag{32}$$

The ability of this method to suppress temperature fluctuations is demonstrated in Fig. 17. While the fundamental mode $f^{[1]}$ of a langasite resonator exhibits frequency shifts of up to 500 Hz upon inlet of different gases, the compensated frequency f_{TC} remains almost constant. The small deviations that are still visible result from the time shift between the measurement of the fundamental mode $f^{[1]}$ and the overtone $f^{[3]}$. Finally, it should be noted that f_{TC} describes mass changes in a different manner [121]:

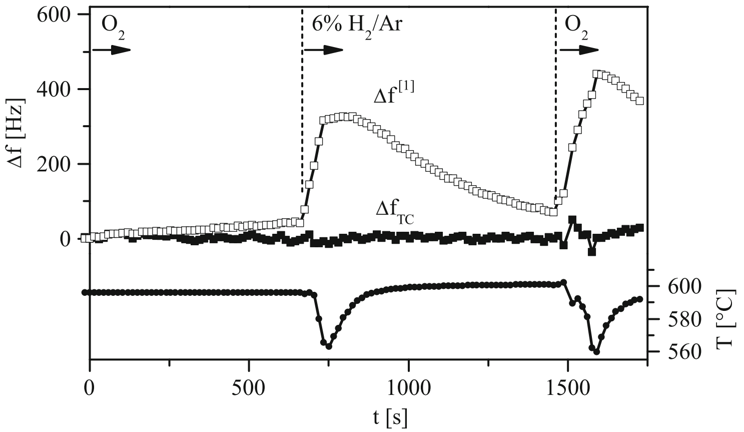

Fig. 17 Frequency fluctuations $\Delta f^{[1]}$ and vanishing frequency shift Δf_{TC} of an uncoated langasite resonator during switching the atmosphere from oxygen to 6% H_2/Ar and reverse

$$S_{\mathrm{TC}} = S^{[1]}\left(1 - \frac{3c^{[1]}}{c^{[3]}}\right) \tag{33}$$

The temperature compensation requires quasi-simultaneous measurement of the fundamental mode and the first overtone resonance which doubles the minimum data acquisition period.

5.3.2 Cross-Sensitivities

The cross-sensitivity of metal oxide films is a general problem. However, specially designed electrodes of resonant sensors enable simultaneous monitoring of the electrical and mechanical sensor film properties. The approach improves the selectivity as described in the application section for the distinction of CO and H_2 at 600°C.

5.3.3 Electromechanical Losses

Electromechanical losses in the resonators potentially limit the accuracy in frequency determination and, thereby, the applicability of resonant sensors at elevated temperatures. However, the use of network analyses to acquire the resonance spectra circumvents this problem. Choosing a reasonable number of data points the uncertainty in resonance frequency determination can be reduced to ±4 Hz at 1,000°C [121].

5.3.4 Aging and Degradation of the Piezoelectric Crystals

Single-crystalline resonator materials show fundamental advantages such as the absence of grain boundaries which are prone to induce aging effects. However, unfavorable conditions, i.e., extremely high temperatures and low p_{O_2}'s, result potentially in the reduction of the crystals or in the loss of constituents. Taking langasite as example, irreversible degradation due to reduction has not been observed. In order to describe the stability of langasite, the formation of oxygen vacancies and the related shift of the resonance frequency can be taken. In nominally hydrogen-free atmospheres, the frequency shift induced by redox-related reactions is expected to exceed a limit of ±4 Hz at fairly low p_{O_2}'s, i.e., below 10^{-36} and 10^{-24} at 600°C and 800°C, respectively. Water vapor is found to shift the resonance frequency already at higher p_{O_2}'s. In an atmosphere containing about 1% hydrogen, langasite can be regarded as a stable resonator material above p_{O_2}'s of about 10^{-20} and 10^{-13} at 600°C and 800°C, respectively [110]. Further, a significant gallium evaporation occurs in strongly reducing atmospheres. The gallium oxide-deficient region reaches down to 1.5 μm below the surface after annealing at 900°C for 12 h. However, a thin alumina layer of only 20 nm suppresses the gallium evaporation [127].

5.4 *Application Examples*

The application examples presented here take advantage of three different effects. Despite being a particle sensor, the first example is a soot sensor where the gravimetric effect is used directly. Secondly, an oxygen sensor is presented which uses the environmental-dependent density of CeO_2 films. The third example is a selective CO/H_2 sensor. Based on the simultaneous determination of electrical and mechanical sensor film parameters, both gases can be distinguished at high temperatures.

Examples for SAW-based sensors are not presented. It should be noted, however, that the conductivity of sensor films causes strong effects due to the high surface-sensitivity of such devices. For example, tungsten oxide films were applied successfully on langasite-based devices to detect hydrogen or ethene at elevated temperatures [128]. Zinc oxide has been tested as a sensitive layer for oxygen detection [129].

5.4.1 Soot Sensor

First, the application of a langasite resonator as soot sensor is presented. Especially in diesel combustion systems there is a high demand for cost-effective sensors to monitor the particle emissions [130]. Common optical particle measurement

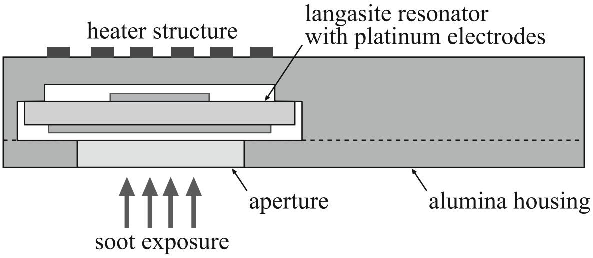

Fig. 18 Schematic cross section of a high-temperature microbalance soot sensor

systems are expensive and error prone for onboard diagnostics, while resistivity-based interdigital sensors do not deliver a continuous sensor signal [131]. They show a threshold as long as no conductive paths are formed by the soot. In contrast, microbalance-based sensors enable a continuous measurement of the soot accumulation at elevated temperatures. Further, the soot can be removed by temporary heating of the langasite-based sensor to temperatures above 600°C. This step cannot be realized with common quartz-based microbalances.

The sensor setup for such a langasite-based soot sensor is shown in Fig. 18. The resonator is coated with keyhole-shaped platinum electrodes and mounted in an alumina housing. The meander-type heater structure can be used to heat the device electrically up to 800°C. A small aperture exposes one electrode to the exhaust gas. The aperture is smaller than the electrode of the resonator to prevent a broadening of the effective electrode diameter by the conductive soot layer.

In order to accumulate soot, the sensor is operated at 200°C and exposed to a sooting flame for 10 s while the temperature-compensated resonance frequency is recorded. After each exposition, a significant shift of the resonance frequency of 70 Hz is observed as visualized in Fig. 19. The temperature compensation described above leads to a reverse sign of the frequency shift. The fundamental mode of the resonator shows a decreased resonance frequency after the exposition, which indicates an increased mass load on the resonator surface. Applying the Sauerbrey equation and assuming a density of soot of 1.1 g/cm^3, the thickness of the deposited soot layer after 10 s of deposition is estimated to be about 60 nm.

5.4.2 Gravimetric Oxygen Sensor

Cerium oxide (CeO_{2-x}) is chosen as a model material since it shows high oxygen nonstoichiometry as a function of the p_{O_2}. The related mass change is measured using a piezoelectric resonator. About 5 µm thick films are deposited on langasite BAW resonators which are investigated at 900°C in the p_{O_2} range from 0.2 bar to 10^{-17} bar. Below 10^{-10} r, changes in the resonance frequency by several 10 Hz could be attributed to mass changes, i.e., to changes in stoichiometry. Thereby, CeO_{2-x} coated langasite resonators are able to monitor the p_{O_2} at elevated

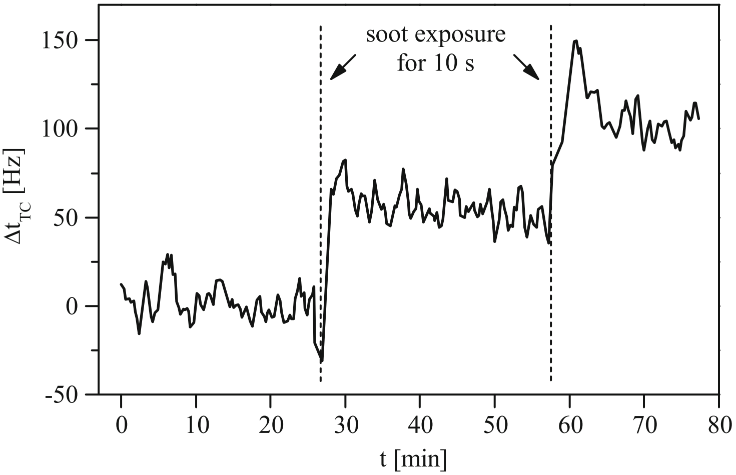

Fig. 19 Shift of the temperature-compensated resonance frequency of a langasite-based soot sensor after expositions to a sooting flame for 10 s

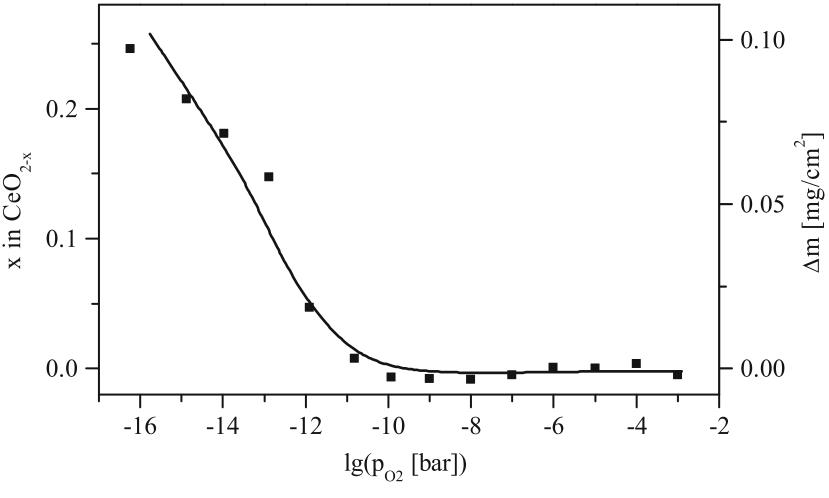

Fig. 20 Nonstoichiometry of $CeO_{2\text{-}x}$ at 900°C as a function of the p_{O_2} determined using a langasite BAW resonator

temperatures and low p_{O_2}'s as visualized in Fig. 20. The data correspond to those shown in Ce–O phase diagrams and are in general accordance with nonstoichiometry data determined by impedance spectroscopy [132]. The application of other sensor film materials like TiO_2 shifts the measurement range to even lower p_{O_2}'s. In other words, the sensor material can be varied to tailor the sensitivity for the p_{O_2} range of interest.

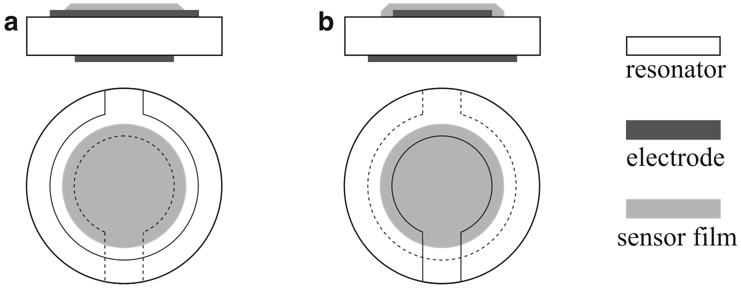

Fig. 21 Electrode and sensor film layout for the microbalance (**a**) and conductivity mode (**b**)

5.4.3 Selective CO/H_2 Sensor

Langasite-based bulk acoustic wave resonators with two different electrode layouts enable to distinguish between conductivity and mechanical effects in metal oxide sensor films. Both electrode layouts (see Fig. 21) are based on keyhole-shaped platinum electrodes of different diameter on front and rear side of the resonator. In order to operate the sensor in the conventional microbalance mode, the sensor film is deposited on the side with the larger platinum electrode. Since the electrode diameter is larger than that of the sensor film, the electrode fixes the electrode area independent of the sensor film conductivity. Consequently, the resonance behavior is solely determined by mechanical properties (density, stiffness, etc.) of the sensor film.

At a given p_{O_2}, CeO_2-coated resonators show different frequency shifts upon changes of the CO and H_2 concentrations in the surrounding atmosphere [133]. The effect can be used if the p_{O_2} is measured by another sensor. A λ-probe would be one option. However, the availability of a data acquisition unit for resonant sensors motivates to use them as p_{O_2} sensor, too. Here, a modified layout is applied which reflects the sensor film conductivity. The property is known to be p_{O_2} dependent in case of, e.g., TiO_2. In the conductivity mode, the sensor film is deposited on the smaller platinum electrode and exceeds its size. Thereby, the sensor film conductivity determines the effective electrode diameter. As a consequence, the width w of the mass sensitivity distribution is altered. Since the mass of the platinum electrode is significantly larger than that of the thin TiO_2 sensor film, the model for inhomogeneous mass loads applies and the frequency shift must be described by Eq. (29). The effect is illustrated in Fig. 22. The increase of the sensor film conductivity results in a bigger effective electrode radius $r_{el}^{Tio_2}$ and, thereby, a broader distribution of the mass sensitivity. As a consequence, the mass sensitivity in the area of the heavy platinum electrode increases and causes a resonance frequency shift.

A sensor setup consisting of a CeO_2 (microbalance mode) and a TiO_2 (conductivity mode)-coated langasite resonator has been tested with respect to its sensitivity and selectivity for H_2 and CO. Gas mixtures of argon with 0.25% CO or H_2 or a mixture of these gases are supplied at 600°C. Thereby, the p_{O_2} is adjusted in the range from 10^{-4} to 10^{-20} bar by adding oxygen to the gas mixture using a zirconia oxygen ion pump (see, e.g., [32]). Figure 23 shows the temperature-compensated

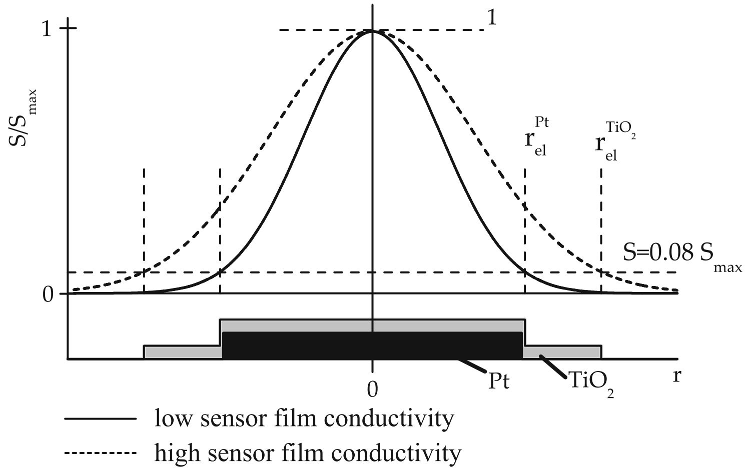

Fig. 22 Displacement distribution on a langasite resonator operated in the conductivity mode for high and low sensor film conductivity

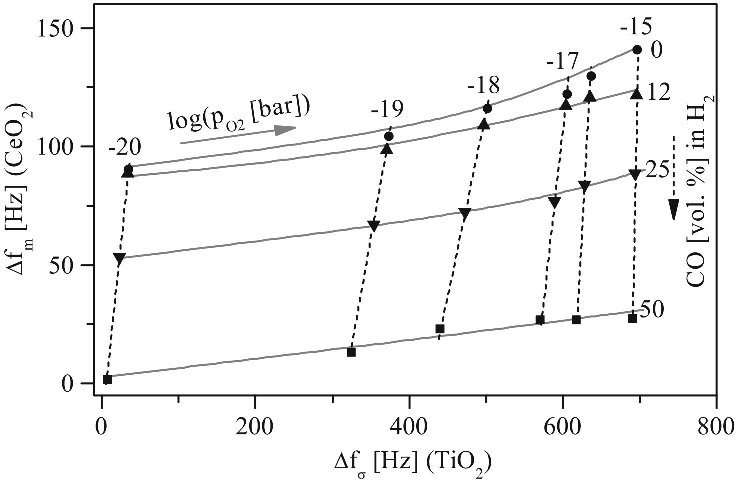

Fig. 23 Temperature-compensated resonance frequency of a TiO_2-coated resonator (conductivity mode) plotted versus the response of a CeO_2-coated resonator (microbalance mode) for different gas mixtures and p_{O_2}'s

resonance frequencies of both resonators. Clearly separated sensor signals for the different p_{O_2}'s and CO/H_2 ratios are found. Considering the uncertainty in frequency determination of about 2.5 Hz and the frequency shift between the different mixtures containing CO and H_2, a relative sensitivity for H_2 of about 2% is calculated. The example demonstrates the ability of the system to distinguish both strongly reducing gases which cannot be done using solely conductivity-based gas sensors.

References

1. Kohl D (2001) Function and applications of gas sensors. J Phys D Appl Phys 34:R125–R149
2. Ivers-Tiffee E, Hardtl KH, Menesklou W, Riegel J (2001) Principles of solid state oxygen sensors for lean combustion gas control. Electrochim Acta 47(5):807–814
3. Moseley PT (1997) Solid state gas sensors. Meas Sci Technol 8(3):223–237
4. Garzon F, Mukundan R, Brosha E (2000) Solid-state mixed potential gas sensors: theory, experiments and challenges. Solid State Ion 136:633–638
5. Miura N, Lu G, Yamazoe N (2000) Progress in mixed-potential type devices based on solid electrolyte for sensing redox gases. Solid State Ion 136:533–542
6. Moos R, Sahner K, Fleischer M, Guth U, Barsan N, Weimar U (2009) Solid state gas sensor research in Germany – a status report. Sensors 9:4323–4365
7. Zosel J, Tuchtenhagen D, Ahlborn K, Guth U (2008) Mixed potential gas sensor with short response time. Sens Actuators B Chem 130(1):326–329
8. Göpel W, Hesse J, Zemel JN (eds) (1992) Optical sensors. VCH, Weinheim
9. Hodgkinson J, Tatam RP (2013) Optical gas sensing: a review. Meas Sci Technol 24 (1):012,004
10. Somorjai GA (1972) Principles of surface chemistry. Prentice-Hall, Englewood Cliffs
11. Ostrovskii VE, Agafonov YA, Gostev BV, Kadyshevich EA, Lapidus AL (2010) Chemisorption of gases and reaction of propane dehydration at chromic oxide. Solid Fuel Chem 44 (4):275–286
12. Geiger GH, Poirier DR (1973) Transport phenomena in metallurgy. Addison-Wesley
13. Sakuma T (1988) Phase transformation and microstructure of partially-stabilized zirconia. Trans Jpn Inst Met 29(11):879–893
14. Ruh R, Mazdiyasni K, Valentine P, Bielstein H (1984) Phase Relations in the System ZrO_2–Y_2O_3 at Low Y_2O_3 Contents. J Am Ceram Soc 67(9):C–190
15. Kröger FA (1964) The chemistry of imperfect crystals. North Holland, Amsterdam
16. Park J, Blumenthal R (1989) Electronic transport in 8 mole percent Y_2O_3-ZrO_2. J Electrochem Soc 136(10):2867–2876
17. Goff J, Hayes W, Hull S, Hutchings M, Clausen K (1999) Defect structure of yttria-stabilized zirconia and its influence on the ionic conductivity at elevated temperatures. Phys Rev B 59 (22):14,202
18. Ramamoorthy R, Dutta P, Akbar S (2003) Oxygen sensors: materials, methods, designs and applications. J Mater Sci 38(21):4271–4282
19. Wiemhöfer H, Göpel W (1991) Interface analysis for solid state electrochemical devices and chemical sensors. Fresenius J Anal Chem 341:106–111
20. Darken LS, Gurry RW (1953) Physical chemistry of metals. McGraw-Hill, New York
21. Fouletier J, Mantel E, Kleitz M (1982) Performance characteristics of conventional oxygen gauges. Solid State Ion 6:1–13
22. Ghetta V, Fouletier J, Henault M, le Moulec A (2002) Control and monitoring of oxygen content in molten metals. Application to lead and lead-bismuth melts. J Phys IV 12:123–140
23. Weppner W (1977) Electronic transport properties and electrically induced p-n junction in ZrO_2 + 10 mol% Y_2O_3. J Solid State Chem 20(3):305–314
24. Friedman L, Oberg K, Boorstein W, Rapp R (1973) Electronic conductivities of commercial ZrO_2+ 3 to 4 Wt Pct CaO electrolytes. Metallur Mater Trans B 4(1):69–74
25. Patterson JW, Bogren EC, Rapp RA (1967) Mixed conduction in $Zr_{0.85}Ca_{0.15}O_{1.85}$ and $Th_{0.85}Y_{0.15}O_{1.925}$. J Electrochem Soc 114:752
26. Fouletier J, Fabry P, Kleitz M (1976) Electrochemical semipermeability and the electrode microsystem in solid oxide electrolyte cells. J Electrochem Soc 123(2):204–213
27. Maskell W, Steele B (1986) Solid state potentiometric oxygen gas sensors. J Appl Electrochem 16(4):475–489

28. Fouletier J, Siebert E, Caneiro A (1984) Accurate monitoring of low oxygen activity in gases with conventional oxygen gauges and pumps. In Science and Technology of Zirconia II. Adv Ceram 12:618–626
29. Fouletier J, Seinera H, Kleitz M (1974) Measurement and regulation of oxygen content in selected gases using solid electrolyte cells. I. discontinuous use of gauges. J Appl Electrochem 4(4):305–315
30. Fleming W (1977) Physical principles governing nonideal behavior of the zirconia oxygen sensor. J Electrochem Soc 124(1):21–28
31. Lide DR (ed) (2003) CRC handbook of chemistry and physics, 84th edn. CRC
32. Schulz M, Brillo J, Stenzel C, Fritze H (2012) Oxygen partial pressure control for microgravity experiments. Solid State Ion 225:332–336
33. Egry I (1991) Surface tension measurements of liquid metals by the oscillating drop technique. J Mater Sci 26:2997–3003
34. Docquier N, Candel S (2002) Combustion control and sensors: a review. Progr Energy Combust Sci 28(2):107–150
35. Riegel J, Neumann H, Wiedenmann H (2002) Exhaust gas sensors for automotive emission control. Solid State Ion 152:783–800
36. Dietz H (1982) Gas-diffusion-controlled solid-electrolyte oxygen sensors. Solid State Ion 6 (2):175–183
37. Saji K, Kondo H, Takahashi H, Takeuchi T, Igarashi I (1988) Influence of H_2O, CO_2 and various combustible gases on the characteristics of a limiting current-type oxygen sensor. J Appl Electrochem 18(5):757–762
38. Göpel W, Reinhardt G, Rösch M (2000) Trends in the development of solid state amperometric and potentiometric high temperature sensors. Solid State Ion 136–137:519–531
39. Baunach T, Schänzlin K, Diehl L (2006) Sauberes Abgas durch Keramiksensoren. Physik J 5:33–38
40. Alkemade U, Schumann B (2006) Engines and exhaust after treatment systems for future automotive applications. Solid State Ion 177(26):2291–2296
41. Twigg M (2003) Automotive exhaust emissions control. Platinum Metals Rev 47(4):157–162
42. Skelton DC, Tobin RG, Lambert DK, DiMaggio CL, Fisher GB (2003) A surface-science-based model for the selectivity of platinum–gold alloy electrodes in zirconia-based NO_x sensors. Sens Actuators B Chem 96(1):46–52
43. Menil F, Coillard V, Lucat C (2000) Critical review of nitrogen monoxide sensors for exhaust gases of lean burn engines. Sens Actuators B Chem 67(1):1–23
44. Somov S, Guth U (1998) A parallel analysis of oxygen and combustibles in solid electrolyte amperometric cells. Sens Actuators B Chem 47(1):131–138
45. Barsoukov E, Macdonald JR (2005) Impedance spectroscopy. Wiley
46. Bhowmik S, Constant KP, Parker JC, Ali M (1995) Electrical characterization of nanocrystalline Titania 1: impedance spectroscopy studies between 300 K and 473 K. Mater Sci Eng A 204:258–266
47. Mather GC, Marques FMB, Frade JR (1999) Detection mechanism of TiO_2-based ceramic H_2 sensors. J Eur Ceram Soc 19:887–891
48. Fleischer M (2008) Advances in application potential of solid state gas sensors: high-temperature semi conducting oxides and ambient temperature Gasfet devices. Meas Sci Technol 19:042001
49. Fleischer M, Wagner V, Hacker B, Meixner H (1995) Comparison of a.c. and d.c. measurement techniques using semiconducting Ga_2O_3 sensors. Sens Actuators B Chem 26–27:85–88
50. Kiss G, Pinter Z, Perczel IV, Sassi Z, Reti F (2001) Study of oxide semiconductor sensor materials by selected methods. Thin Solid Films 391(2):216–223
51. Schwebel T, Fleischer M, Meixner H, Kohl CD (1998) CO-sensor for domestic use based on high temperature stable Ga_2O_3 thin films. Sens Actuators B Chem 49:46–51

52. Barsan N, Weimar U (2001) Conduction model of metal oxide gas sensors. J Electrocer 7(3):143–167
53. Seiyama T, Kato A, Fujishi K, Nagatani M (1962) A new detector for gaseous components using semiconductive thin films. Anal Chem 34:1502–1503
54. Taguchi N (1972) Gas detecting device. US Patent 3,695,848
55. Weimar U, Göpel W (1995) Measurements on tin oxide sensors to improve selectivities and sensitivities. Sens Actuators B Chem 26(1):1318
56. Gerblinger J, Lohwasser W, Lampe U, Meixner H (1995) High temperature oxygen sensor based on sputtered cerium oxide. Sens Actuators B Chem 26–27:93–96
57. Knauth P, Tuller HL (1999) Nonstoichiometry and relaxation kinetics of nanocrystalline mixed praseodymium-Cerium oxide $Pr_{0.7}Ce_{0.3}O_{2-x}$. J Eur Ceramic Soc 19(6):831–836
58. Menesklou W, Schreiner HJ, Härdtl KH, Ivers-Tiffee E (1999) High temperature oxygen sensors based on doped $SrTiO_3$. Sens Actuators B Chem 59(2–3):184–189
59. Moos R, Härdtl KH (1997) Defect chemistry of donor-doped and undoped strontium titanate ceramics between 1000 and 1400°C. J Am Ceram Soc 80(10):2549–2562
60. Rothschild A, Menesklou W, Tuller HL, Ivers-Tiffee E (2006) Electronic structure, defect chemistry, and transport properties of $SrTi_{1-x}Fe_xO_3$. Solid Solutions Chem Mater 18:3651–3659
61. Skinner SJ, Kilner JA (2003) Oxygen ion conductors. Mater Today 6(3):30–37
62. Zhou HD, Goodenough JB (2004) Polaron morphologies in $SrTi_{1-x}Fe_xO_{3-\delta}$. J Solid State Chem 177:1952–1957
63. Hwang JH, McLachlan DS, Mason TO (1999) Brick layer model analysis of nanoscale-to-microscale cerium dioxide. J Electroceram 3:7–16
64. Tuller HL (2000) Ionic conduction in nanocrystalline materials. Solid State Ion 131(1):143–157
65. Butt DP, Park Y, Taylor TN (1999) Thermal vaporization and deposition of gallium oxide in hydrogen. J Nucl Mater 264:71–77
66. Althainz P, Goschnick J, Ehrmann S, Ache HJ (1996) Multisensor microsystem for contaminants in air. Sens Actuators B 33:72–76
67. Frank K, Kohler H, Guth U (2009) Influence of the measurement conditions on the sensitivity of SnO_2 gas sensors operated thermo-cyclically. Sens Actuators B 141:361–369
68. Rothschild A, Tuller HL (2006) Gas sensors: new materials and processing approaches. J Electroceram 17(2–4):1005–1012
69. Fleischer M, Kornely S, Weh T, Frank J, Meixner H (2000) Selective gas detection with high-temperature operated metal oxides using catalytic filters. Sens Actuators B 69:205–210
70. Firebaugh SL, Jensen KF, Schmidt MA (1998) Investigation of high-temperature degradation of platinum thin films with an in situ resistance measurement apparatus. J Microelectromech Syst 7(1):128–135
71. Meyer R, Waser R (2004) Resistive donor-doped $SrTiO_3$ sensors: I, basic model for a fast sensor response. Sens Actuators B Chem 101(3):335–345
72. Baumard JF, Tani E (1977) Electrical conductivity and charge compensation in Nb doped TiO_2 rutile. J Chem Phys 67:857–860
73. Chiang YM, Birnie DP, Kingery WD (1997) Physical ceramics: principles for ceramics science and engineering. Wiley
74. Choi GM, Tuller HL (1988) Defect structure and electrical properties of single-crystal $Ba_{0.03}Sr_{0.97}TiO_3$. J Am Ceram Soc 71(4):201–205
75. Yoo H, Song H, Lee D (2002) $BaTiO_{3-\delta}$ defect structure, electrical conductivity, chemical diffusivity, thermoelectric power, and oxygen nonstoichiometry. J Electroceram 8:5–36
76. Moos R, Menesklou W, Schreiner H, Härdtl K (2000) Materials for temperature independent resistive oxygen sensors for combustion exhaust gas control. Sens Actuators B Chem 67 (1–2):178–183
77. Brixner LH (1968) Preparation and properties of the $SrTi_{1-x}Fe_xO_{3-x/2}/O_{x/2}$ system. Mater Res Bull 3(4):299–308

78. Norby T (2001) Fast oxygen ion conductors – from doped to ordered systems. J Mater Chem 11:11–18
79. Steinsvik S, Bugge R, Gjønnes J, Taftø J, Norby T (1997) The defect structure of $SrTi_{1-x}Fe_xO_{3-y}$ ($x = 0$–0.8) investigated by electrical conductivity measurements and electron energy loss spectroscopy (EELS). J Phys Chem Solids 58:969–976
80. Haines J, Cambon O, Keen D, Tucker M, Dove M (2002) Structural disorder and loss of piezoelectric properties in α-quartz at high temperature. Appl Phys Lett 81:2968
81. Jundt DH, Fejer MM, Norwood RG (1992) Composition dependence of lithium diffusivity in lithium niobate at high temperature. J Appl Phys 72(8):3468–3473
82. Barns R, Carruthers J (1970) Lithium tantalate single crystal stoichiometry. J Appl Crystallogr 3(5):395–399
83. Birnie DP III (1993) Analysis of diffusion in lithium niobate. J Mater Sci 28:302–315
84. Damjanovic D (1998) Materials for high temperature piezoelectric transducers. Curr Opin Solid State Mater Sci 3(5):469–473
85. Fachberger R, Bruckner G, Knoll G, Hauser R, Biniasch J, Reindl L (2004) Applicability of $LiNbO_3$, langasite and $GaPO_4$ in high temperature SAW sensors operating at radio frequencies. IEEE Trans Ultrason Ferroelectr Freq Control 51(11):1427–1431
86. Reindl L, Scholl G, Ostertag T, Scherr H, Wolff U, Schmidt F (1998) Theory and application of passive SAW radio transponder as sensors. IEEE Trans Ultrason Ferroelectr Freq Control 45:1281–1292
87. Bruckner G, Hauser R, Stelzer A, Maurer L, Reindl L, Teichmann R, Biniasch J (2003) High temperature stable SAW based tagging system for identifying a pressure sensor. In: Proceedings of the 2003 I.E. international frequency control symposium and PDA exhibition jointly with the 17th European frequency and time forum, 2003. pp a942–a947
88. Bordui PF, Norwood RG, Jundt DH, Fejer MM (1992) Preparation and characterization of off-congruent lithium niobate crystals. J Appl Phys 71:875
89. Jundt DH, Fejer MM, Byer RL (1990) Optical properties of lithium-rich lithium niobate fabricated by vapor transport equilibration. IEEE J Quant Electr 26:135–138
90. Ohlendorf G, Richter D, Sauerwald J, Fritze H (2008) High-temperature electrical conductivity and electro-mechanical properties of stoichiometric lithium niobate. Diffusion Fundament 8:6–1
91. Epelbaum BM, Nagata S, Bickermann M, Heimann P, Winnacker A (2007) Development of natural habit of large free-nucleated ALN single crystals. Physica Status Solidi B Basic Solid State Phys 244(6):1780–1783
92. Patel ND, Nicholson PS (1990) High-frequency, high-temperature ultrasonic transducers. NDT Int 23(5):262–266
93. Jacobs K, Hofmann P, Klimm D, Reichow J, Schneider M (2000) Structural phase transformations in crystalline gallium orthophosphate. J Solid State Chem 149(1):180–188
94. Krempl P (1997) Quartz homeotypic gallium orthophosphate: a new high-tech piezoelectric crystal. Ferroelectrics 202(1):65–69
95. Krispel F, Reiter C, Neubig J, Lenzenhuber F, Krempl PW, Wallnöfer W, Worsch PM (2003) Properties and applications of singly rotated $GaPO_4$ resonators. IEEE Int Freq Contr Symp 17:668–673
96. Chai B, Lefaucheur JL, Ji YY, Qiu H (1998) Growth and evaluation of large size LGS ($La_3Ga_5SiO_{14}$), LGN ($La_3Ga_5,Nb_{0,5}O_{14}$) and LGT ($La_3Ga_{5,5}Ta_{0,5}O_{14}$) single crystals. In: Proceedings of the 1998 IEEE international frequency control symposium, Crystal Photonics Inc., Sanford, pp 748–760
97. Shimamura K, Takeda H, Kohno T, Fukuda T (1996) Growth and characterization of lanthanum gallium silicate $La_3Ga_5SiO_{14}$ single crystals for piezoelectric applications. J Crystal Growth 163(4):388–392
98. Zhang S, Fei Y, Chai BHT, Frantz E, Snyder DW, Jiang X, Shrout TR (2008) Characterization of piezoelectric single crystal $YCa_4O(BO_3)_3$ for high temperature applications. Appl Phys Lett 92(20):202905-1–202905-3

99. Perloff A (1956) Temperature inversions of anhydrous gallium orthophosphate. J Am Ceram Soc 39(3):83–88
100. Hirano S, Kim P, Orihara H, Umeda H, Ishibashi Y (1990) Dielectric properties of hydrothermally grown gallium orthophosphate single crystals. J Mater Sci 25(6):2800–2804
101. Krempl P, Voborsky G, Posch U, Wallnöfer W (1994) Hydrothermal process for growing large crystals or crystal layers. US Patent 5,375,556
102. Elam JW, Pellin MJ (2005) $GaPO_4$ sensors for gravimetric monitoring during atomic layer deposition at high temperatures. Anal Chem 77(11):3531–3535
103. Thanner H, Krempl PW, Wallnöfer W, Worsch PM (2002) $GaPO_4$ high temperature crystal microbalance with zero temperature coefficient. Vacuum 67(3–4):687–691
104. Haines J, Cambon O, Prudhomme N, Fraysse G, Keen D, Chapon L, Tucker M (2006) High-temperature, structural disorder, phase transitions, and piezoelectric properties of $GaPO_4$. Phys Rev B 73(1):14,103
105. Barz RU, Grassl M, Gille P (2001) Study of anisotropic effects in hydrothermal growth of gallium orthophosphate single crystals. Ann Chim Sci Mat 26:95–98
106. Cambon O, Yot P, Balitsky D, Goiffon A, Philippot E, Capelle B, Detaint J (2001) Crystal growth of $GaPO_4$, a very promising material for manufacturing BAW devices. Ann Chim Sci Mater 26:79–84
107. Jacobs K, Hofmann P, Klimm D (2002) OH impurities in $GaPO_4$ crystals: correlation between infrared absorption and mass loss during thermal treatment. J Cryst Growth 237–239:837–842
108. Jacobs K, Hofmann P, Reichow J (2001) Physico-chemical aspects of the hydrothermal growth of $GaPO_4$. Ann Chim Sci Mater 26:85–90
109. Mill B, Pisarevsky Y (2000) Langasite-type materials: from discovery to present state. In: Proceedings of the 2000 IEEE/EIA international frequency control symposium and exhibition, 2000. Kansas City, MO, USA, pp 133–144
110. Fritze, Holger: High-temperature piezoelectric crystals and devices. J Electroceram 26(1–4):122–161
111. Schulz M, Fritze H (2008) Electromechanical properties of langasite resonators at elevated temperatures. Renew Energy 33(2):336–341
112. Fritze H, Tuller H (2001) Langasite for high-temperature bulk acoustic wave applications. Appl Phys Lett 78(7):976–977
113. Yu F, Zhao X, Pan L, Li F, Yuan D, Zhang S (2010) Investigation of zero temperature compensated cuts in langasite-type piezocrystals for high temperature applications. J Phys D Appl Phys 43:165,402
114. Zhang S, Frantz E, Xia R, Everson W, Randi J, Snyder DW, Shrout TR (2008) Gadolinium calcium oxyborate piezoelectric single crystals for ultrahigh temperature (>1000°C) applications. J Appl Phys 104:084–103
115. Sauerbrey G (1959) Verwendung von Schwingquarzen zur Wägung dünner Schichten und zur Mikrowägung. Zeitschrift für Physik A 155(2):206–222
116. Benes E (1984) Improved quartz microbalance technique. J Appl Phys 56:608–626
117. Martin B, Hager H (1989) Velocity profile on quartz crystals oscillating in liquids. J Appl Phys 65:2630
118. Berlincourt DA, Curran D, Jaffe H (1964) Physical acoustics, principles and methods. In: Piezoelectric and piezomagnetic materials and their function in transducers, vol 1–Part A, Chap. 3. Academic, pp 169–270
119. Ikeda T (1990) Fundamentals of piezoelectricity. Oxford University Press, Oxford
120. Tiersten HF (1969) Linear piezoelectric plate vibration. Plenum
121. Fritze H (2011) High-temperature bulk acoustic wave sensors. Meas Sci Technol 22:012,002
122. Wohltjen H (1984) Mechanism of operation and design considerations for surface acoustic-wave device vapor sensors. Sens Actuators 5(4):307–325
123. Richter D, Sakharov S, Forsén E, Mayer E, Reindl L, Fritze H (2011) Thin film electrodes for high temperature surface acoustic wave devices. Procedia Eng 25:168–171

124. Hornsteiner J, Born E, Fischerauer G, Riha E (1998) Surface acoustic wave sensors for high-temperature applications. In: Proceedings of the 1998 I.E. international frequency control symposium, 1998. Pasadena, CA, USA, pp 615–620
125. da Cunha M, Moonlight T, Lad R, Frankel D, Bernhard G (2008) High temperature sensing technology for applications up to 1000°C. In: Proceedings of the IEEE sensors 2008. Beijing, China, pp 752–755
126. Narine SS, Slavin AJ (1998) Use of the quartz crystal microbalance to measure the mass of submonolayer deposits: Measuring the stoichiometry of surface oxides. J Vac Sci Technol A16:1857–1862
127. Richter D, Schulz M, Sakharov S, Davis ZJ, Fritze H (2013) Surface acoustic wave devices: materials stability in harsh environments. In: MRS proceedings, Boston, Massachusetts, vol 1519
128. Thiele J (2006) High temperature LGS SAW gas sensor. Sens Actuators B Chem 113(2):816–822
129. Zheng P, Chin TL, Greve D, Oppenheim I, Malone V, Cao L (2011) High-temperature langasite SAW oxygen sensor. IEEE Trans Ultrason Ferroelectr Freq Control 58(8):1538–1540
130. Moos R (2005) A brief overview on automotive exhaust gas sensors based on electroceramics. Int J Appl Ceram Technol 2(5):401–413
131. Fleischer M, Pohle R, Wiesner K, Meixner H (2005) Soot sensor for exhaust gases. In: Eurosensors conference XIX, 2005, vol 1. Barcelona
132. Tuller HL, Nowick AS (1979) Defect structure and electrical properties of nonstoichiometric CeO_2 single crystals. J Electrochem Soc 126:209–217
133. Richter D, Fritze H (2009) Selectivity improvement of high-temperature resonant gas sensors using micromachined membrane arrays. In: Proceedings sensor and test conference Nuremberg, Germany
134. Cachau-Herreillat D, Bennazha J, Goiffon A, Ibanez A, Philippot E (1992) X-ray, DTA and crystal growth investigation on $AlPO_4$–$GaPO_4$ and $AlPO_4$–$AlAsO_4$ systems. Eur J Solid State Inorg Chem 29:1295–1307
135. Muraoka Y, Kihara K (1997) The temperature dependence of the crystal structure of berlinite, a quartz-type form of $AlPO_4$. Phys Chem Miner 24(4):243–253
136. Strassburg M, Senawiratne J, Dietz N, Haboeck U, Hoffmann A, Noveski V, Dalmau R, Schlesser R, Sitar Z (2004) The growth and optical properties of large, high-quality AlN single crystals. J Appl Phys 6:5870–5876
137. Ambacher O, Brandt MS, Dimitrov R, Fischer RA, Miehr A, Metzger T, Stutzmann M (1996) Thermal stability and desorption of group III nitrides prepared by MOCVD. J Vac Sci Technol 14:3532–3542
138. Kim K, Zhang S, Huang W, Yu F, Jiang X (2011) $YCa_4O(BO_3)_3$ (YCOB) high temperature vibration sensor. J Appl Phys 109(12):126,103
139. Yu F, Zhang S, Zhao X, Yuan D, Wang Q, Shrout TR (2010) High temperature piezoelectric properties of yttrium calcium oxyborate single crystals. Phys Status Solidi RRL 4:103–105
140. Scott H (1975) Phase relationships in the zirconia-yttria system. J Mater Sci 10(9):1527–1535
141. Ishibashi K, Kashima T, Asada A (1993) Planar type of limiting current oxygen sensor. Sens Actuators B Chem 13(1–3):41–44
142. Saji K, Kondo H, Takahashi H, Futata H, Angata K, Suzuki T (1993) Development of a thin-film oxygen sensor for combustion control of gas appliances. Sens Actuators B Chem 14(1–3):695–696
143. Hoshino K, Peterson NL, Wiley CL (1985) Diffusion and point defects in $TiO_{2\text{-}x}$. J Phys Chem Solid 46(12):1397–1411
144. Ohly C, Hoffmann-Eifert S, Guo X, Schubert J, Waser R (2006) Electrical conductivity of epitaxial $SrTiO_3$ thin films as a function of oxygen partial pressure and temperature. J Am Ceram Soc 89(9):2845–2852

Insect Olfaction as a Natural Blueprint of Gas Sensors?

Bernhard Weißbecker and Stefan Schütz

Abstract Biologically inspired sensory solutions utilize highly developed organs of perception that are evolutionary tuned towards compounds correlated to ecological functions. After millions of years of “survival of the fittest” insects, e.g., are trained to detect specific compounds that serve reliably as cues to find hosts and mating partners, or to avoid enemies and competitors. The multitude of insect species (>1,000,000) and their ecological interactions provide a vast range of possible biosensors based on natural sensory systems. Also biomimetic approaches can lead to various applications for tracking and monitoring of chemical compounds in environmental and industrial processes. Biosensors utilize organic components (e.g., proteins, cells, tissues, or organisms) within a technical appliance. The combination of technical devices with biological sensory units provides detectors which are superior to mere technical solutions in selectivity and sensitivity. For instance, by integrating insect antennae in the gate of a field-effect transistor (BioFET), volatile trace compounds are directly detectable in the ppb range. The complex biochemical detection system in the antenna of the insect serves as a selective detector for compounds that provide vital information about its environment. Thus, knowing the selectivity and sensitivity pattern enables us to design biomimetic semiconductor sensors utilizing the evolutionary experience of insects in combination with reliability and ruggedness of technical semiconductor gas sensors for highly specific gas-sensing tasks.

Keywords Biomimetic sensor, Biosensor, Electroantennography, Insect olfaction, Semiconductor gas sensor, Smoke detection, Volatile organic compounds

---

B. Weißbecker and S. Schütz (✉)
Department of Forest Zoology and Forest Protection, Georg-August University of Göttingen,
Büsgenweg 3, 37077 Göttingen, Germany
e-mail: stefan.schuetz@forst.uni-goettingen.de

C.-D. Kohl and T. Wagner (eds.), *Gas Sensing Fundamentals*,
Springer Series on Chemical Sensors and Biosensors (2014) 15: 47–66
DOI 10.1007/5346_2013_54,

Contents

1 The Key: Observation of Insect Behavior

1.1 Introduction to Insect Behavior

Simply observing animals in nature is often a complex task. Natural behaviors are typically complex composites of distinct subroutines. Differentiating among the behaviors and determining which stimuli elicit which behavior is in many cases challenging. Insects, however, in spite of their minute size, display a wide span of behaviors. Most of them are stereotype and executed in an obligate manner on the presentation of the adequate stimulus. Even a small creature like the honeybee shows a behavioral repertoire of about 60 distinct and recognizable behaviors [1]. Additionally, insects comprise a highly diverse group of organisms and have proven particularly rewarding models in studying olfaction. Insects decode their chemical environment, the peripheral olfactory system adapts evolutionary, and in turn mirrors the adaptive forces acting on the system over evolutionary time [2].

Insects show complex behaviors that are composed of behavior components which are elicited, maintained, or terminated by environmental (external), interindividual (external), and intraindividual (internal) stimuli. Appetitive behavior is such a behavior component that is governing search for vital resources like food, mating partners, and sites for laying eggs.

Most of the time, appetitive behavior is guided by sensors measuring different sensory modalities as olfaction, vision, humidity, temperature, tactile, and gustatory senses. This warrants a multimodal sensory integration [3]. However, in this contribution, we focus on the olfactory sense which is closest related to the tasks of gas sensors. From cybernetic point of view, an appetitive controller for food finding is composed of three main subsystems: chemotaxis, feeding arousal, and integrating behavior controls [4]. Chemotaxis is an innate behavioral response by an organism to an external directional gradient of stimulus intensity, that is, a response to a chemical concentration gradient. Insects use their antennae to detect

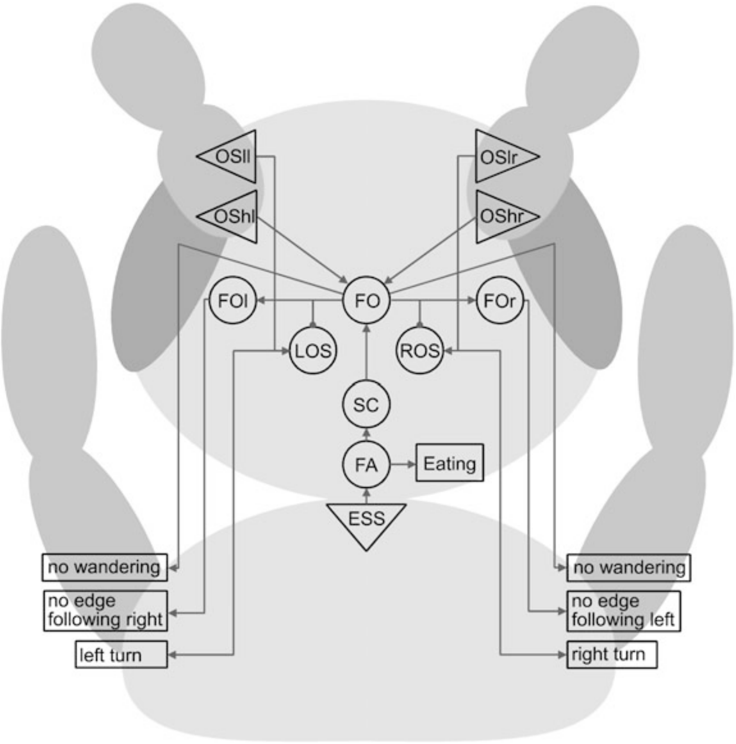

Fig. 1 Cybernetic layout for an appetitive controller. *OSlr* odor sensor low right, *OShr* odor sensor high right, *FO* following odor, *FOl* following odor left, *LOS* left odor strength, *SC* search command, *FA* feeding arousal, *ESS* energy status sensor (from www.mindcreators.com/AppetitiveController.htm, simplified)

quality, quantity, and gradient direction of volatile chemical compounds. Inducers of locomotion towards increasing steps of concentrations are considered as attractants, while repellents result in moving away from the source. Feeding arousal can briefly be described as “hunger” being an important internal subsystem relating current demand of the organism to movement behavior. The final behavior of an insect depends on many internal and external variables, and hunger is one of the most important internal ones. Next, different behaviors are mutually exclusive. Performing random wandering for untargeted exploration of the environment at the same time with targeted movement towards a close food source are not compatible behaviors. Even edge-following behavior which is important to go around possible obstacles between insect and odor source has to be modulated appropriately in order to reach the odor source. Behavior integration neurons provide control when one behavior is active or not (Fig. 1).

Before the insect can feed, it must first be able to find food. The purpose of the chemotaxis control neurons is to orient the insect so that it moves towards a food source it can smell. Thus, the antennal odor sensor neurons are critical for chemotaxis. In our cybernetic model, these neurons are the odor sensor neuron low left (OSll), odor sensor neuron low right (OSlr), the odor sensor neuron high left (OShl), and the odor sensor neuron high right (OShr). The low and high in the odor sensor names refers to the gain which controls the sensitivity of that antenna. An odor sensor with a very high gain will be able to detect smaller quantities of volatile compounds and will thus be able to detect food at a much longer distance (long-range orientation). However, since it has such a high gain, it also means that as it gets closer to the food, the high gain sensors will saturate and the animal will no longer be able to get any useful orientation information from them. Low gain sensors will not be able to detect food unless they are very near to it. But it also means that they will be able to guide the insect even when they are close to immediate contact with the food (close range orientation). The outputs from these odor sensor neurons are fed into left odor strength (LOS) and right odor strength (ROS) neurons. Odor sensors from the left side excite the LOS neurons and inhibit the ROS neurons, and chemical sensors from the right side excite the ROS neurons and inhibit the LOS neurons. This performs a comparison of the odor strength values that are coming from left and right side that can be used to determine which way to turn in order to orient the insect towards the food.

This simplified model example of insect food-finding behavior displays the impact of properties of the antennal odor sensors on behavioral outcome. In turn, observation of insect behavior, especially attraction towards specific odor sources, can provide valuable clues for sophisticated sensor properties.

1.2 Example **M. acuminata, M. atrata***: Long-Range Orientation to Forest Fires*

Already at the beginning of the twentieth century, firemen reported on black beetles that flew in masses towards burning forests, hampering efforts to extinguish fires, and even attacking firemen [5]. Reports on this unusual pyrophilic (“fire-loving”) behavior of the black jewel beetle *Melanophila acuminata* included speculation that the beetle might be able to orientate towards a forest fire through olfactory means [6].

Pyrophilic beetles depend on forest fires for their reproduction. The adult beetles are living inconspicuously in forests with high dead wood content mostly with a predatory lifestyle. At high temperatures and low air humidity, they show an increased flight and searching behavior. Once picking up volatile organic compounds characteristic for forest fires, such insects approach ongoing fires and invade the burnt area immediately after fire. For long-range orientation towards a fire, these insects have special sensors for smoke [7] and infrared radiation [8]. Whereas the olfactory receptors for smoke are located on the antennae, the infrared receptors are housed in sensory organs, which can be found on the thorax or on the abdomen. Two genera of jewel beetles (Buprestidae) can be classified as

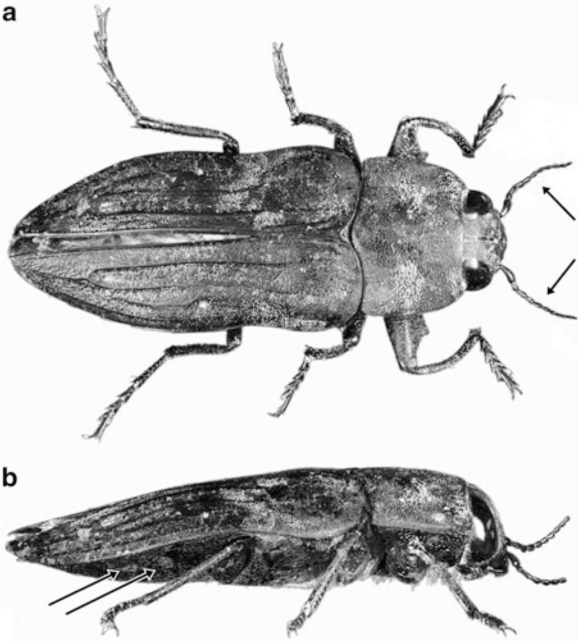

Fig. 2 One example for pyrophilic jewel beetles. The black fire beetle (*Merimna atrata*) occurring in Australia. (**a**) *Top view* antennae marked with arrows, (**b**) *side view* infrared receptors marked with arrows

pyrophilous: more than ten species of the *Melanophila* genus, which are distributed nearly all over the northern hemisphere, and the buprestid beetle *Merimna atrata* (Fig. 2), which is endemic to Australia [9]. Despite the fact that there is some debate about how these beetles are able to approach forest fires over distances of more than 30 km [10, 11], measurements with a biosensor on the basis of intact insect antennae of *M. acuminata* showed significant responses to wood smoke of a 5 m^3 heap of burning wood logs in more than 2 km distance [12], and analogous measurements with intact insect antennae of *M. atrata* showed significant responses to wood smoke of a 15 ha eucalypt forest fire in more than 20 km distance, suggesting a key role of olfaction in long-range attraction to forest fires.

Despite the fact that *Melanophila* and *Merimna* show a similar behavior and belong to the same family of jewel beetles, their infrared receptors are totally different from each other, suggesting that this specialization to fire developed independently in both genera from the northern hemisphere and from Australia [11].

1.3 Example **M. acuminata, M. atrata***: Close-Range Orientation on Burnt Forest Sites*

Arriving on the freshly burnt area, the males of both genera often stay close to burning or smoldering wood looking for females of their species, which are attracted to the fire, too. Infrared receptors might serve here for detecting sites that are not too hot to alight [13]. After mating, the females deposit eggs under the bark of the freshly burnt trees. Only there, the wood-boring larvae of *Melanophila* and *Merimna* can develop by feeding in the weakened and preheated wood of fire damaged trees [14]. Consequently, fire detection is the compulsory precondition for the survival of all these pyrophilous insect species. They are not only able to detect fires from big distances, moreover, they are able to discriminate trees that are charred to the core from trees that still contain preheated, but uncharred wood as substrate for their larvae. Egg deposition behavior was observed exclusively on trees with an uncharred wood core. Consequently, the young larvae started to feed in the transition region between charred and unaffected wood, providing preheated wood with partially depolymerized cellulosis which is easier to digest like in a natural cooking pot. This kind of information is not retrievable by vision or infrared detection but only by the detection of volatile organic compounds specifically generated by early stages of thermal decomposition of wood leaving the charred trunk through thermal shrinking fissures in the wood.

2 The First Step: Analysis of Olfaction by Trace Analysis and Electrophysiology

2.1 Trace Analysis of Smoke Volatiles

In order to analyze traces of airborne volatile compounds, air has to be sampled in a reproducible manner. If the volatile target compounds have a boiling point well below ambient temperature, like permanent gases, they can be sampled in a defined enclosure, like a glass flask or syringe, as a gas sample. If the volatile target compounds have a boiling point within the range or above ambient temperature, direct gas samples will be depleted by adsorption to the walls of the enclosure. Therefore, most volatile organic compounds have to be sampled on an absorbent and have to be desorbed prior to analysis by a gas chromatograph (GC). Moreover, volatile compounds are often present only in high dilutions so that most of the time a pre-concentration is necessary. Most sampling methods use an active sampling approach, sucking a defined volume of air into an enclosure or over an absorbent serving as a trap. Common absorption materials provide a huge internal surface like charcoal or the polymer Tenax® [15]. When sampling smoke volatiles, aerosol particles have to be taken into account. They are prone to distort sampling results and have to be kept out of the volatile samples by special particle filters [16]. Another way to circumvent distortions by airborne particulate matter is to use passive sampling techniques like solid phase microextraction (SPME) suffering the disadvantage of an ill-defined sample volume [17].

The most widespread set-up to analyze volatile organic compound samples is a gas chromatograph coupled to a detector unit allowing to identify and to quantify the separated compounds in a mixture of volatiles. First, the volatile sample has to be transferred into the GC by an injector. In case of direct gas sample, injection or direct headspace techniques [18] can be applied. In case of compounds trapped on an adsorbent, the sample has to be eluted by a solvent (chemodesorption) or evaporated into an inert gas flow by elevated temperatures (thermo-desorption) [17]. After injection the compounds are moved by the inert carrier gas through the GC column. Interactions with the column coating determine which compound is retained longer or which compound is eluting earlier. The retention time of a specific compound depends on geometry and chemistry of the column, carrier gas and carrier gas flow, temperature during the separation, and the identity of the compound. Identification of a compound by retention time requires a separation of aliquots of the sample on at least two different columns. Having passed the column, the compounds can be detected by different detectors like the flame ionization detector (GC-FID) essentially detecting every compound that is combustible in a hydrogen-oxygen flame or like the mass spectrometric detector (GC-MS) that allows structural elucidation of the eluting compounds [19].

2.2 Electroantennographic Analysis of Volatiles

The biochemical transduction pathway in insect olfaction generates membrane depolarizations in olfactory neurons which can be detected as a summed electroantennographic response of the insect antenna. Although intensive research has been conducted on understanding the biochemical interactions involved in insect olfaction, the interactions are not as yet fully understood. Thus, we shortly summarize the current state of knowledge: once an odor plume reaches the airspace around an insect, it enters nanopores in the cuticle of an olfactory sensillum. The cuticle covers the antenna in order to prevent mechanical damage and desiccation of the sensory neurons housed in the sensillum. These wax-filled nanopores allow volatile organic compounds to diffuse into the sensillum lymph that surrounds the neurons inside the sensillum. This kind of enriching unpolar volatiles in cuticular wax provides a pre-concentration of the volatiles enabling insect antennae to perceive volatiles reliably in air and in water. So-called odorant-binding proteins (OBPs), first discovered by Vogt and Riddiford as pheromone-binding proteins (PBPs) [20], selectively bind and transport the mostly hydrophobic odor compounds through the hydrophilic sensillum lymph to the olfactory receptor contained in the neuronal membrane (Fig. 3).

It is proposed that due to the three-dimensional tertiary structure of these monochain proteins, a binding cavity is formed in which functional groups of amino acids are exposed to interact with the peculiar structure and charge distribution of the odor molecule [21]. The lipophilic odor forms a complex with the OBP and can diffuse through the aqueous sensillum lymph towards the dendrite membrane. In the dendrite membrane, the odorant receptor (OR) can form a spatial functional unit with an ion channel [22]. Upon contact of this OR-ion-channel unit with the OBP-odor complex, the ion channel opens allowing an influx of potassium ions into the olfactory neuron causing a dose-dependent depolarization of the olfactory

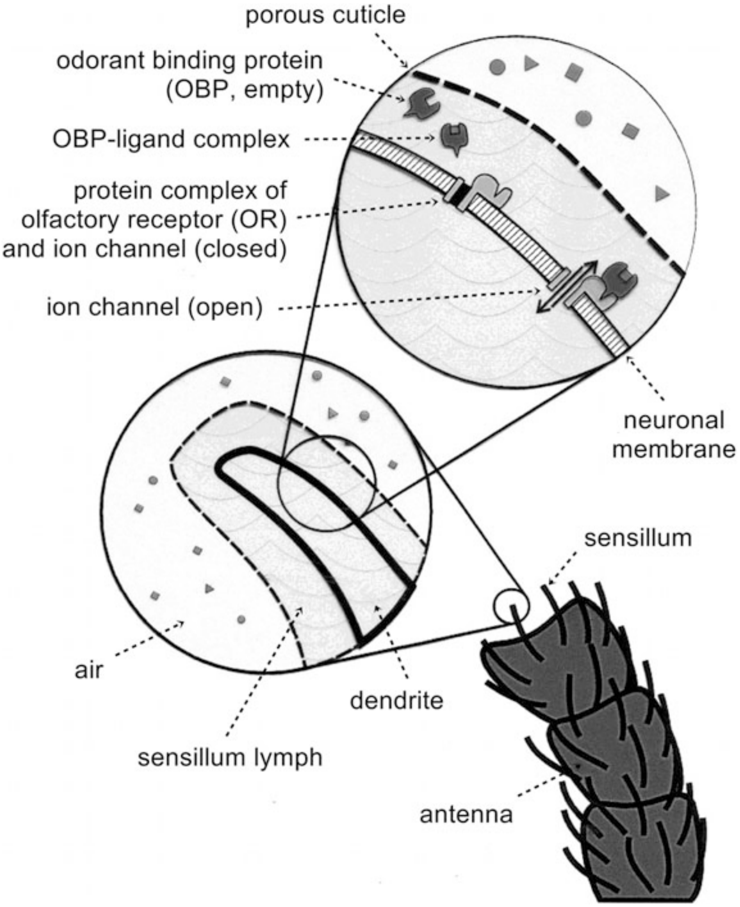

Fig. 3 The functional concept of insect olfaction: odorant receptor proteins (OR) linked to ion channels are embedded in the neuronal membrane of a dendrite inside a sensillum on the antenna. Contact with a complex formed by an odorant-binding protein (OBP) and an odor ligand triggers ion influx, thus causing depolarization of the olfactory neuron, modified from [12]

neuron. A summation of these depolarizations over the antenna can be recorded as EAG signal (Fig. 4). When the odor is present in a detectable concentration, a sufficient number of cascades give rise to membrane depolarizations in different dendrites of one neuron summing up to exceed the neuronal activation threshold. This will lead to an action potential from the sensory neuron which is transferred into the insect central nervous system, where it is further processed into odor perception [23]. Thus, peripheral olfactory transduction is the basis for the sensitivity and selectivity of odor perception, both of single odorant compounds and of odorant mixtures [24].

As the adaptation of the olfactory sense in insects to the distinctive demands for the single species has gone through millions of years of selection of the fittest, the

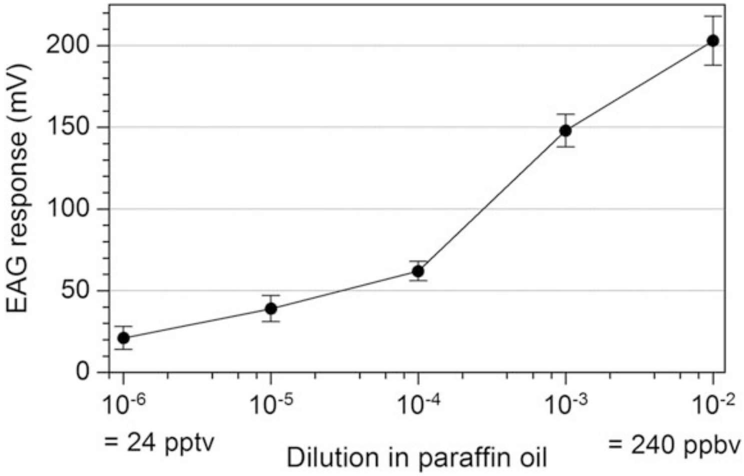

Fig. 4 Dose-response curve of an antenna of *Melanophila acuminata* to guaiacol. The odor dilutions are provided by air in equilibrium with solutions of the odor compound in paraffin oil in decadic dilution steps. The vapor pressure of guaiacol is modified by diluting the compound in paraffin oil according to Henry's law yielding the outlined equilibrium concentrations of guaiacol in air. The EAG response of the antenna exposed to a 0.5 s stimulus of odor laden air is amplified by a factor of 100

resulting compounds can be regarded as marker compounds in the ecological interaction between the insect and its environment. A combination of trace analysis, like gas chromatography mass spectrometry with a parallel electroantennographic detection based on insect antennae resulting in one GC-MS/EAD setup [25], allows the identification of single compounds that are selectively traceable by an insect via scent (setup see Fig. 5, example chromatogram see Fig. 6).

If compounds released by burning pine wood are collected by a charcoal trap, chemodesorbed from the trap by a solvent and injected into the GC-MS/EAD setup, the complex mix of thermal decomposition compounds is separated by the gas chromatographic column and guided in parallel to the mass spectrometer and an EAG equipped with the antenna of *M. acuminata*. Peak formation in the EAG trace marks out compounds that are detected by the insect. Simultaneous peak formation allows the identification of electrophysiologically active compounds by mass spectrometric analysis.

The beetle antenna shows a high sensitivity to different terpenes. *M. acuminata* is able to use them as marker compounds for coniferous trees, the preferred host tree of the beetle. Moreover, the beetle antenna shows a high sensitivity to guaiacol derivatives emerging from the pyrolysis of wood lignin. This enables the beetle to differentiate between grass fires only burning the herbal layer and full forest fires. Only the latter will provide sufficiently damaged trees for its offspring. The relation of guaiacol and substituted guaiacols allows the beetle to assess the fraction of smoldering wood logs and, thus, potential space for egg deposition. Compounds released by forest fires and detected by the antenna of its Australian relative,

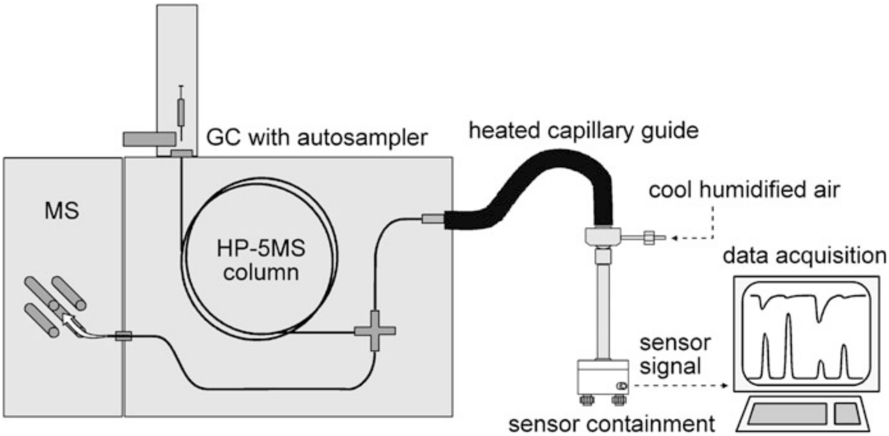

Fig. 5 Schematic of a gas chromatograph coupled in parallel to a mass spectrometer and an electroantennographic detector (GC-MS/EAD), modified from [24]

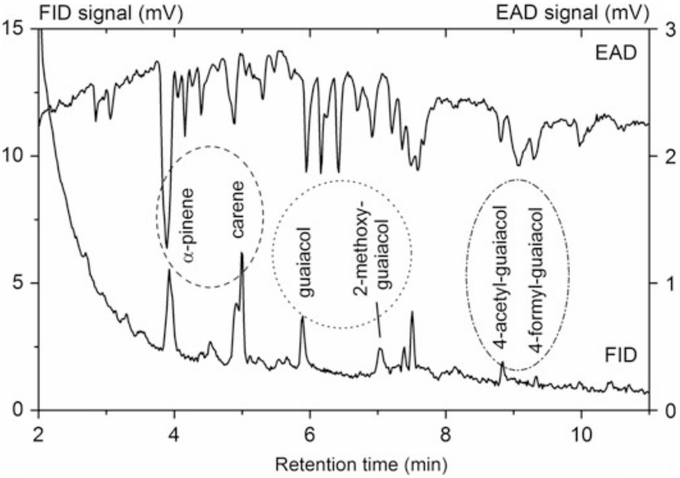

Fig. 6 Result of combined gas chromatography/flame ionization detection (GC-FID/EAD) utilizing the antenna of *Melanophila acuminata*. Simultaneous peak formation allows the identification of electrophysiologically active compounds, in this case guaiacol derivatives and terpene compounds. The differently dashed circles designate different groups of bioactive volatile compounds: marker compounds for wood species burning, marker compounds for burning wood, marker compounds for smoldering wood, modified from [7].

M. atrata can be grouped in the same way, and again, the guaiacol derivatives are used as marker compounds for attractive full forest fires. The utilization of the same kind of marker compounds despite separate development suggests that the guaiacol compounds might provide a robust set of marker compounds for wood smoke detection.

The striking performance of insect olfaction in distinctively responding to ecologically relevant compounds has been verified by many studies [26–29] and can inspire a wide range of biosensor applications. As insect species appear in most ecosystems all over the world and are adapted to many, often very distinct olfaction-based interactions with their environment, the amount of potentially usable marker compounds for biosensors based on insect olfaction is extremely large. The applicability of these marker compounds for economic purposes implies that biodiversity of insects can provide a considerable storehouse of evolutionary improved sensor designs.

3 The Second Step: Utilization of Insect Antennae as Biosensors

3.1 Introduction to Biosensors

One of the main drawbacks of conventional analytical tools is that most of them are not suitable for online measurements during field analysis. These methods are highly sensitive, accurate, and provide reproducible values with suitable detection limits. Nonetheless, they are expensive, large in size, require highly skilled personnel to operate, and are not rugged for field measurements. Therefore, the quest for designing sensitive and selective sensors [30] has now become a major topic in modern research. Miniaturization [31] is important in order to make them suitable for online applications [32]. Biosensors promise to meet this need for small online measuring devices.

Basically, a biosensor is a measuring device that traces chemical compounds, organisms, or physical quantities by spatially and functionally combining a biological component with a physical or chemical transducer [33, 34]. This definition suggests a wide field of possible applications, as it neither refers to any peculiar biological components nor does it describe any concrete physical quantities. Actually, the field of possible realizations of biosensor concepts is quite extensive.

The integrated biological component could, for instance, be an organic molecule, like an enzyme or an antibody. These biochemical structures perform distinctive tasks in organisms and therefore interact with only a selected number of other chemical compounds that occur sometimes only in low concentrations. This selectivity can be utilized in a sensor concept that responds selectively and sensitively towards distinct compounds. The biocomponent can also be an organelle, cell, organ, or a complete organism (Fig. 7).

As a technological part of the sensor, a transducer is defined by its function and not by its mode of operation. Its task is to convert the specific biological/chemical

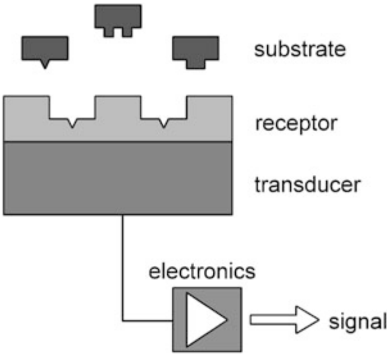

Fig. 7 Functional principle of a biosensor (simplified), modified from [12]

interaction of the biocomponent and an analyte into a physical/chemical response with a measurable output, generally electrical signals. One of the first applications of a biosensor published was a system to measure the concentration of glucose in blood [35]. Here, the enzyme glucose oxidase was immobilized with a dialysis membrane on a platinum electrode. The enzyme metabolizes glucose to gluconolactone while the produced hydrogen is transformed to hydrogen peroxide under consumption of oxygen. Hydrogen peroxide is detected by an amperometric electrode. Alternatively, the consumption of oxygen can be recorded. The biocomponent is in this case the dissolved glucose oxidase and the transducer a platinum oxygen electrode. A permeable membrane keeps the solution around the electrode.

Biosensors can be classified by the type of the used biocomponent, the stage of development (generation), or the type of transducer.

Enzymes (enzyme sensors) and antibodies (immunosensors) are utilized as biocomponents in biosensors where the substrate is detected by docking on a selective protein. One can differentiate between catalytic sensors and affinity sensors depending on whether the formation of a protein/substrate complex yields a metabolic product or not. A microbial sensor utilizes living cells, for instance, coupled to an oxygen electrode that measures respiration processes of the cell by means of the oxygen uptake. This utilization of living cells or tissue opens new perspectives for biosensor applications. However, it also presents a technical challenge to cultivate functional cells on a transducer and to obtain a sufficient storage protocol for the biosensor [36]. Moreover, biological receptors like complete sensing organs, for instance, insect antennae can be used taking advantage of the biological integration of biological receptor and biophysical transduction unit, leaving only the electronic part to the technological side.

The above mentioned glucose sensor of Clark and Lyons uses a membrane in order to immobilize enzymes on an electrode. This setup is also designated as a biosensor of the first generation [33]. Enhancements to this technique are sensors where the biochemical receptors are directly bound to the surface of the transducer (second generation) or immobilized directly on an electronic control device, for instance a transistor (third generation). In particular, field-effect transistors

(FETs) are convenient because of their high input impedance. The combination of a FET with a biocomponent, for instance an insect antenna, is referred to as a BioFET [37, 38].

The most important types of transducers are electrochemical, optical, mass sensitive, or thermal sensors [39]. An example of electrochemical transduction is the amperometric detection especially used for catalytic enzyme reactions. Optical sensors can utilize the absorption, fluorescence, or bioluminescence of molecules and organisms as input.

One technical realization of mass sensitive sensors is the piezoelectric sensor by modifying the surface of a quartz oscillator with an enzyme or antibody. When biocomponents from the surroundings attach to its surface, the total mass of the crystal changes, and due to the Sauerbrey equation, the oscillating frequency of the quartz also changes. Thermal sensors detect the production or consumption of heat during biochemical reactions.

Conventional methods of instrumental chemical analysis, especially GC-MS, require high laboratory costs. In this context, biosensors offer approaches for improved methods that allow real-time on-site analytics [40].

To detect, for instance, a fire marker compound in the woodland, standard methods require sample collection of several hours from ambient air. GC-MS analysis is then performed with a throughput of 20 samples maximum per day. Therefore, the manual labor for sample preparation and the operation of the instrumental setup is very cost intensive, restricting these conventional methods to the survey of a limited number of samples.

A portable measuring device without extensive sample preparation is needed to establish convenient applications for practical on-site use [39]. A biosensor with an appropriate selectivity can detect compounds directly in their matrix without pre-concentration or purification. This will inter alia enable the recording of data in a high spatial and temporal resolution in order to follow a concentration gradient and thereby, localize the source of smoke. However, biosensors provide less accurate quantification of compounds in comparison with conventional techniques of trace analysis.

3.2 A Biosensor on the Basis of Insect Antennae

The basic idea of a biosensor based on insect olfaction is to utilize the extremely high sensitivity and selectivity of olfactory receptors. The silk moth *Bombyx mori*, for example, is able to trace 1,000 molecules per second of the pheromone bombykol in one cubic centimeter of air [41]. This is equivalent to a 1-g sugar lump diluted within and distributed over the whole water volume of Lake Constance (Bodensee). However, this sensitivity is unrivalled yet and can’t be mimicked by technological gas sensors. Moreover, insect antennae display an evolutionary adaption of insect olfaction to the detection of marker compounds even in complex environmental conditions.

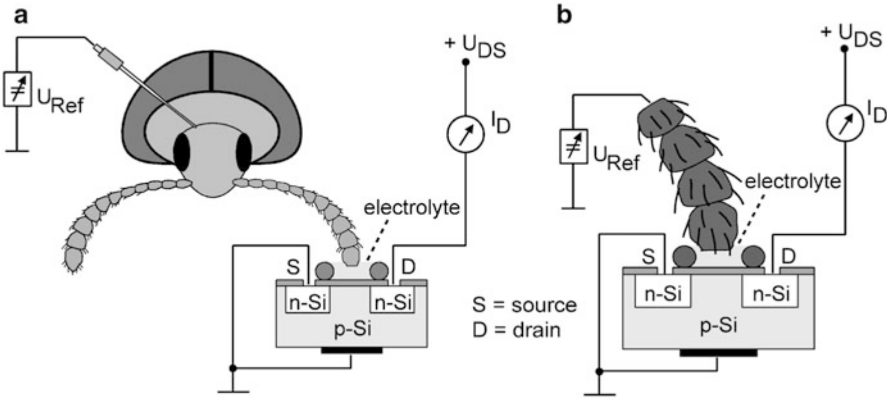

Fig. 8 BioFET hybrid consisting of an insect antenna and a field-effect transistor (FET) with intact pyrophilic beetle (**a**) and isolated antenna setup (**b**), respectively

The black jewel beetle *M. acuminata* can, for instance, detect the burnt scent of a single charred tree over a distance of several kilometers [7]. This striking performance is based on the extremely high sensitivity of the antenna of this insect for guaiacol compounds, reliably detecting guaiacol down to the low pptv (parts per trillion in volume) range (Fig. 4). Therefore, the combination of a highly specialized biochemically operating insect organ with a signal amplifying and processing electronic device can lead to a highly sensitive detection of organic trace compounds combined with a high time resolution in the atmosphere.

The utilization of an intact insect antenna as a biocomponent requires a mechanically and electrically stable junction while avoiding damage to the organ. Electrical and mechanical features of this hybrid device of an insect antenna joint to a field-effect transistor (Fig. 8) rendered this BioFET as particularly reliable [42, 43]. In the case of the “whole-beetle” setup, the antenna of a beetle was directly coupled to the gate of the FET via an electrolyte solution, whereas for the “isolated antenna” setup, it was removed from the beetle. The biochemical cascade inside the antenna finally leads to the formation of an electrical potential drop across the receptor’s cell membrane and thus, to a dipole potential over the whole antenna. The latter modulates the conductance of the FET channel between source and drain, inducing a distinct variation of the drain current I_D, which is dependent on the particular odor concentration [44].

The immanent miniaturization of the insect antenna as well as the miniaturization of the microelectronic part allows manufacture of biosensor circuits of the size of a 1C coin. Such sensor heads are deployable in portable biosensor systems to enable high-resolution data acquisition in situ. As distinctive example an application of biosensors on the basis of insect antennae in smoke detection is described below.

The first possible application that comes into mind is to use the biosensor for the same purpose as the beetles themselves, i.e., detecting forest fires. As laboratory and field experiments revealed, a biosensor on the basis of antennae of *M. acuminata* can detect a fire comprising of only a single tree over a 2-km distance and can be traced by the concentration gradient of smoke components and wind direction through a dense forest stand. Combining the high sensitivity and selectivity for marker compounds of fire with an identification of the kind of fire and the traceability of the source, a biosensor based on the antenna of *M. acuminata* can be a powerful on-site tool to be used as the first link in the fire-fighting chain.

Considering further possible applications of this kind of biosensor, it is important to keep in mind that it detects smoke components such as guaiacol compounds very sensitively and that these compounds originate from the pyrolysis of lignin, one of the basic constituents of wood. However, fossil wood (i.e., coal) contains lignin, too. Thus, combustion products of fossil wood (i.e., coal) can also be detected by the biosensor.

Combustion products of diesel fuel or gasoline do not elicit comparable signals.

This enables the design of a biosensor based on the antenna of *M. acuminata* to differentiate between compounds released by dangerous smoldering fires in coal storage units and frequently occurring background compounds, for example, originating from gasoline or diesel combustion engines. Thus, false alarms caused by engine exhausts can be avoided and a reliable fire tracking system could be based on the performance of the biosensor. However, the limited lifetime of the insect antennae poses a serious obstacle for the design of monitoring systems on the basis of this kind of biosensor. This kind of biosensor is most suitable for on-site applications like high sensitivity detection and track following nicely complementing classical analysis systems.

3.3 Biomimetic Approaches to Sensors on the Basis of Insect Olfaction

Evolutionary processes like selection with respect to efficiency of resource location force the development of highly reliable markers for specific resources. Especially challenging is the inherent high variability of natural sources mostly consisting of entities that do not want to be located.

Chemo-ecological examinations [45] and biosensor development [46] can yield compounds perceived and used by insects for resource location. Because of their short lifetime, biosensors are useful predominantly in on-site and source tracking applications. Monitoring applications have to use sensor technology with lifetimes of several years. Thus, solid-state sensors can be tuned to marker compounds used by insects in order to detect specific resources like burnt wood.

This biomimetic approach has to face several challenges:

- Sensitivity of insect antennae is much higher than of most solid-state sensors causing a restriction of possible applications. Biomimetic long-distance forest fire detection is not possible yet because of the high dilution of smoke volatiles into free atmosphere. However, indoor applications in storage units, buildings, and industrial facilities are possible because of the comparably low dilution of smoke volatiles in the limited air space.

- Selectivity of insect antennae is much higher than of most solid-state sensors. This issue can partly be resolved by an optimization of selectivity utilizing different novel solid-state sensor production techniques like doping and nanocasting and by sophisticated operation procedures like temperature cycling [47]. Moreover, the combination of several compound group specific sensors into an array can improve discriminating power of the solid state sensor system [48].
- Processing in insect brain has to be mimicked by data processing like neural network approaches and sophisticated chemometric methods [49].
- Natural resources to be detected by insects are not completely congruent with warning situations in urban or industrial environment. Thus, not every insect-marker compound is suitable as a marker compound for a technical process. For example, α-pinene, being released by leaves/needles during forest fires [7], is not suitable for smoldering fire early warning in lignite storage units because thermal decomposition products of lignite do not contain terpenes as typical resin compounds. In contrast, other marker compounds like guaiacol derivatives [50] are highly suitable compounds for smoldering fire early warning in lignite storage units. Boundary conditions of technical processes are not identical with the natural, biological environment of the insects. This can result in different interfering compounds. For example, high nitrous oxide concentrations prove to be problematic during detection by solid-state sensors used for early fire warning during an industrial wood particle drying process [50].

A consequential application that comes into mind is to design a biomimetic sensor for the same purpose as the biosensor in coal storage units, i.e., detecting smoldering coal, but on a monitoring basis. A biomimetic solid-state sensor array on the basis of the detection of insect marker compounds [50] has been reliably working for over five years now in several industrial lignite storage units.

Another application can be gleaned from the behavior of the pyrophilic beetle *M. acuminata* after having reached the freshly burned site. Female beetles lay their eggs on stems that were not completely destroyed by fire. To be able to locate an appropriate place for egg deposition, the beetle has to be able to distinguish between different stages of heated or burned wood tissue. This ability is based on the perception of marker compounds that correlate significantly to wood heating and the temperature of the wood beneath the bark. This set of marker compounds, when detected by a semiconductor gas sensor system, can be utilized for fire warning applications detecting wood fires before they show open flame. Such applications can be adapted to wood flake driers in the wood processing industry [51]. Reducing the varying water content of wood flakes (70–50%) down to 8–6% in order to glue and press them into boards requires a large energy input.

As the drying process progresses more efficiently at higher temperatures, it would be more efficient to dry the flakes just below the threshold of self-incension. Under production conditions, temperature is at a level that ensures fire safety by

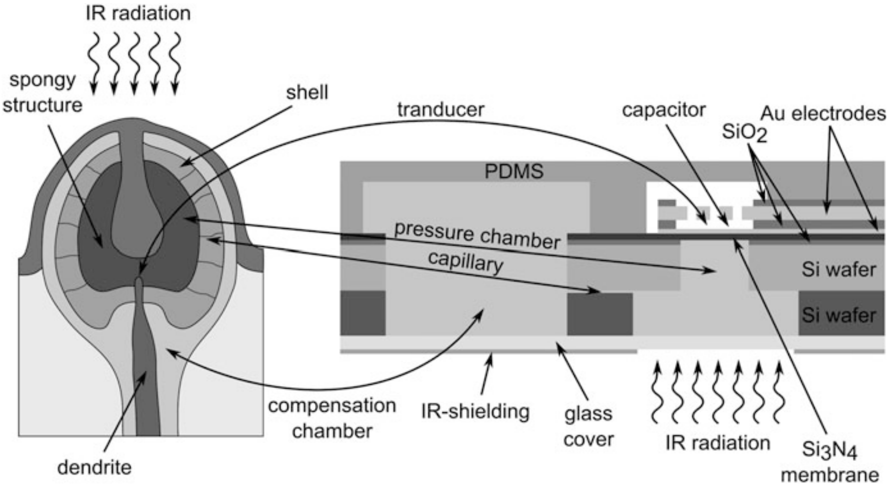

Fig. 9 Biomimetic approach to an uncooled IR sensor on the basis of IR perception by the beetle *M. acuminata*. *Left*: simplified cross section of the IR receptor in *M. acuminata*. *Right*: cross-section of the IR sensor on the basis of MEMS technology (not to scale). Modified from [52]

monitoring the air temperature and installing spark extinguishing systems. Monitoring marker compounds characteristic for heated wood just before self-incension would allow higher temperatures in wood flake driers without increasing the fire hazard. This confers the advantages of reducing energy consumption, avoiding potential loss of material due to fire, and avoiding damage due to the fire itself. As self-incension of sawdust stored in silos as a renewable energy source is one of the problems faced by modern energy plants, such systems could also be installed in biomass storage units. Moreover, fire early warning applications for wooden constructions, like warehouses and hotels are possible, whereas the relatively high-energy consumption of semiconductor gas sensors limits commercial viability in the private market.

Of course, biomimetic sensor approaches are not limited to insect olfaction. *M. acuminata* uses specialized infrared-sensing receptors based on a fluid-filled pressure cell. By absorbing IR radiation, the fluid heats up and expands, the receptor senses the resulting pressure increase using a mechanoreceptor. A biomimetic approach to this type of uncooled IR sensor using MEMS technology uses the deflection of a Si_3N_4 membrane having one electrode of a plate capacitor on top by the pressure increase inside the pressure cell (Fig. 9). A long and narrow channel connects the pressure cell to a compensation chamber.

This chamber is sealed by a thin and elastic PDMS membrane to the outside. The channel enables a slow transfer of fluid to the compensation chamber while the thin PDMS membrane maintains the pressure inside this chamber close to the ambient pressure, protecting the breaking of the Si_3N_4 membrane because of changing ambient pressure or temperature [52].

In technological applications combinations of sensors with different modalities as they occur in nature might be another field of biomimetic inspiration for meeting challenging requirements regarding dependability of sensor outputs.

Acknowledgments Funding by the BMBF for "Biosensors on the basis of insect olfaction" and "BioHot" is gratefully acknowledged. Funding by the Deutsche Forschungsgemeinschaft (DFG) for "Multidimensional EAG" is gratefully acknowledged.

References

1. Chittka J, Niven J (2009) Are bigger brains better? Curr Biol 19:R995–R1008
2. Hansson BS, Stensmeyr MC (2011) Evolution of insect olfaction. Neuron 72:698–711
3. Wessnitzer J, Webb B (2006) Multimodal sensory integration in insects – towards insect brain control architectures. Bioinsp Biomim 1:63–75
4. Mindcreators (2012) http://www.mindcreators.com/AppetitiveController.htm. Accessed 4 September 2012
5. Manee AH (1913) Observations on Buprestidae at Southern Pines, North Carolina (Coleop.). Entomol News 24:167–171
6. Evans WG (1964) Infra-red receptors in *Melanophila acuminata* DeGeer. Nature 202:211
7. Schütz S, Weißbecker B, Hummel HE, Apel K-H, Schmitz H, Bleckmann H (1999) Insect antenna as a smoke detector. Nature 398:298–299
8. Schmitz H, Bleckmann H, Mürtz M (1997) Infrared detection in a beetle. Nature 386:773–774
9. Schmitz H, Schmitz A (2002) Australian fire beetles. Landscope 1:36–41
10. Evans WG (2010) Reproductive role of infrared radiation sensors of *Melanophila acuminata* (Coleoptera: Buprestidae) at forest fires. Ann Entomol Soc Am 103:823–826
11. Schmitz H, Bousak H (2012) Modelling a historic oil-tank fire allows an estimation of the sensitivity of the infrared receptors in pyrophilous *Melanophila* beetles. PLoS One 7(5): e37627
12. Paczkowski S, Weissbecker B, Schöning MJ, Schütz S (2010) Biosensors on the basis of insect olfaction, In: Vilcinskas A (ed) Insect biotechnology Springer Verlag, Dordrecht, Heidelberg, London, New York, pp 225–240
13. Mainz T, Schmitz A, Schmitz H (2004) Variation in number and differentiation of the abdominal infrared receptors in the Australian 'fire-beetle' *Merimna atrata* (Coleoptera, Buprestidae). Arthropod Struct Dev 33:419–30
14. Apel K-H (1989) Zur Lebensweise des schwarzen Kiefernprachtkäfer *Melanophila acuminata*. Entomol Nach Ber 33:278–280
15. Dettmer K, Engewald W (2003) Ambient air analysis of volatile organic compounds using adsorptive enrichment. Chromatographia Suppl 57:339–347
16. Mazzoleni LR, Zielinska B, Moosmüller H (2007) Emissions of levoglucosan, methoxy phenols, and organic acids from prescribed burns, laboratory combustion of wildland fuels, and residential wood combustion. Environ Sci Technol 41:2115–2122
17. Supelco (1998) Solid phase microextraction: theory and optimization of conditions. Supelco Bulletin 923, Bellefonte
18. Drozd J, Novák J (1979) Headspace gas analysis by gas chromatography. J Chromatogr A 165:141–165
19. Tholl D, Boland W, Hansel A, Loreto F, Röse US, Schnitzler JP (2006) Practical approaches to plant volatile analysis. Plant J 45:540–60
20. Vogt RG, Riddiford LM (1981) Pheromone binding and inactivation by moth antennae. Nature 293:161–163

21. Tegoni M, Campanacci V, Cambillau C (2004) Structural aspects of sexual attraction and chemical communication in insects. Trends Biochem Sci 29:257–264
22. Wicher D, Schafer R, Bauernfeind R, Stensmyr MC, Heller R, Heinemann SH, Hansson BS (2008) *Drosophila* odorant receptors are both ligand-gated and cyclic-nucleotide-activated cation channels. Nature 452:1007
23. Weissteiner S, Huetteroth W, Kollmann M, Weißbecker B, Romani R, Schachtner J, Schütz S (2012) Cockchafer larvae smell host root scents in soil. PLoS One 7(10):e45827
24. Kosanke-Schütz K, Gabriel M, Weißbecker B, Reinecke H, Werner D, Koch UT, Schütz S (2012) Sequence matters – selective adaptation in electroantennographic response to binary odour mixtures by the Colorado potato beetle. J Appl Entomol 136:372–385
25. Weißbecker B, Holighaus G, Schütz S (2004) Gas chromatography with mass spectrometric and electroantennographic detection: analysis of wood odorants by direct coupling of insect olfaction and mass spectrometry. J Chrom A 1056:209–216
26. Dötterl S, Jürgens A, Seifert K, Laube T, Weißbecker B, Schütz S (2006) Nursery pollination by a moth in *Silene latifolia*: the role of odours in eliciting antennal and behavioural responses. New Phytol 169:707–718
27. Johne AB, Weissbecker B, Schütz S (2008) Approaching risk assessment of complex disease development in horse chestnut trees. A chemical ecologist’s perspective. J Appl Entomol 132:349–359
28. Thakeow P, Angeli S, Weißbecker B, Schütz S (2008) Antennal and behavioural responses of the fungivorous insect *Cis boleti* to volatiles of its host fungus. Chem Senses 33:379–387
29. Bleeker PM, Diergaarde PJ, Ament K, Schütz S, Johne B, Dijkink J, Hiemstra H, De Gelder R, de Both MTJ, Sabelis MW, Haring MA, Schuurink RC (2011) Tomato-produced 7-epizingiberene and R-curcumene act as repellents to whiteflies. Phytochemistry 72:68–73
30. Valentini L, Cantalini C, Armentano I, Kenny JM, Lozzi L, Santucci S (2004) Highly sensitive and selective sensors based on carbon nanotubes thin films for molecular detection. Diamond Relat Mater 13:1301–1305
31. Rapp M, Reibel J, Voigt A, Balzer M, Bülow O (2000) New miniaturized SAW-sensor array for organic gas detection driven by multiplexed oscillators. Sens Actuators B Chem 65:169–172
32. Hinrichsen V, Scholl G, Schubert M, Ostertag T (1999) Online monitoring of high-voltage metal-oxide surge arresters by wireless passive surface acoustic wave (SAW) temperature sensors. Paper presented at the High Voltage Engineering, 1999. Eleventh International Symposium on (Conf. Publ. No. 467) London , 23–27 August 1999
33. Lowe CR (1985) An introduction to the concepts and technology of biosensors. Biosensors 1:3–16
34. Scheller FW, Schubert F, Renneberg R, Müller H-G, Jänchen M, Weise H (1985) Biosensors: trends and commercialization. Biosensors 1:135–160
35. Clark LC, Lyons C (1962) Electrode systems for continuous monitoring in cardiovascular surgery. Ann NY Acad Sci 102:29–45
36. Rudolph AS, Reasor J (2001) Cell and tissue based technologies for environmental detection and medical diagnostics. Biosens Bioelectron 16:429–431
37. Schügerl K (1985) Sensor-Meßtechniken in der biotechnologischen Forschung und Industrie. Naturwissenschaften 72:400–407
38. Schütz S, Weißbecker B, Hummel HE, Schöning MJ, Riemer A, Kordos P, Lüth H (1997) Field effect transistor-insect antenna junction. Naturwissenschaften 84:86–88
39. Rodriguez-Mozaz S, Lopez de Alda MJ, Barceló D (2006) Biosensors as useful tools for environmental analysis and monitoring. Anal Bioanal Chem 386:1025–1041
40. Badihi-Mossberg M, Buchner V, Rishpon J (2007) Electrochemical biosensors for pollutants in the environment. Electroanal 19:2015–2028
41. Kaissling K-E, Priesner E (1970) Die Riechschwelle des Seidenspinners. Naturwissenschaften 54:23–28

42. Schöning MJ, Schütz S, Schroth P, Weißbecker B, Steffen A, Kordos P, Lüth H, Hummel HE (1998) A BioFET on the basis of intact insect antennae. Sens Actuators B Chem 47:234–237
43. Schroth P, Schöning MJ, Lüth H, Weißbecker B, Hummel HE, Schütz S (2001) Extending the capabilities of an antenna/chip biosensor by employing various insect species. Sens Actuators B Chem 78:1–5
44. Weissbecker B, Schöning MJ, Schütz S (2011) Biosensoren für das Umweltmonitoring. In: Herrmann B, Striegnitz M (eds) Biologische Spurenkunde, vol 2. Umweltmonitoring. Springer Verlag, in press
45. Schütz S, Weißbecker B, Klein A, Hummel HE (1997) Host plant selection of the Colorado potato beetle as influenced by damage induced volatiles of the potato plant. Naturwissenschaften 84:212–217
46. Schütz S, Weißbecker B, Hummel HE (1996) Biosensor for volatiles released by damaged plants. Biosens Bioelectron 11:427–433
47. Gramm A, Schütze A, Rühl T (2002) Identification of organic solvents by a virtual multisensor system with hierarchical classification. Proc IEEE Sens 1:382–387
48. Schieberle P, Hofmann T, Kohl D, Krummel C, Heinert L, Bock J, Traxler M (1998) High resolution gas chromatography – selective odorant measurement by multisensor array". In: Mussinan CJ, Morello MJ (eds) Flavour analysis. ACS Symposium Series 705, Oxford University Press, Oxford
49. Kohl CD (2003) Electronic noses. In: Waser R (ed) Nanoelectronics and information technology – advanced electronic materials and novel devices. Wiley-VCH, Berlin
50. Schütz S, Hummel HE, Schöning MJ, Schroth P, Kordos P, Lüth H, Zimmermann S, Schwarz A, Kohl D, Koczan D (1999) Application and perspective of biosensors based on insect olfaction. Proc Sensor 11:105–110
51. Paczkowski S, Sauerwald T, Weiß A, Bauer M, Kohl D, Schütz S (2011) Biomimetic gas sensors for large-scale drying of wood particles. Proc SPIE 7975:7975051–7975058
52. Siebke G, Holik P, Schmitz S, Lacher M, Steltenkamp S (2013) A µ-biomimetic uncooled infrared sensor. Proc SPIE 8686, doi:10.1117/12.2008951

Sensor Arrays, Virtual Multisensors, Data Fusion, and Gas Sensor Data Evaluation

Peter Reimann and Andreas Schütze

Abstract Selectivity will remain one of the main challenges for gas sensors. The majority of single gas sensors have a broad response spectrum and additional effort is required to provide specific information from the recorded raw data. Sensor arrays comprising a number of different sensors, either of the same basic type or combining different sensor principles, are often employed to improve the selectivity. Another approach is the dynamic operation of a single sensor element leading to a virtual multisensor. Depending on the application, both classification, i.e., recognition of a certain gas or gas mixture, and quantification, i.e., determining the concentration of a target gas, are required. For evaluation of the higher-dimensional data vectors obtained from the sensor system, different methods are commonly used, e.g., unsupervised and supervised multivariate statistics or artificial neural networks. For comprehensive classification, a multistep process is employed, typically comprising data preprocessing, feature extraction, dimensionality reduction, and finally classification. This chapter addresses typical methods used for gas sensor data evaluation and also briefly addresses challenges relating to sensor calibration and drift compensation. Four application examples are shown in detail demonstrating the use of different sensor configurations and data processing approaches: robust ozone quantification, sweat odor assessment trained by correlation with a human sensory panel, fire detection in buildings, and finally underground fire detection in coal mines requiring very high selectivity.

Keywords Artificial neural networks, Fire detection, Multivariate statistics, Odor assessment, Ozone quantification, Sensor array, Virtual multisensor

---

P. Reimann and A. Schütze (✉)
Laboratory for Measurement Technology, Department of Mechatronics, Saarland University, Campus A5.1, 66123 Saarbruecken, Germany
e-mail: schuetze@LMT.uni-saarland.de

C.-D. Kohl and T. Wagner (eds.), *Gas Sensing Fundamentals*,
Springer Series on Chemical Sensors and Biosensors (2014) 15: 67–108
DOI 10.1007/5346_2013_52,

Contents

1 Introduction

Gas sensors are used in many applications today, covering a wide range from comfort applications, e.g., cabin air quality (CAQ) in cars [1, 2] or controlled ventilation in buildings [3], over process monitoring applications [4], and quality control, e.g., leak test of packaged goods [5, 6], to various applications in safety and security [7–9]. However, especially for the latter, the suppression of false alarms is still a major challenge that often cannot be addressed satisfactorily preventing broader use of gas sensors. Even in other applications, selectivity is a key issue for gas sensor systems. For example, demand-controlled ventilation for reduced power consumption in buildings is today primarily based on CO_2 detection, which basically reflects the presence of persons within a room [10, 11]. To suppress the effects of hazardous volatile organic compounds (VOC) such as formaldehyde or benzene leading to the sick building syndrome, future sensor systems should be able to selectively detect hazardous gases while ignoring benign VOC compounds such as ethanol or room freshener [12–14].

Gas sensor applications can be divided not only according to the level of reliability required, which is often directly related to the selectivity of the sensor system, but also according to the target result to be obtained. Many typical safety and security applications define a specific target gas, e.g., CO in parking garages or CH_4 in gas leak detection, combined with a threshold limit value for triggering the alarm. In other applications, not only a threshold is monitored, but the sensor should supply a correct reading of the target gas concentration, independent of interfering gases, to allow a proper analysis and reaction of a higher-level system, e.g., CO_2 monitoring for indoor air quality. Others, e.g., fire detection, depend on the detection and identification of complex gas mixtures which are often not well defined in terms of gas components and respective concentrations but rather simulated, for example, by standardized test fires. For applications based on complex mixtures, gas sensor development is much more difficult as the target to be detected is not uniquely defined. In this contribution, exemplary applications are presented to discuss the respective requirements and possible approaches to achieving the required selectivity and stability through advanced signal processing. Even though quantification is of interest in many applications, in this contribution we will focus mainly on classification of gases or complex gas mixtures.

Very few gas sensor principles actually provide nearly perfect selectivity to a single target gas. Examples are paramagnetic oxygen sensors which are based on the paramagnetism of oxygen [15, 16] or the lambda probe for exhaust gas oxygen sensing which is based on oxygen ion conductance in ZrO [17, 18]; thus, both sensors are based on unique physical or chemical properties. Most other chemical sensor principles exhibit a broad response spectrum: the resistance of metal oxide gas sensors is basically depending on the concentration of adsorbed oxygen and other surface charges leading to band bending and thus energy barriers between individual grains of the material [19, 20]. Pellistor-type sensors only detect the heat generated by combustion of gas components on their catalytically active surface [21, 22]. Gas-sensitive field-effect transistors (GasFETs) detect charges on or in the gate material which influence the current flowing through the transistor channel [23, 24]. Even electrochemical (EC) cells depending on ionization of gas molecules at a catalytically active electrode and providing a current signal caused by the ion conductance in an electrolyte show a response to various gases. Indeed, one and the same EC cell with the exact same combination of materials is sold for different target gases, albeit with different sensitivities. Even seemingly selective gas sensor principles, i.e., the hydrogen GasFET first proposed by Lundström [25] or IR gas detectors, often show severe cross sensitivity to other gases. While the closed Pd gate layer of the Lundström FET only allows diffusion of protons, i.e., atomic hydrogen, to form a charged layer at the interface between gate electrode and insulator, protons can result also from hydrogen-containing gases, i.e., water, ammonia, or hydrocarbons, depending on the catalytic activity of the gate material and the operating temperature [23]. These examples show that the chemical interaction itself, typically involving the gas phase and a catalytically active surface, is responsible for the lack of selectivity. At the same time, it should be noted that this chemical interaction which forms the basis of the various sensor principles is also responsible for drift, aging, and poisoning effects due to reversible or irreversible changes of the sensor interface. However, limited selectivity is also observed for physical sensing principles. For example, IR detection is often employed for monitoring of methane, but, again, other hydrocarbons also absorb IR radiation in the same spectral region as methane. Selective IR measurements would require the use of expensive high-resolution spectrometers, which is often not suitable to typical gas sensor applications in the field.

Increasing the selectivity of chemical sensors, either with optimized materials or realization of specific target interaction, i.e., with molecular imprinted polymers for mass-sensitive devices, is still one of the main challenges for research. The highest selectivity is achieved using biomolecular interaction, i.e., antibodies optimized for specific target molecules [26]. However, one often has to note that reversibility and especially long-term stability are often reduced when selectivity is increased and material optimization requires a long time, especially due to testing and proving the stability of the obtained sensor systems. To overcome the generic problem of selectivity for gas sensor systems, sensor arrays, i.e., a combination of several sensors showing different response to target and interfering gases, have been widely studied. Sensor arrays are often composed of sensors based on the same sensing principle, but can also combine sensors based on different principles. Demonstrated examples range from only a few sensors to many hundreds of sensor elements. Due to the broad response spectrum of the individual sensor elements and the similarities of the gas interaction, the array response often shows many redundancies and is typically evaluated by methods adapted from pattern recognition and interpretation.

However, multisensor arrays pose several problems: the sensor systems are more complicated due to the large number of sensors and required readout electronics. Thus, cost but also size and power consumption are much higher than for conventional sensor systems. In addition, sensor drift becomes highly problematic because a change of the response of a single element in an array changes the overall pattern and can thus lead to false results from the pattern analysis. An alternative can be realized with dynamic operation of a single sensor element, which also leads to a response pattern. A widely used approach is temperature cycling, which changes the chemical interaction at the sensor surface and has been successfully employed for metal oxide gas sensors, pellistors, and GasFETs. Other methods are based on field-effect or impedance measurements. The common goal of all dynamic operating modes is the generation of a response pattern, which is then interpreted using similar methods as for sensor arrays, which also leads to the term “virtual multisensor.” Different methods for realization of virtual multisensors as well as similarities and differences compared to multisensor arrays are discussed in detail in Sect. 2.

There are many methods used for pattern analysis of multisensor data. Depending on the setup of the sensor system, the response of the various sensors or of the virtual multisensor is typically recorded as a multidimensional data vector, which is then interpreted further. This process is known as multisensor data evaluation or data fusion. The latter term, strictly defined, applies to bringing together data from different sensor elements or domains to deduct the desired information from the combined raw data, but is often also used to describe the pattern recognition process in general. Section 3 gives an overview over different methods discussing their advantages and disadvantages. Emphasis is placed on the most widely used techniques based on multivariate statistics, Principal Component Analysis (PCA) and Linear Discriminant Analysis (LDA), and on Artificial Neural Networks (ANN) using the backpropagation training algorithm.

Optimum classification of sensor data requires using not only the most suitable method but also a systematic approach which, as the methods themselves, is also adapted from standard pattern classification. Section 4 shows the typical four-step process composed of data preprocessing, feature extraction, dimensionality reduction and, finally, classification.

Different application scenarios are discussed in Sect. 5 covering quantitative measurement of ozone as an example of a well-defined application (Sect. 5.1), the assessment of odor based on reference analysis by a human sensory panel (Sect. 5.2), and, finally, fire detection both in buildings (Sect. 5.3.1) and in coal mines (Sect. 5.3.2) as examples for complex and safety critical applications.

2 Sensor Arrays and Virtual Multisensors

2.1 The Nose as Ideal Paradigm

Multisensor arrays have been studied since 1982 [27] to improve the selectivity of gas sensors, especially based on the resistive sensor principle, i.e., metal oxide semiconductor and conducting polymer sensors, but also using electrochemical cells or mass-sensitive devices, i.e., bulk acoustic wave (BAW) or surface acoustic wave (SAW) [28]. The general approach is actually derived from the olfactory system of mammals, which is based on a large number of odor receptors. Each odor receptor detects a specific target molecule or functional group of a complex molecule, sending a nerve impulse to the olfactory bulb of the brain, where the information is processed. Different nerve cells with the same odor receptor are combined to achieve higher sensitivity and also redundancy, thus suppressing noise. The mammalian nose has several hundred different odor receptors, thus achieving a wide detection range. Odors can be based on simply one chemical molecule, i.e., H_2S smelling like rotten eggs, but are often a complex combination of many molecules. For example, to emulate the odor of coffee, not less than 22 different chemical components are required to achieve a result that is interpreted as coffee by the human nose [29]. The olfactory bulb thus recognizes combinations of primary odor receptors firing and interprets these patterns as a complex odor which is our sensory perception. A skilled perfumer can distinguish up to 10,000 different odors, thus proving that pattern recognition, i.e., combinations of the response of the few hundred different odor receptors responding to individual molecules or functional groups, plays a decisive role for our sense of smell [30].

Typical detection limits of chemical sensors are in the ppm or upper ppb range, sometimes even considerably higher, e.g., for pellistors. The detection limit of the nose, i.e., the biological “ideal instrumental implementation,” varies widely but can go down to single-molecule detection, e.g., for pheromones for certain insects. One should note that through millions of years of evolution the sense of smell was optimized to detect relevant target molecules at relevant levels of detection.

Thus, both positive (primarily food and potential sexual partners) and negative smells (poisons, enemies, fire) are reliably detected by an animal adapted to its specific surroundings.

2.2 Multisensor Arrays and Electronic Noses

Mimicking the function of the nose, multisensor systems generate a response pattern by recording, e.g., a single response value for each sensor in an array. Sensor arrays can be based on the combination of any number and any kind of gas sensors, but are often composed of sensors based on the same sensing principle. Over the years, many systems have been demonstrated and commercialized starting with only two sensors [31] and going up to dozens of sensor elements [32, 33]. Sensor arrays have been tested for the environmental monitoring, medical diagnostics and health monitoring, process monitoring, food and beverage quality assurance, cosmetics and fragrances, detection of explosives, automotive and aerospace applications, and recognition of natural products [28]. Building a sensor array from sensors of the same type, e.g., metal oxide semiconductor, different sensing materials can be combined. In addition, the basic response of a given material is modified, e.g., by adding different catalysts, modifying the layer structure, i.e., the size of the metal oxide grains and the degree of sintering, or by simply operating the sensors at different temperatures. Sensor arrays have been demonstrated to achieve astounding selectivity, i.e., classification of boar taint in meat [34] or recognition of tuberculosis [35], leading to the often used term "electronic nose."

Combining different sensor materials and/or different sensor principles can reduce the linear dependence of the sensor response, but typically sensor arrays still show a high degree of redundancy. Note that this redundancy is different from the biological redundancy in the nose which is achieved by multiple sensors of the same type. This is necessary, as the biological odor receptors are not long-term stable and are typically replaced after several weeks. Thus, a large number of identical receptors allow a consistent sense of smell even when the individual sensor elements are continuously replaced. This approach, i.e., building large arrays with redundant sensors, has only recently been studied in the EU project NEUROCHEM primarily for better understanding of the sense of smell [36]. Due to the increased complexity and cost of the sensor array and electronic read-out this approach is not used on practical applications.

However, there are crucial differences between the function of the odor receptors and the olfactory bulb in the nose and typical sensor arrays: most important, the odor receptors in the nose are highly selective, thus achieving a response pattern with linearly independent contributions. Multisensor arrays, on the other hand, often show a large degree of similarity between different sensors. For example, in an array based on different tin dioxide sensors, practically all sensors will respond to carbon monoxide (CO) with a reduction of resistance and to nitrogen oxides (NO_x) with an increase in resistance.

Even though multisensor systems are often referred to as electronic noses, the performance achieved today is still far from the biological model. This is not only due to the fact that sensor signal processing is still comparatively simple but also due to differences in the sensors themselves. As already explained, odor receptors in the nose are highly selective. Most important, they ignore common simple molecules like CO, even though these occur in hazardous situations like fires. The reason is simple: CO is produced by not only fire but also numerous other processes. Thus, the information content of detecting CO is low, so that our nose has learned to detect other, more complex, and specific molecules, when it detects "fire." Chemical sensors, on the other hand, often show highest sensitivity towards simple molecules like CO, H_2, NO_x, and especially water (humidity) which makes their interpretation more difficult.

Commercial multisensor systems (see Fig. 1) can be divided into two categories: (1) dedicated systems for a specific application, i.e., fire detection in coal power plants [37, 38], and (2) generic devices, which can be adapted ("trained") for analysis of various application scenarios, often for comparison and classification of n samples [32]. Adaptation is usually performed by calibrating the sensor system with known samples and then comparing the signal patterns obtained for unknown samples to the training patterns. Thus, the whole process is a typical example for classification. Classification results are improved, if the pattern variation is only

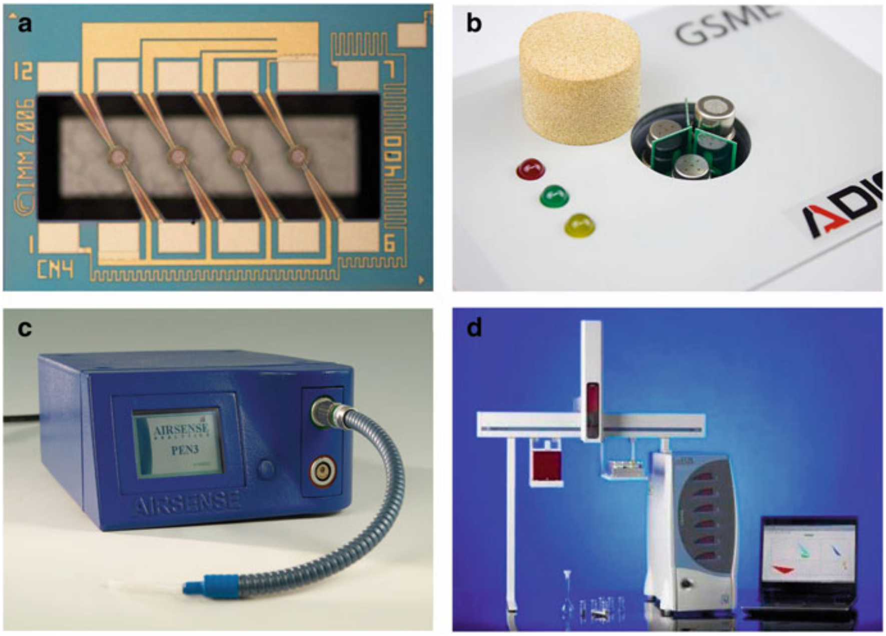

Fig. 1 Examples of sensor arrays, multi gas sensor systems, and electronic noses: (**a**) ultra-low-power micromachined gas sensor array [39] (reproduced with permission); (**b**) gas sensor array for detection of smoldering fires in dusty environments by GTE Industrieelektronik, Germany [40]; generic electronic nose systems; (**c**) Portable Electronic Nose (PEN) with up to 10 sensor elements by Airsense Analytics, Germany [41]; (**d**) FOX laboratory system with up to 18 sensor elements and autosampler by Alpha MOS, France [42]

caused by the target sample, i.e., the characteristic mixture of various gases, and not convoluted, for example, by concentration variations or changes of the background. Thus, generic electronic noses are more resembling laboratory-type equipment used in well-controlled surroundings and typically also including well-defined sampling routines. Dedicated systems, on the other hand, have to perform in a real application environment. Thus, while the range of targets to be identified is reduced, the variation of the ambient conditions has to be taken into account in the calibration.

2.3 Virtual Multisensors

A second approach to generating a complex response pattern lies in the dynamic operation of a single sensor. Thus, the sensor is actively driven, changing its response to various gases, which also results in the response pattern. As this response pattern is obtained from a single sensor, but resembles the response of a multisensor system, this approach is also called a virtual multisensor.

The most widely used approach is the variation of the sensor temperature which can actually be done both in static mode (i.e., n sensors of the same type are operated at different temperatures) or in dynamic mode. As each gas will have a typical temperature profile, i.e., the sensitivity vs. temperature is characteristic of the specific gas [43], the variation of the sensor temperature allows detection of each gas at its highest sensitivity for a given sensor type, which obviously improves detection. In addition, the gas can be identified from the characteristic temperature profile. However, this simple approach will work only for single gases and often only in a limited concentration range with a well-defined background. Due to nonlinear effects caused by variation of the gas concentration and/or interaction of different gas molecules on the sensor surface, the interpretation of signal patterns obtained from gas mixtures is much more complicated. One well-known example of the static approach is the KaMiNa which used a temperature gradient on a single sensor element and a number of electrodes to record the sensor response at different temperatures [44]. This was also combined with changing the sensor layer itself, e.g., the film thickness, to vary the sensor response further and obtain more information from this static array [45].

2.3.1 Temperature Cycled Operation

In comparison, dynamic temperature modulation is more versatile as it allows adaptation of the temperature range as well as the temperature cycle, i.e., T vs. time. Often, sinusoidal modulation is used, but temperature ramps or step changes can also be employed. In addition, dynamic temperature cycling leads to operation of the sensor in non-equilibrium states, thus can achieve results not obtained with static operation. Indeed, we could show that dynamic operation achieves the highest selectivity, when a large hysteresis occurred during temperature cycling. While fast temperature changes, i.e., step changes with maximum rate of change allowed by the driving electronics, achieve the largest hysteresis, this makes the sensor system sensitive to changes in the ambient, i.e., temperature, humidity, and gas flow across the sensor, all of which influence the actual temperature vs. time, i.e., the true temperature cycle and, thus, the interaction between sensor and surrounding gas atmosphere. To allow the interpretation of the sensor response independent of ambient conditions, the sensor operation should be based on exact temperature control, i.e., the sensor temperature is continuously measured and adjusted to the desired set point by the driving electronics. Typically, the heater integrated in the sensor chip is used for temperature measurement and both analog and digital temperature control circuits can be used to achieve high-quality temperature control. Then, a temperature cycle should be selected with maximum temperature increase and decrease rates so that the actual sensor temperature can follow the set point at all times. While the maximum rate for temperature increase depends on the maximum heater power supplied by the driving electronics and is thus in principle unlimited, the cool down rate depends on the passive heat dissipation and is mainly determined by the sensor packaging. Thermal time constants of ceramic type metal oxide gas sensors or bead-type pellistors are on the order of several seconds, while MEMS-type microhotplate sensors have thermal time constants of several tens of ms. For achieving a reliable sensor performance, the data acquisition has to be exactly synchronized with the temperature cycle to allow interpretation of the recorded dynamic sensor response. The data acquisition needs to be adapted to the sensor with a measurement interval of approximately one tenth of the thermal time constant to record all relevant features of the sensor response. The dynamic operation of the sensor increases not only the selectivity but also the sensitivity as the response for a target gas vs. interfering gases can be optimized by adjusting the temperature profile to make maximum use of non-equilibrium states on the sensor surface.

Temperature cycled operation (TCO) was first suggested by Eicker [46] and not only has since then been widely used with metal oxide gas sensors [47–49] but has also been applied to pellistors [50] and recently to GasFETs [51, 52]. In general, any chemical sensor allowing operation at elevated temperature will also allow TCO with a corresponding increase in selectivity because the chemical interaction itself is directly influenced by the operating temperature. Even though the temperature cycle seems to suggest that the response of the sensor is slower compared to static operation, it was demonstrated at least for classification applications that dynamic operation can actually reduce the response time [53]. For identification of the fuel type, i.e., gasoline or diesel, in the tank of a car, a micromachined sensor operating in temperature cycled mode allowed identification of the fuel vapor in as little as one second while the sensor required up to 60 s to achieve steady state when operated at a constant temperature (Fig. 2). TCO has proven suitable for continuous operation also in field tests under challenging ambient conditions, i.e., in a kitchen or a chemical laboratory [54], and also to improve the performance of sensor systems immediately after power-up [55].

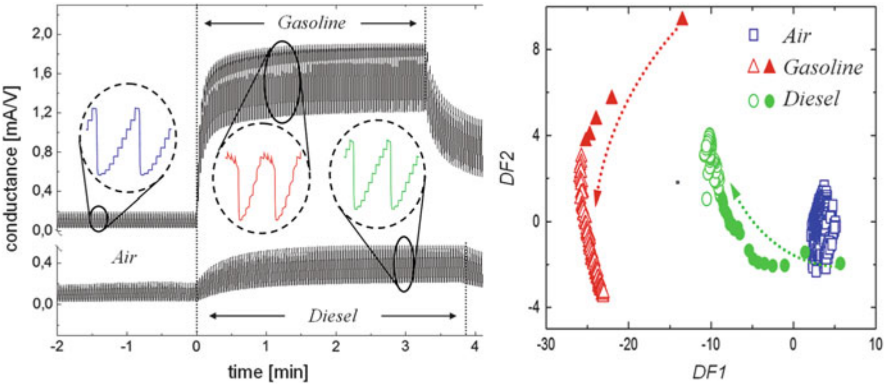

Fig. 2 Virtual multisensor based on TCO demonstrated for the identification of fuel type to prevent false fueling of cars. A microstructured sensor is used with a T-cycle with 2 s duration; the resulting response patterns (*inserts*) allow classification of gasoline after just one cycle and diesel after three cycles, although steady state is reached after approx. 20 and 40 s, respectively

2.3.2 Electrical Impedance Spectroscopy

A second method for generating a dynamic response already widely used for metal oxide sensors is electrical impedance spectroscopy (EIS) where an ac signal is applied to the sensor and the complex sensor response is recorded [56, 57]. Crystalline metal oxide layers can be modeled by a combination of different parallel RC elements representing the electrode-layer interface, the grain boundaries, and the metal oxide grains, respectively [58]. These show different influences of the interaction between the gas-sensitive layer and the gas components [19, 59, 60], which can be probed by measuring the complex impedance over a wide frequency range. The resulting EI spectrum allows separation of the different contributions and thus extraction of features which can be used for gas classification and quantification [56]. Typically, an equivalent circuit model is fitted to the resulting spectrum and the parameters of the components are extracted as features for further evaluation. Different methods can be used for obtaining the EI spectrum, with the most common laboratory method being excitation of the layer with a sinus voltage of defined amplitude being swept over the relevant frequency range and the amplitude and phase of the resulting current flow being recorded to determine the complex impedance [61]. A much simpler approach is excitation of the layer with a short voltage pulse only and recording the resulting current vs. time. As a short pulse also corresponds to a broad frequency spectrum, this is similar but much easier to be implemented in low-cost sensor systems. The resulting pulse response can be directly evaluated using pattern recognition tools similar to the TCO response shape [62]. However, the energy introduced into the sensor, especially for higher frequencies, is low. A good compromise between complexity of the required readout electronics and data acquisition time is the use of Pseudo Random Binary Sequences (PRBS) which can be tailored to the desired frequency range and show an almost constant energy density over the frequency range, similar to a sinus sweep, but can be generated easily as a digital signal thus requiring only a high-speed driver but no complex signal generation [63, 64].

2.3.3 Other Methods of Dynamic Signal Generation

Depending on the sensor type, other methods can be employed to obtain a dynamic sensor response. Examples are field-effect excitation which can be employed both for metal oxide gas sensors [65] and for GasFETs [66]. Gate Bias Cycling for GasFETs has also shown a surprisingly strong hysteresis effect not only providing a wealth of information for signal analysis but also exhibiting very long time constants up to several 10 min duration, which can be interpreted only in terms of ion diffusion into the insulating layer [67]. A method which has received considerable interest in recent years is optical excitation of solid-state gas sensors. The illumination of a semiconductor leads to the generation of charge carriers which can interact with adsorbed gas molecules [68, 69]. Thus, the resulting electrical signal is influenced by the gas interaction and can be used for classification. Finally, the sensor response vs. time is also a suitable method for dynamic evaluation and is actually used in many laboratory e-nose systems by combining the sensor system with suitable sampling. In stand-alone sensor systems in the field, filters – either broadband, like activated charcoal [70], or gas-specific [71] – can be used to switch the gas on and off and record the resulting response patterns.

2.4 Calibration

If the interaction of gas sensors with complex gas mixtures could be predicted, i.e., with a suitable model of the interactions occurring on the sensor surface, the signal patterns could be interpreted by inversing the model to determine the gases and their concentrations for a given response pattern. However, the modeling of chemical sensor is still far away from models that allow not only the interpretation of observed sensor behavior in general terms but also the exact quantitative prediction of the response for an arbitrary gas mixture. Thus, the analysis of sensor response is primarily based on extensive calibration, most often with complex gas mixing systems allowing control of the carrier gas including temperature and relative humidity, admixture of different bottled test gases, and even online generation of test gases by various methods. Figure 3 shows the schematic of a gas mixing system recently set up in our group [72].

Typical situations are recorded with the sensor system by emulating the later application scenario. However, this strategy can only be employed if target and interfering gases and their respective concentrations are known with sufficient accuracy. For more complex applications like fire detection, the application itself is simulated with, for example, specific test fires as defined in the EN 54 standard for fire detectors [73, 74]. Another approach would be the parallel assessment of

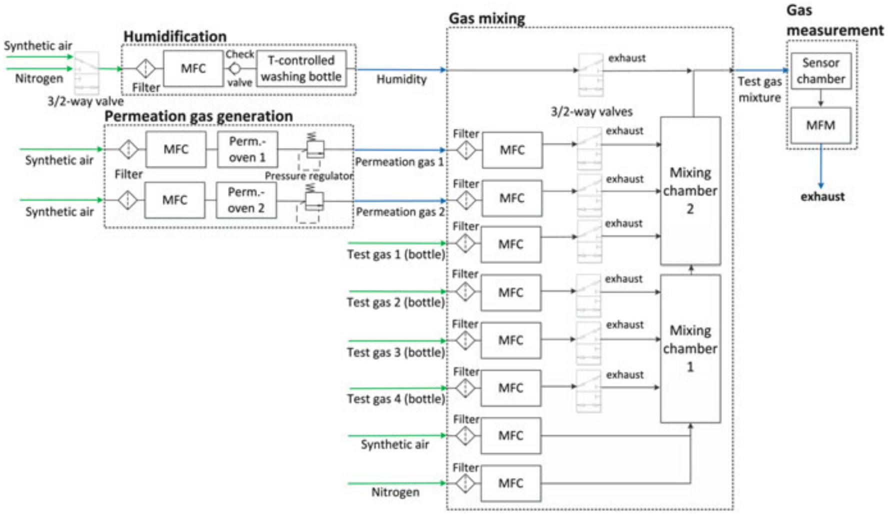

Fig. 3 Schematic of a complex gas mixing system allowing variation of the carrier gas oxygen concentration between 0% and 20%, humidification up to 95% plus admixture of four bottled test gases. In addition, test gases are generated online using two permeation ovens. All gas flows are controlled with mass flow controllers (MFC); test gases are mixed into the carrier gas by 3/2-way valves. A mass flow meter (MFM) placed behind the sensor chamber checks the leak integrity of the system. All parameters are computer controlled allowing automated testing with complex test profiles over days or even weeks [72]

target situations either with reference instruments or even with human sensory panels to obtain a reliable reference, e.g., for smell assessment (see Sect. 5.2).

The result of a calibration is a data set giving the sensor response – in general, an *n*-dimensional vector of raw sensor data – and also containing information on the gas mixture or the scenario for which these measurements were taken. To allow identification of relevant structures in the data, a sufficient number of calibration measurements are required. As a rule of thumb, the number of measurements m should be at least ten times larger than the number of raw sensor data for each measurement. Otherwise, overfitting might result in the subsequent signal processing [75], i.e., patterns are not recognized because of typical characteristic features but instead by random variations of individual measurements. All calibration data are then combined in an $m \times n$ matrix **D** for further analysis where each row i ($1 \leq i \leq m$) contains the raw data obtained for a single sample or measurement and each column k ($1 \leq k \leq n$) contains the values observed for a specific dimension, e.g., a specific sensor in a multisensor array or the resistance at a defined frequency for EIS measurements, over all measurements.

3 Pattern Analysis Methods Used for Gas Sensor Systems

The task of the ensuing pattern analysis is the interpretation of this data vector to obtain the desired information, i.e., gas type and concentration or a more abstract result such as smell intensity. In the simplest form, a yes or no decision is required, i.e., to trigger an alarm. This can be compared to other pattern analysis tasks, e.g., using fingerprint readers or image processing. Here also, the simplest form is a yes or no decision, i.e., for allowing access to a computer, or a classification, i.e., identification of a certain object or person from a range of options but can also go to analog results, i.e., estimating the age of a person in an image. Thus, methods applied for interpretation of gas sensor data are mostly adapted from other pattern analysis applications. Excellent overviews are given in [76, 77].

Methods can be divided into different categories, i.e., linear or nonlinear. The most important distinction is the question how the data analysis is adapted to obtain the desired result. Unsupervised methods are based only on the analysis of response patterns trying to enhance the difference in the multisensor response to different stimuli. Examples for unsupervised methods are PCA [78] or Self-Organizing Maps (SOM), also known as Kohonen maps [79]. Supervised methods, on the other hand, actively seek to identify characteristic differences in the sensor data to allow correct classification while ignoring data variation which does not help with task at hand. The most widely used supervised methods are LDA [78], also referred to as Fishers linear discriminant, and ANN.

3.1 Multivariate Statistics

PCA and LDA are both based on multivariate statistics and lead to linear projections of the data from the high-dimensional space of the sensor data [78].

PCA is an orthogonal transformation of the data space allowing a significant dimensionality reduction while still retaining most of the variance contained in the original data set. The first principal component is the vector, i.e., direction in the n-dimensional data space, along which the data show the greatest variance. The second principal component is the direction with the second highest variance and so on. Thus, the first few principal components already explain most of the variance of the data and thus contain most of the information of the data. Mathematically, the PCA projection is determined by calculating the eigenvectors of the $n \times n$ covariance matrix **A** of the calibration data **D**. The eigenvectors are ordered according to the size of the eigenvalues and the PCA projection is obtained by

$$\underline{x'} = \underline{\underline{A}} \cdot \left(\underline{x} - \underline{\mu}\right) \tag{1}$$

Here, x' denotes the transformed coordinates (principal components), x the original coordinates, and μ the empirical mean of the data. Subtraction of μ thus leads to centering of the data around the origin and multiplication with **A** to a rotation around the origin. Note that the evaluation of the principal component i for a measurement x is simply a vector multiplication, with a_i representing the eigenvector i:

$$\mathrm{PC}_i = \sum_{k=1}^{n} a_{ik} \cdot x_k \tag{2}$$

While PCA is based only on the covariance of the data matrix, LDA as a supervised method also takes the class property of each sample into account. Optimum separation of different groups or classes is achieved by maximizing the distance between groups while minimizing the scatter within the groups by maximizing Γ:

$$\Gamma = \frac{\text{Scatter between groups}}{\text{Scatter within groups}} \rightarrow \max \tag{3}$$

Solving the optimization problem results in a dimensionality reduction (number of classes minus one) with new coordinates (discriminant functions) offering better separation of different classes thus allowing easier classification. The determination of the discriminant value i for a measurement x is again simply a vector multiplication with an added offset b_{i0}, which centers the projected data on zero:

$$\mathrm{DF}_i = b_{i0} + \sum_{k=1}^{n} b_{ik} \cdot x_k \tag{4}$$

Both PCA and LDA are very helpful for the analysis of gas sensor data. Data from sensor arrays and virtual multisensors typically contain a large degree of colinearity or redundancy which is effectively converted into a set of values of linearly uncorrelated variables using PCA while LDA explicitly attempts to model the difference between classes. Though the determination of projection vectors requires large computational effort, later application to new measurements is simple and can thus be implemented even in low-cost systems using cheap microcontrollers. To better understand the differences between unsupervised PCA and supervised LDA it is helpful to view the results in geometrical terms, that is, as projections from higher-dimensional space to one or two dimensions: while PCA selects the viewpoint so that the overall variation, i.e., the area of the shadow, is maximized, LDA selects a viewpoint so that the classes are best separated. This is depicted in Fig. 4. The data shown in this figure can be taken as theoretical measurement results for two different gases with varying concentration being measured by two sensors resulting in the values x_1 and x_2.

The projection obviously shows two separate groups with a large variance caused by the changing concentration and a shift caused by the different gases. Reducing the dimension to one, PCA would plot the data along the first principal component, PC_1, which is resulting from changing concentrations leading to significant overlap of

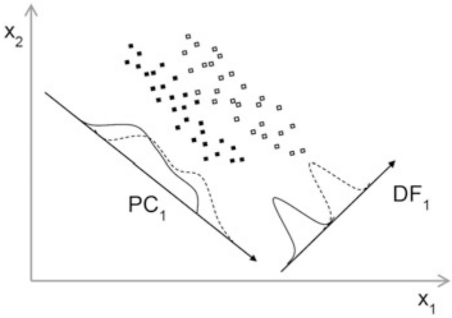

Fig. 4 Comparison of the resulting first variable for PCA and LDA for a data set with two groups: while the PCA projection selects a viewpoint (axis) so that the spread is maximized, LDA selects an axis which provides best separation, i.e., minimum overlap, of the two groups

both groups. LDA, on the other hand, separates the groups along the first discriminant function, DF_1, because the variations caused by changing concentration are suppressed to minimize the scatter within each known group. PCA would be able to separate both gases if the samples were reduced to one concentration, which is one reason why sampling is of great importance to obtain good results with electronic nose systems. While LDA clearly provides a better basis for classification, both methods should usually be employed together to gain a better understanding of the system, e.g., to identify hidden variation in the samples which might interfere with correct classification.

3.2 Artificial Neural Networks

Our brain is especially powerful for pattern recognition [75], able, for example, to recognize a person from a brief glimpse from a long distance away or to discriminate a real person from a computer using captchas [80]. The brain is made up of nerve cells which are highly connected collecting many inputs via dendrites and synapses. Information is processed in a nerve cell basically by calculating a weighted sum of all inputs, i.e., signals from sensory cells or other nerve cells. If the weighted sum (“enervation”) exceeds a threshold, the nerve cell in turn gives out a signal (“fires”) along its single output (“axon”) propagating the information through the network. Even though the individual signal is digital, i.e., a voltage pulse traveling along the axon, analog information is coded in the frequency of the nerve pulses [30].

ANN mimic the information processing in the brain and have been successfully applied to pattern recognition for many years [30, 75]. Nerve cells are simulated by the so-called neurons (Fig. 5, right) forming the basic building blocks of complex networks and evaluating multiple input values to provide a single output. Simulations vary basically with the choice of the neuron features starting from simple digital output (“perceptron”) to analog output using complex output

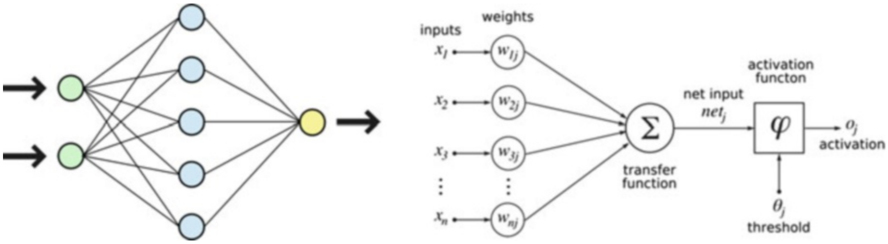

Fig. 5 Schematic of a simple feedforward network (*left*); each neuron in the network calculates the weighted sum of its inputs x_i and gives out the activation o_j (*right*) [81]

functions as well as with the connectivity of the network. The most common method is the so-called feedforward network connecting n input neurons, i.e., representing sensor signals, via a number of hidden layers to one or more output neurons (Fig. 5, left). The output can be either analog, i.e., the concentration of a certain target gas, or digital, i.e., classification of a certain situation like “fire.” The most important feature of ANN is their ability to learn, i.e., to match their output to the desired target output. Learning is most often performed by adapting the connections between neurons, i.e., the weight with which the output of one neuron is multiplied in the next neuron. The most common training scheme for feedforward networks is the backpropagation (BP) algorithm. The name is derived from the way the weights are modified by propagating the resulting error of a prediction, i.e., the difference between actual and desired output based on the training data set, backwards though the network. The mathematical basis of the algorithm is a gradient descent approach based on the overall error of the network, i.e., the sum of all errors over all training patterns, interpreted as a function of the weights. Many modifications, both strictly mathematical and largely empirical, have been developed leading to a wealth of methods under the generic term ANN.

ANNs trained by BP are very powerful, because the network can learn even very complex and nonlinear relationships between sensor signals and underlying gases [30, 31]. While training of the network, especially if different configurations are to be tested, required large computational effort, implementation for evaluation of measurements is much simpler and can be realized also on simple microcontrollers. The main drawback of ANN is their black-box character: due to implicit nature of data evaluation and their nonlinear nature, small changes of input values can actually lead to large changes of the output. Thus, the prediction of the response for data sets outside of the training space is impossible which means that the effect of sensor drift or other errors on the resulting output cannot be predicted. In many applications, especially for safety and security, the correct function of the evaluation algorithm under any circumstances has to be proven, which is up until now not possible for ANN.

In contrast to BP as a supervised training method, Self-Organzing Maps (SOM) is an unsupervised method trying to identify common aspects in complex data sets [79]. Basically, SOM try to represent complex multidimensional data in the form of a two-dimensional map. Training is performed by adapting a predefined number of neurons, i.e., vectors from the original data space, to best represent the total training set. In contrast to related supervised methods (see LVQ below), not only the winner neuron itself is adapted but also the neighboring vectors in the map to preserve the topological properties of the input space. The best image is of an elastic net thrown over the data with the nodes being pulled to best represent the original data. The analysis of the data is performed by labeling of the neurons, i.e., by identifying the correct class of a few training samples and, thus, the neuron on which they are projected. Note, however, that SOM does not guarantee unique labeling of neurons; thus, labeling can lead to false interpretation, especially if the different groups are not clearly separated [82].

3.3 Other Methods

Many other methods have been used for evaluation of gas sensor data, a more extensive, systematic overview can be found in [83].

Fuzzy logic has been applied successfully, especially for transferring experience of users to automatic evaluation. An example is fire detection with multisensor systems for H_2, CO, and other gases in coal power plants, where alarm decisions are based on evaluation of linguistic rules such as "*If* hydrogen concentration and CO concentration are medium *and* both are increasing *and* the H_2/CO ratio is increasing *then* set-off the fire alarm" [38]. Fuzzy logic can also be applied to infer rules from calibration data, e.g., for automatic clustering of data, which is an unsupervised data evaluation method [84].

Learning Vector Quantization (LVQ) is a supervised method closely related to SOM and is often used to find a good representation of a large calibration data set with only a few typical data vectors ("codebook vectors") [85]. A given number of data vectors is assigned to each group and iteratively adapted to best represent the total data set. This can be combined with nearest neighbor classification to allow classification of new data by comparing these with the codebook vectors and assigning the class of the most similar vector to the unknown data. Different variations of the algorithm developed by Kohonen allow optimized adaption of the codebook vectors to represent either the density of the calibration data or to interpret the class boundaries [86].

Support Vector Machine (SVM) is another supervised method. The basic SVM takes a set of input data and predicts, for each given input, which of two possible classes forms the output. It is based on training samples ("support vectors") realizing a non-probabilistic binary linear classifier. Furthermore, SVMs can be extended using the so-called kernel trick to also perform nonlinear classifications, implicitly mapping their inputs into high-dimensional feature spaces and performing a linear classification in this feature space [87].

4 Systematic Data Evaluation Based on Pattern Recognition

To achieve optimum results for sensor array data fusion and interpretation, pattern analysis methods presented above need to be integrated into a systematic structure comprising data preprocessing, feature extraction, and dimensionality reduction before finally allowing classification with high reliability and performance. While this is a step-by-step process, the optimization of this process has to be done taking all steps into account, i.e., by comparing the performance of the final classification. To allow objective comparison of different methods and data evaluation steps, a suitable quality function has to be defined. For classification problem, this is usually considered as the percentage of false classifications, but, more generally, should be defined as an analog “distance function” to allow a comparison even when 100% correct classification is achieved. A distance function can, for example, be defined as the sum of the distance of each sample from false classification over the whole data set. Thus, a smaller quality function value or quality measure would mean that some or many samples are close to other groups and could thus lead to false classification, for example, with added drift or aging. Different distance definitions may be used, but the Euclidean distance is most widely used. However, not all methods provide analog distance values.

Data sets are often divided into two or three subgroups, i.e., one for training and one for testing and sometimes a third for validation. Data processing is based on the training data only, and the test data is used to evaluate the performance. For example, for ANN trained with BP, the overall error for the test set often increases again after some time while the error of the training set is still decreasing which is indicative of overfitting of the data. Leave-one-out cross validation is another method for validation especially for small calibration data sets. Here all values except one are used iteratively and the correct classification of the left out sample is evaluated based on the remaining training set [88].

4.1 Data Preprocessing

Raw data obtained from sensor arrays and virtual multisensors are often subject to noise or other interference, which can be suppressed by averaging or filtering of the sensor raw data. However, care needs to be taken to identify incorrect data transmission to prevent a strong influence on the evaluation. For example, if measurements are averaged over five individual sensor readings, a single faulty bit – in the worst case, the sign of the recorded value – leads to a large error of the average without being as apparent as the sign error in the original reading. This could be suppressed by also calculating the standard deviation σ of the multiple readings and rejecting data where σ exceeds a certain threshold. Also, outliers, which can dominate the subsequent processing, can be suppressed by calculating the empirical mean and standard deviation of the values and eliminating measurements far removed from the mean, again selecting a suitable threshold.

For virtual multisensors, preprocessing is even more powerful as it can often suppress not only noise but also drift in the data. This is due to the fact that all values are recorded from a single sensor; thus drift should influence each reading in a similar way, which is not the case for sensor arrays. Take the example of multiplicative drift of a metal oxide sensor, i.e., resistance R is changed by a constant factor γ. This can be efficiently eliminated by dividing all values recorded in the cycle, i.e., the recorded data vector $\underline{x}$ by the mean value over the whole cycle:

$$\underline{x}^{\text{norm}} = \left(\frac{1}{n} \sum_{k=1}^{n} x_i \right)^{-1} \cdot \underline{x} \tag{5}$$

This method has proven very suitable to suppress not only drift caused by aging but also the influence of changing humidity on the sensor effect which often poses a large problem for MOS sensors [89, 90]. For additive drift, i.e., a variable offset, the mean value of the cycle could be subtracted from each value to eliminate this drift effect. Other methods might include subtraction of or division by the maximum or minimum value in the cycle. Note that the effectiveness of different normalization methods has to be tested but can then provide valuable insight into the sensor itself.

4.2 Feature Extraction

To obtain characteristic and valuable information from the raw data, secondary features are often extracted. For a sensor array measuring a defined gas sample, these are usually the sensor values after a certain exposure time. In order to provide more information, the initial slope of the sensor response, a possible overshoot, etc., could additionally be extracted from the sensor response curves (Fig. 6), as these are characteristic for the interaction between gas sample and sensor. Even the sensor noise might be representative for a specific gas or gas mixture, either due to the interaction of gas and sensor or due to gas currents.

For virtual multisensor systems, different methods of extracting features from the response pattern have been established. Most widely used with impedance spectroscopy, for example, is the determination of a suitable equivalent circuit and extracting the values of the lumped elements by fitting the model to the recorded spectrum using least squares methods, especially the Levenberg–Marquardt algorithm (LEVM) [61].

For periodic signals like those obtained from TCO or gate bias cycling, Fourier and wavelet analyses have been widely used. But there are also numerous other methods from simple features describing the shape of the sensor response (i.e., average and slope in certain sections of the response curve) [89] to fitting of exponential functions to describe the sensor response after step changes [55]. Selection and extraction of suitable features from the raw data is a very important and often overlooked step in data processing. It can provide greatly improved results (see Fig. 7 [89]) and also has a strong influence on the computational effort of the signal evaluation. The prediction of the performance of various features is difficult and, thus, needs to be tested, i.e., the effect of different feature on the overall performance has to be studied. Interesting features can often be identified by observing the typical raw sensor response patterns manually as humans are very efficient at pattern recognition.

Note that after feature extraction, these have to be normalized so that all features have the same range. Otherwise features with large absolute values would dominate further processing based on distance. For example, if the absolute value and the slope of a signal are extracted (cf. Fig. 6), the slope is typically at least an order of magnitude smaller and would thus contribute very little to the overall vector distance. Normalization can be done by linearly mapping all values of a feature to a certain range, i.e., [0; 1] or [−1; 1], based on seeking the minimum and maximum values of this feature in the calibration data set. However, this approach can be sensitive to outliers, i.e., one single value could dominate the linear mapping, which would basically make the feature obsolete. If outliers have not been removed in the preprocessing, then the normalization of feature i can be performed by calculating the empirical mean μ_i and standard deviation σ_i and mapping all features according to

$$x_i^{\text{norm}} = \frac{1}{\sigma_i}(x_i - \mu_i) \tag{6}$$

The resulting feature space is centered at zero and shows the same empirical standard deviation for all features. Some data processing methods implicitly perform normalization, but not all; PCA, for example, requires data normalization, while ANNs, in general, do not. Note that some software implementations include data normalization to account for this requirement.

Fig. 6 Typical sensor response curves for a sensor exposed to a short gas pulse. Normally, only the value at the end of the exposure ① is evaluated. Different response curves are discriminated, for example, by calculating the initial slope of the sensor signal ②, the slope at the end of the gas exposure ③, the overshoot ④, the initial slope of the signal return ⑤, or the undershoot ⑥

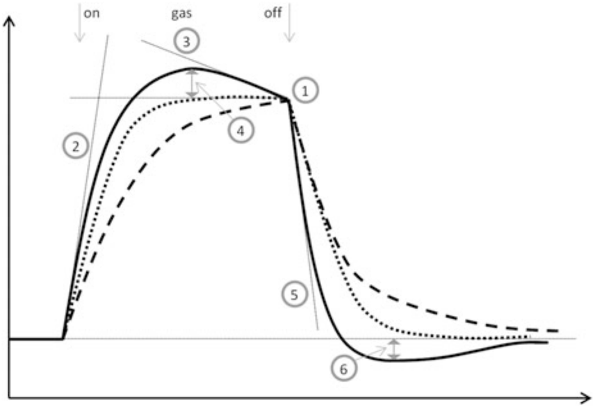

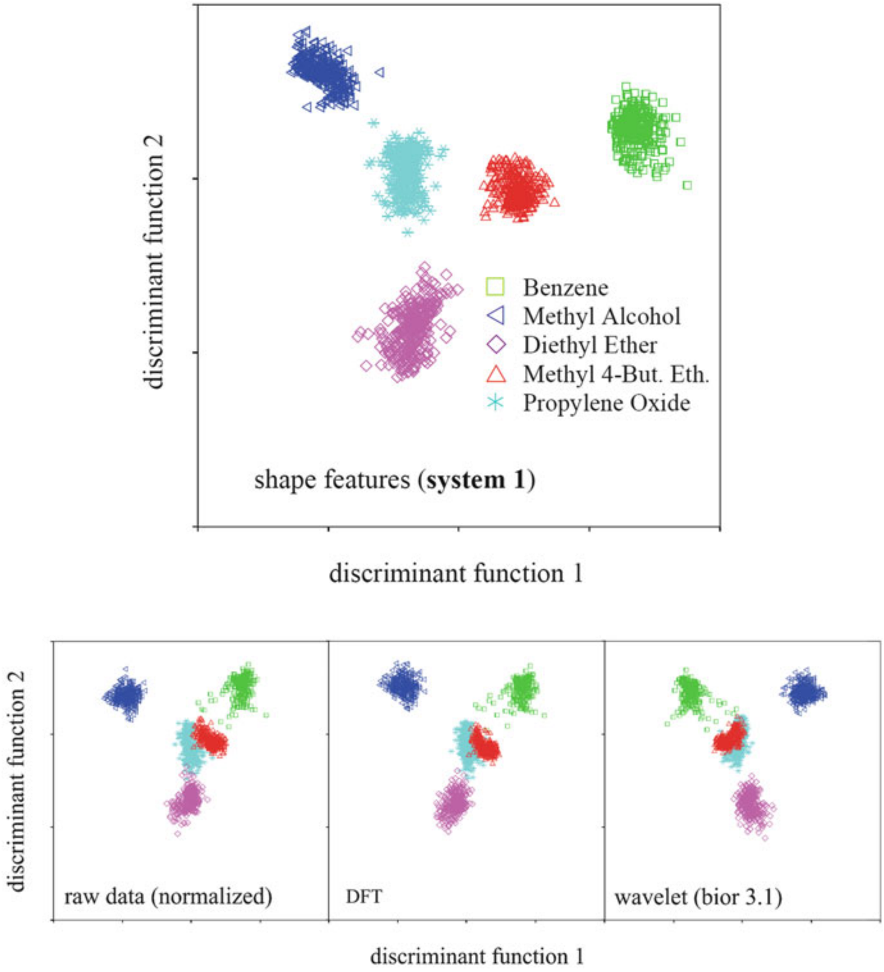

Fig. 7 Comparison of two-dimensional LDA projections obtained from five features extracted by different methods from a gas sensor system based on two temperature cycled sensors. While raw data, discrete Fourier transformation (DFT), and wavelet transformation all lead to overlap, shape features describing the sensor response, i.e., mean values, slopes, and curvature of the TCO patterns, lead to perfect separation of five tested solvents (each group contains measurements in the concentration range 2 to 200 ppm and for 30% and 70% r.h.) ([89], reproduced with permission)

4.3 Dimensionality Reduction

Sensor arrays and virtual multisensors often provide high-dimensional data which, however, show strong redundancy or correlation, i.e., the different dimensions are not linear independent. Note that the generation of secondary features can even increase the dimensionality while obviously not adding any additional information [89].

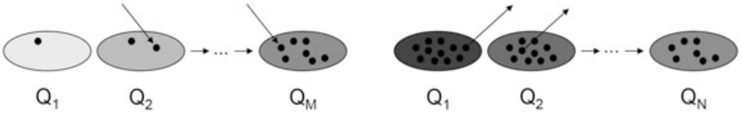

Fig. 8 Schematic of bottom-up (*left*) and top-down (*right*) feature selection based on the quality measure Q

This increases the demand on the data processing, due to higher computational effort and also larger storage requirements for calibration data. In addition, overfitting easily results if the dimensionality of the features is similar to or even larger than the number of calibration measurements. Thus, prior to the final classification, the dimensionality should be reduced, for example, by removing redundancy and transforming the data into a linear-independent, lower-dimension data set. This is the main task of multivariate statistics such as PCA and LDA (see above), which are often employed for dimensionality reduction. PCA results in a data space of the same dimension as the original feature space. However, the dimension can be reduced by omitting higher dimensions. The amount of variance explained by the principal components is known from the "loadings" and, for gas sensor data, the first two or three components often explain more than 90% of the total variance due to the strong correlation of the raw data. LDA directly reduces the dimensionality to the number of classes -1, but even here only the first two discriminant functions are often retained as they show good class separation even for a larger number of classes. For further simplification, the feature space can be reduced to a smaller number of features by retaining only those with large loading, i.e., values for a_i and b_i in (1) and (2), respectively. For LDA, this process is sometimes called stepwise LDA. Note that the resulting classification often profits from the reduced number of features.

Other possibilities include a feature selection process based on a quality function as defined above. While a brute force approach, i.e., calculating the quality measure for all possible combinations of features, is typically not realistic due to the huge amount of combinations for high-dimensional feature spaces, both bottom-up and top-down approaches are suitable (Fig. 8). Bottom-up would mean to first select the one feature which alone gives the highest-quality measure. This feature is kept and additional features are added in an iterative process, so that the new feature achieves the highest increase of the quality measure compared to the previous feature set. Top-down starts with all features and iteratively eliminates features, which show the smallest decrease of the quality measure. The iteration is stopped, for example, when the increase of the quality measure for additional features falls below a certain value for bottom-up or the decrease of the quality measure exceeds a certain value for top-down. Alternatively, overlap between classes could be taken into account, i.e., selecting the minimum number of features which allow correct classification of all samples.

Note that dimensionality reduction is also helpful in obtaining a fast impression of the quality of the data analysis by plotting all training data into the reduced space. This often provides a good impression of the data quality at a glance (cf. Fig. 7), while abstract quality measures are often difficult to interpret.

4.4 Classification

Classification is obtained by comparing data from measurement, i.e., during later operation of the gas measurement system, with calibration data. This can be done implicitly or explicitly. Explicit comparison is often based on the *k* nearest neighbor (*k*NN) classifier [91], which identifies the calibration data vectors closest to the new measurement result and assigns the class of the majority of the *k* nearest neighbors. This classification can actually be performed at any step of the pattern classification process, i.e., based on raw data vectors, feature vectors, or reduced dimension feature vectors. The distance is calculated using the same distance function as for the quality function. To reduce the demand on storage space, a subset of the calibration data is usually selected as reference vectors. For compact LDA projections (see Fig. 9b below), the group centroid is often sufficient as a single reference vector effectively leading to spheres defining the different classes. For more extended groups, i.e., as shown in Figs. 2 right, or 4, more than one reference vector is required to represent the calibration data. LVQ is a suitable method for adapting a certain number of reference vectors to best represent the complete calibration data set [85]. If only the single nearest neighbor is used, false classification can easily occur, especially for extended groups and outliers. Taking more neighboring vectors into account, i.e., three, can lead to more stable classification results. This is further improved by weighting the neighbors to account for the various distances. Equation (7) gives two examples for distance weighing:

$$w'_x(v_i) = 1 - \frac{d[v_x, v_i]}{d[v_x, v_{\max}]}$$

$$w''_x(v_i) = \exp\left(-\frac{d[v_x, v_i]}{R_0}\right) \tag{7}$$

Here, v_x represents the measurement vector to be classified, v_i the vectors of the *k* nearest neighbors, $d[]$ the distance function, and w are weights calculated using different neighborhood definitions. Thus, w' is based on a relative neighborhood region defined by the distance between v_x and $v_{\max}$, i.e., the nearest neighbor with the greatest distance. On the other hand, w'' is based on the same neighboring radius R_0 used for all vectors. For each class, the weights of the vectors belonging to this class are added and the unknown measurement is assigned to the class with largest overall result.

There are of course many other possibilities for defining a classifier, i.e., using LDA as a multidimensional classifier or a combination of binary classifiers, i.e., class *i* vs. all other classes [78] or PLSDA (Partial Least Squares Discriminant Analysis) [92] (see also Sect. 5.3.1 below). Again, as with the other steps in the process, different possibilities have to be compared to identify the classification best suited to the problem at hand. ANN can be used as a classifier, i.e., if binary networks ("perceptrons") are used giving a simple yes or no output for each group [75]. Note that ANN can actually combine the steps *feature extraction*, *dimensionality reduction,* and *classification* in one, as they are very powerful in finding the implicit relationship between recorded sensor data and desired output. However, this can easily require larger networks with more neurons and thus more free parameters, i.e., weights to be adapted by the learning process. As already stressed, the number of training samples should be (much) larger than the number of free parameters to avoid overfitting; a large network therefore requires many samples drastically increasing the calibration effort.

5 Application Examples

5.1 Quantification of Ozone

The first example presented here is based on an application where a gas sensor monitors an ozone (O_3) generator used for indoor air treatment, i.e., to oxidize odorants and germs. The example is discussed in more detail by Lösch et al. [93], while we give a brief overview of the main points here. The control of the resulting ozone concentration is required to prevent adverse health effects. The limit value for ozone is 50 ppb and should be reliably monitored even during aging-induced sensor drift and in the presence of interfering gases like CO or NO_2. A commercial, microstructured metal oxide gas sensor, MiCS 2611 [94], was tested which showed good selectivity vs. CO and NO_2 in static tests. However, the sensitivity varied from sensor to sensor and also from measurement to measurement by nearly a factor of two, which was not acceptable for the desired applications.

To improve the sensor performance, a simple temperature profile consisting of a linear temperature ramp from room temperature up to 400°C and back down to room temperature in 10 s each was developed. The temperature cycle and the resulting sensor response patterns are shown in Fig. 9, top left. Data evaluation is performed by first averaging 10 sensor readings corresponding to a period of 200 ms and then normalizing the sensor response by dividing each value by the mean of the whole cycle (preprocessing). In order to enhance the relevant information, the first and second derivatives of the normalized sensor response curves are determined by simply calculating the differences of subsequent values for the equidistant steps. A total of 17 features, i.e., the extreme values (absolute values and position of maximum and minimum), the zero points, and the number of zero points of the first and second derivatives as well as the resistance at room temperature of the normalized sensor response, are extracted from the sensor response (feature extraction). Using these features, an LDA was calculated for five different ozone concentrations defined as separate classes. The resulting projection of the first and second discriminant function (dimensionality reduction) shows a good correlation between the value of the first discriminant function and the ozone concentration (Fig. 9, top right). In this case, concentration prediction was required and is realized by fitting a second-order

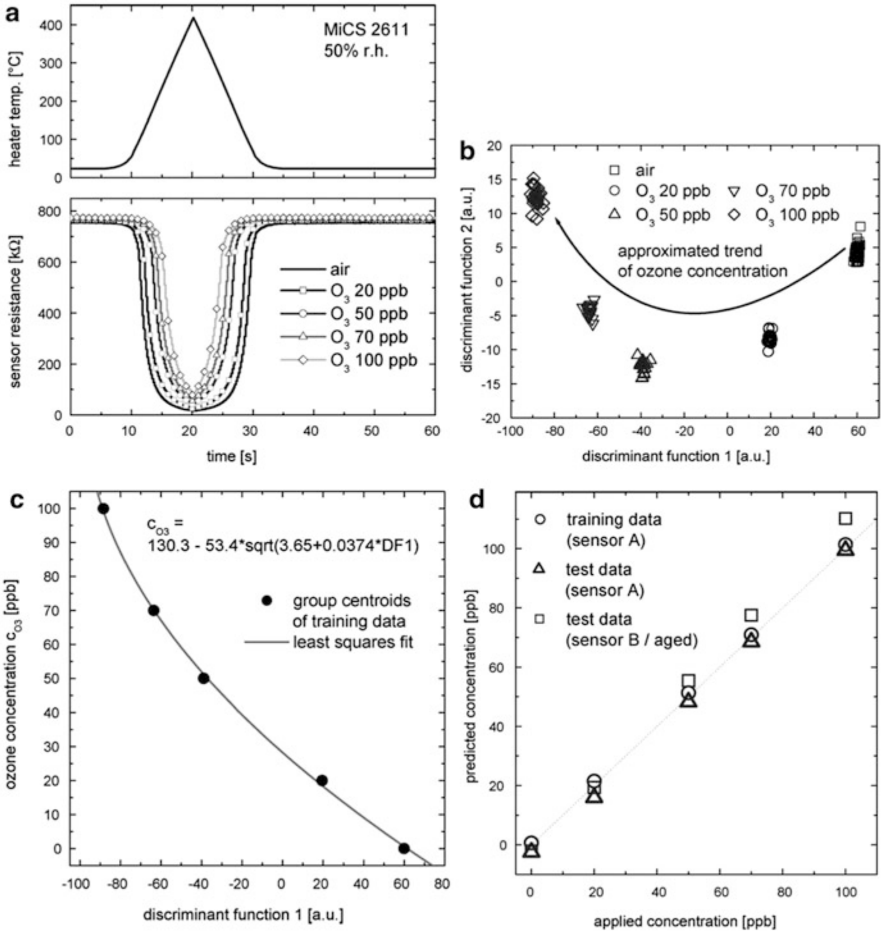

Fig. 9 (**a**) Temperature cycle based on linear ramps from RT up to 400°C and back to RT and resulting sensor response for different O_3 concentrations; (**b**) LDA plot separating the five groups with different ozone concentrations; (**c**) fit function for predicting the ozone concentration based on the values of the first discriminant function; (**d**) predicted vs. applied ozone concentration for the training and test data for sensor A and test data for the aged sensor B showing excellent correlation. ([93], reproduced with permission)

polynomial to the calibration data obtained from the LDA, i.e., the value of the first discriminant function and the corresponding ozone concentration as shown in Fig. 9, bottom left. To validate this approach, the data evaluation was applied to results from a second measurement series using the same sensor and to results from a second, aged sensor operated with the same temperature cycle. Figure 9, bottom right, shows that the predicted ozone concentration shows a maximum deviation of 10 ppb from the applied concentration, which is a drastic improvement compared to the results obtained for static sensor operation. Note that the absolute sensor resistance, i.e., the single value evaluated for static operation, is eliminated from the response by the normalization of the pattern. The number of required features extracted from the response pattern was further reduced to only 10 by describing the hysteresis between ramp up and ramp down instead of evaluating each separately.

In the presence of interfering gases, the unmodified strategy led to larger deviations of the predicted ozone concentration. Especially in the presence of CO which might result from exhaust gases or other combustion processes, the ozone concentration was consistently predicted too low with deviations of 20 ppb. Similar but less relevant deviations occurred in the presence of NO_2, while the combination of CO and NO_2 cancelled each other leading to nearly no deviation of the predicted ozone concentration. To compensate this effect, the background atmosphere is classified and prediction is based on modified fit functions adapted to the background. The identification of the background was realized using the same features extracted from the same temperature cycle. Note that this identification is possible only if no ozone is present, which can be achieved by simply switching the ozone generator off for the background classification.

Thus, TCO and application-specific data evaluation results in a considerable improvement compared to standard static operation of the gas sensor. Even though data processing is based on a method developed for classification, i.e., LDA, an analog concentration prediction is obtained by calculating a fit function between the first discriminant value and the concentration. The evaluation can be performed by any microcontroller since all calculations with large computational effort (LDA and curve fitting) are only performed off-line. The biggest drawback of the presented solution is the long duration of the temperature cycle which leads to a low measurement rate for the final system and can also lead to false results if the gas composition changes during the measurement. However, while the microstructured sensor would allow much faster cycling, the characteristic response features for ozone were only obtained using slow temperature changes.

5.2 Sweat Odor Assessment

The assessment of complex smells is a very difficult problem for gas sensor systems. Typically, sensor arrays or electronic noses can only compare different samples and indicate the degree of their similarity. In this example [94–96], the results obtained with an electronic nose were correlated with the assessment from a human sensory panel. The goal of the project was to prove that sensor systems can take over routine measurements from sensory panels after having been correctly trained. The application studied concerned the assessment of the smell of sweat for shoes and socks. The sensor system should then be used in the development of shoes and socks, testing different materials and material combinations with the goal of reducing the often unpleasant and embarrassing odor. In the project, a number of different shoes, e.g., leather sneakers, sports shoes, and even gumboots, and socks were worn under controlled conditions by a number of test persons. Afterwards, the sweat odor intensity was evaluated by a sensory panel consisting of six test persons on a scale of 1 (no odor) to 5 (very strong sweat odor). In parallel, the smell was measured with commercial ceramic metal oxide gas sensor, UST 1330 [98], operated in TCO mode with a temperature cycle lasting 40 s and spanning the temperature range from 240°C to 420°C. Sampling was performed by placing the shoe or sock in a clean glass test chamber and drawing air from this test chamber over the sensor. Data were recorded over 20 min, resulting in 30 temperature cycled for each sample. To suppress the influence of the ambient, the test chamber was flushed with an excess of humidified pure air. Data evaluation consisted of normalization followed by feature extraction from the TCO pattern: this was divided into four sections and from each section the mean value and the slope were extracted, thus basically describing the shape of the sensor response. PCA and LDA were both tested on a subset of the data to evaluate their suitability for predicting the odor intensity. While PCA does not achieve a grouping of the data with the same odor intensity, LDA again shows a good and nearly linear correlation between odor intensity and the first discriminant function (Fig. 10).

However, the prediction of the odor intensity based on the value of the first discriminant function proved shaky, i.e., resulting in large spread and could not be applied to data obtained in further measurement series. Here, a neural network trained with the features extracted from the temperature cycle proved more suitable. The network structure is a simple feedforward network with eight input neurons for the eight features, one hidden layer, also with eight neurons, and a single analog output neuron trained to predict the odor intensity. While predictions for each single

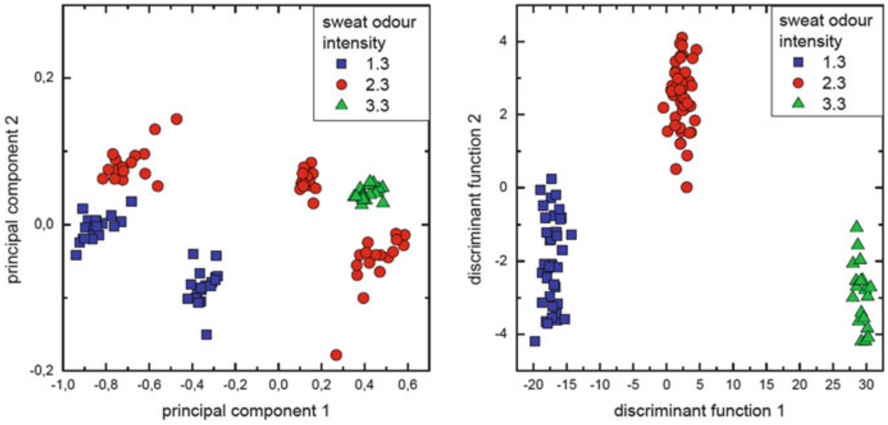

Fig. 10 Comparison of PCA (*left*) and LDA (*right*) plots for the same data for assessment of the sweat odor intensity [96]. While the LDA plot shows good correlation between the value of the first discriminant function and the odor intensity, the PCA plot shows six separate groups corresponding to the measurements of six different shoes with no correlation between the odor intensity and the two first principal components

temperature cycle proved to show large spread, the averaging of the predictions for all temperature cycles for each sample resulted in predictions with an accuracy similar to the standard deviation of the human sensory panel even when applied to three different measurement series spread over a period of several months as shown in Fig. 11.

Thus, even though the sensor shows drift, data obtained from TCO combined with suitable data preprocessing and feature extraction allowed a high-quality prediction and proved that the sensor system can successfully evaluate one specific smell (sweat) in a complex matrix, i.e., the smell of the different materials like leather, synthetics, or rubber. Note, however, that this result might change if different shoes with different materials and, thus, different base smells are evaluated. The sensor performance was probably based on detection and quantification of isovaleric acid, the lead compound in sweat, especially in foot odor. In separate tests with the pure compound, we could show that the sensor used in these experiments actually achieves a sensitivity vs. isovaleric acid similar to the human nose.

5.3 Fire Detection

Fire detection is expected to by one of the next large markets for gas sensors. Already today, gas sensor-based fire detectors have become the standard in specific application environments, where traditional smoke detectors cannot be used, i.e., in areas with a lot of dust or fog. In these cases, multisensor systems have proven very successful for early fire detection by recognizing typical fire gases like CO or H_2 (resulting from hydrolysis of water); these systems make use of advanced signal processing to achieve high reliability and very low false alarm rates [37, 38]. The

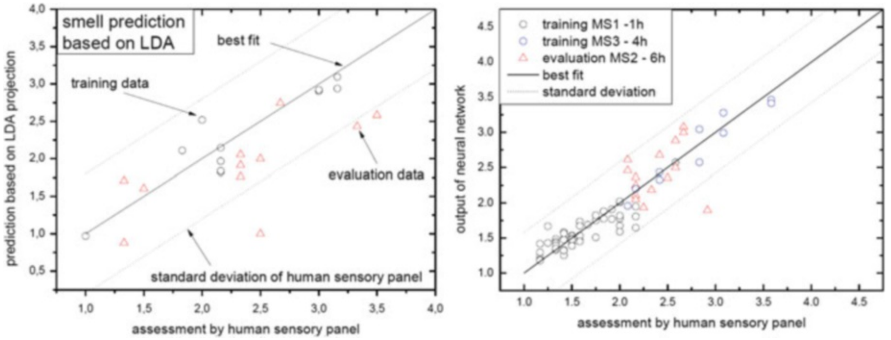

Fig. 11 Prediction of the odor intensity based on LDA projection (*left*) and the output of a neural network trained with backpropagation (*right*), respectively. In both cases, the predictions of all temperature cycles for one sample are averaged; triangles denote evaluation data, i.e., data not used for developing the prediction algorithm. While LDA prediction is shaky even for measurements from one experimental series, the neural network is able to predict the odor intensity with an accuracy similar to the standard deviation of the human sensory panel (*dashed lines*) even for three different measurement series (MS) spread over a period of several months [96]

opportunities for gas sensors in this application are high as all fires are accompanied by typical fire gases being produced which in principle allow not only fast and reliable detection but also a classification, which can help to mitigate the damages caused by the fire and/or an analysis of the cause of fires. On the other hand, fire detection, as applications in safety and security in general, demands high reliability, especially with zero false-negative results and an acceptable suppression of false alarms. Even though gas sensors have been successful in niche applications for many years, more research is required [99, 100].

5.3.1 Fire detection in Buildings

Fire detectors in buildings are installed in huge numbers of several Mio each year with increasing tendency due to stricter regulations demanding fire detectors not only in public buildings but also in private homes. The requirements for fire detectors are defined in EN 54 [73] and are based on the timely detection of different types of test fires, i.e., smoldering and open fires, with and without smoke generation [101]. This is actually one of the main obstacles for introducing gas sensor-based fire detectors as the standard has been written with respect to smoke and heat detectors. However, gas sensor-based detectors can meet these requirements and have proven suitable for all fires defined in the international standard [37]. Another and in practice very relevant limitation is the power consumption: fire detectors in buildings are often battery powered (for private homes) or powered via their data bus (in networked building installations) with a power consumption of less than 1 mW/unit. This seems to exclude many gas sensor principles depending on heated sensors, i.e., MOS-type sensors. Thus, electrochemical cells and gas-sensitive field-effect sensors operating at room temperature are proposed for fire detectors [101, 102]. False alarm suppression, however, usually requires multisensor arrays to be used. For example, CO alone is not significant for fire detection and is often actually used primarily to prevent CO poisoning at high concentrations rather than for early fire detection at low concentrations. Detection levels for smoldering fires are in the range of tens of ppm, which is easily reached also by traffic exhaust introduced into building through open windows.

Hoefer et al. have studied multisensor systems combining MOS sensors, GasFET, EC cells for CO and NO_2, an NDIR cell for CO_2, and temperature and humidity sensors [101] (see Fig. 12). These studies proved that the early detection of fires and even identification of fire type, i.e., open or smoldering fire, is possible with this system using calibration data sets obtained from standardized test fires interpreted by PLSDA. In this method, the different situations to be identified are simply given a numerical value, i.e., -1 for no fire and 1 for fire, and a function is fitted to the multidimensional training data set (variables) to fit the classification (target values) using partial least squares. By selecting a suitable threshold value for the analog prediction resulting from the function applied to new data, a fairly high reliability is achieved. Note that with this threshold, the algorithm can be tuned to be more, i.e., allow faster fire detection, or less sensitive, i.e., achieve better false

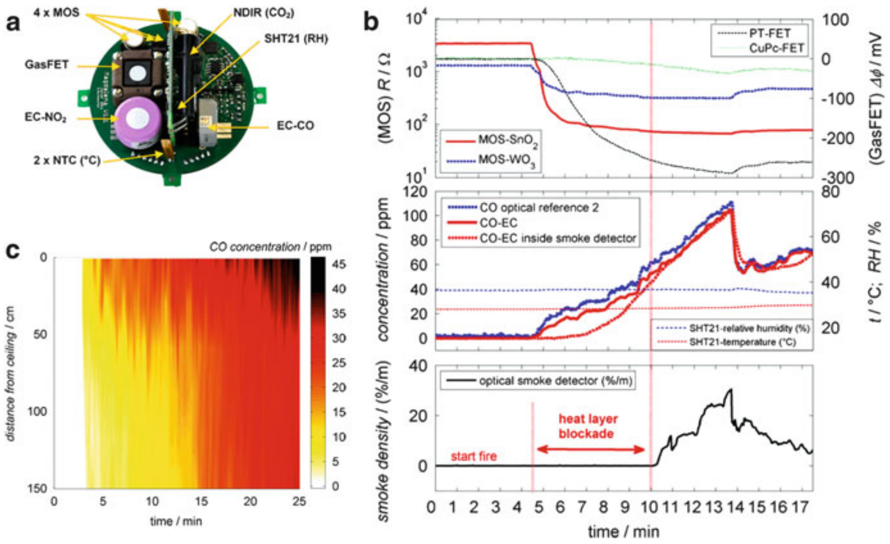

Fig. 12 (**a**) Multisensor array with various gas sensors, temperature, and humidity sensors for fire detection studies; (**b**) sensor signals obtained from the multisensor array for a smoldering wood fire (EN 54, test fire 2) in a room with heated ceiling leading to a significantly delayed response of the smoke detector due to a heat layer at the ceiling; (**c**) modeling of the CO distribution resulting from smoldering cotton shows that the highest concentrations are directly at the ceiling, i.e., the location of the gas sensor system ([101], reproduced with permission)

alarm suppression. Here also, data preprocessing, mainly smoothing, and feature extraction were used to improve the results. For the gas sensor signals, the authors used the sensor signal slope to become independent of the baseline and thus of sensor drift. The discrimination between flaming and smoldering fires and even the recognition of possible false alarm scenarios, i.e., cigarette smoke, were also possible by defining specific target functions for these events again with PLSDA. The authors also noted advantages for gas sensor-based fire detectors especially due to faster detection of fire gases compared to smoke: smoke is often blocked from reaching the fire detector by a heat layer at the ceiling. Especially MOS sensors achieved a detection of some fires in half the time required for standard smoke detectors as shown in Fig. 12b. This is due to CO spreading along the ceiling thus reaching the highest concentrations where the detectors are placed as shown by modeling the gas distribution in fire test chambers (Fig. 12c).

Fire detection in buildings was also studied with a virtual multisensor system based on a single microstructured MOS sensor [54, 94]. This sensor was operated in a temperature cycle with a duration of only 250 ms, i.e., five temperature levels held for 50 ms each, after which the sensor was switched off for 14.75 s to achieve an average power consumption of only 1.3 mW. This sensor-operating mode allowed discrimination of typical fire gases [103] and was trained for discrimination of various fire and non-fire situation simulated in a miniaturized fire test chamber [104]. The sensor systems proved stable during field testing over one year even under harsh environments, for example, in a cafeteria kitchen. At this test sight, an optical smoke detector laced alongside generated more than 600 false alarms plus additional error messages. The gas sensor system, on the other hand, allowed discrimination of typical patterns obtained by cooking activities from the trained fire patterns [54, 105]. Signal analysis was based on the same principles as described for the sweat odor assessment above, i.e., normalization, feature extraction as levels and slopes, and LDA for dimensionality reduction with each test fire and false alarm situation defined as a separate class.

Further studies [106] even showed the potential for discrimination of different fire and non-fire situation, i.e., six test fires as defined in EN 54 plus six false alarm situations (e.g., disco fog, indoor fireworks) and finally background air using a virtual multisensor combined with an artificial neural network for evaluation. The network had 13 output neurons, one for each class, to classify all situations. Training was based on approx. 12 repetitions of fire and non-fire situations simulated in the miniaturized fire test chamber [104]. Of the 260 randomly selected validation data sets, i.e., temperature cycles, 20 for each situation, only six false classifications were observed based on a winner-takes-all approach, i.e., assigning the class of the neuron with the highest output. Furthermore, these false classifications always occurred at the beginning of the test which were similar, i.e., open spirit fire (TF6) and spirit on sugar to simulate flambéing of food. The repetition of the tests after several months showed increasing false classifications due to sensor drift. However, it was possible to train a neural network with data from the first and second series of experiments to take into account the sensor drift. This network which was trained to only give an alarm/no-alarm decision achieved correct classification for more than 95% of all individual T-cycles. By evaluating the predictions of several T-cycles, this could be increased even further showing the large potential for gas sensors for fire detection.

5.3.2 Underground Fire Detection

Fire detection systems are often required for very specific application scenarios. Coal mines, for example, require very sensitive detectors for smoldering coal fires, which can self-start in inactive mine sections. The large weight of the rocks causes immense pressure on the coal leading to increased temperature and (very) slowly developing smoldering fires. If the fire reaches a critical temperature or if fresh air reaches the smoldering coal, an open fire can result which spreads fast and is very difficult to contain. Earlier studies on coal fires have shown that in addition to CO as an indicator for smoldering fire these are characterized by significant generation of ethane (C_2H_4) and a characteristic CO/C_2H_4 ratio of 100/1 [107]. Due to increased fresh air supply in coal mines in Europe, relevant detection limits are approx. 10 ppm for CO and 100 ppb for C_2H_4, respectively. At the same time, typical background concentrations of methane released from the coal are up to 1% during normal operation. In addition, the sensor can be confused by typical operating conditions releasing various gases, such as diesel exhaust (NO_x, CO), blasting fumes (NO_x), and battery chargers (H_2). Thus, a very high selectivity is required, with interfering gases, for example, CH_4 at 1% or 10^4 ppm, having concentrations up to five orders of magnitude higher than the target gases, for example, C_2H_4 at 100 ppb.

We developed a sensor system, again based on a single commercial MOS sensor [98] combined with TCO and advanced signal processing, allowing only detection of this specific fire signature but also discrimination from other situation typical from operating conditions [108]. To achieve this extreme selectivity, the sensor is operated not with step changes in the temperature cycle but instead with temperature ramps allowing exact control of the sensor temperature at each point independent of changes in the ambient. Data evaluation is also based on the normalization of the sensor response to suppress drift effects and feature extraction, i.e., mean values and slopes in different sections of the cycle as described above. However, subsequent dimensionality reduction and classification are not performed on one step. Instead, a hierarchical classification scheme is applied as shown in Fig. 13.

In the first classification step, the ambient humidity level is determined, a value that can either be extracted directly from the sensor response pattern itself (see also [103]) or by using a separate r.h. sensor. In the second step, the CH_4 concentration is determined, again either from the sensor response pattern or from the CH_4 sensors always installed for explosion warning in coal mines. Based on the knowledge of ambient conditions and the concentration of the dominating interfering gas CH_4, the third classification determines if hydrogen is present in the atmosphere, which would otherwise interfere with the data evaluation. In the fourth step, an alarm decision is finally achieved. The corresponding LDA plots obtained for the calibration data based on synthetic gas mixture to simulate the real conditions are shown in Fig. 13b, c for the third and final decision, respectively. Note that the data contain various mixtures with CO and NO_x separately as well as together to simulate typical operating conditions. The alarm decision is based on groups with (fire) and without (no fire) C_2H_4. The warning group is a mixture of all three gases, which can be caused both by a smoldering fire and additional NO_x, for example, from blasting operations, as well as diesel exhaust, which can contain all three gases. The system is therefore not able to discriminate between these situations as they are actually identical in their gas composition. However, while smoldering fires develop over a long time (several hours or even days), blasting fumes and diesel exhaust gases typically appear only briefly for minutes which means that the warning situation should be resolved after some time to obtain a definite result.

This system was also tested underground in field experiments and showed excellent correlation to the existing CO monitoring, also allowing discrimination of various typical operating situations. Over several months, however, the significant drift of the sensor response pattern was observed which did not longer allow reliable

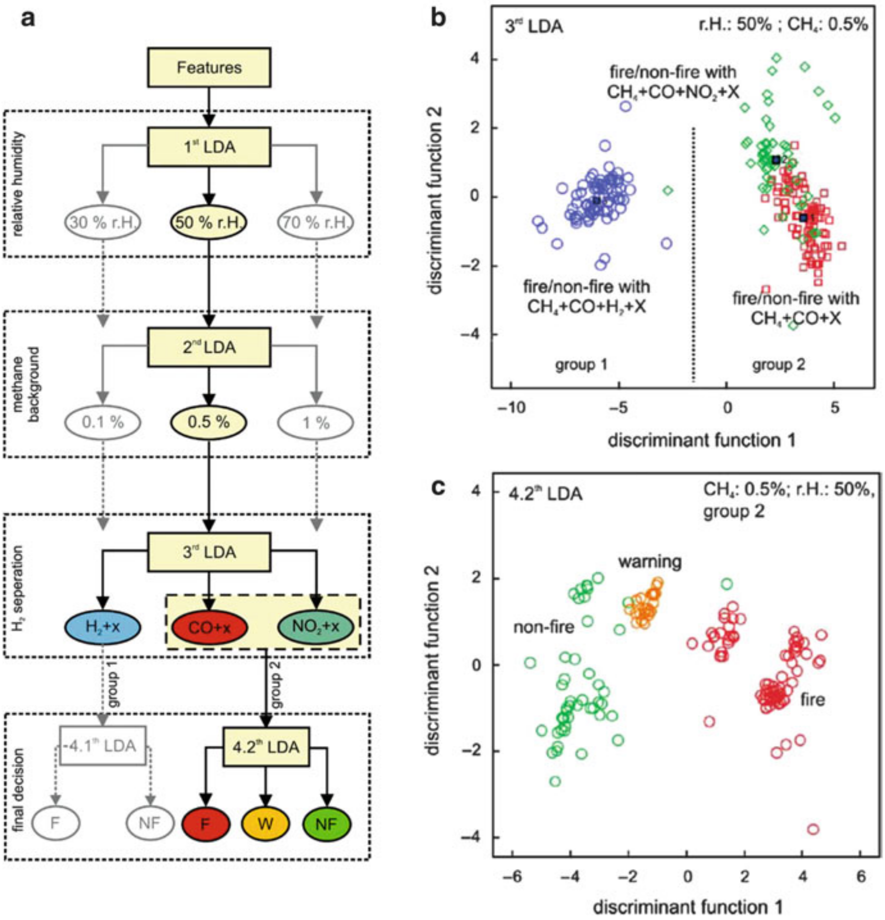

Fig. 13 (**a**) Hierarchical data evaluation for underground smoldering fire detection; (**b**) and (**c**) show the LDA plots for decision 3 (H_2 separation) and decision 4.2 (no fire, warning, fire), respectively, for 50% r.h. and 0.5% CH_4 background. Calibration data are required for the complete range of ambient conditions to allow alarm decisions under any conditions ([108], reproduced with permission)

discrimination of the various situations. To counteract this drift online recalibration based on two test gas mixtures is suggested. Recalibration is performed at the LDA projection level by shifting and rotating the projections so that the sensor patterns recorded during recalibration again match the original training data. In addition, sensor self-monitoring was suggested. This can be achieved either by combining two redundant methods for data extraction, for example, TCO and EIS, or by comparing the predictions obtained from the sensor system (first and second decision in Fig. 13) with data from reference sensors for r.h. and CH_4, respectively, as shown schematically in Fig. 14.

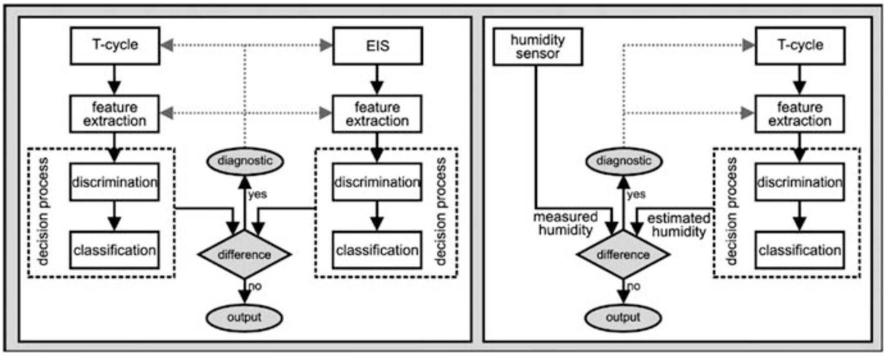

Fig. 14 Self-monitoring and self-diagnosis strategy for safety and security applications based on semiconductor gas sensors: by using a combination of T-cycling and EIS, redundant data from both methods are evaluated separately and the output is checked for differences (*left side*); alternatively, r.h. and/or CH_4 can be estimated from TCO data and compared with the output of a separate humidity sensor or methane sensor (*right side*); in both cases, detected differences are used to signal a possible malfunction and/or change the operating mode to start a self-diagnosis of the system ([108], reproduced with permission)

6 Conclusions

The examples shown above prove the large potential for sensor arrays and data fusion for gas sensor systems. Classic multisensor arrays as generic electronic noses with a broad detection spectrum are excellent for the comparison of complex gas mixtures or odors, but require frequent recalibration due to sensor drift changing the signal pattern. Thus, these systems should be understood as laboratory-type equipment to be used by trained personnel. With adequate care in data acquisition, including sampling, preprocessing, and evaluation, truly astounding results can be obtained. However, one should always be careful to test and verify the results. Otherwise, one might obtain the impression that e-nose systems are suitable for quality control of wines while in fact only the alcohol content is measured.

Dynamic operation, on the other hand, can not only improve the stability of a sensor signal, but can also increase the selectivity drastically by evaluating the response pattern resulting from controlled changes of the operating condition of the sensor. This is most evidently useful for temperature changes, as the chemical interaction between sensor and gas is directly affected, but can also be achieved with other methods like impedance measurement, bias cycling, etc. The main importance of dynamic operation is the increase stability, especially compared to static sensor arrays. This is due mainly to the fact that drift affects the complete sensor and thus still allows (limited) interpretation of the response pattern even if the sensor has changed due to aging or poisoning.

Signal evaluation is a powerful but also complex process which needs to be done methodically and carefully. Standard methods like multivariate statistics or ANN have proven very successful for a wide range of applications at least in lab testing.

However, the true test for gas sensor systems is in the field in which additional effects not simulated in the laboratory might affect the sensor. Making full use of this potential allows development of superior gas measurement systems with high performance and even self-monitoring functionality to indicate changes of the sensor making this approach very attractive also for applications in safety and security. Note, however, that for applications in safety and security some of the data evaluation strategies presented above are not acceptable, at least today. Certification requires data evaluation algorithms to be verifiable, i.e., the behavior of the algorithm for changes of the input signals or fault situations has to be predictable. This actually rules out many nonlinear methods such as ANN as for even tiny changes of the input patterns, the output can change completely. Other methods, especially linear projection based on only a limited number of features extracted from the sensor response, are acceptable. For example, the hierarchical evaluation strategy for underground fire detection presented in Sect. 5.3.2 was evaluated by Dekra/EXAM in the framework of the European project SAFETECH [109], and the potential for this approach and its certification was confirmed.

However, one major obstacle remains for many applications: the calibration process is time-consuming and tedious, with sensor to sensor variation preventing the use of a standardized evaluation algorithm for all systems [89; Kelleter J (private communication)]. Both for static sensor arrays and dynamic virtual multisensor, making full use of the potential of advanced data analysis requires individual and extensive calibration. For low-cost systems this increases the cost dramatically, especially if complex tests have to be performed as required for fire detection. Additional research is required either to improve the repeatability of the sensor performance, for example, by making use of advanced nanotechnologies to obtain very uniform gas-sensitive layers, or to simplify the calibration process. One possible approach could be classification of each sensor according to a range of reference sensor prototypes based on testing with standardized test gases in the production process. This could be improved further by individual adaptation of the signal processing based on application-specific test gas mixtures.

On the other hand, the same general application, for example, fire detection, will have very different gas signatures in the different operating environments, depending on the type of burning materials, background gases, and ambient conditions. Air flow from the source to the sensor or away from the sensor will lead to huge concentration variations; ambient conditions will change the gas mixture because rain can wash out some components and others will not desorb at low temperatures. This variation has to be taken into account also, for example, by installing the sensor systems in their operating environment for several weeks before setting alarm thresholds based on typical sensor patterns observed during this time. It is obvious that this type of adaptation, which is today performed semiautomatically for niche applications [Kelleter J (private communication)], has to be fully automated for low-cost applications, which is another challenge for data fusion and evaluation.

Chemical sensors will always be subject to sensor drift due to the chemical interaction between the transducer itself and the analyte to be tested. Drift needs to be recognized, either by testing in the field or by suitable self-monitoring strategies as outlined above. Recalibration could then be used to adapt the signal processing to allow longer operation of the sensor systems.

Finally, ubiquitous sensor networks not only pose challenges, i.e., due to larger number of sensors, but also offer opportunities, especially if heterogeneous networks are deployed. In environmental monitoring, combining low-cost mobile sensor platforms with high-performance stationary measurement systems allows on-the-fly calibration by using a fixed station as reference whenever a mobile sensor is close to it [110]. Making full use of intelligent sensor networks would allow many new applications from chemical weather forecasting, i.e., localized prediction of concentrations of hazardous air contaminants, to early warning against terrorist threats, for example, with explosives or chemical warfare agents.

To make full use of the potential of gas sensor systems, close interaction between research in materials, transducers, sensor operation and readout and, last but not least, signal evaluation is required.

References

1. Blaschke M, Tille T, Robertson P, Mair S, Weimar U, Ulmer H (2006) MEMS gas-sensor array for monitoring the perceived car-cabin air quality. IEEE Sens J 6(5):1298–1308. doi:10.1109/JSEN.2006.881399
2. Galatsis K, Wlodarski W, Kalantar-Zadeh K, Trinchi A (2002) Investigation of gas sensors for cabin air quality monitoring. Proc COMMAD 2002:229–232. doi:10.1109/COMMAD.2002.1237234
3. Ahmed O (2012) Future building sensing applications. In: Fleischer M, Lehmann M (eds) Solid state gas sensors: industrial application. Springer, ISBN: 978-3-642-28093-1
4. Bachinger T, Haugen J-E (2003) Process monitoring. In: Pearce TC, Schiffman SS, Nagle HT, Gardner JW (eds) Handbook of machine olfaction – electronic nose technology. Wiley-VCH, ISBN: 3-527-30358-8
5. Schütze A, Gramm A, Gottfried-Gottfried R (2003) Fast leak test based on gas sensors for direct integration in the manufacturing process. In: Proceedings of the sensor 2003, vol 1. Nuremberg, 13–15 May 2003, pp 249–254.
6. Gramm A, Schütze A (2006) Sealing testing method for products incorporating a fluid (*Verfahren und Vorrichtung zur Dichtheitsprüfung*), Patent DE 10,316,332, 2006
7. Becher C, Kaul P, Mitrovics J, Warmer J (2010) The detection of evaporating hazardous material released from moving sources using a gas sensor network. Sens Actuators B 146: 513–520. doi:10.1016/j.snb.2009.12.030
8. Wang J (2007) Electrochemical sensing of explosives. Electroanalysis 19(4):415–423. doi:10.1002/elan.200603748
9. Pamula VK (2003) Detection of explosives. In: Pearce TC, Schiffman SS, Nagle HT, Gardner JW (eds) Handbook of machine olfaction – electronic nose technology. Wiley-VCH, ISBN: 3-527-30358-8
10. Persily AK (1997) Evaluating building IAQ and ventilation with indoor carbon dioxide. ASHRAE Trans 103(2)
11. Scheff PA, Paulius VK, Huang SW, Conroy LM (2000) Indoor air quality in a middle school, part I: use of CO_2 as a tracer for effective ventilation. Appl Occup Environ Hyg 15(11): 824–834. doi:10.1080/10473220050175706
12. Batterman S, Peng C (1995) TVOC and CO_2 concentrations as indicators in indoor air quality studies. Am Ind Hyg Assoc J 56(1):55–65. doi:10.1080/15428119591017321

13. Norbäck D, Björnsson E, Janson C, Widström J, Boman G (1995) Asthmatic symptoms and volatile organic compounds, formaldehyde, and carbon dioxide in dwellings. Occup Environ Med 52:388–395. doi:10.1136/oem.52.6.388
14. Schütze A (2012) Chemical sensors for indoor applications. In: Proceedings of the 14th international meeting on chemical sensors, Nürnberg/Nuremberg, 20–23 May 2012, ISBN:978-3-9813484-2-2, pp 630–634. doi:10.5162/IMCS2012/7.4.1
15. Pauling L, Wood RE, Sturdivant JH (1946) An instrument for determining the partial pressure of oxygen in a gas. J Am Chem Soc 68(5):795–798. doi:10.1021/ja01209a029
16. Hummel H (1968) Ein neuer magnetischer Sauerstoff-Messer mit sehr kurzer Einstellzeit und hoher Selektivität. Chemie Ingenieur Technik 40(19):947–951. doi:10.1002/cite.330401903
17. Dietz H, Haecker W, Jahnke H (1977) Electrochemical sensors for the analysis of gases. In: Gerischer H, Tobias CW (eds) Advances in electrochemical sciences and engineering, vol 10. Wiley, New York, pp 1–90
18. Riegel J, Neumann H, Wiedenmann H-M (2002) Exhaust gas sensors for automotive emission control. Solid State Ionics 152–153:783–800. doi:10.1016/S0167-2738(02)00329-6
19. Barsan N, Weimar U (2001) Conduction model of metal oxide gas sensors. J Electroceram 7(3): 143–167. doi:10.1023/A:1014405811371
20. Heiland G (1981–1982) Homogeneous semiconducting gas sensors. Sens Actuators 2:343–361. doi:10.1016/0250-6874(81)80055-8
21. Jones E (1987) The pellistor catalytic gas detector. In: Mosley PT, Tofield BC (eds) Solid state gas sensors, Chap. 2. Adam Hilger, Bristol
22. Gall M (1991) The Si-Planar-Pellistor: a low-power pellistor sensor in Si thin film technology. Sens Actuators B 4:533–538. doi:10.1016/0925-4005(91)80165-G
23. Lundström I, Sundgren H, Winquist F, Eriksson M, Krantz-Rülcker C, Lloyd Spetz A (2007) Twenty-five year of field effect gas sensors research in Linköping. Sens Actuators B 121:247–262. doi:10.1016/j.snb.2006.09.046
24. Lloyd Spetz A, Andersson M (2012) Technology and application opportunities for SIC FET gas sensors. In: Fleischer M, Lehmann M (eds) Solid state gas sensors: industrial application. Springer, ISBN: 978-3-642-28093-1
25. Lundström I, Shivaraman MS, Svensson C, Lundkvist L (1975) A hydrogen-sensitive MOS field-effect transistor. Appl Phys Lett 26(55):55–57. doi:10.1063/1.88053
26. Hock B, Seifert M, Kramer K (2002) Engineering receptors and antibodies for biosensors. Biosens Bioelectron 17(3):239–249. doi:10.1016/S0956-5663(01)00267-6
27. Dodd GH, Persaud KC (1982) Analysis of discrimination mechanisms in the mammalian olfactory system using a model nose. Nature 299:352–355
28. Pearce TC, Schiffman SS, Nagle HT, Gardner JW (eds) (2003) Handbook of machine olfaction – electronic nose technology. Wiley-VCH, ISBN: 3-527-30358-8
29. Mayer F, Grosch W (2001) Aroma simulation on the basis of the odourant composition of roasted coffee headspace. Flavour Frag J 16:180–190. doi:10.1002/ffj.975
30. Schiffman SS, Pearce TC (2003) Introduction to olfaction: perception, anatomy, physiology, and molecular biology. In: Pearce TC, Schiffman SS, Nagle HT, Gardner JW (eds) Handbook of machine olfaction – electronic nose technology. Wiley-VCH, ISBN: 3-527-30358-8
31. Sommer V (1993) Einsatz von katalytisch aktiven Metallen zur Beeinflussung der Nachweisempfindlichkeit und Selektivität von Gassensoren. Dissertation, RWTH Aachen
32. Vanneste E, Geise HJ (2003) Commercial electronic nose instruments. In: Pearce TC, Schiffman SS, Nagle HT, Gardner JW (eds) Handbook of machine olfaction – electronic nose technology. Wiley-VCH, ISBN: 3-527-30358-8
33. Persaud KC, Travers P (1991) Multi-element arrays for sensing volatile chemicals. Intell Instrum Comput 9(4):147–154
34. Annor-Frempong IE, Nute GR, Wood JD, Whittington FW, West A (1998) The measurement of the responses to different odour intensities of “boar taint” using a sensory panel and an electronic nose. Meat Sci 50:139–151. doi:10.1016/S0309-1740(98)00001-1

35. Stetter JR, Penrose WR, McEntegart C, Roberts R (2000) Prospects for infectious disease diagnosis with sensor arrays. In: Proceedings of the 7th international symposium of olfaction and electronic nose, Brighton, 20–24 July 2000, pp 101–104
36. Beccherelli R, Zampetti E, Pantalei S, Bernabei M, Persaud KC (2010) Design of a very large chemical sensor system for mimicking biological olfaction. Sens Actuators B 146(2):446–452. doi:10.1016/j.snb.2009.11.031
37. Kohl D, Kelleter J, Petig H (2001) Detection of fires by gas sensors. Sens Update 9:161–223
38. Kelleter J (1997) Künstliche Nase für gasförmige Emissionen aus unvollständiger Verbrennung, Aufbau und Erprobung eines Multi-Gassensor-System. Dissertation; Justus-Liebig-Universität Gießen; Shaker Verlag, ISBN: 3-8265-2072-6
39. Elmi I, Zampolli S, Cozzani E, Mancarella F, Cardinali GC (2008) Development of ultra-low-power consumption MOX sensors with ppb-level VOC detection capabilities for emerging applications. Sens Actuators B 135(1):342–351. doi:10.1016/j.snb.2008.09.002
40. GTE Industrieelektronik mbH, Viersen, http://www.adicos.de/
41. Airsense Analytics GmbH, Schwerin, http://www.airsense.com/
42. Alpha MOS, Toulouse, http://www.alpha-mos.com/
43. Nitta M, Ohtani S, Haradome M (1980) Temperature dependence of resistivities of SnO_2-based gas sensors exposed to CO, H_2 and C_3H_8 gases. J Electron Mater 9(4):727–743. doi:10.1007/BF02652893
44. Arnold C, Harms M, Goschnick J (2002) Air quality monitoring and fire detection with the Karlsruhe electronic micronose KAMINA. IEEE Sens J 2(3):179–188. doi:10.1109/JSEN.2002.800681
45. Althainz P, Dahlke A, Frietsch-Klarhof M, Goschnick J, Ache HJ (1995) Reception tuning of gas-sensor microsystems by selective coatings. Sens Actuators B 25(1–3):366–369. doi:10.1016/0925-4005(95)85082-1
46. Eicker H (1977) Method and apparatus for determining the concentration of one gaseous component in a mixture of gases, US Patent 4,012,692, 15 March 1977
47. Lee AP, Reedy BJ (1999) Temperature modulation in semiconductor gas sensing. Sens Actuators B 60:35–42. doi:10.1016/S0925-4005(99)00241-5
48. Clifford PK, Tuma DT (1983) Characteristics of semiconductor gas sensors II. Transient response to temperature change. Sens Actuators B 3:255–281. doi:10.1016/0250-6874(82)80027-9
49. Heilig A, Bârsan N, Weimar U, Schweizer-Berberich M, Gardner JW, Göpel W (1997) Gas identification by modulating temperatures of SnO_2-based thick film sensors. Sens Actuators B 43:45–51. doi:10.1016/S0925-4005(97)00096-8
50. Engel M, Baumbach M, Kammerer T, Schütze A (2004) Preparation of microstructured pellistors and their application for fast fuel vapor discrimination. In: Proceedings of the 17th IEEE international conference on micro electro mechanical systems (MEMS 2004), Maastricht, 25–29 January 2004, pp 268–271. doi:10.1109/MEMS.2004.1290574
51. Bur C, Reimann P, Andersson M, Schütze A, Lloyd Spetz A (2012) Increasing the selectivity of Pt-gate SiC field effect gas sensors by dynamic temperature modulation. IEEE Sens J 12(6):1906–1913. doi:10.1109/JSEN.2011.2179645
52. Bur C, Reimann P, Andersson M, Lloyd Spetz A, Schütze A (2012) New method for selectivity enhancement of SiC field effect gas sensors for quantification of NOx. Microsyst Technol 18(7):1015–1025. doi:10.1007/s00542-012-1434-z
53. Kammerer T, Engel M, Schütze A (2003) An intelligent fuel sensor based on a microstructured gas sensor. In: Proceedings of the IEEE sensors 2003, vol 2. Toronto, 22–24 October 2003, pp 1064–1069. doi:10.1109/ICSENS.2003.1279106
54. Ankara Z, Schütze A (2008) low power virtual sensor system based on a micromachined gas sensor for security applications and warning systems. In: Proceedings of the EUROSENSORS, Dresden, pp 495–498, 2008
55. Baumbach M, Kammerer T, Sossong A, Schütze A (2004) A new method for fast identification of gases and gas mixtures after sensor power up. In: Proceedings of the IEEE sensors

conference 2004, vol 3. Vienna, 24–27 October 2004, pp 1388–1391. doi:10.1109/ICSENS.2004.1426443

56. Weimar U, Göpel W (1995) A.c. measurements on tin oxide sensors to improve selectivities and sensitivities. Sens Actuators B 26–27:13–18. doi:10.1016/0925-4005(94)01547-U
57. Fleischer M, Wagner V, Hacker B, Meixner H (1995) Comparison of a.c. and d.c. measurement techniques using semiconducting Ga_2O_3 sensors. Sens Actuators B 26–27:85–88. doi:10.1016/0925-4005(94)01562-V
58. Barsan N, Koziej D, Weimar U (2007) Metal oxide-based gas sensor research: how to? Sens Actuators B 121(1):18–35. doi:10.1016/j.snb.2006.09.047
59. Hoefer U, Steiner K, Wagner E (1995) Contact and sheet resistances of SnO_2 thin films from transmission-line model measurements. Sens Actuators B 26–27:59–63. doi:10.1016/0925-4005(94)01557-X
60. Barsan N, Schweizer-Berberich M, Göpel W (1999) Fundamental and practical aspects in the design of nanoscaled SnO_2 sensors: a status report. Fresenius J Anal Chem 365(4):287–304. doi:10.1007/s002160051490
61. Ross Macdonald J (1987) Impedance spectroscopy – emphasing solid materials and systems. Wiley, New York. ISBN 0-471-83122-0
62. Diehl C (1994) Optimierung von Halbleiter-Gassensoren zum Nachweis von CO und NO in Verbrennungsabgasen, diploma thesis. Institute for Applied Physics, JLU Gießen
63. Schüler M, Darsch S, Reimann P, Schütze A (2010) Low-cost impedance spectroscopy for semiconductor gas sensors – a hardware concept. In: International workshop on impedance spectroscopy, Chemnitz, 13–15 October 2010
64. Reimann P, Dausend A, Schütze A (2010) Optimale Signalanregung zur low-cost Impedanzmessung von Halbleitergassensoren. In: Proceedings of the Sensoren und Messsysteme, VDE Verlag, Berlin, Offenbach; ISBN 978-3-8007-3260-9, pp 93–100
65. Schütze A (1994) Präparation und Charakterisierung von Phthalocyanin-Schichten zum Nachweis oxidierender und reduzierender Gase. Dissertation, Justus-Liebig-Universität Gießen, Shaker Verlag, Aachen, 1995
66. Bur C, Bastuck M, Andersson M, Schütze A, Lloyd Spetz A (2012) Influence of a changing gate bias on the sensing properties of SiC field effect gas sensors. In: Proceedings of the 14th international meeting on chemical sensors, Nürnberg/Nuremberg, 20–23 May 2012, ISBN:978-3-9813484-2-2, pp 140–143. doi:10.5162/IMCS2012/1.5.4
67. Bastuck M, Bur C, Lloyd Spetz A, Andersson M, Schütze A (2013) Identification of ammonia and carbon monoxide based on the hysteresis of a gas-sensitive SiC field effect transistor. In: Proceedings of the transducers, Barcelona, 16–20 June 2013
68. Carotta MC, Cervi A, Fioravanti A, Gherardi S, Giberti A, Vendemiati B, Vincenzi D, Sacerdoti M (2011) A novel ozone detection at room temperature through UV-LED-assisted ZnO thick film sensors. Thin Solid Films 520(3):939–946. doi:10.1016/j.tsf.2011.04.173
69. Herrán J, Fernández-González O, Castro-Hurtado I, Romero T, G^a Mandayo G, Castaño E (2010) Photoactivated solid-state gas sensor for carbon dioxide detection at room temperature. Sens Actuators B 149(2):368–372. doi:10.1016/j.snb.2010.06.050
70. Schütze A, Pieper N, Zacheja J (1995) Quantitative ozone measurement using a Pc thin film sensor and dynamic signal evaluation. Sens Actuators B 23(2–3):215–217. doi:10.1016/0925-4005(94)01281-L
71. Baumbach M, Schütze A, Cheng F, Kelly S, Delprat H, Parret F, Menini P, Soulantica K, Chaudret B, Maisonnat A (2004) Novel mesoporous filters for selective gas absorption. In: Proceedings of the IEEE sensors conference 2004, vol 2. October 24–27, 2004, Vienna, pp 939–942; doi: 10.1109/ICSENS.2004.1426326
72. Helwig N (2013) Konzeption, Aufbau und Programmierung einer Gasmischanlage für Flaschen- und Permeationsgase. Diploma thesis, Lab for Measurement Technology, Saarland University

73. European Standard EN 54-7 (2006) Fire detection and fire alarm systems – part 7: smoke detectors – point detectors using scattered light, transmitted light or ionization; German version EN 54-7:2000 + A1:2002 + A2:2006, Beuth-Verlag
74. European Standard EN 54-9 (1984) Components of automatic fire detection systems – fire sensitivity test; German version EN 54-9:1984; Beuth Verlag, Berlin
75. Zell A (1997) Simulation neuronaler Netze. R. Oldenbourg Verlag, ISBN 978-3-486-24350-5
76. Gutierrez-Osuna R (2002) Pattern analysis for machine olfaction: a review. IEEE Sens J 2(3): 189–202. doi:10.1109/JSEN.2002.800688
77. Marco S, Gutiérrez-Gálvez A (2012) Signal and data processing for machine olfaction and chemical sensing: a review. IEEE Sens J 12(11):3189–3214. doi:10.1109/JSEN.2012.2192920
78. Duda RO, Hart PE, Stork DG (2000) Pattern classification, 2nd edn. Wiley, New-York. ISBN 978-0-471-05669-0
79. Kohonen T (2001) Self-organizing maps. Springer Verlag, ISBN 978-3-540-67921-9
80. von Ahn L, Blum M, Hopper NJ, Langford J (2003) CAPTCHA: using hard AI problems for security, advances in cryptology – EUROCRYPT 2003, Lecture notes in computer science 2656:294–311. doi:10.1007/3-540-39200-9_18
81. Davide FAM, Di Natale C, D'Amico A (1994) Self-organizing multisensor systems for odour classification: internal categorization, adaptation and drift rejection. Sens Actuators B 18(1–3):244–258. doi:10.1016/0925-4005(94)87090-X
82. Hines EL, Boilot P, Gardner JW, Gongora MA (2003) Pattern analysis for electronic noses. In: Pearce TC, Schiffman SS, Nagle HT, Gardner JW (eds) Handbook of machine olfaction – electronic nose technology, Wiley-VCH, ISBN: 3-527-30358-8
83. Höppner F, Klawonn F, Kruse R, Runkler T (1999) Fuzzy cluster analysis. Wiley, Chichester. ISBN 9780471988649
84. Kohonen T (1986) Learning vector quantization for pattern recognition. Technical Report TKK-F-A601, Helsinki University of Technology
85. Crammer K, Gilad-Bachrach R, Navot A, Tishby N (2002) Margin analysis of the LVQ algorithm. In: Becker S, Thrun S, Obermayer K (eds) Advances in neural information processing systems vol 15. pp 462–469, ISBN: 9780262025508
86. Hearst MA, Dumais ST, Osman E, Platt J, Scholkopf B (1998) Support vector machines. IEEE Intell Syst Appl 13(4):18–28. doi:10.1109/5254.708428
87. Kearns M, Ron D (1999) Algorithmic stability and sanity-check bounds for leave-one-out cross-validation. Neural Comput 11(6):1427–1453. doi:10.1162/089976699300016304
88. Gramm A, Schütze A (2003) High performance solvent vapor identification with a two sensor array using temperature cycling and pattern classification. Sens Actuators B 95:58–65. doi:10.1016/S0925-4005(03)00404-0
89. Schütze A, Gramm A, Rühl T (2004) Identification of organic solvents by a virtual multisensor system with hierarchical classification. IEEE Sens J 4(6):857–863. doi:10.1109/JSEN.2004.833514
90. Cover T, Hart P (1967) Nearest neighbor pattern classification. IEEE Trans Inf Theory 13(1): 21–27. doi:10.1109/TIT.1967.1053964
91. Barker M, Rayens W (2003) Partial least squares for discrimination. J Chemom 17(3): 166–173. doi:10.1002/cem.785
92. Lösch M, Baumbach M, Schütze A (2008) Ozone detection in the ppb-range with improved stability and reduced cross sensitivity. Sens Actuators B 130:367–373. doi:10.1016/j.snb.2007.09.033
93. MicroChemical Systems SA, now SGX Sensortech SA, Corcelles, CH; http://www.sgxsensortech.com/
94. Horras S, Gaiotto A, Mayer M, Reimann P, Schütze A (2009) Correlation of an E-nose system for odor assessment of shoe/socks systems with a human sensory panel. In: Proceedings of the 13th international symposium on olfaction and electronic nose. AIP conference proceedings, vol 1137. Brescia, 15–17 April 2009, pp 517–520. doi:10.1063/1.3156600

95. Horras S, Gaiotto A, Mayer M, Reimann P, Schütze A (2009) Evaluation of an E-nose system for objective smell assessment of shoe/socks systems by comparison with a sensory panel. In: Proceedings of the sensor 2009, vol I, ISBN 978-3-9810993-4-8, pp 233–238. doi:10.5162/sensor09/v1/b5.2
96. Stephan Horras (2011) Adaptierbares Messsystem zur Detektion von Gasen und Gerüchen basierend auf Halbleitergassensoren im temperaturzyklischen Betrieb. Dissertation, Saarland University, Shaker-Verlag, Aachen, ISBN 978-3-8440-0101-3
97. UST Umweltsensortechnik GmbH, Geschwenda, http://www.umweltsensortechnik.de
98. Jackson MA, Robins I (1994) Gas sensing for fire detection: measurements of CO, CO_2, H_2, O_2, and smoke density in European standard fire tests. Fire Saf J 22(2):181–205. doi:10.1016/0379-7112(94)90072-8
99. Pfister G (1983) Detection of smoke gases by solid state sensors – a focus on research activities. Fire Saf J 6(3):165–174. doi:10.1016/0379-7112(83)90067-X
100. Gutmacher D, Hoefer U, Wöllenstein J (2012) Gas sensor technologies for fire detection. Sens Actuators B 175:40–45. doi:10.1016/j.snb.2011.11.053
101. Pohle R, Simon E, Schneider R, Fleischer M, Sollacher R, Gao H, Müller K, Jauch P, Loepfe M, Frerichs H-P, Wilbertz C (2007) Fire detection with low power FET gas sensors. Sens Actuators B 120(2):669–672. doi:10.1016/j.snb.2006.03.040
102. Ankara Z, Kammerer T, Gramm A, Schütze A (2004) Low power virtual sensor array based on a micromachined gas sensor for fast discrimination between H_2, CO and relative humidity. Sens Actuators B 100:240–245. doi:10.1016/j.snb.2003.12.072
103. Ankara Z, Kammerer T, Engel M, Nagel H, Schütze A (2005) Efficient and cost-saving test method for fire detectors based on metal-oxide semiconductor gas sensors. In: Proceedings of the sensor 2005, vol 2. pp 109–114
104. Ankara Z (2008) Untersuchung zum Einsatz von mikrostrukturierten Halbleitergassensoren in der heutigen Gebäudebrandmeldetechnik. Dissertation, Saarland University, Shaker-Verlag, Aachen, ISBN 978-3-8322-7310-1
105. Engel M (2008) Untersuchung zur Kalibrierbarkeit von Gassensoren im temperaturzyklischen Betrieb. Dissertation, Saarland University, Shaker-Verlag, Aachen, ISBN 978-3-8322-7446-7
106. Guntau A, Hein N (1994) Entwicklung und Erprobung neuer Verfahren zur Verhütung und Bekämpfung von Selbstentzündungsbränden im Steinkohlebergbau. Final Report 01 HD 018, German Federal Ministry for Research and Technology, Bonn
107. Reimann P, Schütze A (2012) Fire detection in coal mines based on semiconductor gas sensors. Sens Rev 32(1):47–58. doi:10.1108/02602281211197143
108. SAFETECH Optimisation of surveillance, technical equipment & procedures to prevent workers from danger attribute to fire, hazardous or toxic gases, firedamp or climatic conditions; project reference: RFCR-CT-2003-00010, Research Programme of the Research Fund for Coal and Steel (RFCS), 9/2003–2/2007
109. Krutzler C, Unger A, Marhold H, Fricke T, Conrad T, Schütze A (2012) Influence of MOS gas sensor production tolerances on pattern recognition techniques in electronic noses. IEEE Trans Instrument Meas 61(1):276–283. doi:10.1109/TIM.2011.2161015
110. Ketzel M, Jensen SS, Ellermann T, Olesen HR, Berkowicz R, Hertel O (2012) Evaluation of the street pollution model OSPM for measurements at 12 streets stations using a newly developed and freely available evaluation tool. Eur J Environ Civil Eng S1:004. doi:10.4172/2165-784X.S1-004

Carbon Nanotube Gas Sensors

Michele Penza, Philip J. Martin, and John T.W. Yeow

Abstract Carbon nanotubes (CNTs) have exceptional physical properties that make them one of the most promising building blocks for future nanotechnologies in the gas-sensing applications. CNTs may play a key role in the development of innovative gas sensors based on flexible substrates, nanosensors and ultrahigh sensitivity devices at low power consumption for sub-ppm-level gas detection at room temperature. On the basis of these innovations, many applications including CNTs have been demonstrated. Various synthesis processes of CNTs, at single- and multiwalled format, composites and functionalised carbon nanostructures are reviewed. The applications of CNT sensors cover a wide range of detection of targeted gases and volatile organic compounds in the field of environmental monitoring, industrial process control and health-care monitoring. The article concludes with a brief discussion on future prospects of CNT gas sensors in the rapidly emerging fields.

Keywords Applications, Carbon nanotubes, CNT gas sensors, Functional carbon nanotubes

---

M. Penza (✉)
ENEA, Italian National Agency for New Technologies, Energy and Sustainable Economic Development Technical Unit Brindisi Technologies for Materials, PO BOX 51 Br-4, 72100 Brindisi, Italy
e-mail: michele.penza@enea.it

P.J. Martin
CSIRO, Materials Science and Engineering, Lindfield, NSW, Australia
e-mail: phil.martin@csiro.au

J.T.W. Yeow
Systems Design Engineering, University of Waterloo, Waterloo, ON, Canada
e-mail: jyeow@uwaterloo.ca

C.-D. Kohl and T. Wagner (eds.), *Gas Sensing Fundamentals*,
Springer Series on Chemical Sensors and Biosensors (2014) 15: 109–174
DOI 10.1007/5346_2014_59,

Contents

1 Introduction

The detection of chemical compounds and biological species in air, including toxic gases and volatile organic vapours, is of great concern in several fields such as environmental pollution, air quality control, industrial emission monitoring, process control, medical diagnosis, health-care monitoring, homeland security, food control, agriculture, safety and transports. The development of new sensing devices enabled by emerging nanotechnologies and engineered nanomaterials will significantly impact on practical applications in the real world with high benefit for daily life of the citizens.

Engineered materials at nanoscale level including both one-dimensional nanostructures (e.g. nanotubes, nanowires, nanobelts, nanorods, nanoobjects) and two-dimensional monoatomic nanomaterials (e.g. graphene) have strongly emerged. They hold a great promise for the development of miniaturised chemical nanosensors at high performance due to excellent mix of outstanding properties such as greater gas adsorption capacity due to high surface-to-volume ratio, high structural and thermal stability, high modulation of the electrical charge upon gas exposure, tuning of the electrical properties and sensing characteristics by surface modifications with functional materials, ability to tailor composition and size of the building nanoblocks for integrated devices, low-power microelectronics and advanced microsystems with wireless communications and new functionalities.

Carbon nanotubes (CNTs) possess a specific and unique set of electrical, structural, mechanical, thermal, optical and sensing properties which have been stimulating increasing interest in the researchers community for practical applications and proof of concepts [1–12]. Structurally, CNTs can be described as a sheet of graphene rolled into a tube. Depending on the orientation of the tube axis relative to the carbon network, different types of CNTs, described by the indices of their chiral vector, n and m, can be achieved. In fact, *armchair* CNTs ($n = m$) usually show metallic conductivity, while *zigzag* CNTs ($m = 0$) or *chiral* ($n \neq m$) CNTs are semiconducting [13].

Moreover, CNTs can vary by the number of carbon layers in their sidewalls. Single-walled CNTs (SWCNTs), double-walled CNTs and multiwalled CNTs (MWCNTs) have been synthesised and are commercially available.[1] Indeed, this large variety opens the field to many different applications. Whereas semiconductor CNTs, especially SWCNTs, have been used to implement field-effect transistor (FET)-based sensors [8, 14–17], the metallic conducting MWCNTs have been used as electrodes for catalysis [18] and miniaturised devices [12, 17]. Although CNTs are depicted as open-ended tubes for simplicity, their ends are usually capped by fullerene-type hemispheres. The higher curvature at these end groups compared to the sidewalls of the CNTs leads to a difference in the chemical reactivity that can be exploited to selectively functionalise the ends of the CNTs. In addition to covalent functionalisation, the properties of the CNTs can be modified by the deposition of the metal or metal oxide particles and nanoclusters or by the non-covalent attachment of polymers or other supramolecules. These different options add another level to the structural variety of the CNTs and render them a highly customisable material for biosensing and gas sensor applications.

From the discovery of the carbon nanotubes in 1991 by Iijima [19, 20] until the end of 2012, roughly 50,000 scientific reports have been published on this hot topic and related applications.

The electrical properties of CNTs are extremely sensitive to charge transfer and chemical doping effects by various molecules. When electron-withdrawing molecules (e.g. NO_2, O_3, O_2) or electron-donating molecules (e.g. NH_3, CO, H_2S, SO_2, H_2, CO_2, C_2H_5OH, etc.) interact with the p-type semiconducting CNTs, they will change the density of the main charge carriers (i.e. holes) in the nanotube, changing the electrical conductance. This behaviour is the basis for applications of CNTs as electrical chemical gas sensors [21–27].

---

[1] Carbon Nanotechnologies Inc (www.cnanotech.com), USA; Nanocyl SA (www.nanocyl.com), Belgium; Cheaptubes Inc (www.cheaptubes.com), USA; CNT Co Ltd (www.carbonnanotube.biz), South-Korea; Yunnan Guorui Nano-Tech Co Ltd (www.sinotubes.com), China; Sigma-Aldrich (www.sigma-aldrich.com), Italy.

A broad spectrum of variants in the CNT-based domain as highly sensitive nanostructured materials have been developed according to the analyte of interest such as air pollutants [28–30]; volatile organic compounds (VOCs) [14, 24, 31]; nerve-agent stimulants, explosives, toxic gases and chemical warfare agents [32]; and many others. During the last decade various optional nanostructures of carbon nanotubes as gas sensor materials have been explored including single-walled carbon nanotubes [1, 2, 14, 27, 32], multiwalled carbon nanotubes [3, 7, 11, 21, 23, 28–30], metal-functionalised CNTs [21, 23, 28–30, 33–38], CNT composites [25] and hybrid materials based on carbon nanotubes [31]. They offer adequate sensitivity and robustness; the most imperative point in their selection is their processability [39] into thin films or coatings and individual nanotube with suitable applicability to the chemical species to be detected, especially when developing a sensor array to address selectivity and stability.

In this chapter, an overview of the current state of the CNT gas sensor technology will be presented by providing a comparison to existing state of the art, including an outlook for the future CNT-based sensor technologies. This contribution reviews the integration of the carbon nanotubes in gas nanosensors at high performance for various real-world applications such as environmental monitoring, industrial applications and health-care monitoring. In particular, the physical properties of CNTs will be shortly discussed, including the methods of fabrication and growth of the carbon nanotubes. Special session will be devoted to single-walled carbon nanotubes, multiwalled carbon nanotubes, functionalised CNTs and CNT composites for advanced gas-sensing applications. Future challenges and new trends in the CNT-based gas sensors will be discussed as well.

2 Properties of CNTs

2.1 *Structure of CNTs*

Graphene can be rolled up into a tube structure to form single-walled carbon nanotube (SWCNT). Tube diameters can be from 0.4 to 2 nm [40]. The structural feature of SWCNT can be represented by chiral vector $\boldsymbol{C} = n\boldsymbol{a}_1 + m\boldsymbol{a}_2$, where m and n are integers, $\boldsymbol{a}_1 = \left(\frac{\sqrt{3}}{2}a, \frac{1}{2}a\right)$ and $\boldsymbol{a}_2 = \left(\frac{\sqrt{3}}{2}a, -\frac{1}{2}a\right)$ are real space unit vectors and $a = 2.46\,\dot{\mathrm{A}}$ is the lattice constant of graphene [41, 42]. The diameter and the chiral angle of SWCNT can be calculated by Eqs. (1) and (2), respectively:

$$d = \frac{a}{\pi}\sqrt{n^2 + m^2 + mn} \tag{1}$$

$$\theta = \cos^{-1}\frac{2n+m}{2\sqrt{n^2+m^2+mn}} \tag{2}$$

According to the different structural factors, SWCNTs can be classified into three categories: (1) armchair SWCNT with $\theta = 30°$ and $n = m$, (2) zigzag SWCNT with $\theta = 0°$ and $m = 0$; and (3) chiral SWCNT with all the other n and m values and $|\theta| \in (0°, 30°)$ [42].

Multiwalled carbon nanotube (MWCNT) can be presented as either a Russian doll structure (several symmetric SWCNTs with different diameters assembled together) or a Swiss roll-like structure [41]. Most experimental studies have supported a Russian doll structure due to the symmetric fringes, which were observed from micrographs and existence of CNT caps at both ends. Diameters of MWCNTs can be from about 20 nm to up to 100 nm with interspace of about 0.34 nm between walls [40].

2.2 Electronic and Electrical Properties of CNTs

It is shown that all armchair SWCNTs and SWCNTs with value of $n - m = 3q$, where $n > m$ and j is nonzero integer, have metallic properties, while all the other SWCNTs are semiconductors [41]. Armchair SWCNTs are always metallic materials when the tubes are bent. However, the electronic properties of metallic SWCNTs that are not armchair can be modified by tube distortion. The resistance of SWCNT can be 6.5 kΩ, while for semiconducting SWCNTs, the hole mobility was measured higher than 10,000 cm^2/Vs [40].

Both SWCNTs and MWCNTs are considered quantum wires; therefore, the electron transportation in the tubes is ballistic with no scattering by impurities. It was found both theoretically and experimentally that CNTs could carry high density current without significant generation of heat [41].

The background theory, past experiments and studies for CNTs' electronic and electrical properties have been comprehensively reviewed by Prabhakar in [40] and Sinha et al. in [43].

2.3 Mechanical Properties of CNTs

It was found that SWCNTs appear in a curved shape; on the other hand, the shape of MWCNTs is much straighter. This might be due to the larger diameters of MWCNTs than SWCNTs. The stiffness of the tube structure is increased by an increase in the tube diameter.

Shokrieh et al. reported the experimental and theoretical studies of the Young's modulus of CNTs [44]. Experimental results vary from 400 to 3,600 GPa. The disagreements of experimental results were due to the following: (1) different CNT sample size (diameter, length, chirality, fabrication method, etc.), (2) limitation in direct measuring techniques and (3) large amount of uncertainties from indirect measurements. Theoretical studies of CNT Young's modulus have made significant progress. The progress made includes atomistic modelling, analytical continuum mechanics and numerical continuum mechanics based on finite element analysis. The tensile strength measurement of CNTs also attracts much research interests. Yu et al. studied the tensile strength of MWCNTs [45]. They utilised an atomic force microscope (AFM) with a single MWCNT as a strength sensing component. Scanning electron microscope (SEM) was utilised to monitor the whole measurement experiment. It was found that tensile strength of MWCNT ranges from 11 to 63 GPa and the corresponding Young's modulus ranges from 270 to 950 GPa. The tensile strength of SWCNT ropes was also determined based on the same set-up [46]. The SWCNT used in the experiment was (10,10) SWCNT and the diameter was 1.36 nm. The measured tensile strength of SWCNT ranges from 13 to 52 GPa with a mean strength of 30 GPa. The corresponding Young's modulus was determined to range from 320 to 1,470 GPa with a mean value of 1,002 GPa. Wang et al. measured the tensile strength of an individual SWCNT using high-resolution tunnelling electron microscope (TEM) and AFM system [47]. Individual SWCNTs were obtained by in situ removal of MWCNT's outer shells. The diameters of SWCNTs range from 0.7 to 5.9 nm, and the measured tensile strength ranges from 25 to 100 GPa.

2.4 Thermal Properties of CNTs

The predicted thermal conductivity of CNTs can be as high as 6,600 W/mK for (10,10) CNT at room temperature [48]. Thermal conductivity measurements of individual MWCNTs were carried out, but no measurements on individual SWCNTs were reported. Due to the larger diameter of MWCNTs, thermal conductivities measured were less than half that of the predicted value of SWCNTs. Kim et al. measured the thermal conductivity of individual MWCNT with a diameter of 14 nm and a length of 2.5 μm [49]. The measured conductivity was higher than 3,000 K/mK. The outer shell of MWCNT is considered to contribute more heat conduction. The anisotropic properties of MWCNT might also affect the conductivity. Fujii et al. measured the thermal conductivities of three individual MWCNTs with different diameters and length, which were 9.8–5.1 nm–3.7 μm, 16.1–4.9 nm–1.89 μm and 28.2–4.2 nm–3.6 μm (outer diameter–inner diameter–length), respectively [50]. It was reported that the thermal conductivity increases with a decrease in the tube diameter and an increase of the environmental temperature. The conductivity of the one with a diameter of 9.8 nm was measured to be 2,096 W/mK at room temperature.

2.5 *Optical Properties of CNTs*

Raman spectroscopy is the most widely used tool to study the structure of CNTs. Typical Raman spectrum of SWCNT contains four main features that are useful for characterising CNTs [41]: (1) low-frequency peak, Raman shift <200 cm^{-1} (RBM peak), (2) peak with Raman shift around 1,340 cm^{-1} (D-line), (3) peak with Raman shift in the range of 1,550–1,600 cm^{-1} (G-band) and (4) peak with Raman shift around 2,600 cm^{-1} (G'-line).

The radial breathing mode (RBM) peak is especially useful for characterisation of CNT structure since it is inversely related to the tube diameter [42]. RBM peak and G-band features can also be used for discrimination of semiconducting SWCNTs and metallic SWCNTs [41, 51].

3 Fabrication Methods of CNTs

The origin of carbon nanotubes (CNTs), as they are understood today in research and development, may be traced back to Iijima (1991) who observed the now familiar tubular carbon structures. CNT material is typically produced using a technique similar to that use for preparing fullerenes based on an arc discharge evaporation technique. The structures are found to be coaxial tubes of graphite sheets of the order of micrometres in length and varying in diameter from a few nanometres to tens of nanometres. These structures became known as multiwalled carbon nanotubes (MWCNTs), and there have been several extensive reviews of the fabrication methods for CNTs by Jose-Yacaman et al. [52], Journet and Bernier [53], Meyyappan et al. [54–56], Popov [57], Kratschmer et al. [58], Baddour and Briens [59], Kumar and Ando [60], Broza [61] and Tessonnier and Su [62].

There are three basic methods used in the preparation of CNTs. These are arc discharge, laser ablation and catalytic processing.

3.1 *Electrical Arc Discharge*

A schematic of the simple arc discharge method is shown below in Fig. 1 [61]. The two cylindrical electrodes, contained within an argon- or helium-filled vessel at a pressure of approximately 660 mbar, are separated by a small gap ~1 mm. A current of 100 A is passed through the electrodes, and a plasma discharge is ignited which has a temperature of around 4,000 K, resulting in the vaporisation of the anode and the growth of the needle-like structures on the end of the cathode. The anode is continuously moved as the electrode is consumed to maintain the arc discharge gap and a discharge voltage of 30 V. The electrodes are water cooled and the anode diameter is around 6 mm and the cathode diameter 16 mm [53]. The system may be

Fig 1 Scheme of setup for CNT deposition by arc discharge [61]

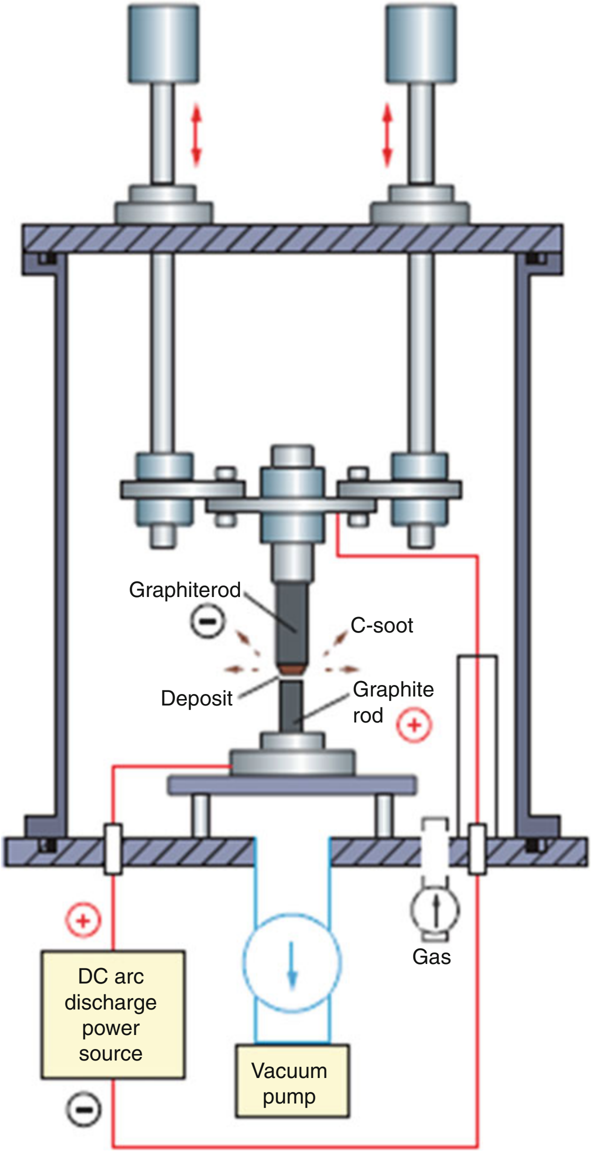

operated in one of the two modes. In the first configuration, the basic arc discharge will produce deposits on the end of the cathode and also soot on the walls of the reactor. The deposit was shown to be a hard outer shell with a softer fibrous core. The hard shell was found to be a fusion of nanoparticles and MWCNTs where the MWCNTs consisted of a number of concentric tubes of a constant spacing of 0.34 nm.

The second configuration used in the arc discharge technique is co-evaporation of a metal and graphite. If a hole of the order of 3.5 mm is drilled into the anode and filled with a metal catalyst and graphite powder, the resulting metal evaporation modifies the structures deposited on the cathode, and for certain metals (catalysts), a high density of single-walled carbon nanotubes (SWCNTs) is formed. The catalysts include Co, Co/Ni, Co/Y, Co/Fe, Ni/Y, Ni/Lu and Ni/Fe, as suggested by Baddour and Briens [59]. The formed SWCNTs have only one graphitic sheet and may be isolated or bundled. The tubes generally have a diameter of 1.2 and 1.4 nm with lengths of several microns. The tips are closed and free of any catalyst species. The production rate of CNTs is dependent upon the pressure, and Co is reported to be the most effective catalyst in the synthesis of the SWCNTs [63].

Aside from CNTs produced during the electric arc process, there are also other products such as amorphous carbon, fullerenes and graphite sheets rendering recovery and purification of the CNTs labour intensive. In summary the method is relatively simple, readily scalable and commonly used, but CNT yield remains challenging.

3.2 Laser Ablation

In this technique (see Fig. 2), graphite is vaporised by laser irradiation in a helium atmosphere. Typically a focused, pulsed or continuous laser (wavelengths 10.6 μm 1064 nm, 532 nm) of minimum power 500 W is used for the irradiation. The production of SWCNTs increases with the power of the laser. The pressures used vary from 27 to 53 kPa, and various gases including helium, argon and nitrogen have been tested. In contrast to the electric arc process, relatively high-purity SWCNTs are produced at room temperature, and the conditions for synthesis are easily tuned by changing gas pressure and species. Relatively high yields of SWCNTs ($>70\%$) were produced by Dai et al. [64], using laser ablation of carbon rods with Ni and Co catalysts. The resulting nanotubes were uniform and combined to form ropes 5–20 nm in diameter and up to hundreds of micrometres long. Both the arc discharge and laser ablation are high-yield methods for the production of nanotubes, but both rely on the vaporisation of carbon from a solid source at temperatures $>3{,}000^\circ$C and the CNTs are tangled containing nanoscale impurities and require purification. One such purification scheme proposed by Liu et al. [65] consists of refluxing in 2.6 M nitric acid, resuspending the CNTs in pH10 water-containing surfactant and then filtering. When the purified suspension is passed through a polytetrafluoroethylene filter, a mat of SWCNT ropes termed ‘bucky paper’ is formed.

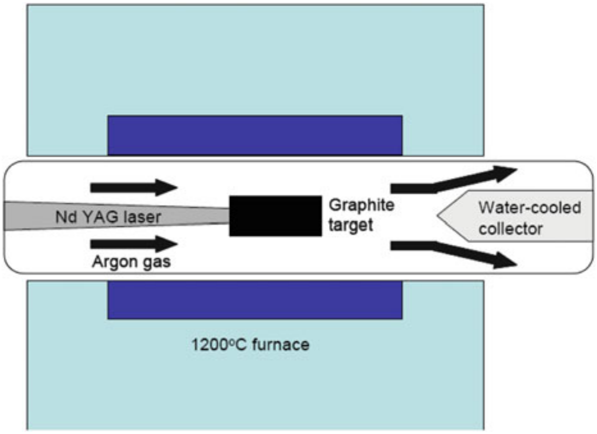

Fig. 2 Scheme of setup for CNT deposition by laser ablation [59]

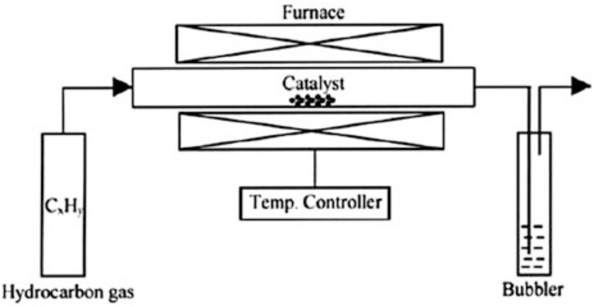

Fig. 3 Scheme of set-up for CNT growth by catalytic deposition [60]

3.3 Synthesis of CNTs by Catalytic Decomposition

The CVD method (see Fig. 3) is relatively simple and economic compared to arc discharge and laser ablation; however, the CNT growth mechanism is still the subject of technical debate. It was first recognised by Yacaman et al. [52] that CNTs could be synthesised by catalytic decomposition of a carbon-containing gas over a metal surface. The material was termed buckytubes that were carbon microtubules with a fullerene structure. The method used involved using catalytic decomposition of acetylene over iron particles at a temperature of 700°C. The resulting CNTs were up to 50 μm long and with a helical structure. The diameter of the tubes was controlled by that of the metal catalyst and the length determined by the reaction time. Two types of tubes were identified, amorphous-like with an underlying graphitic structure and a pure buckytube type. The general principle in chemical vapour deposition (CVD) growth of CNTs is the catalytic decomposition of a carbon-containing gas such as acetylene, ethylene or methane in a glass tube reactor that is held at a temperature in the range of 500–1,000°C. The most commonly used catalysts are Fe, Co or Ni nanoparticles.

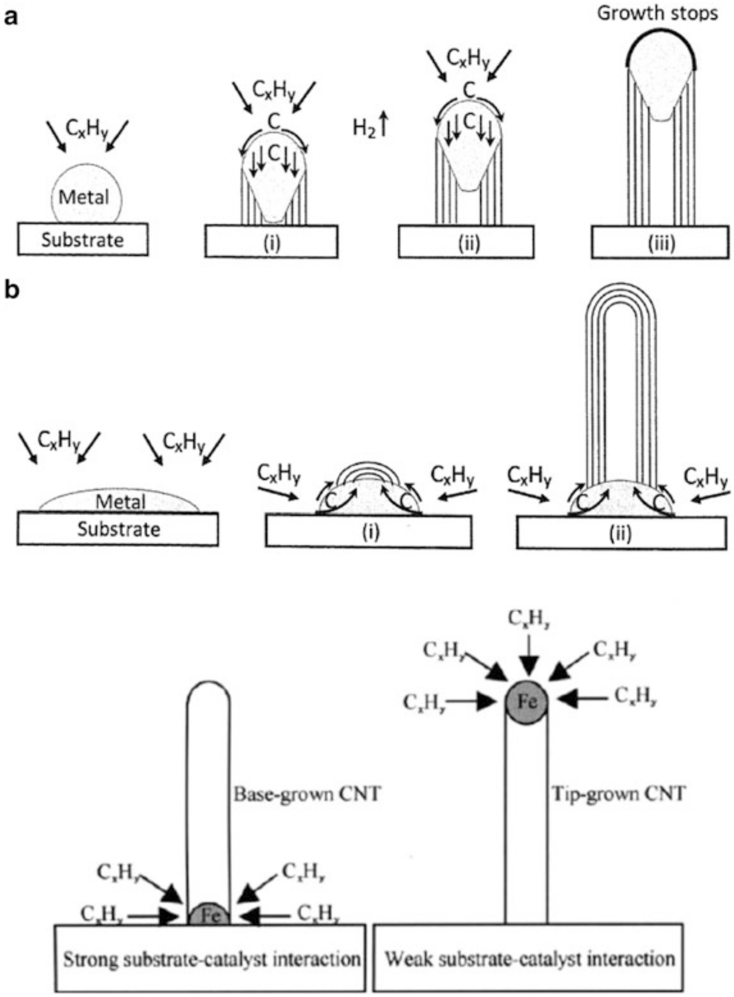

Fig. 4 Models of growth mechanism for CNTs, as adopted by Kumar and Ando [60]. Growth mechanisms for CNTs: (**a**) tip-growth model, (**b**) base-growth model

The most generally accepted growth mechanism is that the hydrocarbon vapour comes into contact with the heated catalyst particles and decomposes into hydrogen and carbon [60]. The scheme of the growth mechanism is depicted in Fig. 4. The hydrogen is removed and the carbon dissolves into the metal. After the carbon solubility limit is reached, the carbon precipitates out and forms a cylindrical network. In the case where the catalyst–substrate interaction is weak, the hydrocarbon decomposes on top of the catalyst particle, and the carbon diffuses through the metal to the bottom of the catalyst, precipitates out and lifts the particle off the substrate. The CNT will continue to grow as long as the supply of carbon is delivered through the surface of the open metal top. Generally growth ceases

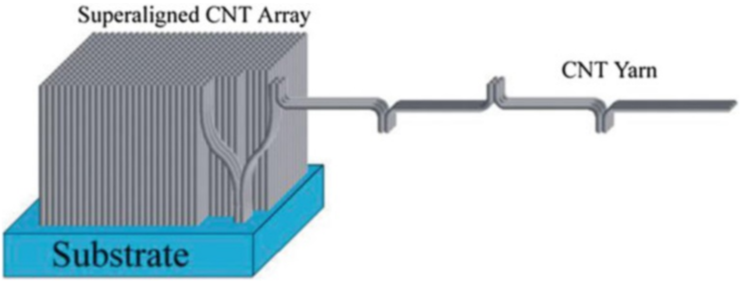

Fig. 5 Scheme of *forest* and *web pulling* of the CNTs, adopted by Zhang [72]

when the top surface is covered with excess carbon. This type of CNT growth is termed a *tip-growth model*. It is also possible for the opposite to occur when the catalyst–substrate interaction is strong. In this instance the particle is not raised, but carbon precipitation occurs on the catalyst top surface and continues following a *base-growth model*. The CNTs form MWCNTs or SWCNTs depending on the size of the catalyst: tens of nm for MWCNTs and a few nm for SWCNTs.

Regular arrays of CNTs can be grown on silicon wafers patterned with micron-scaled catalytic metal islands. Kong et al. [67] used methane to deposit small-diameter SWCNTs and Fe/Co catalysts with a yield of 47%.

3.4 Carbon Nanotube Yarns

Under certain conditions, vertically aligned CNTs may be grown by the CVD method and drawn from the surface after deposition in a continuous web and ultimately spun into a yarn. These highly aligned arrays are described as *forests*. A scheme of the CNTs as *forest* and *yarns* is shown in Fig. 5.

The creation of continuous yarns from carbon nanotubes was first reported by Jiang et al. [68] in 2002. They discovered that while trying to remove a bundle of CNTs from an array of CNTs, several microns high grown on a silicon substrate, a continuous yarn of pure CNTs was obtained. These initial experiments produced a yarn 30 cm long and 200 μm wide. HRTEM images (see Fig. 6) of as-grown CNTs showed the outer diameter was about 15 nm and the inner diameter was about 5 nm. It was estimated that an array 1 cm^2 could generate approximately 10 m of yarn. Incandescent light was emitted from a filament constructed from the yarn, and after 3 h of operation, the tensile strength increased from 1 to 6.4 mN. A UV polariser operating at 325 nm was also demonstrated. Further work on filaments explored the polarised incandescent light emission from a carbon nanotube bundle by Li et al. [69]. The original method used by the Tsinghua University group [68, 70, 71] to grow the drawable CNT *forests* was atmospheric pressure CVD in a 1–2-inch tube furnace using acetylene feedstock and an Fe catalyst on silicon substrates. The diameter of the substrate was later increased to 4 inches and growth of

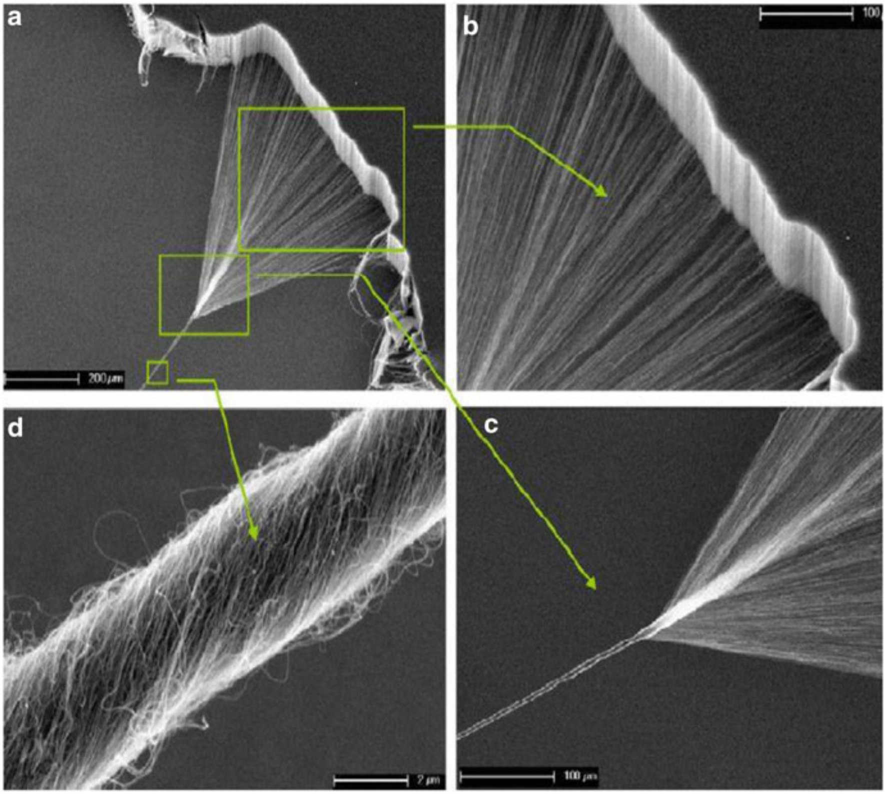

Fig. 6 HRTEM images of the CNT yarns, as adopted by Atkinson [66]. SEM micrographs of a CNT forest in the process of spinning showing the overall process and details. (**a**) Overview, (**b**) self-assembly of CNTs, (**c**) detail of twist insertion and (**d**) yarn structure

super-aligned (drawable) forests obtained at low pressure (2 mbar) and a temperature of 680–720°C [72]. A modification used was to draw the CNT yarn through ethanol to prevent undesirable bonding of the yarn to other surfaces. The tensile stress of these materials was 600 MPa. Heating improved the Young's modulus by a factor of two to 74 GPa. Substrates successfully tested included silicon, oxidised silicon and quartz. A key factor for successful super alignment was reported to be an Fe catalyst thickness of 3.5–5.5 nm deposited by electron beam evaporation at a rate of 0.1 Å s^{-1}.

The tensile strength of yarn spun from super-aligned CNT (SACNT) was improved by twisting and shrinking. The yarns were spun from 235-μm SACNT arrays on 4-inch silicon wafers. The twisted drawn yarn was passed through a solvent comprising water, ethanol or acetone and then subsequently baked at 100°C to remove the solvent. By this method yarns tens to hundreds of metres long were produced. The yarn diameter was reduced by the shrinking technique from 5–41 to 4–34 μm. Yarns with a diameter of 10 μm had the greatest tensile strength of

0.63 GPa before shrinking and 1.10 GPa afterwards. The specific strength was 1.56–1.71 GPa (g cm^{-3})$^{-1}$. Similarly the Young's modulus also improved from ~48 to ~56 GPa. The electrical resistivity decreased with yarn diameter. At diameters less than 20 µm, the resistivity was 1.1×10^{-5} Ω m. After twisting and shrinking, the resistivity of 18-µm-diameter yarn was ~2.5×10^{-8} Ω m, 2–3 orders of magnitude higher than that of gold. The tensile strength of gold wire was ~155 MPa and specific strength ~8 MPa (g cm^{-3})$^{-1}$.

The conductivity of MWCNT yarn has been improved synthesising metal CNT composites [73]. The synthesis was achieved by a simplified electroplating technique in which metallic nanoparticles were incorporated into the yarn. In particular Cu–CNT and Au–CNT composite yarns were prepared with metal-like conductivities of 2–3 × 10^5 S cm^{-1}.

In 2004 Li et al. [74] demonstrated that continuous fibres and ribbons of carbon nanotubes could be spun directly from the CVD synthesis zone of a furnace using a liquid source of carbon and iron catalyst. A carbon source of ethanol containing ferrocene and thiophene was used. The solution was injected into the top of a furnace operated at 1,050 to 1,200°C. An aerogel of CNTs formed and was extracted at the bottom directly onto a drum. The material produced was generally highly reproducible, pure (~95 wt%) MWCNTs. The MWCNT fibres were 30 nm diameter containing 5–10% iron. The Cambridge Process, as this method came to be referred to in the literature, was later improved to produce km of fibre at a rate of 20 m/min. The electrical conductivity was 8×10^5 S/m, the stiffness around 50 GPa/SG, tensile strength 1.0 GPa/SG and the density 1.0 g/cm^3. The density of the drawn fibres was improved by passing the fibre through acetone, and the fibre properties were also improved by reducing the catalyst concentration in the furnace. The maximum tensile strength obtained was 1.46 GPa. However, it was reported that the fibres contain voids, entanglements, catalyst residue and other carbonaceous materials which together have limited the quality of the material and its application to date. In further refinements on the process, electric sparking was performed on macroscopic films and fibres which led to the removal of the amorphous coatings on the CNTs and reshaped them into the nanosize particles consisting of graphite and iron oxide. This led to the formation of the unique heterostructures of the nanoparticles-bonded SWCNT bundles in the sparked film [75].

Zhu et al. [76] of Los Alamos discovered how to grow longer nanotubes, thus opening the door to new uses (e.g. Li et al. [70], Zhang et al. [77]). The most effective way to utilise these new properties is to assemble CNTs into fibres. However, despite extensive worldwide efforts to date, the specific strength and specific stiffness of CNT fibres that have been reported by various research groups are much lower than currently available commercial fibre. Covalent coating of Au nanoparticles onto the CNTs not only significantly enhances conductivity but also changes the conducting mechanism. These results provide insight into the electron transport behaviour in the *p*-conjugated CNT system and useful strategies to manipulate the electronic properties of CNTs for potential applications in electronics, sensing and conducting wires [70, 71]. Many groups have successfully synthesised vertically aligned CNT arrays using Fe film as catalyst. However, there exist only limited reports on the spinning of fibres from such CNT arrays. This raises the question of why some CNT arrays are spinnable while others are not, given that the same catalyst and similar gas composition were used to produce the CNT arrays. Los Alamos group [76] reported the key points to synthesise spinnable CNT arrays depending on the pretreatment of catalysts. They showed that the shortest catalyst pretreatment leads to growth of CNT arrays with the best spinnability, while prolonged catalyst pretreatment results in disordered and nonspinnable CNTs. On the basis of understandings on the crucial role of catalyst pretreatment, they also demonstrated the growth of undulating CNT arrays with uniform and tuneable waviness, which present a class of open-cell foam structures and may find a wide range of applications. Huynh and Hawkins [78] demonstrated that among the critical parameters for spinnable CNT forests are a substrate temperature of 670°C, a critical flow rate of helium of 700 sccm with an upper limit of 3.5–5% acetylene concentration and a deposition time of 20 min. The Fe catalyst thickness is also critical (2.3 ± 0.3 nm) and should be deposited onto a silicon substrate with a thermally grown oxide layer of 50 nm. Small variation from this parameter set can strongly degrade the spinnability. As an example, ethylene can be used as the carbon gas, but the substrate then requires the use of an aluminium oxide buffer layer, a thinner catalyst, hydrogen as the carrier gas and higher growth temperatures.

Guzman et al. [79] reported on the high-yield growth of vertically aligned carbon nanotubes on a continuously moving substrate. A cold wall chamber with a moving platform was able to grow forests to a height of ~1 mm and with substrate speeds up to 2.4 mm h^{-1}. The silicon substrates were coated with 1 nm Fe and 10 nm Al_2O_3 by electron beam evaporation. The carbon feedstock was ethylene, acetylene or ethanol. The forests were comparable to statically grown CNTs, but no drawability was reported.

3.5 Plasma-Enhanced CVD

The successful application of CNTs in applications such as sensing requires controlled growth on both patterned and unpatterned substrates. Plasma-enhanced CVD (PECVD) offers such a process at reduced substrate temperatures and the growth of free-standing carbon nanostructures compared to the tangled arrays produced by conventional CVD from NASA Ames Research group, led by Meyyappan [54–56]. The growth mechanisms are not entirely clear, and the phenomena involved are coupled and complex. These include plasma chemistry particle interactions, surface chemistry, catalyst behaviour, electrical field effects, ion bombardment, heat transfer, etc. The parameters affecting growth are equally complex and involve at least the carbon-containing gas species, type of diluents, flow rates, plasma excitation, plasma power, substrate type and temperature, distribution of the temperature, catalyst type and thickness and distribution.

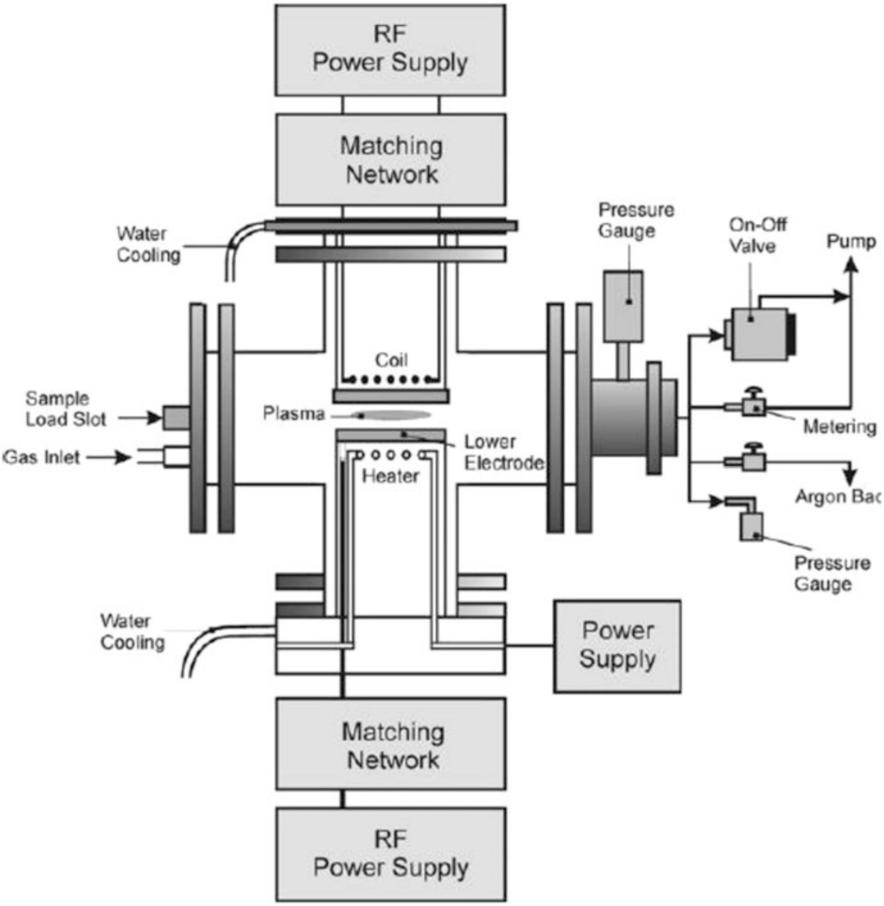

Fig. 7 Schemes of the PECVD setup for growth CNTs, as adopted by Meyyappan et al. [54]

The PECVD reactors (see Fig. 7) used in CNT synthesis are classified according to the excitation source used to enhance the discharge, and the most common variant is a dc plasma discharge. This comprises two parallel plate electrodes mounted in a vacuum chamber. In the common arrangement, the upper electrode is at earth potential and the lower electrode driven by the power supply. The substrates are mounted on the driven electrode. The substrate may also be heated independently of the gas discharge by thermal resistance heaters or infrared lamps. The typical operating pressures are in the range of 5–10 mbar, and dc powers used range typically from 150 to 200 W.

Alternatively the active electrode may be driven by a capacitively coupled RF power supply operating at 13.56 MHz at an operating pressure of 0.1–1.0 mbar. Various configurations have been used where the plasma is generated remotely from the substrate wafer to reduce damage by ion bombardment. Inductively coupled RF discharges are also employed in PECVD reactors where high plasma densities are achieved at relatively lower operating pressures (few mbar). The inductive coil is typically isolated from the discharge chamber by means of a quartz window. In this way contamination is reduced to a minimum from the coil. This type of configuration permits independent biasing of the substrate platform by means of a separate RF or dc supply. A third type of excitation is by means of microwave CVD (MPCVD), where the plasma is driven at 2.45 GHz at operating pressures of 5–10 mbar [56].

With all the PECVD techniques, the most common feedstock gases are C_2H_2/NH_3 and CH_4/H_2, and the frequently used catalysts are Ni, Fe and Co. If catalysts are not used, the resulting material will largely be amorphous carbon or, in the case of specific conditions, diamond. The catalyst must be in the form of nanoparticles and not a continuous smooth film and may be applied to the substrate from solution or by physical vapour deposition. The catalyst is typically <20 nm in thickness and will determine the resulting particle size. The actual substrate temperature during growth is strongly governed by plasma heating, and typical temperatures reported are 600–800°C. In some instances the CNTs grow via a tip-growth mechanism where the catalyst nanoparticle remains on top in contrast to VA-MWCNT where the CNTs grow on top of the catalyst particles. Growth rates for PECVD are slower than CVD and have been reported in the range of 0.5–6 $\mu m\ min^{-1}$ saturating after ~20 min. Cessation of growth has been related to catalyst poisoning where an amorphous carbon deposit forms on top of the catalyst.

SWCNTs have been grown by PECVD [56] by both direct and remote plasma methods at high temperatures and MWCNTs deposited at temperatures as low as 120°C.

The PECVD method has received much attention in the growth of nanostructures and high aspect ratio carbon nanofibres 50–100 nm in diameter in biosensor development [56]. The successful exploitation of PECVD methods in CNT production will ultimately depend on a greater level of understanding of the complex interplay between the many phenomena and process parameters.

4 CNT Gas Sensors

Carbon nanotubes (CNTs) are in the top list of the nanostructured materials for advanced gas-sensing applications. CNTs are intrinsically very gas sensitive to the chemical environment due to very large surface area.

In this paragraph, gas sensors based on CNTs are reviewed with special attention to the pristine single-walled and multiwalled structures. In addition, engineered CNTs modified with functional materials such as metals, polymers, metal oxides and other organic materials are shortly described. Finally, composites with nanofillers of CNTs in different host matrixes are addressed for promising gas-sensing applications. CNT sensors have been proven very efficient for detecting various environmental toxic vapours, hazardous gases and volatile organic compounds for molecular recognition. Here, we would highlight the distinguished sensor applications of the CNT gas sensors.

4.1 Single-Walled Carbon Nanotube Sensors

As a rolled-up layer of graphene, the hollow structure and high surface area-to-volume ratio enable SWCNT to be a good absorber of gas molecules through both physical and chemical absorption. Theoretical studies and simulations of gas molecules absorption on SWCNT and SWCNT bundles have been comprehensively reviewed by Yun et al. [80]. It is believed that the change in electrical property of SWCNT under gas exposure is first related to the electron transfer among gas molecules and SWCNTs. Second, it is related to the carrier lifetime.

Most recently, target gas molecules are usually NO_x, NH_3, H_2 and chemical warfare agents (CWA) such as dimethyl methylphosphonate (DMMP). A summary of SWCNT gas sensors developed in recent years is given in Table 1. Electron donor gases such as NH_3 and H_2 donate electron when gas molecules are absorbed onto the nanotubes. The conductance of SWCNT, which can be measured for gas detection, is then decreased as an effect. Electron acceptor gases such as NO_x and O_2 react with SWCNT inversely and induce a resistance decrease. This principle is widely used for SWCNT-based gas-sensing applications [81–86]. Figure 8 shows a typical structure of a resistor-type SWCNT gas sensor.

It is found that single SWCNT is rarely used for sensor fabrication due to the current limitation of sensor fabrication. Instead of a single SWCNT, dense SWCNT film is mostly applied as a gas-sensing component. SWCNT film can be obtained either by directly growing SWCNTs on a sensor substrate through arc discharge method [81, 82], CVD method [84, 87, 88] or laser ablation technique [85] or by dispersing SWCNT in solutions before applying to a substrate [83, 89]. SWCNTs in the form of dense CNT film enable the possibility of mass production of sensors.

SWCNT can have either a metallic or semiconducting property depending on its chirality. The semiconducting property of SWCNT can be exploited to realise an SWCNT field-effect transistor (SWCNT-FET) [87–89]. Two metal electrodes connected by single SWCNT or SWCNT film with SiO_2/Si substrate are a typical SWCNT-FET structure [87, 88] (Fig. 9). The operating principles of CNT-FET gas sensors are comprehensively reviewed and discussed by Bondavalli et al. [90].

Semiconducting SWCNT is usually *p*-type, which is different from that of the other metal oxide nanowire (*n*-type). Comparing to metal oxide nanowires, such as In_2O_3, SnO_2 and ZnO, the difference in semiconductor type of SWCNT can be exploited for gas molecule discrimination since SWCNT appears to have inverse electrical response when exposed to target gases [87].

SWCNT-based gas sensors are very sensitive with a fast response time. However, the high binding energy between gas molecules and SWCNT makes gas molecules' desorption process difficult, thereby inducing long recovery time. The binding energy of different gas molecules on SWCNT was studied by Zhao

Table 1 Summary of reviewed SWCNT gas sensor developed recently

Target gas	Sensor structure	Operation	Features	References
NO NH_3	In situ deposited SWCNT film with silver IDE with/without methanol treatment	Resistance response vs. concentration change (0–40 ppm)	Simple fabrication process Fast response Poor recovery time at room temperature, but can be improved by temperature increase	[81]
H_2	SWNT film with Pt electrodes	Resistance response measured by fixed voltage with current change vs. existence of 4% hydrogen in dry air	Sensitivity and selectivity can be improved by applying chitosan filter	[82]
DMMP	SWNT film on PDDA-modified polyimide substrate with Ti-Cu IDE	Voltage–current measurement for obtaining resistance response vs. concentration change (1–40 ppm)	Mechanical stability and flexibility Good selectivity (compared to methanol, dichloromethane, xylene, chloroform, hexane) Low detection limit Room temperature measurement Low operation voltage (50 mV)	[83]
DMMP DPGME DMA	Dense SWNT network with heating resistor at the backside	Resistance response vs. concentration change (DMMP, 0.01–0.05 ppm; DPGME, 0.1–0.8 ppm; DMA, 50–200 ppm)	Room temperature measurement Good discrimination among three tested CWA simulants	[84]
NO_2 Ethanol H_2	SWNT together with In_2O_3, SnO_2 and ZnO nanowire as sensing components with hotplate for temperature control	FET set-up with voltage–current measurement vs. different concentrations (H_2, 500/1,000/2,000 ppm; ethanol, 50/100/200 ppm; NO_2, 0.1/1 ppm) Data analysed by principal component analysis for gas discrimination	Ambient temperature detection of H_2 and ethanol with localised heating SWNT acts as discrimination factor due to the different sensing mechanism comparing to metal oxide nanowire	[87]

(continued)

Table 1 (continued)

Target gas	Sensor structure	Operation	Features	References
NO_2 NH_3	SWNT film on SiO_2/Si substrate with source and drain indium electrodes by low temperature bonding	FET set-up with voltage–current measurement vs. concentration change (NO_2, 10–50 ppm; NH_3, 24.1–149.1 ppm)	No extra steps in fabrication process to remove metallic components Easier for mass production	[88]
NO NO_2	SWNT film	Resistance response vs. concentration change (SWNT, 2–10 ppm; MWNT, 2–50 ppm)	SWNT sensor is more sensitive to NO than MWNT sensors (≈200 ppb)	[85]
Octane Butanol Butyl acetate	CMOS-based set-up with SWCNT deposited	Resistance response vs. concentration change (octane, 2k–10 kppm; butanol, 1k–5 kppm; butyl acetate, 1k–5 kppm)	Good linearity and sensitivity Fast response time	[89]

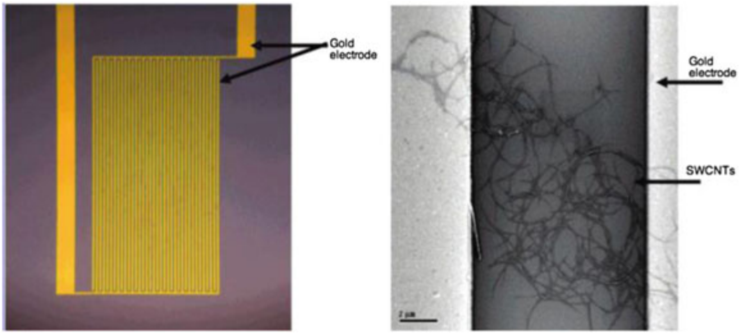

Fig. 8 Resistance type SWCNT gas sensor [3]

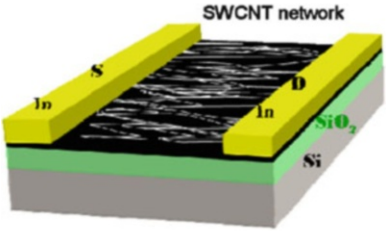

Fig. 9 SWCNT-FET sensor structure [88]

et al. [91]. Micro-heating components were integrated with the gas sensors in order to decrease the recovery time of SWCNT-based sensors [84, 87, 89].

Temperature has been shown to have an effect on the sensitivity of the sensor. Horrillo et al. [84] compared the resistance response of SWCNT gas sensor under different temperatures. It is determined that sensors appear to have higher sensitivity at lower temperature (22°C compared to 77, 145 and 230°C).

It is found that factors such as film thickness, density, porosity, alignment of SWCNTs (parallel, vertical or random casting), contacts among SWCNTs and impurities from the synthesis process will also affect gas-sensing performance.

Hoa et al. [81] compared 'as-deposited SWCNT (AD-SWCNT)' gas sensor and 'methanol-treated SWCNT (MT-SWCNT)' gas sensor. The resistance of the two types of sensors has significant differences. The resistance of SWCNT sensor can be decreased from about 25 kΩ to about 310 Ω. They believed that the obvious resistance decrease is due to the increase of contacts among SWCNTs. This technique was also applied in gas sensor developed by Li et al. [82] to increase the contact between SWCNT film and substrate.

Ueda et al. [85] compared SWCNT-based NO_x sensors with MWCNT-based NO_x sensors of the same sensor structure. They found that SWCNT-based sensors have a higher sensitivity than MWCNT-based sensors. They thought that this phenomenon might be induced by the charge leakage at the Fe/Al catalytic layer.

4.2 Multiwalled Carbon Nanotube Sensors

There are two basic configurations that employ CNTs in gas sensing [92, 93]. These are the chemiresistor and the back-gated chemical field-effect transistor (Chem FET). The simple chemiresistor is based on the use of a positive and negative electrode with the CNTs bridging the gap. The CNTs may be single, a composite, a yarn or other state. The current is passed through the bridging CNTs and the resistance is measured. Any interaction between the surface atoms of the CNTs with adsorbed gas results in a change of resistance through charge transfer processes. These processes may be enhanced by functionalising the CNTs via surface treatment and coating with metal nanoparticles. In the FET configuration the conductance of the CNT between source and drain is modulated by a gate electrode. The FET arrangement is based on using semiconducting SWCNTs. In the chemiresistor configuration, the CNTs may be grown directly on the sensor by CVD or PECVD processing. Alternatively the CNTs may be drop cast in a solution of a suitable solvent on top of interdigitated electrodes, for example. Some posttreatment of the CNT solution may also be performed.

In detecting inorganic vapour, the sensitivity may be improved if poly(*o*-anisidine) is coated onto the CNTs. This is attributed to direct charge transfer with electron hopping influencing intertube conductivity through the adsorbed polymer [94]. MWCNT sensors for CO detection have been reported where the sensing mechanism was attributed to electrochemical oxidation of the carbon monoxide [95, 96].

Penza et al. [23] used vertically aligned CNTs grown on alumina substrates with an Fe catalyst in a miniature gas sensor for monitoring landfill gases (see Fig. 10). The forest-like structure of CNTs was 10 μm high, and the tube diameters ranged from 5 to 35 nm. A comparison was made between unmodified CNTs and CNTs loaded with 5 nm of sputtered nanoclusters of Pt, Ru and Ag of diameter 5–50 nm. Chemical analysis of multicomponent gas mixtures of CO_2, CH_4, H_2, NH_3, CO and NO_2 was made. The CNT:Ru sensor was able to detect 330 ppb NO_2 with a relative change in resistance of 0.55% at a sensor temperature of 150°C. The sensor recovery rate was increased by pulse heating to 110°C.

Organic vapour has also been investigated with MWCNT chemiresistors by Slobodian et al. [97]. An MWCNT network or entangled pure and oxidised nanotubes were used to detect iso-pentane, diethyl ether, acetone and methanol. Functionalisation by $KMnO_4$ improved the response to the organic solvents with oxygen functional groups. Shukla et al. [98] also detected organic vapours of dichloroethane, toluene, chloroform, methanol and benzene at concentrations as low as 100 ppm with sensitivities up to 49%. They used thin film composites of polymethyl methacrylate with MWCNTs. The tubes were functionalised with oxygenated groups using an electrostatic corona discharge.

A chemiresistor was used by Yoo et al. [99] to measure relative humidity fabricated from plasma-treated MWCNT–polyimide composite film. The sensitivity was 0.0047% RH and had a linear correlation of 0.9999. The sensing

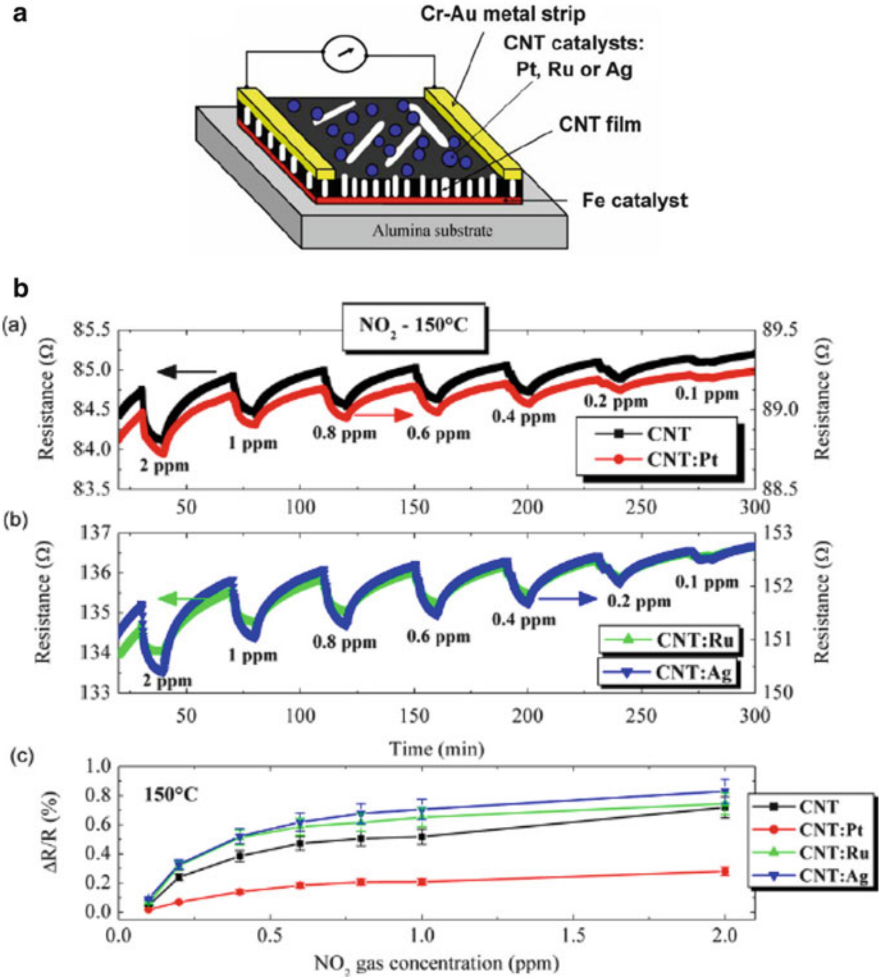

Fig. 10 NO_2 gas-sensing characteristics of the vertically aligned CNT layers and functionalized by Pt, Ru and Ag nanoclusters, as adopted by Penza et al. [23]

mechanism was attributed to charge transfer between adsorbed water molecules and the composite film. The MWCNT concentration strongly influenced the detection sensitivity.

Cava et al. [100] developed a self-assembly method to make MWCNT films for use in an oxygen chemiresistor sensor. An MWCNT assembly, formed by a conventional drop cast method, was compared to a chemical-based self-assembly technique based on a liquid–liquid interface system of toluene and water. The resulting films were deposited onto interdigitated electrodes acting as a sensor and tested at 160°C. The resistance decreased with oxygen exposure indicating a *p*-type behaviour (mostly metallic) of the MWCNTs where the oxygen molecules act as a hole dopant and increase the conductivity. Both sensors had a fast recovery time of 0.9 s, but the self-assembled sensor improved the response to oxygen by 3.4 times, the result being attributed to the improved distribution of the self-assembled MWCNTs and better intertube contact.

4.2.1 Ionisation Sensors

The basic requirements for sensing include sensitivity, reversibility, selectivity and robustness. The gas ionisation sensor offers selectivity through exhibiting a characteristic breakdown voltage for the gas under test [101–104]. In these devices MWCNT arrays are used to intensify the electric field and reduce the operating voltages.

A novel, high-efficiency helium detector was first described by Riley et al. [105], in which MWCNTs were used as the active element. The CNTs were grown by CVD on a steel support by catalytic decomposition of acetylene on an etched stainless steel wire. The CNT-coated steel tip was exposed to a helium background of 4×10^{-5} mbar and a positive high voltage applied. At around 7 kV, ionisation was observed and helium ions detected. The general concept of using a CNT ionisation microsensor for gas detection was developed by Modi et al. [106]. The scheme is reported in Fig. 11. The sensor consisted of an anode, containing vertically aligned MWCNT emitters grown on an oxidised silicon wafer, separated from a cathode by a glass insulator spacer 180 μm thick. The CNTs were 30 μm long and 25–30 nm in diameter. The sharp radius of the CNT tip (~15 nm) creates high non-linear electric fields which causes gas breakdown through corona around the tip area. The voltage between the anode and cathode is increased until a discharge current is detected. The breakdown voltage and current are characteristic of the gas species and concentration, respectively. The sensor was able to distinguish between NH_3, air, Ar, He and O_2. The device showed promise for room temperature detection of gas concentrations of the order of 1% in air.

A two-sensor array was developed by Zhang et al. [107], in which 4-μm-long CNTs with ~50-nm separation between the nanotubes were employed. By using different gaps between the anode and cathode of 100 and 170 μm, a breakdown voltage relationship for each was established for CH_4–CO mixture in a N_2 carrier gas and the gases identified without separation. Kim [108, 109] produced a compact version of the ionisation sensor using silicon–glass anodic bonding and glass patterning processes. The power consumption was tens of milliwatts and the gas sensitivity around 10^{-7} to 10^{-4} mol/L of argon. A modification of the simple CNT array on a silicon wafer was made by Chen et al. [95, 96] in which anodized aluminium oxide (AAO) templates were used as the CNT substrate. The device was found to discriminate between acetic acid, alcohol, acetone and water vapour, the highest sensitivity being 50 μg/L for acetic acid.

Zikai et al. [110] was able to demonstrate gas selectivity with a 4-sensor array system also using AAO templates. Anode–cathode gaps of 120 and 180 μm were used for each pair of sensors and fixed by means of insulating polyimide films. The

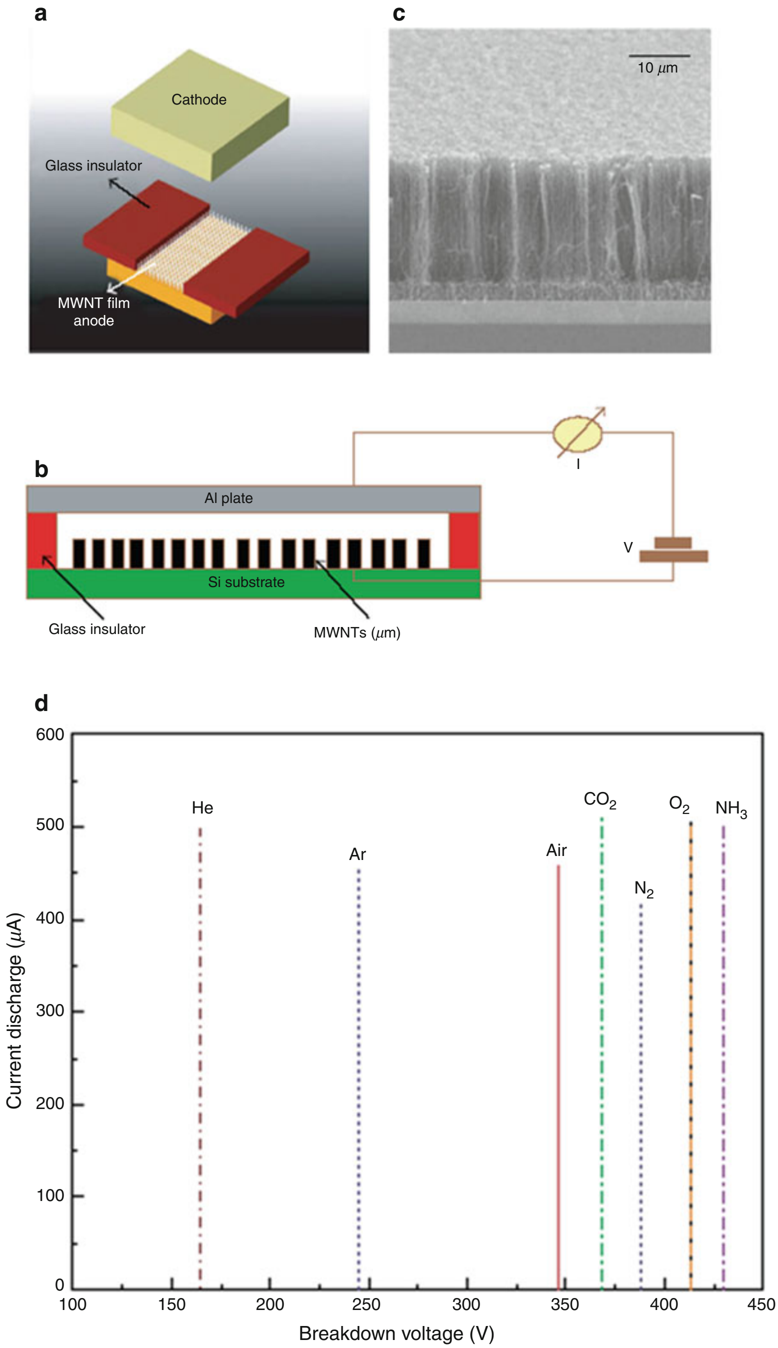

Fig. 11 The nanotube gas ionisation sensor. (**a**) Exploded view of sensor showing MWCNT film as anode, 180-μm-thick glass insulator plates and Al plate as cathode. (**b**) Scheme of test set-up. (**c**) SEM image of the CVD-grown vertically aligned MWCNT film used as anode. (**d**) I–V curves for NH_3, CO_2, N_2, O_2, He, Ar and air, showing distinct breakdown voltages. Reprinted with permission from *Nature*, as adopted by Modi et al. [106]

electrode areas were 2 × 2 cm. This arrangement successfully distinguished between Ar, CO_2, N_2 and air. The noise in gas ionisation sensors was reduced by Meng et al. [111] by use of pre-breakdown current measurement. Stable and reproducible results were obtained for acetic acid detection although no sensitivity figures were available. Huang et al. [112] successfully detected NH_3 with a basic sensor of area 2 × 3 mm. Again using the pre-breakdown current, gas sensitivity to 1 ppm NH_3 in air was demonstrated with response times of the order of 3–6 s.

Bent MWCNTs were used by Baghgar et al. [113] and compared to vertically aligned tubes in a sensor arrangement. The bent tubes were grown by CVD under an electric field. With an anode–cathode spacing of 200 μm, it was found that the bent MWCNTs had a lower breakdown voltage than the vertically aligned CNTs. Sensitivity was demonstrated for H_2, C_2H_2, O_2, Ar and air, and gas pressures as low as 0.3 mbar were tested.

Other recent designs include the use of porous silicon substrates for the CNT arrays [114] where a sensitivity of 500 ppm helium was shown. A novel sensor employing branched treelike CNTs was constructed by Darbari et al. [115] and H_2, O_2, Ar and C_2H_2 detected down to 10^{-2} mbar.

A model of the gas ionisation process was developed by Mahmood et al. [116] in 2011. The model takes into account the field emitting properties of CNTs and the density and aspect ratio variations. The model was able to simulate gas breakdown behaviour with CNT field emission and demonstrated that electrostatic screening effects are reduced to a minimum when the intertube spacing is equal to the tube height. The field emission was also found to increase for moderate CNT density on the electrode. The model was based on a CNT diameter of 55 nm and tube height of 5 μm.

4.2.2 CNT Rope and Yarn Sensors

The development of gas sensors based on MWCNT has largely concentrated on individual tubes, strands of tubes, assemblies of single or multiwall tubes, etc. functionalised with nanoparticles and operating in a chemiresistor configuration. More recently it has been shown that yarn or ropelike structures can be used to detect a range of gases.

Long MWCNT ropes have been used to detect NH_3 [160] with good sensitivity to high and low concentrations. The ropes were made by a floating catalyst CVD process using xylene as the carbon source. Strands that formed during the high-temperature reaction were spun into ropes 10–80 μm in diameter 15–20 cm long and cut into short lengths. These shorter sections were mounted on insulating substrates of 500-nm SiO_2 on Si and the electrical response to NH_3 assessed using a 4-point probe resistance system. It was shown that concentrations as low as 50 ppm could be detected with a response of 0.7% change in resistivity and 4.5% change for 1,000 ppm. Exposure to dry air after NH_3 did not produce full recovery. When higher concentrations of gas were used, the conductance continued to decrease. The mechanism was thought to be related to adsorbed NH_3 donating an electron pair to the CNTs so that charge transfer decreases the conductance. Temperature measurements suggested that the MWCNT ropes are metallic at room temperature and resistance increases with temperature. Desorption of NH_3 occurred at elevated temperature offering a mechanism for reversibility.

An MWCNT yarn was also used to detect NH_3 by Randeniya et al. [117]. The yarn was decorated with nanocrystalline Au particles (see Fig. 12). The Au particles enhanced the sensitivity and gas concentrations down to ~500 ppb readily detected. A plasma treatment of the yarn prior to decoration was found to enhance the response due to the formation of a dense coverage of Au nanoparticles with sizes smaller than 3 nm. In addition larger particles in the range of 10–20 nm were also present. The enhancement was believed to be a consequence of the change in charge transfer characteristics at the Au–CNT interfaces caused by the absorption of gas molecules to the Au particles. Gas adsorption onto the Au particles modifies the conductance and sensing response. The small size distribution of the dense Au nanoparticles was considered to be an important aspect of the sensor response resulting in an order of magnitude improvement relative to uncoated yarn.

Quantum electron conductance calculations by Zanolli et al. [118] confirmed that MWCNT decorated with Au nanoparticles after oxygen plasma treatment improved the detection sensitivity for NO_2 and CO. The Fermi energy shift was computed, and the charge transfer directly correlated with resistance change. Electronic mechanisms therefore play a major role in determining the Au–CNT interaction during exposure to specific gas molecules.

A similar behaviour also occurs for yarns treated with Pd and Pd/Pt in hydrogen detection by Randeniya et al. [119]. The yarn chemiresistor was sensitive to 20 ppm hydrogen in nitrogen at room temperature decorated with nanocrystalline Pd and 5 ppm when decorated with Pt–Pd. A response of 4% was found for 400 ppm with full recovery within 60 s.

4.3 Functionalised Carbon Nanotube Sensors

The functionalisation of the CNTs is a powerful strategy to improve gas sensitivity and fabricate selective nanomaterials. Functionalising the surface of these nanostructures offers another route for expanding their chemical sensing capability. In fact, the charge exchange between an adsorbate and the CNTs changes the electron density in the nanomaterial, modifying the carrier density in the nanostructure. The surface modifications in the carbon nanostructures can enhance the charge transfer by applying external perturbations (e.g. electric field, electromagnetic radiation, thermal heating, ultrasonication), attachment of functional groups or catalytically functionalising sidewalls of carbon-based nanomaterials.

Recently, gas sensors based on functionalised CNTs have been proposed capable of detecting small gas concentrations with high specificity. In fact, successful attempts of functionalised CNT sensors have been covered by a wide variety of functionalising materials such as polymers [25, 120–126], enzymes [127, 128],

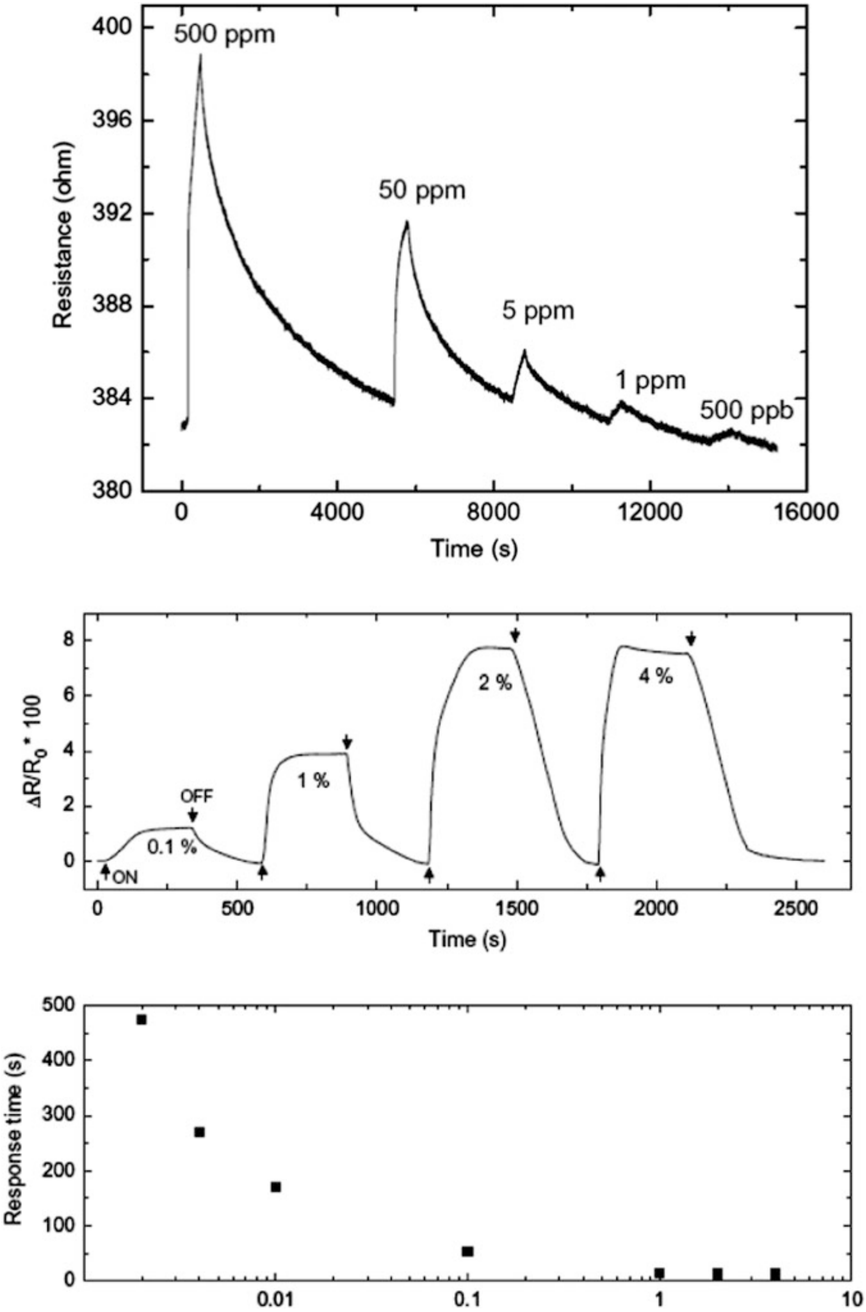

Fig. 12 Gas-sensing characteristics of CNTs yarns, as adopted by Randeniya et al. [119]. Response and recovery of Pd-MWCNT chemiresistors as a function of time and hydrogen concentration

proteins [129–134], antibodies [135, 136], DNA [137–139], semiconducting metal oxides [140–152], metalloporphyrins [153] and metallic nanoclusters [21, 23, 28–30, 33–38, 154] using different processing methods for functional materials integrated in several transducers. Furthermore, nanoclusters of noble metals (Au, Pt, Pd, Ag, Ru, etc.) have been used as metal decorations onto sidewalls to enhance the gas sensitivity [23, 28–30, 33–35, 155–157, 160, 161, 163] of the CNT networks, operating at a sensor temperature ranging from 20 to 250°C, to detect various gas molecules of NO_2, NH_3, H_2, CH_4, H_2S, C_6H_6 and volatile organic solvents.

Here, the CNTs functionalised with noble metal nanoclusters and other functional materials (e.g. metal oxides, polymers and organic materials) are surveyed for gas-sensing applications.

4.3.1 Metal Nanoclusters

Special attention has been paid by materials scientists to the metal catalysts, especially in the form of nanoclusters, as functional materials for advanced CNT-based gas sensors. Metals exhibit a broad range of electronic, chemical and physical properties that are often highly sensitive to changes in the chemical environment. They are mechanically and chemically robust and stable, and thus, compared to polymer-functionalised sensors, metal-modified sensors are able to operate not only at room temperature but also at higher temperatures in harsh environments. Typically, Pd and Pt are widely used in commercial sensors to catalyse combustible gases such as H_2, CH_4, CO, LPG and so on for rapid detection at room temperature in order to avoid a possible trigger of explosion in the chemical detection at elevated temperatures.

Kong et al. [155] demonstrated room temperature H_2 sensors based on palladium (Pd) nanoparticle-modified SWCNTs prepared by electron beam evaporation of ~5 Å of palladium over the entire substrate containing the SWCNT device. Pd-functionalised SWCNTs were shown to be highly sensitive to H_2, with 50% greater response of up to 50% relative resistance change towards 400 ppm H_2 in air compared to bare SWCNT bundles. Response time was recorded as 5–10 s, and the recovery time was measured as ~400 s. It was established that at room temperature, the adsorbed H_2 molecules on the surface of Pd nanoparticles are dissociated by spillover effect into hydrogen atoms that dissolve into Pd at high solubility, leading to a decrease in the Pd work function. This causes electron transfer from Pd to SWCNTs and reduces the hole carriers in the *p*-type carbon nanotube and hence causes a decrease in the electrical conductance. This process is reversible as dissolved atomic hydrogen in Pd can combine with adsorbed O_2 in air to form OH groups which further combine with atomic hydrogen to form H_2O and leave the Pd–SWCNT system, thus recovering the sensor initial conductance giving reversibility to the device.

Penza et al. [21, 30] demonstrated the impact of the tailored load of Au nanoclusters functionalising the sidewalls of the MWCNT networks on

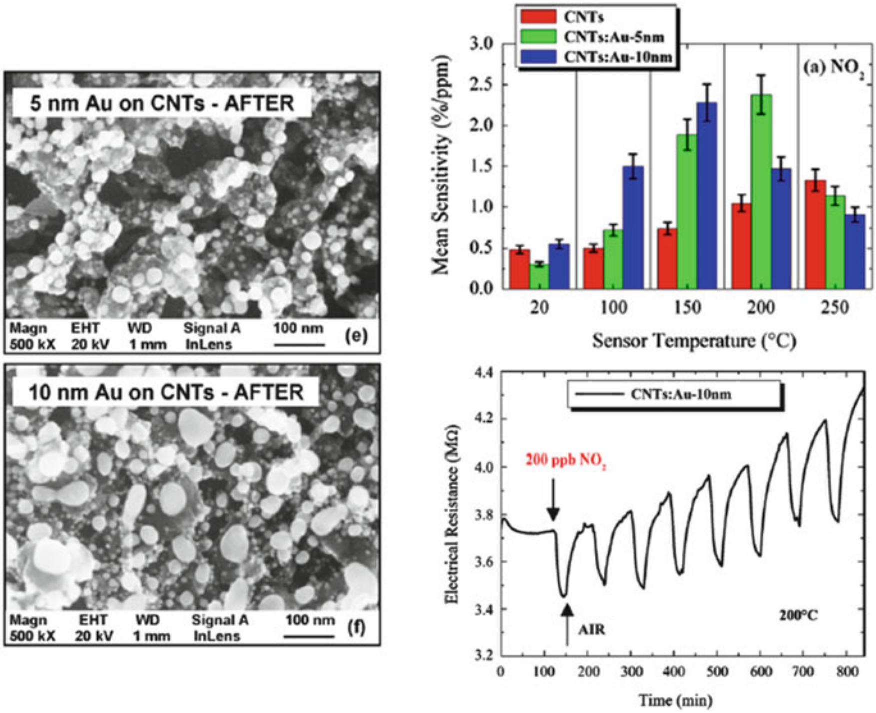

Fig. 13 SEM image of the CNT networks with Au clusters of loading 5 nm (*e-left*) and 10 nm (*f-left*), after thermal annealing. (*Top-right*) Comparison of the mean sensitivity for three chemiresistors based on unmodified CNTs, 5-nm and 10-nm loaded Au-modified CNT nets, vs. temperature. (*Down-right*) Repeatability of the sensor response to eight pulses of 200 ppb NO_2 at 200°C. This figure is reprinted and adapted with permission from Elsevier [30]

gas-sensing properties of a chemiresistor, working at a temperature ranging from 20 to 250°C. Au nanoclusters with increasing size of 5–15, 5–30 and 5–60 nm enhanced gas response compared to unmodified CNT sensors for various reducing gases (NH_3, H_2S) and an oxidising gas (NO_2), down up to a sub-ppm level of detection limit. Negligible responses were recorded to CO, N_2O and SO_2. Figure 13 shows the Au nanoclusters onto CNT sidewalls and the gas-sensing performance. The effect of the sensor temperature on gas sensitivity is also reported. An optimal operating temperature for each Au-modified CNT sensor exposed to NO_2 gas has been recorded, e.g. the temperature of maximum NO_2 gas sensitivity for CNTs loaded with Au nanoclusters of 5 nm was 200°C. Good repeatability of the electrical response of the Au-modified CNT sensor towards 200 ppb NO_2 is also measured, at 200°C.

Llobet and co-workers [34] prepared hybrid materials consisting of oxygen plasma-treated MWCNTs decorated with metal nanoparticles (e.g. Rh, Pd, Au or Ni) for tailored gas recognition of benzene vapours below 50 ppb with high sensitivity and selectivity, at room temperature. Espinosa et al. [158] decorated plasma-treated CNT films with Au or Ag clusters by evaporation for detecting NO_2 up to a 500 ppb level at room temperature. Star et al. [35] decorated SWCNTs by selective electroplating with either Pt, Pd, Au or Rh for detecting a large variety of gases such as CO, NO_2, CH_4, H_2S, NH_3 and H_2. Also, Meyyappan et al. [3] employed Pd-coated SWCNTs for room temperature methane detection [157] and for discriminating NO_2, HCN, HCL, Cl_2, acetone and benzene using the multivariate technique of the principal component analysis (PCA) [26]. Wongwiriyapan et al. [159] demonstrated highly sensitive detection of CO down to 1 ppm at room temperature using Pt-decorated SWCNT layer. Xie et al. [162] demonstrated Pt-decorated SWCNT layer for a highly sensitive glucose biosensor.

4.3.2 Other Functional Materials

Another class of functional materials based on *metal oxides*, e.g. nanocrystals of tin dioxide (SnO_2), for CNT-miniaturised sensors has been recently investigated [148, 152]. Existing SnO_2 sensors are very sensitive and typically operate at temperatures over 200°C to enhance the surface adsorption/reaction kinetics and sensitivity that requires continuous heating of the sensor, considerable electrical power consumption and increased sensor cost. The rutile-structured tin dioxide thin film sensors are *n*-type semiconducting materials widely used in gas-sensing applications and commercial devices. Their main drawbacks are cross-sensitivity, lack of selectivity and high-temperature operations. An emerging strategy to overcome these limitations is the use of SnO_2 nanocrystals as functional material onto *p*-type CNT networks for enhanced gas sensing. Under control of thickness and size of the *n*-type SnO_2 nanocrystals, the electrical properties of hybrid material SnO_2/CNT can change from *p*-type to *n*-type due to charge transfer induced by gas adsorption. Figure 14 shows the device and sensing performance of the proposed sensor.

Lu et al. [148] demonstrated the feasibility to fabricate a gas sensor configured as SnO_2 nanocrystals functionalising the CNT networks for improved gas detection of 25, 50 and 100 ppm NO_2, 100 ppm CO and 0.1% and 1% H_2 diluted in air, operating at room temperature. This hybrid platform as a sensing element is potentially superior to either of its constituent components.

Also, Yang et al. [152] demonstrated the promising sensing properties of hybrid material based on sputtered SnO_2 nanoparticles functionalising the SWCNT networks for improved H_2 gas detection down to 100 ppm and working at room temperature. The gas-sensing behaviour of SnO_2-SWCNT network sensors was changed from *p*-type to *n*-type with increasing SnO_2 deposition time, i.e. increasing surface coverage of SnO_2 on SWCNT.

Furthermore, *polymers* are used in chemical sensing due to their reactivity with gas molecules caused by changes in their physical (e.g. volume changes upon exposure) and chemical (e.g. change of oxidation state) properties. They exhibit, particularly the class of the conducting polymers, very attractive and interesting electronic, optical, magnetic and mechanical properties and processing advantages.

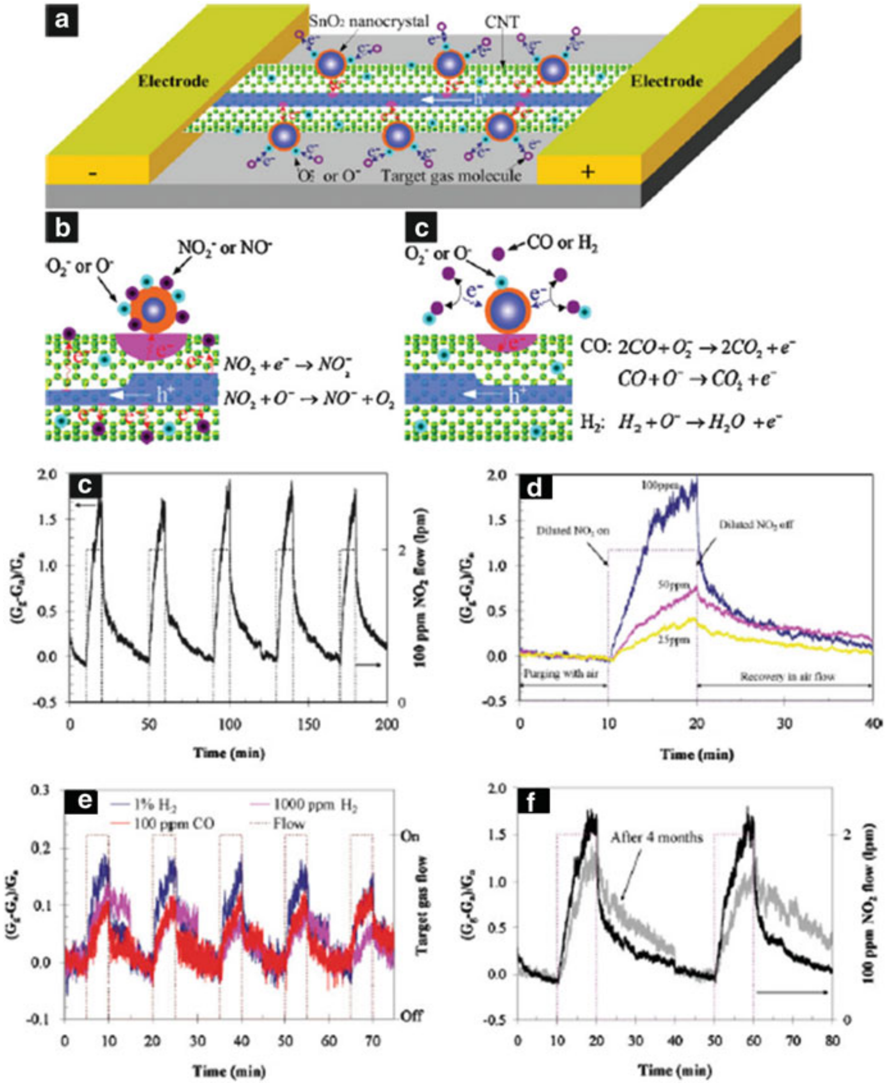

Fig. 14 (*a-Top*) Discrete SnO_2 nanocrystals supported on an individual CNT used as gas-sensitive platform. Possible gas-sensing mechanisms include (*b-Top*) direct adsorption of target molecules (NO_2) onto SnO_2/CNT surface inducing electron transfer and changing the sensor conductivity (mechanism 1) and (*c-Top*) catalytic reaction between target gas molecules (H_2 and CO) and oxygen adsorbates releasing electrons back into SnO_2/CNT surface and changing sensor conductivity (mechanism 2). Electrical sensing performance. (*c-Down*) Dynamic response of SnO_2/CNT sensor for room temperature detection of 100 ppm NO_2. (*d-Down*) Dependence of sensor response on NO_2 concentrations of 100, 50 and 25 ppm. (*e-Down*) Room temperature responses of SnO_2/CNT sensor to 1% and 0.1% H_2 and 100 ppm CO diluted in air. (*f-Down*) Comparison of sensing performance of the as-fabricated SnO_2/CNT sensor with that of the same sensor after a four-month period. The gas sensor performance degrades, but the device is still working. This figure is reprinted and adapted with permission from Wiley-VCH [148]

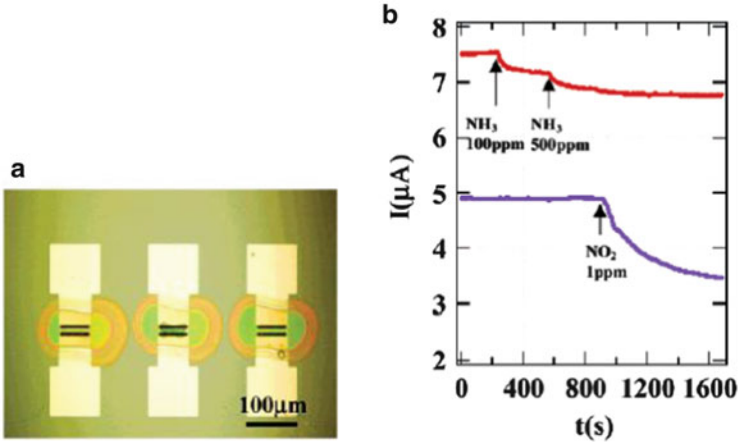

Fig. 15 (**a**) Optical image showing three CNT devices after microspotting with droplets of polymer CNT solutions. (**b**) *Red* (*top*) *curve*: a device coated with Nafion exhibits response towards 100 and 500 ppm of NH_3 in air, and no response when 1 ppm of NO_2 was introduced to the testing environment. *Blue* (*bottom*) *curve*: in contrast, a PEI-coated device exhibits no response towards 100 and 500 ppm of NH_3 and a large conductance decrease towards 1 ppm of NO_2. This figure is reprinted and adapted with permission from ACS [164]

Star et al. [120] fabricated non-covalently functionalised SWCNT field-effect transistors (FETs) by simply submerging nanotube network FETs in an aqueous solution of polyethyleneimine (PEI) and starch overnight. PEI–starch polymer-coated SWCNT-FET devices had electrical *n*-type characteristics and were used as CO_2 gas sensors. The proposed sensing mechanism was based on chemical interactions briefly discussed: starch polymer is hygroscopic and its presence will locally increase the amount of water. Due to the presence of water, the amine groups of the PEI can react with dissolved CO_2 gas molecules to form carbamates. These introduce scattering centres that decrease the carrier mobility in the SWCNTs, thereby increasing the electrical resistance. With this polymer CO_2 gas recognition layer, the functionalised SWCNT-FET sensors exhibited a high sensitivity, fast time, good linearity and complete reversibility for CO_2 concentrations widely ranging from 0.05 (500 ppm) to 10% in air.

Furthermore, Dai et al. [164] developed an SWCNT sensor modified with two distinct polymers of polyethyleneimine (PEI) and Nafion by imparting high sensitivity and selectivity to NO_2 and NH_3, respectively. Figure 15 shows the optical image of three CNT sensors with microelectrodes prepared by dropping CNT–polymer solutions. Arrays of devices comprising multiple SWCNTs bridging metal electrodes were obtained by CVD nanotubes across prefabricated electrode arrays. This ensemble of modified nanotubes exhibited specifically large electrical conductance changes under chemical gating. Polymer modification was used to impart high sensitivity and selectivity to the sensors towards ammonia and nitrogen dioxide. PEI coating affords *n*-type nanotube devices capable of detecting NO_2 at less than 1 ppb concentrations while being insensitive to NH_3. In the contrast, Nafion blocks NO_2 and allows for selective sensing of NH_3. Detection of molecules in a gas mixture was demonstrated by using the multiplexed nanotube sensors.

CNTs have been used as good transducing nanoplatforms for molecular recognition with biosensing capability by *functional organic materials*.

Functionalisations of the CNTs have been performed by DNA [137, 139, 165–168] for hybridisation purposes, by antibodies [136] to study selective antigen–antibody reactions, by proteins [134, 138] and enzymes [127, 128] for efficient induced electrical charge modulation and by modified SWCNT microelectrodes for electrochemical measurements of epinephrine in the presence of ascorbic acid [169]. Additionally, it was demonstrated [170] that nanotube tips with the capability of chemical and biological discrimination can be created with acidic functionality and by coupling basic or hydrophobic functionalities or biomolecular probes to the carboxyl groups that are present at the open tip ends.

Lieber et al. [170] had used these modified nanotubes as AFM tips to titrate the acid and base groups, to image patterned samples based on molecular interactions and to measure the binding force between single protein–ligand pairs. As carboxyl groups are readily derivatised by a variety of reactions, the preparation of a wide range of functionalised nanotube tips should be possible, thus creating molecular probes with potential applications in many areas of nanotechnology, chemistry and biology.

4.4 Composite Carbon Nanotube Sensors

A great attention has been paid to the *composite materials* for gas-sensing applications due to their possibility to operate at room temperature with high performance. Compared to counterpart metal oxide sensors, the CNT-based nanocomposites work at room temperature and are easy to fabricate.

Generally, composite materials consist of a polymeric matrix which acts as an insulating matrix and dispersed particles, e.g. nanotubes, of conducting materials which act as conducting path of the nanocomposite materials. The gas-sensing behaviour of conducting filler–matrix composite materials can be described by the volumetric change of the matrix due to adsorbed vapour and the accompanying change of the percolation-type conductivity. This type of composite material shows a drastic change in the electrical conductivity around a critical composition described as *percolation threshold*. Usually, it depends on the shape of the conducting filler. Generally, the composite with higher aspect ratio of the conducting filler shows the lower threshold and the sharper change in the conductivity around the threshold. Therefore, composite materials equipped with conducting filler of higher aspect ratio, like CNTs, are expected to show higher sensitivities at room temperature.

An et al. [151] prepared an SWCNT/polypyrrole (PPy) nanocomposite by a simple and straightforward in situ chemical polymerisation of a pyrrole and

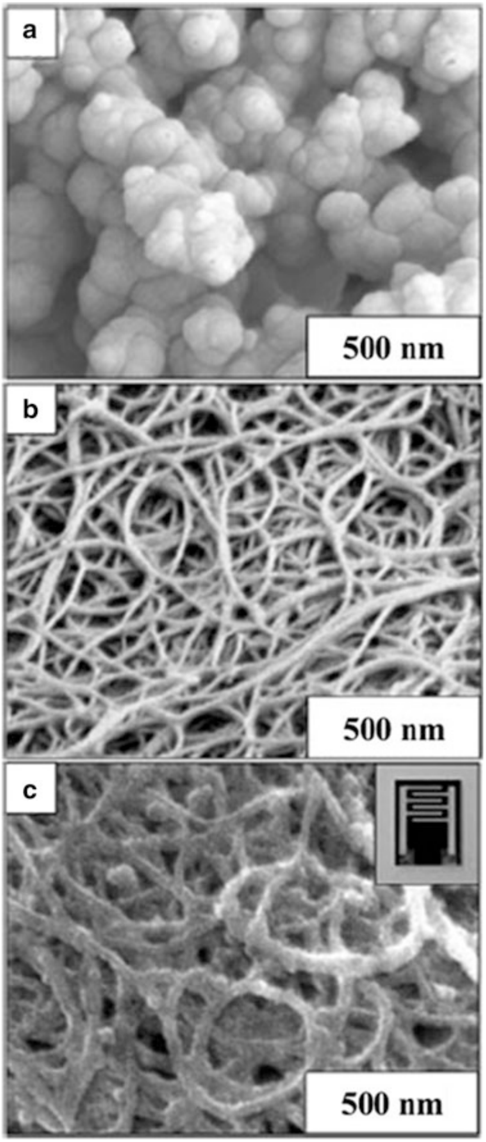

Fig. 16 SEM image of (**a**) pure polypyrrole (PPy), (**b**) purified CNT bundles (diameter of 20 nm) and (**c**) the SWCNT/PPy nanocomposite. The *inset* shows the optical microscope image of the sensor Au/Ti microelectrodes, prepared by sputtering onto SiO_2/Si substrate. This figure is reprinted and adapted with permission from Wiley [151]

SWCNT mixture. The composite was then spin coated onto pre-patterned IDE for electrical resistance measurements towards exposure of tested gases. Figure 16 shows the SEM image of the PPy matrix, SWCNT bundle filler with a diameter of 20 nm and SWCNT/PPy nanocomposite. This nanocomposite showed a better sensitivity to NO_2 gas than both pure materials of SWCNTs and PPy that was due to the enhanced conductivity of the composite material by dispersed CNTs. This

PPy–CNT nanocomposite sensor exhibited signal degradation under long time exposure.

Bavastrello et al. [171] fabricated a nanocomposite of MWCNTs embedded in the poly(2,5-dimethylaniline) (PDMA) by oxidative polymerisation. The nanocomposite PDMA–MWCNTs showed a progressive spontaneous undoping process along the time associated with the instability of the doping agent, constituted by HCl vapours, inside the polymeric matrix. The instability of doping process allowed to fabricate a spontaneous reversible sensor for acid vapours by setting up a comparative potentiometric circuit and engineering the sensitive element directly onto a circuit board.

Philip et al. [122] developed composite thin film of polymethyl methacrylate (PMMA) with unmodified MWCNTs or oxidation-modified MWCNTs (f-CNTs) as nanofillers for gas sensing. The resistance changes of both nanocomposites were evaluated upon exposure towards different gases including dichloromethane, chloroform, acetone and other volatile organic compounds. Both CNT/PMMA and f-CNT/PMMA composites showed increasing resistance upon exposure to these vapours at room temperature. This behaviour was explained on the basis of the volume expansion and polar interaction of the CNT surface with vapour molecules under test. The f-CNT/PMMA showed a significant improvement on the sensor's behaviour including sensitivity, response time and recovery time. This can be attributed by the effects of oxidation on the electronic properties of the CNT fillers in the nanocomposite.

Penza et al. [172] demonstrated that highly sensitive microacoustic vapour sensors based on SAW 433 MHz oscillators were able to detect volatile organic compounds (VOCs) at room temperature using a nanocomposite film of HiPco single-walled carbon nanotubes (HPNTs) embedded in a cadmium arachidate (CdA) amphiphilic organic matrix prepared by the LB technique with a different weight SWCNT filler content. The structural properties and the surface morphology of the nanocomposite were examined by X-ray diffraction, transmission and scanning electron microscopy, as shown in Fig. 17. HRTEM image revealed that the pristine as-received SWCNTs were organised in tangled bundles with diameters of several tens of nanometres. They appear coated by CdA host matrix and randomly distributed in tangled nets of nanotubular chains densely aggregated. The sensing characteristics for acoustic devices indicated that sensitivity to polar and nonpolar tested VOCs of the SWCNT–CdA composite increased with the SWCNT filler content.

Furthermore, *macromolecules* are used to functionalise the CNTs for enhanced gas-sensing properties, even at room temperature.

Particularly, *metalloporphyrins* (MPPs) are among the functional materials characterised by flexible and multiple molecular recognition properties. The basic porphyrin ring is an extended aromatic system formed by four pyrrolic rings linked by methynic bridges. This basic structure is turned into a metalloporphyrin when a transition metal atom (Fe, Co, Ni, Cu, Mo, Zn, Mn, etc.) replaces the two hydrogen atoms at the central core. Also, other modifications include compounds at the lateral positions. Thus, a metalloporphyrin can offer a wide variety of interaction

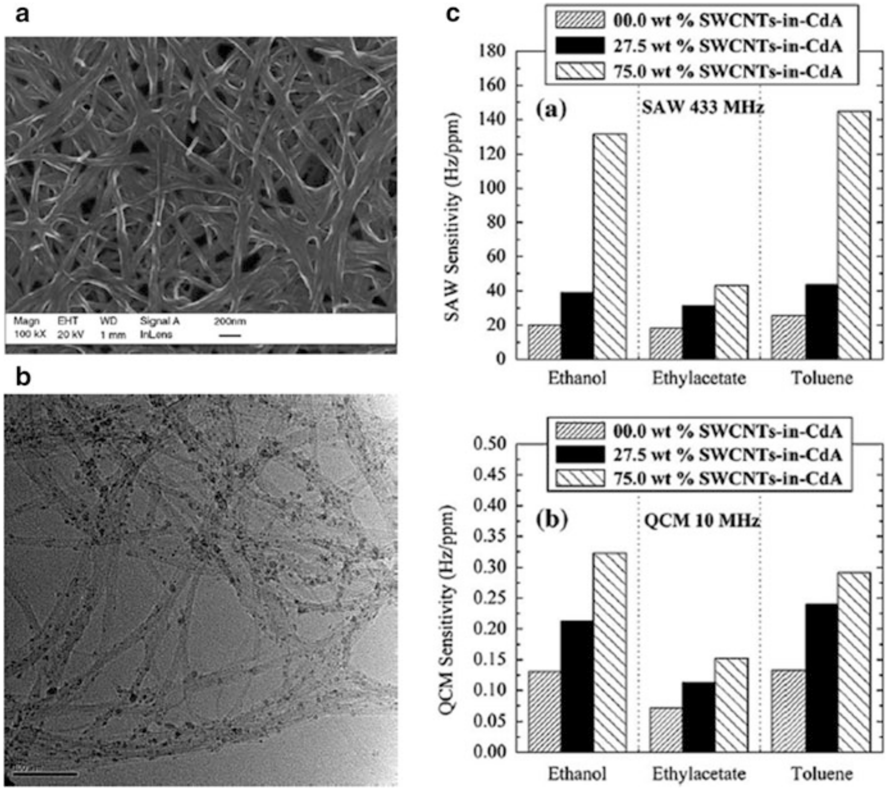

Fig. 17 (**a**) SEM image of the SWCNT–CdA 27.5 wt.% LB nanocomposite film. (**b**) TEM image of pristine HiPco SWCNT material used as filler in the nanocomposite. (**c**) Comparison of room temperature sensitivity of the nanocomposite SWCNT–CdA LB film with a different weight filler content onto SAW 433-MHz and QCM 10-MHz transducer. This figure is reprinted and adapted with permission from Elsevier [172]

mechanisms that can be exploited for gas sensing. Recently, Penza et al. [153] demonstrated the effect of the surface functionalisation of the CNT-networked films with spray MPP layer on gas sensitivity. MPP-modified CNT networks exhibited an increased sensitivity of the electrical resistance towards concentrations of common volatile organic compounds of alcohols, amines, aromatics and ketones, at room temperature. The gas adsorption properties of the MPP-functionalised CNTs exhibited broad selectivity and high sensitivity. PCA analysis was performed using the gas response of a sensors array by providing a capability of the compounds recognition. These results were considered very promising for the development of arrays of CNT-based gas nanosensors with broad selectivities for fingerprinting analysis of gaseous complex samples.

Furthermore, CNT networks modified with *functional groups* attached to walls and as nanofiller in composite materials to engineer *nanocomposites* with different matrix embedding CNTs as one-dimensional structures are shortly surveyed for gas-sensing applications.

The physically and chemically activated surface modifications in the CNT networks involve non-covalent or covalent attachments of foreign functionalising materials and anchored functional groups changing the electronic properties useful for chemical sensing applications. In fact, the chemical modifications [173–175] represent an important area in the sidewall chemistry and doping of the CNTs for sensor nanomaterials applications.

Sin et al. [176] demonstrated the electrical resistance response of the chemically functionalised MWCNTs (f-CNTs) to alcohol vapours with ultralow power consumption. For the fabrication of the sensor, purified MWCNTs were sonicated in 3:1 concentrated sulphuric acid and nitric acid for different time intervals. By this method, the MWCNTs can be oxidised and COOH groups will be grafted along the sidewall and the tube ends of the MWCNTs. It is believed that with the polar COOH groups attached onto the nanotube surface, the sensors will give higher responses towards the alcohol vapours under test as their absorption efficiency with these volatile organic compounds will be increased due to the dipole–dipole interactions (mainly hydrogen bonding) between the COOH and the polar organic molecules.

In addition, Bekyarova et al. [177, 178] developed SWCNTs with covalently attached functional groups of poly(*m*-aminobenzene sulphonic acid) (PABS) to sidewalls exhibiting improved sensor performance for NH_3 detection. SWCNTs produced by arc discharge (P2-SWNT) were dispersed in DMF by sonication to obtain dispersions of 0.2 mg/mL. SWNT–PABS (1 mg/mL) with attached functional groups were produced by Carbon Solution, Inc., and prepared by sonication. Both dispersions were deposited on an array of gold interdigitated (IDE), with a gap between the fingers of 80 μm. The deposition was performed by spraying the dispersions with air brush in several steps until the desired resistance ranging from 0.2 to 20 kΩ was obtained. Figure 18 shows the sensor device; the typical responses towards NH_3; the comparison of the ammonia response exhibited by the different SWCNTs, with and without PABS functional groups attached to sidewalls; and the scheme of the interaction of SWNT–PABS with NH_3. Compared to purified SWNTs, devices fabricated with SWNT–PABS have shown more than two times higher change of resistance upon NH_3 exposure. Importantly, the SWNT–PABS sensors rapidly recover their resistance when NH_3 is replaced with nitrogen. Exposure to NH_3 induces significant changes in the electronic structure of the SWNT–PABS, which allow detection of ammonia at concentrations as low as 5 ppm.

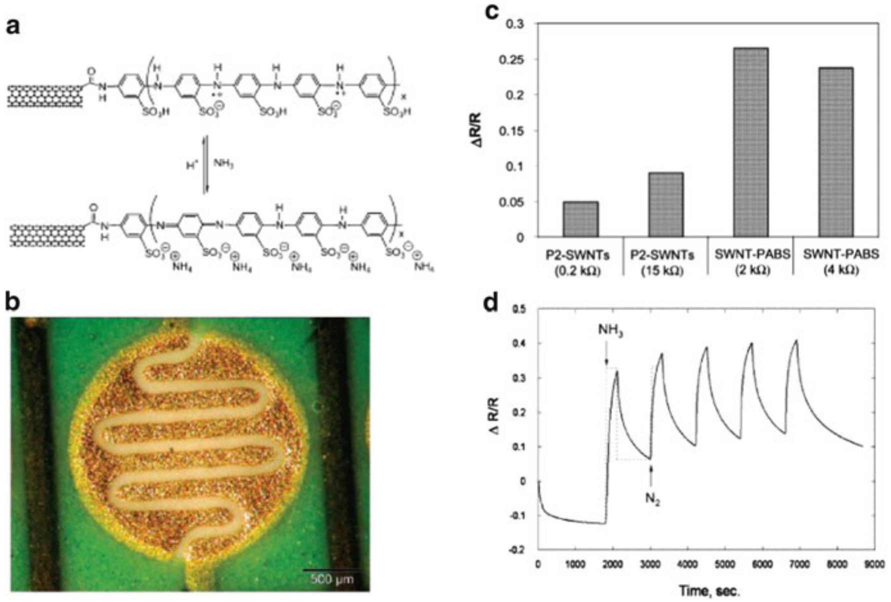

Fig. 18 (**a**) Interaction scheme of the modified SWNT–PABS, having functional groups attached of poly(*m*-aminobenzene sulphonic acid) (PABS), with NH_3 gas molecules. (**b**) Optical image of the interdigitated electrode used for the CNT-based sensor. (**c**) Response of the unmodified (P2-SWNTs) with different electrical resistance and the PABS-modified SWCNTs (SWCNT-PABS) with different electrical resistance. (**d**) Response curves of the PABS-modified SWCNTs (SWNT–PABS) towards 100 ppm NH_3. This figure is reprinted and adapted with permission from ACS [177]

5 CNT Nanosensors

Due to the limitations of the fabrication technique and the difficulties of mass production, CNTs in form of thin film, as opposed to single strands of CNTs, are widely applied for gas-sensing applications. However, interesting development on single CNT sensor deserves some attention.

Kong et al. developed a NO_2/NH_3 gas sensor that is based on an FET structure by incorporating individual semiconducting SWCNTs [1]. When the sensor (see Fig. 19) was exposed to 200 ppm NO_2 at room temperature, it showed a fast response time of about 2–10 s, but a slow recovery time of about 12 h. However, the recovery time can be shortened to 1 h by heating the sensor to 200°C. When compared to the result of NO_2 sensing, the sensor response to NH_3 was slower (1–2 min) with less sensitivity. It was also found that the response time of the sensor decreased when there is a decrease in gas concentration.

Almost all of the CNT-based gas sensors were designed based on the property of charge/hole mobility modification due to gas molecules absorption on CNTs. Thus, most CNT-based electrical components can be considered potential platform for

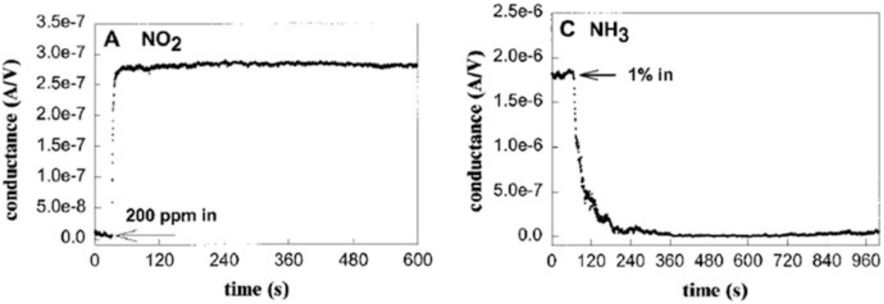

Fig. 19 Response of individual SWCNT-FET to 200 ppm NO_2 and 1% NH_3 in Ar flow. This figure is reprinted and adapted with permission from Science [1]

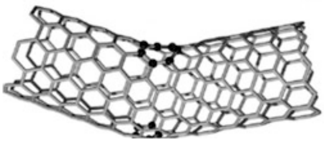

Fig. 20 Connection of armchair and zigzag SWCNT with pentagon–heptagon defect. This figure is reprinted with permission from Nature [179]

gas sensing. Thus, in addition to an FET structure, diodes constructed by individual CNT can also be considered.

CNT diodes can be realised either by connecting a metallic SWCNT and a semiconducting SWCNT or by doping to form a *p*–*n* junction (Fig. 20). The connection of metallic and semiconducting CNTs can be realised by bending SWCNT to create pentagon–heptagon defects, which is illustrated in [179].

Zhou et al. designed a diode by doping potassium (K) to half of the semiconducting SWCNT, thereby forming the *n*-type section, and the remaining half with no dopant remains *p*-type [180]. The SWCNT has a diameter of about 2 nm and length of 3.5 μm. The structure of K-doped SWCNT diode is illustrated in Figure 21.

6 Applications

CNTs promise to be essential parts of many future electronic components such as transistors, switches, emitters and sensors. Assemblies of metallic and semiconducting CNTs can be used to produce macroscopic devices integrating individual tubes for nanoelectronics.

CNTs are widely considered as natural sensing elements in the format of a key nanotube or nanowire architecture that has been identified as providing high sensitivity. Several aspects of the CNT properties have been discussed in the

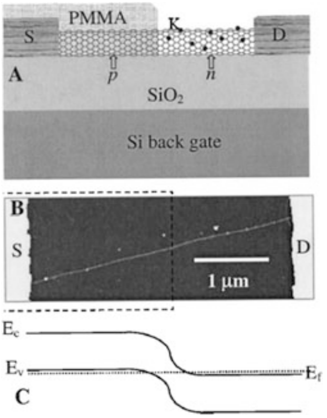

Fig. 21 K-doped SWCNT as a rectifying component. This figure is reprinted and adapted with permission from Science [180]

context of the practical applications in order to design and fabricate advanced sensory systems. Specifically, CNTs are functionalised with molecular units imparting high sensitivity and selectivity to make advanced resistive or FET sensor devices. CNT sensors have the great potential for smart integration into electronic circuits, miniaturisation, low power consumption and low cost.

Nevertheless, there are several challenges associated with their synthesis, purification, processing and fabrication into devices. CNTs are good candidates for a variety of applications in the field of environmental monitoring, industrial process control and health monitoring.

Here, many applications of pristine and modified CNTs integrated into innovative proof of concepts are reviewed in the emerging sectors.

6.1 Environmental Monitoring

CNTs are innovative nanostructured materials for new sensing technologies for low-cost air quality control and environmental monitoring. This is of strategic importance for the sustainable development and green economy, including protection of the public health. In the past, noticeable scientific efforts have been realised to develop functional materials and devices for air quality control (AQC), mainly cost-effective nanosensors. These are not commercialised yet.

The current research for materials tackles both the specifications of continuous and ubiquitous environmental monitoring and the industrial demands for device integration. Moreover, strong inputs are pushing the development of new low-dimensional nanostructured materials for gas detection of ppb level at low power consumption and low cost.

Carbon nanomaterials such as nanotubes and graphene are rapidly developing and offer the potential for increased surface area and composition control in order to address gas detection as low as ppb level in real-world applications by considering

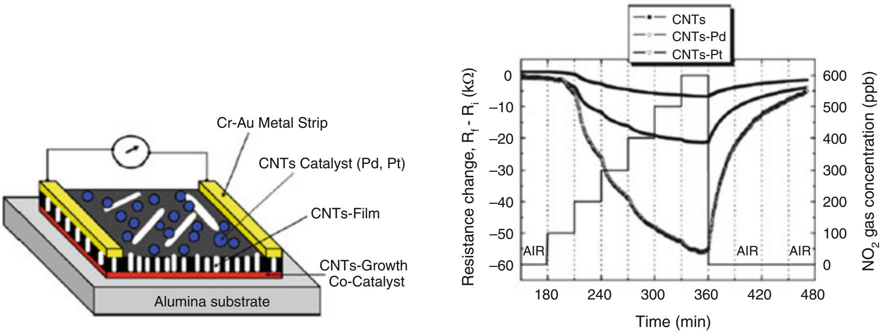

Fig. 22 (*Left*) Schematic view of two-pole chemiresistor based on MWCNT-networked films functionalized with Pt and Pd nanoclusters. (*Right*) Time response of three sensors based on unmodified CNTs, 5-nm loaded Pd- and Pt-modified CNTs, exposed to various 30-minute pulses of NO_2 gas ranging from 100 to 600 ppb, at a sensor temperature of 200°C. This figure is reprinted and adapted with permission from Elsevier [29]

the interfering effects of temperature and humidity. Here, a survey of CNT-based sensors for air and water applications is shortly discussed.

6.1.1 Air Quality Control

Penza et al. [29] demonstrated a gas chemiresistor fabricated directly onto alumina substrates using RF-PECVD-grown MWCNTs for gas detection of air pollutants, at a working temperature of 200°C. Functionalisations of MWCNTs tangled bundle films with nominally 5-nm-thick Pt and Pd nanoclusters, prepared by sputtering, provided higher sensitivity for significantly enhanced gas detection of NO_2, H_2S, NH_3 and CO up to a low limit of sub-ppm level. The electrical resistance at room temperature of unmodified and Pt- and Pd-functionalised MWCNTs was measured as 32.5, 14.1 and 13.4 kΩ, respectively. Thus, the metal modification of CNTs was found to decrease electrical resistance of CNT-networked films. The measured electrical conductance of the metal-functionalised MWCNTs upon gas exposure was modulated by charge transfer with *p*-type semiconducting characteristics. Pt- and Pd-cluster-functionalised MWCNT sensors exhibited better performance compared to unmodified MWCNTs, making them promising candidates for air pollutants' environmental monitoring. The calculated limit of detection of the most performing Pt-modified CNT sensor was as low as 3 ppb NO_2, 4 ppb H_2S, 200 ppb NH_3 and 4 ppm CO, working at 200°C. Figure 22 shows the scheme of fabricated chemiresistor. Also, a simple electronic interface for chemiresistor has been developed with a voltage output of sensor signal. Figure 22 shows the detection at sub-ppm level ranging from 100 to 600 ppb NO_2 in the 30-min step-pulse format using the three CNT sensors, at the operating temperature of 200°C. Both metal-functionalised CNT sensors are more sensitive than unmodified CNT sensor due to the catalytic effect of the spillover with highest sensitivity for

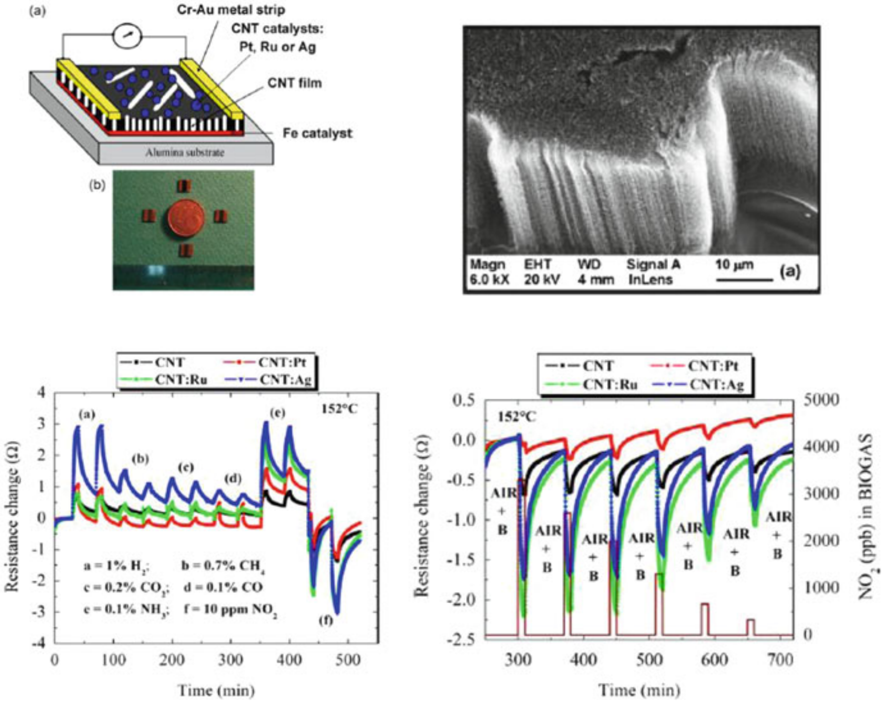

Fig. 23 (*Top-left*) (**a**) Schematic view of two-pole chemiresistor based on MWCNT films functionalized with Pt, Ru and Ag clusters. (**b**) Image of four CNT chemiresistors. (*Top-right*) SEM image of vertically aligned MWCNTs grown by Fe catalyst PECVD. (*Down-left*) Response to 1% H_2, 0.7% CH_4, 0.2% CO_2, 0.1% CO, 0.1% NH_3 and 10 ppm NO_2 of a four-sensor array based on unmodified CNTs and Ru-, Pt- and Ag-modified MWCNTs vertically aligned *forest-like* networks, at 152°C. (*Down-right*) Response of a four-sensor array to a multicomponent gas mixture of landfill gas with various content of the target NO_2 gas (3.3 ppm to 330 ppb) by unmodified and metal-functionalized CNT. The sensor temperature is 152°C. The gas mixture B of the landfill gas is composed of 550 ppm CO_2, 660 ppm H_2, 460 ppm CH_4 and 260 ppm NH_3 in air. This figure is reprinted and adapted with permission from IOP [23]

Pt-modified CNT sensor able to detect 100 ppb NO_2. This limit represents the actual NO_2 attention level for environmental monitoring in the Italian regulations. The resistance change induced by 100 ppb NO_2 in the Pt-modified CNT sensor is extremely high as 5.1 kΩ and is higher than that of about 4 Ω reported in the literature [181] for unmodified CNT-based NO_2 gas sensors. These results able the metal-functionalised CNT gas sensors for environmental air monitoring applications.

Additionally, Penza et al. [23] demonstrated vertically aligned MWCNT layers RF-PECVD synthesised on Fe-coated alumina substrates as *forest-like* nanostructure, as shown in Fig. 23. A miniaturised CNT-based gas sensor array was developed for monitoring landfill gas (LFG) at a temperature of 150°C. The sensor array was composed of four sensing elements with unmodified CNT and CNT loaded with 5-nm nominally thick sputtered clusters of Pt, Ru and Ag. Chemical analysis of the multicomponent gas mixtures constituted of CO_2, CH_4, H_2, NH_3, CO and NO_2 was performed by array sensor responses and pattern recognition based on principal component analysis (PCA). PCA results demonstrated that the metal-decorated and vertically aligned CNT sensor array is able to discriminate the NO_2 presence in the multicomponent mixture LFG. The size of metal clusters decorating CNT top surface varied in the range of 5–50 nm. Functional characterisation based on electrical charge transfer sensing mechanisms in the metal-modified CNT chemiresistor array demonstrated high sensitivity providing minimal sub-ppm-level detection down up to 100 ppb NO_2, at 150°C.

Varghese et al. [182] demonstrated impedance spectroscopy used to study the gas-sensing characteristics of both capacitance and resistance of sensors employing MWCNTs as active gas-sensing element. These studies revealed the chemisorption of the tested reducing gases upon the surface of MWCNT layer. Increasing sensor impedance was observed with increasing humidity or partial pressures of NH_3, CO and CO_2. The impedance changes were attributed to *p*-type conductivity in the semiconducting MWCNTs and the formation of Schottky barriers between metallic and semiconducting nanotubes in the carbon bundles. Reversible responses were recorded for MWCNT sensors exposed towards relative humidity, CO and CO_2, while they were strongly responsive towards NH_3 behaving as dosimeters.

Cantalini et al. [181, 183, 184] demonstrated that PECVD-grown CNT sensors were fabricated onto Si_3N_4/Si substrates equipped with Pt electrodes for gas-sensing applications. The CNT diameter ranged 30–40 nm and length 100–200 nm. CNTs showed cross-sensitivities towards NH_3, H_2O and C_2H_5OH and exhibited high sensitivity towards NO_2 gas in the gas concentrations range of 10–100 ppb. The highest NO_2 gas sensitivity was measured at 165°C working temperature. No response was found towards CO and CH_4 gases in the operating temperature range of 25–250°C. Additionally, NO_2 gas sensitivity resulted to be improved by annealing the as-grown films at temperatures higher than 330°C. This was attributed to structural changes induced by temperature exceeding 250°C providing a support for a phase transition causing an electrical change from a metallic to a semiconducting response of the CNT film.

Someya et al. [14] measured the conductance of semiconducting SWCNTs in FET structures and investigated the device response to alcoholic vapours. The semiconducting SWCNTs were synthesised by CVD onto heavily doped Si substrate capped with 100-nm-thick SiO_2, and the electrode contacts were formed by evaporating Cr–Au with metal shadow masks. Figure 24 shows significant changes at room temperature in FET drain current measured when the device was exposed to various alcoholic vapours of methanol, ethanol, 1-propanol, 2-propanol, 1-butanol, 1-pentanol, 1-octanol and tertiary-butanol with a gate voltage of -20 V and a source–drain voltage of -100 mV. The response time was within 5–15 s. The reversibility and reproducibility were considered good. Short recovery time (few seconds) can be obtained if the gate voltage is released briefly and restored before the next gas-exposure cycle. Moreover, the different response characteristics of the

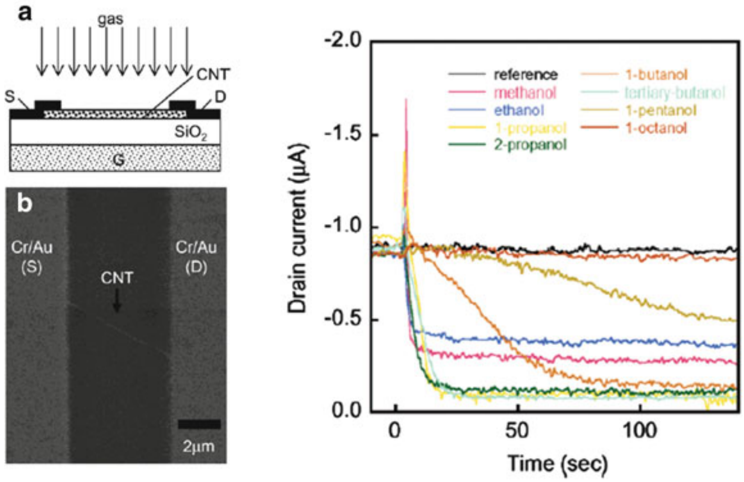

Fig. 24 (**a**-*Left*) Schematic view of the SWCNT-based FET sensor integrated in SiO_2/Si substrate. (**b**-*Left*) SEM image of the nanotube FET: a single-walled carbon nanotube bridges source and drain Cr–Au electrodes with a spacing of 5 μm. (*Right*) Drain currents (V_{SD} = -100 mV; V_G = −20 V) as a function of time upon exposure to saturated vapours of various alcohols: methanol, ethanol, 1-propanol, 2-propanol, 1-butanol, tertiary-butanol, 1-pentanol and 1-octanol. This figure is reprinted and adapted with permission from ACS [14]

CNT-FET device to several alcohols considered also suggested its potential application for the identification of the gas sources in the air quality control applications.

Kuzmych et al. [185] demonstrated a chemically functionalised CNT-FET for nitric oxide (NO) gas detection. The NO gas to be detected was passed through acidic gas scrubbing, oxidation and conductivity measurements by CNT-FET. Gas mixtures containing NO were passed through an Ascarite scrubber and then an oxidising material (CrO_3) which converted NO to NO_2. This gas was delivered to the CNT-FET modified with PEI polymer. Interaction of NO gas with PEI-modified CNT-FET resulted in a conductivity change depending proportionally on NO gas concentration. A wide range of NO gas concentrations were measured from 2 ppb to 5 ppm. A detection limit was measured as 5 ppb NO at a relative humidity of 30%. Cross-sensitivity to CO_2 and O_2 was measured as well, modelling human breath conditions. Compared to chemiluminescence methods for monitoring NO, this sensor offers the advantages of low cost, compact size and simplicity for self-diagnostics and home care.

Novak et al. [32] demonstrated the use of CNTs as FET sensors for chemical detection at sub-ppb level of nerve agents, such as the simulant of DMMP for sarin. These sensors are intrinsically selective against interferent signals from hydrocarbon vapours and humidity. They used a special filter based on a flow cell coated with chemoselective polymer films. The CNT-FET device uses a miniaturised flow cell, and the response towards 1 ppb DMMP was measured with successful detection.

Meyyappan and co-workers [3] fabricated a gas sensor by casting of an SWCNT-networked layer on interdigitated electrodes (IDE) for gas and organic vapour detection, at room temperature. The sensor response is linear for gas concentrations from sub-ppm to hundreds of ppm with a detection limit of 44 ppb for NO_2 and 262 ppb for nitrotoluene. The response time is in the range of a few seconds, and the recovery time is longer in the range of minutes by using UV illumination. The gas sensitivity is less than 6% for all tested devices, comparable with commercial gas sensors. The extended detection capability from gas to organic vapours is attributed to a direct charge transfer on the individual semiconducting SWCNTs' conductivity with additional electron hopping effects on intertube conductivity through physically adsorbed molecules between individual SWCNTs. A model of gas adsorption into CNT networks has been proposed by Meyyappan et al. [3] to distinguish two different effects in the electrical charge transfer: *intratube modulation* and *intertube modulation*. In the first case, a direct charge transfer between gas molecules and an individual nanotube can lead to the modulation of the Fermi level in the semiconducting tubes causing a conductivity change. In the second case, gas adsorption occurs in the interstitial space between nanotubes to form a CNT–molecule junction leading to a hopping mechanism for intertube charge transfer between individual nanotubes in the bundle with a consequent change in the conductivity. These effects of charge modulation can be enhanced depending on adsorbed target gas, tube nanostructure and defective status in the nanomaterials. It also demonstrated that the recovery time for NO_2 desorption is very long, on the order of various hours, because of the high bonding energy between SWCNTs and adsorbed NO_2 molecules. A strategy proposed to reduce the recovery time was the UV light illumination upon recovery cycle simultaneously with recovery nitrogen gas. The UV exposure decreased the desorption energy barrier to promote the NO_2 desorption up to a few minutes. However, this UV light method was already employed by Dai et al. [186] to accelerate molecular photo-desorption from SWCNTs by using an ultraviolet light source with a wavelength of 254 nm, intensity of 2 mW/cm^2 and photon flux of $2.5 \times 10^{15}/cm^2$ s.

6.1.2 Water Quality Control

Nanomaterials for environmental protection are emerging for new practical applications. In particular, carbon nanomaterials are good candidates for water quality control and liquid applications.

CNTs have some important advantages for fabricating carbon material-based electrochemical sensors including the good electrical conductivity, the biocompatibility, the large specific area, the well-defined nanotube structure, the modifiable surface, the functional groups on the surface with pretreatment and the capability of being solubilised or dispersed in solutions. Based on these unique properties, a large variety of research works and reviews [187] have been dealt with CNT-based electrochemical sensors. An extensive review on the electrochemical CNT-based sensors for applications has been proposed by Hu and Hu [188].

An electrochemical sensor is mainly composed by a three-electrode cell with a working electrode (e.g. the new carbon nanomaterial to be assessed), a reference electrode (e.g. Ag/AgCl for aqueous media, Ag/Ag^+ for nonaqueous solutions) and an auxiliary electrode (counter electrode) principally consisting of a material similar to the working electrode. The electrodes are commonly immersed in a specific solution of one or more electrolytes for measuring the characteristic current–potential curves in the cyclic voltammetry.

Barisci et al. [189–191] demonstrated the possibility to use CNTs to modify the electrodes in the electrochemical sensors immersed in aqueous and nonaqueous solutions. In particular, an electrochemical quartz crystal microbalance (QCM) was modified with SWCNTs for studying the voltammetric properties of various electrolytic solutions showing that the QCM electrode mass increased with increasing negative potentials and was associated with double-layer charging in the CNT electrode. Liu et al. [192] demonstrated the usage of carbon nanotube powder in electrochemical microelectrodes for nitrite detection in acidic solutions with a low detection limit as 10^{-7} M at signal-to-noise ratio of 4.

Wang et al. [193] demonstrated a carbon nanotube/Teflon composite as electrochemical sensors and biosensors for marked electro-catalytic activity towards hydrogen peroxidase providing low-potential amperometric detection of glucose and ethanol. Additionally, Weeks et al. [194] demonstrated an enzymatic amperometric biosensor using vertically aligned carbon nanofibres for biosensing applications.

Valentini et al. [169] demonstrated functionalised SWCNTs modified microsensors for the selective response of epinephrine in the presence of ascorbic acid. Modified stainless steel microelectrodes (microwire diameter, 300 mm) were assembled using functionalised SWCNTs deposited by the electrophoretical deposition process (EPD) method. The functionalised SWCNTs, which covered the microelectrode surfaces, showed an improved sensitivity and selectivity towards the electrochemical detection of epinephrine. These chemical sensors hampered the voltammetric responses of ascorbic acid (AA) and uric acid (UA), while the electrochemical oxidation of epinephrine was significantly enhanced. Using the differential pulse voltammetry technique, epinephrine showed a very well-resolved peak centred around 240 mV, while 1 mM of AA (present in the same solution) was not detected. This optimisation resulted in microsensors with a good linear range (2–100 μM) epinephrine, a good sensitivity (28.1 A M^{-1} cm^{-2}) and interelectrode reproducibility ($RSD\% = 7.0$, $n = 6$), a detection of limit ($LOD = 3\sigma$) of 2 μM, a response time of 6 s, a significant operational stability (13 h in continuous working conditions) and long-term stability (1 month).

Consales et al. [195] developed an optical fibre coated by SWCNT LB films at the distal end for detection of toluene (20–80 ppm) in water environment. The good stability, high sensitivity (1.2×10^{-4} ppm), detection limit as low as 5 ppm and good dynamics in the response and recovery (few minutes) confirmed the potentiality of this optical device for detecting chemicals in aqueous solutions.

6.2 Industrial Applications

The widespread adoption of CNT sensors for industrial applications will depend on the development of sensors that can detect a number of gases at specific concentrations with sufficient sensitivity and selectivity, reproducibly and cost-effectively. Manufacturing costs and complexity will also be a major consideration. One can then easily envisage CNT sensors appearing in many areas such as environment, food processing, agriculture, medicine, mining, defence, etc.

CNTs have immense potential in sensing due to superior chemical and electronic properties [196] and can be employed not only as the sensing element but also as part of the transduction system. The fabrication of CNT sensors is in essence the integration of CNT morphology through their chirality, diameter and length with the substrate and interconnections in a transistor or resistor configuration. Some significant progress was reported on the commercialisation of such devices.

Progress has also been reported on the basic technological methods for integrating CNTs in different applications with wafer-level approaches by Hermann et al. [197]. The support–catalyst system can be controlled to adapt the CNT growth for the needs of specific applications. For example, the CNT growth can be completely inhibited in thermal CVD when tungsten is employed as a support for the Ni catalyst. The W suppresses catalyst seed formation and prevents CNT growth. This deactivation of catalyst activity can be exploited for site-selective CVD growth of CNTs.

Sensors based on a single SWCNT are not considered suitable for widespread manufacture of devices due to the variability in the electronic properties of individual SWCNTs [199]. Lee et al. [198] have proposed the use of an SWCNT network-base channel which uses a number of SWCNTs. By this method the electronic properties are averaged over the assembly of tubes and promise a pathway to practical applications.

A major potential area for CNT sensor-based technology is believed to be in the biomedical industry [43]. A typical example is the measurement and control of sugar levels in the medication of diabetes. The size of the CNT sensor and low power consumption also render it suitable for implantation for applications that may include pulse rate monitoring, blood glucose levels or other diagnostics.

6.2.1 Automotive

The automotive industry has great potential for the adoption of CNT sensor technology from the improvement of performance through the monitoring of oil degradation to antitheft technology. Engine oils are susceptible to degradation by oxygen, temperature and stresses [200]. The degradation of oil can generate acidic by-products and lead to the reduction in lubrication efficiency and eventual engine damage and failure. Sensors are able to monitor acidity, viscosity and conductivity [201]. Conductometric sensors have been reported for automotive oil monitoring based on a polymer-multiwalled carbon nanotube composite. MWCNTs with a diameter of 6–20 nm and lengths of the order of 1–5 μm were used as the conductive linkages in polymers such as polyurethane. Such devices can monitor the quality of lubricating oil at temperatures up to 80°C.

It is predicted that hydrogen will become increasingly important as an alternative fuel in the automotive industry and as such the detection of low concentrations will be important. To ensure maximum safety in hydrogen-based automotive applications, a number of sensors are required [202]. Sensors available on the market do not respond with sufficient sensitivity to hydrogen for automotive requirements, and much research is dedicated to this area. A recent example is the work of Ventura et al. [203] who have developed a cross-linked aminated MWCNT paper as a hydrogen sensor. The paper was used as a substrate for the immobilisation of palladium nanoparticles. Aminated MWCNTs were cross-linked with benzoquinone to produce a material similar to bucky paper. The device was demonstrated to detect 360 ppm of hydrogen with a resistance change of 0.14 Ω. The detection of toxic gases in industrial and automotive emissions is also an area of intense development. Recently Cho et al. [204, 205] have developed an energy-efficient chemical sensor system that operates at room temperature with a power consumption of 32 μW and has a measurement accuracy of 1.34% across the 10 kΩ–9 MΩ range. A detection limit of 50 ppm NO_2 was demonstrated.

6.2.2 Food Industry

Nanotechnology is finding many applications in food quality safety and security and the subdomains of agricultural production food processing and packaging and distribution [206]. In the case of CNT sensors, direct quantification of specific analytes (e.g. proteins, metabolites and nucleic acids) is used to identify the presence of microbes. Nanosensor devices that use CNTs are small enough to trap and measure proteins and molecules [207]. The addition of synthetic colourants to food can also be problematic where quinoline yellow, for example, has been shown to be genotoxic. Zhao et al. [208] have developed an MWCNT electrode to detect such colourant and successfully applied it to detection in commercial soft drinks at a level equivalent to liquid chromatography with a sensitivity limit of 0.5 mg L^{-1}.

Nano-biosensors with pore sizes equivalent to bacteria can be used as fast detectors for peptides at the single molecule level. The electrochemical reactivity of CNTs permits their use in effective low-potential, amperometric biosensing [209]. For amperometric monitoring of lactate CNT–mineral oil, paste sensing is employed. The accelerated electron reaction of hydrogen peroxide at the CNT-based paste electrode permits high sensitivity. Tang et al. [210] have reported on an ultrasensitive electrochemical immunoassay of staphylococcal enterotoxin B in food using a CNT device. Staphylococcus enterotoxin B is one of the major toxins responsible for food poisoning. High sensitivity was demonstrated down to a level of 10 pg/mL.

A novel system for assessing food quality was reported by Park et al. [211]. They developed an olfactory-nanovesicle-fused carbon nanotube-transistor biosensor that can effectively mimic the response of a canine nose. The bioelectronic sensor could detect hexanol, an indicator of the oxidation of food, down to 1 fM concentration in real time. Similarly a portable electronic nose was reported by Wongchoosuk et al. [212] based on carbon nanotube–SnO_2 gas sensors and used to detect methanol contamination in whiskeys. A composite mixture of CNTs and SnO_2 was evaporated over interdigitated electrodes equipped with a heater on the rear. The composite mixture gave a response 65% greater than pure tin oxide and could detect EtOH and MetOH down to 100 ppm.

The detection of illegal growth chemicals in cattle has also been investigated using carbon nanotube-based electrochemical immunosensing by Liu et al. [213]. Clenbuterol (CLB) is used to increase growth, reduce fat and improve protein accretion in livestock but can result in adverse clinical effects in humans and is therefore illegal. The monitoring of residual CLB is therefore of interest from a public health and food industry perspective. Liu et al. [213] used a conjugate of MWCNTs and goat anti-mouse-immunoglobulin G as a sensing medium. A detection limit as low as 0.1 ng/mL was demonstrated with a rapid assay time of 16 min.

Agriculture and fishing in general represent areas where CNT sensors can play important roles. This may include humidity control, CO_2 monitoring and pH measurements [43]. The measurement of xanthine is important in the diagnosis and control of gout, xanthinuria and hyperuricaemia. In addition xanthine is important in quality control of fish. Devi et al. [214] immobilised xanthine oxidase on a composite film of zinc oxide nanoparticle/chitosan/carboxylated MWCNT/polyaniline electrodeposited onto a Pt electrode. Using this system a response time of 4 seconds was found and a detection limit of 0.1 μM demonstrated.

A major area in food production is the control of fruit ripening which plays an important part in transportation and packaging. Ethylene initiates the ripening of fruit and promotes seed germination and flowering [215]. A reversible chemoresistive sensor has been developed by Esser et al. that can detect sub-ppm concentrations of ethylene. The sensor was highly selective towards ethylene and easily constructed from commercial materials. The basis was an ethylene-sensitive material comprising a mixture of SWCNTs with a copper complex based on a fluorinated tris(pyrazole) borate ligand. This material is able to react with ethylene and induce a change in conductivity. The concentrations required for fruit ripening are between 0.1 and 1 ppm which the sensor was readily able to detect. The limit reported was approximately 0.5 ppm ethylene.

6.2.3 Other Applications

High-level protection for military, firefighters, law enforcement and medical personnel is a priority when dealing with biological, chemical and other threats. Nanotechnology and carbon nanotube-based sensors have applications in this area [216]. In case of the detection of explosives, nitrotoluene and 2,4-dinitrotoluene have been employed for the development of the 2,4,6-trinitrotoluene (TNT) sensors [8]. Chemical warfare agents include sarin, soman and nerve-agent precursors. Among the works reporting on the use of CNT sensors in this field is Li et al.'s [3] which reported on the detection of 262 ppb for 3-nitrotolune using SWNTs drop cast onto interdigitated electrodes.

CNTs have been used as electrochemical platforms for microbiological, toxins and pesticides detection as well as for explosives [217]. Two common organophosphorus insecticides used in agriculture are methyl parathion and chlorpyrifos. Self-assembled monolayers of the SWCNT wrapped by thiol-terminated single-strand oligonucleotide on gold were used to fabricate a nanosize polyaniline matrix for acetylcholinesterase enzyme immobilisation. The acetylcholine enzymatic reaction results in changes in pH near the electrode surface to permit detection [218]. The dynamic range for the determination of methyl parathion and chlorpyrifos was found to be between 1.0×10^{-11} and 1.0×10^{-6} M, whereas the detection limit for both was 1×10^{-12} M. In general CNT-based sensors are found to be more efficient compared to liquid or gas chromatography, and they are fast, more responsive and low cost. At the same time they have superior electrical, mechanical, chemical and structural properties over conventional materials [219].

CNT sensing has also been applied to in situ detection of impact damage in composite materials used in aeronautical, space and automotive applications. Proper et al. [220] showed that by infiltrating an MWCNT network into the composite structure, it was possible to detect, in real time, impact-induced internal damage by monitoring localised changes in the conductivity. The regions observed had a spatial size of approximately 0.5 in. Rausch and Mader [221] used a similar approach to monitor the health of glass fibre-reinforced thermoplastics. Percolated CNTs were incorporated into the composite structure. Pre-dispersed CNTs were added to an aqueous film former and deposited onto the glass fibre. The main factors influencing the change in resistance under loading were the CNT weight fraction of the film former and the solid content of the film former/CNT system on the glass fibre. Similarly, Saafi [222] has used CNT networks to monitor the health of concrete structures. SWNTs were mixed with concrete and integrated with an off-the-shelf wireless system. Changes in resistance under varying loads were then monitored as the test system was deflected. The device was sensitive and highly reproducible and with low hysteresis. Crack initiation was manifested by a sudden increase in the effective resistance. Tan et al. [223] have developed a corrosion sensor for structural health monitoring based on MWCNT and Nafion. The electrical impedance of the CNTs was used as the sensing parameter whilst immersed in buffer and saline solutions. When corrosion occurs on the metal surface, the corrosive ions penetrate into the surface of the CNTs and change the electrical resistance.

6.3 Health-care Monitoring

Health-care monitoring includes the following: (1) environmental monitoring around a patient, such as gas, radiation and atmospheric pressure; (2) patient monitoring, such as pulse rate, sugar level, breathing, blood flow, temperature and so on; and (3) patient pose monitoring, such as duration of a pose and the condition of devices that hold the patient pose. Sensors for health-care monitoring are required to be real time, long lasting, accurate, easily operated and low cost. CNT-based sensors are small, sensitive and power efficient. All of these properties make CNT suitable for implant applications and specifically for health-care monitoring.

Temperature is an important factor for health-care monitoring. Patel developed a type of surgical suture that is integrated with temperature sensors for measuring temperature at a wound [224]. If an infection occurs, temperature at the wound will increase; therefore, infection condition can be effectively monitored by temperature monitoring. Dorozhkin et al. developed an MWCNT-based temperature sensor using a single nanotube [225]. The resistance of a single MWCNT that is filled with liquid form of Gallium (Ga) decreases linearly when the temperature is increased. As a result, MWCNTs can be used as a temperature sensor for infection monitoring.

Lab-on-a-chip can be used as a fast, compact and portable blood analysis device for on-site blood condition monitoring. Shahini et al. reported the use of MWCNT for electrical cell lysis application can decrease voltage requirement by 50% [226]. The voltage reduction is due to the concentration of electric field at the tip of CNTs.

Measurement of blood glucose level is an important factor indicating human health condition. Real-time insulin dosage adjustment enabled by continuous glucose level measurements will greatly benefit diabetics [227]. CNT can be utilised as sensing electrodes of glucose sensors to increase sensitivity and shorten response time. The sensing principles related to CNT-based glucose sensing have been reviewed comprehensively by Zhu et al. [227].

X-ray devices have been widely applied in medical applications. Accurate assurance of radiation environment is an important safety issue for patients and x-radiation system operators. CNTs have shown to respond to irradiation. Kang et al. [228] studied the resistance response of semiconducting SWCNT network to X-ray radiation.

Fluctuation of pH value in human body might be useful for indicating health status. Lei et al. [229] filtered MWCNT-suspended solution by vacuum filtration through metal electrodes deposited filtering paper. After a drying process, the paper-type pH sensor based on CNTs was fabricated. The resistance of the sensor was found to decrease when the pH value of the measurand increases. Rastogi et al. [230] studied the interaction between CNTs and DNA. The binding of DNA to CNT presents high fluorescent intensity and also induces conductance change due to the change of charge carrier concentration. This property indicates the ability of

CNTs for DNA detection, which can be useful for early detection of DNA-related health problems. More importantly, it is believed that not only DNA but also any biomolecules are expected to induce a change in electrical property after interacting with CNTs. Thus CNTs are extremely suitable for biosensor applications.

Besides the usage of CNTs in the aforementioned applications, CNTs can also be used for blood pressure sensing and flow sensing [43]. Even though CNTs are well suitable for biosensing applications, the toxicity of CNTs should be taken into account before applying CNTs to real-world applications. According to the review study of Smart et al. [231], the toxicity of unrefined CNTs is contributed by the catalytic transition metal components, while pure CNTs present little cytotoxicity. Therefore, the CNT fabrication process and purification procedure should ensure that any CNT toxicity is eliminated to safeguard public safety.

7 Future Trends in CNT Gas Sensors

CNT sensors are being developed for a wide range of applications, and common to all such successful developments will be improvements in stability, response time detection limits, selectivity and sensitivity. The application areas cover agriculture, food production, health, safety, manufacturing, automotive, construction security, etc. In a decade of research and development in CNT-based sensors, the advantages over conventional technologies have been demonstrated in terms of low cost, stability, reproducibility, high sensitivity and multi-detection arrays. Further work is required to understand the response mechanisms and further improve performance. CNTs have large surface-to-volume ratios and unique electrical properties. To increase the response of CNTs in detection, researchers continually develop methods for functionalising the CNT surface with conducting polymers and nanoparticles. Developments will proceed in a number of targeted areas, and the following are some immediate examples.

Musameh et al. [219] have reviewed extensively the application of CNT sensors and biosensors in the detection of organophosphate pesticides. They conclude that the stability of the CNT-modified surfaces in harsh environments, such as sewage water, strongly affects the reproducibility and lifetime of the sensor. Further work is required to develop more robust forms of CNT and composite materials that can withstand such environments. In addition, the selectivity can be increased by incorporating specific biorecognition elements such as antibodies. The use of new forms of enzymes with greater affinity for organophosphides will further increase sensitivities and detection limits.

A very promising development is the mimicking of the canine nose reported by Park et al. [211]. Here an olfactory-nanovesicle-fused carbon nanotube-transistor biosensor has been successfully demonstrated in the detection of the oxidation of food through hexanol sensing down to the 1 f. concentration level. Hexanol is also a specific marker in lung cancer. A natural extension of this breakthrough is to fabricate an array of sensors decorated with diverse olfactory receptors on a single chip. In this way a bioelectronic nose function can be replicated. Appropriate numerical methods to analyse sensor array data and high-throughput nanomanufacturing techniques for mass production of devices will become increasingly important [6].

One of the largest potentials for CNT-based sensor technology is the area of low-power, portable sensors. CNTs can readily be integrated into solid-state microscale electronic sensor technologies, and arrays can be easily fabricated [8]. The development of sensor arrays will enable simultaneous screening of multiple analytes. Room temperature operation will also simplify the architecture by removing the requirement for internal heating and control elements. It will also be necessary to develop not only low-power sensors but also the capability of wireless communication. This approach has been taken by Dowling and Tentzeris [232] using CNT wireless gas and pressure sensors. The sensors were inkjet-printed to form a passive RFID system. The printed SWCNT film functions as a tuneable resistor with a value dependent upon the gas concentration, and the RFID reader monitors the backscattered power level. As the gas concentration changes, the load resistance alters and is manifested in a power level change. This approach offers ultrasensitive sensors for wide range of applications. Thai et al. [233] have used a CNT-based sensor to monitor the sensed gas concentration directly in the form of a transmitted wireless signal. The sensing element, or transducer, produces a change in resistance in response to the gas dosage, and this change is converted into a voltage via an operational amplifier signal conditioner connected to a microcontroller. The signal is then sent to an integrated wireless module that uses an antenna to communicate with a remote station.

8 Conclusions

Recent research and development of CNT-based gas sensors was reviewed at the current state of the art. CNTs exhibit a large surface area and outstanding structural, electrical, optical, thermal and mechanical properties, which make them some of the most exciting nanomaterials as promising candidates for the next generation of chemical sensors. To overcome some of the limitations of the pristine CNTs, great efforts have been directed towards functionalisation and surface modifications of CNTs by different methods and technologies and with a wide range of functionalising materials such as polymers, metals, metal oxides, DNA, proteins, enzymes, antibodies and so on.

Generally, modified CNTs offer an enhanced performance in chemical detection related to raw material. The large variety of functionalisation methods and technologies combined to a wide choice of functional materials make the modified CNTs one of the most performing building blocks for gas micro-nanosensors and sensor arrays. However, challenges for the fabrication of reliable commercial devices are still numerous and open. They include the fundamental understanding of the sensing mechanisms and its employment for engineered sensing nanomaterials, including the development of specific, fast and stable gas nanosensors and sensor arrays, the optimisation of numerical methods of signal processing to analyse sensor array output for pattern recognition applications and the development of suitable manufacturing techniques enabling mass production of CNT-based sensors.

At the present, significant progress has been realised in these sectors, but commercial devices based on CNTs will become successful when these mentioned challenges become routine and innovation with adequate technology transfer has occurred. Decreased manufacturing costs together with the incorporation of available wireless technology in the sensor systems may allow the implementation of wireless sensor networks for accurate chemical mapping of structures or large areas with low-cost single node/sensor.

Furthermore, the current study of the CNT-based gas sensors should move from the fundamental gas-sensing performance in laboratories towards real-world applications in actual working scenario. In particular, CNT-based sensors have been demonstrated as proof of concepts in the field of environmental monitoring, especially air quality control, industrial process control and health-care monitoring.

In addition, CNTs are very important platforms for biosensing applications. Numerous reports fix remarkably these technical questions showing high capability of the carbon-nanostructured materials. In any case, despite the great opportunities in integrating biomolecules with CNTs, these carbon-based nanomaterials are not the answer for all applications in bio-nanotechnology. The biosensing potential of these materials is enormous in medicine and biology, but there are examples in literature that the application of the CNTs gives no advantages compared to other technologies.

Finally, the future of CNT-based gas sensors looks very bright in combination to the various transducers used, but continued progress needs to overcome the current challenges, move towards the development of reliable commercial devices and lead to a class of sensor nanomaterials with superior sensitivity, reduced sizes, low cost, stable response, selectivity and extended lifetimes for a wide range of environments and applications.

Acknowledgements The authors are indebted to EU COST Office—*Cooperation in Science and Technology*—by networking of the COST Action TD1105 *EuNetAir*, *European Network on New Sensing Technologies for Air-Pollution Control and Environmental Sustainability*, under Memorandum of Understanding (MoU oc-2011-1-9706) signed by 25 COST countries (EU-zone) and 5 non-COST countries (extra-EU including Australia, Canada, China, Russia, the USA) on December 2012, including over 75 research teams from academia, research institutes, agencies and industry.

References

1. Kong J, Franklin NR, Zhou C, Chapline MG, Peng S, Cho K, Dai H (2000) Nanotube molecular wires as chemical sensors. Science 287:622–625

2. Collins PG, Bradley K, Ishigami M, Zettl A (2000) Extreme oxygen sensitivity of electronic properties of carbon nanotubes. Science 287:1801–1804
3. Li J, Lu Y, Qi Y, Cinke M, Han J, Meyyappan M (2003) Carbon nanotube sensors for gas and organic vapor detection. Nano Lett 3:929–933
4. Cao Q, Rogers JA (2009) Ultrathin films of single-walled carbon nanotubes for electronics and sensors: a review of fundamental and applied aspects. Adv Mater 21:29–53
5. Yang W, Thordarson P, Gooding JJ, Ringer SP, Braet F (2007) Carbon nanotubes for biological and biomedical applications. Nanotechnology 18:412001
6. Zhang T, Mubeen S, Myung NV, Deshusses MA (2008) Recent progress in carbon nanotube-based gas sensors. Nanotechnology 19:332001
7. Penza M, Cassano G, Rossi R, Rizzo A, Signore MA, Alvisi M, Lisi N, Serra E, Giorgi R (2007) Effect of growth catalysts on gas sensitivity in carbon nanotube film based chemiresistive sensors. Appl Phys Lett 90:103101
8. Kauffman DR, Star A (2008) Carbon nanotube gas and vapour sensors. Angew Chem Int Ed 47:6550–6570
9. Collins PG, Avouris P (2000) Nanotubes for electronics. Sci Am 2000:62–69
10. Mahar B, Laslau C, Yip R, Sun Y (2007) Development of carbon nanotube-based sensors. A review. IEEE Sensors J 7:266–284
11. Valentini L, Cantalini C, Armentano I, Kenny JM, Lozzi L, Santucci S (2004) Highly sensitive and selective sensors based on carbon nanotubes thin films for molecular detection. Diam Relat Mater 13(4–8):1301–1305
12. Dericke V, Auvray S, Borghetti J, Chung C-L, Lefevre R, Lopez-Bezanilla A, Nguyen K, Robert G, Schmidt G, Anghel C, Chimot N, Lyonnais S, Streiff S, Campidelli S, Chenevier P, Filoramo A, Goffman MF, Goux-Capes L, Latil S, Blase X, Triozon F, Roche S, Burgoin J-P (2009) Carbon nanotube chemistry and assembly for electronic devices. Comptes Rendus Phys 10:330–347
13. Dresselhaus MS, Dresselhaus G, Avouris PH (2001) In: Carbon nanotubes - synthesis, structure properties and applications. Topics Applied Physics, vol 80. Springer-Verlag: Berlin
14. Someya T, Small J, Kim P, Nuckolls C, Yardley JT (2003) Alcohol vapour sensors based on single-walled carbon nanotube field effect transistors. Nano Lett 3:877–881
15. Martel R, Schmidt T, Shea HR, Hertel T, Avouris P (1998) Single and multi-wall carbon nanotube field-effect transistors. Appl Phys Lett 73:2447–2449
16. Tans S, Verschueren S, Dekker C (1998) Room-temperature transistor based on single carbon nanotube. Nature 393:49–52
17. Avouris P (2002) Molecular electronics with carbon nanotubes. Acc Chem Res 35:1026–1034
18. Schnorr JM, Swager TM (2011) Emerging applications of carbon nanotubes. Chem Mater 23:646–657
19. Iijima S (1991) Helical microtubules of graphitic carbon. Nature 354:56–58
20. Iijima S, Ichihashi T (1993) Single-shell carbon nanotubes of 1 nm diameter. Nature 363:603–605
21. Penza M, Rossi R, Alvisi M, Cassano G, Signore MA, Serra E, Giorgi R (2008) Surface modification of carbon nanotube networked films with Au nanoclusters for enhanced NO_2 gas sensing applications. J Sensors 2008:107057
22. Dai H (2002) Carbon nanotubes: synthesis, integration, and properties. Acc Chem Res 35:1035–1044
23. Penza M, Rossi R, Alvisi M, Serra E (2010) Metal-modified and vertically-aligned carbon nanotube sensors array for landfill gas monitoring applications. Nanotechnology 21:105501
24. Penza M, Cassano G, Aversa P, Cusano A, Cutolo A, Giordano M, Nicolais L (2005) Carbon nanotubes acoustic and optical sensors for volatile organic compound detection. Nanotechnology 16:2536–2547

25. Li J, Lu Y, Meyyappan M (2006) Nano chemical sensors with polymer-coated carbon nanotubes. IEEE Sensors J 6:1047–1051
26. Lu Y, Partridge C, Meyyappan M, Li J (2006) A carbon nanotube sensor array for sensitive gas discrimination using principal component analysis. J Electroanal Chem 593:105–110
27. Park Y, Dong K-Y, Lee J, Choi J, Bae G-N, Ju B-K (2009) Development of an ozone gas sensor using single-walled carbon nanotubes. Sensors Actuators B 140:407–411
28. Penza M, Cassano G, Rossi R, Alvisi M, Rizzo A, Signore MA, Dikonimos T, Serra E, Giorgi R (2007) Enhancement of sensitivity in gas chemiresistors based on carbon nanotube surface functionalized with noble metal (Au, Pt) nanoclusters. Appl Phys Lett 90:173123
29. Penza M, Rossi R, Alvisi M, Cassano G, Signore MA, Serra E, Giorgi R (2008) Pt- and Pd-nanoclusters functionalized carbon nanotubes networked films for sub-ppm gas sensors. Sensors Actuators B 135:289–297
30. Penza M, Rossi R, Alvisi M, Cassano G, Serra E (2009) Functional characterization of carbon nanotube networked films functionalized with tuned loading of Au nanoclusters for gas sensing applications. Sensors Actuators B 140:176–184
31. Penza M, Tagliente MA, Aversa P, Re M, Cassano G (2007) The effect of purification of single-walled carbon nanotube bundles on the alcohol sensitivity of nanocomposite Langmuir-Blodgett films for SAW sensing applications. Nanotechnology 18:185502
32. Novak JP, Snow ES, Houser EJ, Park D, Stepnowski JL, McGill MA (2003) Nerve agent detection using networks of single-walled carbon nanotubes. Appl Phys Lett 83:4026–4028
33. Penza M, Rossi R, Alvisi M, Signore MA, Cassano G, Dimaio D, Pentassuglia R, Piscopiello E, Serra E, Falconieri M (2009) Characterization of metal-modified and vertically-aligned carbon nanotube films for functionally enhanced gas sensor applications. Thin Solid Films 517:6211–6216
34. Leghrib R, Felten A, Demoisson F, Reniers F, Pireaux J-J, Llobet E (2010) Room-temperature, selective detection of benzene at trace levels using plasma-treated metal-decorated multiwalled carbon nanotubes. Carbon 48:3477–3484
35. Star A, Joshi V, Skarupo S, Thomas D, Gabriel JCP (2006) Gas sensor array based on metal-decorated carbon nanotubes. J Phys Chem B 110:21014–21020
36. Zhao Q, Nardelli MB, Lu W, Bernhoc J (2005) Carbon nanotubes-metal cluster composites: a new road to chemical sensors. Nano Lett 5:847–851
37. Kumar MK, Ramaprabhu S (2006) Nanostructured Pt functionalized multiwall carbon nanotubes based hydrogen sensor. J Phys Chem B 110:11291–11298
38. Guo M, Pan M, Chen J, Mi Y, Zhang X, Chen Y (2006) Palladium modified multi-walled carbon nanotubes for benzene detection at room temperature. Chin J Anal Chem 34:1755–1758
39. Singh V, Joung D, Zhai L, Das S, Khondaker SI, Seal S (2011) Graphene based materials: past, present and future. Prog Mater Sci 56:1178–1271
40. Bandaru PR (2007) Electrical properties and applications of carbon nanotube structures. J Nanosci Nanotechnol 7:1–29
41. Harris PJF (2009) Carbon nanotube science, synthesis, properties and applications. Cambridge University Press, Cambridge
42. Saito R, Dresselhaus S, Dresselhaus MS (2003) Physical properties of carbon nanotubes. World Scientific, London
43. Sinha N, Ma J, Yeow JTW (2006) Carbon nanotube-based sensors. J Nanosci Nanotechnol 6: 573–590
44. Shokrieh MM, Rafiee R (2010) A review of the mechanical properties of isolated carbon nanotubes and carbon nanotube composites. Mech Compos Mater 46:155–172
45. Min-Feng Y, Lourie O, Moloni K et al (2000) Strength and breaking mechanism of multiwalled carbon nanotubes under tensile load. Science 287:637–640
46. Min-Feng Y, Files BS, Arepalli S et al (2000) Tensile loading of ropes of single wall carbon nanotubes and their mechanical properties. Phys Rev Lett 84:5552–5555

47. Wang M-S, Golberg D, Bando Y (2010) Tensile tests on individual single-walled carbon nanotubes- linking nanotube strength with its defects. Adv Mater 22:4071–4075
48. Berber S, Kwon Y-K, Tománek D (2000) Unusually high thermal conductivity of carbon nanotubes. Phys Rev Lett 84:4613–4616
49. Kim P, Shi L, Majumdar A, McEuen PL (2001) Thermal transport measurements of individual multiwalled nanotubes. Phys Rev Lett 87:215502
50. Fujii M, Zhang X, Xie H (2005) Measuring the thermal conductivity of a single carbon nanotube. Phys Rev Lett 95:065502
51. Jorio A, Souza Filho AG, Dresselhaus G (2002) G-band resonant raman study of 62 isolated single-wall carbon nanotubes. Phys Rev 65:155412
52. Yacaman JM, Miki-Yoshida M, Rendon L, Santiesteban JG (1993) Catalytic growth of carbon microtubules with fullerene structure. Appl Phys Lett 62:201–204
53. Journet C, Bernier P (1998) Production of carbon nanotubes. Appl Phys A 67:1–9
54. Meyyappan M, Delzeit L, Cassell A, Hash D (2003) Carbon nanotube growth by PECVD: a review. Plasma Sources Sci Technol 12(2):205
55. Meyyappan M (2005) Carbon nanotubes science and applications. CRC, Boca Raton
56. Meyyappan M (2009) Catalyzed chemical vapour deposition of one-dimensional nanostructures and their applications. Prog Cryst Growth Charact Mater 55(1–2):1–21
57. Popov VN (2004) Carbon nanotubes: properties and application. Mat Sci Eng R Reports 43 (3):61–102
58. Krtschmer W, Lamb LD, Fostiropoulos K, Huffman DR (1990) Slid C_{60}: a new form of carbon. Nature 347:354–358
59. Baddour CE, Briens C (2005) Carbon nanotube synthesis: A review. Int J Chem Rect Eng 3:1–20
60. Kumar M, Ando Y (2010) Chemical vapour deposition of carbon nanotubes: a review of growth mechanism and mass production. J Nanosci Nanotech 10:3739–3758
61. Broza G (2010) Synthesis, properties, functionalisation and applications of carbon nanotubes: a state of the art review. Chem Chem Technol 4(1):35–45
62. Tessonnier JP, Su DS (2011) Recent progress on the growth mechanism of carbon nanotubes: a review. ChemSusChem 4(7):824–847
63. Bethune DS (1993) Cobalt-catalysed growth of carbon nanotubes with single atomic layer walls. Nature 363:605–607
64. Dai H, Rinzler AG, Nikolaev P, Thess A, Colbert DT, Smalley RE (1996) Single-wall nanotubes produced by metal-catalyzed disproportionation of carbon monoxide. Chem Phys Lett 260:471–475
65. Liu Y, Gao L, Sun J, Zhaeng S, Jiang L, Wang Y, Hishahi K, Li Y, Noda K (2007) A multistep strategy for cutting and purification of single-walled carbon nanotubes. Carbon 45 (10):1972–1978
66. Zhang M, Atkinson KR, Baughman RH (2004) Multifunctional carbon nanotube yarns by downsizing and ancient technology. Science 306:1358
67. Kong J, Soh HT, Cassell AM, Quate CF, Dai H (1998) Synthesis of individual single-walled nanotubes. Phys Rev B 58:14013–14019
68. Jiang K, Li Q, Fan S (2002) Spinning continuous carbon nanotube yarns. Nature 419:801
69. Li P, Jiang K, Liu M, Li Q, Fan S (2003) Polarized incandescent light emission from carbon nanotubes. Appl Phys Lett 82:1763–1765
70. Li Q, Zhang X, DePaula RF, Zheng L, Zhao Y, Stan L, Holesinger TG, Arendt PN, Peterson DE, Zhu YT (2006) Sustained growth of ultralong carbon nanotube arrays for fiber spinning. Adv Mater 18:3160–3163
71. Li QW, Li Y, Zhang XF, Chikkannanavar SB, Zhao YH, Dangelewicz AM, Zheng LX, Doorn SK, Jia QX, Peterson DE, Arendt PN, Zhu YT (2007) Structure-dependent electrical properties of carbon nanotube fibers. Adv Mater 19:3358–3363

72. Zhang X, Jiang K, Feng C, Liu P, Zhang L, Kong J, Zhang T, Li Q, FanS (2006) Spinning and processing continuous yarns from 4-inch wafer scale super-aligned carbon nanotube arrays. Adv Mater 18:1505–1517
73. Randeniya LK, Bendavid A, Martin PJ, Tran C (2010) Composite yarns of multiwalled carbon nanotubes with metallic electrical conductivity. Small 6(16):1806–1811
74. Li Y, Kinloch I.A. Windle A.H (2004), Direct spinning of carbon nanotube fibers from chemical vapour synthesis. Science 304: 276–278
75. Li Y, Zhong XH, Windle AH (2008) Structural changes of carbon nanotubes in their macroscopic films and fibers by electric sparking processing. Carbon 46:1751–1756
76. Zhang X, Li Q, Tu Y, Li Y, Coulter JY, Zheng L, Zhao Y, Jia Q, Peterson DE, Zhu Y (2007) Strong carbon-nanotube fibers spun from long carbon-nanotube arrays. Small 3(2):244–248
77. Zhang Y, Zou G, Doorn S, Htoon H, Stan L, Hawley ME, Sheehan CJ, Zhu Y, Jia Q (2009) Tailoring the morphology of carbon nanotube arrays: From spinnable forests to undulating foams. Nano 3:2157–2162
78. Huynh CP, Hawkins SC (2010) Understanding the synthesis of directly spinnable carbon nanotube forests. Carbon 48:1105–1115
79. Guzman de Villoria R, Figueredo SL, Hart AJ, Steiner SA III, Slocum AH, Wardle BL (2009) High-yield growth of vertically aligned carbon nanotubes on a continuously moving substrate. Nanotechnology 20:405611–405619
80. Yun Wang and John. T. W. Yeow (2009) A review of carbon nanotubes-based gas sensors. Journal of Sensors 2009.
81. Hoa ND, Van Quy N, Cho Y (2009) Porous single-wall carbon nanotube films formed by in Situ arc-discharge deposition for gas sensors application. Sensors Actuators B Chem 135:656–663
82. Li W, Hoa ND, Kim D (2010) High-performance carbon nanotube hydrogen sensor. Sensors Actuators B Chem 149:184–188
83. Wang Y, Yang Z, Hou Z et al (2010) Flexible gas sensors with assembled carbon nanotube thin films for DMMP vapor detection. Sensors Actuators B Chem 150:708–714
84. Horrilloa MC, Martía J, Matataguia D et al (2011) Single-walled carbon nanotube microsensors for nerve agent simulant detection. Sensors Actuators B Chem 157:253–259
85. Ueda T, Katsuki S, Takahashi K et al. (2008) Fabrication and characterization of carbon nanotube based high sensitive gas sensors operable at room temperature. Diam Relat Mater 17:1586–1589
86. Penza M (2012) Carbon nanotubes for gas sensing applications: principles and transducers. In: Terranova ML, Rossi M, Orlanducci S (eds) Carbon nanomaterials for gas adsorption. Pan Stanford Publishing, Singapore
87. Chen P-C, Ishikawa FN, Chang H-K et al (2009) A nanoelectronic nose- a hybrid nanowire/carbon nanotube sensor array with integrated micromachined hotplates for sensitive gas discrimination. Nanotechnology 20: 125503
88. Wang L-C, Tang II K-T, Teng I-J et al (2011) A single-walled carbon nanotube sensing device. Sensors 11:7763–7772
89. Tian W-C, Lu H-L, Kuo C-Y et al (2011) A carbon nanotube gas sensor using CMOS-based platform. In: IEEE conference on sensors 2011, Limerick, Ireland, pp 1036–1039
90. Bondavalli P, Legagneux P, Pribat D (2009) Carbon nanotubes based transistors as gas sensors – state of the art and critical review. Sensors Actuators B Chem 140:304–318
91. Zhao J, Buldum A, Han J et al (2002) Gas molecule adsorption in carbon nanotubes and nanotube bundles. Nanotechnology 13:195–200
92. Wang Y, Yeow JTW (2009) A review of carbon nanotubes-based gas sensors. J Sensors 2009:493904–493928
93. Zhao Z, Hui G, Pan M, Chen YA (2009) Novel method for gas classification by means of an array of carbon nanotubes gas sensors. In: 3rd International conference on bioinformatics and, biomedical engineering 2009, Beijing, China

94. Trojanowicz M (2006) Analytical applications of carbon nanotubes: a review. TrAC Trends Anal Chem 25(5):480–489
95. Chen X, Guo Z, Huang J, Meng F, Zhang M, Liu J (2008) Fabrication of gas ionization sensors using well-aligned MWCNT arrays grown in porous AAO templates. Coll Surf A 313:355–358
96. Chen X, Wang Y, Wang Y, Hou Z, Xu D, Yang Z, Zhang Y (2010) A breath sensor using carbon nanotubes operated by field effects of polarization and ionization. Sensors Actuators A 158:328–334
97. Slobodian P, Riha P, Lengalova A, Svoboda P, Saha P (2011) Multi-wall carbon nanotube networks as potential resistive gas sensors for organic vapor detection. Carbon 49(7):2499–2507
98. Shukla P, Bhatia V, Gaur V, Jain VK (2011) Electrostatically functionalized multiwalled carbon nanotube/PMMA composite thin films for organic vapor detection. Polym Plastics Technol Eng 50(11):1179–1184
99. Yoo KP, Lim LT, Min NK, Lee MJ, Lee CJ, Park CW (2010) Novel resistive-type humidity sensor based on multiwall carbon nanotube/polyimide composite films. Sensors Actuators B 145(1):120–125
100. Cava CE, Salvatierra RV, Alves DCB, Ferlauto AS, Zarbin AJG, Roman LS (2012) Self-assembled films of multi-wall carbon nanotubes used in gas sensors to increase the sensitivity limit for oxygen detection. Carbon 50(5):1953–1958
101. Sadeghian RB, Kahrizi M (2007) A novel miniature gas ionization sensor based on free-standing gold nanowires. Sensors Actuators A 137:248–255
102. Kermany AR, Mohamed NM, Singh BSM (2010) Ionization based gas sensor using aligned MWCNTs array. In: IEEE Proceedings of the international conference on semiconductor electronics (ICSE), Melaka, Malaysia doi:10.1109/smelec.2010.5549361
103. Kermany AR, Mohamed NM, Singh BSM (2011) Characterization of aligned MWCNTs array as the sensing element for ionization gas sensor. J Appl Sci 11(7):1243–1248
104. Lin J, Liu J (2010) A two-component gas analyzer based on self-sustaining dark discharge carbon nanotube film cathode gas sensor. Adv Mater Res 121:181–191
105. Riley DJ, Mann M, Maclaren DA, Dastoor PC, Allison W, Teo KBK, Amaratunga AJ, Milne W (2003) Helium detection via field ionization from carbon nanotubes. Nano Lett 3(10):1455–1458
106. Modi A, Koratkar N, Lass E, Wei B, Ajayan PM (2003) Miniaturized gas ionization sensors using carbon nanotubes. Nature 424:171–174
107. Zhang Y, Liu J, Li X, Tang X, Zhu C (2005) Study of improving identification accuracy of carbon nanotube film cathode gas sensor. Sensors Actuators A 125:15–24
108. Kim S (2005) Detection of inert gases by cold electron emission from carbon nanotube emitters. Modern Phys Lett 19(24):1207–1211
109. Kim S (2006) CNT sensors for detecting gases with low adsorption energy by ionization. Sensors 6:503–513
110. Zikai S, Guohua H, Min P, Yuquau C (2009) A novel method for gas classification by means of an array of carbon nanotubes gas sensors. In: 3rd International conference on bioinformatics and biomedical engineering (ICBBE) 2009, IEEE Press, Beijing, China, pp 1–4
111. Meng F, Li M, Chen Y, Jia Y, Liu J, Huang J, Liu J (2009) Dynamic prebreakdown current measurement of nanotips-based gas ionization sensor application at ambient atmosphere. IEEE Sensors J 9(40):435–440
112. Huang J, Wang J, Gu C, Yu K, Meng F, Liu J (2009) A novel highly sensitive gas ionization sensor for ammonia detection. Sensors Actuators A 150:218–223
113. Baghgar M, Abdi Y, Arzi E (2009) Fabrication of low-pressure field ionization gas sensor using bent carbon nanotubes. J Phys D 42:135502–135507
114. Nikfarjam A, Zad AI, Razi F, Mortazavi SZ (2010) Fabrication of gas ionization sensor using carbon nanotube arrays grown on porous silicon substrate. Sensors Actuators A 162:24–28

115. Darbari S, Abdi Y, Mohajerzadeh S (2010) A novel carbon gas sensor based on field ionization from branched nanostructures. Eur Phys J Appl Phys 52:30602–30607
116. Mahmood S, Burhanudin ZA, Hamid NH (2011) Effects of CNT density variation in field emission model of ionization gas sensor. In: IEEE regional symposium on micro and nanoelectronics (RSM), Kuala Lumpur, pp 266–269
117. Randeniya LK, Martin PJ, Bendavid A (2011) Ammonia sensing characteristics of carbon-nanotube yarns decorated with nanocrystalline gold. Carbon 49(15):5265–5270
118. Zanolli Z, Leghrib R, Felton A, Pireaux JJ, lLobet E, Charlier JC (2011) Gas sensing with Au-decorated carbon nanotubes. ACS Nano 5(6):4592–4599
119. Randeniya LK, Martin PJ, Bendavid A (2012) Detection of hydrogen using multi-walled carbon-nanotube yarns coated with nanocrystalline Pd and Pd/Pt layered structures. Carbon 50(5):1786–1792
120. Star A, Han T-R, Joshi V, Gabriel J-CP, Gruner G (2004) Nanoelectronic carbon dioxide sensors. Adv Mater 16:2049–2052
121. An KH, Jeong SY, Hwang HR, Lee YH (2004) Enhanced sensitivity of a gas sensor incorporating single-walled carbon nanotube-polypyrrole nanocomposites. Adv Mater 16:1005–1009
122. Philip B, Abraham JK, Chandrasekhar A (2003) Carbon nanotube/PMMA composite thin films for gas-sensing applications. Smart Mater Struct 12:935–939
123. Wei C, Dai L, Roy A, Tolle TB (2006) Multifunctional chemical vapor sensors of aligned carbon nanotube and polymer composites. J Am Chem Soc 128:1412–1413
124. Kim S, Lee HR, Yun YJ, Ji S, Yoo K, Yun W-S, Koo J-Y, Ha D-H (2007) Effects of polymer coating on the adsorption on gas molecules on carbon nanotube networks. Appl Phys Lett 91:093126
125. Chen H-W, Wu R-J, Chan K-H, Sun Y-L, Su P-G (2005) The application of CNT/Nafion composite material to low humidity sensing measurement. Sensors Actuators B 104:80–84
126. Abraham JK, Philip B, Witchurch A, Varadan VK, Reddy CC (2004) A compact wireless gas sensor using a carbon nanotube/PMMA thin film chemiresistor. Smart Mater Struct 13:1045–1049
127. Besteman K, Lee J-O, Wiertz FGM, Heering HA, Dekker C (2003) Enzyme-coated carbon nanotubes as single-molecule biosensors. Nano Lett 3:727–730
128. Wang J, Liu G, Lin Y (2006) Amperometric choline biosensor fabricated through electrostatic assembly of bienzyme/polyelectrolyte hybrid layers on carbon nanotubes. Analyst 131:477–483
129. Yang W, Thordarson P, Gooding JJ, Ringer SP, Braet F (2007) Carbon nanotubes for biological and biomedical applications. Nanotechnology 18:412001
130. Chen RJ, Zhang Y, Wang D, Dai H (2001) Noncovalent Sidewall Functionalization of Single-Walled Carbon Nanotubes for Protein Immobilization. J Am Chem Soc 123:3838–3839
131. Shim M, Kam NWS, Chen RJ, Li Y, Dai H (2002) Functionalization of carbon nanotubes for biocompatibility and biomolecular recognition. Nano Lett 2:285–288
132. Contarino MR, Sergi M, Harrington AE, Lazareck A, Xu J, Chaiken I (2006) Modular, self-assembling peptide linkers for stable and regenerable carbon nanotube biosensor interfaces. J Mol Recognit 19:363–371
133. Zhong J, Song L, Meng J, Gao B, Chu W, Xu H, Luo Y, Guo J, Marcelli A, Xie S, Wu Z (2009) Bio-nano interaction of proteins adsorbed on single-walled carbon nanotubes. Carbon 47:967–973
134. Wang J, Liu G, Jan MR (2004) Ultrasensitive electrical biosensing of proteins and DNA: carbon-nanotube derived amplification of the recognition and transduction events. J Am Chem Soc 126:3010–3011
135. Maehashi K, Katsura T, Kerman K, Takamura Y, Matsumoto K, Tamiya E (2007) Label-free protein biosensor based on aptamer-modified carbon nanotube field-effect transistors. Anal Chem 79:782–787

136. Erlanger BF, Chen B-X, Zhu M, Brus L (2001) Binding of an anti-fullerene IgG monoclonal antibody to single wall carbon nanotubes. Nano Lett 1:465–467
137. Dwyer C, Guthold M, Falvo M, Washburn S, Superfine R, Erie D (2002) DNA-functionalized single-walled carbon nanotubes. Nanotechnology 13:601–604
138. Keren K, Berman RS, Buchstab E, Sivan U, Braun E (2003) DNA-templated CNFET. Science 302:1380–1382
139. Staii C, Johnson AT Jr, Chen M, Gelperin A (2005) DNA-decorated carbon nanotubes for chemical sensing. Nano Lett 5:1774–1778
140. Gong J, Sun J, Chen Q (2008) Micromachined sol–gel carbon nanotube/SnO_2 nanocomposite hydrogen sensor. Sensors Actuators B 130:829–835
141. Liu Y-L, Yang H-F, Yang Y, Liu Z-M, Shen G-L, Yu R-Q (2006) Gas sensing properties of tin dioxide coated onto multi-walled carbon nanotubes. Thin Solid Films 497:355–360
142. van Hieu N, Thuy LTB, Chien ND (2008) Highly sensitive thin film gas sensor operating at room temperature based on SnO_2/MWCNTs composite. Sensors Actuators B 129:888–895
143. Wang J, Liu L, Cong S-Y, Qi J-Q, Xu B-K (2008) An enrichment method to detect low concentration formaldehyde. Sensors Actuators B 134:1010–1015
144. Fu Q, Lu C, Liu J (2002) Selective coating of single wall carbon nanotubes with thin SiO_2 layer. Nano Lett 2:329–332
145. Du N, Zhang H, Chen B, Ma X, Liu Z, Wu J, Yang D (2007) Porous indium oxide nanotubes: layer-by-layer assembly on carbon-nanotube templates and application for room-temperature NH_3 gas sensors. Adv Mater 19:1641–1645
146. Liang YX, Chen YJ, Wang TH (2004) Low-resistance gas sensors fabricated from multiwalled carbon nanotubes coated with a thin tin oxide layer. Appl Phys Lett 85:666–668
147. Chen Y, Zhu C, Wang T (2006) The enhanced ethanol sensing properties of multi-walled carbon nanotubes/SnO_2 core/shell nanostructures. Nanotechnology 17:3012–3017
148. Lu G, Ocola LE, Chen J (2009) Room-temperature gas sensing based on electron transfer between discrete tin oxide nanocrystals and multiwalled carbon nanotubes. Adv Mater 21:2487–2491
149. Dai C-L, Chen Y-C, Wu C-C, Kuo C-F (2010) Cobalt oxide nanosheet and CNT micro carbon monoxide sensor integrated with readout circuit on chip. Sensors 10:1753–1764
150. Ueda T, Takahashi K, Mitsugi F, Ikegami T (2009) Preparation of single-walled carbon nanotube/TiO_2 hybrid atmospheric gas sensor operated at ambient temperature. Diam Relat Mater 18:493–496
151. An G, Na N, Zhang X, Miao Z, Miao S, Ding K, Liu Z (2007) SnO_2/carbon nanotube nanocomposites synthesized in supercritical fluids: highly efficient materials for use as a chemical sensor and as the anode of a lithium-ion battery. Nanotechnology 18:435707
152. Yang M, Kim D-H, Kim W-S, Kang TJ, Lee BY, Hong S, Kim YH, Hong S-H (2010) H_2 sensing characteristics of SnO_2 coated single wall carbon nanotube network sensors. Nanotechnology 21:215501
153. Penza M, Rossi R, Alvisi M, Signore MA, Serra E, Paolesse R, D'Amico A, Di Natale C (2010) Metalloporphyrins-modified carbon nanotubes networked films-based chemical sensors for enhanced gas sensitivity. Sensors Actuators B 144:387–394
154. Penza M, Rossi R, Alvisi M, Signore MA, Serra E (2009) Effects of reducing interferers in a binary gas mixture on NO_2 gas adsorption using carbon nanotube networked films based chemiresistors. J Phys D Appl Phys 42:72002
155. Kong J, Chapline MG, Dai H (2001) Functionalized carbon nanotubes for molecular hydrogen sensors. Adv Mater 13:1384–1386
156. Wong YM, Kang WP, Davidson JL, Wisitsora-at A, Soh KL (2003) A novel microelectronic gas sensor utilizing carbon nanotubes for hydrogen gas detection. Sensors Actuators B 93:327–332
157. Lu Y, Li J, Han J, Ng H-T, Binder C, Partridge C, Meyyappan M (2004) Room temperature methane detection using palladium loaded single-walled carbon nanotube sensors. Chem Phys Lett 391:344–348

158. Espinosa EH, Ionescu R, Bittencourt C, Felten A, Erni R, Van Tenderloo G, Pireaux J-J, Llobet E (2007) Metal-decorated multi-wall carbon nanotubes for low temperature gas sensing. Thin Solid Films 515:8322–8327
159. Wongwiriyapan W, Inoue S, Ito T, Shimazaki R, Maekawa T, Suzuki K, Ishikawa H, Honda S, Oura K, Katayama M (2008) Highly sensitive detection of carbon monoxide at room temperature using platinum-decorated single-walled carbon nanotubes. Appl Phys Express 1:014004
160. Li YH, Zhao YM, Zhu YQ, Rodriguez J, Morante JR, Mendoza E et al (2006) Mechanical and NH_3 sensing properties of long multiwalled carbon nanotube ropes. Carbon 44:1821–1825
161. Suehiro J, Hidaka S-I, Yamane S, Imasaka K (2007) Fabrication of interfaces between carbon nanotubes and catalytic palladium using dielectrophoresis and its application to hydrogen gas sensor. Sensors Actuators B 127:505–511
162. Xie J, Wang S, Aryasomayajula L, Varadan VK (2007) Platinum decorated carbon nanotubes for highly sensitive amperometric glucose sensing. Nanotechnology 18:065503
163. Li C, Su Y, Lv X, Xia H, Wang Y (2010) Electrochemical acetylene sensor based on Au/MWCNTs. Sensors Actuators B 149:427–431
164. Qi P, Vermesh O, Grecu M, Javey A, Wang Q, Dai H (2003) Towards large array of multiplex functionalized carbon nanotube sensors for highly sensitive and selective molecular detection. Nano Lett 3:347–351
165. Berti F, Lozzi L, Palchetti I, Santucci S, Marrazza G (2009) Aligned carbon nanotube thin film for DNA electrochemical sensing. Electrochim Acta 54:5035–5041
166. Li J, Ng HT, Cassell A, Fan W, Chen H, Ye Q, Koehne J, Han J, Meyyappan M (2003) Carbon nanotube nanoelectrode array for ultrasensitive DNA detection. Nano Lett 3:597–602
167. Daniel S, Rao TP, Rao KS, Rani SU, Naidu GRK, Lee H-Y, Kawai T (2007) A review of DNA functionalized/grafted carbon nanotubes and their characterization. Sensors Actuators B 122:672–682
168. Chen C-L, Yang C-F, Agarwal V, Kim T, Sonkusale S, Busnaina A, Chen M, Dokmeci MR (2010) DNA-decorated carbon-nanotube-based chemical sensors on complementary metal oxide semiconductor circuitry. Nanotechnology 21:095504
169. Valentini F, Palleschi G, Lopez Morales E, Orlanducci S, Tamburri E, Terranova ML (2007) Functionalized single-walled carbon nanotubes modified microsensors for the selective response of epinephrine in presence of ascorbic acid. Electroanalysis 19:859–869
170. Wong SS, Joselevich E, Woolley AT, Cheung CL, Lieber CM (1998) Covalently functionalized nanotubes as nanometre-sized probes in chemistry and biology. Nature 394:52–55
171. Bavastrello V, Stura E, Carrara S, Erokhin V, Nicolini C (2004) Poly(2,5-dimethylaniline)-MWNTs nanocomposite: a new material for conductometric acid vapours sensors. Sensors Actuators B 98:247–253
172. Penza M, Tagliente MA, Aversa P, Cassano G, Capodieci L (2006) Single-walled carbon nanotubes nanocomposite microacoustic organic vapor sensors. Mater Sci Eng C 26:1165–1170
173. Fischer JE (2002) Chemical doping of single-wall carbon nanotubes. Acc Chem Res 35:1079–1086
174. Sun Y-P, Fu K, Lin Y, Huang W (2002) Functionalized carbon nanotubes: properties and applications. Acc Chem Res 35:1096–1104
175. Niyogi S, Hamon MA, Hu H, Zhao B, Bhowmik P, Sen R, Itkis ME, Haddon RC (2002) Chemistry of single-walled carbon nanotubes. Acc Chem Res 35:1105–1113
176. Sin MLY, Chow GCT, Wong GMK, Li WJ, Leong PHW, Wong KW (2007) Ultra-low power alcohol vapour sensors using chemically functionalized multiwalled carbon nanotubes. IEEE Trans Nanotechnol 6:571–577
177. Bekyarova E, Davis M, Burch T, Itkis ME, Zhao B, Sunshine S, Haddon RC (2004) Chemically functionalized single-walled carbon nanotubes as ammonia sensors. J Phys Chem B 108:19717–19720

178. Zhang T, Mubeen S, Bekyarova E, Yoo BY, Haddon RC, Myung NV, Dreshusses MA (2007) Poly(m-aminobenzene sulfonic acid) functionalized single-walled carbon nanotubes based gas sensors. Nanotechnology 18:165504
179. Yao Z, Postma HWCh, Balents L et al (1999) Carbon nanotube intramolecular junctions. Nature 402:273–276
180. Zhou C, Kong J, Yenilmez E et al (2000) IND3 Modulated chemical doping of individual carbon nanotubes. Science 290:1552–1555
181. Valentini L, Armentano I, Kenny JM, Cantalini C, Lozzi L, Santucci S (2003) Sensors for sub-ppm NO_2 gas detection based on carbon nanotube thin films. Appl Phys Lett 82:961–963
182. Varghese OK, Kichambre PD, Gong D, Ong KG, Dickey EC, Grimes CA (2001) Gas sensing characteristics of multi-wall carbon nanotubes. Sensors Actuators B 81:32.41
183. Cantalini C, Valentini L, Lozzi L, Armentano I, Kenny JM, Santucci S (2003) NO_2 gas sensitivity of carbon nanotubes obtained by plasma enhanced chemical vapor deposition. Sensors Actuators B 93:333–337
184. Cantalini C, Valentini L, Armentano I, Lozzi L, Kenny JM, Santucci S (2003) Sensitivity to NO_2 and cross-sensitivity analysis to NH_3, ethanol and humidity of carbon nanotubes thin film prepared by PECVD. Sensors Actuators B 95:195–202
185. Kuzmych O, Allen BL, Star A (2007) Carbon nanotube sensors for exhaled breath components. Nanotechnology 18:375502
186. Chen RJ, Franklin NR, Kong J, Cao J, Tombler TW, Zhang Y, Dai H (2001) Molecular photodesorption from single-walled carbon nanotubes. Appl Phys Lett 79:2258–2260
187. Wang J (2005) Nanomaterial-based electrochemical biosensors. Analyst 130:421–426
188. Hu C, Hu S (2009) Carbon nanotube-based electrochemical sensors: principles and applications in biomedical systems. J Sensors 2009:ID 187615
189. Barisci JN, Wallace GG, Baughman RH (2000) Electrochemical characterization of single-walled carbon nanotube electrodes. J Electrochem Soc 147:4580–4583
190. Barisci JN, Wallace GG, Baughman RH (2000) Electrochemical studies of single-wall carbon nanotubes in aqueous solutions. J Electroanal Chem 488:92–98
191. Barisci JN, Wallace GG, Baughman RH (2000) Electrochemical quartz crystal microbalance studies of single-wall carbon nanotubes in aqueous and non-aqueous solutions. Electrochim Acta 46:509–517
192. Liu P, Hu J (2002) Carbon nanotube powder microelectrodes for nitrite detection. Sensors Actuators B 24:194–199
193. Wang J, Musameh M (2003) Carbon nanotube/teflon composite electrochemical sensors and biosensors. Anal Chem 75:2075–2079
194. Weeks ML, Rahmanb T, Frymier PD, Islam SK, McKnightc TE (2008) A reagentless enzymatic amperometric biosensor using vertically aligned carbon nanofibers (VACNF). Sensors Actuators B 133:53–59
195. Consales M, Crescitelli A, Campopiano S, Cutolo A, Penza M, Aversa P, Giordano M, Cusano A (2007) Chemical detection in water by single-walled carbon nanotubes-based optical fiber sensors. IEEE Sensors J 7:1004–1005
196. Fam DWH, Al P, Tok AIY, Liedberg B, Moochhala SM (2011) A review on technological aspects influencing commercialisation of carbon nanotube sensors. Sensors Actuators B 157:1–7
197. Hermann S, Fiedler H, Haibo Y, Loschek S, Bonitz J, Schultz SE, Gessner T (2012) Wafer level approaches for the integration of carbon nanotubes in electronic and sensor applications. In: International multi-conference systems, signals and devices (SSD) 2012, Chemnitz
198. Lee BY, Sung MG, Lee J, Baik KY, Kwon YK, Lee MS, Hong S (2011) Universal parameters for carbon nanotube network based sensors: can nanotube sensors be reproducible? ACS Nano 5:4373–4379
199. Lee SU, Belosludov RV, Mizuseki H, Kawazoe Y (2009) Designing nanogadgetry for nanoelectronic devices with nitrogen-doped capped carbon nanotubes. Small 5:1769–1775

200. Latif U, Dickert FL (2011) Conductometric sensors for monitoring degradation of automotive engine oil. Sensors 11:8611–8625
201. Mujahid A, Dickert FL (2012) Monitoring automotive oil degradation: analytical tools and onboard sensing technologies. Anal Bioanal Chem. doi:10.1007/s00216-012-6186-1
202. Kerroum I, El Matbouly H, Domingue F (2012) Survey of commercial sensors and emerging miniaturized technologies for safety applications in hydrogen vehicles. In: 2012 IEEE sensors applications symposium, University of Brescia, Italy, 7–9 February 2012
203. Ventura DN, Li S, Baker CA, Breshike CJ, Spann AL, Strouse GF, Kroto HW, Acquah SFA (2012) A flexible cross-linked multi-walled carbon nanotube paper for sensing hydrogen. Carbon 50:266–2674
204. Cho TS, Lee Kj, Kong J, Chadrakasan AP (2008) The design of a low power carbon nanotube chemical sensor, system. J Phys Chem C 112(22):8319–8323
205. Cho TS, Kj L, Kong J, Chadrakasan AP (2009) A 32-μW 1.83-kS/s carbon nanotube chemical sensor system. IEEE J Solid State Circuits 44:659–669
206. Robinson DKR, Morrison M (2011) Nanotechnologies for improving food quality, safety and security. In: Frewer LJ, Norde W, Fischer A, Kampers F (eds) Nanotechnology in the agri-food sector: implications for the future. Wiley-VCH, Weinheim
207. Sharon M, Choudhary AK, Kumar R (2010) Nanotechnology in agricultural diseases and food safety. J Phytol 2(4):83–92
208. Zhao J, Zhang Yu WK, Chen J, Zhou Y (2011) Electrochemical sensor for hazardous food colourant quinoline yellow based on carbon nanotube-modified electrode. Food Chem 128:569–722
209. Otles S, Yalcin B (2012) review on the application of nanobiosensors in food analysis. Acta Sci Pol Technol Aliment 11(1):7–18
210. Tang D, Tang J, Su B, Chen G (2010) Ultrasensitive electrochemical immunoassay of staphylococcal enterotoxin B in food using enzyme-nanosilica-doped carbon nanotubes for signal amplification. J Agric Food Chem 58:10824–10830
211. Park J, Lim JH, Jin HJ, Namgung S, Lee SH, Park TH, Hong S (2012) A bioelectronic sensor based on canine olfactory nanovesicle-carbon nanotube hybrid structures for the fast assessment of food quality. Analyst 137:3249–3254
212. Wongchoosuk C, Wisitsoraat A, Tuantranont A, Kerdcharoen T (2010) Sensors Actuators B 147:392–399
213. Liu G, Chen H, Peng H, Song S, Gao J, Lu J, Ding M, Li L, Ren S, Zou Z, Fan C (2011) A carbon nanotube-based high sensitivity electrochemical immunosensor for rapid and portable detection and control. Biosens Bioelectron 28:308–313
214. Devi R, Yada S, Pundir CS (2011) Amperometric determination of xanthine in fish meat by zinc oxide nanoparticle/chitosan/multiwalled carbon nanotube/polyaniline composite film bound xanthine oxidase. Analyst 137:754–759
215. Esser B, Schnorr JM, Swager TM (2012) selective detection of ethylene gas using carbon nanotube-based devices: utility in determination of fruit ripeness. Angew Chem Int Ed 51:1–6
216. Turaga U, Singh V, Lalagiri M, Kiekens P, Ramkumar SS (2012) Nanomaterials for defense applications. 2012 Annual meeting 28 October–2 November 2012, Pittsburgh, PA, USA
217. Marin S, Merkoci A (2011) Nanomaterials based electrochemical sensing applications for safety and security. Electroanalysis 24(3):459–469
218. Viswanathan S, Radecka H, Radecki J (2009) Electrochemical biosensor for pesticide based on acetylcholinesterase immobilised on polyaniline deposited on vertically assembled carbon nanotubes wrapped with ssDNA. Biosens Biolectron 24:2772–2777
219. Musameh MM, Gao Y, Hickey M, Kyratzi IL (2012) Application of carbon nanotubes in the extraction and electrochemical detection of organophosphate pesticides: a review. Anal Lett 45:783–803

220. Proper A, Zhang W, Bartolucci S, Oberai AA, Koratkar N (2009) In-situ detection of impact damage in composites using carbon nanotube sensor networks. Nanosci Nanotechnol Lett 1:3–7
221. Rausch J, Mader E (2010) Health monitoring in continuous glass fibre reinforced thermoplastics: manufacturing and application of interphase sensors based on carbon nanotubes. Composite Sci Technol 70:1589–1596
222. Saafi M (2009) Wireless and embedded carbon networks for damage detection in concrete structures. Nanotechnology 20:3995502
223. Tan A, Cha Y, Joo J, Inpil K (2011) Novel corrosion sensor based on carbon nanotube composites for structural health monitoring. In: Yildiz B (ed) Proceedings of the thermal and materials nanoscience and nanotechnology for structural health monitoring, Begell House, Hotel Dedeman, Antalya, Turkey, pp 1–7. http://eprints.qut.edu.au/46098/
224. Patel P (2012) Smart sutures that detect infections. Technology review. http://www.technologyreview.com/news/428969/smart-sutures-that-detect-infections/?ref=rss. Accessed 16 Sept 2012
225. Dorozhkin PS, Tovstonog SV, Golberg D et al (2005) A liquid-Ga-filled carbon nanotube: A miniaturized temperature sensor and electrical switch. Small 1:1088–1093
226. Shahini M, Yeow JTW (2011) Carbon nanotube for voltage reduction and throughput enhancement of electrical cell lysis on a lab-on-a-chip. Nanotechnology 22:325705
227. Zhu Z, Garcia-Gancedo L, Flewitt AJ et al (2012) A critical review of glucose biosensors based on carbon nanomaterials: carbon nanotubes and graphene. Sensors 12:5996–6022
228. Kang Q, Yeow JTW, Barnett R (2012) The use of semiconducting single-walled carbon nanotube films to measure X-ray dose. Carbon 50:2197–2201
229. Lei KF, Lee K-F, Yang S-I (2012) Fabrication of carbon nanotube-based pH sensor for paper-based microfluidics. Microelectron Eng 100:1–5
230. Rastogi R, Dhindsa N, Raman Suri C et al (2012) Interfacing of DNA with carbon nanotubes for nanodevice applications. Mater Chem Phys 135:268–276
231. Smart SK, Cassady AI, Lu GQ et al (2006) The biocompatibility of carbon nanotubes. Carbon 44:1034–1047
232. Dowling J, Tentzeris MM (2009) Smart house and smart energy applications of low-power RFID-based wireless sensors. In: Proceedings of the microwave conference 2009 (APMC 2009), Asia Pacific, Singapore, 7–10 December 2009, pp 2412–2415
233. Thai TT, Yang L, DeJean GT, Tentzeris MM (2011) Nanotechnology enables wireless gas sensing. IEEE Microw Mag 12(4):84–95

New Sensing Model of (Mesoporous) In_2O_3

Thorsten Wagner, Nicola Donato, and Michael Tiemann

Abstract Recently indium oxide (In_2O_3) attracted attention as a material for sensing layers in semiconducting gas sensors. Compared to frequently investigated materials like tin dioxide (SnO_2), tungsten trioxide (WO_3), or gallium oxide (Ga_2O_3) indium oxide offers some unique properties. The most prominent one is its selectivity to oxidizing gases such as ozone (O_3) or nitrogen dioxide (NO_2) at low operating temperatures (<150°C). Combined with the photoreduction properties of *nanocast*, *porous* In_2O_3 highly selective sensing layers with a fast response can be prepared. In some cases even room temperature measurements are possible; therefore this material allows for designing low-power sensors without the need for special sensor substrates (e.g., μ-hotplates). Detailed analysis of the sensing mechanism reveals that known sensing models are not able to describe the observed effects. Therefore a new sensing model for ordered nanoporous In_2O_3 is presented which will be applicable for nonstructured material too.

Keywords Indium oxide, Low power, Ordered mesoporous, Photoreduction, Sensing model

Contents

T. Wagner (✉) and M. Tiemann
Department of Chemistry, University of Paderborn, Warburger Straße 100, 33098 Paderborn, Germany
e-mail: Thorsten.Wagner@upb.de

N. Donato
Department of Matter Physics and Electronic Engineering, University of Messina, Italy

C.-D. Kohl and T. Wagner (eds.), *Gas Sensing Fundamentals*,
Springer Series on Chemical Sensors and Biosensors (2014) 15: 175–212
DOI 10.1007/5346_2013_57,

1 Introduction

Because of their robust construction, high selectivity, and the low per-unit price chemoresistors based on semiconducting sensing layers are qualified for mass application. They find use in cars and buildings for air quality monitoring, i.e., detecting volatile organic compounds (VOCs) and nitrogen oxides (NO_x), respectively. To tune the selectivity there are a variety of methods beginning with the choice of the sensing material and catalysts (e.g., [1]), multi-signal generation by cyclic temperature (e.g., [2]), or measurement voltage variation [3] to the point of using (catalytic) filter layers [4, 5]. However, one big drawback for many (mobile or battery-powered) applications is the high energy consumption caused by the need of operating temperatures of several hundred degrees to maintain a fast and stable operation (for some target gases the temperature is also needed to trigger the chemical reactions, but this is not within the scope of this article). One way to counteract this problem is the reduction of the heater power by miniaturization [6] or by pulsed-mode operation [7] which typically leads to increased production costs.

The approach presented in the following makes use of photocatalytic effects in (ordered mesoporous) In_2O_3 for low-power detection of oxidizing gases. In the last few years (since 2000) the number of scientific publications on In_2O_3 sensors has increased strongly. However, there are only a few examples of commercial sensors based on In_2O_3, e.g., for aqueous ozone detection (New Cosmos Electric Co [8]). In the low temperature range (100–150°C) cubic In_2O_3 (Bixbyite-type) is specifically sensitive to oxidizing gases as ozone (O_3) or nitrogen dioxide (NO_2) [9] but is nearly insensitive to reducing gases as CO, NH_3, or other hydrocarbons [10]. However, as it is known, low-temperature operation of metal oxides typically leads to long signal stabilization times, slow sensor reactions, and long recovery times. In the case of In_2O_3, this drawback can be overcome by illumination with light. For In_2O_3 nanoparticles a decrease in recovery times and faster desorption of adsorbates was observed by illumination with UV light (400 nm) [11]. But even though this significantly improves the sensing behavior slow lattice diffusion of oxygen [12] is still predominant over short-term effects caused by surface adsorbates in the dense nanoparticle layers. This is mainly ascribed to the fact that the UV light penetration depth for these layers is rather poor (in the order of 10 nm [13]). This is important since, as will be argued in the following pages, illumination with UV light not only affects desorption of adsorbates but also leads to photoreduction of the bulk phase (inner region of the particles) of the material which leads to increased diffusion coefficients and therefore faster signal stabilization. Hence ordered mesoporous structured In_2O_3 with its thin pore walls (<10 nm) and high accessibility offers superior properties compared to the nonstructured material. The surface-dominated mesoporous material also seems to be prone to a new type of diffusion which is related to the reduced ordering in the surface-near region (reduced Landau ordering) [14].

The following chapter will first cover basic material properties of In_2O_3 and then relate them to specific changes caused by the ordered mesoporous structure. Photoreduction and diffusion measurements will be presented which allow for a new sensing model for In_2O_3. At the end applications for the mesoporous In_2O_3 in room-temperature ozone and nitrogen dioxide sensing will be presented.

2 Working Principle of Semiconducting Gas Sensors

In a typical semiconducting gas sensor device the electronic resistance change of a sensitive layer is measured during gas exposure (see Fig. 1). This concept allows for the design of simple, robust, and low-cost sensing elements. Even though the design of the sensing element is simple the reactions of the target gas on the sensing layer are a complex process. For most metal oxides a surface-chemical reaction of gas molecules changes the oxygen coverage of the metal oxide surface. This leads to a change in the electronic depletion layer formed by the oxygen adsorbates affecting conductance by increasing the energy barrier between adjacent metal oxide grains. These grain contacts are crucial for the signal generation. In this simplified picture the interior regions of the semiconductor particles therefore do not contribute to the sensor response. For this reason newly developed synthesis methods try to reduce this inner region and thereby increase the sensor's response. Since the size of the depletion layers is of the order of nanometers the target is to prepare metal oxides with structures in this same region.

3 Basic Properties of In_2O_3

3.1 Crystal Structure

The most stable In_2O_3 crystal structure is the space-centered cubic Bixbyite modification (space group 206, $Ia\overline{3}$) [15, 16]. There are other modifications, e.g.,

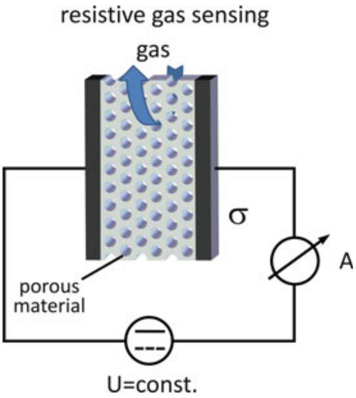

Fig. 1 Schematic of a typical setup of a resistive gas sensor. Electronic resistance σ of a (porous) material is measured upon interaction with target gas. Typically a constant measurement voltage is applied via interdigitated electrodes and the current or the resistance is recorded, respectively [5]. Reproduced by permission of the Royal Society of Chemistry

a corundum type (space group 167, $R\overline{3}c$), synthesized under high pressure of 5–57 GPa and high temperatures of 800–1,250°C. However, these metastable structures will typically transform to the Bixbyite-type structures at normal pressure and 300°C [17, 18]. Therefore it is assumed that under typical working conditions of semiconducting gas sensors only Bixbyite-type In_2O_3 is present, which is consistent with powder X-ray diffraction results.

The lattice constant of Bixbyite-type In_2O_3 is 10.117 Å. The unit cell contains 40 atoms but typically the cubic unit cell with 80 atoms is used (see Fig. 2).

The Indium atoms are located at two nonequivalent positions (marked in Fig. 2 with a green and a brown polyhedron). The alignment of the six oxygen atoms coordinating the Indium is different (see Fig. 3). The figure also shows the oxygen-interstitial sites of the ideal crystal.

Figure 4 shows a section of the cubic unit cell along the (111)-direction. The two nonequivalent Indium sites are marked with colored polyhedra. Additionally the possible interstitial sites for Indium are marked (two possibilities). In the following the Wyckoff notation is used to refer to the different sites. In a simplified view the Wyckoff notation is used to denote groups of "equivalent" sites (more precisely conjugate subgroups of the space group), e.g., "8b" means that there are eight atoms situated on b-sites where the number, distance to, and the angle between the next neighbors is equal (the actual use for this notation is more complex but for the following description the simplified version seems appropriate).

3.2 *Oxygen Diffusion*

There are only a few publications about oxygen diffusion in In_2O_3 which seem to deliver reliable data on oxygen diffusion coefficients. This is probably due to the fact that the preparation of dense In_2O_3 layers is a challenging task. Only Wirtz et al. [12] show results on bulk-phase oxygen diffusion in densely packed In_2O_3 films which

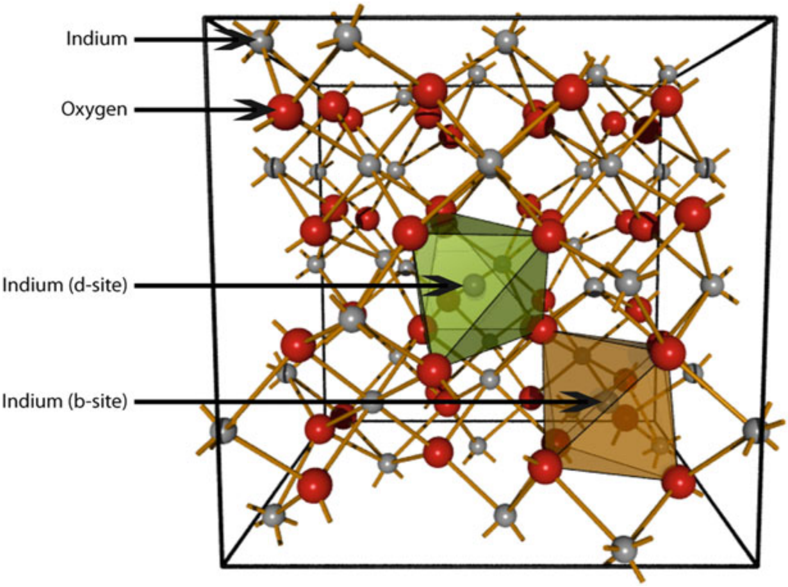

elem.	no.	oxidation	Wyckoff -pos.	X	Y	Z
In	1	3	8b	0.25	0.25	0.25
In	2	3	24d	0.4668(1)	0.0	0.25
O	1	-2	48e	0.3905(13)	0.1529(11)	0.3832(13)

Fig. 2 *Top*: unit cell of cubic (Bixbyite-type) In_2O_3 (80 atoms); the two nonequivalent positions for Indium are marked (see text). *Bottom*: structural data used to generate the graphics [19]

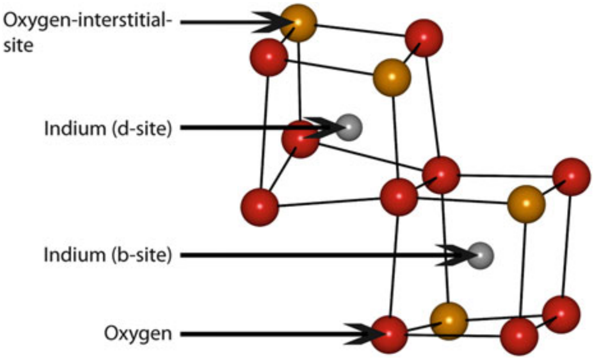

Fig. 3 Depiction of the two nonequivalent indium positions in the crystal lattice. The alignment of the oxygen atoms differs for both positions, at the so-called b-site oxygen interstitial sites are located at the space diagonal, at the d-site they are at the face diagonal of the cube

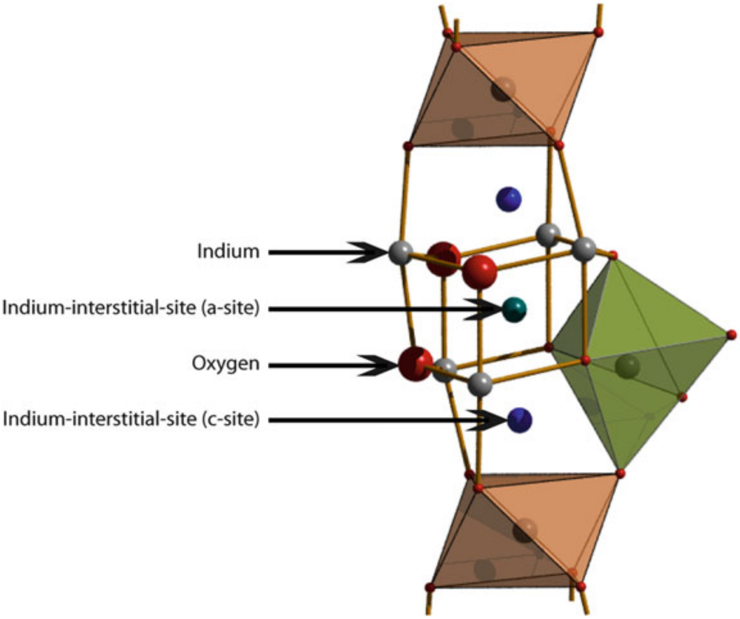

Fig. 4 Section of the unit cell in (111)-direction: the nonequivalent Indium sites are marked with *green* and *brown* polyhedra. The two possible indium interstitial sites are marked *blue* (c-site) and *green* (a-site)

have been prepared by vapor deposition (see Fig. 5). The measurements were performed at temperatures between 727 and 1,027°C and under different oxygen partial pressures. The results cannot be transferred unambiguously to nanostructured materials since these materials are strongly dominated by boundary layer effects, but they allow at least an estimation of the contribution of the bulk part.

Results show that there are two mechanisms for oxygen diffusion. Below 10 μbar the diffusion coefficient increases with decreasing oxygen partial pressure. This is explained by defect diffusion. Above 10 μBar the diffusion coefficient increases with increasing oxygen partial pressure. In this regime oxygen migrates over interstitial sites. Activation energies for interstitial and defect diffusion are 1.72 and 1.97 eV, respectively.

3.3 Sensing Mechanism of Nonstructured In_2O_3

The above-described oxygen-interstitial sites are characteristic for the Bixbyite-type structure (compared to other typical sensing materials as, e.g., SnO_2 which has a close-packed oxygen sublattice) and allow easy oxygen incorporation via free interstitial sites at the surface at low temperature [20]. Therefore Ivanovskaya

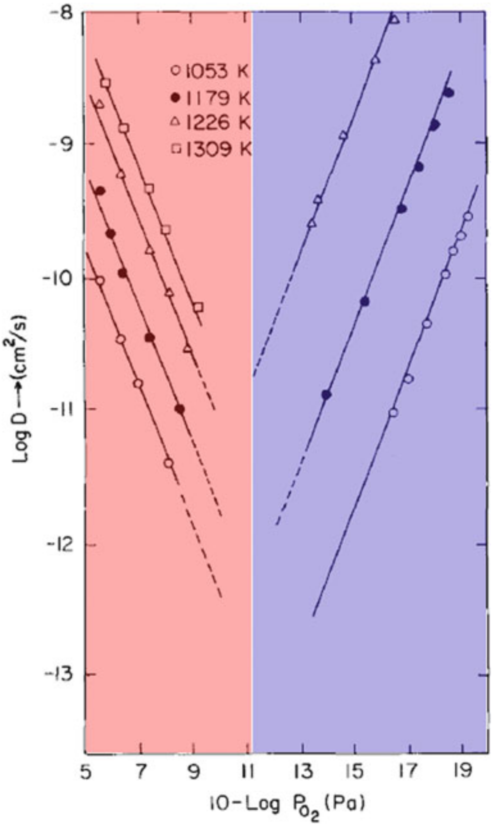

Fig. 5 Oxygen diffusion coefficients in In_2O_3 bulk phase for different oxygen partial pressures [12]. In the high-pressure regime (*red*) the oxygen diffusion via interstitial sites dominates; in the low-pressure regime (*blue*) the oxygen diffuses via defects

et al. assume that there is no chemisorbed oxygen at the surface and the sensor reaction is best described as oxidation and reduction of the In_2O_3 [21].

The sensing layers used by the authors have been prepared by sol–gel method. Other results by Korotcenkov et al. show a correlation of the sensing reaction with the surface structure (In_2O_3 synthesized by spray pyrolysis) [22, 23]. They conclude that this is an indication for a mixed mechanism (ionosorption and redox-type).

However, a consistent picture for the In_2O_3 sensing mechanism is still missing. Only in more recent works Golovanov et al. developed a preliminary model for the sensing properties based on a combination of experimental data (In_2O_3 films by spray pyrolysis) and density functional theory [24]. The authors explain the observed behavior by different mechanisms for the response to oxidizing and reducing gases:

- Oxidizing gases: sensor reaction is dominated by diffusion processes.
- Reducing gases: the reaction is controlled by redox and catalytic effects in a thin surface-near region.

This model is used as basis for the following discussions.

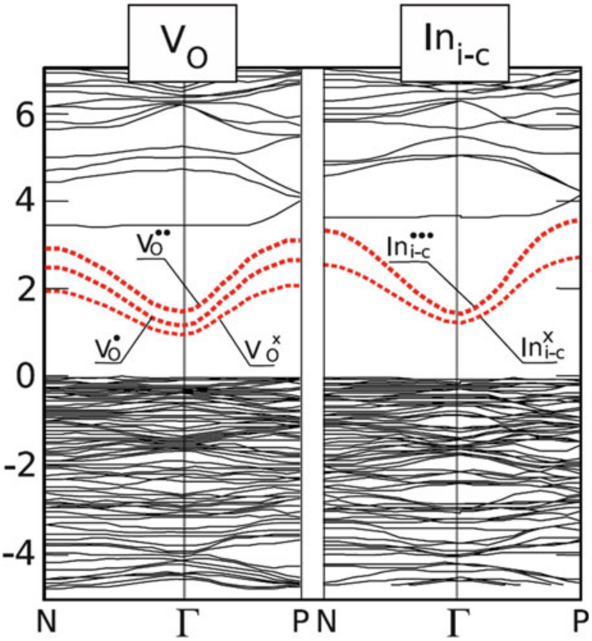

Fig. 6 Results of band structure calculations with oxygen vacancies (*left*) and indium interstitials (*right*) including energy level shift depending on charged state. Both defects show similar properties like a second band gap at higher energies as well as similar energy level shift [28]

3.4 Defect Model

Indium oxide offers a remarkably high conductivity, even without doping, with charge carrier concentrations up to 10^{19} cm^3 [25, 26]. Under equilibrium condition (up to 1% oxygen deficiency in the lattice) as well as under reducing conditions the number of intrinsic defects is high [27].

However, there is an ongoing discussion about the nature of these defects. Therefore a short review about the different possibilities will be given. For the undoped material there are two possibilities which are oxygen defects or indium located at interstitial sites (see Fig. 6).

Band structure calculations [28] show that the effect for both types, oxygen defects and interstitial indium, on the band structure is similar (see Fig. 6). To clarify this thermodynamic stability of the defects has also to be taken into account. Besides the two influence factors impurities are discussed as a reason for the high charge carrier concentration as well; the most prominent one is hydrogen.

In principle all intrinsic defects offer shallow donor levels. Furthermore the calculated energy of formation of oxygen defects is lower than the formation of interstitial indium [28]. Therefore oxygen deficiency seems to contribute the largest part to the nonstoichiometry of the In_2O_3. This is supported by density functional theory calculations by Lany and Zunger [29]. They conclude that nonstoichiometry up to 1% is caused by oxygen defects rather than indium interstitials.

The intrinsic donors (oxygen defect and indium interstitial) are shallow. However, at room temperature without further activation, calculations reveal that they can only be responsible for charge carrier concentrations up to 10^{14} cm^3.

Also, so-called electron killers, e.g., interstitial oxygen which is unstable and reduces the charge carrier concentration even further, have been proposed by the same authors.

To explain the discrepancy between deep color centers and high conductivity they introduced an optically activated, metastable, and conducting oxygen defect state. However, so far there is no experimental evidence for this.

For the following considerations oxygen defects will be assumed to be the reason for the high charge carrier concentration.

There are other approaches to explain for the high charge carrier concentration, such as interstitial indium acting as donor [30] or hydrogen impurities [31, 32], but there are even more problems explaining the observed effects and most of them describe synthesis routes which do not comply with the one presented in this work.

3.5 Band Structure

Even though In_2O_3 is a material with many applications there is still an ongoing discussion about the size and type of the electronic band gap. In this work we will assume a direct band gap [33] of 2.6 eV which cannot be observed in bulk material because of forbidden transitions from the valence band maximum to the conduction band minimum [34]. Since the properties of the nanostructured samples in this work are strongly dominated by their surface it is reasonable to assume transitions even below this energy.

This assumption is motivated by literature. Early work proved the existence of a direct 3.75 eV excitation [35, 36]. But already then there were first hints on an indirect transition of about 2.6 eV [35]. The literature values for this indirect transition are between 2.1 and 2.7 eV [35, 37] and also the position of the valence band maximum differs [20, 38]. Despite these experimental results DFT calculations do not show any indirect transition for defect-free In_2O_3 [33].

Only recent developments in the synthesis of highly crystalline In_2O_3 layers allow the separation of effects related to the volume from surface effects. Figure 7 shows that there is an absorption below 3.5 eV (which was supposed to be the direct transition) for the cubic Bixbyite-type structure [39]. This was interpreted before as an evidence for an indirect band gap. Only recently Walsh et al. [34] showed that the transition from valence band maximum to conduction band minimum is forbidden. Therefore experiments only show the transition from a deeper level of the valence band to the conduction band. In the presence of additional phonons the transition rules are softened so that this transition experimentally behaves like an indirect band gap.

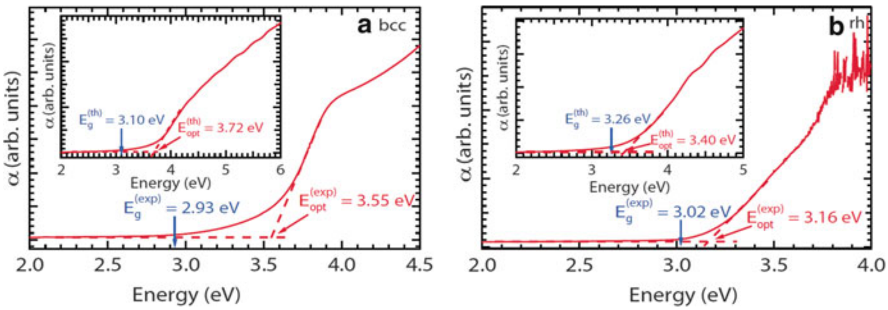

Fig. 7 Absorption coefficient α for Bixbyite-analogue In_2O_3 (*left*) and corundum-type In_2O_3 (*right*); *insets* show calculated coefficients [39]

Table 1 Charge carrier concentration of various In_2O_3 samples; the last value (*grey*) was used for the later presented estimations (see text)

Charge carrier concentration (cm^{-3})	Preparational method	References
4×10^{19}–1.4×10^{20}	Magnetron sputtered films, 150 nm thickness, polycrystalline	[45]
1–5 × 10^{19}	Ion beam sputtering	[46]
1–3 × 10^{20}	Ion beam sputtering	[43]
8.45×10^{18}	Oxygen ion-assisted thermal evaporation, near stoichiometric films	[47]
1×10^{17}	Sol–gel	[48]

3.6 *Other Properties*

For estimations used later in this article there are other relevant properties which are summarized in the following:

- Work function: utilizing internal photoemission (for details to this method see [40] or [41]) the work function was measured to be 5 eV [42].
- Electron mobility: for sputtered In_2O_3 layers typical mobilities of 60 cm^2 V^{-1} s^{-1} [43] are measured.
- Permittivity: the relative permittivity is 10.2 [44].
- Charge carrier concentration: there is a strong variation in the literature values depending on the synthesis method. For the results presented in the following the value 1×10^{17} cm^3 in Table 1 (grey) was used since the preparation method is similar to the one presented here.

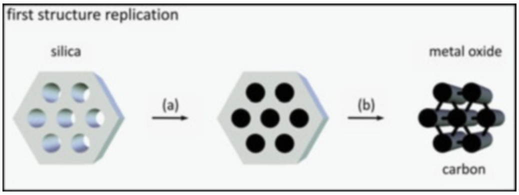

Fig. 8 Schematic of the nanocasting process to retain negative metal oxide (or carbon, see text) replica of the silica matrix

4 Ordered Mesoporous In_2O_3

The following experimental results were obtained by using ordered mesoporous In_2O_3 as model system. The unique properties of this type of material, like well-defined porosity (and therefore high gas accessibility and easy light penetration) and large specific surface area, allow a deeper understanding of the sensing mechanism in In_2O_3.

The fairly new concept of structure replication of nanostructured solid materials ("nanocasting" [49–52]) allows the preparation of mesoporous In_2O_3 as well as numerous other periodically ordered materials (e.g., metal oxides [49–51, 53–58], carbon[59, 60] and organic materials [61]). Besides the application in gas sensing (see [5]) these materials offer also interesting properties for catalysis [62].

Contrary to conventional sol–gel synthesis routes a regular nanostructure is achieved in the material by replication of a rigid structure matrix, such as porous silica (SiO_2). The pores of this matrix are impregnated with a precursor compound, typically a metal salt, by, e.g., wet impregnation, incipient wetness, melt impregnation technique, or two-solvent impregnation [5].

After conversion of the precursor into the product the matrix is removed, typically by chemical etching, resulting in a negative replica of the structure matrix (see Fig. 8). As depicted in there is also the possibility to synthesize mesoporous carbon which can be utilized to achieve positive replica by repeating the replication process. However, since this method is not applied here, it is referred to the literature for more details [5].

Typical structure matrices for replication are ordered mesoporous silica materials like SBA-15 or KIT-6 which are synthesized by utilization of self-assembled supramolecular aggregates of amphiphiles serving as structure directors ("soft templates"). This method is also applicable to the synthesis of a few metal oxides directly without the need of additional replication steps [63, 64]. However, besides the lower quality of the structure, there are other drawbacks such as the narrow temperature range during synthesis which results in low crystallinity.

In the following ordered mesoporous In_2O_3 materials will be discussed which were synthesized by structure replication from cubic KIT-6 silica (space group: $Ia\overline{3}d$) [65]. There are also other examples of mesoporous In_2O_3 in the literature [66–68], but with no particular focus on the details of the nanocasting synthesis or gas-sensing application. Figure 9 shows typical structural properties of the In_2O_3 samples presented here [65]. With the chosen matrix an average pore size of

Fig. 9 *Top:* N_2 physisorption isotherm and resulting pore-size distribution (DFT-based method, *inset*) of the samples after different temperature treatments; *middle:* low-angle and wide-angle (*inset*) powder X-ray diffraction (XRD) pattern showing good mesoscopic order as well as crystallinity; *bottom:* transmission electron microscopic (TEM) image and selected area electron diffraction pattern (SEAD, *inset*) [65]

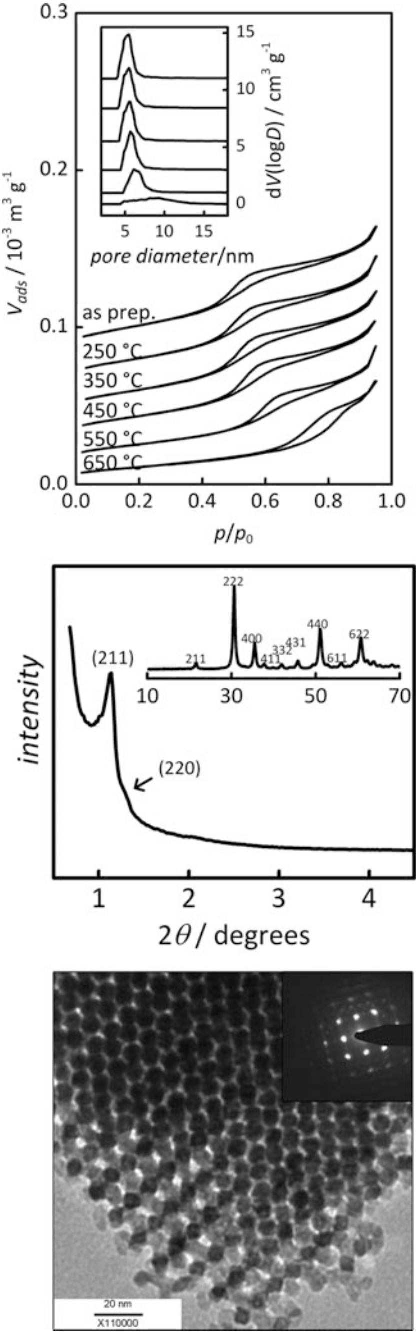

ca. 6 nm was achieved (measured by nitrogen physisorption). The pore size distribution and low-angel X-ray diffraction (XRD) confirm the uniformity and periodicity of the samples. These results are consistent with transmission electron microscopy (TEM) and selected area electron diffraction (SAED). This synthesis method further results in a high thermal stability of the nanostructure up to 450°C [65] likely due to a higher crystallinity achieved by heating the material to elevated temperatures prior matrix removal. This also allows sintering of the nanomaterial while still being structurally stabilized by the structure matrix. More details can be found in [69]. Even though the presented applications in this article cover low-temperature measurements it has been shown that the increased thermal stability offers advantages in high-temperature sensing [65, 70, 71].

Another important feature for sensing applications, especially for preparation of sensing layers, is the size and morphology of the mesoporous structured particles. However, since this is also not covered in this article, we refer to the literature for more details [5]. Other properties regarding the sensing characteristics will be discussed below.

5 Sensing Model

The sensing mechanism in semiconducting metal oxides is typically related to oxygen exchange of the material with the surrounding and, as explained above, the sensing mechanisms of In_2O_3 seems to be dominated by redox reactions; therefore oxygen transport properties are of major interest.

To identify the mechanism responsible for the gas-triggered change in conduction optical measurements will be presented. As was also mentioned before oxygen vacancies are thought to be the main source of free electrons in the conduction band (donor levels). The energy of this donor level was measured by FT-IR.

In the last part of this section results are combined to a sensing model for ordered mesoporous In_2O_3 which is also applicable to nonporous material.

5.1 Oxygen Diffusion

As mentioned at the beginning there is no spectroscopic evidence for oxygen adsorbates even in the case of ozone sensing [72]; oxygen species seem to be incorporated very quickly into the crystal lattice of In_2O_3. This leads to the conclusion that the transient behavior of In_2O_3-based sensors at low temperature ($<$150°C) is strongly dominated by oxygen diffusion in the lattice. Since typical methods of measuring oxygen diffusion are not applicable to the porous material an indirect method is used. Sensing layers of the mesoporous and a nonporous reference material have been exposed to different oxygen partial pressures at room temperature. As can be seen in Fig. 10 there are effects at three different time domains which can be identified as presented in Fig. 11:

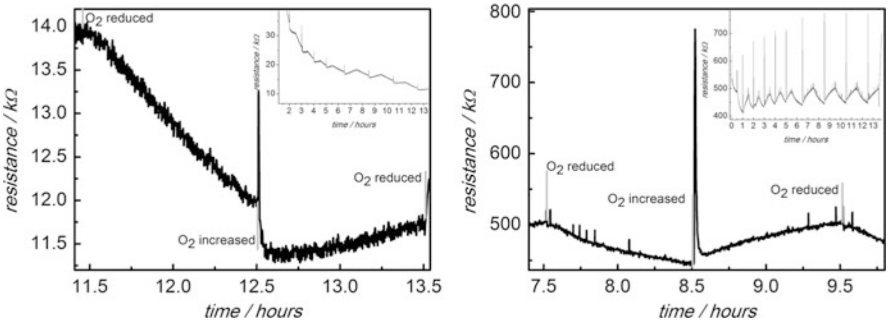

Fig. 10 Reaction of non-ordered (*left*) and ordered mesoporous (*right*) In_2O_3 to cyclic O_2 partial pressure change (achieved by mixing dry synthetic air with nitrogen). *Plots* show a single cycle; *insets* show the entire measurement [73]

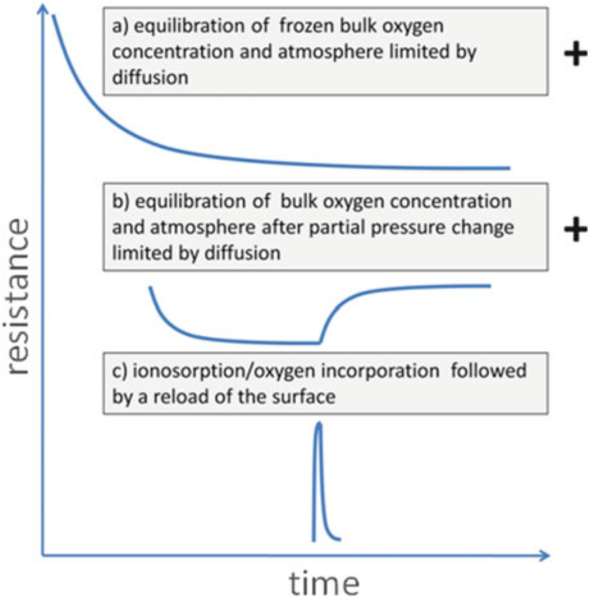

Fig. 11 Schematic depicting different superimposed components in sensor signal at O_2 partial pressure changes [73]

1. Slowest process: equilibration of frozen bulk oxygen concentration and the oxygen concentration in the surrounding atmosphere limited by diffusion.
2. Intermediate: equilibration of bulk oxygen concentration and atmosphere after partial pressure changes limited by diffusion.
3. Fastest process: ionosorption or oxygen incorporation followed by a reload of the surface.

Depending on the specific properties of the sensing material (structured or nonstructured) the different effects are superimposed, resulting in different sensing behavior. As can be seen in inset in Fig. 10 the mesoporous sensor stabilizes faster. Also the equilibration between surface and volume is faster for the mesoporous material (see single cycles Fig. 10). The last effect which was attributed to reload of the surface is stronger in the mesoporous case. In the following the three effects will be discussed in more detail.

5.1.1 Faster Baseline Stabilization of the Mesoporous Material

To clean the surface prior to the experiment the sensors were heat-treated in clean synthetic air to remove unwanted adsorbates. During this process the equilibration of the surrounding atmosphere with the bulk oxygen concentration at elevated temperature is faster than at low temperature. This is caused by the thermal activation of the involved diffusion processes [74]. Cooling of the sensor then leads to a decrease in thermally activated free charge carriers (e^-), which causes the formation of a potential barrier at the surface (e.g., in SnO_2) [75]. This leads to desorption of adsorbates and therefore to a shift of the adsorption/desorption equilibrium towards desorption. Oxygen diffuses from the interior of the crystal lattice to the surface. Since the diffusion is thermally activated it is further suppressed during the cooling procedure resulting in a nonequilibrium state at room temperature. The equilibration time constant is of the order of 2–3 days for the nonporous material. Since it has been shown that the oxygen diffusion in the bulk leads to changes in conductivity (and therefore to a baseline drift) [76] this is believed to be the reason for the observed effect. In contrast, the mesoporous material has a much higher surface-to-volume ratio (specific surface area of ca. 80 m^2/g for the mesoporous material as compared to ca. 20 m^2/g in the nonporous material) which causes a much faster stabilization (ca. 2 h) of the baseline. Consistently there is no baseline drift observed for both materials at elevated operating temperature (250°C) because then the diffusion processes are activated (measurements not shown).

Therefore the oxygen diffusion is the rate-determining step in the sensor reaction [24]. For the most commonly used sensor material, SnO_2, equilibration times at 200°C are of the order of days [77, 78] although they should amount to ca. 200 s assuming that diffusion is the limiting factor [79]. In this case the exchange reaction of oxygen at the surface is the rate-determining step.

5.1.2 Faster Equilibration Between Surface and Volume for Mesoporous Material

In analogy to the equilibration of the baseline oxygen diffusion again determines the equilibration time after lowering the O_2 partial pressure. The reduced oxygen concentration at the near-surface region causes increased oxygen diffusion out of the bulk. The mesoporous material equilibrates faster (time constant ca. 30 h) than the nonstructured material (not determinable). Again this is supported by the behavior at elevated temperatures. At 150°C the thermally activated diffusion reduces the time constant to the order of minutes; at 250°C there is no significant difference between the reaction of mesostructured and nonstructured material.

5.1.3 Recharging Effects

There are two possible explanations for the fast change in the sensor resistance after switching the test gas.

Even though ionosorption of oxygen is not expected to be the time-determining process at an elevated temperature of 250°C [21, 23], it may lead to a strong and fast decrease (few seconds) of free charge carriers in the surface-near region at room temperature. This causes the formation of a depletion layer and the recharging of the surface which is responsible for the slow regeneration (minutes) of the resistance.

The second (less likely) explanation is the direct incorporation of oxygen into the lattice. Such incorporation would also lead to a strong decrease of free charge carriers in the surface-near region with a subsequent slow regeneration also due to surface recharging. However, even if the incorporation of oxygen is promoted by the open lattice structure of cubic In_2O_3, the O_2 molecules have to dissociate first. Therefore we presume that ionosorption is the reason for the observed sensing behavior. Apart from a much higher intensity of the mesoporous In_2O_3 there is no qualitative difference of this effect. This increased intensity compared to nonstructured material is attributed to the higher surface-to-volume ratio.

As mentioned before, there are only sparse data on oxygen diffusion in undoped In_2O_3 available in the literature. For nonporous, compact, and thick polycrystalline layers, interstitial diffusion is dominating with a diffusion constant of

$$D_\mathrm{I} = 0.01\ \mathrm{cm^2 s^{-1}} \cdot \mathrm{e}^{(-1.72\mathrm{eV}/k_\mathrm{B}T)}.$$

Here the activation energy is roughly twice as high in comparison to the commonly used SnO_2 [76]

$$D_\mathrm{I} = 0.02\ \mathrm{cm^2 s^{-1}} \cdot \mathrm{e}^{(-0.9\mathrm{eV}/k_\mathrm{B}T)}.$$

Hence oxygen diffusion in bulk In_2O_3 at room temperature is ca. 10–30 times lower and therefore negligible.

The low oxygen diffusion combined with the fast incorporation of oxygen caused by the open lattice structure of cubic In_2O_3 [20] leads to a new concept of depletion layer formation. The high charge carrier density of up to $10^{20}\ \mathrm{cm^{-3}}$ in undoped In_2O_3 theoretically causes thin depletion layers of about 1 nm thickness even at high amounts of surface states. However, UV photoelectron spectroscopy (UPS) suggests thicker depletion layers for which a so-called chemical depletion

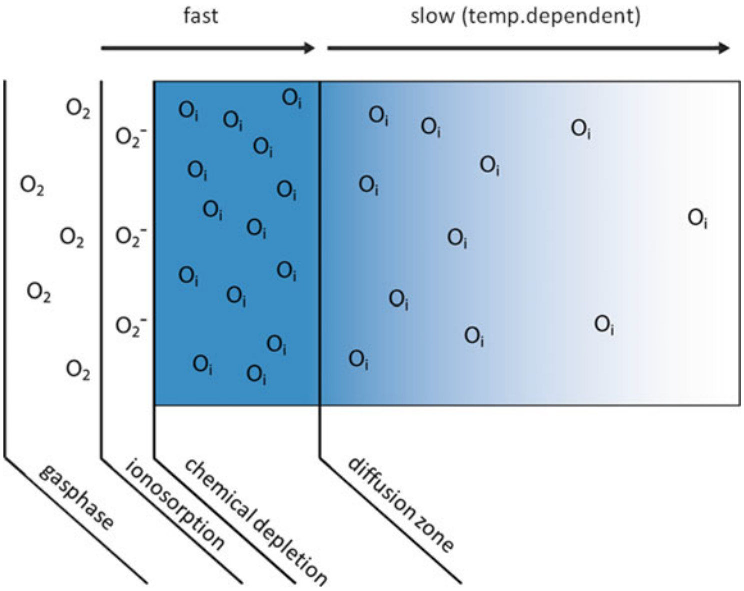

Fig. 12 Chemical depletion effect: ionosorbed oxygen from the gas phase is rapidly incorporated into the crystal lattice. Because of suppressed lattice diffusion at low temperatures, it is accumulated at the surface-near region [73]

layer is held responsible [20]. Caused by increased oxygen concentration compared to the bulk phase (and therefore reduced dopant concentration) in the surface-near region the free-charge-carrier concentration is reduced. Compared to conventional depletion layers which are caused by compensation of surface charges the chemical depletion and the resulting shift of the Fermi level is not linked to charge. In fact chemical depletion forms because of the strongly suppressed oxygen diffusion at low temperature. The surface of the Bixbyite-type structure allows incorporation of oxygen also at low temperature.

Because of suppressed diffusion into the bulk the incorporated oxygen is accumulated at the surface (see Fig. 12). Therefore only specifically structured material with high surface-to-volume ratio combined with diffusion enhancement by UV light allows room-temperature measurements.

5.2 *Photoreduction Properties*

As explained above there is an ongoing discussion about the origin of the high free-charge-carrier concentration even in undoped In_2O_3. As for gas sensing it is assumed in this article that oxygen vacancies are the relevant species. However, there are no experimental data for the ionization energy of the electrons of this oxygen vacancy so far. Therefore in the following different measurements will be

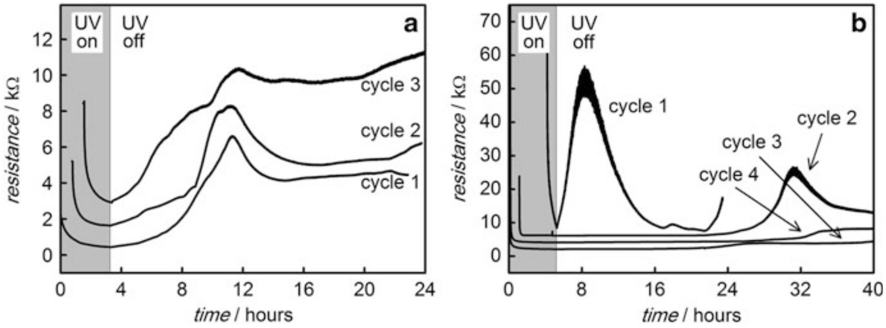

Fig. 13 Change in electronic resistance of mesoporous In_2O_3 in (*left*) synthetic air (20.5% O_2, 79.5% N_2) and (*right*) pure nitrogen (N_2) upon repeated illumination with UV light [80]

presented to further support the idea of oxygen vacancies donors and to quantify the ionization energy. In addition, these results show the possible application of the material as a room temperature sensor for certain gases when illuminated with UV light (see last section: applications).

In a first step the influence of illumination (UV light, 350 nm, ca. 3.5 eV) of the material under oxidizing (synthetic air (20.5% O_2, 79.5% N_2) and reducing (N_2 atmosphere) atmospheric conditions has been investigated (see Fig. 13). A substantial drop in resistance is observed immediately after turning on the UV light under both conditions. After turning the light source off, however, there is a significant difference in the behavior between air and N_2. Moreover in N_2 there is also a change in resistance from cycle to cycle. In synthetic air all cycles show the same order of magnitude for the recovery time whereas in N_2 the time span increases for each cycle and recovery is not observed at all (within the measured time frame of 40 h) in the fourth cycle. In both cases, a transient peak is observed before signal recovery.

To explain the observed light-induced phenomena first the most common effects of UV illumination, electron–hole pair generation [29], desorption of oxygen adsorbates [81], and photoreduction [82] will be reviewed:

5.2.1 Electron–Hole Pair Generation

As explained above the nature of the band gap of In_2O_3 is not fully elucidated. Still, for the mentioned reasons, we assume that the excitation energy used in our experiments (350 nm, 3.5 eV) is sufficient for electron excitation from the valence band to the conduction band. This way UV light induces direct changes in conductivity which are considered as a possible explanation for the change in electronic resistance of In_2O_3, since recombination of these pairs is suppressed [29]. However, some of the observed effects cannot be accounted for by this explanation alone (see below).

5.2.2 Desorption of (Oxygen-) Adsorbates

There are two mechanisms closely related to the electron excitation which lead to a direct desorption of adsorbates caused by UV light. First, a binding electron may be excited to the conduction band causing the adsorbate to desorb. Second, a light-generated hole in the valence band may combine with the binding electron. In principle these mechanisms have already been experimentally proven in 1959 for single-crystalline zinc oxide (ZnO) [81]. In these studies optically activated desorption evoked a change in conductance by several orders of magnitude. Analogous to the electron–hole pair generation in nanostructured materials these mechanisms are known to apply to UV light energies even below the band gap energy [83]. As will be shown in the applications section this effect leads to higher dynamics and sensitivities for the detection of oxidizing gases (at room temperature) [84].

5.2.3 Photoreduction

The last effect discussed here has the strongest influence on the electronic conduction. Due to a recombination of a hole (generated by optical electron–hole pair generation) with the binding electron from within the In–O bond the bond breaks and the oxygen atom is set free to diffuse out of the crystal lattice causing photoreduction of the In_2O_3 and leaving behind an oxygen vacancy (V_O) [82, 85]. This was also predicted by DFT calculations [28]. As stated before the oxygen vacancy is considered to be responsible for the high charge carrier concentration (10^{19} cm^{-3} [25, 26] or an even higher concentration in the case of doped In_2O_3).

Figure 14 shows a schematic of the three possible mechanisms. Even though each of them in principle could lead to the observed resistance drop upon UV light illumination only photoreduction can explain the partial irreversibility of this effect (i.e., a nonvanishing photoconductivity). Since reoxidation is suppressed under pure nitrogen atmosphere the asymmetric behavior of the mesoporous material in different atmospheres under illumination stands to reason.

To further clarify this, the experiment was also conducted with nonporous (bulk) In_2O_3 (average grain size: 40 nm; Fig. 15). Compared to the mesoporous material the response shows two significant differences:

- The resistance drop after turning the UV light on is much lower than for mesoporous In_2O_3 in synthetic air and pure nitrogen.
- No accumulation effect is observed (results are supported by measurements on polycrystalline layers of In_2O_3 after UV illumination at 365 nm [86]).

We conclude that both effects, the strong decrease in resistance and the accumulative effect, are related to the unique structural properties of mesoporous In_2O_3. The main differences between the samples are the lateral dimensions. The mesoporous material can be described as a network of branched, crystalline In_2O_3 ribbons of about 5.7 nm diameter whereas the bulk material mainly consists of sphere-like particles with ca. 40 nm diameter (see Fig. 16). The penetration depth of

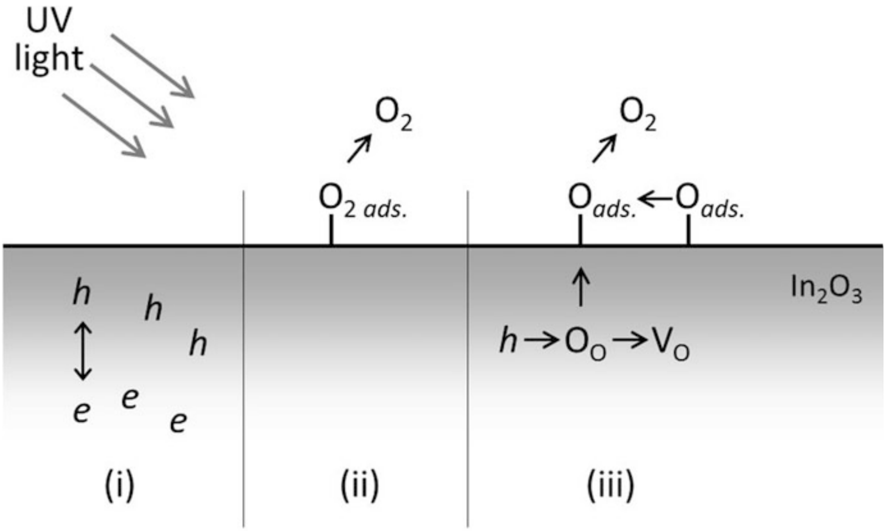

Fig. 14 Schematic of the most common processes occurring upon illumination (light energy above band gap energy) of In_2O_3: *i*) electron–hole-pairs generation; (*ii*) direct desorption of oxygen adsorbates; (*iii*) photoreduction; in the last case recombination of an illumination-induced hole with a lattice In–O binding electron eventually leads to desorption of the respective lattice oxygen atom [80]

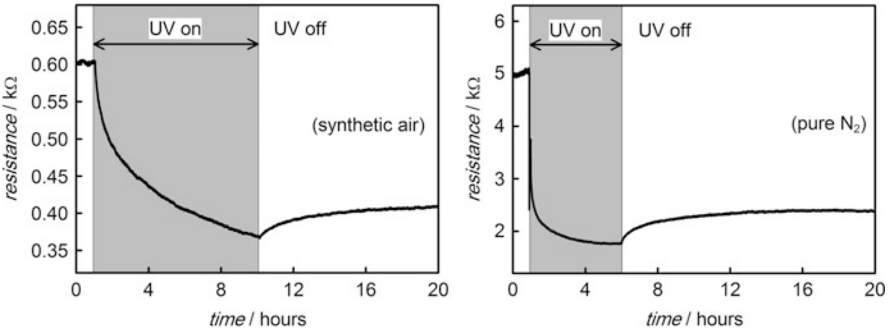

Fig. 15 Comparison of the sensor resistance change of nonporous (bulk) In_2O_3 in (*left*) synthetic air (20.5% O_2, 79.5% N_2) and (*right*) pure nitrogen (N_2) upon repeated illumination with UV light [80]

light-induced effects such as photoreduction has been shown to be ca. 10 nm [13, 36]. This means that the mesoporous structured In_2O_3 is nearly completely affected by the illumination (photoreduction) whereas only the surface-near region of the bulk material will be influenced. In the latter case the core region of each grain is unaffected and will further act as reservoir of non-reduced In_2O_3 allowing oxygen atoms to slowly diffuse to the reduced surface-near regions. Since the oxygen vacancies created by photoreduction are metastable and conducting (shallow donors) [28, 29] the diffusion leads to a gradual increase in resistance

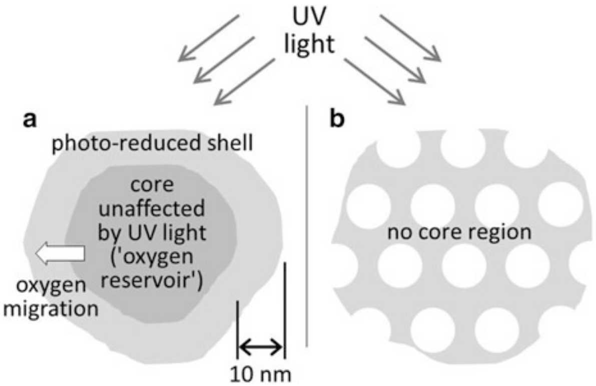

Fig. 16 Grain sizes significantly above the UV light penetration depth lead to slow oxygen migration effects in bulk-phase (granular) In_2O_3 (**a**) whereas mesoporous In_2O_3 with a nanostructure (**b**) is entirely affected by UV illumination [80]

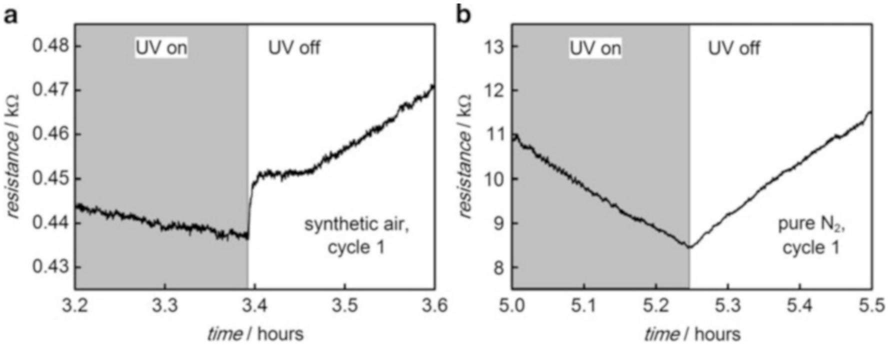

Fig. 17 Detailed analysis of the electronic resistance change after UV light is turned off (mesoporous In_2O_3). There is a different reaction in (**a**) synthetic air (20.5% O_2, 79.5% N_2) and (**b**) pure nitrogen (N_2) which suggests that this effect is not due to electron–hole pair generation but rather desorption or photoreduction effects (see text) [80]

after the UV light is turned off. In the mesoporous material there is only a small fraction of non-photoreduced material which is why this regeneration effect is strongly suppressed here. Also, the smaller reservoir is depleted after a few illumination cycles which explains the abovementioned accumulation behavior.

The other two effects, desorption and electron–hole pair generation, may still contribute to the UV light-induced change in electronic resistance. However, especially electron–hole pair generation will occur on a much faster time scale. In Fig. 17 the behavior of the electronic resistance immediately after the UV light is turned off is shown in more detail. A clear difference between the reaction in air and pure nitrogen is apparent. Since the direct effect of the electron–hole pair generation should be independent of the surrounding atmosphere the observed change in

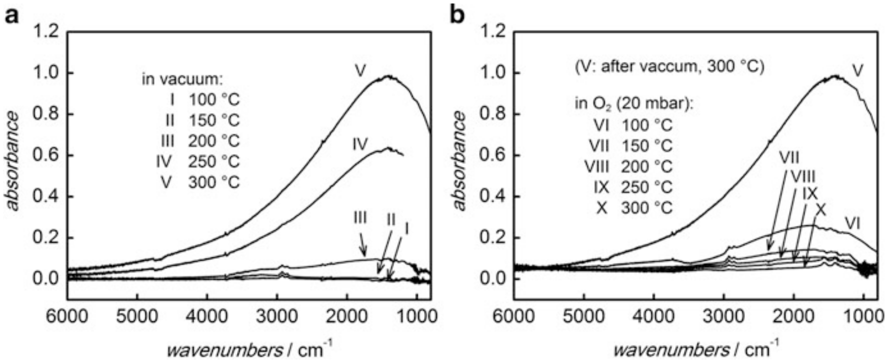

Fig. 18 Results of the in situ FT-IR measurements of mesoporous In_2O_3 (**a**) during heating from 100 to 300°C in vacuum and (**b**) during subsequent heating in O_2 (20 mbar). Reference spectra of the sample after isothermal treatment at 300°C in vacuum and in O_2 have been subtracted [80]

case of synthetic air is likely to be an indirect effect (desorption or photoreduction). Hence the direct electron–hole pair generation should be negligible.

5.3 *In Situ FT-IR Spectroscopy*

As mentioned above we consider fluctuations in oxygen vacancy concentration in In_2O_3 (caused by photoreduction) as the cause for resistance changes under illumination and in different gas atmospheres. Therefore further investigations by temperature-resolved in situ FT-IR spectroscopy have been carried out. Spectra of a mesoporous In_2O_3 sample have been recorded at increasing temperature from 100 to 300°C in vacuum and in pure oxygen atmosphere, respectively (see Fig. 18). In vacuum the formation of a broad absorption band at ca. 1,450 cm^{-1} (180 meV) is observed. The gradual erosion (with increasing temperature) of this band in oxygen atmosphere suggests that this is related to oxygen defects either in the crystal lattice or at the surface of the In_2O_3. In both cases the absorption will be caused by photo-ionization of (preexisting) oxygen vacancies. The energy of ca. 180 meV is in accordance with energies observed for other n-type metal oxides [87–95], caused by the first photo-ionization of the oxygen vacancy (see basics section). This is also supported by photoluminescence studies on In_2O_3 ([96] and references therein).

However, desorption/adsorption of anionic oxygen species at the surface must be ruled out, since no surface chemisorption is observed for In_2O_3 [21]. Therefore the effect is attributed to oxygen in- and out-diffusion into or out of the crystal lattice annihilating or creating oxygen vacancies.

Apart from the above-reported photoreduction properties the IR results also account for the highly asymmetric behavior in the reaction to oxidation (oxygen treatment) and reduction (outgassing). Compared to, e.g., SnO_2 [97], significant in-diffusion of oxygen is observed already at a temperature as low as 100°C. The absorption is reduced to about 20% of the initial intensity. To generate a significant amount of oxygen vacancies on the other hand treatment at 200°C in vacuum is necessary. At lower temperatures there is no visible effect (Fig. 18, spectra I and II).

As will be shown in the application section this is also consistent with the gas-sensing behavior. At lower temperature (<150°C) the mesoporous In_2O_3 responds highly specific to oxidizing gases.

5.4 Sensing Model: Band Structure

The above-made considerations clearly show that the often-used chemisorption model does not adequately describe the behavior of (mesoporous) In_2O_3 at low temperature. In fact the mechanism can be described by the oxidation and reduction of the bulk of the sensing material. As confirmed by temperature resolved FT-IR a shallow donor state (ca. 180 meV) caused by the oxygen vacancies exists. The following estimation shows that this is sufficient to explain the observed conductivity changes. Afterwards the sensing mechanism in mesoporous In_2O_3 will be described by means of a simple band diagram.

The calculations in the following are based on the fact that oxygen vacancies induce donor-level defects in mesoporous In_2O_3. Since there is no chemisorption observed for In_2O_3 [21] the energy bands at the surface are assumed to be flat. The neutrality condition is then expected to be the same as for bulk material, i.e.:

$$n = p + \sum_i Z_i N_i, \tag{1}$$

with the charge Z_i (in units of electronic charge) of the impurity of type $\underline{i}$ and the concentration N_i of said impurity. In a simplified picture the interaction of the bulk with the gas phase is described by

$$\tfrac{1}{2}\,\mathrm{O_2} + \mathrm{V^+} + \mathrm{e^-} \rightleftharpoons \mathrm{O_O}. \tag{2}$$

Calculated formation energies for the defect states in In_2O_3 show that this is a realistic assumption [28]. The reaction can be split into the in- and out-diffusion of neutral oxygen and the subsequent ionization:

$$\tfrac{1}{2}\,\mathrm{O_2} + \mathrm{V^0} \rightleftharpoons \mathrm{O_O}, \tag{3}$$

$$\mathrm{V^O} \rightleftharpoons \mathrm{V^+} + \mathrm{e^-}, \tag{4}$$

with an enthalpy of the reaction (4) of about 180 meV (see above).

In-diffusion of oxygen reduces the doping level (3) causing a downshift of the Fermi level (E_F) in the gap leading to reduced electron occupancy of oxygen vacancies.

The transition from V^0 to V^+ is controlled by (4) so the peak of absorbance in the FT-IR spectra corresponds to excitation of electrons from this defect state (as was already assumed above). Hence, when the oxygen concentration increases (or oxidizing gases are offered), the in-diffusion from environment into the bulk is favored and the downshift of the E_F explains the increase in resistance (see application section).

Without band bending and assuming that there are no holes in the valence band ($p = 0$) the density of electrons in the conduction band (CB) n is equal to the density of ionized donors:

$$n = N_c e^{[(E_F - E_{CB})/k_B T]} \tag{5}$$

To calculate N_c an effective mass of the electron of 0.3 m_o, with the electron rest mass m_o [98], is assumed. All energies refer to E_{CB}.

Utilizing the Fermi–Dirac distribution the probability of finding an ionized vacancy can be calculated by [98]

$$f = 1/\left(1 + e^{\left[(E_F - E_D)/k_B T)\right]}\right), \tag{6}$$

where k_B is the Boltzmann constant and T the absolute temperature. Multiplying (6) with the density of V_o results in the number of electrons in the conduction band. After substitution of (5) the following equation is obtained:

$$N_c e^{\left(\frac{E_F}{k_B T}\right)} = \frac{[V_c]}{1 + e^{\left(\frac{E_F - E_D}{k_B T}\right)}}. \tag{7}$$

As a practical example two oxygen vacancy concentrations far enough from degeneracy are considered. The doping level should be reduced by two orders of magnitude by oxygen in-diffusion at 300°C (sample in oxygen atmosphere after outgassing in vacuum, see FT-IR results Fig. 18). Evaluating (7) with $T = 300°C$, $E_D = -0.18$ eV, $k_B T = 0.049$ eV, and $N_c = 10^{19}$at/cm^3 results in a E_F of ca. 0.16 eV below E_{CB} with $[V_o] = 10^{18}$ at/cm^3 in reducing atmosphere, and 0.35 eV below E_{CB} when $[V_o] = 10^{16}$ at/cm^3 in oxidizing atmosphere.

This shift of 0.2 eV in E_F is in accordance with the observed variation in the FT-IR spectra as well as the observed conductance changes in oxidizing atmosphere with respect to dry air. Hence, the postulated mechanism explains the sensing effect in In_2O_3.

The scheme in Fig. 19 depicts the gas-sensing model for In_2O_3. The signal is not generated by a change in surface states but rather by a change in the bulk donor concentration caused by diffusion-controlled change in oxygen vacancy concentration. The calculations confirm that this effect can induce Fermi level shifts which are strong enough to explain the observed response behavior.

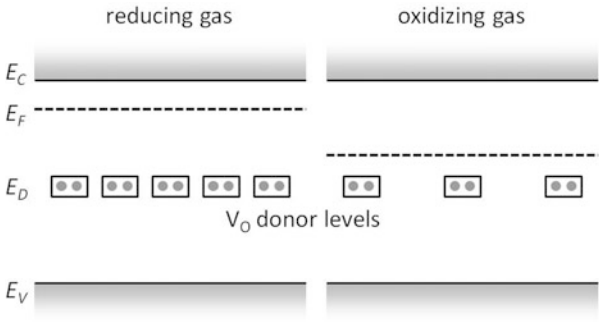

Fig. 19 Band diagram of an In_2O_3-sensing layer under reducing (*left*) and oxidizing (*right*) conditions: oxygen vacancies are depicted as *boxes* with *double dots* mark. They are capable of allocating electrons to the conduction band (shallow donors). Depending on the donor concentration the Fermi level (E_F) shifts. *Note*: since there are no ionosorbed oxygen species there is no band bending at the surface-near region (E_C: conduction band energy; E_D: donor level energy; E_V: valence band energy) [80]

6 Application: Low Temperature Sensing of Oxidizing Gases

6.1 Ozone Sensing

Since In_2O_3 is specifically sensitive to oxidizing gases at low temperature, ozone is a suitable candidate for room-temperature measurements. It is highly reactive and does not need additional activation energy.

The first measurements have been carried out with and without illumination. A blue LED (459.6 nm with a FWHM of 40.5 nm) was used as a light source. As mentioned before it is possible to activate electrons into the conduction band with sub-bandgap light because of the high amount of lattice defects at the surface of the mesoporous material. Figure 20 shows the sensor response to ozone concentrations of 1.2 and 2.4 ppm under dry conditions at room temperature. In the illuminated case the response is five times higher for 1.2 ppm ozone and 30 times higher for 2.4 ppm ozone concentration, respectively (see Table 2).

In addition to the general signal increase upon illumination there is also a strong nonlinearity in the sensors response. Doubling the concentration leads to five times higher response. In the non-illuminated case, however, the sensor seems to be saturated already at 1.2 ppm ozone. The response even decreases at the higher concentration due to drift effects in the baseline resistance.

The saturation effect can be described by a saturation of active surface sites of the In_2O_3. Even though it was stated before that the sensing mechanism is not dominated by ionosorbed oxygen species there will be at least intermediate adsorbed states. The ozone needs to dissociate before the oxygen can be incorporated into the In_2O_3 lattice. It is assumed that O_2^- is the dominant intermediate

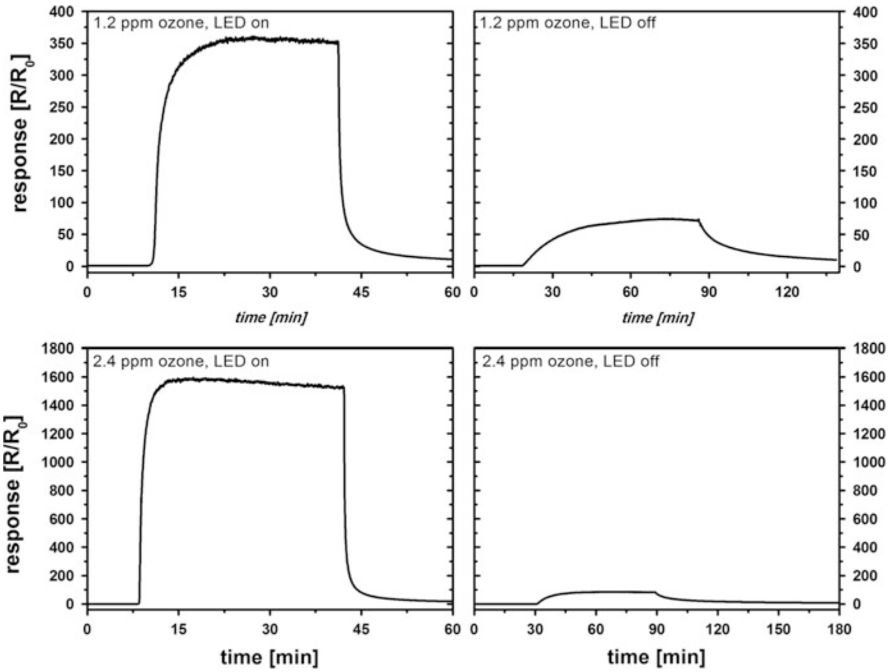

Fig. 20 Sensor response (R/R_0) to different ozone concentrations with and without illumination with blue light [84]

Table 2 Sensor response (R/R_0) and t_{90} values for different ozone concentrations with and without illumination [84]

Ozone concentration (ppm)	LED	Response	t_{90} response (min)	t_{90} decay (min)
1.2	On	353.26	5.4	3.6
2.4	On	1,764.60	2.0	1.3
1.2	Off	72.20	34.8	>50
2.4	Off	62.30	15.86	75

oxygen species. The occurrence of O_3^- cannot be ruled out entirely at temperatures below 150°C [72, 99] but it has been proposed that O_3^- is not stable even at low temperatures [100].

The reaction mechanism can be formulated as follows:

$$O_{3,g} + e^- \rightleftharpoons O_{3,g} + e^- \rightleftharpoons O_{3,s}^- \rightleftharpoons O_{2,s}^- + \tfrac{1}{2}O_2, \qquad (8)$$

with the subscript g denoting the gas phase and s referring to a surface-adsorbed site.

Electron–hole pair generation by illumination with blue light leads to desorption of adsorbates and photoreduction of the In_2O_3, as was stated before. For the surface effect this can be described by the following equations:

$$O_{3,s}{}^{-} + h_{vb}{}^{+} \rightarrow O_{3,g}, \tag{9}$$

$$O_{2,s}{}^{-} + h_{vb}{}^{+} \rightarrow O_{2,g}. \tag{10}$$

By illumination the redox equilibrium is hence shifted towards the reduction side leading to a shift of the saturation of the sensor signal to higher concentrations.

Besides this increase in sensitivity the response and decay times are substantially faster in the illuminated case. Also the asymmetry between response and decay time is reversed (t_{90} times for response and decay are shown in Table 2).

The response time in the illuminated case is slightly longer at low and high ozone concentrations (e.g., $t_{90\ \mathrm{res.,2.4\ ppm}} = 2.0$ min, $t_{90\ \mathrm{dec.,\ 2.4\ ppm}} = 1.3$ min). This behavior is typically observed for “redox”-type mechanisms [101].

In the non-illuminated case the decay time is more than twice as long as the response time (e.g., $t_{90\ \mathrm{res.,2.4\ ppm}} = 15.86$ min, $t_{90\ \mathrm{dec.,\ 2.4\ ppm}} = 75$ min) which is a known behavior for an adsorption-/desorption-dominated sensing mechanism. This is consistent with the asymmetric behavior of In_2O_3 to oxidizing and reducing gases. Oxygen incorporation into the lattice is fast while reduction is rather slow.

For most gas-sensing measurements a cross-sensitivity to humidity occurs. Especially at low temperature it is expected to play a major role since relatively stable hydroxyl groups can be formed at the surface. Therefore the influence of humidity to the illuminated In_2O_3 sensor was also studied.

Figure 21 shows the sensor’s characteristic to ozone at concentrations (from 20 ppb to 1.5 ppm) at 20% and 40% relative humidity, respectively. For both humidity levels the response is not linear but shows a saturating behavior. As described before there is an equilibration between oxidation and reduction of the material involving intermediate ionosorbed species at the surface. The number of surface states available will modulate the sensors response. Therefore it seems reasonable to use a model that describes surface coverage, such as the Langmuir model, as a first approximation for the sensor’s behavior. A least-square fit of the Langmuir equation,

$$\mathrm{Response} = \frac{c \cdot K_L \cdot q_{\max}}{1 + K_L \cdot c}, \tag{11}$$

(with the ozone concentration c, an empirical, material-specific constant K_L, and the maximum adsorbate concentration at the surface $q_{\max}$), results in the data presented in Table 3.

It has to be kept in mind, though, that the relation between the response and the number of adsorbed molecules is not quantitatively defined. As discussed before, the sensing signal, especially for In_2O_3, is not only correlated to ionosorption effects. The detailed reaction mechanism also plays a major role.

However, since the constant K_L accounts for the curvature of the graph, it may be used as a measure for some semiquantitative statements as, e.g., the correlation of the saturation behavior with other influence factors. A higher coefficient corresponds to saturation at lower adsorbate partial pressure. Since

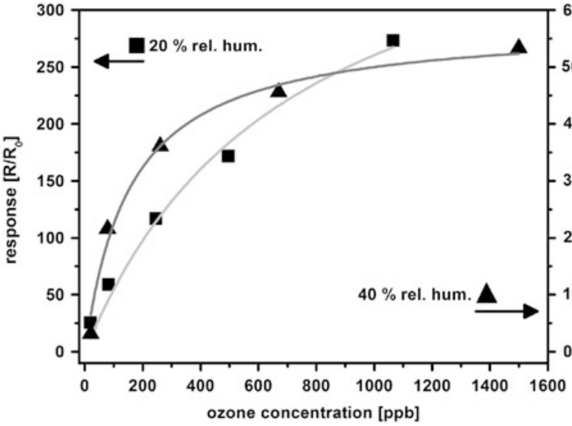

Fig. 21 Sensor response values of an illuminated sensor at room temperature. Characteristic curves have been recorded at 20% (*squares*) and 40% (*triangles*) relative humidity; a least-square fit of the Langmuir isotherm was performed (the *solid lines*, see text) [84]

Table 3 Fitting results (least-square method) of the Langmuir isotherm equation to the sensors response vs. ozone concentration (Fig. 21)

Humidity (%)	K_L	q_{max}
20	0.0014	447
40	0.0064	579

K_L is the "Langmuir coefficient"; q_{max} is the maximum surface coverage of adsorbed molecules [84]

this effect is not in the main scope of this article, results are only summarized briefly. It is assumed that the difference in the two characteristics is based on the different number of surface hydroxyl groups blocking the active sites of the metal oxide [102]. There are two major effects of these groups: First, hydroxyl groups are known to catalyze the ozone decomposition [9]. In case of a high amount of surface hydroxyl groups the number of ozone molecules reaching the surface and therefore the resistance change associated with this will be diminished. Second, at the same time, the baseline resistance is lower for hydroxylated In_2O_3 surface leading to an overall increase in response. The hydroxyl groups are also responsible for the second effect. Since they block ozone reaction sites at the surface the surface saturates faster at higher relative humidity (for more details see [84]).

6.2 NO_2 Sensing

Another important target gas with oxidizing properties is NO_2 which is a hazardous product in various combustion processes. Similar to ozone it is also highly reactive at low temperature. In the following comparative measurements with ordered mesoporous and nonstructured In_2O_3 are presented. Also various operating temperatures have been tested with and without illumination by a UV

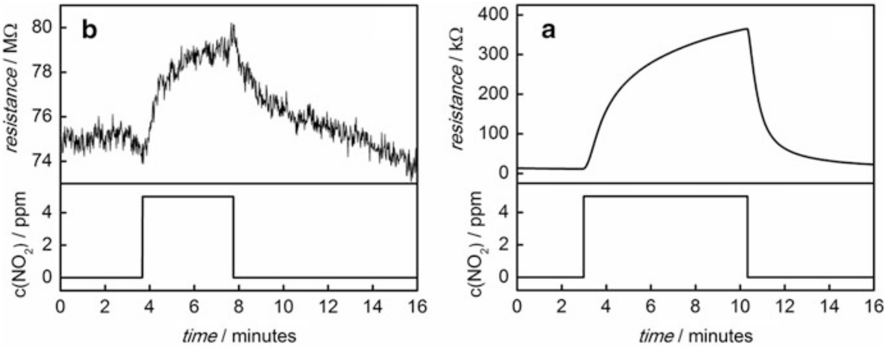

Fig. 22 Reference resistance measurement of nonstructured In_2O_3 (*left*) compared to ordered mesoporous In_2O_3 (*right*) in dry synthetic air at 200°C operating temperature and 5 ppm NO_2 exposure [73]

LED with a peak emission wavelength of 400 nm. To investigate the influence of the illumination reference measurements have been performed without illumination. Figure 22 shows the resistance of ordered mesoporous and nonstructured In_2O_3 upon exposure to 5 ppm NO_2 at 200°C. Both sensing layers respond to NO_2; however the baseline resistance of the nonstructured material is much higher (about 76 MOhm) than that of the mesoporous material (12 kOhm). The high resistance is one reason for the low response (defined again as R/R_0 where R and R_0 are the electronic resistances in the presence and absence of the test gases, respectively) of only 0.06 compared to 26.3 for the mesoporous material. This is mainly attributed to the 10 times larger number of grain-to-grain contacts in the nonstructured In_2O_3 sensing layer. The grain size of the nonstructured material is ca. 40 nm whereas the ordered mesoporous particles are up to 300 nm in size. Additionally the mesoporous material offers a higher specific surface area which also will increase sensor response.

Besides the lower response the nonstructured material fails to qualify for practical (room temperature) applications since with typical (inexpensive) measurement circuits it is not possible to measure such high resistance values. As can be seen in Fig. 22 the noise level is already rather high even under laboratory conditions. This is the reason why a temperature of 200°C was chosen for this measurement even though it is above the optimum operating temperature for NO_2 detection (see next pages).

The situation is substantially improved when the sensors are illuminated with UV light. Because of the above-described effects (electron–hole pair generation, photoreduction) the charge carrier density increases and the baseline resistance for both materials decreases. This facilitates gas-sensing measurements even at room temperature. In Fig. 23 the gas response for both materials at various temperatures under UV light exposure and 5 ppm NO_2 is shown. The optimum operating temperature in this measurement was 100°C for both materials. Even though it is possible to measure a gas response with the nonstructured material with

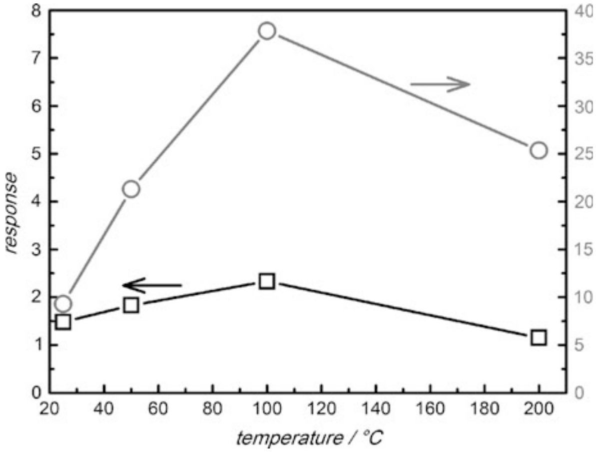

Fig. 23 Comparison of the response to 5 ppm NO_2 of nonstructured (*black*) and mesoporous In_2O_3 (*grey*) in dry synthetic air at various temperatures exposed to UV light [73]

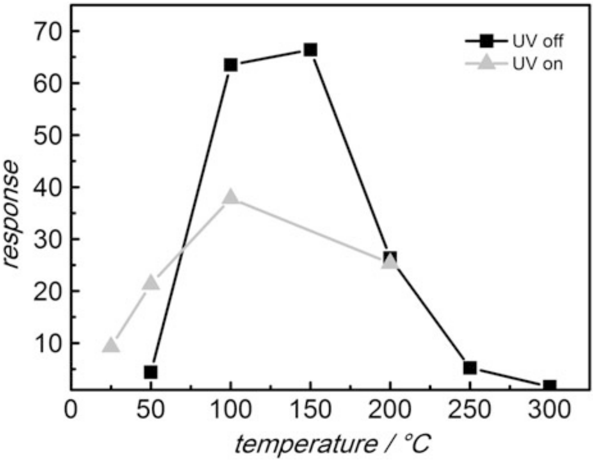

Fig. 24 Response of mesoporous In_2O_3 in dry synthetic air to 5 ppm NO_2 with and without UV illumination at various temperatures [73]

illumination at room temperature the mesoporous material shows a better performance (response of 37.8 at 100°C compared to 2.3 at 100°C for the nonstructured In_2O_3). Similar to the above-discussed ozone measurements the response of the mesoporous material is slightly lower in the illuminated case (25.3 with UV light compared to 26.3 without light at 200°C, see Fig. 24). This is again explained by photoreduction caused by the UV light.

To further analyze the influence of the UV light the response of the mesoporous material was also recorded without illumination at various operating temperatures (see Fig. 24). It is noticeable that at low temperatures ($<$100°C) the non-illuminated sensor shows a lower response than with illumination. Above this temperature (100°C $< T <$ 200°C) the response is lower in the illuminated case. This indicates that there are concurrent mechanisms dominating the different temperature regimes. The behavior in the low-temperature region can be explained analogously

Fig. 25 Comparison of the gas response of mesoporous In_2O_3 at 50°C operating temperature to 5 ppm NO_2 in dry synthetic air with and without UV illumination [80]

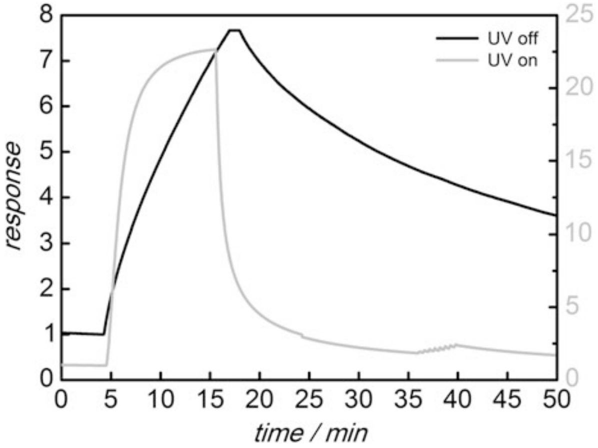

to the above-described behavior of the nonstructured material in the illuminated case. The decrease in baseline resistance is caused by free charge carriers induced by illumination leading to a higher response. Since at elevated temperature thermal activation starts to dominate (over the optical activation) there is an increasing amount of free charge carriers in the conduction band in both cases (illuminated and non-illuminated). Hence, the behavior is then controlled by photoreduction caused by illumination which overcompensates oxidation by NO_2. As a result the sensor response decreases compared to the non-illuminated case. Another reason for the decreasing response may be related to photodissociation of NO_2 caused by the UV light [103].

Even though the response is lower for the illuminated case this leads to higher dynamics of the sensor and saturation occurs at higher concentration (see last section, ozone measurements).

For practical purposes not only the response but also the transient behavior, e.g., reaction and regeneration rates of the sensor signal, is important. Figure 25 shows the comparison of the response of the illuminated and the non-illuminated mesoporous material at 50°C operating temperature to 5 ppm NO_2. The non-illuminated sensor does not reach a stable value after 15 min and an estimated t_{90} time is in the order of a few hours. The regeneration is even slower. That means that the sensor cannot be used without illumination for another measurement for a couple of days if it is not regenerated, e.g., by a heat treatment in between. However, as can be seen in the Fig. 25, the illumination does not only strongly increase response but also accelerate the response rate substantially. The t_{90} time is now less than 3.5 min. Likewise, regeneration occurs much faster for the illuminated signal; 10% of the maximum value is reached after ca. 15 min.

7 Conclusion

In_2O_3, especially in ordered mesostructured form, allows for a new type of room-temperature sensors especially for oxidizing gases. As could be demonstrated standard sensor models are not capable of describing the observed behavior of In_2O_3 in this temperature region. It was shown that, compared to standard materials like, e.g., tin dioxide (SnO_2), tungsten trioxide (WO_3), or gallium oxide (Ga_2O_3) indium oxide, the sensing mechanism is dominated by the in-and-out diffusion of oxygen into the crystal lattice leading to a change in donor concentration. The first activation energy of the related oxygen vacancy was measured utilizing temperature resolved in situ FT-IR to be 180 meV (which is a typical value for oxygen defects in metal oxides). Qualitative (mathematical) estimations prove that this is sufficient to explain the observed change in conductivity. Even though the redox-type model was introduced based on measurements on mesoporous structured In_2O_3 it is also applicable for nonstructured materials. In this case however slow oxygen diffusion into and out of the bulk leads to formation of thin chemical depletion layers (compared to the total grain size) which makes it difficult to distinguish it from chemisorption. Only the atypical selectivity to oxidizing gases such as ozone suggests some other mechanisms.

Another important property resulting from the proposed sensor model is the behavior under UV illumination (photoreduction) which accelerates the sensors reaction and regeneration. Especially for the mesoporous material which is due to the porous structure with its thin pore walls highly accessible to light and gas molecules this leads to improved sensing properties as was demonstrated on UV-enhanced ozone and NO_2 detection. With the mesoporous In_2O_3 room-temperature sensing seems possible. Because of the reduced energy consumption this therefore allows for application in battery-powered devices.

Acknowledgments The authors thank Claus-Dieter Kohl, Sara Morandi, Cesare Malagù, Mariangela Latino, and Giovanni Neri for the valuable discussions.

References

1. Morrison SR (1987) Selectivity in semiconductor gas sensors. Sens Actuator 12(4):425–440. doi:10.1016/0250-6874(87)80061-6
2. Kunt TA, McAvoy TJ, Cavicchi RE et al (1998) Optimization of temperature programmed sensing for gas identification using micro-hotplate sensors. Sens Actuators B Chem 53 (1–2):24–43. doi:10.1016/S0925-4005(98)00244-5
3. Sauerwald T (2007) Untersuchung von Oberflächenprozessen mit Einfluss auf die Multisignalgewinnung von SnO_2- und WO_3-Gassensoren. Dissertation, Justus-Liebig-Universität
4. Cabot A, Arbiol J, Cornet A et al (2003) Mesoporous catalytic filters for semiconductor gas sensors. In: Papers from the 3rd international seminar on semiconductor gas sensors, vol 436. pp 64–69. doi:10.1016/S0040-6090(03)00510-8

5. Wagner T, Haffer S, Weinberger C et al (2013) Mesoporous materials as gas sensors. Chem Soc Rev 42(9):4036–4053. doi:10.1039/C2CS35379B
6. Vincenzi D, Butturi MA, Guidi V et al (2001) Development of a low-power thick-film gas sensor deposited by screen-printing technique onto a micromachined hotplate. Proceeding of the eighth international meeting on chemical sensors IMCS-8 – Part 2. Sens Actuators B Chem 77(1–2):95–99. doi:10.1016/S0925-4005(01)00679-7
7. Faglia G, Comini E, Cristalli A et al (1999) Very low power consumption micromachined CO sensors. Sens Actuators B Chem 55(2–3):140–146. doi:10.1016/S0925-4005(99)00044-1
8. Takada T, Tanjou H, Saito T et al (1995) Aqueous ozone detector using In_2O_3 thin-film semiconductor gas sensor. Proceedings of the fifth international meeting on chemical sensors. Sens Actuators B Chem 25:548–551. doi:10.1016/0925-4005(95)85119-4
9. Takada T, Suzuki K, Nakane M (1993) Highly sensitive ozone sensor. Sens Actuators B Chem 13(1–3):404–407. doi:10.1016/0925-4005(93)85412-4
10. Ivanovskaya M, Gurlo A, Bogdanov P (2001) Mechanism of O_3 and NO_2 detection and selectivity of In_2O_3 sensors. Proceeding of the eighth international meeting on chemical sensors IMCS-8 – part 2. Sens Actuators B Chem 77(1–2):264–267. doi:10.1016/S0925-4005(01)00708-0
11. Wang CY, Cimalla V, Kups T et al (2007) Integration of In_2O_3 nanoparticle based ozone sensors with GaInN/GaN light emitting diodes. Appl Phys Lett 91(10):103509
12. Wirtz GP, Takiar HP (1981) Oxygen diffusion in vapor-deposited indium oxide films. J Am Ceram Soc 64(12):748–752. doi:10.1111/j.1151-2916.1981.tb15900.x
13. Bender M, Katsarakis N, Gagaoudakis E et al (2001) Dependence of the photoreduction and oxidation behavior of indium oxide films on substrate temperature and film thickness. J Appl Phys 90(10):5382–5387
14. Vollath D (2008) Nanomaterials: an introduction to synthesis, properties and application. Wiley-VCH, Weinheim, ISBN-10: 3527333797
15. Hoekstra HR, Gingerich KA (1964) High-pressure B-type polymorphs of some rare-earth sesquioxides. Science 146(3648):1163–1164
16. Prewitt CT, Shannon RD, Rogers DB et al (1969) The C rare earth oxide-corundum transition and crystal chemistry of oxides having the corundum structure. Inorg Chem 8(9):1985–1993. doi:10.1021/ic50079a033
17. Gurlo A, Kroll P, Riedel R (2008) Metastability of corundum-type In_2O_3. Chem Eur J 14 (11):3306–3310. doi:10.1002/chem.200701830
18. Chu D, Zeng Y, Jiang D et al (2007) Tuning the phase and morphology of In_2O_3 nanocrystals via simple solution routes. Nanotechnology 18(43):435605
19. Marezio M (1966) Refinement of the crystal structure of In_2O_3 at two wavelengths. Acta Cryst 20(6):723–728. doi:10.1107/S0365110X66001749
20. Harvey SP, Mason TO, Gassenbauer Y et al (2006) Surface versus bulk electronic/defect structures of transparent conducting oxides: I. Indium oxide and ITO. J Phys D Appl Phys 39 (18):3959–3968
21. Ivanovskaya M, Bogdanov P, Faglia G et al (2000) The features of thin film and ceramic sensors at the detection of CO and NO_2. Sens Actuators B Chem 68(1–3):344–350
22. Korotcenkov G, Brinzari V, Cerneavschi A et al (2002) Crystallographic characterization of In_2O_3 films deposited by spray pyrolysis. Sens Actuators B Chem 84(1):37–42
23. Korotcenkov G, Brinzari V, Cerneavschi A et al (2004) The influence of film structure on In_2O_3 gas response. Thin Solid Films 460(1–2):315–323
24. Golovanov V, Mäki-Jaskari MA, Rantala TT et al (2005) Experimental and theoretical studies of indium oxide gas sensors fabricated by spray pyrolysis. Sens Actuators B Chem 106(2):563–571
25. de Wit JHW (1973) Electrical properties of In_2O_3. J Solid State Chem 8(2):142–149
26. Weiher RL (1962) Electrical properties of single crystals of indium oxide. J Appl Phys 33 (9):2834–2839
27. de Wit JHW (1975) The high temperature behavior of In_2O_3. J Solid State Chem 13 (3):192–200

28. Agoston P, Erhart P, Klein A et al (2009) Geometry, electronic structure and thermodynamic stability of intrinsic point defects in indium oxide. J Phys Condens Matter 21(45):455801
29. Lany S, Zunger A (2007) Dopability, intrinsic conductivity, and nonstoichiometry of transparent conducting oxides. Phys Rev Lett 98(4):45501
30. Tomita T, Yamashita K, Hayafuji Y et al (2005) The origin of n-type conductivity in undoped In_2O_3. Appl Phys Lett 87(5):51911–51913
31. Cox SFJ, Davis EA, Cottrell SP et al (2001) Experimental confirmation of the predicted shallow donor hydrogen state in zinc oxide. Phys Rev Lett 86(12):2601. doi:10.1103/PhysRevLett.86.2601
32. Cox SFJ (2003) The shallow-to-deep instability of hydrogen and muonium in II–VI and III–V semiconductors. J Phys Condens Matter 15(46):R1727
33. Erhart P, Klein A, Egdell RG et al (2007) Band structure of indium oxide: indirect versus direct band gap. Phys Rev B 75(15):153205–4
34. Walsh A, Da Silva JLF, Wei S et al (2008) Nature of the band gap of In_2O_3 revealed by first-principles calculations and X-ray spectroscopy. Phys Rev Lett 100(16):167402–167404
35. Weiher RL, Ley RP (1966) Optical properties of indium oxide. J Appl Phys 37(1):299–302
36. Xirouchaki C, Kiriakidis G, Pedersen TF et al (1996) Photoreduction and oxidation of as-deposited microcrystalline indium oxide. J Appl Phys 79(12):9349–9352. doi:10.1063/1.362612
37. Matino F, Persano L, Arima V et al (2005) Electronic structure of indium-tin-oxide films fabricated by reactive electron-beam deposition. Phys Rev B 72(8):85437
38. Gassenbauer Y, Klein A (2006) Electronic and chemical properties of tin-doped indium oxide (ITO) surfaces and ITO/ZnPc interfaces studied in-situ by photoelectron spectroscopy. J Phys Chem B 110(10):4793–4801
39. King PDC, Veal TD, Fuchs F et al (2009) Band gap, electronic structure, and surface electron accumulation of cubic and rhombohedral In_2O_3. Phys Rev B 79(20):205211–10
40. Williams R (1965) Photoemission of electrons from silicon into silicon dioxide. Phys Rev 140(2A):A569
41. Abstreiter G, Prechtel U, Weimann G et al (1986) Internal photoemission – a suitable method for determining band offsets in semiconductor heterostructures. Surf Sci 174(1–3):313–317
42. Pan CA, Ma TP (1980) Work function of In_2O_3 film as determined from internal photoemission. Appl Phys Lett 37(8):714–716
43. Sarath Kumar SR, Kasiviswanathan S (2009) Role of oxygen vacancies in the high-temperature thermopower of indium oxide and indium tin oxide films. Semicond Sci Tech 24(025028):1–7
44. Abdullaev MA, Kamillov IK, Magomedova DK et al (2004) Effects of the preparation procedure and In_2O_3 thickness on the electrical and photovoltaic properties of In_2O_3 $CuInSe_2$ heterostructures. Inorg Mater 40(11):1181–1185. doi:10.1023/B:INMA.0000048218.96266.25
45. Li X, Zhang Q, Miao W et al (2006) Transparent conductive oxide thin films of tungsten-doped indium oxide. Thin Solid Films 515(4):2471–2474
46. Bellingham JR, Phillips WA, Adkins CJ (1990) Electrical and optical properties of amorphous indium oxide. J Phys Condens Matter 28:6207
47. Cho J, Yoon KH, Koh S (2000) Microstructure of indium oxide films in oxygen ion-assisted deposition. Thin Solid Films 368(1):111–115
48. Oprea A, Gurlo A, Barsan N et al (2009) Transport and gas sensing properties of In_2O_3 nanocrystalline thick films: a Hall effect based approach. Sens Actuators B Chem 139 (2):322–328
49. Tiemann M (2008) Repeated templating. Chem Mater 20(3):961–971
50. Lu A, Schüth F (2006) Nanocasting: a versatile strategy for creating nanostructured porous materials. Adv Mater 18(14):1793–1805. doi:10.1002/adma.200600148
51. Yang H, Zhao D (2005) Synthesis of replica mesostructures by the nanocasting strategy. J Mater Chem 15(12):1217–1231. doi:10.1039/B414402C
52. Roggenbuck J, Waitz T, Tiemann M (2008) Synthesis of mesoporous metal oxides by structure replication: strategies of impregnating porous matrices with metal salts. Micropor Mesopor Mat 113(1–3):575–582

53. Schüth F (2003) Endo- and exotemplating to create high-surface-area inorganic materials. Angew Chem Int Edit 42(31):3604–3622. doi:10.1002/anie.200300593
54. Valdés-Solís T, Fuertes AB (2006) High-surface area inorganic compounds prepared by nanocasting techniques. Mater Res Bull 41(12):2187–2197. doi:10.1016/j.materresbull.2006.04.018
55. Wan Y, Yang H, Zhao D (2006) "Host – Guest" chemistry in the synthesis of ordered nonsiliceous mesoporous materials. Acc Chem Res 39(7):423–432. doi:10.1021/ar050091a
56. Kondo JN, Domen K (2007) Crystallization of mesoporous metal oxides†. Chem Mater 20 (3):835–847. doi:10.1021/cm702176m
57. Lu A, Zhao D, Wan Y (2010) Nanocasting. A versatile strategy for creating nanostructured porous materials. RSC Nanoscience & Nanotechnology, Royal Society of Chemistry, Cambridge
58. Ren Y, Ma Z, Bruce PG (2012) Ordered mesoporous metal oxides: synthesis and applications. Chem Soc Rev 41(14):4909–4927. doi:10.1039/C2CS35086F
59. Liang C, Li Z, Dai S (2008) Mesoporous carbon materials: synthesis and modification. Angew Chem Int Ed 47(20):3696–3717. doi:10.1002/anie.200702046
60. Xia Y, Yang Z, Mokaya R (2010) Templated nanoscale porous carbons. Nanoscale 2 (5):639–659. doi:10.1039/B9NR00207C
61. Thomas A, Goettmann F, Antonietti M (2008) Hard templates for soft materials: creating nanostructured organic materials†. Chem Mater 20(3):738–755. doi:10.1021/cm702126j
62. Tüysüz H, Schüth F (2012) Ordered mesoporous materials as catalysts. Adv Catal 55:127–239
63. Soler-Illia GJ, Sanchez C, Lebeau B et al (2002) Chemical strategies to design textured materials: from microporous and mesoporous oxides to nanonetworks and hierarchical structures. Chem Rev 102(11):4093–4138
64. Wan Y, Zhao D (2007) On the controllable soft-templating approach to mesoporous silicates. Chem Rev 107(7):2821–2860. doi:10.1021/cr068020s
65. Waitz T, Wagner T, Sauerwald T et al (2009) Ordered mesoporous In_2O_3: synthesis by structure replication and application as a methane gas sensor. Adv Funct Mater 19 (4):653–661. doi:10.1002/adfm.200801458
66. Yang H, Shi Q, Tian B et al (2003) One-step nanocasting synthesis of highly ordered single crystalline indium oxide nanowire arrays from mesostructured frameworks. J Am Chem Soc 125(16):4724–4725. doi:10.1021/ja034005i
67. Tian B, Liu X, Yang H et al (2003) General synthesis of ordered crystallized metal oxide nanoarrays replicated by microwave-digested mesoporous silica. Adv Mater 15 (16):1370–1374. doi:10.1002/adma.200305211
68. Prim A, Pellicer E, Rossinyol E et al (2007) A novel mesoporous CaO-loaded In_2O_3 material for CO_2 sensing. Adv Funct Mater 17(15):2957–2963. doi:10.1002/adfm.200601072
69. Tiemann M (2007) Porous metal oxides as gas sensors. Chem Eur J 13(30):8376–8388. doi:10.1002/chem.200700927
70. Waitz T, Becker B, Wagner T et al (2010) Ordered nanoporous SnO_2 gas sensors with high thermal stability. Sens Actuators B Chem 150(2):788–793. doi:10.1016/j.snb.2010.08.001
71. Wagner T, Krotzky S, Weiß A et al (2011) A high temperature capacitive humidity sensor based on mesoporous silica. Sensors 11(12):3135–3144. doi:10.3390/s110303135
72. Gurlo A, Barsan N, Ivanovskaya M et al (1998) In_2O_3 and MoO_3-In_2O_3 thin film semiconductor sensors: interaction with NO_2 and O_3. Sens Actuators B Chem 47(1–3):92–99
73. Wagner T, Kohl C, Malagù C et al (2013) UV light-enhanced NO_2 sensing by mesoporous In_2O_3: interpretation of results by a new sensing model. Sens Actuators B Chem 187:488–494. doi:10.1016/j.snb.2013.02.025
74. Bourgoin JC, Corbett JW (1978) Enhanced diffusion mechanisms. Radiat Eff 36(3):157–188. doi:10.1080/00337577808240846
75. Ding J, McAvoy TJ, Cavicchi RE et al (2001) Surface state trapping models for SnO_2-based microhotplate sensors. Sens Actuators B Chem 77(3):597–613

76. Bárdos L, Libra M (1989) Effect of the oxygen absorption on properties of ITO layers. Special issue polymer physics. Vacuum 39(1):33–36
77. Kissine VV, Voroshilov SA, Sysoev VV (1999) A comparative study of SnO_2 and SnO_2:Cu thin films for gas sensor applications. Thin Solid Films 348(1–2):304–311
78. Ruhland B, Becker T, Müller G (1998) Gas-kinetic interactions of nitrous oxides with SnO_2 surfaces. Sens Actuators B Chem 50(1):85–94
79. Kamp B, Merkle R, Maier J (2001) Chemical diffusion of oxygen in tin dioxide. Sens Actuators B Chem 77(1–2):534–542
80. Wagner T, Kohl C, Morandi S et al (2012) Photoreduction of mesoporous In_2O_3: mechanistic model and utility in gas sensing. Chem Eur J. doi:10.1002/chem.201103905
81. Heiland G, Mollwo E, Stöckmann F (1959) Electronic processes in zinc oxide. Adv Solid State Phys 8:191
82. Fritzsche H, Pashmakov B, Claflin B (1994) Reversible changes of the optical and electrical properties of amorphous InO_x by photoreduction and oxidation. Special issue dedicated to Professor Bernhard Seraphin. Sol Energ Mat Sol C 32(4):383–393
83. Faglia G, Baratto C, Comini E et al (2004) Metal oxide nanocrystals for gas sensing. In: IEEE sensors 2004 conference, Vienna. p 182
84. Wagner T, Hennemann J, Kohl C et al (2011) Photocatalytic ozone sensor based on mesoporous indium oxide: influence of the relative humidity on the sensing performance. Special section: proceedings of 7th international workshop on semiconductor gas sensors. Thin Solid Films 520(3):918–921. doi:10.1016/j.tsf.2011.04.181
85. Pashmakov B, Claflin B, Fritzsche H (1993) Photoreduction and oxidation of amorphous indium oxide. Solid State Commun 86(10):619–622
86. Dixit A, Panguluri RP, Sudakar C et al (2009) Robust room temperature persistent photoconductivity in polycrystalline indium oxide films. Appl Phys Lett 94(25):252105–3
87. Ghiotti G, Chiorino A, Boccuzzi F (1993) Surface chemistry and electronic effects of H2 (D2) on two different microcrystalline ZnO powders. Surf Sci Lett 287–288:A380. doi:10.1016/0167-2584(93)90425-I
88. Ghiotti G, Chiorino A, Prinetto F (1995) Chemical and electronic characterization of pure SnO_2 and Cr-doped SnO_2 pellets through their different response to NO. Proceedings of the fifth international meeting on chemical sensors. Sens Actuators B Chem 25:564–567. doi:10.1016/0925-4005(95)85123-2
89. Chiorino A, Ghiotti G, Prinetto F et al (1997) Characterization of SnO_2-based gas sensors. A spectroscopic and electrical study of thick films from commercial and laboratory-prepared samples. Sens Actuators B Chem 44(1–3):474–482. doi:10.1016/S0925-4005(97)00238-4
90. Lenaerts S, Roggen J, Maes G (1995) FT-IR characterization of tin dioxide gas sensor materials under working conditions. Spectrochim Acta A Mol Biomol Spectrosc 51 (5):883–894. doi:10.1016/0584-8539(94)01216-4
91. Jarzebski ZM (1976) Physical properties of SnO_2 materials. J Electrochem Soc 123(9):299C. doi:10.1149/1.2133090
92. Jarzebski ZM (1976) Physical properties of SnO_2 materials. J Electrochem Soc 123 (10):333C. doi:10.1149/1.2132647
93. Göpel W, Lampe U (1980) Influence of defects on the electronic structure of zinc oxide surfaces. Phys Rev B 22(12):6447–6462. doi:10.1103/PhysRevB.22.6447
94. Hausmann A, Schallenberger B (1978) Interstitial oxygen in zinc oxide single crystals. Z Physik B 31(3):269–273. doi:10.1007/BF01352351
95. Samson S, Fonstad CG (1973) Defect structure and electronic donor levels in stannic oxide crystals. J Appl Phys 44(10):4618–4621
96. Cao H, Qiu X, Liang Y et al (2003) Room-temperature ultraviolet-emitting In_2O_3 nanowires. Appl Phys Lett 83(4):761–763
97. Malagu C, Giberti A, Morandi S et al (2011) Electrical and spectroscopic analysis in nanostructured SnO_2: "Long-term" resistance drift is due to in-diffusion. J Appl Phys 110 (9):93711–93715

98. Shur M (1990) Physics of semiconductor devices. Prentice Hall series in solid state physical electronics. Prentice Hall, Englewood Cliffs
99. Naydenov A, Stoyanova R, Mehandjiev D (1995) Ozone decomposition and CO oxidation on CeO_2. J Mol Catal A 98(1):9–14
100. Mills A, Lee S, Lepre A (2003) Photodecomposition of ozone sensitised by a film of titanium dioxide on glass. J Photoch Photobio A 155(1–3):199–205
101. Korotcenkov G, Ivanov M, Blinov I et al (2007) Kinetics of indium oxide-based thin film gas sensor response: the role of "redox" and adsorption/desorption processes in gas sensing effects. Thin Solid Films 515(7–8):3987–3996. doi:10.1016/j.tsf.2006.09.044
102. Thiel PA, Madey TE (1987) The interaction of water with solid surfaces: fundamental aspects. Surf Sci Rep 7(6–8):211–385. doi:10.1016/0167-5729(87)90001-X
103. Roehl CM, Orlando JJ, Tyndall GS et al (1994) Temperature dependence of the quantum yields for the photolysis of NO_2 near the dissociation limit. J Phys Chem 98(32):7837–7843. doi:10.1021/j100083a015

SAW and Functional Polymers

Adnan Mujahid and Franz L. Dickert

Abstract In modern sensor design, researchers are focused to develop accurate, miniaturized, portable, and highly sensitive devices for online monitoring in different fields. Surface acoustic wave (SAW) resonators are center of interest for their excellent response, exceptional transducing ability, small size, ruggedness, and tunable frequency for getting superior sensitivity. Based on the dimensions of interdigital electrodes, type of substrate material, and coating interface, they can be tailored according to desired application and nature of working environment. The sensing interface of SAW devices can be fabricated with a variety of suitable materials ranging from metal oxide films, nanoparticles, supramolecular structures, molecular imprinted polymers, carbon nanotubes and their composites, self-assembled monolayers, and other polymeric hybrid materials. Their sensor applications cover a wide range, e.g. detection of toxic volatile organic compounds, explosive vapors, chemical warfare agents, humidity, NO_x, and a variety of other gaseous analytes. SAW-based multisensor arrays are of utmost importance due to their outstanding recognition ability in complex mixtures and thus making them ideally suited for designing e-noses. This article deals with the potential sensor applications of SAW devices coated with different polymeric receptor materials.

Keywords Piezomaterials, Polymers, SAW, Sensor array, Volatile organic compounds

---

A. Mujahid
Department of Analytical Chemistry, University of Vienna, Waehringerstrasse 38,
1090 Vienna, Austria

Institute of Chemistry, University of the Punjab, Quaid-i-Azam campus,
Lahore 54590, Pakistan

F.L. Dickert (✉)
Department of Analytical Chemistry, University of Vienna, Waehringerstrasse 38,
1090 Vienna, Austria
e-mail: franz.dickert@univie.ac.at

C.-D. Kohl and T. Wagner (eds.), *Gas Sensing Fundamentals*,
Springer Series on Chemical Sensors and Biosensors (2014) 15: 213–246
DOI 10.1007/5346_2013_55,

Contents

1 Introduction

Recent developments in sensor technology clearly indicate that scientists are paying more attention to accurate and small devices having relatively much lower cost for various analyses. One of the main drawbacks of conventional analytical tools is that most of them are not efficient for online measurements during field analysis. Undoubtedly, they are highly sensitive, accurate and provide reproducible values with suitable detection limits. Nonetheless, they are expensive, being large in size, required highly skilled personnel to operate and are not rugged for field measurements. Therefore, the quest for designing sensitive and selective sensors [1] has now been extended vastly in modern research. Miniaturization [2] is the key in order to make them real alternative for online applications [3]. Their ruggedness is also an important point when working in harsh environments [4] and complex matrices. Eventually keeping all these valuable features, the cost of chemical sensor should be low enough for commercialization and routine use.

Surface acoustic wave (SAW) devices offer all these characteristics for being employed as principal transducer for building advanced chemical sensors [5]. They are small in size, possess high resonating frequency, robust for multifaceted analysis and have relatively low cost. SAW, basically are mass-sensitive resonators [6] which provides a direct change in resonance frequency upon interaction with target analyte.

Although the market of optical biosensors [7] is much broad in contrast to acoustic devices, however, later one offers more advantages over the former one. The most striking feature is their label or marker-free detection [8] of binding events which makes them universal transducers for the sensing of virtually all types of analytes. In former cases, SAW usually operates in gaseous phase only since it cannot be subjected to liquid medium due to excessive damping issues. The new generation of SAW devices [9] can work excellently in liquid environments without serious problems. Choice of the substrate material and cutting angle solves the problem thus avoiding too much loss of acoustic energy.

The selection of SAW sensing element is also very important in order to obtain highly selective response of target analytes. There is a broad spectrum of sensitive materials that have been developed according to the analyte of interest such as volatile organic compounds (VOCs) [10], nerve agent stimulants [11], explosives, toxic gases, chemical warfare agents [12] and many others. During the last decade, various materials have been explored including metal oxide nanoparticles [13] and nanorods [14], supramolecular structures [15], carbon nanotubes [16], molecular imprinted polymers [17], hyper-branched hydrogen-bond acidic [18], basic [19] polymers, and other artificial receptors. They offer adequate sensitivity and robustness; however, the most imperative point in their selection is their processability [20] into thin films and applicability to diverse analyte species especially when developing a sensor array [21]. Regeneration of sensor surface is also essential so as to use them for several times with reproducible results.

Polymers [22] are the most favorite choice for crafting state-of-the-art sensor materials [23] in accordance with SAW devices. They accomplish high class selectivity for binding the target molecule, robust against severe media actions, reusable and moreover preferred for pattern recognition in constructing sensor arrays. The functionality of the polymers can be tuned to establish desired chemical interactions with a wide variety of analytes of varying polarity and size. Some of the polymers are commercially available and by slight modification they can be grafted on SAW interface. However, to deal with diverse analytes and aiming high performance, we have to synthesize different polymers, e.g. molecular imprinted polymers and hydrogen-bond acidic hyperbranched polymers. During the synthesis, they are tailored for geometrical fit, solubility, and electrostatic interactions with host polymer chains. They can be coated on SAW devices in several ways such as spin coating, spray coating, and Langmuir–Blodgett.

In this chapter, we will spell out the basic principle, theory, and transduction mechanism of SAW devices both in gas and liquid environments following the polymer sensor chemistry and their prospective applications in different fields.

2 Basic Principle and Theory of SAW Resonators

SAW devices are basically mass-sensitive or acoustic resonators [24] those are made of piezoelectric crystal materials [25]. Piezoelectric effect was pointed first by Pierre Curie and Jacques Curie [26, 27] in 1880 when they observed that applied mechanical stress polarized the piezoelectric crystals. The reverse was also true as mathematically

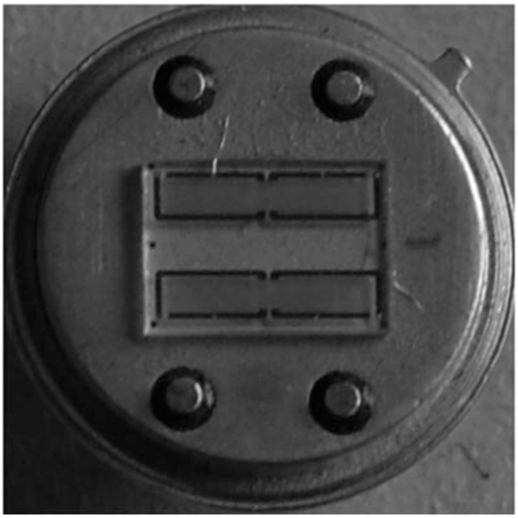

Fig. 1 A typical SAW dual delay line device (Siemens Munich)

calculated by Lippman in 1881[28] and later confirmed by Curie brothers. The idea of surface waves was presented in 1885 by Lord Raleigh [29] in his historical paper in which he discovered the phenomena of surface waves and explained the wave propagation at the interface of elastic solids. Since from name it is understandable that in these devices the oscillations are confined to surface of the substrate material. They had broad range of applications in building oscillators, narrow bandwidth frequency filters, micro and nanostructuring in computer chips and most prominently in development of biosensors. A technological image of a dual delay line SAW resonator has been shown in Fig. 1.

In principle, surface waves have both longitudinal and shear wave components that can couple with the substrate surface and travel nondispersively. If we follow the design of a classical SAW resonator, interdigital electrodes are fabricated in a comblike structure on piezosubstrate. A chemical sensitive layer is uniformly coated on transmitter and receiver end, i.e. called interdigital transducers (IDT). On applying voltage across the electrodes, the surface particles of piezocrystal are displaced from their position and as a result Rayleigh waves are produced that propagate along the surface of substrate material and travel through chemical sensor layer. These waves are collected at receiver transducer where they are retransformed into electronic signal. The wave energy is concentrated to the surface layer and thus is independent of the bulk substrate material. The absorbers or reflectors absorb/reflect back the Rayleigh waves to the transducers ensuring the proper resonance of the device. The typical design of SAW resonator has been illustrated in Fig. 2. In the design of SAW resonators, the dimension, i.e. length, width, and depth of interdigital electrodes, strongly influences the performance of the device.

The IDT can be fabricated by photolithographic process [30] using light sensitive coating on substrate. The dimensions of IDT can also be optimized with high accuracy in size and depth following lift-off technique. This method enables to

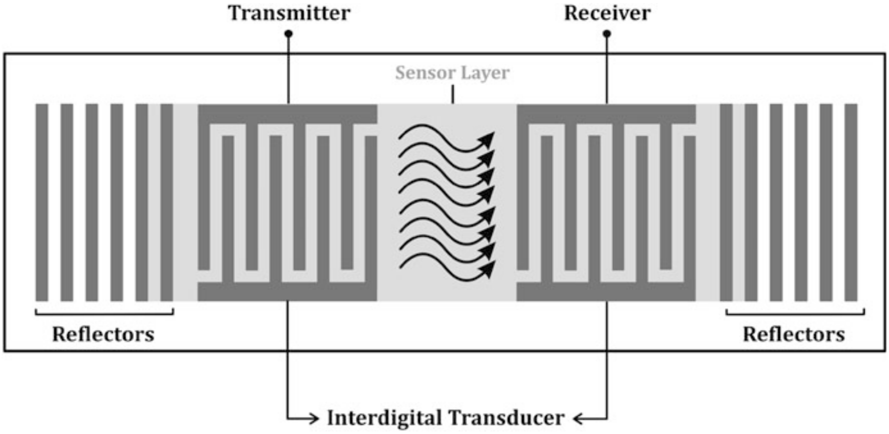

Fig. 2 Design and propagation of surface waves in SAW devices

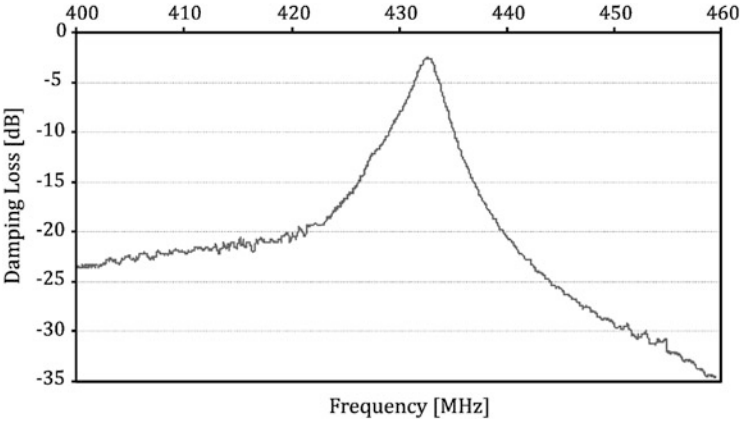

Fig. 3 Resonance spectrum of 433 MHz SAW

control the microstructuring on substrate minimizing undesirable features in contrast to the conventional etching process. The damping spectrum of 433 MHz has been shown in Fig. 3.

2.1 Piezomaterials for SAW Manufacturing

For manufacturing SAW devices, there are several piezoelectric materials [31, 32] both natural and synthetic those are used; quartz is the most common material that is taken in ST-cut form. The choice of piezomaterial depends upon nature of application such as temperature coefficients, wave propagation mode, dielectric constant of substrate, and the ultimate cost of the material. Quartz [33] is most widely used

Table 1 Characteristics of common piezomaterials used for SAW manufacturing

Piezomaterial	Cutting angle	Temperature coefficient (ppm/°C)	Dielectric constant	Piezoelectric constant (pC/N)	SAW velocity (m/s)
Quartz	ST–X	0	3.7	2.3	3,158
$LiTaO_3$	X–112°Y	–18	52	9.2	3,290
$LiNbO_3$	128°Y–X	–74	83	6.0	3,960
ZnO–glass	–	–15	10	12.4	3,150

piezomaterial because of its minor temperature coefficient and relatively much lower cost; however, it cannot be used above 500°C temperature due to phase transition problem. Gallium orthophosphate ($GaPO_4$) [34] and Langasite ($La_3Ga_5SiO_{14}$) [35] are similar to quartz but very stable at high temperatures and can be adopted for above 900°C applications. For instance, quartz has a small dielectric constant, i.e. 3.8, that restricts its use in polar environments; thus piezomaterials with high dielectric constants are needed. Lithium tantalate ($LiTaO_3$) [36] has dielectric constant of nearly 40 and is suitable for liquid-phase operation. Table 1 gives a concise picture of different piezomaterials with their characteristic features for building SAW resonators.

2.2 SAW Resonators in Liquid Phase

SAW devices are usually applied for gas phase sensing; they are not suitable for liquid-phase operations. The reason is quite obvious that longitudinal component of Rayleigh waves propagates [37] perpendicular to the surface which results in high damping loss due to the viscosity of the liquids at solid SAW interface. The situation becomes more critical when in contact liquid is highly polar and substrate material has also high electromechanical coupling constant. This contributes to high dielectric loss, e.g. quartz has dielectric value 3.8, so when it is in contact to water that has dielectric constant near 80 as a result a short circuit is produced, and we see no resonance as shown in Fig. 4.

The problem can be solved in two ways: first, the cutting angle of piezomaterial is rotated in such a way that shear transverse waves are generated. Shear waves propagate entirely along the surface in contrast to Rayleigh waves thus consequently less damping loss. Second, the selection of a piezomaterial of relatively high dielectric constant. In this regard, $LiTaO_3$ has dielectric value 40 which is fairly comparable to water and so short circuiting can be avoided. A damping spectrum of quartz and $LiTaO_3$ in water [38] has been plotted in Fig. 4. As one can see that there is virtually no resonance for quartz in water while $LiTaO_3$ has suitable resonance. Love waves are also considered for liquid-phase sensor operations. If we categorize, there are three general types of SAW devices used for sensors:

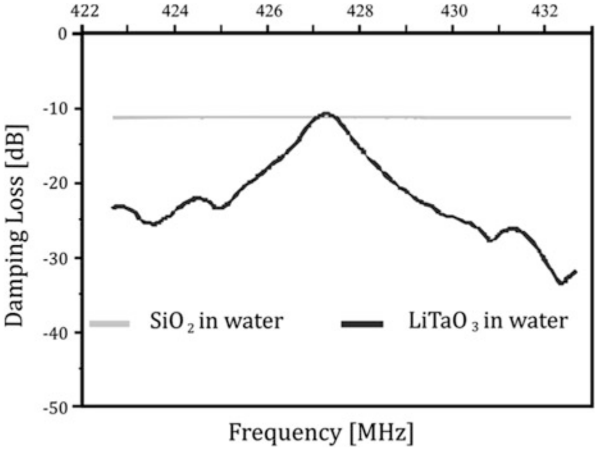

Fig. 4 Resonance spectrum of Quartz (SiO_2) and $LiTaO_3$ in water, adopted from [38]

- Rayleigh wave sensors
- Lamb/flexural plate wave sensors
- Love wave sensors

In the first two types of sensors, wave propagation is perpendicular to the substrate surface; therefore, they are used mostly in gaseous phase as the waves are damped in liquids. However, Lamb wave or flexural plate wave [39] sensors with extremely fine thickness can be used in liquid environments since they do not dissipate all the energy. Lamb waves travel with less velocity in films than in liquids which render small energy loss in contrast to SAW devices. But due to very small thickness of the device, i.e. few micrometers, makes them fragile; thus the microstructuring of electrodes and handling become extremely difficult.

Love wave sensors are most sensitive acoustic devices and can be used in liquids [40] since in these devices shear horizontal waves are produced in guiding layer, i.e. a solid overlayer is deposited on substrate material. Guiding layer confines the energy between upper and lower interface which helps for making detection on either side. In this way, one side contains the IDT which are isolated from conductive and isotropic liquids, while other side works as sensing interface. This also helps in protecting the electrodes from solvent effects.

2.3 Frequency Sensitivity Relationship

In SAW devices, the measured sensor response is the corresponding shift in resonating frequency of the device. Sauerbrey [41] had provided a quantitative relationship between fundamental resonance frequency and the deposited mass on acoustic device. The character of piezoelectric substrate material, i.e. density and shear modulus, piezoelectric active area, loaded mass, and intrinsic frequency, all contribute to the sensor effect. However, keeping all the constants apart, sensor signal is directly proportional to the square of the fundamental resonance frequency provided that the loaded mass is rigid. The nature of deposited mass greatly influences the performance of SAW resonator since viscoelastic behavior of coated material effects the device frequency and propagation speed.

$$\Delta f = (k_1 + k_2)\rho h {f_o}^2 - k_2 h {f_o}^2 \left[\frac{4\mu(\lambda + \mu)}{V^2(\lambda + 2\mu)} \right]$$

Above equation summarizes the sensor response of SAW device [42] coated with a thin layer of nonconductive material. This relationship covers all the physical aspects of coated substance and their influence on wave propagation. In this equation, h is the film height, ρ is the density of film, μ is the shear modulus of film, v is the propagation velocity, f_o is the fundamental frequency, k_1 and k_2 are substrate constants, λ is the Lamb constant, Δf is the change in frequency or pure sensor effect due to mass loading.

In SAW devices, the amplitude of the waves decays exponentially with increasing thickness of substrate and as we know acoustic energy is confined to the surface, this make these devices extremely sensitive to any change at chemical layer interface.

Fundamental resonance frequency is the most important factor to attain higher sensitivity and thus lowering the detection limits, i.e. below one picogram. Since sensor response is directly proportional to the square of fundamental frequency. In principle, with the increasing resonance frequency of SAW devices, the penetrating depth decreases. Generally, SAW devices are operated between 25 and 500 MHz; however, in some cases higher-frequency resonators up to 1 GHz [43] are also reported for sensor applications. Further higher-frequency device is very difficult to realize for sensor applications due to IDT design constraints.

The thickness of coating material plays also a vital role for getting pronounced sensitivity and controlling the noise level of device. Films with greater thickness interact with high sample volume thus leading to an increased surface roughness and noise. This becomes more evident when working in liquid environments; it has been observed that films with reduced layer heights work more efficiently. The other advantage is that the thin layers respond much faster than more thick films.

2.4 Sensitivity Interfering Factors

In SAW sensors, a shift in frequency is not always an indicator for mass loading on thin films. This could also be due to the changes in density of medium and viscoelastic coupling phenomena. These factors strongly affect the wave propagation velocity and phase thus leading to false sensor signals. Of course, these factors are more critical when developing SAW sensors for liquid phase and thus become the real challenge. We had earlier explained the possibilities to overcome these problems in Sect. 2.2; however, there are some other important factors that also lead to unwanted sensor response. For example, temperature [44] and relative humidity [45] level of working environment have significant contribution on SAW frequency shift. It has been noticed that 1 K rise in temperature increases frequency of SAW resonator about 40–100 Hz in gaseous phase which is large enough to interfere with pure sensor response. In liquid phases, temperature affects more seriously due to the much higher density and viscosity. A dual port SAW resonator [46] would be suitable for temperature compensation while performing differential measurements. In this way, frequency shifts due to temperature variations can be avoided.

Relative humidity [47] also plays its role on sensor performance and becomes more crucial when the coating element is hydrophilic in nature. However, in some cases, SAW resonators have been used for monitoring relative humidity levels. Greibl et al. [48] had observed that uncoated SAW resonator at humidity level below 20% increases the frequency slightly due to change in elastic behavior. Whereas going above from 20%, there is a substantial decrease in frequency due to strong interaction of water vapors with silanol group at substrate interface, i.e. quartz.

In general, SAW devices are state-of-the-art sensors which have several advantages over conventional analytical tools and other sensing devices. Miniaturized design, exceptionally high sensitivity and the compatibility with various coating materials are the hallmark of these transducers. Therefore, they are considered most suitable devices for monitoring the binding events at chemical layer interface. Despite the fact that SAW sensors are mostly applied for gas phase application, they however have suitable potential for being used in liquids with adequate sensitivity. The other noticeable feature is that being an acoustic device, they offer marker-free detection, i.e. giving a direct change in frequency shift on mass loading. Carefully crafted chemical layer brings selectivity, i.e. more responsive towards the target analyte in comparison to other analogous compounds. In any sensor design apart from transducer characteristics, coating material has to play the major role for getting enhanced sensitivity and selectivity. There are various sensitive materials available for coating SAW sensors; nevertheless, as earlier mentioned functional polymers are highly suitable as sensing interface. Following section will discuss the potential of polymers as sensing element for SAW devices.

3 Polymers as Sensing Interface

In selection of a suitable coating matrix, one has to think about their processability with the transducer surface. The inherent robustness and rigidness are also vital for getting stable and harder layers that are resistive against extreme environments and useful for longer use. Straightforward regeneration of the sensor layer after analyte adsorption is highly desirable for getting reproducible results. In general, every coating material is not solely responsive towards a particular analyte but it shows a certain pattern for structurally related compounds. However, coating matrices can be optimized to interact more specifically and minimize the unwanted adherence. Polymeric layers have been widely adopted as SAW sensor coatings for meeting all these prerequisites. One of the prominent features is that they can easily be processed into thin films of customized layer height for coating SAW resonators.

A variety of polymers have been studied as sensing element with SAW devices including functional organic polymers, conductive polymers, molecular imprinted polymers, hyper-branched acid polymers and others.

3.1 Functional Organic Polymers

Functional organic polymers have been widely studied for a number of sensing applications along with SAW devices. Already available polymer coatings have shown excellent results for adsorption of different VOCs and especially differentiating wine vapors [49] thus developing e-noses. The sorption of analytes with polymers follows the hydrogen bonding, polar or induced dipolar and other affinity interactions. The selectivity pattern is determined by calculating the partition coefficient of vapor sorption [50] on polymer network. Many research groups have followed the linear solvation energy relationship (LSER) models [51] to understand analyte sorption behavior at polymer interface. The idea is that vapor molecules are considered as solute that is solvated in polymer which leads to the development of solubility scales for a particular polymer vapor system. Solvation values of a broad range of organic compounds have already been calculated and various other are reported in different articles. LSER models predict that the analyte vapors will only be solvated in polymer if the properties of both, i.e. polymer and vapor, are complementary to each other. These findings are very important and build the basis of chemical vapor sensing strategies. Grate et al. [52] had investigated the potential of different polymeric materials for chemical vapor sorption in order to design a sensor array. They had followed the inverse least square (ILS) methods to predict the response of an each type of vapor in sensor array. This technique was fairly compatible with LSER since the polymer vapor interaction information can easily be collected without knowing the advance polymer parameters. However, for the training phase a large number of calibration data set is required for predicting the sensor response of each vapor on a particular polymer layer. Therefore, authors utilized twenty different polymers for eighteen diverse analyte vapors using SAW resonators as transducing device.

In order to collect almost all sort of interactions with analytes, a large variety of polymer is also required including dipolar, polarizable, and hydrogen-bond acidic hyper-branched polymers. As earlier mentioned, most of the polymers are commercially available; however, some of them, i.e. hydrogen-bond acidic polymers, have to be tailored accordingly to obtain better sensitivity and selectivity performance while designing an array. Hartman et al. [53] had developed such hyper-branched acidic polymers coated on SAW devices for the detection of analytes having hydrogen-bond basic features. These polymers yield a substantially higher sensor response that drops over a period of time which could be due to the loss of sensing element from surface and unavailability of the interaction sites. This could be overcome by functionalization of polymer with stable groups and ensuring a completely reversible sorption process of analytes on polymer.

Tepper et al. [54] had adopted rapid expansion of supercritical solutions (RESS) technique for attaining high surface polymer coating materials as chemical vapor sensors. They had compared these layers with the bulk films of the same polymer for organic vapor sensing. They had found that films generated by RESS are much more sensitive than bulk films and exhibit much faster response. This approach can be extended even to those polymers having low analyte vapor permeability since RESS is highly suitable for crafting different polymers into thin films on SAW devices which are difficult to coat by conventional methods.

The frequency shift in SAW devices is not purely attributed to the adsorption of analyte vapors, but it is also due to the change in the modulus of polymer. The layers cause strong influence on the wave propagation velocity depending upon the extent of viscoelastic behavior of the polymers. Grate et al. [55] had developed a model where the frequency shift was explained as a combined effect of vapor mass adsorption and due to swelling of the polymer layer. Since the analyte adsorption also tends to increase the volume of the polymer layer ultimately leading to swelling. This swelling behavior of polymer was compared to the expansion in volume due to thermal effects. They had concluded that the change in the polymer modulus has major contribution in resultant frequency shifts, whereas the mass change has much smaller role in overall SAW sensor response. Therefore, polymer films that expand their volume drastically on vapor sorption would respond with much higher-frequency shifts than the hard polymer coatings provided the mass of analyte is the same.

3.2 Molecular Imprinted Polymers

Molecular imprinting [56] gives a new spin to conventional polymer systems in order to design highly selective artificial receptors. In this technique, template or analyte molecule is added along the monomers and cross linker in a suitable solvent to carryout polymerization. After completion of reaction or reaching the gel point, it can be fabricated into thin films on SAW device of desired thickness. Template molecules are washed away that leaves behind the cavities of adapted shapes analogous to analyte species. If the removal of template does not require any covalent bond rupture, then this technique is non-covalent imprinting which is most frequently adopted for designing sensor materials. However, in covalent imprinting each time the bond has to be cleaved for eliminating template. Covalent imprinting does not find much sensor applications and is usually applied when there is no functional group present at analyte molecule. Pauling [57, 58] was the first who introduced the concept of lock and key mechanism which is analogous to imprinting strategy. Wulff and Sarhan [59] had designed imprinted polymers for resolution of racemates thus providing the foundation for the development of artificial receptors. Mosbach [60] had significant contribution in the progress of non-covalent imprinting polymers as chemosensitive coatings for bio-recognition.

In the synthesis of imprinted polymers, the degree of cross linking controls the shape of molecular hollows for reversible analyte interactions and also the rigidness of

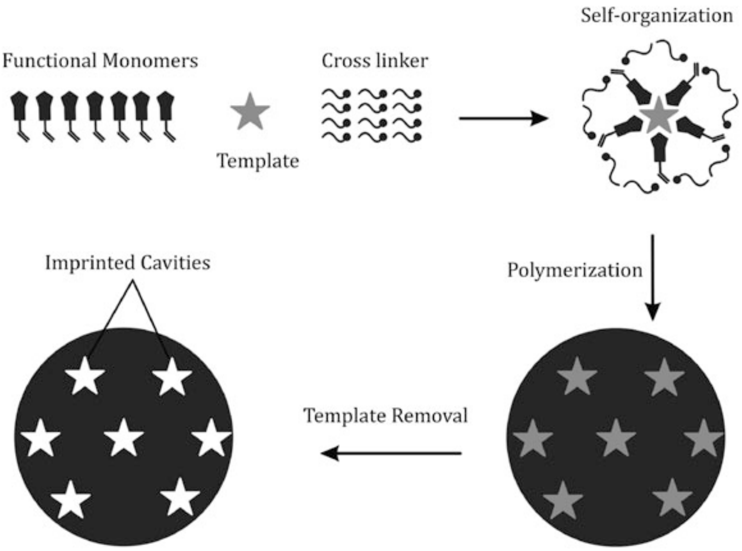

Fig. 5 Principle of molecular imprinting

the structure so that generated cavities are not immediately collapsed. Highly cross-linked polyurethane layers have shown substantial sensor response in the detection of polycylic aromatic hydrocarbons (PAHs). In fact, functional monomers and cross linkers are pre-organized around the template molecules interacting via non-covalent attractive forces before the polymerization. A schematic representation of molecular imprinting has been illustrated in Fig. 5. After the reaction, the templates are excluded, while the rest of the polymer architecture holds the memory of print analyte and therefore, behave as synthetic receptors. Analyte–polymer interactions are very much similar to antibody–antigen binding that leads to astonishing selectivity. Non-covalent interactions such as hydrogen bonding, π—π interactions, dipolar, and van der Waals forces accomplish the recognition of target analyte in complex mixtures. During the last decade, molecular imprinted polymers have been widely studied for sensing applications [61] including the detection of various biological analytes, environmental toxins both in liquid and gaseous phase, degradation products and various others. Depending upon the size of analytes, the template molecules can be imprinted only at polymer surface using soft lithographic technique which is termed as surface imprinting. Analytes with larger sizes are difficult to exclude from bulk material consequently it leads to incomplete regeneration and blocking of active sites. This ultimately leads to irreversible attachment of analyte and gradual decrease in sensor signal in successive measurements. Dickert et al. [62] had successfully imprinted various bio analytes such as yeast [63], red blood cells [64], bacteria, and viruses [65] at imprinted polymer interface. The foremost advantage of imprinting technology is that these materials are much easily processable into thin films of desired layer height, thus can be coated on transducer surface uniformly. Their unique selectivity, reversible interactions with analyte, rigid and robust coatings, and compatibility with sensor devices make this technique extremely useful for sensor applications.

3.3 Conducting Polymer Coatings

In recent years, conducting polymers are getting increasing interest in the design of acoustic wave sensor coatings since analyte interaction at polymer surface leads to change in the conductivity of SAW resonators. In contrast to metal oxide structures, conducting polymers can work efficiently even at room temperature. The other important feature is that they can be easily fabricated to transducer surface of tunable layer height and with structural modifications according to the analyte of interest. That is why conducting polymers, i.e. polyaniline, polypyrrole, and polythiophene, are proving to be real alternative to metal oxides and thus preferred for developing smart sensor materials. Conducting polymers have strong conjugated π-electronic system that undergoes electronic changes upon analyte interaction. Generally, their synthesis follows oxidative polymerization where the amount and nature of doping element controls their conductivity.

Ricco et al. [66, 67] had first reported lead phthalocyanine (PbPc) conducting thin films as SAW sensor coatings for NO_2 detection. The interaction of NO_2 with PbPc surface strongly enhances its conductivity astonishingly, thus enabling to detect a large amount of NO_2, i.e. 10^{16} molecules/cm^3 of PbPc. These conducting polymeric sensors are 1000 times more sensitive in comparison to pure mass response of SAW devices. As a result of continuous exposure to analyte gases, the sensor film is oxidized severely and that leads to a strong drift in sensor signal. In addition, humidity interference also influences SAW response.

Conducting polymers in the form of nanofibers [68] are usually deposited on SAW surface as sensitive layer. In case of polyaniline, nanofibers are synthesized by reaction of acid dopant under relatively low temperature as the diameter and the conductivity of polyaniline depends upon dopant. A shift in the conductivity of polymer film upon analyte interactions influences the velocity of the propagation wave through piezoelectric substrate. Since the frequency depends on the speed of acoustic waves, therefore, a corresponding change in resonance frequency is observed, i.e. sensor response of the device. The extent of change in velocity would depend on the concentration of analyte thus giving quantitative information. Authors had further explored the potential of polyanisidine [69] and polypyrrole [70] for the detection of hydrogen gas. Conductive polymers are sensitive, environmentally stable and easily convertible into thin films. However, one serious concern in their performance is that a change in the conductivity of polymer results in the reshuffling of already bounded charges on substrate surface which leads to weaken the piezoelectric character of SAW.

3.4 Polymer Hybrid Materials

Apart from using pure polymeric coatings for SAW sensing applications, they can also be merged with other useful materials to develop finer, homogenous films with controlled surface morphology, since the major objection in using thin polymer films is their uncontrolled layer height and droplet surface tension. However, introducing CNTs, nanoparticle composites with polymeric materials, the droplet surface tension, and layer inhomogeneity can be reduced. Furthermore, these composite materials have synergic effect as it contains the characteristics of both types of materials which have important contribution in getting enhanced response. Polymer composites with CNTs have been extensively studied for SAW sensor coatings. Penz et al. [71] had conducted in-depth studies on pure CNTs and their composites for gas sensing purpose; however, CNTs with thin polymer films have also been investigated for gas sensing. Sayago et al. [72] had developed polyisobutylene CNT composites for the detection of environmental pollutants, i.e. toluene and octane. They had experienced that polyisobutylene with 2% MWCNTs lead to best sensitivity for toluene and octane sensing. The sensor response was reversible and reproducible as indicated by continuous six weeks measurements.

Carbon black is used with different functional organic polymers for the detection of VOCs at low concentrations, since carbon black possesses high surface area, very small size, i.e. 12 nm, and having considerable conductive properties. Recently, Nicolae et al. [73] had embedded nanoparticles in polymer films following the matrix-assisted pulsed laser evaporation (MAPLE) technique. The key point in using this method is to improve the SAW sensor performance by introducing nanoparticles into polymer and controlling the layer uniformity and homogeneity. This system has limited applications for polymers; however, one can find out the optimum combination of polymer and nanoparticles and laser wavelength.

4 Exemplary Applications

SAW sensors particularly with thin polymer films have been proven very efficient for detecting various environmental toxic vapors and gases and developing e-noses for product classification. Their high sensitivity, robust nature, and versatility make them a very special sensing technology for commercial applications. The sensitivity and selectivity can be optimized by selecting high resonating frequency device coated with suitable polymeric sensitive layer. Here, we would highlight the distinguished sensor applications of SAW resonators.

4.1 VOCs Sensing

SAW sensors have been most extensively studied for the detection of VOCs as they are flammable, highly toxic for living beings and noticeably destroying ozone surface.

Table 2 Comparison of different SAW sensors used for DMMP detection

Substrate	Frequency (MHz)	Coating interface	Tested concentration (mg m^{-3})	Reference
ST-cut quartz	250	Hexafluoroisopropanol	348	[76]
ST-cut quartz	250	Fluoropolyol	1,500	[77]
ST-cut quartz	300	Poly(*o*-phenylenediamine)	0.5	[78]

Therefore, rapid, inexpensive, and convenient methods for the detection of VOCs in environment are of utmost importance. Various research groups had developed different SAW chemoselective coating materials for the molecular recognition of organic vapors.

In 1979, Wohltjen [74] had for first time made the detection of organic vapors by using SAW resonators. The pioneering work of Grate and Wohltjen on vapor adsorption at polymer surface is very valuable in understanding their interactions and thus resulted in the development of early SAW vapor sensors. In another study, Grate et al. [75] had exploited the hydrogen-bond acidic polymers for the detection of basic organic vapors. This strategy was very useful for designing sensor materials for a particular class of organic vapors either having acidic or basic features.

Hartmann et al. [18, 19, 53] had synthesized hyper-branched hydrogen-bond acidic polymers and functionalized them for the detection of nerve gas agents and explosives, i.e. dimethyl methylphosphonate (DMMP) and dinitrotoluene, respectively. Author had also reported hydrogen-bond basic polymers as well for SAW sensors using phosphonate groups on siloxane polymer. As the DMMP belongs to the group of chemical warfare agents (CWA) which are very dangerous in battlefield and can be used in terrorist attacks therefore, a number of papers have been reported for DMMP sensing by SAW resonators. Wen et al. [78] had fabricated 10 nm molecular imprinted polymer film that enable to lower the detection limit down to 0.5 mg/m^3 which is remarkable. The detection limit is relatively superior when compared to other reported results for DMMP detection as indicated in Table 2.

The designed sensor setup has a broad dynamic range that can be seen in Fig. 6 showing a linear response for concentration range of 0.5–100 mg/m^3.

Du et al. [79] had used polysiloxane material and lowered the response time to 30 s which is good to make faster decisions; furthermore, normalized sensor signal for DMMP is much higher in contrast to common interfering vapors as indicated in Fig. 7. Nimal et al. [80] had developed SAW sensors for explosives and CWA. They reported a detection limit of 3 ppb for sarin, i.e. CWA with response time of 15 s which is significant while comparing to other SAW-based sensors.

Explosive vapors such as trinitrotoluene (TNT) and dinitrotoluene (DNT) are generally present at very low concentrations in air over land mines; therefore, their detection is extremely difficult. Their sensing is also important in mine fields and forensic analysis. Houser et al. [81] had tested a series of different hydrogen-bond acidic polymers for explosive detection following FTIR analysis. Authors had proposed that by extrapolating the results a detection limit of 92 ppt can be achieved.

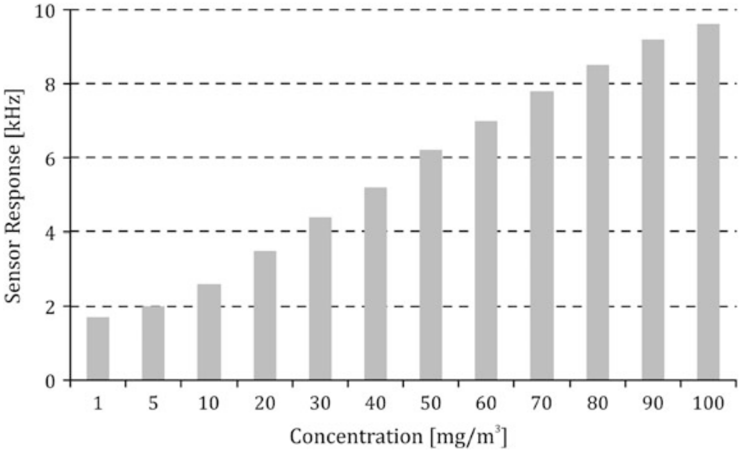

Fig. 6 Sensor response of 300 MHz SAW device for different concentrations of DMMP, adopted from [78]

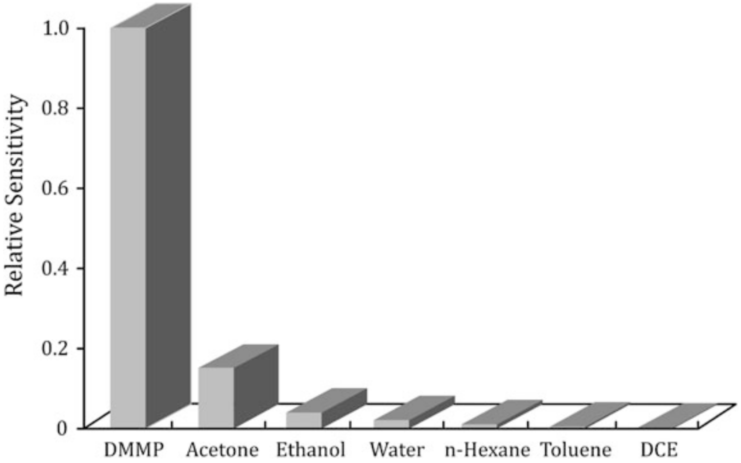

Fig. 7 Relative sensor effect of different vapors of equal concentrations indicating the selectivity of polysiloxane for DMMP, adopted from [79]

Kannan et al. [82] had reported carbowax-1000 polymer as sensing element for explosive detection. The intention was to detect the major impurity, i.e. 2,4 DNT, that has more tendency to vaporize itself than TNT. Since carbowax possess hydrogen-bond acidic character and thus has strong affinity towards nitroaromatics. A frequency shift of 0.56–1.1 Hz/ppb for DNT was reported with recovery time of less than 2 min. SAW-based sensor systems have also been considered for the detection of chlorinated hydrocarbons and other aromatic vapors that pose serious threats to human health. Dickert et al. [83] had significantly contributed to the development of high-frequency SAW sensors [43] for the detection of toluene,

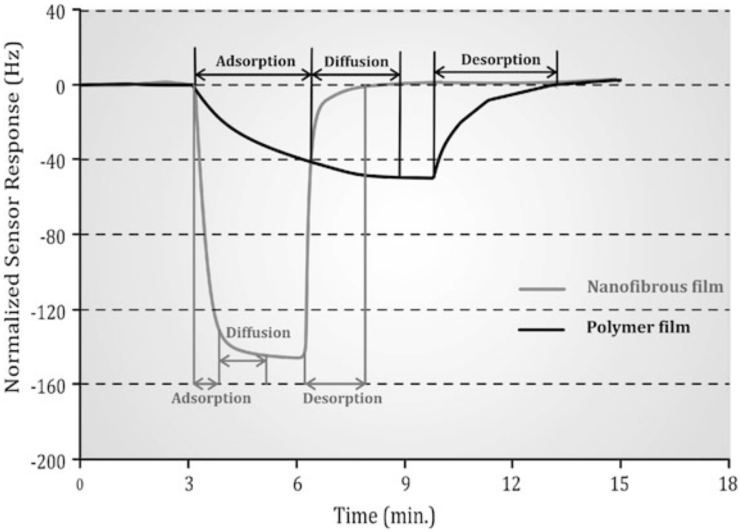

Fig. 8 Comparison between SAW sensor response of nanofibrous film and polymer film, adopted from [85]

isomers of xylene, chlorinated hydrocarbons, and other organic vapors using supramolecular structures [84]. Recently, polyethylene oxide nanofibrous films have been reported for SAW vapor sensors. Liu et al. [85] had coated these films by electrospinning method as in this way the contact surface between analyte and polymer have been improved and the loss of acoustic energy across polymer films was also reduced. While comparing to conventional polymer films, the diffusion times and length is also shortened which leads to fast sorption and desorption process of analytes. They had tested nanofibrous polymer films for the detection of isopropanol, nitrobenzene, toluene, and hydrogen peroxide. It is interesting to note that SAW sensors for hydrogen peroxide have been rarely reported keeping in view its use in explosives for terrorist attacks. Authors had compared drop coated polymer film with nanofibrous film taking hydrogen peroxide as model analyte. From Fig. 8, it is clear that nanofibrous film exhibits faster adsorption, diffusion, and desorption of analyte vapors. In addition, sensor response is also superior which suggest that nanofibrous films are much better choice in contrast to conventional polymer films.

4.2 Multisensor Array for VOCs Sensing

Taking into account the challenges concerning SAW vapor sensors, an advance step is the development of multisensor array that can discriminate individual analyte in complex mixtures. The idea is to mimic the real time environments and thus to design the SAW devices accordingly. Ballantine and Grate et al. [86] had first reported SAW vapor sensor array for evaluating vapor-polymer interactions using twelve coating materials exposed to eleven different vapors following pattern recognition strategies. Grate et al. [87] had proposed that solubility interactions can be useful in the selection of coating materials while designing multisensor system. In another study, Patrash et al. [88] had designed a SAW sensor array coated with four different types of polymers that were exposed to a series of thirty-nine diverse organic vapors. Data of sensor frequency shifts was applied to determine solubility and solvation parameters which are associated with polymeric coatings. The developed solubility and solvation model was useful to predict sensor response of SAW array. Ricco et al. [67] had for first time used cluster analysis technique [89] for evaluating the frequency response for SAW-based sensor array. They concluded that in the design of an array, each of the coating material should be of diverse nature which would be extremely useful for pattern recognition [90] and indentifying several vapors. This point is particularly important as the discriminating capability is not relying on transducer nature. Furthermore, they suggested in future heterogeneous sensor array, i.e. different types of transducers integrated on a platform would be more advantageous for getting independent chemical information. Rapp et al. [2] had shown in a SAW sensor array the sensitivity can be influenced by set phase position. In addition, the thickness and the morphology of the coating material have strong influence on frequency shifts of SAW resonators. Owing to the intense research in the design of multisensor array, statistical tools for data handling have been more frequently considered to interpret results. Penz et al. [91] had adopted PCA and artificial neuronal network (ANN) strategies for vapor sensing applications. Former method was used as preprocessing tool, whereas later one was adopted as pattern classifier. These tools enable us to recognize individual components in binary mixtures, e.g. methanol and 2-propanol.

SAW-based sensor arrays are not restricted only for toxic and hazardous organic vapors since they can be applied in food analysis. Garcia-Gonzalez et al. [92] had developed a versatile e-nose-based SAW sensor array to discriminate lampante from nonlampante virgin olive oils. They had combined SAW array with solid phase micro extraction (SPME) for enrichment of volatile compounds. Different factors including extraction time, sample temperature and carrier gas flow were optimized for SPME process. The performance of designed mathematical set for proposed application was examined by external samples. It has been observed that SPME along with SAW array coated with different polymers is highly suitable for distinguishing olive oil samples. In a similar fashion, Barie et al. [93] had developed SAW sensor array for monitoring food quality of fruits and sugars. The designed e-nose was sensitive enough to respond to low ppm and ppb concentrations of volatile compounds. Authors had measured headspace volatiles of different variety of apples and ripe and unripe pineapples and differentiating between different sugar samples including pure and off-flavor sugars. In another study, Horrillo and coworkers [94] had build-up e-nose SAW array for differentiating different red wine samples. ANN and probabilistic neuronal network (PNN) were adopted for classification and data interpretation with success rate of 95%. Horrillo et al. [95, 96] had used a thin layered structure, i.e. ZnO–SiO_2–Si, to overcome the incompatibility of common piezoelectric materials including quartz, $LiTaO_3$, and $LiNbO_3$ with

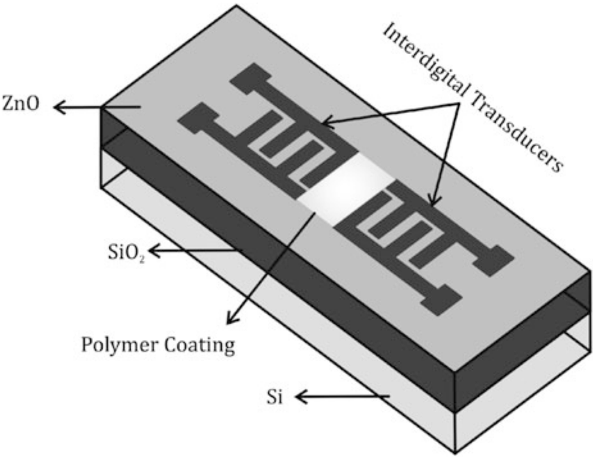

Fig. 9 Schematic representation of ZnO–SiO_2 SAW resonator having polymeric coatings, adopted from [96]

integrated circuits. High electromechanical coupling coefficient, good bonding character with silicon, and high temperature stability make ZnO a suitable choice. The design can be seen in Fig. 9 where polymeric layer is coated on ZnO surface. As for pattern recognition, PCA, PNN, and PLS techniques were adopted.

Xie et al. [97] had used carbon black polymer coatings for detecting mixed vapors, e.g. acetone, ethanol, toluene, methanol, and tetrahydrofuran, at low concentrations using pattern recognition approach. Independent component analysis (ICA) method was used by Yadava et al. [98] for pattern recognition in SAW sensor array, since ICA provides a direct and more useful understanding about analyte solvation parameters. Sensor arrays are highly desirable for monitoring and discriminating different CWAs during field analysis. Joo et al. [99] had constructed SAW array for measuring four distinct classes of CWA including blood, nerve, vesicant, and choking agents. In this study, DMMP, acetonitrile (CH_3CN), dichloromethane (CH_2Cl_2) and dichloropentane (DCP) were chosen as simulant gases. The design of IDT electrodes, layer heights and the composition of different sensing polymers were optimized for getting enhanced sensitivity and selectivity.

From Fig. 10, it can be seen that a layer height of 2.7 μm and IDT with electrode width of 3 μm are best suited for DMMP detection. Authors had adopted principal component analysis (PCA) for pattern recognition and resolving different vapors as shown in Fig. 11. All four types of CWA can easily be distinguished from each other indicating the selectivity of array.

Alizadeh et al. [100] had also reported a multisensor array coated with different polymeric materials for sensing of CWA. They had optimized recognition tools for better classification of simulant gases. Hao et al. [101] had developed a portable e-nose-based SAW array for organic vapor detection. They concluded that selection of a proper statistical algorithm is highly beneficial to collect selective sensor signals. In a recent study, Horrillo and coworkers [102] had investigated the optimal polymeric materials in terms of enhanced sensitivity and selectivity for CWA detection. Especially, authors had reported extremely low detection limits of 0.05

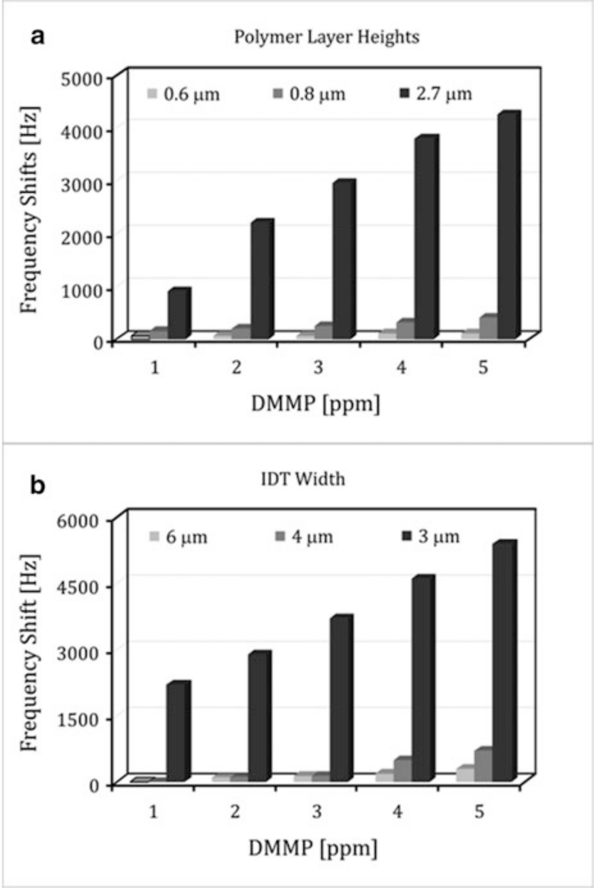

Fig. 10 Frequency shifts for different DMMP concentrations as it can be seen that polymer layer of 2.7 µm and interdigital transducer width is 3 µm are best suited. Adopted from [99]

and 0.5 ppm for DMMP and dipropylene glycol monomethyl ether (DPGME), respectively, which are even below the toxic level of CWA. Apart from explosives and nerve gas simulants sensing, Chen et al. [103] had designed SAW sensors with polyisobutylene for the detection of typical organic vapors present in the breath of lung cancer patients. They had measured eleven different vapors at low concentrations, i.e. 10^{-9} to 10^{-12} M. Authors had combined this e-nose system with gas chromatography that works for separation purpose, and SAW resonators measured these components. The data set was treated with back propagation ANN for recognition of lung cancer patients.

4.3 Gas Sensing Applications

For gas sensing applications, usually electrochemical sensors having metal oxide frameworks are preferred; however, they need to be heated at higher temperatures,

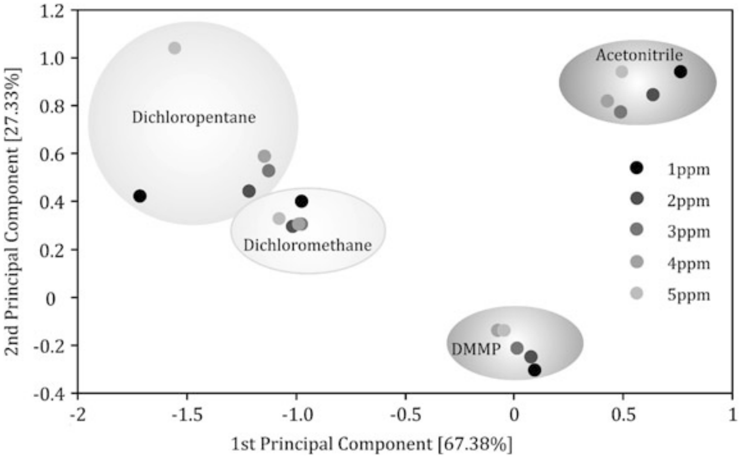

Fig. 11 Principal component analysis (PCA) for each type of gas in the mixture, adopted from [99]

i.e. 350–500°C. Contrary, SAW resonators in combination with suitable coating material can be applied for gas sensing applications at ambient conditions. Hoyt et al. [104] had designed two types of polymer material for CO_2 and relative humidity at room temperature using SAW resonators. They specifically selected polyimide of layer height 370 nm and poly *N*-vinyl pyrrolidone (PNVP) of 40 nm for measuring CO_2 and H_2O concentrations, respectively. The layer height of polymer coatings is essential to operate SAW devices under same temperature coefficients. It has been observed that PNVP films offer suitable quantitative information about relative H_2O in the entire measured range, whereas for CO_2 detection polyimide layer suffers from humidity interference. However, at low humidity levels, sensors for CO_2 work more efficiently thus providing more reliable quantitative data. Wu et al. [45] had crafted polyaniline nanofibers doped with camphorsulfonic acid (CSA) as coating interface for designing SAW humidity sensors. The designed sensor works in the range of 5–90% relative humidity at room temperature with excellent reproducibility. High sensitivity was due to the fact that nanostructured material possess high surface-to-volume ratio with fast electron mobility.

Sadek et al. [14] had used polyaniline nanofibrous material as sensing element for hydrogen gas detection at room temperature using ZnO layered $LiNbO_3$ SAW devices. Polyaniline nanofibers were doped with HCl and CSA and characterized by transmission electron microscopy (TEM). They had observed sensor response of 3 and 14.6 kHz for HCl doped and CSA doped polyaniline, respectively towards 1% H_2. The designed sensor exhibits fast response with suitable reversibility as signal retains its baseline stability for both analytes. Al-Mashat et al. [70] had first time combined polypyrrole nanofibers with 36° YX $LiTaO_3$ SAW resonator for sensing of H_2 and NO_2 gases at room temperature. Since NO_2 is an extremely poisonous gas and high value environmental pollutant, a number of sensors for NO_2 have been proposed.

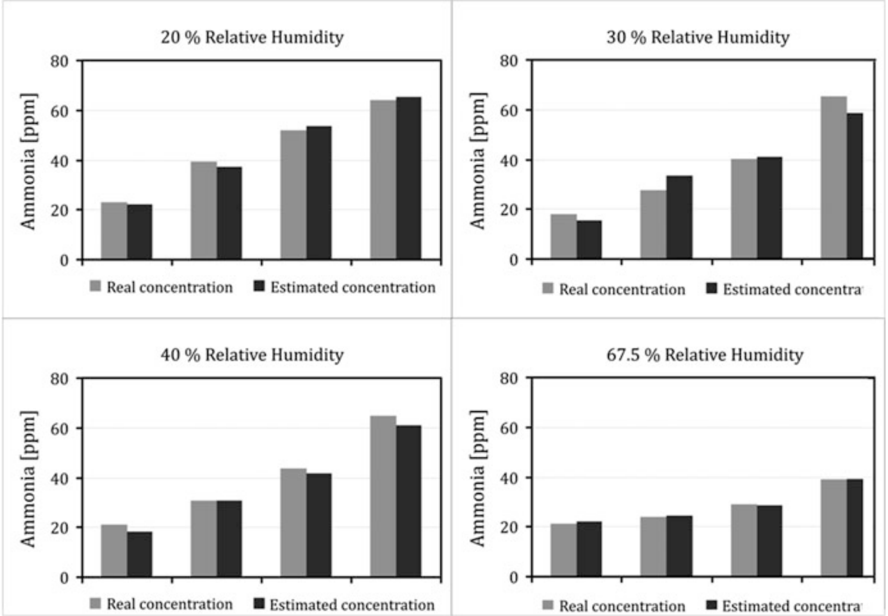

Fig. 12 Comparison between real concentrations and estimated concentration of ammonia vapors at different relative humidity levels, adopted from [105]

In this work, polymer nanofibrous materials are supposed to be suitable alternate to metal oxide structures for gas sensing since polypyrrole is a conducting polymer and its nanofibrous framework, i.e. diameter of 18 nm, is very favorable for high sensitivity. NO_2 is a strong oxidizing agent that can oxidize polymer chain thus ultimately disturbing conjugated system of conducting polymer which is a serious concern regarding reversibility and reproducibility. It has been observed that polypyrrole nanofibers shows frequency shift of 20 kHz against 1% H_2 which is higher when compared to polyaniline based SAW sensor.

Shen et al. [105] had coated polyaniline film on shear horizontal (SH-SAW) devices for the detection of ammonia gas at ppm level. This sensor can detect ammonia in the concentration range from 20 to 70 ppm with a response time of nearly 150 s. The behavior of sensing film is quite different in dry nitrogen and in humid environments. It has been experienced that the elastic effect is relatively smaller than mass loading effect. They had measured a series of different concentrations of ammonia at various humidity levels. At increased humidity levels, cross sensitivity also enhanced indicating a strong interference of water vapors with polyaniline layer. This problem was overcome by getting regression functions for defined humidity environments. Since thirty-six data points were applied and out of them sixteen points were tested, i.e. four data points for four different relative humidity levels. Results illustrated in Fig. 12 clearly indicate that the estimated concentration of ammonia is very much similar to the real concentration at all four humidity levels. Authors believe that by applying statistical tools the frequency shifts due to humidity interference can be reduced.

4.4 Sensing Applications in Liquids

Although STW resonators [106, 107] have solved the problem of high damping loss in solutions, these sensors have not been studied exclusively in liquid mediums. As earlier mentioned in Sect. 2.2, two technical features are critical, first is the selection of substrate material and second is the alteration in cutting angle of resonator. In general, piezoelectric material of high dielectric constant is considered for working in highly polar environment, e.g. $LiTaO_3$ dielectric constant is 40 and therefore preferred over quartz that has 3.8. The second part is associated with the adjustment of cutting angle that allows wave propagation all along the surface avoiding loss in acoustic energy. Dickert et al. [108] had first employed MIP films as sensitive coatings for polycyclic aromatic hydrocarbons (PAHs) detection using both surface and bulk acoustic devices. Highly cross-linked polyurethane layers prove very effective for pyrene sensing [109] in water samples at extremely low concentrations. Prior to mass-sensitive measurements, the selectivity and sensitivity of imprinted layers was examined by fluorescence studies. Polyurethane layers were fabricated on 428-MHz 36° YX-$LiTaO_3$ material that exhibit complete shear waves minimizing the damping loss. A sensor response of nearly 1.5 kHz was observed for 3.5 μg/L pyrene concentration in water which suggests that using STW resonators detection limit can be lowered down to ppb level. In another study, authors [110] had tested the shear wave resonator with same frequency for yeast cell detection.

Recently, Dickert and co-workers had developed STW sensors for engine oil degradation monitoring [38]. As automotive engine oil is a complex mixture of various additives and possesses high viscosity therefore, sensor layer should be highly corrosion resistive and possess thermal durability since degradation takes place at higher temperatures. Titania sol-gel layers imprinted with capric acid model template was applied as sensing element on STW devices. It had been observed that thinner films work more efficiently as diffusion path length and time is considerably lowered down with reduced layer heights. Sensor response increases with the increasing engine oil age. It has been observed that using STW devices of higher resonance frequency, sensor signal increases parabolically. Frequency shifts of three different STW devices for 266-hour used engine oil samples have been shown in Fig. 13. Relatively small size of STW transducer, i.e. 2 mm for 430 MHz, is significant for realizing miniaturized sensor devices.

Josse et al. [111] had used $LiTaO_3$ SH-SAW resonators for the detection of toluene, trichloroethane, and tetrachloroethylene in deionized water. Authors had investigated electrical passivation of transducer in polar medium, loss in acoustic energy and their impact on sensor characteristics. The devices were coated with 0.4 μm poly isobutylene layer over poly methyl methacrylate (PMMA) waveguide layer. Thin guiding layers of PMMA successfully protect IDTs from being directly in contact with liquid media. They found that PMMA guiding layers having

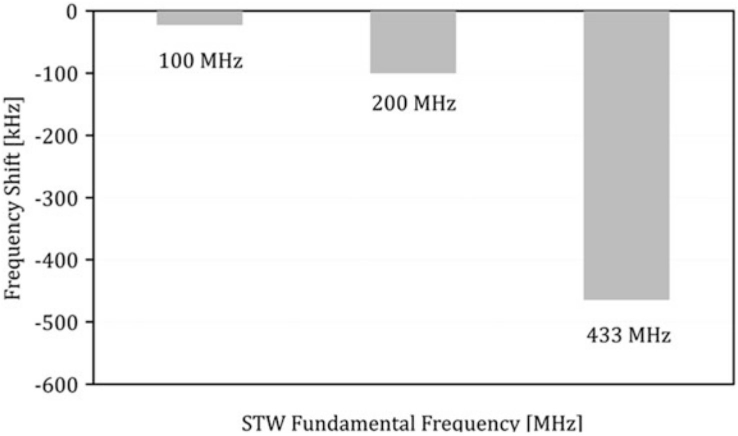

Fig. 13 Sensor response of 100, 200, and 433 MHz STW resonator for 266-hour aged engine oil sample, adopted from [38]

Table 3 Sensor response (Hz/ppm) of three SH-SAW devices with different guiding layers, adopted from [111]

Sr. no.	Solvents	Without (PMMA)	PMMA (0.3 μm)	PMMA (1.8 μm)
1	Trichloroethane	−16	−16.3	−10.6
2	Toluene	−46	−41	−21.5
3	Tetrachloroethylene	−130	−124	−116

thickness of 0.3 μm showed better response than films of 1.8 μm thickness as shown in Table 3. The low sensor response for 1.8 μm thick PMMA film indicates its pronounced viscoelastic contributions which eventually influence mass sensing performance.

5 SAW Resonators Among Acoustic Wave Sensors

Acoustic or mass-sensitive resonators are generally of two types, i.e. SAW and bulk acoustic wave (BAW) resonators, since the classification is made on the basis of wave propagation mode in piezoelectric materials. Contrary to SAW resonators, BAW devices exhibit complete shear wave that propagate in entire piezoelectric material thus showing maximum displacement at upper and lower interfaces. That is why these devices are called as thickness shear mode (TSM) resonators or more commonly quartz crystal microbalance (QCM) [112]. Keeping in view the wave propagation of QCMs, their sensitivity is restricted since high resonance frequency demands more thin quartz wafers which eventually make QCMs fragile. Commercially available QCMs have fundamental resonance frequency in the range of 5–30 MHz as beyond this limit it is difficult to manufacture or handle thin quartz sheets. Taking SAW resonators into consideration, devices with fundamental resonance frequency up to

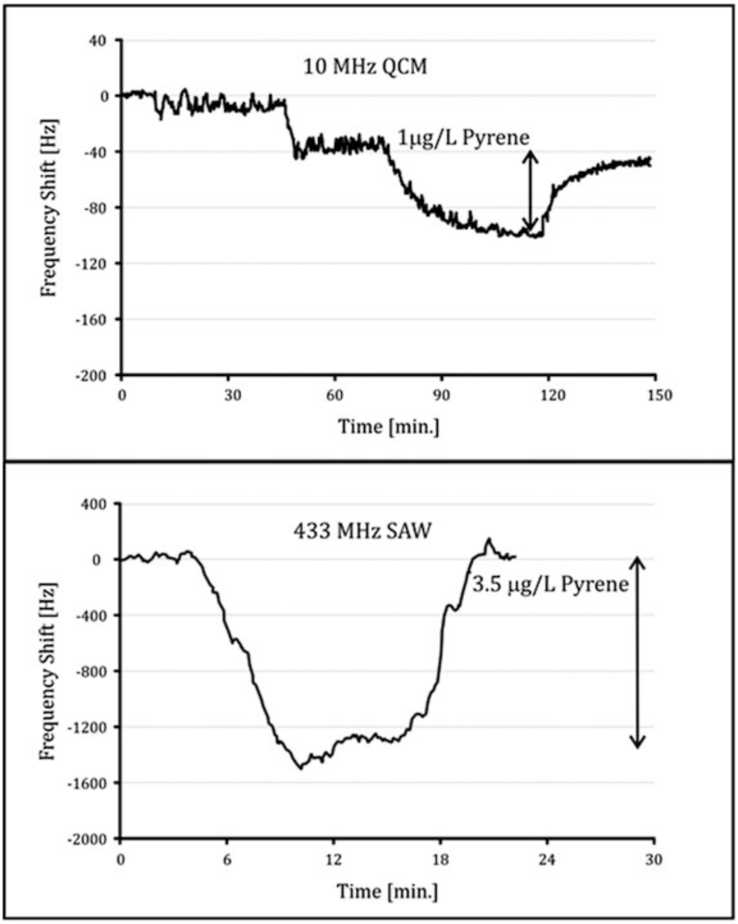

Fig. 14 Comparison between 10 MHz QCM and 433 MHz SAW resonator for pyrene detection in water, adopted from [108, 109]

1 GHz are reported for sensing applications. This means SAW devices are much more superior to QCMs in terms of sensitivity and also offer the ease of manufacturing. Sensor response of 10 MHz QCM with 433 MHz SAW resonator can be compared for the detection of pyrene in water at lower concentrations using imprinted polyurethane sensor layer. Result indicated in Fig. 14 provides clear evidence that SAW sensors are highly responsive and offers unmatched sensitivity.

In QCMs, the acoustic energy is distributed in the bulk of piezocrystal; this limits the sensitivity, while in SAW devices the energy path is confined to the guiding layer at interface which makes them extremely responsive to any surface perturbations. Apart from acoustic energy confinement, wave propagation also depends upon nature of in contact medium particularly in case of liquids. In contrast to QCMs, SAW devices suffer serious acoustic energy loss due to excessive damping in liquid media.

This problem can be solved by using love wave sensors that can operate in liquids with minimum energy loss. Therefore, SAW devices can practically overcome the problem of working in liquids and compete with QCM sensors.

6 Limitations and Challenges

SAW resonators were principally adopted for military purpose; however, the scope can be extended to other different fields particularly for biosensing using suitable coating interface. The devices are highly sensitive, small in size, cost effective, and therefore possess huge potential for commercialization. At the moment, there are various SAW-based sensors available in market for security and industrial applications.

However, there are serious problems associated with SAW devices concerning selectivity since intrinsically they are nonselective. It becomes more important while working in a complex matrix. Other competing sensing approaches such as ion mobility spectroscopy and fluorescent and enzymatic labeling offer much better selectivity than SAW-based sensors. Therefore, most of the bio-recognition events are generally captured by abovementioned analytical technologies. In case of SAW devices, nonselective binding can be minimized by tailored chemical sensor layer. In this regard, a number of approaches have been developed for crafting highly selective synthetic receptors including functional polymeric materials. Combining SAW devices with customized coatings can make these sensors versatile and more attractive for biosensing applications. Frequency shifts apart from bonded surface mass always remain challenging for acoustic wave sensors. Despite selectivity issue, SAW devices are highly susceptible to various environmental factors, e.g. temperature, relative humidity, flow rate variations, and electrical and mechanical fluctuations. These factors produce noise and drift during measurement which ultimately reduces sensitivity and therefore necessary to eliminate. Unwanted signals due to temperature and humidity variations can be minimized by calibrating sensor setup at defined experimental conditions so as to compensate ambient environmental effects. The operation of SAW devices is restricted in liquid phase as the high viscosity of medium leads to excessive damping. The cutting angle of substrate can be adjusted to demonstrate complete shear wave and with no longitudinal components. Thus, the acoustic energy loss due to viscosity of medium can be avoided. Lamb wave and love wave sensors can also operate in fluids; however fine thickness of the device makes them fragile and so difficult for fabrication. Although love wave sensors are highly sensitive, the relative cost is also high. Not only the viscosity but the ionic strength of the liquid has also serious impact on surface wave propagation. For instance, SAW made from quartz substrate shows practically no resonance in water, while in n-heptane it exhibits some resonance which is due to entirely different dielectric constants of water and n-heptane, i.e. 1.9 and 80, respectively. This problem can be figured out by using substrate material of high dielectric value. Therefore, the design and nature of substrate material govern liquid-phase sensing of SAW devices. The promising way to compensate all the nonspecific frequency shifts is by performing differential measurements not only to eradicate all the spurious signals but also make them more selective and reliable. This would certainly make possible to obtain precise and accurate results in complex field measurements thus developing highly competitive SAW sensors for commercial view point.

7 Outlook

SAW device had been widely used as highly sensitive detectors in military and defense applications for more than 25 years. Microsensor Systems, Inc. (MSI) developed by Wohltjen in 1985 was perhaps the first company that introduced SAW-based commercial sensors. They were intended to monitor trace levels of nerve gases, blistering agents and other industrial gases. Moreover, they have been picked up for mine safety applications as well. Their major achievement is on field analysis of explosives having nitro groups, e.g. TNT and cyclotrimethylenetrinitramine (RDX). The design of sensor interface can be improved to achieve unmatched selectivity, reversibility, and long-term stability in SAW devices. Therefore, structuring of synthetic sensor coatings is currently under intense research to develop smart sensor materials of enhanced sensitivity and selectivity. Although there are some research articles published concerning SAW applications in liquids, however, this subject has not been investigated exclusively. SAW sensors possess huge potential for monitoring bio-recognition in fluids especially of extremely small-size species, e.g. bacteria, virus, and food pathogen. This could only be possible with improved version of device and layer interface. The integration of sensor array would be very beneficial for multifaceted analysis with suitable reliability. Combining SAW resonators with other exciting technologies such as surface plasmon resonance (SPR) would not only broaden the scope of the device but also give additional information about kinetic and conformational changes in protein structure. SAW have also been considered for lab-on-a-chip approach where the flow cell volume down to 60 nL can be achieved which appreciably reduces sample volume and cut down analysis time for up to few minutes. Apart from chemical applications, SAW resonators act as band pass filters in mobile phones. Wireless integrated SAW sensor arrays would be very attractive for continuous monitoring of real time sample matrix. With the emergence of new surface technologies along with SAW, it would be possible to measure only targeted analyte interaction without any undesired frequency shifts. Recent highlights of SAW clearly indicate that this field has bright future and there are a number of opportunities for researchers to design more sophisticated sensors.

References

1. Valentini L, Cantalini C, Armentano I, Kenny JM, Lozzi L, Santucci S (2004) Highly sensitive and selective sensors based on carbon nanotubes thin films for molecular detection. Diamond Relat Mater 13(4–8):1301–1305
2. Rapp M, Reibel J, Voigt A, Balzer M, Bülow O (2000) New miniaturized SAW-sensor array for organic gas detection driven by multiplexed oscillators. Sens Actuators B Chem 65(1–3): 169–172

3. Hinrichsen V, Scholl G, Schubert M, Ostertag T (1999) Online monitoring of high-voltage metal-oxide surge arresters by wireless passive surface acoustic wave (SAW) temperature sensors. Paper presented at the high voltage engineering 1999. Eleventh international symposium on (Conf. Publ. No. 467) London, 23–27 August 1999
4. Wolff U, Dickert FL, Fischerauer GK, Greibl W, Ruppel CCW (2001) SAW sensors for harsh environments. IEEE Sens J 1:4–13
5. Mujahid A, Lieberzeit PA, Dickert FL (2010) Chemical sensors based on molecularly imprinted sol–gel materials. Materials 3(4):2196–2217
6. Ballantine DS (1997) Acoustic wave sensors theory, design, and physico-chemical applications. Academic. http://worldcat.org. http://www.engineeringvillage.com/controller/servlet/OpenURL?genre=book&isbn=9780120774609
7. Cooper MA (2002) Optical biosensors in drug discovery. Nat Rev Drug Discov 1:515–528
8. Länge K, Bender F, Voigt A, Gao H, Rapp M (2003) A Surface acoustic wave biosensor concept with low flow cell volumes for label-free detection. Anal Chem 75(20):5561–5566
9. Smith JP, Hinson-Smith V (2006) The new era of SAW devices. Anal Chem 78(11):3505–3507
10. Penza M, Cassano G, Aversa P, Antolini F, Cusano A, Consales M, Giordano M, Nicolais L (2005) Carbon nanotubes-coated multi-transducing sensors for VOCs detection. Sens Actuators B Chem 111–112:171–180
11. Cattanach K, Kulkarni RD, Kozlov M, Manohar SK (2006) Flexible carbon nanotube sensors for nerve agent simulants. Nanotechnology 17(16):4123
12. Nimal AT, Mittal U, Singh M, Khaneja M, Kannan GK, Kapoor JC, Dubey V, Gutch PK, Lal G, Vyas KD, Gupta DC (2009) Development of handheld SAW vapor sensors for explosives and CW agents. Sens Actuators B Chem 135(2):399–410
13. Korotcenkov G (2007) Metal oxides for solid-state gas sensors: what determines our choice? Mater Sci Eng B 139(1):1–23
14. Sadek AZ, Wlodarski W, Li YX, Yu W, Li X, Yu X, Kalantar-zadeh K (2007) A ZnO nanorod based layered ZnO/64° YX LiNbO3 SAW hydrogen gas sensor. Thin Solid Films 515(24):8705–8708
15. Dickert FL, Geiger U, Keppler M, Reif M, Bulst WE, Knauer U, Fischerauer G (1995) Supramolecular receptors for SAW and QMB devices: solvent recognition evaluated by FT-IR spectroscopy and BET adsorption analysis. Sens Actuators B Chem 26(1–3):199–202
16. Penza M, Antolini F, Antisari MV (2004) Carbon nanotubes as SAW chemical sensors materials. Sens Actuators B 100:47–59
17. Sellergren B (ed) (2001) Molecularly imprinted polymers: man-made mimics of antibodies and their applications in analytical chemistry. Techniques and instrumentation in analytical chemistry, vol 23. Elsevier, Amsterdam
18. Hartmann-Thompson C, Hu J, Kaganove SN, Keinath SE, Keeley DL, Dvornic PR (2004) Hydrogen-bond acidic hyperbranched polymers for surface acoustic wave (SAW) sensors. Chem Mater 16(25):5357–5364
19. Hartmann-Thompson C, Keeley DL, Gallagher S (2006) Hydrogen-bond basic siloxane phosphonate polymers for surface acoustic wave (SAW) sensors. Sens Actuators B Chem 115(2):697–699
20. Garzella C, Comini E, Tempesti E, Frigeri C, Sberveglieri G (2000) TiO_2 thin films by a novel sol–gel processing for gas sensor applications. Sens Actuators B Chem 68(1–3):189–196
21. Fang M, Vetelino K, Rothery M, Hines J, Frye GC (1999) Detection of organic chemicals by SAW sensor array. Sens Actuators B Chem 56(1–2):155–157
22. Mujahid A, Dickert FL (2010) Surface nano-patterning of polymers for mass-sensitive. In: Carrara S (ed) Bio-detection, nano-bio-sensing. Springer, New York, Dordrecht, Heidelberg, London, pp 45–82. ISBN 978-1-4419-6168-6. doi:10.1007/978-1-4419-6169-3

23. Dickert FL, Hayden O, Lieberzeit P, Haderspoeck C, Bindeus R, Palfinger C, Wirl B (2003) Nano- and micro-structuring of sensor materials – from molecule to cell detection. Synth Met 138(1–2):65–69
24. Hoummady M, Campitelli A, Wlodarski W (1997) Acoustic wave sensors: design, sensing mechanisms and applications. Smart Mater Struct 6(6):647
25. Gualtieri JG, Kosinski JA, Ballato A (1994) Piezoelectric materials for acoustic wave applications. IEEE Trans Ultrason Ferroelectr Freq Control 41(1):53–59
26. Curie J, Curie P (1880) Contractions et dilatations produites par des tensions dans les cristaux hémièdres à faces inclines. C R Acad Sci Gen 93:1137–1140
27. Curie J, Curie P (1880) Development by pressure of polar electricity in hemihedral crystals with inclined faces. Bull Soc Min Paris 3:90–102
28. Lippmann G (1881) Principe de la conservation de l'électricité. An Chim Phys 24:145
29. Rayleigh L (1885) On waves propagated along the plane surface of an elastic solid. Proc Lond Mathemat Soc s1–17(1):4–11
30. Hesjedal T, Seidel W (2003) Near-field elastomeric mask photolithography fabrication of high-frequency surface acoustic wave transducers. Nanotechnology 14(1):91
31. Steinem C, Janshoff A (2005) SENSORS piezoelectric resonators. In: Editors-in-Chief: Paul W, Alan T, Colin P (eds) Encyclopedia of analytical science, 2nd edn. Elsevier, Oxford, pp 269–276
32. Gautschi G (2002) Piezoelectric sensorics : force, strain, pressure, acceleration and acoustic emission sensors, materials and amplifiers. Springer, Berlin
33. Da Cunha MP, De Azevedo FS (1999) Investigation on recent quartz-like materials for SAW applications. IEEE Trans Ultrason Ferroelectr Freq Control 46(6):1583–1590
34. Krempl P, Schleinzer G, Wallnofer W (1997) Gallium phosphate, $GaPO_4$: a new piezoelectric crystal material for high-temperature sensorics. Sens Actuators A Phys 61 (1–3):361–363
35. Dubovik MF, Andreyev IA, Shmaly YS (1994) Langasite ($La_3Ga_5SiO_{14}$) an optical piezoelectric: growth and properties. In: Proceedings of the 48th IEEE international frequency control symposium, Boston, MA. 1–3 June 1994, pp 43–47
36. Hashimoto KY, Yamaguchi M, Mineyoshi S, Kawachi O, Ueda M, Endoh G (1997) Optimum leaky-SAW cut of $LiTaO_3$ for minimised insertion loss devices. In: Proceedings of the IEEE ultrasonics symposium, vol 241. Toronto, Ont. 5–8 October 1997, pp 245–254
37. Calabrese GS, Wohltjen H, Roy MK (1987) Surface acoustic wave devices as chemical sensors in liquids. Evidence disputing the importance of Rayleigh wave propagation. Anal Chem 59(6):833–837
38. Mujahid A, Afzal A, Glanzing G, Leidl A, Lieberzeit PA, Dickert FL (2010) Imprinted sol–gel materials for monitoring degradation products in automotive oils by shear transverse wave. Anal Chim Acta 675(1):53–57
39. Cai Q-Y, Park J, Heldsinger D, Hsieh M-D, Zellers ET (2000) Vapor recognition with an integrated array of polymer-coated flexural plate wave sensors. Sens Actuators B Chem 62(2): 121–130
40. Kovacs G, Vellekoop MJ, Haueis R, Lubking GW, Venema A (1994) A love wave sensor for (bio)chemical sensing in liquids. Sens Actuators A Phys 43(1–3):38–43
41. Sauerbrey G (1959) Verwendung von schwingquarzen zur waegung dunner schichten und zur mikrowaegung. Zeitschrift für Physik 155(2):206–222
42. Afzal A, Dickert FL, (2011) Surface acoustic wave (SAW) sensors for chemical applications. In: Korotcenkov G (ed) Chemical sensors: comprehensive sensor technology, vol 4. Solid State Sensors. Chap. 10, Momentum, New Jersey, ISBN: 978-1-60650-233-4.
43. Dickert FL, Forth P, Bulst W-E, Fischerauer G, Knauer U (1998) SAW devices-sensitivity enhancement in going from 80 MHz to 1 GHz. Sens Actuators B Chem 46(2):120–125
44. Liron Z, Greenblatt J, Frishman G, Gratziani N, Biran A (1993) Temperature effect and chemical response of surface acoustic wave (SAW) single-delay-line chemosensors. Sens Actuators B Chem 12(2):115–122

45. Wu T-T, Chen Y-Y, Chou T-H (2008) A high sensitivity nanomaterial based SAW humidity sensor. J Phys D Appl Phys 41(8):085101
46. Penza M, Cassano G (2000) Relative humidity sensing by PVA-coated dual resonator SAW oscillator. Sens Actuators B Chem 68(1–3):300–306
47. Shen C-Y, Hsu C-L, Hwang R-C, Jeng J-S (2007) The interference of humidity on a shear horizontal surface acoustic wave ammonia sensor. Sens Actuators B Chem 122(2):457–460
48. Greibl W, Hayden O, Achatz P, Fischerauer G, Scholl G, Dickert FL (2002) Surface phenomena with organic coatings for chemical sensing. In: Vo-Dinh T, Buettgenbach S (eds) Proceedings of the SPIE, vol 4576. Advanced Environmental Sensing Technology II, Boston, MA. 22 February 2002, pp 160–168. doi:10.1117/12.456953
49. García M, Fernández MJ, Fontecha JL, Lozano J, Santos JP, Aleixandre M, Sayago I, Gutiérrez J, Horrillo MC (2006) Differentiation of red wines using an electronic nose based on surface acoustic wave devices. Talanta 68(4):1162–1165
50. Abraham MH, Fuchs R (1988) Correlation and prediction of gas-liquid partition coefficients in hexadecane and olive oil. J Chem Soc Perkin Trans 2(4):523–527
51. Grate JW, Abraham MH, Du CM, McGill RA, Shuely WJ (1995) Examination of vapor sorption by fullerene, fullerene-coated surface acoustic wave sensors, graphite, and low-polarity polymers using linear solvation energy relationships. Langmuir 11(6):2125–2130
52. Grate JW, Patrash SJ, Kaganove SN, Abraham MH, Wise BM, Gallagher NB (2001) Inverse least-squares modeling of vapor descriptors using polymer-coated surface acoustic wave sensor array responses. Anal Chem 73(21):5247–5259
53. Hartmann-Thompson C, Keeley DL, Dvornic PR, Keinath SE, McCrea KR (2007) Hydrogen-bond acidic polyhedral oligosilsesquioxane filled polymer coatings for surface acoustic wave sensors. J Appl Polym Sci 104(5):3171–3182
54. Levit N, Pestov D, Tepper G (2002) High surface area polymer coatings for SAW-based chemical sensor applications. Sens Actuators B Chem 82(2–3):241–249
55. Grate JW, Klusty M, McGill RA, Abraham MH, Whiting G, Andonian-Haftvan J (1992) The predominant role of swelling-induced modulus changes of the sorbent phase in determining the responses of polymer-coated surface acoustic wave vapor sensors. Anal Chem 64 (6):610–624
56. Wulff G (1995) Molecular imprinting in cross-linked materials with the aid of molecular templates – a way towards artificial antibodies. Angewandte Chemie Int Edn English 34(17): 1812–1832
57. Pauling L (1940) A theory of the structure and process of formation of antibodies. J Am Chem Soc 62:2643–2657
58. Pauling L, Campbell DH (1942) The production of antibodies in vitro. Science 95:440–441
59. Wulff G, Sarhan A (1972) Uber die Anwendung von Enzymanalog gebauten Polymeren zur Racemattrennung. Angew Chem 84:364
60. Klaus M (1994) Molecular imprinting. Trends Biochem Sci 19(1):9–14
61. Dickert FL, Hayden O (1999) Molecular imprinting in chemical sensing. TrAC Trends Anal Chem 18(3):192–199
62. Dickert FL, Lieberzeit P, Tortschanoff M (2000) Molecular imprints as artificial antibodies – a new generation of chemical sensors. Sens Actuators B Chem 65(1–3):186–189
63. Seidler K, Polreichová M, Lieberzeit P, Dickert F (2009) Biomimetic yeast cell typing—application of QCMs. Sensors 9(10):8146–8157
64. Hayden O, Mann K-J, Krassnig S, Dickert FL (2006) Biomimetic ABO blood-group typing. Angew Chem Int Ed 45(16):2626–2629
65. Hayden O, Bindeus R, Haderspöck C, Mann K-J, Wirl B, Dickert FL (2003) Mass-sensitive detection of cells, viruses and enzymes with artificial receptors. Sens Actuators B Chem 91(1–3): 316–319
66. Ricco AJ, Martin SJ, Zipperian TE (1985) Surface acoustic wave gas sensor based on film conductivity changes. Sens Actuators 8(4):319–333

67. Ricco AJ, Crooks RM, Osbourn GC (1998) Surface acoustic wave chemical sensor arrays: new chemically sensitive interfaces combined with novel cluster analysis to detect volatile organic compounds and mixtures. Accounts Chem Res 31(5):289–296
68. Sadek AZ, Baker CO, Powell DA, Wlodarski W, Kaner R, Kalantar-zadeh K (2007) Polyaniline nanofiber based surface acoustic wave gas sensors – effect of nanofiber diameter on H_2 response. IEEE Sens J 7(2):213–218
69. Al-Mashat L, Tran HD, Wlodarski W, Kaner RB, Kalantar-zadeh K (2007) Hydrogen gas sensor fabricated from polyanisidine nanofibers deposited on 36°YX $LiTaO_3$ layered surface acoustic wave transducer. SPIE BioMEMS Nanotechnol III 6799:67991B–67998B
70. Al-Mashat L, Tran HD, Wlodarski W, Kaner RB, Kalantar-zadeh K (2008) Polypyrrole nanofiber surface acoustic wave gas sensors. Sens Actuators B Chem 134(2):826–831
71. Penza M, Antolini F, Vittori-Antisari M (2005) Carbon nanotubes-based surface acoustic waves oscillating sensor for vapour detection. Thin Solid Films 472(1–2):246–252
72. Sayago I, Fernández MJ, Fontecha JL, Horrillo MC, Vera C, Obieta I, Bustero I (2011) Surface acoustic wave gas sensors based on polyisobutylene and carbon nanotube composites. Sens Actuators B Chem 156(1):1–5
73. Nicolae I, Viespe C, Grigoriu C (2011) Nanocomposite sensitive polymeric films for SAW sensors deposited by the MAPLE direct write technique. Sens Actuators B Chem 158(1): 418–422
74. Wohltjen H, Dessy R (1979) Surface acoustic wave probe for chemical analysis. I. Introduction and instrument description. Anal Chem 51(9):1458–1464
75. Grate JW (2008) Hydrogen-bond acidic polymers for chemical vapor sensing. Chem Rev 108(2): 726–745
76. McGill RA, Chung R, Chrisey DB, Dorsey PC, Matthews P, Pique A, Mlsna TE, Stepnowski JL (1998) Performance optimization of surface acoustic wave chemical sensors. IEEE Trans Ultrason Ferroelectr Freq Control 45(5):1370–1380
77. Dominguez DD, Chung R, Nguyen V, Tevault D, McGill RA (1998) Evaluation of SAW chemical sensors for air filter lifetime and performance monitoring. Sensors and Actuators B: Chemical 53(3):186–190
78. Wen W, Shitang H, Shunzhou L, Minghua L, Yong P (2007) Enhanced sensitivity of SAW gas sensor coated molecularly imprinted polymer incorporating high frequency stability oscillator. Sens Actuators B Chem 125(2):422–427
79. Du X, Ying Z, Jiang Y, Liu Z, Yang T, Xie G (2008) Synthesis and evaluation of a new polysiloxane as SAW sensor coatings for DMMP detection. Sens Actuators B Chem 134(2): 409–413
80. Nimal AT, Mittal U, Singh M, Khaneja M, Kannan GK, Kapoor JC, Dubey V, Gutch PK, Lal G, Vyas KD, Gupta DC (2009) Development of handheld SAW vapor sensors for explosives and CW agents. Sens Actuators B Chem 135(2):399–410
81. Houser EJ, Mlsna TE, Nguyen VK, Chung R, Mowery RL, Andrew McGill R (2001) Rational materials design of sorbent coatings for explosives: applications with chemical sensors. Talanta 54(3):469–485
82. Kannan GK, Nimal AT, Mittal U, Yadava RDS, Kapoor JC (2004) Adsorption studies of carbowax coated surface acoustic wave (SAW) sensor for 2,4-dinitro toluene (DNT) vapour detection. Sens Actuators B Chem 101(3):328–334
83. Lieberzeit P, Greibl W, Jenik M, Dickert F, Fischerauer G, Bulst W-E (2007) Cavities generated by self-organised monolayers as sensitive coatings for surface acoustic wave resonators. Anal Bioanal Chem 387(2):561–566
84. Dickert FL, Bäumler UPA, Stathopulos H (1997) Mass-sensitive solvent vapor detection with calix[4]resorcinarenes: tuning sensitivity and predicting sensor effects. Anal Chem 69(6): 1000–1005
85. Liu S, Sun H, Nagarajan R, Kumar J, Gu Z, Cho J, Kurup P (2011) Dynamic chemical vapor sensing with nanofibrous film based surface acoustic wave sensors. Sens Actuators A Phys 167(1):8–13

86. Ballantine DS, Rose SL, Grate JW, Wohltjen H (1986) Correlation of surface acoustic wave device coating responses with solubility properties and chemical structure using pattern recognition. Anal Chem 58(14):3058–3066
87. Grate JW, Abraham MH (1991) Solubility interactions and the design of chemically selective sorbent coatings for chemical sensors and arrays. Sens Actuators B Chem 3(2):85–111
88. Patrash SJ, Zellers ET (1993) Characterization of polymeric surface acoustic wave sensor coatings and semiempirical models of sensor responses to organic vapors. Anal Chem 65:2055–2066
89. Julian WG (1991) Detection of vapours and odours from a multisensor array using pattern recognition. Part 1. Principal component and cluster analysis. Sens Actuators B Chem 4(1–2): 109–115
90. Nakamoto T, Fukunishi K, Moriizumi T (1990) Identification capability of odor sensor using quartz-resonator array and neural-network pattern recognition. Sens Actuators B Chem 1(1–6): 473–476
91. Penza M, Cassano G (2003) Application of principal component analysis and artificial neural networks to recognize the individual VOCs of methanol/2-propanol in a binary mixture by SAW multi-sensor array. Sens Actuators B Chem 89(3):269–284
92. García-González DL, Barie N, Rapp M, Aparicio R (2004) Analysis of virgin olive oil volatiles by a novel electronic nose based on a miniaturized SAW sensor array coupled with spme enhanced headspace enrichment. J Agric Food Chem 52(25):7475–7479
93. Barié N, Bücking M, Rapp M (2006) A novel electronic nose based on miniaturized SAW sensor arrays coupled with SPME enhanced headspace-analysis and its use for rapid determination of volatile organic compounds in food quality monitoring. Sens Actuators B Chem 114(1): 482–488
94. Lozano J, Fernández MJ, Fontecha JL, Aleixandre M, Santos JP, Sayago I, Arroyo T, Cabellos JM, Gutiérrez FJ, Horrillo MC (2006) Wine classification with a zinc oxide SAW sensor array. Sens Actuators B Chem 120(1):166–171
95. Horrillo MC, Fernández MJ, Fontecha JL, Sayago I, García M, Aleixandre M, Gutiérrez J, Gràcia I, Cané C (2006) Optimization of SAW sensors with a structure ZnO–SiO_2–Si to detect volatile organic compounds. Sens Actuators B Chem 118(1–2):356–361
96. Fernández MJ, Fontecha JL, Sayago I, Aleixandre M, Lozano J, Gutiérrez J, Gràcia I, Cané C, MdC H (2007) Discrimination of volatile compounds through an electronic nose based on ZnO SAW sensors. Sens Actuators B Chem 127(1):277–283
97. Xie H, Yang Q, Sun X, Yang J, Huang Y (2006) Gas sensor arrays based on polymer-carbon black to detect organic vapors at low concentration. Sens Actuators B Chem 113(2):887–891
98. Yadava RDS, Chaudhary R (2006) Solvation, transduction and independent component analysis for pattern recognition in SAW electronic nose. Sens Actuators B Chem 113(1):1–21
99. Joo B-S, Huh J-S, Lee D-D (2007) Fabrication of polymer SAW sensor array to classify chemical warfare agents. Sens Actuators B Chem 121(1):47–53
100. Alizadeh T, Zeynali S (2008) Electronic nose based on the polymer coated SAW sensors array for the warfare agent simulants classification. Sens Actuators B Chem 129(1):412–423
101. Hao HC, Tang KT, Ku PH, Chao JS, Li CH, Yang CM, Yao DJ (2010) Development of a portable electronic nose based on chemical surface acoustic wave array with multiplexed oscillator and readout electronics. Sens Actuators B Chem 146(2):545–553
102. Matatagui D, Martí J, Fernández MJ, Fontecha JL, Gutiérrez J, Gràcia I, Cané C, Horrillo MC (2011) Chemical warfare agents simulants detection with an optimized SAW sensor array. Sens Actuators B Chem 154(2):199–205
103. Chen X, Cao M, Li Y, Hu W, Wang P, Ying K, Pan H (2005) A study of an electronic nose for detection of lung cancer based on a virtual SAW gas sensors array and imaging recognition method. Measure Sci Technol 16(8):1535
104. Hoyt AE, Ricco AJ, Bartholomew JW, Osbourn GC (1998) SAW Sensors for the room-temperature measurement of CO_2 and relative humidity. Anal Chem 70(10):2137–2145

105. Shen C-Y, Liou S-Y (2008) Surface acoustic wave gas monitor for ppm ammonia detection. Sens Actuators B Chem 131(2):673–679
106. Baer RL, Flory CA, Tom-Moy M, Solomon D (1992) STW chemical sensors. In: Proceedings of the IEEE ultrasonics symposium, 1992, vol 291. 20–23 October 1992, pp 293–298
107. Avramov ID, Rapp M, Voigt A, Stahl U, Dirschka M (2000) Comparative studies on polymer coated SAW and STW resonators for chemical gas sensor applications. In: Proceedings of the 2000 IEEE/EIA international frequency control symposium and exhibition, Kansas City, MO 2000. pp 58–65
108. Dickert FL, Tortschanoff M, Bulst WE, Fischerauer G (1999) Molecularly imprinted sensor layers for the detection of polycyclic aromatic hydrocarbons in water. Anal Chem 71(20): 4559–4563
109. Lieberzeit P, Halikias K, Afzal A, Dickert F (2008) Polymers imprinted with PAH mixtures – comparing fluorescence and QCM sensors. Anal Bioanal Chem 392(7):1405–1410
110. Dickert FL, Hayden O (2002) Bioimprinting of polymers and Sol–Gel phases. Selective detection of yeasts with imprinted polymers. Anal Chem 74:1302–1306
111. Josse F, Bender F, Cernosek RW (2001) Guided shear horizontal surface acoustic wave sensors for chemical and biochemical detection in liquids. Anal Chem 73(24):5937–5944
112. Latif U, Mujahid A, Afzal A, Sikorski R, Lieberzeit P, Dickert F (2011) Dual and tetraelectrode QCMs using imprinted polymers as receptors for ions and neutral analytes. Anal Bioanal Chem 400(8):2507–2515

Percolation Effects in Metal Oxide Gas Sensors and Related Systems

Tilman Sauerwald and Stefanie Russ

Abstract The percolation model has successfully been applied to gas sensors in the past few years. We will describe which kind of sensor properties have been explained or predicted by percolation effects, as, e.g., digital sensor characteristics, tailor-made sensor properties, and resettable dosimeters. Clearly, it is a challenging and nontrivial task to reduce the whole complexity of an experimental system to fit into a mathematical model, as the percolation model. By giving a comprehensive introduction, we will point out which properties of the percolation theory are universal and therefore best suited for the comparison to the experimental results. Furthermore, practical hints for the fitting procedure will be discussed. The focus will be on the metal oxide gas sensors, but we keep in mind that there are further interesting examples for percolation gas sensors and sketch important related systems. We believe that a combined understanding of theoretical and experimental aspects will open new fields for the utilization of percolation effects for metal oxide gas sensor and beyond.

Keywords Percolation, Gas sensors, Digital sensors characteristics, Tailor-made sensor properties, Resettable dosimeter

Contents

T. Sauerwald (✉)
Lab of Measurement Technology, Saarland University, 66123 Saarbrücken, Germany
e-mail: t.sauerwald@lmt.uni-saarland.de

S. Russ
Institut für Theoretische Physik, Freie Universität Berlin, 14195 Berlin, Germany
e-mail: russ@physik.fu-berlin.de

C.-D. Kohl and T. Wagner (eds.), *Gas Sensing Fundamentals*,
Springer Series on Chemical Sensors and Biosensors (2014) 15: 247–278
DOI 10.1007/5346_2013_53,

1 Introduction

Gas sensors based on *n*-type semiconducting metal oxide have been invented more than 50 years ago [1]. Today these sensors normally consist of a granular ceramic, e.g., a sinter pellet [2] or a thick film [3, 4]. A great variety of materials has been investigated, with the *n*-type semiconductor tin dioxide as the most important material [3]. Other important materials are tungsten trioxide, indium oxide, and gallium oxide. Also *p*-type semiconductors, e.g., $SrTi_{1-x}Fe_xO_3$ [5], as well as mixtures of *n*- and *p*-semiconductors [6] have been investigated. A lot of research and development has been done to improve the sensor properties in terms of sensitivity, selectivity, and stability. Most of the research on the sensor principle is nevertheless focusing on the properties of a single grain–grain contact, and it is only recently that also collective, network, or percolation effects have been taken into account.

When we talk about "percolation" in physics, we should be aware that this expression has one more popular and one more specific meaning. The first sense originates from the Latin word "percolare" and describes filtering processes or the dripping of a liquid through a sieve. The second meaning of the word "percolation" describes a mathematical model for systems, where small objects like single atoms, grains, or single bonds have been connected to each other in a random process to form large but still fragile clusters, large enough to spread over the whole system in which they are embedded. When we speak about percolation and percolation theory in this article, we refer to this second meaning. In this sense, the "percolation model" describes a system property linked directly to the geometry of the system and should not be confused with processes (such as diffusion processes) occurring on the system. "Percolation theory" covers a broad range of phenomena that can roughly be subdivided into static and dynamical aspects of the percolation systems. The static aspects consider the geometrical shape and appearance of the percolation clusters itself, while the dynamical aspects investigate, e.g., transport processes on the percolation cluster. We will treat static and dynamical aspects in two different sections in some detail, before we finally come to the use of the percolation model for gas sensing purposes.

The first traces of today's percolation theory can be found about 70 years ago [7, 8]. There, it was described how small molecules connect themselves to larger macromolecules, thereby forming more and more bonds between them in a process of polymerization and gelation (see [9–11] and references therein). In an early publication from the year 1957 on the mathematical fundamentals of percolation, Broadbent and Hammersley [12] created the expression “percolation process” in order to describe how a fluid diffuses through a random porous medium. With the term “percolation process,” they wanted to express that the randomness of the medium (and not the randomness of the diffusion process itself) was the source for the observed phenomena. Today, the percolation model has become a standard model to describe phase transitions, as, e.g., the transition between an insulating and a conducting phase.

Specifically, we want to summarize in which context the percolation model has already been used to better understand the properties of conductance sensors, especially of gas sensors using conductance changes as signals. It is probably clear to the reader that a sensor basically is a system that changes some of its physical properties (as, e.g., color, conductance, shape) under the influence of an external effect or parameter to be detected. Percolation theory, on the other hand, is a very powerful and nevertheless very simple model to describe phase transitions, as, e.g., the transition between the insulating and the conducting phase of a disordered system. It is straightforward that this may be of immense help to describe, e.g., a conductance sensor. When going into the mathematical details, one faces quite ambitious tasks, as, e.g., renormalization techniques, fractal concepts, and scaling behavior. Even if these subjects are not the main focus of this article, we will show where they have been proven meaningful to explain or predict one or another aspect of gas sensors. In the following, we are first going to describe the basic features of the percolation model itself, before we explain the possible applications for gas sensing purposes and describe examples, where the percolation model has already been used or where we think that it could be helpful.

2 The Concept of Percolation: Geometrical Properties

First, we introduce the static properties of a percolation system, i.e., its geometrical shape and appearance. There are different types of percolation models, such as site percolation, bond percolation, continuous percolation, site-bond percolation, invasion percolation, and dynamical percolation. They all describe some random clustering of small units to a large “spanning” cluster and are used in statistical physics as simple models to understand various statistical properties (as, e.g., size, shape, or self-similarity) or dynamical properties (as, e.g., conductance or vibrational properties) of certain disordered systems. To explain the concept of percolation, we concentrate on the site-percolation model that we consider as the most simple one.

In order to create a site-percolation system, we start with an empty lattice (here a square lattice) and assign random numbers r_i (between 0 and 1) to each lattice point i. Then, we choose a desired concentration p of occupied sites, which means that each lattice site with a random number $r_i < p$ is being occupied, while all other sites are left empty. Other types of percolation are similar. If, e.g., we want to create

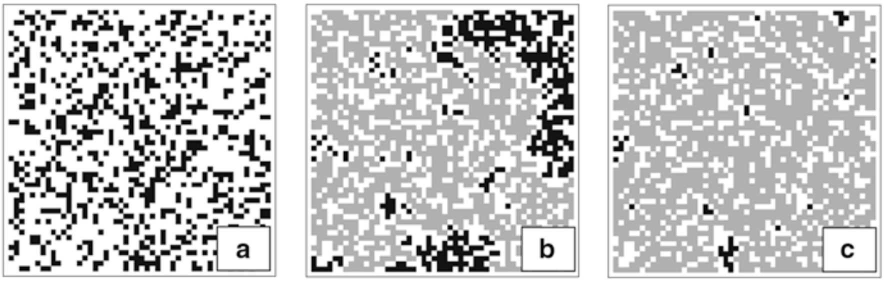

Fig. 1 Examples for site-percolation clusters on a square lattice of side length $L = 50$ and a concentration of (**a**) $p = 0.3$, (**b**) $p = 0.597$ (close to p_c), and (**c**) $p = 0.7$ of occupied sites. Empty sites are indicated by *white color*, occupied sites forming finite clusters by *black*, and occupied sites that belong to the infinite cluster are indicated by the *gray color*

a bond-percolation system, the bonds between the sites (instead of the sites) are occupied (or left empty) according to a random process. For bond percolation and other percolation types, we refer to [9–11].

Figure 1a shows a site-percolation system for a comparatively small value of p, i.e., for $p = 0.3$. Nearest neighbors of occupied sites form clusters of size s ("s-clusters"), where s is the number of the connected occupied sites. So, we call a single unconnected site a "1-cluster," a cluster of two nearest-neighbor sites a "2-cluster," and so on. For small p, only clusters with comparatively small values of s appear, while the clusters increase with p. Figure 1b shows a situation of larger p, where enough sites are occupied to form a cluster that connects two opposite sides of the system. This cluster is called the "infinite" or "spanning" cluster, and in the figure, its sites are indicated by the gray color, while occupied sites that belong to the non-spanning ("finite") clusters are indicated in black. The concentration, where the infinite percolation cluster appears (in average) for the first time, is named the "critical concentration" p_c, and for site percolation we have $p_c \approx 0.5927$ on a square and $p_c \approx 0.3116$ on a simple cubic lattice [11]. The values of p_c depend on the geometry of the lattice and also differ between site- and bond percolation, a behavior that is called "nonuniversal." The values for p_c are normally found numerically, and a table for the most important lattice geometries can, e.g., be found in [10, 11].

When p increases beyond p_c, as it can be seen in Fig. 1c, more and more connections between the infinite cluster and the finite clusters are being formed, so that the latter also become part of the infinite cluster. This way, the infinite cluster gets a more compact appearance and the mean size of the finite clusters decreases again. It is interesting to know that exactly at p_c and for infinite system sizes, also the finite clusters diverge to $<s> \to \infty$. This is illustrated in Fig. 2, where we show, how the mean size $<s>$ of the finite (non-spanning) clusters depends on p. For $p << p_c$ and $p >> p_c$, the value of $<s>$ is small, but close to p_c, it extends to very large values (infinitely large values for infinite system sizes). The so-called correlation length ξ describes the average radius of a finite cluster and

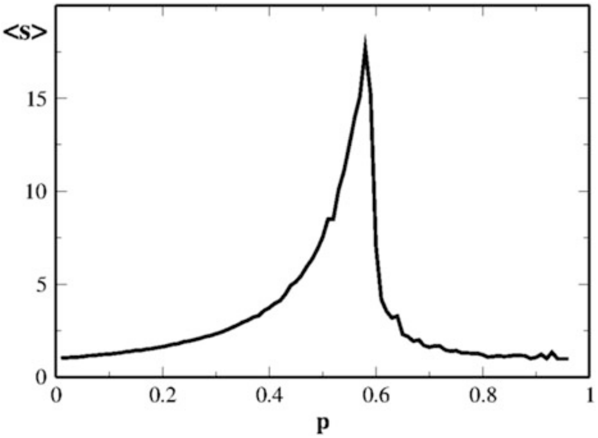

Fig. 2 The mean cluster size $<s>$ of the finite (non-spanning) clusters is plotted versus the occupation probability p. The data have been found by numerical simulations on a 300×300 lattice and an average over 10,000 systems has been performed. For infinite system size, the peak would have a still more symmetric shape with an infinite height

similar to $<s>$, it diverges to infinity at p_c. Note that $<s>$ would be a more symmetric curve for larger system sizes. For finite system sizes, the shape of $<s>$ becomes a bit deformed ("finite-size effect").

Exactly at p_c the infinite cluster is self-similar or fractal, which means that it contains holes, dangling bonds, half-islands, and all kinds of geometrical structures in infinitely many different lengthscales. Please note that the holes of the infinite cluster originate from finite clusters that have been removed (which can also be seen from Fig. 1b). Therefore, in the same way as the finite clusters, also the holes of the infinite cluster exist in all lengthscales at p_c. In Fig. 3, we illustrate the mathematical meaning of fractality, a concept that was invented by Benoit Mandelbrot [13] and has become a key concept for the description of many disordered materials as resins, branched polymers, gels, and others. When one draws d-dimensional circles of radius R on a regular (crystalline) lattice with or without defects, one knows that the number N of occupied sites inside this circle scales with $N \sim R^{\mathrm{d}}$. When one does the same on a percolation cluster, the embedded holes increase with R. As a consequence, N now only increases as $N \sim R^{d_f}$, where d_{f} is called the "fractal dimension" and is smaller than d. Contrary to p_c, d_{f} is universal, i.e., it depends only on the dimension of the lattice but is the same for site- and bond percolation and for all kinds of lattice geometries (simple cubic, diamond, fcc, and so on). The values of d_{f} are known as $d_{\mathrm{f}} = 91/48$ for percolation in $d = 2$ and $d_{\mathrm{f}} = 2.5$ in $d = 3$ [10, 11].

As a direct consequence of the self-similarity and the divergence of the relevant lengthscale, ξ, p_c marks the transition between two different phases of the system and can mathematically be described by standard theories of phase transition [10, 11]. To this end, we imagine, e.g., that the occupied sites are of some

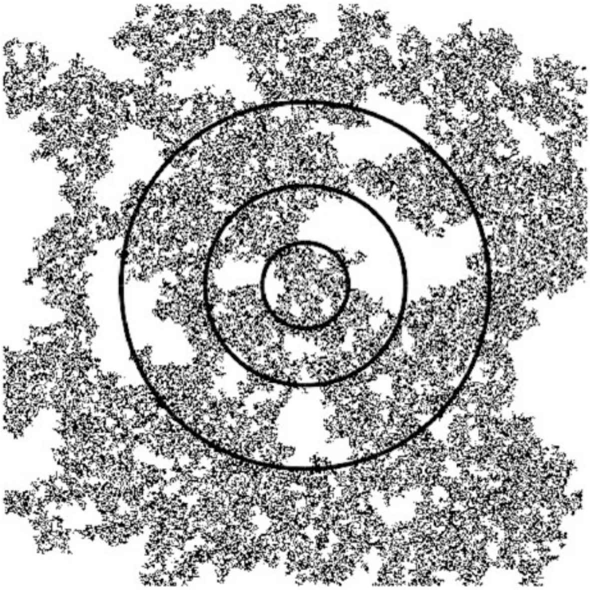

Fig. 3 Illustration of the self-similarity of the infinite percolation cluster at p_c, here in $d = 2$. When circles of increasing radii R are cut out of it, the number N of sites inside the circles scales with $N \sim R^{d_f}$, $d_f < 2$, instead of $N \sim R^2$, as one would expect for a regular (crystalline) system. The reason is that with increasing R, also the sizes of the embedded holes (that arise from the finite clusters that have been removed) are increasing on all lengthscales

conducting material while the empty sites are of insulating material or represent voids. In this case, it is clear that the entire system becomes conducting when for the first time, a percolating conducting pathway appears that ranges from one side of the system to the opposite side. The percolation transition is characterized by critical phenomena, with a correlation length that diverges as $\xi \sim |p - p_c|^{-\nu}$ with the critical exponent ν that is also universal. Also other quantities describing the percolation transition obey power laws, from which we will only introduce the most important ones. Apart from the fractal dimension d_f, we have already introduced the correlation length ξ and the mean cluster size $<s>$:

$$\xi \sim |p - p_c|^{-\nu} \qquad < s > \sim |p - p_c|^{-\gamma}. \tag{1}$$

We can also find quantities that are zero for $p < p_c$ and follow a power law for $p > p_c$. One of these quantities is the probability P_∞ that an occupied site belongs to the spanning cluster. Obviously, P_∞ must be zero below p_c, where no spanning cluster exists. Above p_c, it increases rapidly, as more and more finite clusters become part of the infinite cluster, i.e., $P_\infty \sim |p - p_c|^\beta$ with the critical exponent β. It is interesting to know that P_∞ also plays the role of the order parameter of the percolation phase transition. Closely related to P_∞ is the electrical conductance σ

that naturally is determined by the existence and shape of the conducting pathways between two opposite sides of the lattice. Also σ is zero for $p < p_c$ and increases rapidly above p_c, when the size of the infinite cluster and therefore the number of conducting pathways increases. The critical exponent μ that describes the increase of σ is, however, different from β, because not all sites of the cluster are really contributing to the electrical current. Also this is easy to understand, when one takes a closer look at the structure of the spanning cluster: one quickly realizes that a lot of dangling bonds and wedges exist that are dispensable for the transport properties. In summary, we also introduced the following two power laws that are valid only above p_c:

$$P_\infty \sim (p - p_c)^\beta \qquad \sigma \sim (p - p_c)^\mu \text{ for } p > p_c. \tag{2}$$

The exponents ν, γ, β, μ, and d_f are – contrary to the value of p_c – universal, i.e., they depend only on the dimension d of the system (where $d = 2$ or $d = 3$ applies for our purposes here) and not on geometrical details and on the type of percolation (site or bond). We will need the exponent μ later. Its value is equal to 1.3 for percolation systems in $d = 2$ and equal to 1.99 for percolation in $d = 3$ [14].

It is worth noting that the percolation transition is a statistical one and that all relations and values mentioned above are valid as statistical averages over many different configurations. So, the infinite cluster appears in a statistical way and also "untypical" realizations, where an infinite cluster is already existing below p_c (or nonexistent above p_c), are possible for finite systems. However, with increasing system size L, the phase transition becomes sharper until, at $L \to \infty$, the probability that a system contains the infinite cluster jumps from 0 to 1 exactly at p_c.

3 Dynamical Aspects of Percolation: Numerical Simulations of the Conductivity

The percolation model – among other things – is used to simulate the mobility μ_{el} (and thereof the conductivity σ) of the considered material. This is usually done by random-walk simulations [15] that represent a very powerful tool to gain access to the dynamical properties of the given lattice. The list of topics, where random-walk simulations have already been applied, is very long and reaches from crystalline systems over ion glasses, random binary systems to irregular pores as in zeolites (for a summary see, e.g., [16]). Before discussing some of these applications, we first want to provide the reader with the necessary background to understand the opportunities and challenges but also the possible problems of this method.

It is well known that σ is given by

$$\sigma = e\ n\ \mu_{el}\ , \tag{3}$$

with the unit charge e and the electron density n. It goes back to Einstein and his explanation of the Brownian motion (see, e.g., [17]) that μ_{el} can be expressed by the Nernst–Einstein relation as

$$\mu_{\mathrm{el}} = \frac{eD}{k_{\mathrm{B}}T}, \tag{4}$$

with temperature T, Boltzman constant k_{B}, and diffusion coefficient D leading to

$$\sigma = \frac{e^2 n\, D}{k_{\mathrm{B}}T}. \tag{5}$$

Therefore, the problem is reduced to finding the diffusion coefficient D and eventually the electron density n (if the latter cannot be considered as constant). This is usually done by random-walk simulations that we will now explain in some detail. To do so, we first look at some non-fractal lattice that is either perfectly ordered or has some constant impurity density, i.e., a certain density of missing sites or bonds or of bonds with some altered strength. We now imagine a so-called random walker, e.g., an electron that moves through this lattice by hopping from one lattice site to the other, normally only over nearest-neighbor sites. In this picture, one normally translates the bonds with jump probabilities (and missing bonds with zero jump probability) and considers all sites as identical. (Also other pictures are possible, as one can refer waiting times to the sites by claiming that the random walker spends a certain time on every site before trying its next jump.)

For simplicity, we stay in the first picture, where all jump probabilities are either equal to 1 (nearest-neighbor site is occupied) or equal to 0 (nearest-neighbor site empty). This way, the computer simulation of a random walk consisting of N' time steps of length τ is straightforward and resembles even a game with random numbers. The important quantity that is related to the mobility μ_{el} via the diffusion constant D is the so-called mean square displacement $<r^2(t)>$, i.e., the mean squared distance that the walker has traveled during time $t = N'\tau$. According to the Einstein relation that applies on non-fractal systems, $<r^2(t)>$ is proportional to t. In order to obtain $<r^2(t)>$, one therefore has to perform a large number of different walks (starting at different points of the lattice) and calculate $r(t)$ for each walk, where r measures the distance that the walker has traveled from its starting point. Then, one performs the average of $r^2(t)$ for each value of t over many walks and gets the diffusion coefficient D of a d-dimensional lattice as

$$D = \lim_{\mathrm{t}\to\infty} < r^2(t) > / \ (2d\ t). \tag{6}$$

As $<r^2(t)>\sim t$ on a regular lattice (see above), D is a constant. We obtain σ from (5) by setting the electron density n as proportional to the number N of the conducting (and connected) sites of the lattice, where N is constant on regular lattices.

The described procedure is comparatively simple, if we work on a non-fractal system with well-defined Euclidian dimension d. The situation changes for fractal structures as percolation systems, where $<r^2(t)>$ is no longer proportional to t. Exactly at p_c, the mean squared displacement on fractal systems scales as

$$< r^2(t) > \sim t^{2/d_w}, \tag{7}$$

with the "random-walk dimension" d_w that is bigger than 2. This kind of diffusion is called "anomalous diffusion" [15] (for details, see also [18]) and does not straightforwardly lead to the diffusion coefficient D. Fortunately, the considered systems are normally not exactly at the critical concentration p_c, but (slightly) below or above. If $p < p_c$, we only have finite clusters, so that $<r^2(t)>$ converges to some constant value for large t. In this case, according to (6), D and σ are equal to zero, which is of course what one would expect when the conducting sites are not forming a spanning cluster. If $p > p_c$, the infinite cluster is self-similar only on lengthscales smaller than the correlation length ξ. Accordingly, (7) applies only until the walker has traveled a distance of $r \approx \xi$, i.e., for smaller times. For larger t (corresponding to larger r), the diffusion becomes normal and (6) applies. This means that one can obtain D from (6), under the condition that the random walk is performed for a quite long time, so that the regime of normal diffusion is reached. The necessary time can become very long, particularly close to p_c, which makes the simulations technically difficult. We have already introduced the conductance σ in (2). The number N of sites belonging to the infinite cluster is no longer constant but proportional to $P_\infty \sim (p - p_c)^\beta$, so that the behavior of μ_{el} and σ now differs, i.e., $\mu_{el} \sim (p - p_c)^{\mu-\beta}$.

On the experimental side, this concept has, e.g., been applied to interpret the diffusion and phase correlation lengths of electron diffusion in thin gold films close to the percolation threshold [19]. If on the other hand, one wishes to analyze experimental data of the conductance σ or the mobility μ_{el} (diffusion coefficient D), it is normally a nontrivial task to decide if percolation effects could play a role. Imagine that one has, e.g., found a steep increase in σ when plotted against the concentration of well-conducting sites or some related quantity. If p_c is known, it is straightforward to plot either σ or μ_{el} against $(p - p_c)$ in a double-logarithmic plot, which gives – according to (2) – a straight line of slope μ or $\mu - \beta$ for σ or μ_{el}, respectively. If, however, p_c is not known (remember that p_c is nonuniversal and normally differs for each lattice geometry), it can be quite difficult or even impossible to obtain a clear picture, as already slight deviations from the correct value of p_c lead to enormous deviations from the correct slopes and even from the straight lines. This is demonstrated in Fig. 4, where we show how the simple relation $\sigma \sim (p - p_c)^\mu$ from (2) with $p_c = 0.593$ and $\mu = 1.3$ may be distorted, depending on the type of presentation. Figure 4a shows the data in a half-logarithmic presentation, where we plotted σ versus p and here, the percolation transition is clearly recognizable. In Fig. 4b, we plotted σ versus $p - p'_c$ in a double-logarithmic plot by assuming that the exact value of p_c was not known

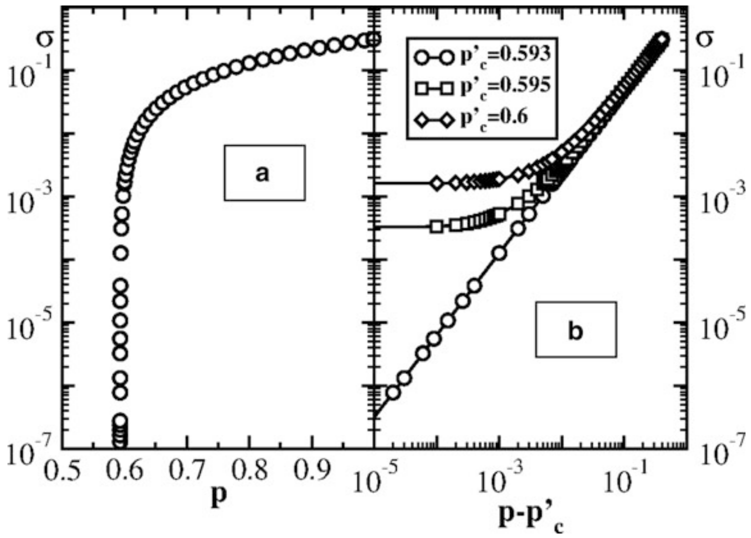

Fig. 4 The conductance σ is plotted versus the concentration in different ways. (**a**) Semi-logarithmic plot of σ versus p. (**b**) Double-logarithmic plot of σ versus $p{-}p'_c$ with several values of p'_c. The figure shows that only a very high accuracy for $p'_c = p_c$ leads to the desired straight line of slope μ

and several approximate values p'_c have been used instead. One can see that it is quite difficult to obtain the correct power-law behavior. For the first curve (circles), the correct value of $p'_c = p_c = 0.593$ was used, and we can see, that here, the data follow a perfect straight line of the correct slope. In the two other cases, $p'_c = 0.595$ (squares) and $p'_c = 0.6$ (diamonds) were used, and we can see that this disturbs the presentation significantly, especially for small values of $p - p'_c$.

In cases, where real data from nonideal systems are used that might be fluctuating and might contain some background conductance, saturation effects, and others, it may therefore be extremely difficult to extract the values of μ, even if the percolation transition and the steep increase might be clearly visible.

4 Geometrical Percolation Effects: Systems with Fixed Occupation Probability

In this chapter, we discuss percolation effects in systems that are related to metal oxide gas sensors. We are interested in the transition between the (electrically) insulating state and the conducting state of those systems. We discuss two types of systems. In Sect. 4.1 the percolation effects are occurring during the system preparation, while in Sect. 4.2 the percolation effects in the systems occur during the operation in response to the change of some parameter. Of a special interest to us are systems where the switching is reversibly dependent on external parameters and that are therefore of importance for sensor applications. We aim to understand the switching processes by only slight changes in composition.

4.1 Percolation Aspect in Sensor Preparation: Composition-Specific Sensor Systems

In some cases it is important to regard percolation effects already in the sensor preparation, while the sensor operation is conducted at fixed concentration p, without using any variation of the percolation properties with time. Specifically this implies the definition of a preparation method for a sensor, which requires two phases of different behavior and is in need for a percolating cluster (commonly a conducting cluster). One could assume that all granular gas sensors fall into this class, since they consist of a sensor material with voids which serve as gas diffusion channels and are therefore essential. Nevertheless for the preparation of most of the granular sensors percolation theory is not applied. The simple reason is that there is no ultimate impetus to increase the fraction of the void to the maximum. Consequently, other aspects of the preparation method, e.g., the film stability, are accentuated. In other words, percolation theory is applied when the properties of the insulating phase are very important and the conductive phase should be reduced to an absolute minimum. An important material where percolation effects are applied is the conductive elastomer (rubber) [20–22]. Most polymers that can be utilized as elastomers are insulating. If a conductive material is required, the elastomer can be homogeneously mixed (filled) with a conducting material (e.g., carbon black) with the fraction of conducting material obviously above the percolation threshold. The material has a lot of applications that range from the utilization as a flexible conductor (e.g., polymer foams that prevent electrostatic damage, electronic devices, or sealing for electromagnetic field absorbing gasket) to numerous sensor applications that will be discussed in the following sections.

The adjustments of percolation properties are also important for disordered (disperse) layers of gas sensor materials. These aspects can be found in literature especially in the case of SnO_2 nanowires [23–25] but also in homogeneous granular material [26] and in the case of systems with two or more types of grains [27]. We want to emphasize one interesting example for the occurrence of binary systems showing a percolation threshold that depends on preparation parameters and is presented by Sahner et al. [27] for a system of lanthanum cuprate-lanthanum ferrate (La_2CuO_4–$LaFeO_3$). This material is used as an oxygen sensor. The system is obtained by co-firing of lanthanum oxide, copper oxide, and iron oxide powders in various molecular fractions forming a compact ceramics (with only a few pores). The ceramic obtained by a solid-state reaction is a phase mixture of lanthanum cuprate (La_2CuO_4) and lanthanum ferrate ($LaFeO_3$). The lanthanum cuprate is the active phase of the sensor but also prone to sulfur poisoning. The $LaFeO_3$ is preventing the poisoning effect but has much lower sensitivity. La_2CuO_4 has a much higher conductivity than $LaFeO_3$, so the conductance of a phase mixture should be dominated by lanthanum cuprate pathways. The aim of the work is to design a material that combines both positive attributes in a way that on one hand the cuprate content is high enough to dominate the conductance, but on the other hand as low as possible in order to increase the content of stable ferrate. In this work, the authors experimentally determine the conductance of different phase mixtures that they are modeling by using a general effective media theory – GEMT ([27] and references therein). The experimental results show that a mixture with a volume fraction of 10% La_2CuO_4 is already above the threshold leading to percolation of La_2CuO_4 through the system. Based on the experimental results, the authors calculate the threshold using the GEMT to a volume fraction of 8%.

Another example for a percolation transition in the preparation process can be found for gallium oxide [28]. Gallium oxide is a very poor semiconductor and it is an important material for a gas sensor working at a high temperature (e.g., 800°C). Up to a certain extent, it is resistant to reducing atmospheres, as, e.g., in exhaust gases [29]. The first hints for percolation effects in metal oxide gas sensors have been found for gallium oxide sensors (see [30] and references therein).

Nagarajan et al. were investigating films of gallium oxides prepared by pulsed laser deposition on an alumina substrate using a gallium oxide (Ga_2O_3) target. The deposition in argon atmosphere yields an amorphous layer with high gallium excess (Ga:O $\approx$ 45:55). This sub-stoichiometric phase of Ga(III)oxide tends to disproportionate into stoichiometric Ga(III) oxide and a phase with high gallium excess. By density functional theory (DFT) calculation on a $Ga_{24}O_{24}$ supercell (thus Ga:O $\approx$ 50:50), the author could prove that the electrons of the highest occupied states become delocalized whereas for a $Ga_{20}O_{24}$ supercell the states are localized. The material therefore exhibits a metallic behavior at a certain gallium excess. When the as-prepared films (Ga:O $\approx$ 45:55) were heated, the authors observed a metal-insulator transition at a temperature of 663 K and therefore a jump of conductivity over seven orders of magnitude. The authors interpret the results as following. With the rise of temperature, there is a formation of stoichiometric Ga_2O_3 nuclei. With increasing temperature, the nuclei grow to larger crystallites and consume oxygen of a certain surrounding "shell" of the amorphous gallium oxide. The shells become conducting due to the increasing gallium excess. At a certain temperature the shells are connecting to a percolation pathway and the whole sample becomes conducting.

4.2 Change of Composition by Morphological Changes in One of the Phases

The most natural principle for the use of percolation effects in sensor applications is to use systems consisting of two (or more) phases, where the geometrical parameters (as, e.g., the grain size) are changed (e.g., inflated or shrank) by an external parameter, so that the whole system is driven over the percolation threshold.

One important example is the conducting polymers that can have a broad variety of applications that utilize the geometric change of the polymer backbone. Among these applications are temperature control [31, 32], strain sensors [33], and gas sensors [34–36]. The temperature control by thermal expansion is a well-known example for the usage in resettable fuses [31] that already have numerous applications. In this case, the devices are made of a mixture of isolating polymers with a conductor. The mixture is above the percolation threshold at normal temperature. Due to ohmic heating, the temperature of the polymer is increasing for high currents. At higher temperatures the isolating polymer is expanding. At a certain threshold current, respectively, temperature, the concentration of the conducting particles is falling below the percolation threshold and the conductance of the fuse is steeply decreasing (triggering of the fuse). As a result, the voltage dissipates mainly in the fuses (of course the energy dissipation at the fuse in the non-triggered/percolating state would typically be very low compared to the total load of the electric circuit), and therefore the heated (low conducting) state is maintained, until the supply voltage falls below a predefined limit (reset). This kind of fuses is available from different manufactures, e.g., [32]. For the gas sensors, different kinds of conducting polymers are used. The geometric change can be an isotropic expansion, evoked, e.g., by thermal expansion, or a swelling due to the incorporation of organic compounds into the polymer backbone [34–36].

An interesting system in which the percolation effect is related to the reversible volume growth of one phase is reported by Dankert and Pundt [37]. In their work, hydrogen sensors based on granular palladium (Pd) films are investigated; in this example the first phase will be represented by the palladium as a metallic conductor, while the second phase is air that can be considered as a perfect insulator. Palladium can absorb large amounts of hydrogen leading to volume expansion. This can be considered as a discontinuous Pd film that is initially insulating, i.e., slightly below the percolation threshold. As a result of the growth of Pd particles, the film might go beyond the threshold and become therefore conducting. In a previous work, Favier et al. [38] show that this effect can be used to make a mesoscopic Pd-wire switch between a nonconducting and a conducting state. Dankert and Pundt demonstrated this effect on a discontinuous thin film and interpreted the results in the framework of percolation theory. The discontinuous film (just below the percolation threshold) was obtained using a sputtered film (10 nm) and Joule heating. The Joule heating leads to an agglomeration of particles. As the ideal case of a percolation transition, the conductance of the films without hydrogen incorporation should be zero. Nevertheless, the prepared films (without hydrogen incorporation) already revealed a significant conductance of approximately 1 mS that the authors attribute to remaining conduction pathways in the film. The conductance was measured at a certain hydrogen uptake. The observed conductance change of the film was as low as 50% for a hydrogen concentration of 5×10^3 Pa. Based on this results, the proposed percolation transition could be questioned. Nevertheless, the research for resistive-type palladium structures for hydrogen sensing is continued by several groups due to the simplicity of the system and the high selectivity of the sensor film. Using enhanced preparation methods, films with improved switching behavior have been demonstrated, e.g., by Xu et al. [39]. The investigation shows that the use of a siloxane self-assembled monolayer as substrate coating leads to a formation of smaller nanoclusters as compared to bare glass substrates. These films show a significant switching point at approximately 2,500 ppm hydrogen. Xu also was able to show the development of additional pathways under hydrogen incorporation using atomic force microscopy [39]. This proves that the concept of establishing percolation pathways by hydrogen-induced volume growth is feasible even though a detailed study of the percolation properties has not yet been reported.

5 Metal Oxide Gas Sensing Principles

We now turn to so-called homogeneous semiconducting gas sensors that usually consist of a polycrystalline oxide layer and change their conductance, when exposed to the gas to be measured. The signal is derived by two electrodes that measure the conductance G between two opposite sides of the layer, and the gas is detected via a change of G. The conductance ($G = \sigma l/A$) is of course depending linearly on the conductivity (cf. Sect. 3) by the macroscopic dimensions, i.e., the length l and the cross-section A of the layer.

Homogeneous metal oxide gas sensors are in the majority n-type semiconductors with a conductance that is basically caused by oxygen vacancies inside the bulk material acting as donors. They are usually considered as belonging to two different classes, depending on their operating temperature. At higher temperatures, the oxygen vacancies are mobile enough to reach equilibrium with the exterior oxygen pressure quite fast, so that the number of bulk charge carriers depends in a very sensitive way on the oxygen concentration that surrounds the sensor [3, 40]. These sensors are called semiconducting lambda probes, because they can replace the Nernstian ceramic lambda sensors for oxygen detection [27].

At lower temperatures, typically below 500°C, surface effects are considered as more important than reactions in the bulk [40], giving rise to a “surface-sensitive” sensor-type utilizing variations of the surface charge and the resulting conductance change from grain to grain (see, e.g., [2]). The surface charge in normal air is typically dominated by (ionosorbed) oxygen which traps electrons from the n-type semiconductor bulk, thereby creating an electron depletion zone (space-charge layer). Conductance from grain to grain occurs via different mechanisms [2, 41–43], first by electron flow through the open necks and second by electron hopping over the grain boundaries. Both mechanisms are disturbed by the depletion layer: first, the area of the conducting channel between two grains is reduced by the thickness of the depletion layer and second, the surface charge is forming a huge barrier (V_{barrier}) of typically several hundred millivolts for the electronic conductance. The transport mechanism over this barrier is usually considered as due to thermionic emission, and therefore this part of the conductivity σ is proportional to $\exp(-eV_{\mathrm{barrier}}/k_BT)$. Thus the conductance variation is high even for small changes of the surface charge.

Gases like CO, H_2, and CH_4 are capable of reducing the surface charge (i.e., making surface charges less negative) either by direct ionosorption or by reactions with ionosorbed oxygen. The resulting change of the conductance is used as the sensor signal. The relative change of conductance $(G_{\mathrm{gas}} - G_{\mathrm{air}})/G_{\mathrm{air}}$ is often attributed as sensitivity S or sensor response. As a direct consequence of this sensing mechanism, the selectivity (i.e., the capability of a sensor to react in different ways to different gases) is not very high, given that all reducing gases generally reduce the surface charge and therefore increase the conductance, whereas oxidizing gases increase the surface charge and therefore decrease the conductance. For sensor application, often a selective detection of a certain gas is required and a lot of techniques have to be studied to achieve selectivity, including sensor temperature [44–46], special sensor, or doping material providing selectively active sites [41, 47, 48], adlayers, and the variation of the film thickness [49–51].

6 Percolation in Homogenous Surface-Type Gas Sensors

SnO_2 is an n-semiconducting material, whose ability as a gas sensor has been known for many years [1]. In practice these sensors consist of SnO_2 grains arranged in a disordered sintered layer that forms a network between two electrodes. While in normal air the conductance of the grains and thus of the total system is poor, a dramatic increase of the conductivity σ takes place, when the sensor is exposed to a reducing gas, such as CO. The reducing gas is thus detected via a change of σ, which is (at not too high temperatures, see above) microscopically explained by a standard model [24, 40, 52]: in normal air, oxygen molecules are adsorbed on the grain surfaces and trap electrons from the conduction band. This way, a negative surface charge of the trapped electrons arises that is accompanied by a positively charged depletion layer of thickness $\lambda \approx 10$ nm (space-charge layer). When a reducing gas is offered, λ becomes smaller, which is often explained by the picture that the gas carries the oxygen away, thereby releasing the trapped electrons (see Fig. 5).

The influence of the grain sizes and the depletion layer on the conductance is explained either by the deterioration of the conductance through the single grains or by a deterioration or even breaking of the bonds between the grains [42]. For a long time, rather the properties of single grains and of single bonds than the network effects have been regarded, and the possibility that whole grains might become insulating or bonds might be broken (i.e., become of zero conductance) has not been taken into account. The possibility that percolation effects should come into play, when the grain radii become comparable to the thickness λ of the depletion layer has first been theoretically proposed and corroborated by numerical simulations in [30, 53]. In this work, a quantitative model has been proposed, where within the

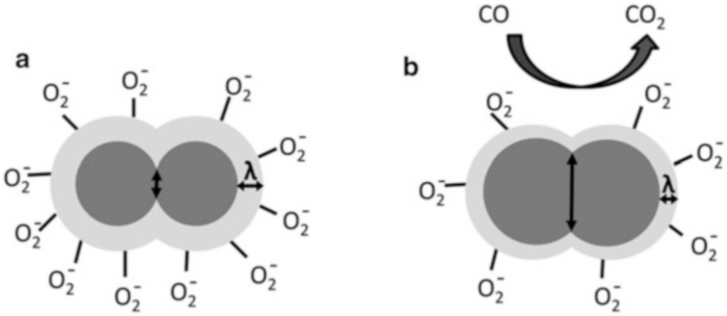

Fig. 5 Sketch of the sensor principle of a neck-controlled sensor under exposure of reducing gas. (**a**) Shows the situation without reducing gas (where λ is at its maximum value), while (**b**) shows a situation of smaller λ, where many oxygen molecules have been removed by the gas (CO)

Schottky approximation (similar as in [43]) and assuming acceptor/donor compensation, the thickness of the depletion layer has been calculated as

$$\lambda \approx (N_{\mathrm{ox}} - N_{\mathrm{r}})/N_{\mathrm{D}},$$

where N_{r} and N_{ox} are the surface densities of the reducing gas and the initially adsorbed oxygen, respectively, while N_{D} is the donor density of the metal oxide bulk material. This means that for grain sizes in the range of a few nanometers, whole grains might become totally depleted of electrons and can therefore be considered as insulating and also bonds between neighboring grains might become broken.

Figure 6a shows a scanning electron microscope picture of a typical SnO_2 grain cluster, while in Fig. 6b, the underlying model picture of [30, 53] is illustrated. This schematic picture shows a network of sintered grains, with connections in the shape of necks between them. Typical parameters for the grain diameters D_i, the sintering parameter Θ, the coordination number k, and the density D_n of donor atoms have been taken from experimental values [43]. In this picture, there is only a sensing signal, if a conducting path from one side of the system to the opposite side is existing, which brings us quite naturally to the percolation model. To model such a system, it has been assumed that from the original number $V_i D_n$ of free electrons in the conduction band of grain i of volume V_i, a certain number $(N_{\mathrm{ox}} - N_{\mathrm{r}})S_{\mathrm{exp},i}$ is trapped by the oxygen. $S_{\mathrm{exp},i}$ is the "exposed surface" of grain i, i.e., the surface that is not blocked by other grains but exposed to the gas. This leads to the number difference $\Delta N_{\mathrm{e}} = V_i D_n - (N_{\mathrm{ox}} - N_{\mathrm{r}})S_{\mathrm{exp},i}$ between the number of electrons coming from the donor atoms and the number of trapped electrons. In a mean-field type approximation, it has been assumed in [30, 53] that a grain, where $\Delta N_{\mathrm{e}} < 0$ applies, is insulating (completely depleted of electrons), while a grain with $\Delta N_{\mathrm{e}} > 1$ is conducting. All grains between these two limits have been considered conducting with a probability $p_{\mathrm{e}} = \Delta N_{\mathrm{e}}$.

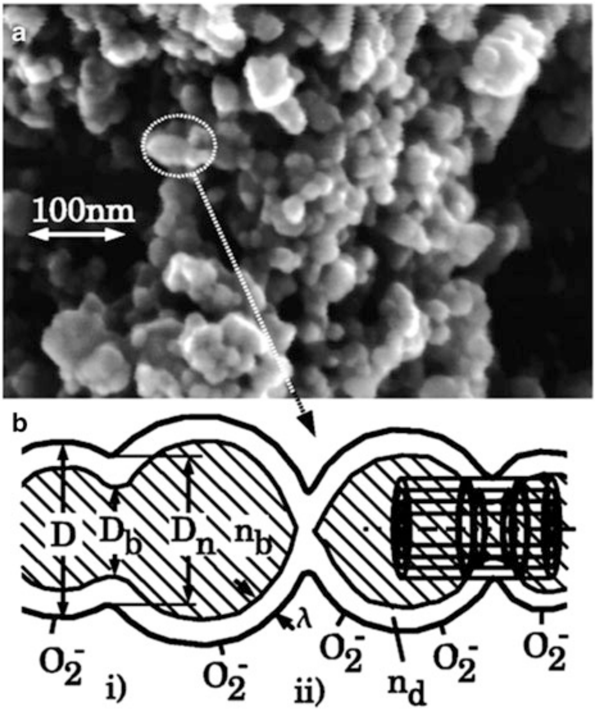

Fig. 6 (**a**) A scanning electron microscope picture of a typical SnO_2 grain cluster. (**b**) The types of grain intersections. Oxygen molecules are ionosorbed at the grain surface by extracting conduction electrons from the grain. This leads to a depletion layer with thickness λ in which the electron density is much smaller than the electron density in the bulk volume ($<D>$: mean grain diameter, D_n: neck diameter). *i*) Open neck (with channel diameter D_b), (*ii*) closed neck. *Right-hand side* (reprint with permission [53])

The conductance of a two-dimensional network built up by grains with a broad distribution of diameters D_i has been investigated by random-walk simulations [30, 53], similar to the ones described above. To find the jump probabilities between two neighboring grains, the diameter of the geometrical overlap (of the "neck") between them was identified. This channel was considered as consisting of the outer depletion zone of thickness λ and (eventually) also a conducting interior part.

This way, it was shown that for not too large grains, the conductance of the gas sensor indeed shows a percolation characteristic curve when plotting it versus the density N_r of reducing gas. Below a certain critical gas density N_{crit} , the system is insulating, while above N_{crit} , the structure becomes conducting. This is shown in Fig. 7, where σ is plotted versus N_r for several systems of different mean grain diameter $<D>$ and coordination number k. One can see that for larger $<D>$ and larger k, the systems are conducting for all gas concentrations N_r, i.e., that no percolation transition can be seen. For smaller grains and smaller values of k, on the other hand, σ is zero for small values of N_r and starts at a threshold value

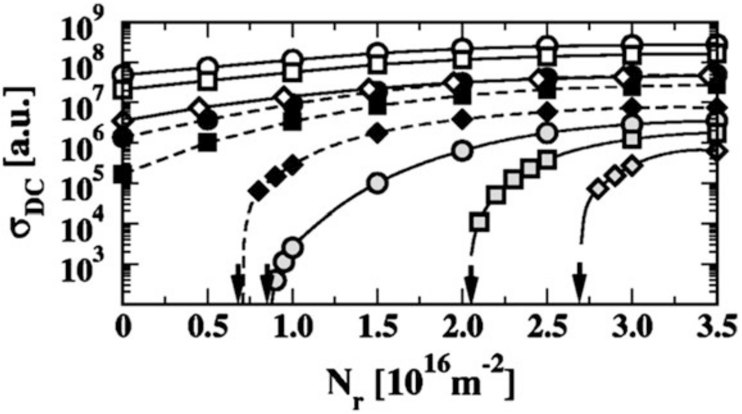

Fig. 7 The (numerically obtained) conductance σ is plotted versus the density N_r of adsorbed gas for systems of different occupation probabilities $p = 0.6$ (*diamonds*), $p = 0.8$ (*squares*), and $p = 1$ (*circles*) and different mean grain sizes $<D> = 50$ nm (*white symbols*), $<D> = 30$ nm (*black symbols*), and $<D> = 12$ nm (*gray symbols*). The *small arrows* indicate the percolation thresholds (reprint with permission from [53])

(indicated by the arrows) with a steep increase. Technical applications that could use this quite special characteristic curves ("digital sensor") have also been proposed in [53]. The experimental verification of this percolation transition in SnO_2-sensors is, however, still pending.

The model of [53] for a nanoporous SnO_2 gas sensor has been considerably improved and extended by Dräger et al. [54] (with the participation of the present authors). In this work, a special three-dimensional site-bond percolation model for mono- and polydisperse systems (grains of equal and of unequal sizes, respectively) has been investigated analytically and numerically. While in [53], the bonds between the sites have been chosen from a realistic distribution, but randomly distributed over the lattice, in [54] the bonds between two neighboring sites have been explicitly calculated from the actual overlap between them (by considering only conductances through open necks that seems to be more relevant for smaller and well-sintered grains [43]). As a main result, the phase transition due to the interruption of the conducting pathways has been described as a complex interplay of three different effects: (1) bond-percolation effects, when too many bonds are cut; (2) site-percolation effects, when too many grains become insulating; and (3) the deterioration of the existing bonds. While the last point is probably clear, the first two points can best be understood from Fig. 8, where the two situations are illustrated in a schematic picture for monodisperse grains. In Fig. 8a, according to the condition of [30, 53], the grains are still conducting, i.e., ΔN_e is still bigger than 1, due to a relatively large volume of the grains (and not too small values of N_D). Figure 8b shows the other limit that is realized for smaller grains, namely, that the overlaps between neighboring grains and therefore also the bonds between them are still intact, when the grains itself become already too small to host free electrons.

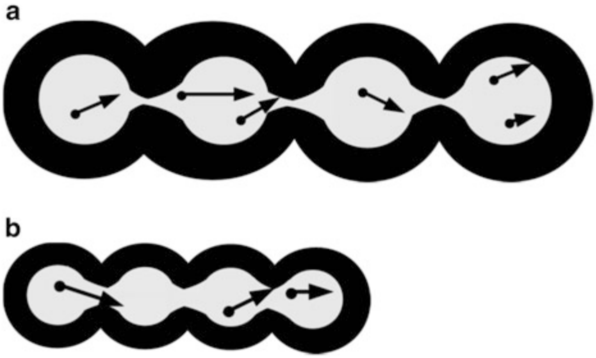

Fig. 8 Sketch of the two possibilities that may lead to a breakdown of the conductance when λ increases: (**a**) The bonds between large grains may become interrupted while the cores are still large and therefore conducting. (**b**) The cores of small grains may become too small to host free electrons, while the bonds are still conducting. Both situations should be understood as just before the breakdown

The reader may notice that these two conditions, (1) the breakdown of overlapping bonds and (2) the breakdown of conducting grains at a given gas concentration N_r, do not necessarily impose a classical percolation transition similar to the one of Fig. 1, with a self-similar spanning cluster and with a universal critical exponent μ originating from (2), but that, e.g., a simultaneous breakdown of all bonds at a given gas concentration N_r in a monodisperse lattice may lead to a similar phase transition with a different critical exponent μ. Indeed, it is shown in [54] that the abovementioned effects compete for their determining role and that therefore a thorough research for the differences between mono- and polydisperse, crystalline, and disordered systems had to be performed.

For a monodisperse system, this whole problem could be solved analytically: considering that the conductance between neighboring grains scales with the area of the conducting overlap between two neighboring sites, one can calculate the case of Fig. 7a analytically and derive the shape of the characteristic curve for the case that the bonds break down while the sites are still intact as

$$\mu_\mathrm{el} \sim \left(N_\mathrm{r} - N_\mathrm{crit}^{(\mathrm{bond})}\right)^2 \text{ with } N_\mathrm{crit}^{(\mathrm{bond})} = N_\mathrm{ox} - \Theta N_\mathrm{D}\frac{< D >}{2}. \tag{8}$$

This means that the “critical” exponent of the phase transition in this case is equal to 2, independent of the geometry and even of the dimension d. In the other case, namely, when the grains become depleted of electrons, while the bonds are still intact, another critical gas concentration was derived in [54], that inflicts an additional cutoff condition for the characteristic sensor curve:

$$N_\mathrm{crit}^{(\mathrm{site})} = N_\mathrm{ox} - \frac{N_\mathrm{D}\pi < D >^3}{6S_\mathrm{exp}} + \frac{p_\mathrm{c}^{(\mathrm{site})}}{S_\mathrm{exp}} \;. \tag{9}$$

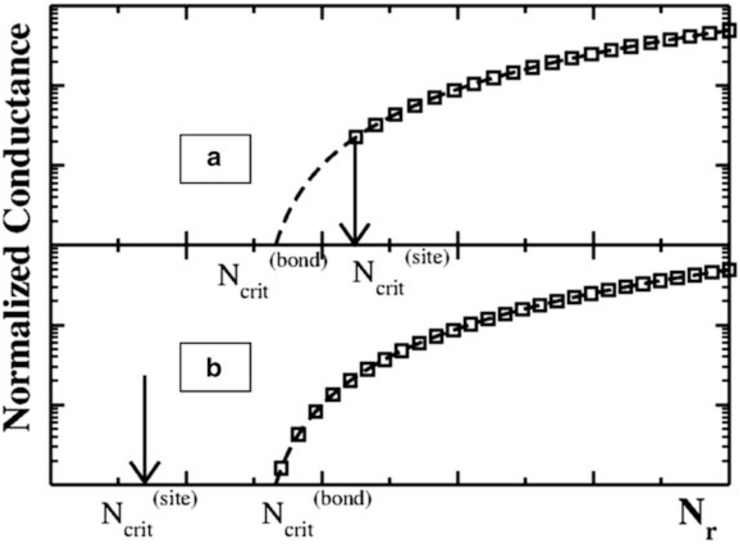

Fig. 9 Sketch of the theoretical prediction for the normalized conductance versus N_r for (*a*) $N_{crit}^{(site)} > N_{crit}^{(bond)}$ and (*b*) $N_{crit}^{(site)} < N_{crit}^{(bond)}$. The theoretical curve for $N_{crit}^{(bond)}$ is indicated by the *dashed curve* and the cutoff value $N_{crit}^{(site)}$ by the *arrows*. The expected experimental values in both cases are shown by the *symbols*. Note the jump of the conductance in (*a*) and the steep increase (high sensitivity) in (*b*)

Here, $p_c^{(site)}$ is the site-percolation threshold of the system (that depends on the geometry and the thickness of the layer).

In Fig. 9, we illustrate the role of the two critical gas thresholds $N_{crit}^{(bond)}$ and $N_{crit}^{(site)}$ in schematic diagrams. While only $N_{crit}^{(bond)}$ influences the shape of the characteristic curve, $N_{crit}^{(site)}$ defines a cutoff value, i.e., $\sigma = 0$ for $N_r < N_{crit}^{(site)}$. The theoretical curve of (8) is indicated by the dashed line and the expected experimental values of the characteristic curves by the symbols. We can see from the figure that two basically different situations are possible: Case 9(a) describes the situation $N_{crit}^{(site)} > N_{crit}^{(bond)}$ and can be realized for smaller grains and smaller values of N_D. In this case, $N_{crit}^{(site)}$ marks a cutoff value, where the conductance jumps from a finite value to zero. We think that this jump could technically be used to design sensors with an inherent threshold value. Case 9(b), on the other hand, that can be realized for larger grains, larger values of N_D, and higher sintering parameters is shown in Fig. 9b. In this case, the expected experimental values follow the critical curve until its end. Depending on the desired application, one or the other case could be desirable.

The results of Fig. 9 have been gained for monodisperse systems. However, it was shown in [54] that also polydisperse systems follow the theoretical curves of Fig. 9 to a large extent. For the case $N_{crit}^{(site)} < N_{crit}^{(bond)}$, the bonds play the major role and no noticeable differences between mono- and polydisperse systems have been found. For $N_{crit}^{(site)} > \mathrm{N}_{crit}^{(bond)}$, on the other hand, the curves for mono- and

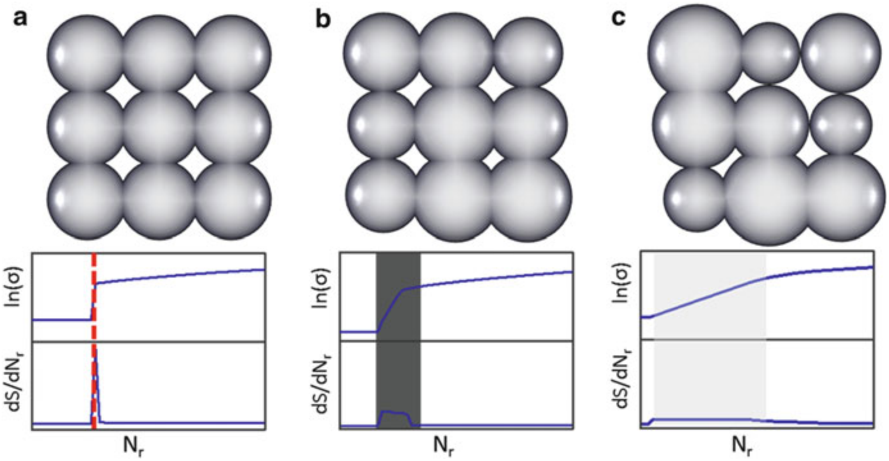

Fig. 10 Schematic illustration of the influence of the grain-size distribution on the sensing properties calculated in [54]: (**a**) Uniform grain sizes with a sharp percolation transition, (**b**) narrow grain-size distribution covering a small concentration range, (**c**) broad grain-size distribution with a wide range of gas concentration

for polydisperse systems match each other only for large values of N_r , while close to the percolation transition the polydispersivity leads to smaller values of the mobility μ_{el} (and therefore σ). In particular, the discrete jump at $N_r = N_{crit}{}^{(site)}$ is washed out and replaced by a smoother increase of σ when N_r increases. Also this continuous increase covers the same interval $\Delta\sigma$, which leads to an enhanced sensitivity of polydisperse as compared to monodisperse systems.

From these numerical results, we can see that percolation theory can help to design not only gas sensors that monitor a single threshold value but also a certain desired gas concentration interval ΔN_r in which the relevant conductance increase takes place. In other words, one could trigger the sensitivity by choosing the grain-size distribution appropriately.

This is shown in Fig. 10 on three schematic pictures. While the three upper pictures indicate systems of the same mean grain size $<D>$ but with different distribution widths, the lower pictures show the expected behavior of the conductance (provided that the other system parameters stay fixed and are chosen such that $N_{crit}{}^{(site)} > N_{crit}{}^{(bond)}$, according to Fig. 9a).

In summary, a monodisperse grain-size distribution as shown in Fig.10a (with appropriate system parameters as explained above) is the best representation when one wishes a sensor monitoring a predefined gas threshold. For the monitoring of a concentration range, one needs a polydisperse system with a certain grain-size distribution. In Fig. 10b, c, we sketched two special examples with a small and a large width of the distribution, respectively. The corresponding concentration ranges (smaller range in (b) and larger in (c)) are also shown in the lower parts of the figure.

7 Composite np-Systems

A more complex approach that has come into focus during the last decade is the use of composite sensors, and among them systems built up by a mixture of semiconducting *n*- and *p*-grains. The motivation for this approach is the search for selective sensors that respond with different characteristic curves to different gases. Composite gas sensors of *p*-type CuO and *n*-type ZnO have been investigated in [55, 56] with respect to their electrical properties and their sensitivity towards CO, which turned out to depend strongly on the volume fraction between the CuO and the ZnO grains and on further doping of the CuO. Selectivity between the gases CO and H_2 has been found in composites of SnO_2 and Zn_2SnO_4, when measuring the resistance of the system under the influence of these gases at fixed concentration [57].

In composite sensors built up of sintered TiO_2 grains in the two different modifications anatase and rutile, a selective behavior towards the gases CO and CH_4 has been reported at high temperatures [6, 58, 59] and interpreted as due to percolation effects. In the experiments to this work, a sensor composed uniquely of anatase grains showed a conductance that increased with the amount of reducing gas, while the conductance of a sensor composed uniquely of rutile grains decreased. The authors interpreted this behavior by assuming that anatase was an *n*-semiconductor while rutile was basically a *p*-material. Since the rutile is obtained from the heat treatment of the anatase, both materials must have the same impurity concentration. Several arguments can be found in the work of [6] for the change of the conductance mechanism during the rutile formation.

Both grains have been considered as sensitive to the ambient atmosphere via the adsorption of molecules on the surfaces. It has been assumed that the conductance of n-grains is increased by a reducing gas (via the mechanisms described above), while the conductance of *p*-grains is decreased by a reducing gas. In this picture, it is again assumed that oxygen reacts with electrons from the outer shell of the grains, which causes additional holes in the case of a *p*-grain and thus an increase of the density of the major carriers. One may question, if surface effects are still the relevant mechanism at the relatively high temperatures (600°C) used for gas measurements in this work, as for SnO_2 sensors, lower temperatures are usually applied in order to stay in the regime of surface-sensitive sensors. However, there are reports on TiO_2 sensors that favor the surface model until at least 600°C [59, 60].

The composite np-sensors of [6] show very different characteristic curves, depending on their volume fraction of anatase to rutile and on the considered gas, i.e., CO or CH_4. Sensors of appropriate anatase-to-rutile fraction were able to show a selective behavior, i.e., an increase of σ with increasing gas concentration N_r towards CO and a decrease of σ with increasing N_r or eventually no response towards CH_4. Only systems with more than 75% *p*-grains showed a decrease of σ with increasing N_r, while already systems with 25% n-grains showed an increase of σ (under the influence of CO) or at least no response (in the case of CH_4).

For the explanation of this behavior, a special kind of a percolation model was proposed in [6] that is based on the following assumptions: Between n-anatase and the p-rutile grains, there are in principle nn-, pp-, and np-connections. It was assumed that only percolating pathways consisting either of pure nn- or of pure pp-connections should contribute to the conductance, while np-bonds were neglected due to the rectifier effect. The nn- and the pp-pathways were considered as parallel resistances, so that for the conductivity σ of the lattice

$$\sigma = < \sigma_{\mathrm{nn}} > + < \sigma_{\mathrm{pp}} >,$$

was assumed with the effective conductances $<\sigma_{\mathrm{nn}}>$ and $<\sigma_{\mathrm{pp}}>$ of the nn- and the pp-pathways, respectively. Both effective conductances were assumed to obey a percolation behavior according to (2)

$$< \sigma_{\mathrm{nn}} > \sim (p_{\mathrm{nn}} - p_{\mathrm{c,nn}})^{\mu'}, < \sigma_{\mathrm{pp}} > \sim (p_{\mathrm{pp}} - p_{\mathrm{c,pp}})^{\mu'},$$

where p_{nn} and p_{pp} play a similar role as the bond occupation probabilities in a bond-percolation model and are estimated by the surface fractions of the n- and the *p*-grains and by the hypothetical surface area of the empty sites (voids). $p_{\mathrm{c,nn}}$ and $p_{\mathrm{c,pp}}$ are the respective critical occupation probabilities. Analyzing the geometrical values of the anatase and the rutile particles from scanning electron micrographs, the authors estimated the critical rutile-to-anatase volume ratio, where for the first time a conducting pathway either of nn- or of pp-bonds should appear, in agreement with the conductance measurements. This means that according to these estimations, a percolating pp-pathway should only exist when the volume ratio of rutile was bigger than 75%, while nn-pathways should be present between 0% and 94–95% of rutile, and both pathways should simultaneously exist between 75% and 94–95% volume ration of rutile.

These measurements have preliminarily been tested [61] by numerical random-walk simulations on composite np-systems, where it has been assumed that different reducing gases possess different capabilities to remove the oxygen from the grain surfaces. Also in the simulations, a selective behavior between different gases has been found. Contrary to the assumptions of [6], the np-bonds have been found important to explain the appearance of five well-distinct sensor curves for the five ratios of anatase:rutile.

8 Gas Sensors Utilizing Bulk Reactions

We now turn to a special variety of solid-state gas sensors that utilize bulk reactions as sensor principle instead of surface reactions as described in Sect. 5. By "bulk reaction" we mean a chemical reaction of the metal oxide in a way that a new chemical phase is generated. Also combinations of the two principles are reported when both bulk reactions and surface reactions are influencing the sensor signal [41, 62]. The behavior of the sensors using a bulk reaction can be very similar to sensors using surface effects, since for practical reasons the bulk reaction will be limited only to the near-surface layer to prevent slow solid diffusion processes and has to be fully reversible in order to achieve a fast sensor response and recovery. Furthermore, typical conductance changes are used as sensor signals in both sensor types. In the case of bulk-reaction gas sensors, thus the two solid phases ought to have great differences in conductivity. It is straightforward that percolation effects might come into play in this type of sensor, when highly conductive and hardly conductive phases are coexisting. Several examples for bulk reactions utilized in gas sensors can be found in literature, as, e.g., the formation of alkali metal nitrate from their oxides or carbonates used as a nitrogen oxide sensor [63] or the formation of nickel sulfide from nickel oxide [64] used for the detection of the sulfur poisoning of catalysts. An important example concerning percolation effects is the sulfurization of copper oxide to copper sulfide. Copper is very prone to the formation of sulfides. Therefore, at low temperatures (typically below 200°C) already small concentrations of hydrogen sulfide (H_2S) applied to copper oxide lead to a formation of copper sulfide according to the following equation:

$$\mathrm{CuO} + \mathrm{H_2S} \ \rightarrow\ \mathrm{CuS} + \mathrm{H_2O}. \tag{10}$$

Whereas CuO is a poorly conductive *p*-type semiconductor [65], CuS is a highly conductive material (*p*-type) showing a metallic hole conduction [66]. The formation of copper sulfide, in the following called sulfurization, has been proven under similar conditions by using X-ray photoemission spectroscopy (XPS) by independent groups [62] [67] and by using TOF-SIMS measurements [68]. A second reaction competes to the process of sulfurization, namely, the reaction of copper sulfide with oxygen-forming copper oxide and sulfur dioxide (11). This reaction is dominant at higher temperatures:

$$\mathrm{CuS} + \mathrm{H_2S} \ \rightarrow \mathrm{CuO} + \mathrm{SO_2}. \tag{11}$$

In the metallurgy, this process, in the following called desulfurization, has been used for centuries for the conditioning of sulfuric ores (so-called roasting) at very high temperatures (e.g., 800°C). For the sensor application, the copper-sulfur phase is only occurring as fine-disperse clusters at the near surface so that usually lower temperatures are sufficient. For partially sulfurized copper oxide fibers, it has been proven with energy dispersive X-ray spectroscopy (EDX) that a short heat treatment at 350°C leads to a complete removal of sulfur [71].

The first reports about the utilization of copper oxide in solid-state gas sensing have been made by the group of Yamazoe [41, 62]. They presented a tin dioxide (SnO_2) gas sensor decorated with CuO clusters. To this end, the SnO_2 powder was loaded with a copper acetate solution. After a subsequent heat treatment, the powder contained 5 wt% CuO. The CuO phase located at the SnO_2 surface was observed to lower the conductance compared to pure SnO_2. This is attributed by the authors as an additional electronic depletion of the SnO_2 at the *p*-*n* junction (remind that CuO is a *p*-type semiconductor). The sensor shows a very high response (i.e., the relative change in conductance) to hydrogen sulfide (H_2S) at a temperature of 200°C. The relative change in conductance after applying 50 ppm hydrogen sulfide is as high as 35,000. The response to other sulfur-containing gases is significantly lower (150 for methyl sulfide and 2.2 for dimethyl sulfide); for reducing gases without sulfur, e.g., ethanol, the sensitivity is almost negligible. The authors interpret these results by the following processes:

They claimed that the phase transformation (10) leads to a decrease of the depletion of the (SnO_2/CuO) $p - n$ junction and thus to the observed conductance increase. Although the concentration of copper oxide is relatively high (5 wt %) and the copper oxide is located at the SnO_2 surface, the authors did not take the possibility into account that the forming of (highly conducting) CuS pathways could be the reason for the observed increase of the conductance.

The very high sensitivity for hydrogen sulfide is only present for temperatures of 200°C and below; at higher temperatures the sensitivity is many orders of magnitude smaller (e.g., $S = 10$ at 300°C). According to the authors, this is due to the contribution of the oxidation process of the CuS sulfide (cf. (11)). The bulk reaction has therefore proven to be inevitable for the detection mechanism, but still the transduction mechanism was of a surface type. Beside the utilization of CuO as decorating or doping material on surface effect sensors, there have been recent reports of pure CuO sensors [67–72]. Some of these papers concentrate on the high temperature mode where the desulfurization process is dominant and therefore no large amount of the copper sulfide phase is present at the surface [67, 69, 72]. In a recent paper with our participation [70, 71], a new type of hydrogen sulfide (H_2S) sensor is presented using percolation effects on near-surface CuS directly as a sensor signal. It has been observed that porous CuO fibers show a sudden increase in the conductance when the amount of H_2S delivered to the sensor exceeds a certain value. Several indications of the experimental curves suggest that percolation effects based on a bulk reaction are responsible for the observed effect. This finding can directly be utilized as sensor principle in a dosimeter-type gas sensor.

The CuO nanofibers used in this work have been obtained by an electrospinning process using a copper precursor (copper nitrate) in a polymer matrix (polyvinylbutyrate). After thermal decomposition of the polymer and oxidation of the copper precursor, the process yields porous copper oxide fibers which are highly accessible to gas. Networks of randomly orientated fibers placed on alumina substrates with platinum electrodes were used as sensors. Scanning electron micrographs (SEM) at various magnifications (see Fig. 11a–c) show a section of the sensor surface which is covered by CuO wires (a). The fibers are spanning two fingers of the interdigitated electrodes with an in-between gap of approximately 20 μm. The network is very thin with little interconnections between wires (see Fig. 11b). The lengths of the wires are much higher than the electrode gap. The conductance of the network, therefore, is dominated by the conductance of parallel fibers. It is assumed that weak connections between fibers are not contributing significantly. It can be seen that the fibers themselves are mesoporous (see Fig. 11c) with a grain and pore size in the order of approximately 50 nm. Therefore, not only the outer surface but rather the whole inner surface of the fiber is considered to be active for a sulfurization process.

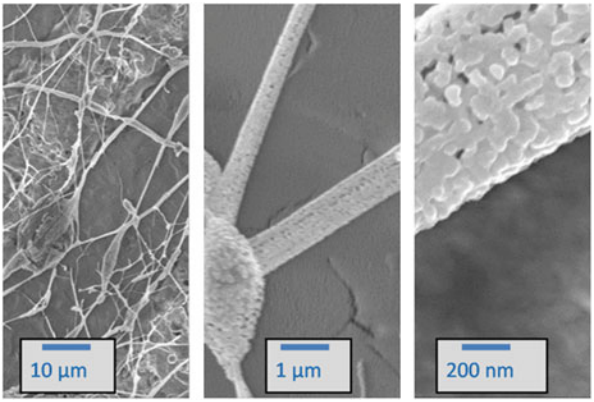

Fig. 11 Scanning electron micrographs of the CuO fibers on a sensor substrate with different magnifications (M): (**a**) on the left ($M = 1{,}000$) the interconnections between the electrodes are shown [10]; (**b**) in the middle ($M = 10{,}000$) the connection of two fibers is visible; (**c**) on the right ($M = 50{,}000$) the grains and pores of a single fiber are depicted [68]

The observed effect after the exposure of the sensors to diluted hydrogen sulfide at an operating temperature of 160°C can be attributed to three regimes. In the first regime (i) the sensor shows a typical behavior of a p-type semiconductor exposed to reducing gas. In this regime, the resistance is decreasing by about 20% at 5 ppm. In the second regime (ii), the sensor shows a steep increase of the conductance over several orders in magnitude. In the third regime (iii) the sensor shows a slow increase of conduction.

The authors interpret the measurement with a continuously growing amount of CuS at the surface of the sensor. During the first regime, the CuS clusters on the surface form only single insulated clusters, so that their contribution to the networks conductance is weak and the conductance in this regime is dominated by the CuO fibers. In the second regime, very probably a percolating cluster is present, so that the highly conducting pathways via the CuS islands are almost immediately dominating the conductance. The time t_c, where the steep increase of σ is starting, can be drawn from the figure. Plotting the conductance σ versus $(t - t_c)$, a power-law $\sigma \sim (t - t_c)^a$, has been found valid over several orders of magnitude using the value $a = 1.99$ (corresponding to the value μ (cf. (2)) in percolation systems in $d = 3$). One straightforward way to interpret this experimental finding is to assume that the density of CuS sites on the CuO surface increases linearly with time t ($p \sim \mathrm{t}$) and that the critical concentration p_c is proportional to t_c. One should be aware that many effects could disturb this simple dependence, as, e.g., saturation effects, nonideal surfaces (where, e.g., not every CuO site can really be transformed into CuS), surfaces with fractures that must be filled or cannot be overcome by the percolation paths, and different molar volumes of the two species. To test the linear dependence of p on t, measurements of the copper-to-sulfur ratio have been performed by EDX measurements [71] and indicated that in the regimes (i) and

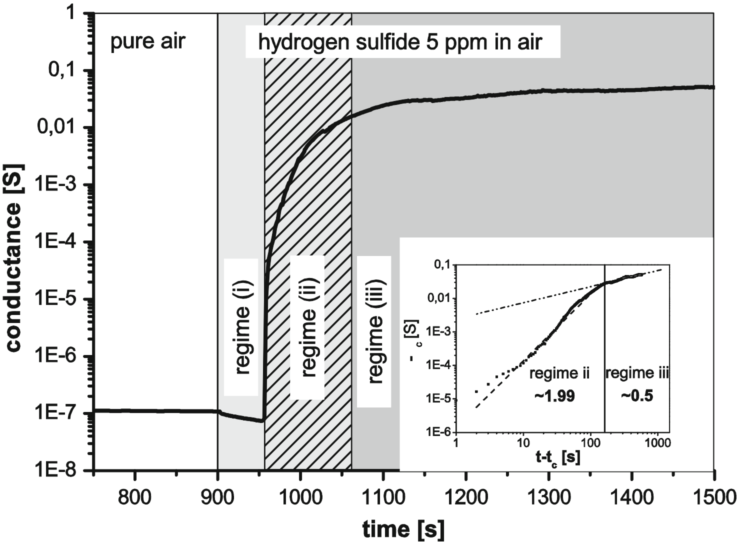

Fig. 12 Conductance of the CuO nanofiber sensor under H_2S exposure. Note that the conductance is on a logarithmic scale. The three regimes of the sensor conductance changes are highlighted with different background pattern. Inset: the change in conductance after the percolation threshold in a log–log plot. The percolation regime (*ii*) and the bulk diffusion regime (*iii*) can be clearly distinguished by the different slopes in the log–log plot. The straight lines of slopes 1.99 and 0.5 are guides to the eye

(ii) the sulfur-to-copper ratio is indeed growing linearly in time. However, it is important to remark that this indication for a linear growth of the CuS-fraction p should be considered with some caution. First of all, EDX is only feasible of measuring the atomic fractions of the sample and therefore only conclusive under the additional assumption that the sulfur is completely bonded in the form of copper sulfide. Second, the accuracy of EDX measurement is limited. Due to the complex morphology of the sample, a quantitative TOF-SIMS seems to be unachievable so that further investigations are necessary to approve or refute the assumption of the linear growth of p with t. Nevertheless, the exponent $a \approx \mu$ that has been found in the experimental curves for a great number of measurements in the range of 0.1–5 ppm at least strongly suggests the explanation by percolation effects.

One can see in the inset of Fig. 12 that the straight line of slope 1.99 in regime (ii) deviates from the experimental values at small values of $(t - t_c)$. One possible source of error is the resistance of the CuO backbone that is varying to a small amount. However, comparing the inset of Fig. 12 to Fig. 4b, it seems very probable that the deviations are due to inaccuracies in the determination of the correct value of t_c. In the experimental procedure, there is no possibility for measuring the percolation threshold with very high precision. Knowing that very small errors in the determination of the percolation threshold lead to large deviations from the correct slopes in the regime close to t_c (or to p_c), one may understand why reports on percolation transitions are not yet very numerous in the literature.

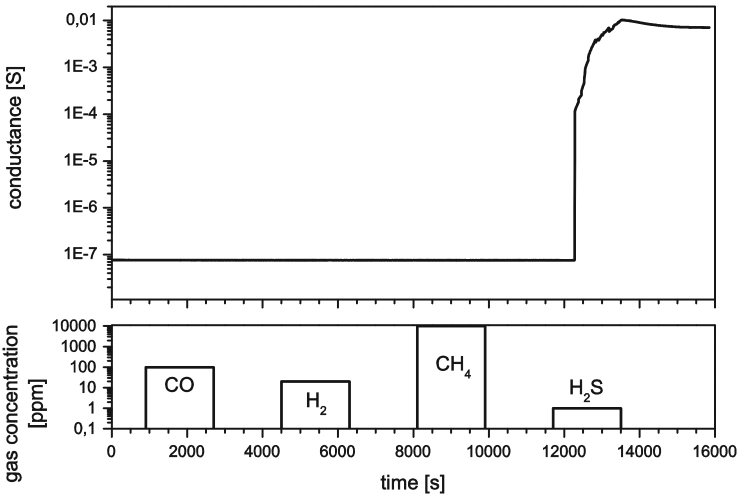

Fig. 13 Conductance change of CuO fiber sensor under exposure to various gases (Reprint with permission from [70])

In the third regime, i.e., for very long exposures of the sensor to H_2S, the conductance is growing with a smaller exponent. The authors attribute this to a growth perpendicular to the CuS when the growth is limited by the diffusion in solid phase. The dependency of the growth rate versus time in first-order approximation scales with the film thickness δ as $\delta \sim t^{0.5}$.

As a direct consequence of the sensor mechanism, one would assume that there is no cross sensitivity to non-sulfur-containing reducing gases. This is a major advantage as compared to surface-type gas sensors. This assumption has been proven for the exposure to carbon monoxide (CO), hydrogen (H_2), methane (CH_4) [70], and ammonia (NH_3) [71]. The conductance of a CuO sensor at 160°C under the exposure of either 100 ppm CO, 50 ppm H_2, 10,000 ppm methane, or 2 ppm H_2S (all in synthetic air at 30% relative humidity) is shown in Fig. 13. The resistance change due to surface effects is negligible and the switching due to the bulk reaction is only occurring for the H_2S exposure.

The authors propose to use the time span between H_2S exposure and percolation transition directly as a sensor signal. Most remarkably, the switching time t_c was shown to be reciprocal to the concentration in the range of 100 ppb to 5 ppm [71]. In other words, the percolation transition takes place, when a specific dose of H_2S is reached. In order to compare the t_c-values independently from small conductance changes caused by surface effects or drift, t_c was defined as the time when the conductance exceeds 10^{-6} S. The sensor cannot be operated in a continuous way since the desulfurization needs an elevated temperature. However, it could be shown that there are possible quasi-continuous modes of operation [68]. The authors propose and demonstrate the following procedure using three conductance thresholds. Two thresholds are used to control the sensor operating temperatures (I) and therefore switching the sensor from the sulfurization to the desulfurization regime, and one is used to measure t_c and therefore to generate a sensor signal (II):

I. Reaching a “regeneration” threshold (e.g., 10^{-3} S) triggers an operation temperature increase (350°C) leading to a desulfurization of the fibers even if the sensor is exposed to 10 ppm H_2S in air. This regeneration phase persists until the sensors conductance does fall below the “measurement” threshold (e.g., 2×10^{-6} S). Then the operating temperature is decreased to 170°C and the CuO fibers start to accumulate sulfur. This point is also used as the starting point for the signal generation.
II. Reaching the switching point (e.g., 10^{-5} S) the conductance marks the end of one measurement cycle. Since the increase is very steep, it might be beneficial to choose a value well above the baseline conduction in order to avoid false switching caused, e.g., by electrical noise. The reciprocal time span between the starting point for signal generation and switching point could be defined as sensor signal. Higher concentrations of H_2S lead to shorter time span values and therefore higher reciprocal time span values.

9 Conclusion

We have described the percolation model in some detail and have shown in which ways it has already been used to describe and to understand the properties of gas sensors. It turns out that percolation effects are suited to improve the performance of metal oxide gas sensors in many ways. For a surface-type gas sensor, percolation theory is a tool to describe the key parameters of the best sensor preparation in a way that mean grain-size, grain-size distribution, crystallinity or disorder, mono- or polydispersivity, and various other parameters can be adapted to the desired sensor properties, as, e.g., in order to create sensors with an inherent threshold. Sensors using (surface-near) bulk reactions can exhibit strong percolation effects. In case of the hydrogen sulfide sensor, utilizing the copper oxide/copper sulfide phase transition, this allows the design of completely selective gas sensors. Clearly, the concept of percolation is not limited to metal oxide sensors as we could sketch exemplary on sensors based on conducting polymers or disperse palladium films. In general, we recognize that the interaction between modeling aspects and experimental results in the literature could be improved. However, we could show in which way experimental error margins show up in the data analysis. Therefore, we made some suggestions, how the data should be treated in order to benefit at most from the knowledge of the universal parameters of percolation theory and in order to keep realistic expectations on the agreement between experimental and theoretical data. We hope that this discussion may help to bring the aspects of modeling and experiment closer together.

Acknowledgements We would like to thank C.-D. Kohl and J. Hennemann for the many valuable advices and the Deutsche Forschungsgemeinschaft for the financial support.

References

1. Seiyama T, Kato A, Fujiishi K, Nagatani M (1962) A new detector for gaseous components using semiconductive thin films. Anal Chem 34(11):1502–1503
2. Morrison SR (1982) Semiconductor gas sensors. Sens Actuators 2:329–341
3. Kohl D (2001) Function and applications of gas sensors. J Phys D Appl Phys 34:R125–R149
4. Barsan N, Weimar U (2003) Understanding the fundamental principles of metal oxide based gas sensors; the example of CO sensing with SnO_2 sensors in the presence of humidity. J Phys Condens Matter 15:R813–R839
5. Sahner K, Matam RMM, Tunney JJ, Post M (2005) Hydrocarbon sensing with thick and thin film p-type conducting perovskite materials. Sens Actuators B 108:102–112
6. Savage N, Chwieroth B, Ginwalla A, Patton BR, Akbar SA, Dutta PK (2001), Composite n−p semiconducting titanium oxides as gas sensors. Sens Actuators B 79:17
7. Flory PJ (1941) Molecular size distribution in three dimensional polymers. I. Gelation. J Am Chem Soc 63:3083
8. Stockmayer WH (1943) Theory of molecular size distribution and gel formation in branched chain polymers. J Chem Phys 11:45
9. Stauffer D, Aharony A (1994) Introduction to percolation theory. Taylor and Francis, London
10. Bunde A, Havlin S (1996) Percolation I and percolation II. In: Bunde A, Havlin S (eds) Fractals and disordered systems, 2nd edn, Springer, Berlin
11. Sahimi M (1994) Application to percolation theory. Taylor and Francis, London
12. Broadbent SR, Hammersley JM (1957) Percolation processes. Math Proc Cambridge Philos Soc 53:629641. doi:10.1017/S0305004100032680
13. Mandelbrot BB (1982) The fractal geometry of nature. W. H. Freeman, San Francisco
14. Bunde A, Kantelhardt L (1996) Introduction to percolation theory. In: Kärger J, Haberlandt R (eds) Diffusion in condensed matter. Vieweg Verlag, Wiesbaden
15. Ben-Avraham D, Havlin S (2000) Diffusion and reactions in fractals and disordered systems. Cambridge University Press, Cambridge
16. Bunde A, Havlin S (eds) (1999) Percolation and disordered systems: theory and applications. In: Proceedings of the international conference on percolation and disordered systems, Schloss Rauischholzhausen, University of Giessen, Giessen, 14–17 July 1998, Elsevier Science B.V., Oxford
17. Bisquert J (2008) Interpretation of electron diffusion coefficient in organic and inorganic semiconductors with broad distributions of states. Phys Chem Chem Phys 10:3175
18. Dräger J, Russ S, Bunde A (1995) Localization in random self-similar structures: universal behaviour. Europhys Lett 31:425
19. Dumpich G (1991) Anomalous electron diffusion in fractal systems at low temperatures. Adv Solid State Phys 31:59
20. Polley MH, Boonstra BBST (1957) Carbon Blacks for highly conductive rubber. Rubber Chem Technol 30(170):179
21. Andrade JS, Ito N, Shibusa Y (1996) Percolation transition in conducting polymer networks. Phys Rev B 54:3910–3915
22. Sau KP, Chaki TK, Khastgir D (1997) Conductive rubber composites from different blends of ethylene–propylene–diene rubber and nitrile rubber. J Mater Sci 32:5717–5724
23. Sysoev VV, Goschnick J, Schneider T, Strelcov E, Kolmakov A (2007) A gradient microarray electronic nose based on percolating SnO_2 nanowire sensing elements. Nano Lett 7(10): 3182–3188
24. Sysoev VV, Schneider T, Goschnick J, Kiselev I, Habicht W, Hahn H, Strelcov E, Kolmakov A (2009) Percolating SnO_2 nanowire network as a stable gas sensor: direct comparison of long-term performance versus SnO_2 nanoparticle film. Sens Actuators B 139:699–703
25. Go J, Sysoev VV, Kolmakov A, Pimparkar N, Alam MA (2009) A novel model for (percolating) nanonet chemical sensors for microarray-based E-nose applications' ECE Faculty Publications. Paper 57. doi:10.1109/IEDM.2009.5424266

26. Yamazoe N, Shimanoe K (2012) Proposal of contact potential promoted oxide semiconductor gas sensor. Sens Actuators B. doi:10.1016/j.snb.2012.10.048
27. Moos KSJSR (2006) Cuprate-ferrate compositions for temperature independent resistive oxygen. Sensors 16:179–186
28. Nagarajan L, De Souza RA, Samuelis D, Valov I, Börger A, Janek J, Becker KD, Schmidt PC, Martin M (2008) Highly non-stoichiometric amorphous gallium oxide – prototype material for a chemically driven insulator-metal transition. Nat Mater 7(5):391–398
29. Höfer U, Frank J, Fleischer M (2001) High temperatures Ga_2O_3-gas sensors and SnO_2-sensors: a comparison. Sens Actuators B 78:6–11
30. Ulrich M, Kohl C-D, Bunde A (2001) Percolation model of a nanocrystalline gas sensitive layer. Thin Solid Films 391:299–302
31. Sherman RD, Middleman LM, Jacobs SM (1983) Electron transport processes in conductor-filled polymers. Polym Eng Sci 23:36–46. doi:10.1002/pen.760230109
32. Tyco Electronics (2008) Product documentation. http://www.te.com/content/dam/te/global/english/products/Circuit-Protection/knowledge-center/documents/circuit-protection-psw-fundamentals.pdf. Accessed 26 May 2013
33. Alamusi NH, Fukunaga H, Atobe S, Liu Y, Li J (2011) Piezoresistive strain sensors made from carbon nanotubes based polymer nanocomposites. Sensors 11:10691–10723. doi:10.3390/s111110691
34. Abraham JK, Philip B, Witchurch A, Varadan VK, Reddy CC (2004) A compact wireless gas sensor using a carbon nanotube/PMMA thin film chemiresistor. Smart Mater Struct 13:1045–1049
35. Chen J, Tsubokawa N (2000) Novel gas sensor from polymer-grafted carbon black: vapor response of electric resistance of conducting composites prepared from poly(ethylene-block-ethylene oxide)-grafted carbon black. J Appl Polym Sci 77:2437–2447
36. Hayashi S, Naitoh A, Machida S, Okazaki M, Maruyama K, Tsubokawa N (1998) Grafting of polymers onto a carbon black surface by the trapping of polymer radicals. Appl Organometal Chem 12:743–748
37. Dankert O, Pundt A (2002) Hydrogen-induced percolation in discontinuous films. Appl Phys Lett 81(2002):1618–1620
38. Favier F, Walter EC, Zach MP, Benter T, Penner RM (2001) Hydrogen sensors and switches from electrodeposited palladium mesowire arrays. Science 293:2227–2231
39. Xu T, Zach MP, Xiao ZL, Rosenmann D, Welp U (2005) Self-assembled monolayer-enhanced hydrogen sensing with ultrathin palladium films. Appl Phys Lett 86:203104. doi:10.1063/1.1929075
40. Kohl D (1989) Surface processes in the detection of reducing gases with SnO_2-based devices. Sens Actuators 18:71–113
41. Yamazoe N (1991) New approaches for improving semiconductor gas sensors, Sens Actuators B 5:7–19
42. Xu C, Tamaki J, Miura N, Yamazoe N (1992) Grain size effect on gas sensitivity of porous SnO_2-based elements. Sens Actuators B 3147–3155
43. Wang X, Yee SS, Carey WP (1995) Transition between neck-controlled and grain-boundary-controlled sensitivity of metal-oxide gas sensors. Sens Actuators 24–25:454–457
44. Eicker H, Kartenberg HJ, Jacob H (1981) Untersuchung neuer Meßverfahren mit Metalloxidhalbleitern zur Überwachung von Kohlenoxid-Konzentrationen Technisches Messen 48:421–430
45. Lalauze P (1984) A new approach to selective detection of gas by an SnO_2 Solid state sensor. Sens Actuators 5:55–63
46. Gramm A, Schütze A (2003) High performance solvent vapor identification with a two sensor array using temperature cycling and pattern classification. Sens Actuators B Chem 95(1–3):58–65
47. Morrison SR (1987) Selectivity in semiconductor gas sensors. Sens Actuators 12:425–440
48. Kohl D, Felde N (2011) Gas sensing investigation in characterizing textile fibers in solid state gas sensors. In: Fleischer M, Lehmann M (eds) Industrial application. Springer, Berlin Heidelberg
49. Sakai G, Matsunaga N, Shimanoe K, Yamazoe N (2001) Theory of gas-diffusion controlled sensitivity for thin film semiconductor gas sensor. Sens Actuators B 80:125–131

50. Mandayo GG, Castaño E, Gracia FJ, Cirera A, Cornet A, Morante JR (2003) Strategies to enhance the carbon monoxide sensitivity of tin oxide thin films. Sens Actuators B95:90–96
51. Heilig A, Barsan N, Weimar U, Göpel W (1999) Selectivity enhancement of SnO_2 gas sensors: simultaneous monitoring of resistances and temperatures. Sens Actuators B 58:302–309
52. Park CO, Akhbar S (2003) Ceramics for chemical sensing. J Mat Sci 38:4611
53. Ulrich M, Bunde A, Kohl C-D (2004) Percolation and gas sensitivity in nanocrystalline metal oxide films. Appl Phys Lett 85:242
54. Dräger J, Russ S, Sauerwald T, Kohl C-D, Bunde A (2013) Percolation transition in the gas-induced conductance of nanograin metal oxide films with defects. JAP 113. J Appl Phys 113:223701. http://dx.doi.org/10.1063/1.4809572
55. Yoon DH, Yu JH, Choi GM (1998) CO gas sensing properties of ZnO–CuO composite. Sens Actuators B 46:1523
56. Jun S-T, Choi GM (1998) Composition dependence of the electrical conductivity of ZnO (n)–CuO(p) ceramic composite. J Am Ceram Soc 81:695–699
57. Moon WJ, Yu JH, Choi GM (2001), Selective CO gas detection of SnO_2-$ZnSnO_4$ composite gas sensor. Sens Actuators B 80:21
58. Savage N, Akbar SA, Dutta PK (2001) Titanium dioxide based high temperature carbon monoxide selective sensor. Sens Actuators B 72:239–248
59. Li X, Ramasamy R, Dutta PK (2009) Study of the resistance behavior of anatase and rutile thick films towards carbon monoxide and oxygen at high temperatures and possibilities for sensing applications. Sens Actuators B 143:308–315
60. Dutta PK, Ginwalla A, Hogg B, Patton BR, Chwieroth B, Liang Z, Gouma P, Mills M, Akbar SA (1999) Interaction of Carbon monoxide with anatase surfaces at high temperatures: optimization of a carbon monoxide sensor. J Phys Chem B 103:4412–4422
61. Russ S (in preparation) Selective resistance behavior of composite semiconducting np systems, (to be submitted, 2013)
62. Tamaki T, Maekawa NM, Yamazoe N (1992) CuO–SnO_2 element for highly sensitive and selective detection of H_2S. Sens Actuators B 9:197–203
63. Groß A, Beulertz G, Marr I, Kubinski DJ, Visser JH, Moos R (2012) Dual mode NO_x sensor: measuring both the accumulated amount and instantaneous level at low concentrations. Sensors 12(3):2831–2850
64. Fremerey P, Jess A, Moos R (2012) Direct in-situ detection of sulfur loading on fixed bed catalysts. In: The 14th international meeting on chemical sensors (IMCS 2012). 20–23 May 2012, Nürnberg. doi:10.5162/IMCS2012/1.1.5
65. Jeong YK, Choi GM (1996) Nonstoichiometry and electrical conductivity of CuO. Phys Chem Solids 57:81–84
66. Nozaki H, Shibata K (1991) Metallic hole conduction in CuS. J Solid State Chem 91:306
67. Ramgir S, Kailasa Ganapathi S, Kaur M, Datta N, Muthe KP, Aswal DK, Gupta SK, Yakhmi JV (2010) Sup-ppm H_2S sensing at room temperature using CuO thin films. Sens Actuators B 151:90–96
68. Sauerwald T, Hennemann J, Kohl C-D, Wagner T, Russ S (2013) H_2S detection utilizing percolation effects in copper oxide. Proc Sens 2013 pp 656-660; ISBN 978-3-9813484-3-9
69. Chen J, Wang K, Hartman L, Zhou W (2008) H_2S detection by vertically aligned CuO nanowire array sensors. J Phys Chem C 2008(112):16017–16021
70. Hennemann J, Sauerwald T, Kohl C-D, Wagner T, Bognitzki M, Greiner A (2012) Physica Status Solidi 209(5):911–916
71. Hennemann J, Sauerwald T, Wagner T, Kohl C-D, Dräger J, Russ S (2012) Electrospun copper (II)oxide fibers as highly sensitive and selective sensor for hydrogen sulfide utilizing percolation effects. In: Proc of the 14th international meeting on chemical sensors (IMCS 2012), 20–23 May 2012, AMA Service GmbH, Nuremberg pp 197–200; ISBN: 978-3-9813484-2-2, doi:10.5162/IMCS2012/2.3.4
72. Steinhauer S, Brunet E, Maier T, Mutinati GC, Köck A, Freudenberg O, Gspan C, Grogger W, Neuhold A, Resel R (2012) Gas sensing properties of novel CuO nanowire devices. Sens Actuators B Chem doi:10.1016/j.snb.2012.09.034

Calorimetric Gas Sensors for Hydrogen Peroxide Monitoring in Aseptic Food Processes

Patrick Kirchner, Steffen Reisert, and Michael J. Schöning

Abstract For the sterilisation of aseptic food packages it is taken advantage of the microbicidal properties of hydrogen peroxide (H_2O_2). Especially, when applied in vapour phase, it has shown high potential of microbial inactivation. In addition, it offers a high environmental compatibility compared to other chemical sterilisation agents, as it decomposes into oxygen and water, respectively. Due to a lack in sensory detection possibilities, a continuous monitoring of the H_2O_2 concentration was recently not available. Instead, the sterilisation efficacy is validated using microbiological tests. However, progresses in the development of calorimetric gas sensors during the last 7 years have made it possible to monitor the H_2O_2 concentration during operation. This chapter deals with the fundamentals of calorimetric gas sensing with special focus on the detection of gaseous hydrogen peroxide. A sensor principle based on a calorimetric differential set-up is described. Special emphasis is given to the sensor design with respect to the operational requirements under field conditions. The state-of-the-art regarding a sensor set-up for the on-line monitoring and secondly, a miniaturised sensor for in-line monitoring are summarised. Furthermore, alternative detection methods and a novel multi-sensor system for the characterisation of aseptic sterilisation processes are described.

Keywords Calorimetric gas sensor, Hydrogen peroxide, Multi-sensor system

Contents

P. Kirchner, S. Reisert, and M.J. Schöning (✉)
Institute of Nano- and Biotechnologies FH Aachen, Campus Jülich, Heinrich-Mussmann-Str. 1, 52428 Jülich, Germany
e-mail: schoning@fh-aachen.de

C.-D. Kohl and T. Wagner (eds.), *Gas Sensing Fundamentals*,
Springer Series on Chemical Sensors and Biosensors (2014) 15: 279–310
DOI 10.1007/5346_2013_51,

1 Introduction

1.1 Hydrogen Peroxide

Hydrogen peroxide (H_2O_2) was discovered for the first time by L. J. Thénard in 1818. He produced it by a reaction of diluted nitric acid with barium peroxide (BaO_2) and named it first oxygenated water [1]. After the discovery of H_2O_2, the production of aqueous H_2O_2 solutions with concentrations up to 50% w/w was performed by slightly improved processes of the reaction described by Thénard. During this time, it was thought that pure H_2O_2 must be unstable due to the fact that H_2O_2 gradually decomposed resulting from traces of metallic and organic impurities of the aqueous solutions [2]. In 1894, R. Wolffenstein gained almost pure H_2O_2 (99% w/w) by vacuum distillation for the first time and demonstrated its stability under cleanest conditions [3]. Until the end of the nineteenth century, different formulas of H_2O_2 have been proposed, where finally P. Melikishvili and L. Pizarjevski determined that the correct formula of H_2O_2 must be H–O–O–H [4].

H_2O_2 (CAS No.: 7722-84-1) is a clear, colourless liquid, which is weakly acid and has a moderately pungent odour [5]. It has strong oxidising properties and is very reactive under certain circumstances, which makes it attractive for many applications, wherein reactive oxidants are required. In comparison with water, H_2O_2 is heavier as well as slightly more viscous. It is miscible with water in any proportion, even though they do not form an azeotropic mixture, so that H_2O_2 could be fully separated by distillation [6]. In Table 1, the main physical properties of H_2O_2 and the corresponding properties of water are summarised. A comprehensive overview of the physical and chemical properties of H_2O_2 over a wide temperature range is given elsewhere [7].

H_2O_2 occurs as a ubiquitous substance in the environment. It naturally exists in surface water, wherein it is mainly produced by a photochemical process of ultraviolet light and dissolved organic compounds [9]. In atmosphere, H_2O_2 is produced by photolysis of ozone or aldehydes [10]. It can be found in living cells as a by-product of aerobic cell metabolism [11]. Exhale breath of humans contains

Table 1 Physical properties of H_2O_2 and water (adapted from [8])

Property	Hydrogen peroxide	Water
Molar mass (g/mol)	34.016	18.015
Melting point (°C)	−0.43	0.0
Boiling point (°C)	150.2	100
Heat of melting (J/g)	368	334
Heat of vaporisation at 25°C (J/(g K))	1,519	2,445
Specific heat at 25°C (J/(g K))	2.629	4.182
Critical temperature (°C)	457	374
Critical pressure (MPa)	20.99	21.44
Relative density at 25°C (g/m^3)	1.4425	0.9971
Viscosity at 20°C (mPa s)	1.249	1.002
Refractive index	1.4084	1.3330

also small amounts of endogenously formed H_2O_2 [12]. Furthermore, a special insect with regard to H_2O_2 is the bombardier beetle, which produces concentrated amounts of H_2O_2 up to 25% w/w for defence purposes [13].

Even though the industrial production of H_2O_2 could be carried out by various wet chemical, electrochemical and organic oxidation processes as shown in [8], almost the total amount of hydrogen peroxide is gained by the organic autoxidation process with anthraquinone today. Therein, 2-alkyl-anthraquinone reacts with hydrogen in the presence of a catalyst (e.g., palladium) to form 2-alkyl-anthrahydroquinone in a first step. After removing the catalyst, the hydroquinone is oxidised usually in ambient air under the formation of hydrogen peroxide, which is extracted in water and the process begins anew [14]. The organic autoxidation process enables large-scale production of H_2O_2 and permits its widely usage in a variety of industrial, medical and environmental application fields. Today, hydrogen peroxide is commercially available as aqueous solutions up to 90% w/w. Due to the fact that hydrogen peroxide could easily decompose on traces of impurities, the solutions are generally stabilised by added weak organic acids [15].

In 2008, the global production of H_2O_2 amounted to be three million tons [16]. According to a new market report from Global Industry Analysts, a H_2O_2 world market of 4.3 million tons is forecast for 2015 [17]. The paper and pulp industry represents the main field of application of estimated 50% of the total H_2O_2 production, wherein it is used for bleaching and delignification [16, 18, 19]. The textile industry deploys H_2O_2 as bleaching agent as well [20]. In metallurgy and mining, it is applied for leaching processes and for the detoxification and destruction of cyanides [21, 22]. Highly concentrated H_2O_2 up to 90% is used as rocket propellant in space technology [23]. Today, it is increasingly applied for environmental protection in industrial plants, especially to detoxify industrial effluents and exhaust gases [8]. The chemical industry uses H_2O_2 for the production of other chemicals such as peroxide compounds, for epoxidation as well as for etching and cleaning processes during the fabrication of micro-machined/semiconductor devices [14]. Last but not least, H_2O_2 at low concentrations of 3% w/w is a highly efficient disinfectant for

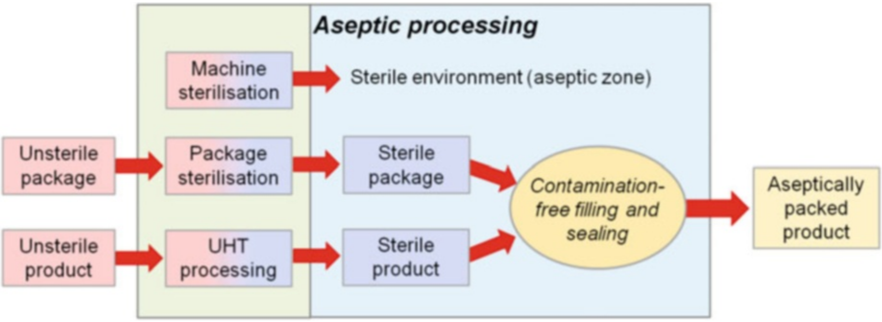

Fig. 1 Schematic flow diagram of aseptic food processing (modified from [29])

medical applications, and at high concentrations up to 35% w/w it is used as sterilant in the food and the pharmaceutical industry as well [24, 25].

1.2 Aseptic Food Processes

1.2.1 Introduction

Packaging is a key element in food processing in order to ensure a high safety standard and quality assurance of a packed product by avoiding any physical, chemical as well as microbiological interaction between the product and environment within its shelf life [26]. Today, aseptic food processing is one of the most important food-packaging methods, which allows to keep up with the great demand of the food industry for long-term preservation of food products at ambient temperature [27]. It is defined as the filling and hermetic sealing of microbiologically stable products (e.g., ultra-high temperature-processed (UHT) milk) into pre-sterilised packages under sterile conditions in an aseptic zone so that microbiological recontamination is prevented [28]. A schematic flow diagram of an aseptic food process is depicted in Fig. 1.

The result of aseptic processing is a safe, packed product with long shelf-life that does not require preservatives or refrigeration during storage. Thus, aseptically packed products offer beneficial attitudes to the consumer, the food manufacturer and to the distributor compared to conventionally canned products: the product retains most of its natural nutrients and of the original sensory characteristics (flavour, texture and colour), and it enables high savings on logistics (no cold chain is required) and on packaging material (do not need to be long-term stable at high temperature and pressure such as cans) [30, 31].

1.2.2 Package Sterilisation

A decisive step within aseptic food processing is the sterilisation[1] of the packaging material prior to the food filling due to the fact that the material could get contaminated by operational staff, surrounding air or even by recontaminated machine components [34, 35]. According to Ansari and Datta, the sterilisation of the packaging material must fulfil the following requirements [24]:

- Rapid, reliable and economical microbicidal effectiveness;
- Compatibility to the packaging material;
- Almost complete removal of residues of the sterilisation agent;
- Harmlessness for the consumer at highest possible residue level;
- No adverse effect on product at highest possible residue level;
- Compatibility to environment.

The sterilisation of the packaging material could be carried out by various physical methods in form of heat and irradiation or chemical sterilants such as ethylene oxide, formaldehyde, peracetic acid or hydrogen peroxide [24, 36, 37]. However, some of the mentioned chemicals are unsuitable for package sterilisation. While ethylene oxide and formaldehyde show strong microbicidal effectiveness, they could not be used in food processing because they are toxic, carcinogenic and potentially explosive leading to a careful handling [38]. Peracetic acid possesses a rapid microbicidal effectiveness even at low concentration levels. However, it decomposes to water and acetic acid, which could generate an off-flavour of the food product and moreover, its vapour is very pungent [24, 28].

1.2.3 Hydrogen Peroxide as Sterilant

Today, hydrogen peroxide (H_2O_2) is the most frequently used sterilant for package-sterilisation processes. Amongst its benefits, it is non-toxic at residual concentrations and it decomposes to environment-friendly products, namely water vapour and oxygen, in a net reaction [39]. Due to the fact that H_2O_2 has merely a low microbicidal effect at room temperature, in most instances, a combination of hydrogen peroxide and heat or even irradiation is applied, in order to increase its microbicidal effectiveness [24, 37, 40]. In general, the microbicidal effectiveness of sterilisation processes with H_2O_2 depends in particular on the H_2O_2 concentration besides other process parameters, such as temperature, humidity and gas velocity [41, 42]. Furthermore, the effectiveness is significantly enhanced through the usage of gaseous H_2O_2

---

[1] According to Wallhäußer, sterility is defined as the total absence of viable microorganisms and transferable genetic material [32]. Besides this general definition, “commercial sterility” is an established term in the food industry. It is defined as “the absence of microorganisms capable of growing in food at normal non-refrigerated conditions at which the food is likely to be held during manufacture, distribution and storage” [33]. In this work, sterilisation stands always for “commercial sterilisation” except where noted otherwise.

[25, 43]. In this case, H_2O_2 is active against a broad spectrum of microorganisms: bacteria, yeasts, fungi, viruses and spores [38, 44]. It acts as an oxidant that affords inactivation most likely through formation of free hydroxyl radicals as intermediate products induced by heat, irradiation or even by transition-metal ions contained in microorganisms [25, 45]. The hydroxyl radicals serve as electrophilic surfactants with high reactivity, which could damage essential cell components such as DNA, proteins, lipids and carbohydrates very site-specific [46–50]. The decisive inactivation step for viable microorganisms during H_2O_2 treatment relies on the DNA damage through strand breaks caused by the formed radicals [45, 51, 52]. However, numerous studies have been conducted, wherein various inactivation mechanisms of bacterial spores through H_2O_2 treatment are supposed. Bacterial spores offer a much higher resistance towards oxidants, like hydrogen peroxide, than their vegetative counterparts due to their thick, proteinaceous spore coats [47], the low water content of the spore core [53, 54], the high impermeability of the inner spore membrane [55] and the protection of the DNA encased by special proteins of spores, the so-called small, acid-soluble spore proteins (SASP) [52, 56, 57]. The latter one blocks DNA damage occurring by viable bacteria through free radicals [57]. Shin et al. and King and Gould found out that H_2O_2 at elevated concentrations causes dissolution of the outer and inner spore coat as well as lysis of the cortex, which could end up in a degradation of the spore core or protoplast structures [58, 59]. However, at lower lethal concentrations, treated spores remain fully their shape, so that dissolution of spore coats seems not to be the initial step of the spores' lethality [58, 60]. Further studies have shown that possible targets of H_2O_2 are enzymes within spores, which are important for the bacterial metabolism after germination, or enzymes, which are involved in the germination (e.g., hydrolysis of the cortex) [52, 60]. Whereas Cortezzo et al. found out that H_2O_2 attacks the spore's inner membrane by creating pores or channels, so that the membrane become leaky for substances of the spore core [61]. Nevertheless, the decisive inactivation process, which is of major significance in order to understand the inactivation mechanism of spores by H_2O_2, is not effectually identified at present time.

1.2.4 Inactivation Kinetics

To determine the sterilisation effectiveness, the reduction of the most resistant bacterial spores for the used chemical sterilant has to be considered. For sterilisation processes, wherein hydrogen peroxide is applied, spores of *Bacillus atrophaeus* (ATCC 9372) or *Bacillus subtilis* SA 22 are typically used as test organisms [62]. The microbial inactivation kinetic is expected to follow a first-order reaction [63]:

$$\frac{\mathrm{d}N}{\mathrm{d}t} = -k \cdot N \tag{1}$$

Here, N is the number of spores and k is the inactivation-rate constant.

By integration of (1), one can obtain a more familiar expression for the microbial reduction:

$$\ln\frac{N_{\mathrm{t}}}{N_0} = -k\cdot t \tag{2}$$

where N_{t} and N_0 are the survived spore number at time t and the initial spore number, respectively.

A general parameter to evaluate the microbicidal effectiveness is the D-value, which is calculated from the survivor curves (survived spores versus time). The D-value represents an exposure time (Δt) at a constant temperature setting that results in 90% reduction of the initial spore number:

$$D = \frac{\Delta t}{\lg N_0 - \lg N_{90\%}} = \frac{2.303}{k} \tag{3}$$

However, for chemical sterilisation agents, the microbicidal effectiveness is often merely determined by the logarithmic cycle reduction (LCR). This is expressed mathematically as follows [64]:

$$\mathrm{LCR} = \lg\frac{N_0}{N_{\mathrm{t}}} \tag{4}$$

1.3 H_2O_2 Monitoring in Gas Phase: State of the Art

During the last two decades, intensive efforts have been focused on detecting gaseous or vaporised H_2O_2 by diversified strategies such as infrared spectroscopy, colorimetry, mass spectroscopy, chemiluminescence as well as amperometric methods. Even though most of this detecting principles could merely be used for low concentrations, or are not suitable either for harsh environmental conditions or for measurement applications in package sterilisation processes, a brief introduction to this methods is given below.

For detecting H_2O_2 by IR spectroscopy, the strong absorbance band of H_2O_2 at 1,420 nm serves as indication peak, whose intensity is used for determining the H_2O_2 concentration. However, water vapour shows also a strong absorbance in this wavelength range and interferes with the H_2O_2 band. Therefore, a correction must be done by identifying at first the amount of water vapour at a further peak (i.e., at 1,360 nm) and by following determining the ratio of water vapour and H_2O_2 at the absorbance band of 1,420 nm [65–67].

In a further sensor approach, colorimetric indicators are described, which are based on a colour change, after they have been exposed to H_2O_2. For instance, Xu et al. described paper-based vapour detection of H_2O_2, wherein a cellulose substrate has been impregnated by Ti(IV) oxo complexes for binding and reacting with H_2O_2 and generating a yellow colour formation [68].

For monitoring H_2O_2 in workplace atmosphere, amperometric sensors are particularly suited [69–71]. In its easiest form, such a sensor consists of a two-electrode arrangement (working and counter electrode), and between both electrodes a solid electrolyte (e.g., Nafion) is situated as ion-exchange material. At an appropriate potential of the working electrode (in general, at 600 mV), hydrogen peroxide becomes oxidised by an anodic reaction and released hydrogen ions trapped in the membrane are reduced at the counter electrode by a cathodic reaction. As a result a current is generated, which depends on the present H_2O_2 concentration.

A further H_2O_2-detection principle is described in [72], which is based on chemiluminescence. Therein, a reaction between a peroxalate compound and vapour-phase H_2O_2 can generate a high-energy intermediate (dioxetanedione) that quickly decomposes producing carbon dioxide and photons, which could further chemically excite a fluorescent dye resulting in an efficient luminescence. This detection principle has been established to selectively detect H_2O_2 at low concentrations.

In [73], a mass-spectrometric method for the detection of gaseous H_2O_2 using a chemical ionisation source is introduced. Therein, oxygen ions are produced from the ionisation of ambient air, which react with H_2O_2 to form stable, ionised clusters of H_2O_2 and oxygen, whose specific mass-to-charge ratio was detected by a time-of-flight mass spectrometer. The intensity of the mass-to-charge ratio can be used to determine the present H_2O_2 gas concentration.

Even though diversified sensing techniques for gaseous H_2O_2 have been developed in the last two decades, they are not suitable for monitoring H_2O_2 during the package sterilisation in aseptic food processes.

1.4 Necessity to Monitor H_2O_2

In current research there exists the necessity to develop a gas sensor for monitoring the H_2O_2 concentration during the package sterilisation in aseptic filling machineries. In sterilisation processes with gaseous H_2O_2, the gas concentration must be sufficiently high enough to ensure the sterility of the packaging material. Furthermore, a homogeneous distribution of the gaseous H_2O_2 must be maintained within the short contact time between the H_2O_2 and packaging material. Due to the fact that the H_2O_2 concentration seems to be the decisive factor for a sufficient sterilisation effect, the sensor should conduce to verify an effectual sterility of the packages treated by H_2O_2 through continuous measurements in aseptic filling machineries. Thus, the sensor could contribute to the control and to the optimisation of the package-sterilisation process with regard to finding out the relevant parameter settings for the gas flow, H_2O_2 dosage as well as contact time between the packaging material and gaseous H_2O_2.

For industrial application, the sensor must fulfil certain requirements. It has to operate reliably under harsh environmental conditions of the sterilisation process. This means that the sensor has to be suitable and approved for elevated gas temperatures, strong gas flows and H_2O_2 concentrations up to the percentage range. For an accurate measurement of the H_2O_2 concentration, the sensor's concentration-dependent signal should not be interfered by altering the gas temperature, gas velocity as well as the humidity in the ambient gas atmosphere.

2 Calorimetric Gas Sensors: A Brief Overview

Gas sensors based on calorimetry can generally be divided into three different types: catalytic gas sensors, adsorbent-based gas sensors and thermal conductivity gas sensors. All of them detect a change in temperature induced by either a chemical reaction on the sensor surface with a gas species or a change of thermal conductivity of the sensor's surrounding gas atmosphere. The elementary sensing element is based on the conversion of temperature in an electrical signal, which is one of the most important physical transduction principles with well-known sensitivity and accuracy for each temperature detector [74]. In general, temperature-resistance detectors, monolithic thermopiles or even pyroelectric sensors are embedded as temperature detectors in calorimetric sensing devices [75]. Therein, the choice of which temperature detector to use depends on the operational conditions – the range of temperature change that has to be detected, the scope of application, the gas concentration as well as the calorimetric sensor type itself.

2.1 Catalytic Gas Sensors

At the beginning of the twentieth century, several oil and gasoline tanker ship-wrecks occurred, which were caused by gas explosions in the storage tanks. Consequently, the Standard Oil Company of California sponsored the investigation of detectors for explosive gases [76]. With the financial support of the oil company, Oliver W. Johnson developed the first portable gas detector in 1927, whose sensing principle relies on the catalytic combustion of flammable gases on a heated platinum filament generating a temperature rise in reference to an enclosed compensation filament [76, 77]. The portable detector was applied to prevent fuel explosions in storage tanks of oil and gasoline tankers. This became the birth of the catalytic gas sensors. In the 1950s, the catalytic detection principle was broadened to quantitatively monitor methane concentrations as critical combustible gas in coal mines. The resulting hazard-alert tool enabled miners to protect them from gas explosions and to replace unspecific flame-safety lamps most frequently deployed before [78]. Even today, catalytic gas sensors are used for monitoring the presence of combustible gases such as hydrogen and hydrocarbons (e.g., methane) in concentration levels up to their respective lower explosive limit (LEL) [79]. The LEL is defined as lowest concentration of the combustible gas in air, which is sufficiently large enough to result in an explosion initiated through an ignition source [80]. For example, the LEL of methane amounts to be 4.6% v/v [81]. The detected gas concentration of the sensing device is often expressed in percentage of LEL [80].

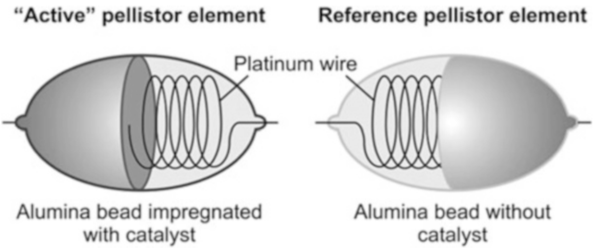

Fig. 2 Schematic view of an "active" pellistor element with platinum wire embedded in an alumina bead that is impregnated with a catalyst (*left*) and a reference pellistor element with platinum wire embedded in an alumina bead without catalyst (*right*)

Current catalytic gas sensors are still also derived from the detection principle firstly introduced by Johnson, and applied in diversified industrial sectors (oil and gas industry, mining, chemical plants). They are simply made up of two coils of platinum wires, where both of them are embedded in identical porous ceramic beads (in most instances, alumina beads). One of the ceramic beads is additionally impregnated with an active catalyst made up of platinum, palladium, rhodium or iridium [82], whilst a corresponding bared bead serves as a reference (see Fig. 2). This sensor arrangement is called pellistor (or catalytic bead sensor) and was first named by A. Baker [83].

The sensor arrangement detects the reaction heat evolved during the catalytic combustion of a flammable gas component on the heated "active" pellistor element in form of a temperature rise leading to a resistance change of the platinum wire, whereas the corresponding reference pellistor element compensates effects occurring in form of altering temperature of the surrounding gas atmosphere [84]. The combustion induced on the hot catalyst surface proceeds in form of an exothermic reaction between a flammable gas and an oxidant of ambient air accompanied by the liberation of heat. In an exothermic reaction, the total energy required for breaking the bonds of a chemical substance is less than the total energy released, while the chemical bonds of the products are formed [73]. Thus, the resulting excess of energy is liberated from the chemical reaction known as reaction enthalpy. The reaction enthalpy ($\Delta_R H^\Theta$) can be described by Hess's law [85]:

$$\Delta_R H^\Theta = \sum n_i \cdot \Delta_R H^\Theta_{\mathrm{prod},i} + \sum n_j \cdot \Delta_R H^\Theta_{\mathrm{react},j} \tag{5}$$

where n_i and n_j are the number of moles, and $\Delta_R H_{\mathrm{prod},i}$ and $\Delta_R H_{\mathrm{react},j}$ are the heat of formation of the products and reactants at standard conditions.

For example, the combustion of hydrocarbons (here, methane) with oxygen of ambient air occurs in the following net reaction:

$$CH_4 + 2O_2 \rightarrow CO_2 + 2H_2O + \Delta_R H \tag{6}$$

Here, $\Delta_R H$ is the reaction enthalpy and in case of methane amounts to −891 kJ/mol at standard conditions [86].

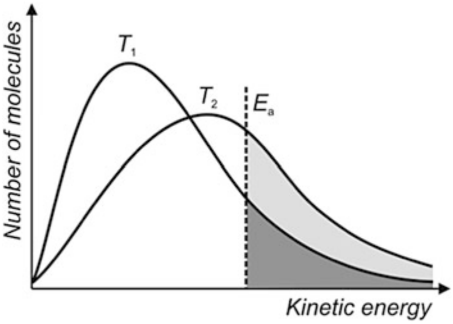

Fig. 3 Distribution (according to Boltzmann) of the molecules' kinetic energy for two different temperatures $T_1 < T_2$ in relation to the activation energy (E_a)

In absence of a catalyst, combustion of a flammable gas is only initiated and sustained if the gas temperature reaches the ignition temperature of the gas species (autoignition) or if an external ignition source (e.g., a spark) is present in order to yield enough kinetic energy of the reactants above the required activation energy of the chemical reaction (see Fig. 3) [87, 88]. Consequently, the reaction rate rises with increasing temperature considerably. This fact is expressed by the Arrhenius equation, which defines the rate constant of the reaction (k) as a function of temperature (T) and activation energy (E_a) [88]:

$$k = A \cdot \mathrm{e}^{-\frac{E_a}{R \cdot T}} \tag{7}$$

with A as pre-exponential factor and R as gas constant.

Moreover, in absence of a catalyst, the concentration range of the flammable gas has to be at a specific level between the LEL – lowest concentration level – and the upper explosive limit (UEL) – highest concentration level – so that combustion can proceed [80].

In contrast to that, the presence of a solid catalyst enables combustion at a temperature much lower than the ignition temperature and even in a concentration range of the flammable gas below its LEL [89]. The catalytic gas sensor is electrically heated through the platinum coil to reach a temperature usually of about 500°C, so that catalytic combustion readily occurs on the "active" pellistor element [82, 90]. The chemical reaction between the reactants, flammable gas and oxygen is accomplished in contact with the catalyst surface forming the combustion products, whereby the catalyst itself is not consumed. Therefore, the catalyst provides an alternative reaction pathway, wherein lower activation energy is required for the reaction process, and as a consequence the rate of the combustion reaction is enhanced according to the Arrhenius equation (see (7)). The catalytically promoted reaction pathway can be divided into a sequence of several intermediate steps (see Fig. 4) referring to [91]. In a first step, the reactants, the flammable gas and oxygen are adsorbed on the catalytic surface, which is in most instances an exothermic process by liberation heat of adsorption. Here, the adsorption predominantly occurs in form of chemisorption, wherein the electronic states of the catalyst and adsorbates are strongly perturbed. The heat of adsorption of the reactants must be low enough to reduce the activation

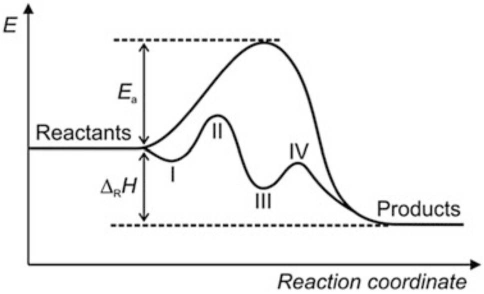

Fig. 4 Energy profile of a homogeneous exothermic reaction without catalyst (*upper curve*) and of a heterogeneous catalysis (*lower curve*) with the intermediate steps: adsorption of the reactants (I), reaction of the adsorbates (II), adsorbed products (III) and desorption of the products (IV) (modified from [91])

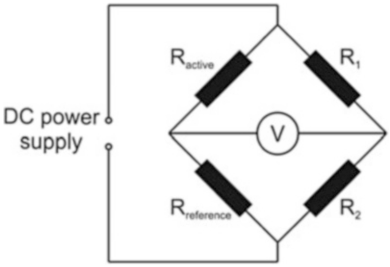

Fig. 5 Wheatstone-bridge configuration of a catalytic gas sensor with “active” pellistor element and reference pellistor element situated in opposing arms of the bridge circuit

energy for oxidation, but high enough to ensure an almost complete surface coverage of the adsorbed reactants [82]. If the catalyst is made up of a transition metal such as platinum or palladium, known as good catalysts for flammable gases with variable oxidation states and with partially filled d-orbitals leading to a surface with unsaturated valencies, the reactants become adsorbed by an electron exchange with the catalyst surface [75]. In a following step, the adsorbates react with each other resulting in an intermediate transition complex as precursor to form the final products, which are first adsorbed on the catalytic surface and finally, desorb from the surface.

For sensor operation, the catalytic gas sensor is electrically connected in a Wheatstone-bridge circuit, wherein the two pellistor elements are wired into opposing arms of it (see Fig. 5) [82, 92]. The pellistor elements are heated to their operating temperature through a constant power supply in form of an applied constant bias voltage or bias current. When the sensor is operated in air free of flammable gas components, the two pellistor elements are balanced and a stable baseline voltage is generated across the bridge. However, the presence of combustible gas components in air causes a change of the resistance of the “active” pellistor element due to the exothermic reaction on the catalyst that generates an out-of-balance voltage across the Wheatstone bridge [82, 93]. The out-of-balance voltage constitutes directly as sensor-output signal, which increases almost linearly with rising gas concentration of the flammable gas component in air [93].

Conventional catalytic gas sensors designed as pellistors feature a high response with low susceptibility to environmental changes and high durability due to the fact that they are rugged even in harsh environments [79]. Furthermore, they are easy to fabricate and afford sensor operation with low complexity in circuit design. But pellistors have also a few drawbacks such as non-specific response to various combustible gases, limited for concentration measurements up to the LEL and high power consumption between 300 and 700 mW [94]. The latter could be overcome by using micro-machined catalytic gas sensors, which are based on micro-hotplates, resulting in a low power consumption, in most cases below 100 mW [90, 94, 95]. This makes micro-machined catalytic gas sensors especially attractive for usage in portable gas detectors, wherein the sensors are driven by battery. Krawczyk and Namiesnik introduced also a new method to detect hydrogen concentrations above the LEL and up to the UEL by driving the catalytic gas sensor with an altered bias voltage [96]. In further studies, the selectivity of catalytic gas sensors was improved. Instead of using a catalyst made up of a noble metal and an insulation layer or dielectric ceramic pellet, the platinum heating wire is covered by a semiconducting metal oxide of SnO_2 or In_2O_3 enabling a gas-specific detection through selective adsorption of the gas species [79, 97]. This extraordinary kind of catalytic gas sensor is also called one-electrode semiconductor gas sensor or semistor.

2.2 *Gas Sensors Based on Adsorption Effects*

The detection mechanism of a further type of calorimetric gas sensor relies on the liberation or the abstraction of heat, since a gas species adsorbs on a selective organic compound. Although the heat of adsorption is rather low, especially for physical adsorption compared to the reaction heat of combustible gases detected by catalytic gas sensors, the adsorption of gas molecules on a corresponding adsorbent in form of an inclusion reaction between a gas species and an adsorbent on the sensor surface is highly selective. To measure the change in temperature resulting from the adsorption process with an accurate resolution in the sub-Kelvin range, monolithic thin-film thermopiles with enlarged Seebeck coefficient are used. On top of the “hot” junctions of a thermopile, a gas-selective polymeric membrane as host compound is applied [98]. This type of calorimetric gas sensors has been used in gas-sensing microsystems to seek out volatile compounds in unknown gas atmosphere [99, 100]. At present time, however, gas sensors based on adsorption effects are still subject of current research.

2.3 *Thermal Conductivity Gas Sensors*

The detection mechanisms of the two calorimetric sensor types described above rely on the chemical reaction between the sensor surface and gas species that is to be detected. The sensor based on thermal conductivity, however, exploits the heat transfer from a heated sensing element to the surrounding gas influenced by the thermal conductivity of the gas as a quantitative measurement principle without any chemical interaction [75]. The thermal conductivity sensor, also called katharometer or hot-wire detector, is one of the oldest gas sensors that was first mentioned by the Siemens and Halske Company in 1913 for the detection of methane in binary gas mixtures [101]. Today, thermal conductivity sensors are mainly applied as non-selective or low-selective but reliable detectors in gas chromatography [75, 102] and as monitoring devices for combustible gases even at high gas concentrations implicating the concentration range above the LEL, wherein they are often used in complementary combination with catalytic gas sensors [82, 103, 104].

The thermal conductivity sensor consists of two platinum or tungsten filaments, which are electrically heated up to an operating temperature of about 300°C and both are situated in a Wheatstone bridge. One of the filaments is exposed to the surrounding gas acting as “active” filament and the other one is either enclosed in a sealed housing for compensating temperature changes of the surrounding gas or exposed to a reference gas [92, 105]. If the sensor is exposed to a gas mixture with air as carrier gas and wherein the thermal conductivity of present gas compounds is higher than the conductivity of air, then heat is dissipated from the “active” heated filament. The dissipation of heating power (P) of the “active” filament can be described by [92]:

$$P = \alpha_{\mathrm{TCS}} \cdot \lambda_{\mathrm{M}} \cdot \Delta T \tag{8}$$

Here, α_{TCS} is a constant defined by the geometry of the heated filament of the sensor, λ_{M} is the thermal conductivity of the surrounding gas and ΔT is the temperature difference between the filament and surrounding gas.

The power dissipation causes a change in the resistance of the filament that can be measured then by generating an out-of-balance voltage in a Wheatstone bridge. For an adequate sensor operation, the heated filaments must be protected from contact with water vapour, since the thermal conductivity of water vapour could strongly interfere with the thermal conductivity of the gas mixture [92]. Even though the detection mechanism seems to be trivial, a precise calculation of the thermal conductivity of an unknown gas mixture depends on temperature and does not end up in a linear function of the mole fraction of the gas components, as considered for ideal binary gas mixtures. A precise description of the thermal conductivity of a non-binary gas mixture is given by an empirical equation from Wassiljewa [106, 107]:

$$\lambda_{\mathrm{M}}(x_i, T) = \sum_{i=1}^{n} \frac{x_i \cdot \lambda_i(T)}{\sum_{j=1}^{n} x_j \cdot \Phi_{ij}(T)} \tag{9}$$

wherein x_i and x_j are the mole fractions of the gas components i and j, λ_i is the thermal conductivity of the component i and Φ_{ij} is a correction factor depending on the viscosity of each gas component according to Mason and Saxena [108]:

$$\Phi_{ij}(T) = \frac{\left(1 + \sqrt{\eta_i(T)/\eta_j(T)} \cdot \sqrt[4]{M_j/M_i}\right)^2}{\sqrt{8 \cdot \left(1 + M_i/M_j\right)}} \tag{10}$$

Here, η_i and η_j are the viscosities of the gas compounds i and j, and M_i and M_j are the molecular weights of the compounds i and j.

3 Calorimetric Gas Sensors for H_2O_2 Monitoring

For the detection of H_2O_2 concentrations up to the percentage range in sterilisation processes, calorimetric gas sensors based on the catalytic reaction mechanism have been developed. For an industrial application of these gas sensors, they must fulfil some operational requirements. The sensor arrangements must continuously operate under harsh environmental conditions, e.g., they have to endure elevated gas temperatures; they must be stable under high gas flows, and they should be robust against vibrations. Furthermore, the sensors' output signal should not be interfered by gas-temperature fluctuations and high amounts of water vapour.

The envisaged sensor set-up comprises a calorimetric differential set-up made up of two temperature-sensing elements. One of them acts as "active" sensor element that is additionally covered by a catalyst, whereas another one is encapsulated by an inert material serving as a reference. If the sensor set-up is exposed to gaseous H_2O_2 atmosphere, a temperature difference between the two temperature-sensing elements can be detected that is caused by the released reaction enthalpy of an overall exothermic reaction on the catalytically active surface area according to:

$$2H_2O_2(g) \rightarrow 2H_2O\,(g) + O_2(g) + \Delta_R H \tag{11}$$

with $\Delta_R H$ of -105.3 kJ/mol.

In contrast to conventional, catalytic gas sensors for the detection of combustible gases, the envisaged sensor set-up for H_2O_2 monitoring does not require oxygen for the exothermic reaction so that it could also be applied for H_2O_2 detection under vacuum conditions. In addition, the sensor set-up must not be actively heated. Instead, the elevated temperature of the gas atmosphere itself is exploited to provide a sufficient sensor-surface temperature. Furthermore, in place of detecting the raised temperature only on the "active" sensing element, the temperature difference between the "active" element and the reference serves as sensor signal, so that altering temperatures of the gas atmosphere are compensated.

Fig. 6 Schematic view of the sensor arrangement for continuous H_2O_2 monitoring; (**a**) calorimetric differential set-up on transistor outline (TO) socket and (**b**) sensor shielded by a TO header and a stainless steel mesh disk

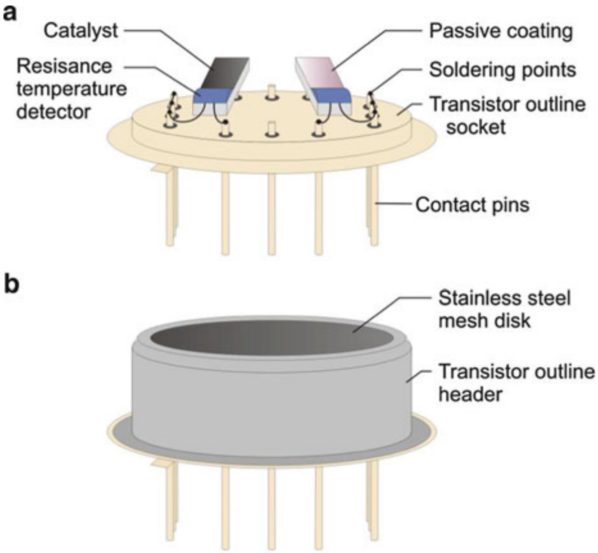

3.1 Sensor Arrangement for On-line Monitoring

3.1.1 Sensor Preparation

For continuous H_2O_2 monitoring, a calorimetric differential set-up was built on top of a conventional transistor outline (TO) socket (see Fig. 6). As temperature-sensing elements, two resistive temperature detectors in form of commercial Pt100 sensors are situated in opposing positions on the TO socket and are soldered on the socket's contact pins. One of the temperature-sensing elements was treated by a catalytically active material, whereas the second element was covered by a passive coating.

In a preliminary study, different potential catalysts and passive coatings were investigated with regard to their response to gaseous H_2O_2 in a well-defined concentration range relating to the deployed concentration in sterilisation processes [109, 110].

As passive materials, electro-deposited nickel, stainless steel cladding and dip-coated perfluoralkoxy (PFA) were examined. Therein, PFA was the passive coating of choice due to its chemical inertness against H_2O_2, excellent temperature stability and hydrophobicity to avoid water condensation on the sensor surface. For the sensor passivation, the temperature-sensing element was first treated by a PFA primer solution and afterwards, dip-coated in an aqueous PFA dispersion, which was then heat-treated at a temperature of 360°C for 30 min.

As catalytically active materials, electro-plated copper as well as diversely deposited manganese oxide coatings (electro-plating with and without heat treatment, chemical deposition from aqueous $HMnO_4$ solution and in powder form)

Table 2 Sensitivities of the different investigated, catalytically active materials

Material	Sensitivity (°C/(% v/v)
Copper (electro-plated)	5.4
Manganese oxide (electro-plated)	1.3
Manganese oxide (electro-plated and heat-treated)	1.7
Manganese oxide (chemically deposited)	4.6
Manganese oxide (powder)	8.6

were investigated with regard to their response against H_2O_2 listed in Table 2. Here, manganese oxide in powder form showed a high sensitivity compared to the other tested catalysts. Thus, one of the temperature-sensing elements of the sensor arrangement was coated by a manganese(IV) oxide powder linked in a PFA matrix and baked at a temperature of 350°C for 25 min.

Once, the catalytically active layer and passive layer were deposited on the temperature-sensing elements, the sensor was finally shielded by a TO header with an opened window enclosed by a stainless steel mesh disk (see Fig. 6).

3.1.2 Sensor Response in H_2O_2 Atmosphere

The investigation of the sensor response in gaseous H_2O_2 was conducted in a sterilisation rig, whereby the process conditions of a H_2O_2-gas flow derived from the industrial aseptic apparatuses were reproduced. The test rig consists of a compressed air-supply unit to provide a carrier-gas stream regulated by a flow-control unit, a dosing system feeding the carrier-gas stream with aqueous H_2O_2 solution and/or deionised water to form an aerosol with liquid H_2O_2/H_2O mixture that has to be thoroughly transferred into the gas phase. This is done by an evaporation unit that consists of two heating elements, wherein the aerosol is first heated up to a temperature directly below its boiling point and afterwards, completely evaporated. The evaporation unit is controlled by the gas temperature at its gas outlet. The gaseous H_2O_2 is then equally dispensed out of the gas nozzles situated in an enclosed sterilisation chamber. In the sterilisation chamber of the test rig, the sensor arrangement was fixated directly in the gas flow, where typically the products, which have to be sterilised, are introduced. In this way, a wide range of gas compositions, flow rates and gas temperatures can be adjusted, as for industrial sterilisation processes. A block diagram of the sterilisation rig is shown in Fig. 7.

A set of parameters, which represents the most common process settings, has been chosen to carry out the sensor-response characterisation. An aqueous H_2O_2 solution of 35% w/w technical grade has been used. Amounts between 250 and 1,100 μL/s have been fed to the carrier-gas stream. Thereby, H_2O_2 concentrations up to 7.5% v/v in the gas phase have been realised at an elevated gas temperature of 270°C on the outlet of the evaporation unit and a gas flow of 10 m^3/h. A typical sensor response to gaseous H_2O_2 is shown in Fig. 8. Therein, a temperature rise on both the "active" and "passive" sensor element with increasing H_2O_2 concentration can be clearly noticed, whereby the rise on the active element is significantly higher

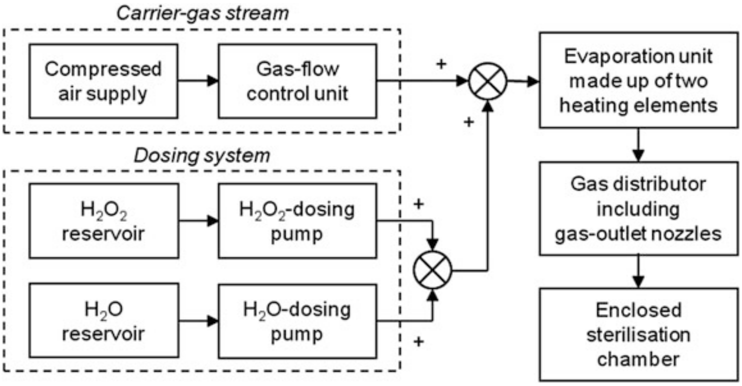

Fig. 7 Block diagram of the sterilisation rig for investigating the sensor-response characteristics

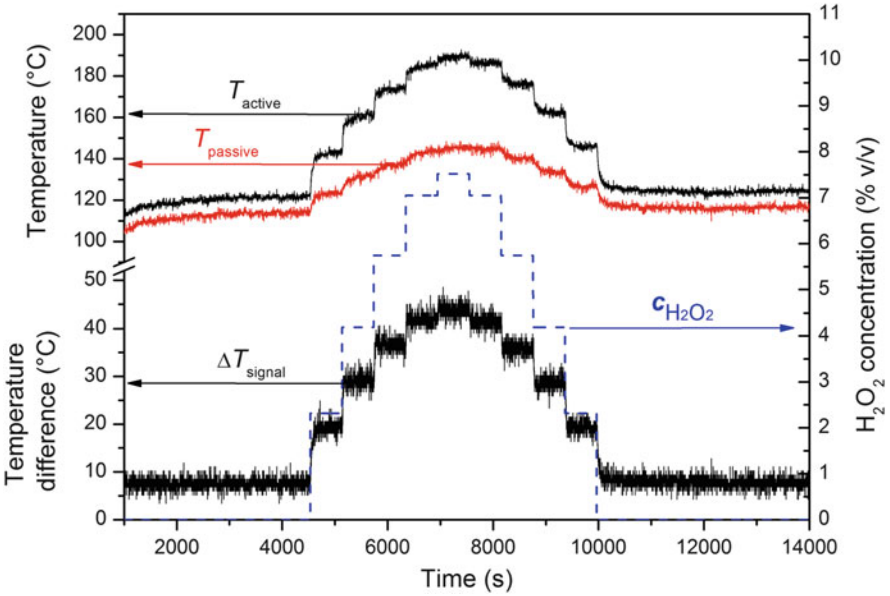

Fig. 8 Sensor-response behaviour for H_2O_2 concentrations between 0 and 7.5% v/v; temperature on the "active" and "passive" sensor element (*upper curves*) as well as temperature difference of both sensor elements (*lower curve*)

than that one of the passive element. The elevated temperature on the passive sensor element at increased H_2O_2 concentrations results from a change in heat capacity of the gas mixture, whereas the temperature on the active element is mainly generated by the catalytically promoted, exothermic reaction. Thus, the resulting temperature difference serving as sensor signal depends solely on the present H_2O_2 concentration in form of a linear function (see Fig. 9):

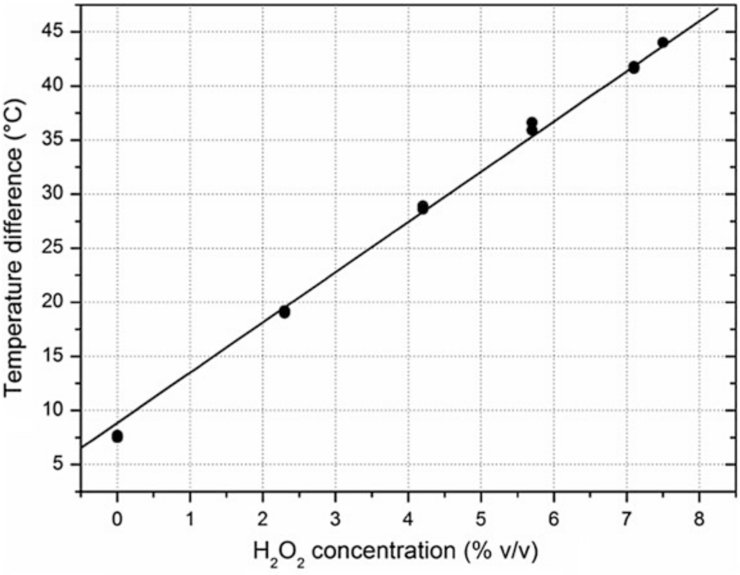

Fig. 9 Temperature difference of the sensor arrangement versus H_2O_2 concentration as calibration plot

$$\Delta T_{\text{signal}} = S \cdot c_{H_2O_2} + \Delta T_0 \tag{12}$$

Here, S is the sensitivity, $c_{H_2O_2}$ is the H_2O_2 concentration and ΔT_0 is the temperature off-set.

The resulting sensor characteristic from the calibration plot shown in Fig. 9 can be described as:

$$\Delta T_{\text{signal}} = 4.6 \cdot c_{H_2O_2} + 8.9 \tag{13}$$

3.1.3 Monitoring System for Industrial Applications

In industrial processes, in particular in aseptic sterilisation processes employing H_2O_2 vapour, a monitoring of the H_2O_2 concentration during machine operation is desired. The sensor described in Sect. 3.1.1 has been designed to be suitable for use under field conditions. In short, the operational requirements are a high thermal, mechanical and chemical stability under continuous operation in H_2O_2 atmosphere. Furthermore, the sensor response should not be influenced by water vapour or fluctuations of the gas temperature. On account on this a monitoring system by means of a handheld device has been developed [111]. This device comprises the

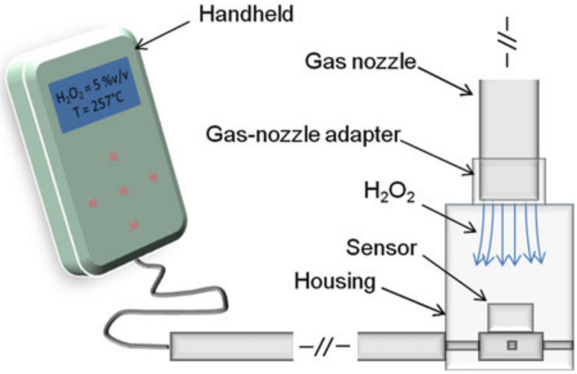

Fig. 10 Schematic of the handheld device when used under the gas nozzle (adapted from the original contribution of the authors [111])

calorimetric H_2O_2 sensor, which is mounted into a housing, and a handheld to display the measured concentration and gas temperature. The sensor housing was designed to be easily adapted to the gas nozzle of an aseptic sterilisation machine, ensuring that the sensor is located in the regular distance from the gas outlet. A schematic of the handheld-sensor system is shown in Fig. 10.

Measurements with the handheld sensor device at the sterilisation test rig as well as at a manufacturer's sterilisation machine have shown a good linearity in the range between 0 and 8% v/v H_2O_2. No influences by water vapour or fluctuations of the gas flow could be observed in the range of interest. The response time of the sensor was 35 s and the absolute accuracy was determined to be 0.2% v/v in a single measurement. All in all, it could be shown that the sensor is suitable for field use. It can be either applied for process monitoring or implemental for optimising the parameter set to increase the sterilisation efficiency.

3.2 Catalytic Surface Reaction and Sensor-Response Modelling

Undoubtedly, the decomposition of H_2O_2 on the catalyst surface occurs in a net reaction as described by (11), wherein H_2O_2 reacts to oxygen and water vapour, releasing a reaction enthalpy of $\Delta_R H$ of -105.3 kJ/mol. On this basis reaction, a theoretical consideration of the sensor response in terms of the concentration-dependent temperature rise can be made.

Therefore, a simplified model is applied, wherein an overall H_2O_2 decomposition on the sensor surface is presupposed and influences of the gas flow, diffusion effects as well as the sensor geometry are being neglected. First of all, the maximum temperature rise is simply calculated by considering the change of the reaction enthalpy. Assuming that the decomposition occurs at constant pressure, the total heat released from the catalytic surface reaction can be described by:

$$\Delta Q = n_V \cdot \Delta_R H = \rho_c \cdot c_p \cdot \Delta T_\infty \tag{14}$$

where n_V is the number density of H_2O_2, ρ_c and c_p are the density and specific heat of the carrier-gas stream and ΔT is the resulting temperature rise.

The number density can be described by:

$$n_V = \frac{\dot{n}_{H_2O_2}}{\dot{V}_c} \tag{15}$$

Here, $\dot{n}_{H_2O_2}$ is the molar flow of H_2O_2 and $\dot{V}_c$ is the volume-flow rate of the carrier-gas stream.

The resulting temperature rise (ΔT_∞) defines the upper limit of the sensor response. For a reaction enthalpy of -105.3 kJ/mol, a maximum concentration-dependent sensor response amounts to be:

$$\Delta T_\infty = c_{H_2O_2} \cdot 24.1°\mathrm{C}/(\%\ v/v) \tag{16}$$

In field experiments the highest response was achieved for manganese oxide powder, in case of the calorimetric differential set-up, which had been built up on a TO transistor socket. The resulting sensitivity amounted to be 8.6°C/(%v/v). However, the calculated upper limit of the temperature rise can only be attained for low gas flows and an overall decomposition of the hydrogen peroxide at the catalyst surface. Furthermore, diffusion effects and the sensors' geometry had not been taken into account for the simulation. Currently running experiments extending this simplified model will consider these effects in more detail to explain the discrepancy between the performed and expected sensitivity values, respectively.

4 Limitations and Challenges

The H_2O_2 concentration certainly is a critical process parameter for aseptic sterilisation processes and their monitoring appears to be very helpful in terms of process control. However, besides the absolute H_2O_2 concentration in the sterilising gas, its local distribution on the surface to be sterilised plays a major role. When sterilising preformed packaging material, its geometry has to be considered, for instance. Areas of stagnant flow may arise, for example, at folding edges or especially in the corners of the packaging material. Such areas, which are hardly reached by the sterilising agent because of their geometry are called "critical spots". To ensure that sufficient contact with hydrogen peroxide has taken place at these critical spots, a local measurement of the H_2O_2 concentration would be desirable.

On the other hand, even though the exact mechanism of microbial inactivation has not yet been uncovered completely, it is believed that the inhibition of microbial growth by hydrogen peroxide is not solely the direct result of its oxidative properties in its molecular state, but the consequence of the activity of other strongly oxidant, chemical species derived from it. In fact, hydrogen peroxide is an excellent source of singlet oxygen, superoxide radicals ($O_2^{\bullet -}$) and hydroxyl radicals ($OH^{\bullet}$) that are highly reactive and very toxic for microorganisms [112]. Furthermore, the kinetic of formation of said species is dependent on a number of other influencing factors, like the temperature, humidity or the presence of catalysts [113]. Having that in mind, it seems reasonable that the microbial inactivation also is indirectly depending on these factors. This implies that solely monitoring the H_2O_2 concentration is therefore not sufficient for an overall convincing evaluation of the sterilisation process.

Accordingly, the challenges for "tomorrow's" sensor systems are first, the local detection of the H_2O_2 concentration and second, the identification and detection of the sum of variables that are responsible for the microbial inactivation process.

5 Further Sensor Approaches

Besides the sensor system for the on-line monitoring of the H_2O_2 concentration, efforts on the development of chip-based calorimetric sensors for the local detection of the H_2O_2 concentration on the items to be sterilised have been made. Here, a fast sensor response for the in-line monitoring during a short contact time of the package with the gaseous H_2O_2 as well as a flat sensor design for its fixation on the particular item is required. Even if the sensor arrangements are developed for two different areas of application, both of them are based on the same catalytic detection principle, namely a differential set-up of a catalytically activated and a passivated temperature-sensitive device. A first generation of these chip-based calorimetric sensors has been realised on silicon substrates, wherein the temperature-sensitive elements were based on either thin-film resistances or thermocouples [110, 114]. Though, due to their high thermal mass, accompanied with a poor response time in the range of 7 s, they did not meet the requirements for an in-line measurement with a short contact time of the analyte to be detected.

However, the second generation of thin-film sensors has been realised on a flexible polyimide sheet with a thickness of 25 μm [115]. The reason for using polyimide instead of conventional silicon as sensor substrate relies on the low thermal conductivity of 0.147 $Wm^{-1} K^{-1}$ (compared to 156 $Wm^{-1} K^{-1}$ for silicon) to guarantee a high sensitivity by avoiding the heat transfer between the active and passive sensor segment. In addition, polyimide shows a chemical inertness against hydrogen peroxide and an expedient mechanical stability as well as a sufficient thermal endurance up to 400°C. As catalyst, again a dispersion of manganese(IV) oxide has been chosen, whereas the electrical insulation was achieved by an SU-8 photo-resist layer on top of the resistance structures. A sample of this type of sensor is depicted in Fig. 11.

With the polyimide-based sensor, sensitivities up to approximately 7.1°C/% v/v could be achieved in the range between 0 and 8% v/v H_2O_2 in the gaseous phase [116], which is comparable to the "macroscopic" sensors for on-line monitoring. The response time (t_{90}) of the polyimide-based sensors was determined to be 5.7 s. Therewith, the response is faster by a factor of approximately 6 compared to the sensors built up on a TO socket. Advantageously using a new "read-out" strategy for

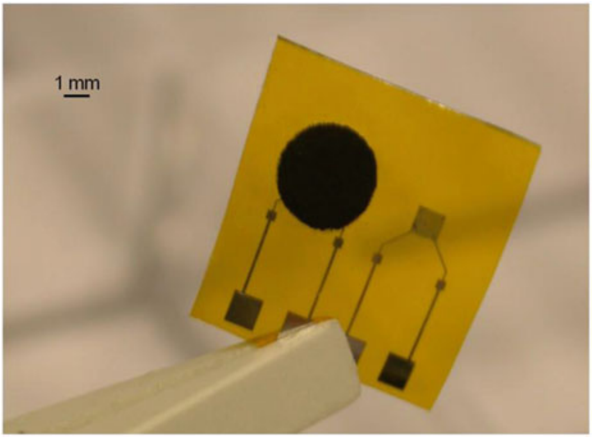

Fig. 11 Calorimetric gas sensor based on a differential set-up of a catalytically activated (*left*) and a passivated (*right*) temperature-sensitive thin-film resistance, realised on a 25 μm polyimide sheet with a size of 10 × 10 mm^2

evaluation of the sensor signal [117] now offers the possibility to quantitatively monitor the H_2O_2 concentration on-line as well as in-line in a single package during each sterilisation step.

Another promising feature of these polyimide-based sensors relies on their flexibility, allowing them to be installed in nearly any position on the packaging material, including edges and corners.

To exploit the full potential of these foil-based sensors and to make them suitable for in-line monitoring, for example, by integrating them into a test package, which can be carried through the sterilisation process, an adequate signal transmission has to be adapted still. In this context, a wireless transmission by means of an RFID circuit seems to be an appropriate option. One proposal for such a circuit is as follows [110], consisting of a

- transmission system, containing a passive RFID transponder (inside the aseptic filling system), inductively coupled to an RFID transceiver (outside of the aseptic filling system) and a
- calorimetric H_2O_2 gas sensor embedded inside of a test package and connected to a transponder.

If sensor and transponder are fabricated on chip level together with an integrated low-power circuit, the transceiver could not only be used for reading the sensor data but also to power the transponder circuit via electromagnetic induction. This way, an additional power supply is not required on the part of the test package.

Another approach, which aims to monitor the sterilisation effect, takes benefit from the use of an array of different types of chemical sensors with varying degrees of response. In so doing, not a quantitative approach, but in a narrow sense, a more qualitative approach is pursued. That means, not a monitoring of the individual parameters itself, like absolute values of concentration or temperature, but rather an abstract representation – a chemical image – of the gas composition is intended. Originally, this attempt was used as a method for artificial olfaction.

As mentioned earlier, the sterilising effect by hydrogen peroxide is not solely attributed to its presence or concentration, but rather arises from the decomposition of the same and resulting reactive intermediates. These intermediates, mainly hydroxyl radicals, even they are of transitory nature, are being related to a high potential of microbial inactivation.

The mechanism of decomposition of hydrogen peroxide occurs in two different ways: Once after recondensation of the hydrogen peroxide at surfaces, as well as in gaseous phase, more precisely during the transition from the liquid phase into the gaseous phase initiated by the evaporation process. The rate of decomposition in turn depends on a number of factors. Essentially, these are the chemical stabilisation of the H_2O_2 solution, its concentration in aqueous solution, the temperature (more precisely the temperature gradient) as well as the texture of the surface and the presence of active sites or catalysts. Concerning the sterilisation by H_2O_2 vapour, typically one tries to avoid condensation of the sterilising agent on the surface of the packaging material, as residues may affect the product to be packaged. In this particular case, the effects that take place at the surface of the packaging material only play a minor role, so that the focus may mainly be directed to the gaseous phase.

Investigations with a metal-oxide semiconductor gas sensor have shown that this type of sensor offers a response upon exposure to hydrogen peroxide [113, 118, 119]. In general, these sensors, although not being very specific, are associated with a high sensitivity to oxidising and reducing gases. This is because the electrical resistance of semiconductors is affected by adsorption of almost any gaseous species. In said studies, a commercially available metal-oxide gas sensor of an n-type semiconductor material has been investigated on its response to H_2O_2 gas mixtures that are used for packing sterilisation, under varying conditions in terms of concentration, humidity, temperature and flow. It was found that for these gas sensors, contrary to the accepted opinion that n-type semiconductors respond with an increase of their electrical resistance on exposure to oxidising gases (such as hydrogen peroxide) in fact, a reduction in the resistance was observed. However, it could be shown that the sensor response had merely been evoked by the influence of intermediate species, in first instance, hydroxyl ions and radicals, respectively, which act as electron donors and directly increase the conductivity of the metal oxide. In the same course, the sensor was tested for its cross-sensitivity on water vapour. It was found that the sensor is in the same manner responsive to water vapour. However, the response was lower by a factor of almost ten compared to hydrogen peroxide.

In recent studies, three types of sensors have been investigated on their response to the influencing factors by the sterilisation with H_2O_2 vapour, namely the concentrations of H_2O_2 in gaseous phase, the level of humidity, the gas temperature as well as the flow rate [113]. These included four metal-oxide semiconductor gas sensors (MOX), which differ by the semiconductor material and its doping, an electrochemical type of sensor (λ-probe) as well as a calorimetric type of sensor for the detection of hydrogen peroxide, as had previously been described. Simultaneously, microbiological tests with spores of *Bacillus atrophaeus* have been carried out in parallel by means of the LCR test, in order to determine the microbicidal effectiveness. Summarising in short, it could be demonstrated that the influencing factors of the

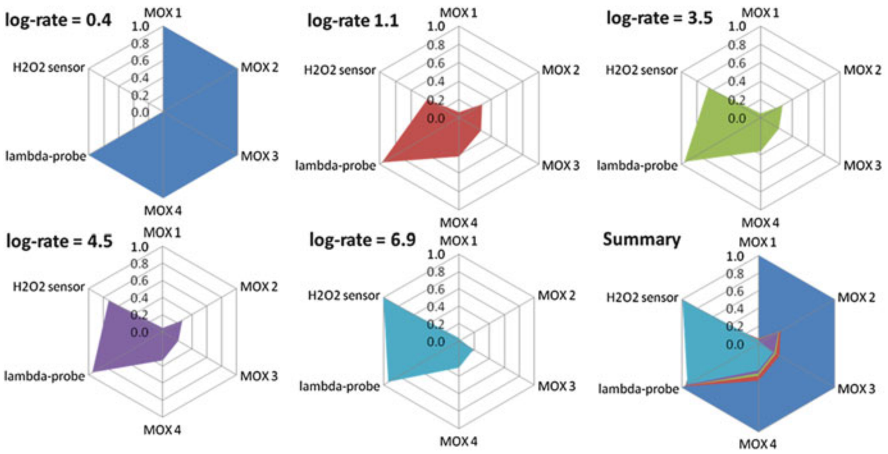

Fig. 12 Radar plots of the resulting sensor signals of six different gas sensors during a series of measurements, correlated with the achieved log-rates during the microbiological tests (Figure adapted from open access journal [113] as original contribution of the authors)

sterilisation by H_2O_2 vapour affected all sensors under investigation, whereas the response of the individual sensors was of varying degree. In this context, patterns generated from the sensor signals, which are represented as the ratio of the signal strengths of the individual sensors by means of a radar plot, are being contrasted with the results of the microbiological tests (see Fig. 12). It turns out that on the basis of the variability of the chemical images obtained, a clear distinction between the different gas compositions and resulting log-rates (same as LCR) can be made.

This approach seems to be highly promising, especially, since it can help to understand the mechanism of action of hydrogen peroxide. Nevertheless, further investigations are necessary both to increase the number of measurements in terms of improving the data (reliability) and to study the long-term behaviour of such an electronic-type gas sensor system (array).

6 Outlook

The steady increase in the output of production of aseptic filling goods, increasing cost pressure as well as the consumers demand for safe foods require a sustainable solution in terms of the quality management of aseptic filling processes. One of the most critical factors is the sterilisation of the packaging material. To the present day it has not succeeded to establish appropriate rapid tests for the monitoring of sterilisation processes employing H_2O_2 vapour as sterilant on the market, although this represents one of the most frequently used techniques.

Thorough tests under field conditions during the last years have demonstrated that the calorimetric gas sensor is a suitable candidate for the monitoring of hydrogen peroxide in aseptic sterilisation processes. It offers the advantage of a rugged construction that makes it operable under harsh environmental conditions, in particular at elevated concentrations of hydrogen peroxide up to 10% v/v and gas temperatures up to 300°C. In addition, it can be produced at low costs [109, 120]. It is therefore becoming apparent that these sensors will soon find their way into practice. A further milestone particularly is represented by the development of chip-/(foil-)based calorimetric gas sensors, which enable an in-line monitoring of the H_2O_2 concentration. It should be mentioned again that this opens access to monitor the local H_2O_2 concentration at critical spots of the packaging material, so as to ensure a sufficient sterilisation. But not only the focus is on the certainty over a sufficient sterilisation of a single package; rather, these sensors can also be applied to analyse the flow of the sterilising agents inside the packages in order to optimise the sterilisation process with regard to the flow characteristics. The sensors based on polyimide foil are already in an advanced state of technology. However, inductive power supply and data acquisition during in-line operation are still a remaining challenge.

A future trend in the monitoring of aseptic sterilisation processes is associated by the use of multi-sensor systems. Initial studies have shown that different types of sensors, including metal-oxide semiconductor gas sensors and electrochemical sensors are responsive to intermediate species that are involved in the process of microbiological inactivation. Such sensor systems could contribute to the understanding of the mechanism of action of hydrogen peroxide, which is still far from being completely understood. To get ahead in this regard, further investigations have to be raised on both, the mechanism of action of hydrogen peroxide on microorganisms and its interaction with the sensors deployed.

References

1. Thénard LJ (1818) Observations sur des nouvelles combinaisons entre l'oxigéne et divers acides. Annales de Chimie et de Physique 8:306–312
2. Schumb WC, Satterfield CN, Wentwoth RL (1955) Hydrogen peroxide. Reinhold Publishing Corporation, New York
3. Wolffenstein R (1894) Koncentration und Destillation von Wasserstoffsuperoxyd. Berichte der Deutschen Chemischen Gesellschaft 27(3):3307–3312
4. Pokhodenko VD (1994) Life and work of academician L. V. Pisarzhevskii (on the 120th anniversary of his birth). Theoretical Exp Chem 29(6):313–319
5. Ayling GW (1981) Waste treatment with hydrogen peroxide. Chem Eng 88(24):79–82
6. Eul W, Moeller A, Steiner N (2000) Hydrogen peroxide. In: Kirk-Othmer encyclopedia of chemical technology. Wiley, Hoboken
7. Yaws C, Setty H (1974) Water and hydrogen peroxide. Chem Eng 81(27):67–74
8. Jones CW, Clark JH (eds) (1999) Applications of hydrogen peroxide and its derivatives. The Royal Society of Chemistry, Cambridge
9. Cooper WJ, Zika RG, Petasne RG, Plane JMC (1988) Photochemical formation of hydrogen peroxide in natural waters exposed to sunlight. Environ Sci Technol 22(10):1156–1160
10. Calvert JG, Stockwell WR (1983) Acid generation in the troposphere by gas-phase chemistry. Environ Sci Technol 17(9):428–443
11. Armogida M, Nistico R, Mercuri NB (2012) Therapeutic potential of targeting hydrogen peroxide metabolism in the treatment of brain ischaemia. Br J Pharmacol 166(4):1211–1224

12. Halliwell B, Clement MV, Long LH (2000) Hydrogen peroxide in the human body. FEBS Lett 486(1):10–13
13. Schildknecht H, Holoubek K (1961) Die Bombardierkäfer und ihre Explosionschemie V. Mitteilung über Insektenabwehrstoffe. Angewandte Chemie 73(1):1–7
14. Goor G, Goor G, Glenneberg J, Jacobi S (2000) Hydrogen peroxide. In: Ullmann's encyclopedia of industrial chemistry. Wiley-VCH, Weinheim
15. Nederhoff E (2000) Hydrogen peroxide for cleaning irrigation system. Comm Grower 55 (10):32–34
16. KEMI Swedish Chemicals Agency (2010) Information on substances – hydrogen peroxide. Technical report
17. Global Industry Analysts, Inc. (2012) Hydrogen peroxide – a global strategic business report. Document
18. Hage R, Lienke A (2006) Anwendung von Übergangsmetallkomplexen zum Bleichen von Textilien und Holzpulpe. Angewandte Chemie 118(2):212–229
19. Miro S, Argyropoulos DS (2001) Catalysis and activation of oxygen and peroxide delignification of chemical pulps: a review. In: ACS symposium series, vol. 785. American Chemical Society, pp. 2–43
20. Spiro M, Griffith WP (1997) The mechanism of hydrogen peroxide bleaching. Textile Chemist Colorist 29(11):12–13
21. Antonijevic M, Dimitrijevic M, Jankovic Z (1997) Leaching of pyrite with hydrogen peroxide in sulphuric acid. Hydrometallurgy 46(1–2):71–83
22. Kitis M, Akcil A, Karakaya E, Yigit N (2005) Destruction of cyanide by hydrogen peroxide in tailings slurries from low bearing sulphidic gold ores. Miner Eng 18(3):353–362
23. Wernimont E, Ventura M, Garboden G, Mullens P (1999) Past and present uses of rocket grade hydrogen peroxide. Technical report, General Kinetics, LLC
24. Ansari I, Datta A (2003) An overview of sterilization methods for packaging materials used in aseptic packaging systems. Food Bioproducts Process 81(1):57–65
25. McDonnell G, Russell AD (1999) Antiseptics and disinfectants: activity, action, and resistance. Clin Microbiol Rev 12(1):147–179
26. Muranyi P (2008) Einsatz eines Atmosphärendruckplasmas zur Entkeimung von lebensmittelrelevanten Verpackungen aus Kunststoff. Dissertation, Technische Universität München
27. Wu JSB, Hsu H-Y, Yang B-HB (2012) Aseptic processing and packaging. In: Handbook of fruits and fruit processing. Wiley, Ames, pp 175–187
28. von Bockelmann BAH, von Bockelmann ILI (1986) Aseptic packaging of liquid food products: a literature review. J Agric Food Chem 34(3):384–392
29. Muranyi P, Wunderlich J, Dobosz M (2006) Sterilisation von Abfüllmaschinen: Standardisierung von Bioindikatoren, Untersuchungsmethoden und Validierungsverfahren. Chemie Ingenieur Technik 78(11):1667–1673
30. Buchner N (ed) (1999) Verpackung von Lebensmitteln, 1st edn. Springer, Berlin
31. David JRD, Graves RH, Carlson VR (eds) (1996) Aseptic processing and packaging of food: a food industry perspective. CRC, New York
32. Wallhäußer KH (ed) (1988) Praxis der Sterilisation, Desinfektion, Antiseptik und Konservierung – Keimidentidentifizierung-Betriebshygiene, 4th edn. Thieme, Stuttgart
33. Codex Alimentarius Commission Code of hygienic practice for aseptically processed and packaged low-acid food (1993) Technical report CAC/RCP 40
34. Cerny G (1990) Packstoffsterilisation beim aseptischen Abpacken. Internationale Zeitschrift für Lebensmittel-Technik, Marketing, Verpackung und Analytik 41(1–2):54–58
35. Gould GW (1996) Methods for preservation and extension of shelf life. Int J Food Microbiol 33(1):51–64
36. Russell AD (1990) Bacterial spores and chemical sporicidal agents. Clin Microbiol Rev 3(2): 99–119
37. Reuter H (1986) Aseptisches Verpacken von Lebensmitteln – Grundlagen und Stand der Technik. Chemie Ingenieur Technik 58(10):785–793

38. Heckert RA, Best M, Jordan LT, Dulac GC, Eddington DL, Sterritt WG (1997) Efficacy of vaporized hydrogen peroxide against exotic animal viruses. Appl Environ Microbiol 63(10): 3916–3918
39. Cardoso CF, JdAF F, Miranda Walter EH (2011) Modeling of sporicidal effect of hydrogen peroxide in the sterilization of low density polyethylene film inoculated with *Bacillus subtilis* spores. Food Contr 22(10):1559–1564
40. Bayliss CE, Waites WM (1982) Effect of simultaneous high intensity ultraviolet irradiation and hydrogen peroxide on bacterial spores. Int J Food Sci Technol 17(4):467–470
41. Engelhard P, Kulozik U (2006) Packstoffentkeimung mittels Wasserstoffperoxid – Methoden und Kombinationsverfahren. Chemie Ingenieur Technik 78(11):1717–1722
42. Unger-Bimczok B, Kottke V, Hertel C, Rauschnabel J (2008) The influence of humidity, hydrogen peroxide concentration, and condensation on the inactivation of *Geobacillus stearothermophilus* spores with hydrogen peroxide vapor. J Pharm Innov 3(2):123–133
43. Engelhard P (2005) Inaktivieren von Mikroorganismen auf festen Oberflächen mittels Atmosphären aus feuchter Luft/Wasserstoffperoxid und IR-Behandlung. Dissertation, Technische Universität München
44. Block SS (ed) (1991) Desinfection, sterilization and preservation. Lea and Febiger, Philadelphia
45. Imlay JA, Linn S (1988) DNA damage and oxygen radical toxicity. Science 240(4857): 1302–1309
46. Mohan A, Dunn J, Hunt MC, Sizer CE (2009) Inactivation of *Bacillus atrophaeus* spores with surface-active peracids and characterization of formed free radicals using electron spin resonance spectroscopy. J Food Sci 74(7):M411–M417
47. Riesenman PJ, Nicholson WL (2000) Role of the spore coat layers in *Bacillus subtilis* spore resistance to hydrogen peroxide, artificial UV-C, UV-B, and solar UV radiation. Appl Environ Microbiol 66(2):620–626
48. Imlay JA (2003) Pathways of oxidative damage. Annu Rev Microbiol 57(1):395–418
49. Baldry M (1983) The bactericidal, fungicidal and sporicidal properties of hydrogen peroxide and peracetic acid. J Appl Microbiol 54(3):417–423
50. Setlow B, Setlow CA, Setlow P (1997) Killing bacterial spores by organic hydroperoxides. J Ind Microbiol Biotechnol 18(6):384–388
51. Linley E, Denyer SP, McDonnell G, Simons C, Maillard J-Y (2012) Use of hydrogen peroxide as a biocide: new consideration of its mechanisms of biocidal action. J Antimicrob Chemother 67(7):1589–1596
52. Melly E, Cowan A, Setlow P (2002) Studies on the mechanism of killing of *Bacillus subtilis* spores by hydrogen peroxide. J Appl Microbiol 93(2):316–325
53. Popham DL, Sengupta S, Setlow P (1995) Heat, hydrogen peroxide, and UV resistance of *Bacillus subtilis* spores with increased core water content and with or without major DNA-binding proteins. Appl Environ Microbiol 61(10):3633–3638
54. Gilmore ME, Bandyopadhyay D, Dean AM, Linnstaedt SD, Popham DL (2004) Production of muramic δ-lactam in *Bacillus subtilis* spore peptidoglycan. J Bacteriol 186(1):80–89
55. Setlow P (2006) Spores of *Bacillus subtilis*: their resistance to and killing by radiation, heat and chemicals. J Appl Microbiol 101(3):514–525
56. Setlow B, Setlow P (1993) Binding of small, acid-soluble spore proteins to DNA plays a significant role in the resistance of *Bacillus subtilis* spores to hydrogen peroxide. Appl Environ Microbiol 59(10):3418–3423
57. Setlow P (1995) Mechanisms for the prevention of damage to DNA in spores of *Bacillus* species. Annu Rev Microbiol 49(1):29–54
58. Shin S-Y, Calvisi EG, Beaman TC, Pankratz HS, Gerhardt P, Marquis RE (1994) Microscopic and thermal characterization of hydrogen peroxide killing and lysis of spores and protection by transition metal ions, chelators, and antioxidants. Appl Environ Microbiol 60 (9):3192–3197
59. King WL, Gould GW (1969) Lysis of bacterial spores with hydrogen peroxide. J Appl Microbiol 32(4):481–490

60. Palop A, Rutherford GC, Marquis RE (1996) Hydroperoxide inactivation of enzymes within spores of *Bacillus megaterium* ATCC19213. FEMS Microbiol Lett 142(2–3):283–287
61. Cortezzo D, Koziol-Dube K, Setlow B, Setlow P (2004) Treatment with oxidizing agents damages the inner membrane of spores of *Bacillus subtilis* and sensitizes spores to subsequent stress. J Appl Microbiol 97(4):838–852
62. Verband Deutscher Maschinen- und Anlagenbauer (VDMA) (2008) Filling machines of VDMA hygiene class V: testing the effectiveness of packaging sterilization devices. Code of practice 6
63. Bazin MJ, Prosser JI (eds) (1988) Physiological models in microbiology, vol 2. CRC, Boca Raton
64. Institute For Thermal Processing Specialists (IFTIPS) (2011) Guidelines for microbiological validation of the sterilization of aseptic filling machines and packages, including containers and closures. Document G.005.V1
65. Adams D, Brown GP, Fritz C, Todd TR (1998) Calibration of a nearinfrared (NIR) H_2O_2 vapor monitor. Pharm Eng 18(4):66–85
66. Corveleyn S, Vandenbossche GMR, Remon JP (1997) Near-infrared (NIR) monitoring of H_2O_2 vapor concentration during vapor hydrogen peroxide (vhp) sterilisation. Pharm Res 14 (3):294–298
67. Haney RL (2011) Principal component analysis for enhancement of infrared spectra monitoring. Ph.D. thesis, Auburn University
68. Xu M, Bunes BR, Zang L (2011) Paper-based vapor detection of hydrogen peroxide: colorimetric sensing with tunable interface. ACS Appl Mater Interfaces 3(3):642–647
69. Toniolo R, Geatti P, Bontempelli G, Schiavon G (2001) Amperometric monitoring of hydrogen peroxide in workplace atmospheres by electrodes supported on ion-exchange membranes. J Electroanal Chem 514(1–2):123–128
70. Kuwata S, Sadaoka Y (2000) Detection of gaseous hydrogen peroxide using planar-type amperometric cell at room temperature. Sens Actuators B Chem 65(1–3):325–326
71. Huang H, Dasgupta PK, Genfa Z, Wang J (1996) A pulse amperometric sensor for the measurement of atmospheric hydrogen peroxide. Anal Chem 68(13):2062–2066
72. Zheng JY, Yan Y, Wang X, Shi W, Ma H, Zhao YS, Yao J (2012) Hydrogen peroxide vapor sensing with organic core/sheath nanowire optical waveguides. Adv Mater 24(35):194–199
73. Chen LC, Yu Z, Hiraoka K (2010) Vapor phase detection of hydrogen peroxide with ambient sampling chemi/chemical ionization mass spectrometry. Anal Methods 2(7):897–900
74. Barsony I, Dücso C, Fürjes P (2009) Thermometric gas sensing. In: Comini E, Faglia G, Sberveglieri G (eds) Solid state gas sensing. Springer, New York
75. Walsh PT, Jones TA (1991) Calorimetric chemical sensors. In: Göpel W, Hesse J, Zemel JN (eds) Sensors – a comprehensive survey, vol 2. Wiley-VCH, Weinheim
76. Henderson RE (2002) Portable gas detectors used in confined space and other industrial atmospheric monitoring programs. Technical report, PK safety
77. Kleven BA (2001) Summary of gas detection. Technical report, Advanced calibration designs
78. Unwin ID (2007) Mine monitoring for safety and health. Monograph
79. Korotcenkov G (2007) Practical aspects in design of one-electrode semiconductor gas sensors: status report. Sens Actuators B Chem 121(2):664–678
80. Erickson PA (ed) (1996) Practical guide to occupational health and safety. Academic, San Diego
81. De Smedt G, de Corte F, Notele R, Berghmans J (1999) Comparison of two standard test methods for determining explosion limits of gases at atmospheric conditions. J Hazard Mater 70(3):105–113
82. Jones TA, Walsh PT (1988) Flammable gas detection. Platinum Metals Rev 32(2):50–60
83. Baker A (1962) Improvements in or relating to electrically beatable filaments. UK Patent 892,530
84. Jones E (1987) The pellistor catalytic gas sensor. In: Moseley P, Tofield B (eds) Solid state gas sensors. Adam Hilger, Bristol

85. Glassman I (ed) (1996) Combustion, 3rd edn. Academic, San Diego
86. Haynes WM (ed) (2012) Handbook of chemistry and physics, 93rd edn. CRC, Colorado
87. McAllister S, Chen J-Y, Fernandez-Pello AC (eds) (2011) Fundamentals of combustion processes, Mechanical engineering series. Springer, New York
88. Liberman MA (ed) (2008) Introduction to physics and chemistry of combustion. Springer, Berlin
89. Cottilard SA (ed) (2011) Catalytic combustion. Chemical engineering methods and technology. Nova Science Publisher, New York
90. Moseley P (1997) Solid state gas sensors. Meas Sci Technol 8(3):223–237
91. Gentry S, Jones T (1986) The role of catalysis in solid-state gas sensors. Sens Actuators 10 (1–2):141–163
92. Korotcenkov G (ed) (2010) Chemical sensors: fundamentals of sensing materials, vol 1, Sensor technology series. Momentum, New York
93. Firth J, Jones A, Jones T (1973) The principles of the detection of flammable atmospheres by catalytic devices. Combustion Flame 20(3):303–311
94. Krebs P, Grisel A (1993) A low power integrated catalytic gas sensor. Sens Actuators B Chem 13(1–3):155–158
95. Vauchier C, Charlot D, Delapierre G, Accorsi A (1991) Thin-film gas catalytic microsensor. Sens Actuators B Chem 5(1–4):33–36
96. Krawczyk M, Namiesnik J (2003) Application of a catalytic combustion sensor (pellistor) for the monitoring of the explosiveness of a hydrogen-air mixture in the upper explosive limit range. J Automated Methods Manag Chem 25(5):115–122
97. Williams G, Coles GS (1999) The semistor: a new concept in selective methane detection. Sens Actuators B Chem 57(1–3):108–114
98. Lerchner J, Seidel J, Wolf G, Weber E (1996) Calorimetric detection of organic vapours using inclusion reactions with organic coating materials. Sens Actuators B Chem 32(1): 71–75
99. Lerchner J, Caspary D, Wolf G (2000) Calorimetric detection of volatile organic compounds. Sens Actuators B Chem 70(1–3):57–66
100. Hagleitner C, Hierlemann A, Lange D, Kummer A, Kerness N, Brand O, Baltes H (2001) Smart single-chip gas sensor microsystem. Nature 414(6861):293–296
101. Company SH (1913) Verfahren und Einrichtung zum Anzeigen von Gasbeimengungen in der Luft, insbesondere von Grubengasen. Patent DRP 283,677
102. McNair HM, Miller JM (eds) (2009) Basic gas chromatography, 2nd edn. Wiley, Hoboken
103. Accorsi A, Delapierre G, Vauchier C, Charlot D (1991) A new microsensor for environmental measurements. Sens Actuators B Chem 4(3–4):539–543
104. Simon I, Arndt M (2002) Thermal and gas-sensing properties of a micromachined thermal conductivity sensor for the detection of hydrogen in automotive applications. Sens Actuators A Phys 97–98:104–108
105. Brown JE, Lipták BG (1995) Thermal conductivity detectors. In: Lipták BG (ed) Instrument engineers' handbook: process measurement and analysis, vol 1. CRC, Boca Raton
106. Poling BE, Prausnitz JM, O'Connell JP (eds) (2001) The properties of gases and liquids, 5th edn. McGraw-Hill, New York
107. Wassiljewa A (1904) Wärmeleitung in Gasgemischen. Physikalische Zeitschrift 5(22): 737–742
108. Mason EA, Saxena SC (1958) Approximate formula for the thermal conductivity of gas mixtures. Phys Fluids 1(5):361–369
109. Näther N, Henkel H, Schneider A, Schöning MJ (2009) Investigation of different catalytically active and passive materials for realising a hydrogen peroxide gas sensor. Physica Status Solidi A 206(3):449–454
110. Kirchner P, Li B, Spelthahn H, Henkel H, Schneider A, Friedrich P, Kolstad J, Keusgen M, Schöning MJ (2011) Thin-film calorimetric H_2O_2 gas sensor for the validation of germicidal effectivity in aseptic filling processes. Sens Actuators B Chem 154:257–263

111. Reisert S, Henkel H, Schneider A, Schäfer D, Friedrich P, Berger J, Schöning MJ (2010) Development of a handheld sensor system for the online measurement of hydrogen peroxide in aseptic filling systems. Physica Status Solidi A 207(4):9103–918
112. Labas MD, Zalazar CS, Brandi RJ, Cassano AE (2008) Reaction kinetics of bacteria disinfection employing hydrogen peroxide. Biochem Eng J 38(1):78–87
113. Reisert S, Geissler H, Flörke R, Weiler C, Wagner P, Schöning MJ (2013) Characterization of aseptic sterilization processes using an electronic nose. Int J Nanotechnol 10(5/6/7):470–484
114. Kirchner P, Ng YA, Spelthahn H, Schneider A, Henkel H, Friedrich P, Kolstad J, Berger J, Keusgen M, Schöning MJ (2010) Gas sensor investigation based on a catalytically activated thin-film thermopile for H_2O_2 detection. Physica Status Solidi A 207(4):787–792
115. Kirchner P, Oberländer J, Friedrich P, Berger J, Rysstad G, Keusgen M, Schöning MJ (2012) Realisation of a calorimetric gas sensor on polyimide foil for applications in aseptic food industry. Sens Actuators B Chem 170:60–66
116. Kirchner P, Oberländer J, Friedrich P, Berger J, Suso HP, Kupyna A, Keusgen M, Schöning MJ (2011) Optimisation and fabrication of a calorimetric gas sensor built up on a polyimide substrate for H_2O_2 monitoring. Physica Status Solidi A 208(6):1235–1240
117. Kirchner P, Oberländer J, Suso H-P, Rysstad G, Keusgen M, Schöning MJ (2013) Towards a wireless sensor system for real-time H_2O_2 monitoring in aseptic food processes. Physica Status Solidi A 210(5):877–883
118. Reisert S, Geissler H, Flörke R, Näther N, Wagner P, Schöning MJ (2011) Towards a multi-sensor system for the evaluation of aseptic processes employing hydrogen peroxide vapour (H_2O_2). Physica Status Solidi A 208(6):1351–1356
119. Reisert S, Geissler H, Flörke R, Wagner P, Schöning MJ (2011) Controlling aseptic sterilization processes by means of a multi-sensor system. IEEE Workshop on merging fields of computational intelligence and sensor technology (CompSens), 18–22
120. Näther N, Juarez LM, Emmerich R, Berger J, Friedrich P, Schöning MJ (2006) Detection of hydrogen peroxide (H_2O_2) at exposed temperatures for industrial processes. Sensors 6: 308–317

Group III-Nitride Chemical Nanosensors with Optical Readout

Jörg Teubert, Sumit Paul, Andreas Helwig, Gerhard Müller, and Martin Eickhoff

Abstract In order to fully profit from the increased sensitivity of nanoscale transducer structures appropriate readout techniques are required. In this context optical methods are highly promising as they allow parallel probing of large ensembles of nano-objects without manipulating or processing single nanostructures. Furthermore, optical readout techniques feature significant advantages for certain applications as, e.g., measurements in potentially hazardous environments that prohibit any form of electricity at the point of measurement. In this article we discuss a novel type of gas-sensitive nanophotonic probes that are based on the photoluminescence response of group III-nitride nanostructures. This material class offers manifold possibilities for the synthesis of nano-objects as well as for the realization of complex semiconductor heterostructures. The latter is inevitable to fully exploit this optical approach by utilizing band engineering methods for a targeted control of the emission properties (such as the absorption behavior, the emission wavelength and intensity, as well as the temperature stability of the emission). In recent years, significant progress in terms of gas sensing applications has been obtained using GaN/AlN quantum dot systems as well as GaN nanowire ensembles with embedded heterostructures of either GaN/AlGaN or GaN/InGaN. These nanoscale transducer structures are highly suitable for the development of optical sensor systems and proved to be fully competitive to conventional sensor concepts. The state of the art of group III-nitride opto-chemical gas sensors is reviewed in the present chapter.

Keywords GaN, III-nitride nanostructures, Nanophotonics, Nanowires, Opto-chemical sensors, Quantum dots

---

J. Teubert (✉) and M. Eickhoff
I. Physikalisches Institut, Justus-Liebig-Universität Gießen, 35392 Gießen, Germany
e-mail: joerg.teubert@exp1.physik.uni-giessen.de; eickhoff@physik.uni-giessen.de

S. Paul, A. Helwig, and G. Müller
EADS Innovation Works, 81663 Munich, Germany

C.-D. Kohl and T. Wagner (eds.), *Gas Sensing Fundamentals*,
Springer Series on Chemical Sensors and Biosensors (2014) 15: 311–338
DOI 10.1007/5346_2014_58,

Contents

1 Introduction

Detection of gas species is often based on the adsorption of molecules on the sensor surface and the subsequent transduction of this adsorption process into an electrical or optical signal. In such cases, nanoscale transducer structures promise higher sensitivities as well as lower detection limits as they offer a higher surface-to-volume ratio compared to devices based on thin films. Therefore, the application of semiconductor nanostructures such as quantum dots (QDs) and nanowires (NWs) based on metal oxides, silicon, zinc oxide, gallium nitride (GaN), or carbon nanotubes, as highly sensitive structures, has been proposed in different works (e.g., [1–9]).

Among the broad range of possibilities for nanostructure fabrication by different combinations of top-down and bottom-up techniques, processes based on the self-organized formation of nanostructures are favorable for the realization of nanoscale transducers as they allow for the minimization of processing efforts. This includes, e.g., the strain-driven formation of QDs [10] or the utilization of strongly anisotropic growth processes to realize semiconductor NWs [11, 12]. As in many cases neither the post-growth sensor processing nor the actual device operation does impose strong requirements on the surface morphology, the intrinsic randomness of the self-assembly process is tolerable.

For readout of the sensor signal mainly conductometric methods have been realized so far. Here, the small dimensions of nanostructures enable detection principles that are often more sensitive than the well-known detection mechanisms at metal-oxide surfaces [13, 14] or of gas-sensitive MOS structures [15–17]: Dangling bonds at semiconductor surfaces give rise to electronic surface states that often lie within the band gap and which cause a surface band bending, i.e., the presence of surface electric fields. In semiconductor NWs which have typical lateral dimensions well below 100 nm, the resulting depletion width can be comparable to the NW diameter (providing that the free carrier concentration in the NW bulk is not too high). As a result, the conductivity of semiconductor NWs is strongly determined by the density and properties of surface states and thus very sensitive to surface adsorbates [18].

With regard to these transduction effects, valuable insight has been gained by investigations on single NWs, in particular on single SnO_2 NWs (exposure to NO_2) [19], single NW transistors made of In_2O_3 NWs (exposure to NO_2 and NH_3) [1], or ZnO NWs (exposure to O_2) [2]. Also in the case of GaN NWs, Chen et al. have reported the dependence of conductivity, photocurrent, and photocurrent decay time on ambient conditions in single-wire measurements [18]. Although these works have demonstrated the possibility of single NW chemical sensors, they have also drawn attention to the problem of large wire-to-wire variations in the electronic properties due to size fluctuations. Further drawbacks result from the high technological effort for NW manipulation and realization of reliable Ohmic contacts as well as from the inevitably complex measurement equipment.

Many technological problems of single NW measurements are avoided by employing nanowire ensembles as transducers. For example, Comini et al. processed conductometric sensor structures using bundles of SnO_2 nanobelts, reporting responses to CO and NO_2 [20]. Zhou et al. found response of Si nanowire bundles to NH_3 [4]. Wang et al. reported room-temperature-selective H_2-sensing using multiple Pd-coated ZnO NWs [21]. Works reporting H_2-sensitivity of GaN-NW-based sensor devices used irregular meshes of GaN NWs covered with a catalytic metal [5, 22, 23].

Although electrical readout has been realized and gas sensitivity has been demonstrated in numerous works, many details of the detection mechanisms remain unclear, as, e.g., the impact of NW–NW junctions and metal-NW junctions on the gas sensitivity in structures involving interconnected NW bundles or meshes. Besides, there are several drawbacks of the conductometric approach: Electrical measurements require complex electrical wiring and feedthroughs which can be unfavorable in safety critical applications. Contact areas often have to be protected from aggressive media and suffer from limited long-term stability. Furthermore, the conductivity of nanostructures is often affected by ambient light irradiation resulting in persistent photocurrent effects [6, 24, 25] that are superimposed to the sensor signal. Thus, proper packaging is required to carefully protect the sensor structures and maintain stable operation.

Due to these restrictions, conductometric sensor concepts are not applicable in some situations. One example is leak monitoring in H_2 and hydrocarbon (HC)-carrying installations. These gases are important carriers of energy but become safety hazards when critical concentrations in the order of 3–5% are reached in ambient air environments (O_2). For the detection of such combustible and explosive atmospheres sensors must not form ignition sources by themselves and, thus, any form of electrical wiring needs to be avoided at the spot of measurement, i.e., within the potentially explosive medium. Possible applications are the detection of leaks in fuel and hydraulic lines in commercial aircrafts or the safety monitoring of fuel cell power units.

This requirement of electricity-free measurements inside a potentially explosive atmosphere is naturally fulfilled by optical readout techniques that are based on the change of optical material properties due to the interaction with the chemical environment. Here, the electricity-carrying detection elements and signal processing circuitry can be separated from the actual sensing element in contact with the potentially dangerous medium. As an example, the first optical H_2-sensor concept was presented by Butler et al. in 1984 who measured the H_2-induced expansion of a Pd-coated optical fiber using an interferometric method [26]. Since then, a multitude of signal conversion phenomena based, e.g., upon changes in absorbance, reflectance, refractive index, or photoluminescence (PL) have been used for the implementation of optical sensor concepts (an overview on recent advances in opto-chemical sensors for the detection of different gases can be found in [27]).

In this chapter we discuss an opto-chemical readout technique that is based on the ambient-sensitive PL characteristics of group III-nitride (III-N) semiconductor nanostructure ensembles. The PL process involves incident photons with energies above the semiconductor band gap. Upon absorption these excite electrons from the filled valence band into an empty state in the conduction band, thereby creating electron–hole pairs. Electrons and holes will then relax by phonon scattering towards the band extrema (or trap states inside the band gap) before recombining under photon emission, i.e., formation of PL light which forms the sensor signal. The competing process of non-radiative recombination via surface states is strongly influenced by surface adsorbates [28–30]. Due to the large surface-to-volume ratio of nanostructures, adsorbate-related effects can be detected with a high sensitivity. As the adsorption of gas molecules on the semiconductor surface is directly detected by the resulting changes in the nanostructure's PL characteristics this method is largely independent of the measurement geometry such as the optical path length in the test volume.

The idea of using luminescence properties of semiconductor nanostructures in context with gas sensors was first introduced in 2005 by Faglia et al. [31]. In this work reversible quenching of the defect luminescence of SnO_2 nanobelts by exposure to ppm concentrations of NO_2 at room temperature has been reported. By using nanobelt ensembles manipulation and processing of individual nano-objects is not necessary and large numbers of NWs can be probed simultaneously. Although very promising, this first attempt for an optical readout suffered from a weak PL signal, a poor temperature stability, and hardly controllable luminescence properties, all problems arising out of the defect nature of the PL emission. A truly successful implementation of this optical readout technique requires a good control of the emission wavelength to reach compatibility with commercially available excitation sources and an optimization of the PL intensity and its temperature stability to arrive at a reproducible and acceptable sensor performance.

All these issues can be addressed by an adequate quantum mechanical confinement of the photo-generated charge carriers. In this context, band engineering methods, i.e., a proper design of semiconductor heterostructures, are important as it allows for a spatial definition of nanoscale regions with appropriate confinement potentials [32, 33]. All bulk semiconductor materials show a strong quenching of their band gap PL with increasing temperature which is in conflict with typical operating temperatures of gas sensors, i.e., room temperature and above. Spatial localization due to carrier confinement prevents photo-generated carriers from reaching non-radiative recombination centers which significantly improves the temperature stability of the luminescence. Furthermore, the energy of the confined states determines the emission wavelength while the band gap of the barrier material strongly influences the absorption behavior.

It should also be noticed that the realization of spatially separated confinement potentials restricts the charge carrier diffusion length which allows for a detection of chemical surface processes with high spatial resolution, in principle only limited by the dimensions of the employed nanostructures.

In this respect, the III-N-material system provides all necessary ingredients to realize nanowire-based transducers with a temperature-stable and controllable optical readout. This material system not only allows for a self-assembled growth of different types of nanostructures from quantum dots (for a review see, e.g., [34]) to nanowires [35, 36] and truly one-dimensional quantum wires [37] but also offers manifold possibilities for band gap engineering within the nanowires themselves. Starting from GaN it is possible to increase or decrease the fundamental band gap by alloying with Al or In, respectively, thus allowing realization of structures with strong carrier localization [38–48]. Additionally, in contrast to organic dyes as alternative gas-sensitive PL-based probes, GaN material shows high chemical inertness and is stable also at elevated temperatures above 300°C.

In recent years the concept of an optical readout using the PL signal of group III-nitride (III-N) nanostructures has been demonstrated in several works. This includes GaN/AlN quantum dot systems as well as GaN nanowire ensembles with embedded GaN/AlGaN or GaN/InGaN heterostructures. In the following sections we will discuss these promising novel types of nanophotonic chemical probes.

2 GaN/AlN Quantum Dots

Polar GaN quantum dots in an AlN matrix can be grown by plasma-assisted molecular-beam epitaxy on AlN-on-sapphire templates. These heterostructures feature large band discontinuities of 1.925 and 0.696 eV for the conduction and valence bands, respectively [49]. Together with the three-dimensional embedding of the quantum dots, this results in strong carrier localization. As a consequence GaN/AlN quantum dots feature a high temperature stability of their PL intensity [50, 51], which enables room-temperature optoelectronic applications. This is illustrated by the Arrhenius plot of the temperature-dependent QD-related PL emission shown in Fig. 1 (blue circles). The figure also contains results from structures to be discussed in the following sections (GaN/AlGaN and InGaN/GaN nanowire heterostructures) as well as two reference systems (InGaN-quantum wells and GaN NWs without heterostructures) for comparison. It is evident that GaN/AlN QDs provide the best temperature stability among all discussed systems with an intensity loss by only a factor of ~2.2 between 7 K and room temperature.

A response in the PL intensity of GaN/AlN QD multilayers to chemically induced changes of the surface potential was first demonstrated by Weidemann et al. [53]. The samples investigated in that work consisted of stacks of one and five

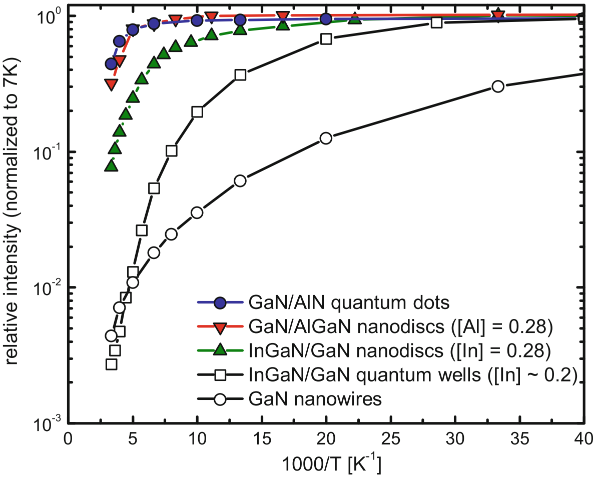

Fig. 1 Temperature stability of the respective PL signal for the different structures discussed in this chapter. Results for InGaN-quantum wells [51] and GaN nanowires without heterostructures [52] are given for comparison

GaN/AlN QD layers deposited on a Si-doped $Al_{0.6}Ga_{0.4}N$ contact layer, as schematically depicted in Fig. 2a. The QD structures were grown on 1 μm thick (0001)-oriented AlN-on-sapphire templates by plasma-assisted molecular-beam epitaxy (PAMBE). The GaN QDs form truncated hexagonal pyramids with $\left\{1\bar{1}03\right\}$ facets, with a height of ~1–2 nm and a base diameter of ~10 nm, as illustrated in the high-resolution transmission electron microscopy (HRTEM) image in Fig. 2b. Further information on the growth process was reported in [54].

In that work, excitation of the PL light was performed using the 244 nm line of a frequency-doubled Ar-ion laser. Due to absorption in the $Al_{0.6}Ga_{0.4}N$ contact layer PL excitation had to be performed from the sample's front side while the PL emission could be detected through the sapphire substrate. It should be noted that, by using a longer wavelength light source, transparency of the substrate material to the PL and excitation light is possible.

To achieve sensitivity to hydrogen, a semitransparent catalytic Pt top layer was evaporated. It has been investigated in numerous works ([55] and references therein) that hydrogen response of metal–oxide–semiconductor (MOS) structures is induced by a catalytic metal. It is assumed that after catalytic dissociation at the metal surface atomic hydrogen diffuses through the metal layer and forms an interface dipole by adsorption between the metal layer and the oxidized semiconductor surface. This dipole layer lowers the effective Schottky barrier height and reduces the surface band bending in the semiconductor.

The presence of an oxidic intermediate layer is required to establish H_2-sensitivity as shown in [56] for Pd/GaN structures. This effect can be directly transferred towards optical detection methods. The reduction of the surface band bending due to hydrogen dipoles results in a variation of the confinement potential (and thus of the confined electronic states) of QDs close to the surface.

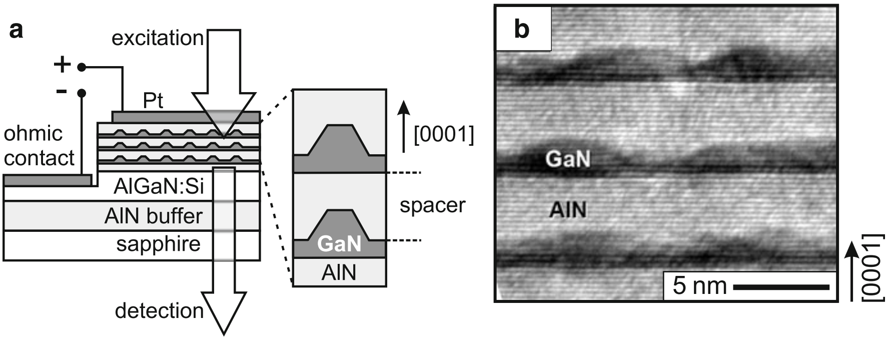

Fig. 2 (**a**) Schematic of the GaN/AlN QD sample structure and the optical path for the PL measurements. (**b**) High-resolution transmission electron micrograph of a GaN/AlN QD stack viewed along the $(11\bar{2}0)$ axis. Reprinted with permission from [53]. Copyright (2009), American Institute of Physics

Figure 3a depicts the luminescence enhancement of the Pt-covered QD structures observed upon exposure to molecular hydrogen. The transient response to hydrogen exposure for a hydrogen concentration of 10% in nitrogen obtained by recording the intensity at a fixed detection wavelength near the emission maximum is shown in Fig. 3b. At this hydrogen concentration the device is already saturated; i.e., even exposure to pure hydrogen atmosphere does not lead to a higher response. On the other hand, a concentration as low as 500 ppm of hydrogen in a synthetic air carrier gas could be clearly resolved (cf. insert in Fig. 3a).

To elucidate the detection mechanism, in particular the effect of hydrogen-induced variations of the surface band bending on the confined QD states, measurements under controlled variations of the surface potential were performed. Using the Pt-top contact and the AlGaN:Si back contact allowed PL characterization in externally applied electric fields and photocurrent measurements that revealed detailed information about the detection mechanism.

Polar III-N semiconductors are characterized by polarization-induced internal electric fields which affect the potential profile in III-N heterostructures. In particular, polarization-induced electric fields in the QDs can determine the PL characteristics via the quantum-confined Stark effect (QCSE) by inducing electron–hole separation and a related red shift of the emission [57–60]. Externally applied electric fields (or those generated by interfacial H-adsorption) superimpose the internal fields and result in an amplification or suppression of the QCSE. According to the QCSE a blue shift (red shift) is accompanied by an increase (quenching) of the PL which was observed for samples with a barrier thickness of 7 nm as depicted in Fig. 4a.

In contrast, QD multilayer samples with thin AlN spacers (3 nm) show decreasing emission energy with increasing PL intensity. This effect was attributed to the influence of a significant tunneling photocurrent, acting as a competing mechanism to radiative recombination inside the GaN QDs [53]. This assumption is supported

Fig. 3 (**a**) PL spectra in pure H_2 and N_2 atmosphere at a bias voltage of −4 V. The inset shows the response of the peak intensity to two pulses of 500 ppm H_2 in synthetic air as carrier gas. (**b**) Response of the PL intensity to introduction of 10% H_2 in an N_2 atmosphere for samples with one and five QD layers. The PL intensity was recorded at a fixed detection wavelength near the emission maximum (due to a different size of the QDs the maximum of the PL emission is located at an energy of 3.9 eV for the single QD layer). Reprinted with permission from [53]. Copyright (2009), American Institute of Physics

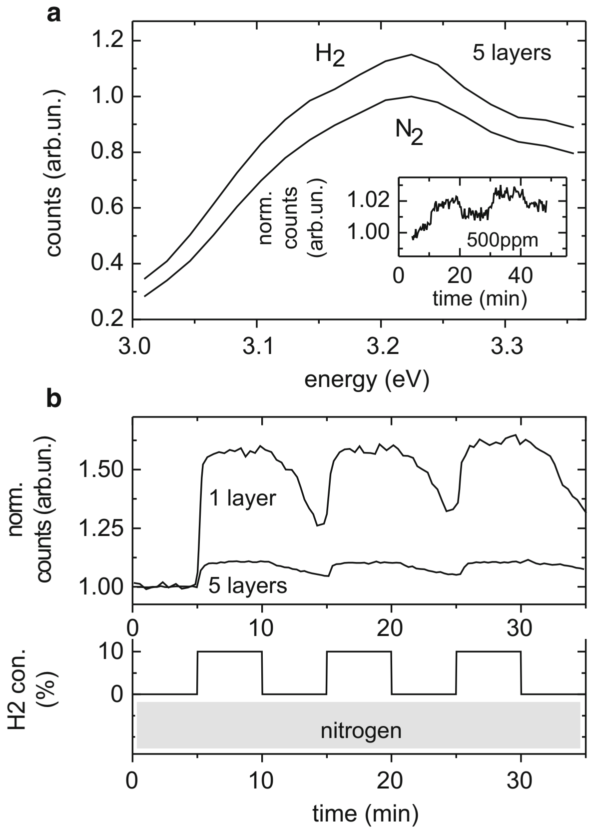

by bias-dependent vertical photocurrent measurements and its correlation with the integrated PL intensity, as depicted in Fig. 5a. In addition to the quenching of the PL, negative bias results in an increasing photocurrent due to enhanced tunneling of photo-generated electron–hole pairs through the barrier layers.

The situation is illustrated in Fig. 5b: The partial compensation of the electric field in the QDs with negative bias leads to a displacement of the electron and hole wave functions and thereby to a decrease of the effective barrier height and width between the QDs and an improved alignment of the QD electronic levels. These effects favor the extraction of photo-generated carriers by tunneling transport in competition with radiative recombination. Positive bias, on the other hand, suppresses the photocurrent so that the PL intensity increases. The overall relative variation of the PL intensity that can be achieved is significantly higher for samples with thin spacers. The enhancement of the photocurrent due to a decreased spacer thickness leads to a significant enhancement of the sensitivity of the PL emission intensity to an external electric field.

The proposed detection mechanism implies that the hydrogen adsorption mainly affects the topmost QD layers and proposes a stronger relative response for

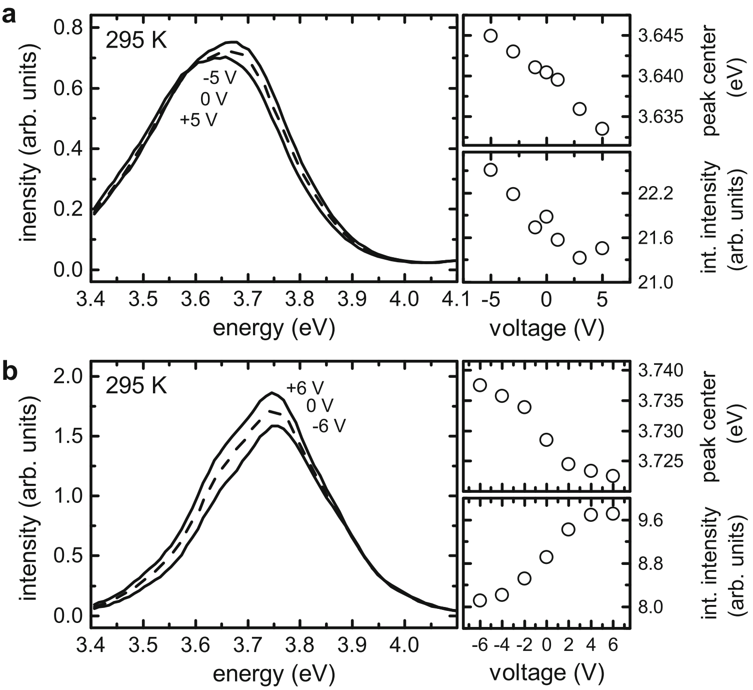

Fig. 4 Bias-dependent PL spectra of 5× QD multilayers with two different spacer thicknesses, (**a**) 7 nm, (**b**) 3 nm. Also shown is the dependence of the emission energy and the integrated emission intensity on the applied bias

structures with a smaller number of layers. This behavior is demonstrated in Fig. 3b, where the relative response of a sample with one layer of QDs (60%) is compared to that of a sample with five layers (10%).

These results demonstrate that optical gas detection with substrate-supported quantum dot structures is not only possible but also offers several unique advantages. As transparency of the substrate to the excitation light can be easily achieved, the realization of optoelectronic chemical sensor systems with built-in separation of media is possible. Here, the sensor structure itself can act as a window between the test medium and the outer environment. This possibility can be further exploited by a reduction of the QD emission energy, e.g., by a transition to InGaN/GaN QD structures. Here, also the excitation of the wetting layers/barriers can be accomplished with commercial and cost-efficient light emitters (such as UV light-emitting diodes or laser diodes) with a subsequent increase of the luminescence intensity. With this respect it is noteworthy that backside illumination/detection has been recently demonstrated using InGaN QDs in GaN matrix in contact with a liquid environment as pH-sensitive devices with optical readout [61].

The possibility to form highly conductive back contact layers allows for the application of external bias and photocurrent measurement that give valuable

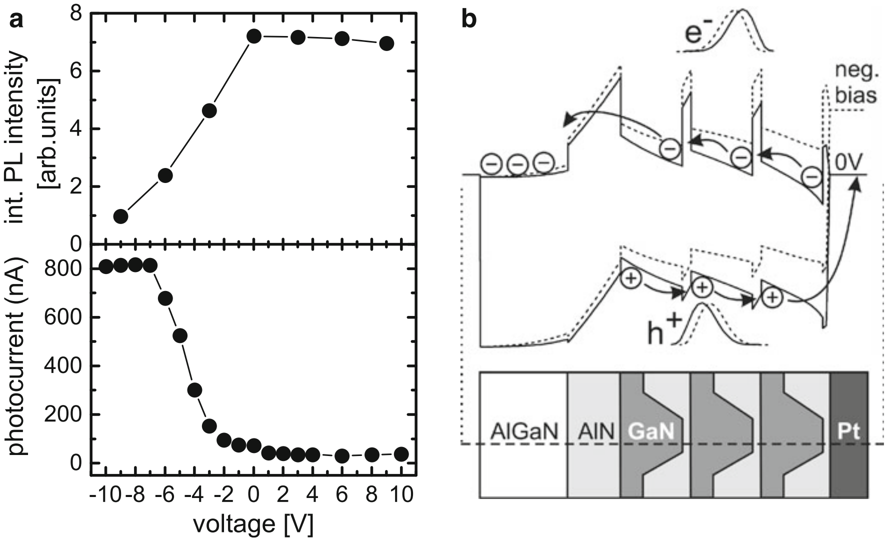

Fig. 5 (**a**) PL intensity and photocurrent as a function of bias for a sample with 3 nm spacers. (**b**) Schematic of the band diagram of a three-layer structure based on simulations using a one-dimensional Schrödinger–Poisson solver illustrating the current transport due to tunneling of photo-excited carriers. Negative external bias leads to a reduction of the effective tunneling barrier thickness due to the displacement of electron and hole wave functions. (**b**) Reprinted with permission from [53]. Copyright (2009), American Institute of Physics

insight into the underlying sensor mechanisms. Besides that, biasing can be used to optimize the device sensitivity and constitute an important advantage in comparison with semiconductor nanoparticles [61, 62]. With these results it becomes apparent that a manipulation of the QDs' internal electric fields via the QCSE alone is not sufficient to achieve maximum sensitivity. Instead, chemically induced activation/suppression of additional non-radiative recombination channels (tunneling photocurrent in the case of GaN/AlN QDs) is a promising concept.

3 GaN/AlGaN Nanowire Heterostructures

While the QD structures discussed in the previous paragraph provide exceptional temperature stability so that optical readout can be realized, the area exposed to the gaseous environment is the same as for conventional thin film devices due to the two-dimensional geometry of the sample surface. In contrast, by using semiconductor nanowire ensembles, the contact area can be significantly increased by approximately a factor of 50–200 (depending on the aspect ratio and the NW density) compared to thin films of the same substrate area.

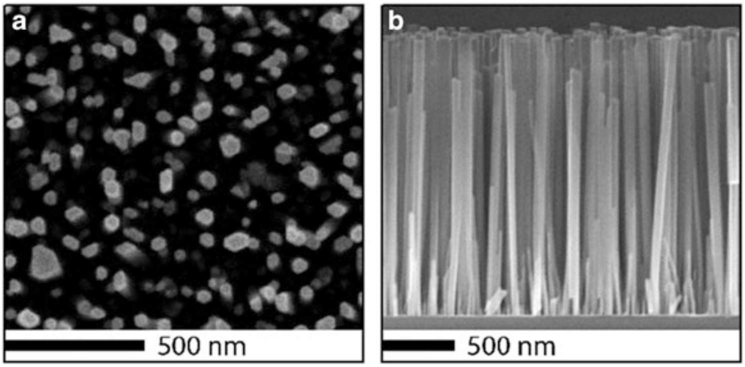

Fig. 6 SEM images of PAMBE-grown GaN nanowires on Si(111) substrate. (**a**) *Top view and* (**b**) *side view*

The growth of $(000\overline{1})$-oriented GaN NWs by PAMBE was first reported in [35] using a self assembled, catalyst-free growth process under nitrogen-rich growth conditions on Si(111) substrates. Due to the possibility for strain relaxation at the lateral surfaces the NWs are characterized by a low density of structural defects compared to GaN thin films. Details of the growth process for the NW structures discussed here can be found in [36].

Figure 6 depicts SEM images of GaN nanowire ensembles revealing typical values of the diameter and NW density of 40 nm and 200 NW/μm^2, respectively. Due to the small lateral dimensions and low density of intrinsic charge carriers self-assembled GaN NWs grown by MBE have been shown to be depleted of free charge carriers [24]. Depletion arises due to the spatial extent of the surface band bending which significantly exceeds the NW diameter as described above. As a result, the lateral band profile of non-intentionally doped (n.i.d.) NWs is essentially flat compared to thermal energies of charge carriers at room temperature.

By alloying with Al it is possible to increase the fundamental band gap of the NW material which allows realization of GaN/AlGaN nanowire heterostructures (NWHs) to obtain quantum confinement in the form of nanodiscs (NDs) as shown by different groups [41, 63–65]. In the context of opto-chemical nanosensors the NWHs provide a high surface-to-volume ratio and quantum mechanical confinement and can act as optical probes with controllable PL emission wavelength for detection of surface adsorbates.

As an example, Fig. 7 presents TEM images of a NWH with 9 GaN NDs embedded in AlN (a) and $Al_{0.72}Ga_{0.28}N$ barriers (b) [32, 41]. The deposition of the $Al_xGa_{1-x}N$ barrier material typically results in lateral growth covering preceding sections of the NWH in a lateral shell of barrier material as shown in Fig. 7a. Depending on growth conditions and Al content, the lateral growth rate can reach 10% of the axial growth rate (cf. Fig. 7a) or can be significantly reduced (cf. Fig. 7b) [41].

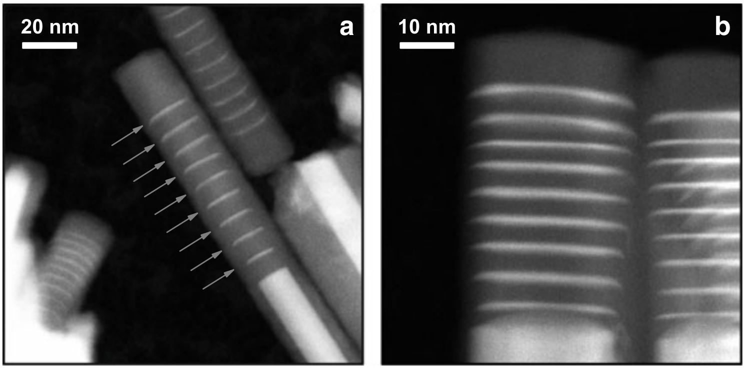

Fig. 7 (**a**) HAADF STEM (high-angle annular dark-field scanning transmission electron microscopy) image of nanowires with 1.7 nm thick GaN NDs surrounded by AlN barriers. The GaN appears in bright contrast, the surrounding AlN in dark. (**b**) HAADF image of a sample with $Al_{0.72}Ga_{0.28}N$ using growth conditions to reduce lateral growth. Reprinted with permission from [41]. Copyright (2011), American Physical Society

As a major difference to III-N two-dimensional heterostructures, the carrier confinement of NWHs (and thus the PL properties) is not solely determined by the material composition (band offsets, polarization charges) and the ND height or width. Moreover, it is governed by a complex interplay between strain relaxation, polarization-induced internal electric fields, and surface band bending. In this context, the presence of a lateral shell plays an important role [41]. Nevertheless, it is possible to control the PL emission characteristics to a large extent (i.e., to tune the emission energy or to optimize the emission intensity) by adjusting the structure geometry and material composition. By proper design of NWHs it is possible to achieve flat band conditions in lateral direction for optimization of the signal intensity and a temperature stability comparable to that of GaN/AlN QDs (cf. Fig. 1). Thus, NWHs combine a large surface area where gas molecules have lateral access to the active structures with excellent temperature stability of a controllable PL signal.

Teubert et al. first demonstrated that the PL properties of GaN NDs embedded in GaN/AlGaN NWs sensitively respond to exposure to hydrogen and oxygen [52]. While hydrogen sensitivity was achieved by deposition of a semitransparent catalytic Pt film (nominal thickness of 5 nm), the strongest response to oxygen was observed for bare NW surfaces.

Figure 8 depicts the PL spectra of as-grown NWH ensembles in dry nitrogen atmosphere. They are dominated by an emission band originating from the NDs at 3.67 eV (3.64 eV) at a temperature of $T = 153$ K (303 K). Luminescence from the GaN base at 3.48 eV (3.43 eV) appears only as a shoulder on the low energy side.

Transient measurements of the ND-related PL signal are depicted in Fig. 9a for different gas atmospheres. In particular, the results for concentrations of 1,000 ppm of H_2 in synthetic air and O_2 in nitrogen at a temperature of 150°C are shown for as-grown and Pt-coated samples. While the presence of H_2 induces an increasing

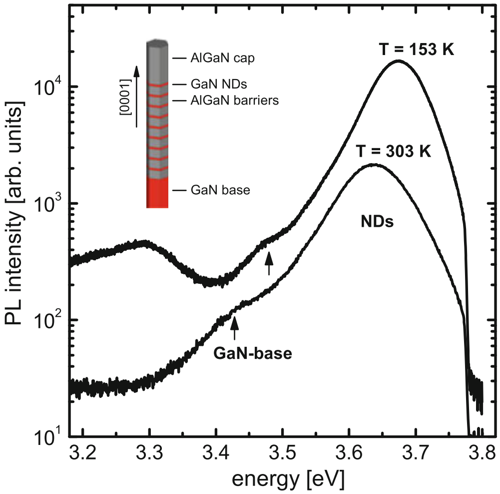

Fig. 8 PL spectra of NWH ensembles at 153 and 303 K. The spectra are dominated by the ND emission. A schematic illustration of the sample structure is shown in the inset. Reproduced with permission from [52]. Copyright (2011), IOP Publishing

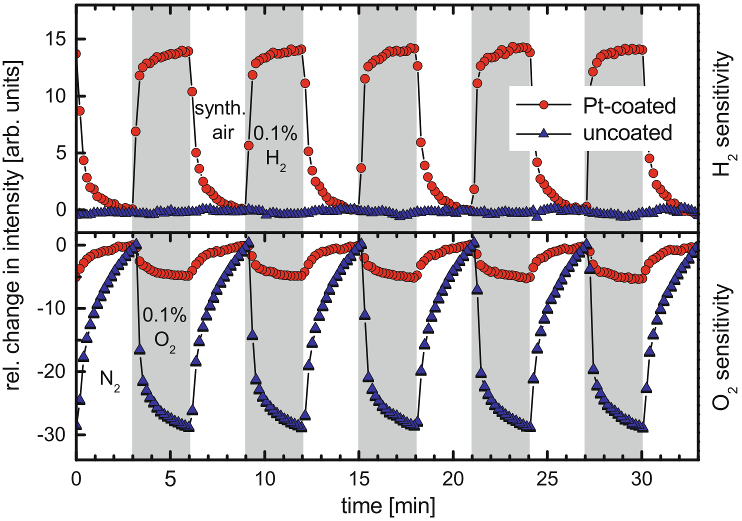

Fig. 9 Transient response of the relative PL intensity to variations of the ambient gas composition ($T = 150°C$, detection at ND-signal maximum). In the presence of hydrogen (H_2 concentration of 0.1% in synthetic air) an increase of the PL intensity for Pt-coated NWs is observed. In contrast, a decrease of the PL signal is detected in the presence of oxygen (O_2 concentration of 0.1% in nitrogen) which can be suppressed by Pt coating. Reproduced with permission from [52]. Copyright (2011), IOP Publishing

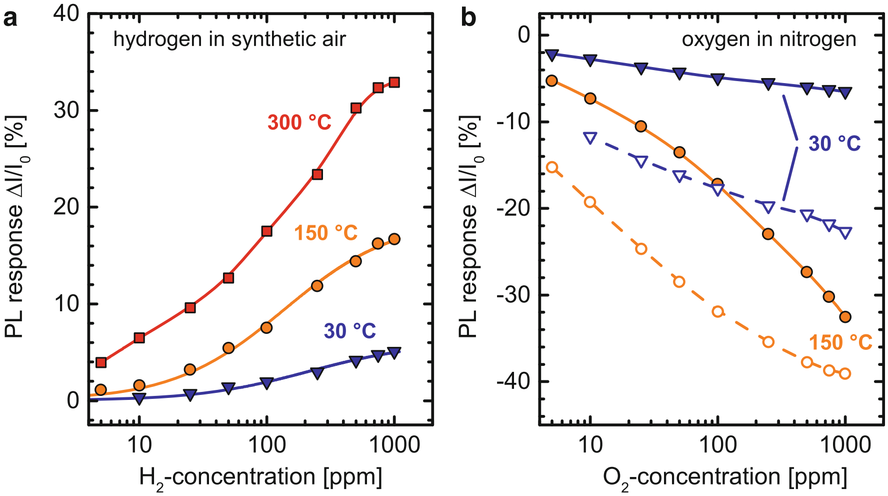

Fig. 10 Relative changes of the integrated ND emission intensity as a function of hydrogen concentration in synthetic air (**a**) and oxygen concentration in nitrogen (**b**). *Lines* serve as guide to the eye. *Open symbols* and *broken lines* in (**b**) represent results from an additional sample with reduced shell thickness (synthesized using the same growth process as the sample in Fig. 7b). Reproduced with permission from [52]. Copyright (2011), IOP Publishing

PL intensity of Pt-coated ND samples, the exposure to O_2 substantially quenches the PL intensity of as-grown structures. Uncoated structures only show a negligible response to hydrogen (of the order of 1%). The $H_2(O_2)$-induced PL increase (decrease) of Pt-coated (uncoated) structures amounts to 16% (−23%). The O_2 response of Pt-coated samples is attenuated to −5%.

It is evident from Fig. 9 that the oxygen response is suppressed by surface coating with Pt. The remaining small response was attributed to incomplete coverage [52]. The small PL increase of uncoated NWHs in the presence of hydrogen might be attributed to the removal of adsorbed residual oxygen from the NW surface by the formation of water.

Figure 10 depicts the H_2- and O_2-induced relative variations of the PL intensity as a function of the respective test gas concentration for 30, 150, and 300°C. Operation of uncoated NWH ensembles in oxygen-containing atmosphere above 200°C resulted in a degradation of the response properties, most likely due to surface oxidation. Therefore, measurements of the oxygen sensitivity were carried out up to 150°C only. For both gases an increase of the relative PL response with increasing temperature was found, featuring a detection limit below 5 ppm at $T = 150°\mathrm{C}$ (limited by the restrictions of the measurement setup).

The PL response of NWs to surface adsorbates cannot be explained within the same model discussed for the QD structures in the previous paragraph. In case of GaN NWs, a modification of the axial polarization-induced electric fields can be excluded due to the high aspect ratio and the lateral access of the gas molecules to all NDs on the nonpolar sidewalls. Instead, the response to adsorption can be

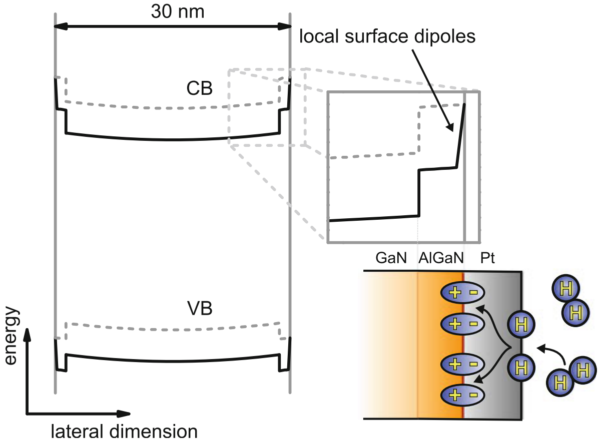

Fig. 11 Schematic illustration of the effect of hydrogen adsorption on the lateral band profiles inside the NDs (surface band bending exaggerated). *Gray dashed lines* represent a clean surface; *black solid lines* reflect the effect of hydrogen induced local surface dipoles at the semiconductor/metal interface. Reproduced with permission from [52]. Copyright (2011), IOP Publishing

understood in terms of suppression (in case of hydrogen) and enhancement (oxygen) of non-radiative surface recombination processes. Due to the large surface area these processes are expected to form an important recombination channel for thin NWs. As the density of photo-generated electron–hole pairs remains constant any variations in surface recombination probability are strongly reflected in the PL intensity. For the presence of a thin lateral shell (thickness of approximately 2 nm for the samples discussed here) the carrier motion to the surface is suppressed but still possible via quantum mechanical tunneling.

According to the discussion in [52, 66] the surface band bending of n.i.d. NWs can be neglected for measurements at room temperature and above, which makes the surface equally well accessible to electrons and holes. This situation is presented in the schematic band diagram of Fig. 11 by the gray dashed line (the potential steps close to the NW surface arise from the AlGaN material of the surrounding shell and are not affected by hydrogen adsorption). In this case a variation of the surface potential only weakly modifies the lateral band profile inside the NDs. Instead, by variation of the surface potential, the band edges within the NW are shifted to higher or lower energies without significant changes of the lateral electric field in the NWs [52].

In contrast, the formation of surface or interface dipole layers at the lateral interface to the metal due to hydrogen adsorption gives rise to a sharp potential drop within an atomic monolayer while the lateral band profile inside the NDs remains almost unchanged (cf. Fig. 11, solid black line). The magnitude of this potential drop depends on the hydrogen coverage and can reach values up to several hundred meV [55]. The resulting improvement of the carrier confinement in the conduction band suppresses tunneling of photo-generated electrons from the ND through the AlGaN-shell to the lateral surface and attenuates non-radiative surface recombination. Consequently, the exposure of Pt-coated NWH ensembles to H_2 results in an increasing PL intensity of the ND emission.

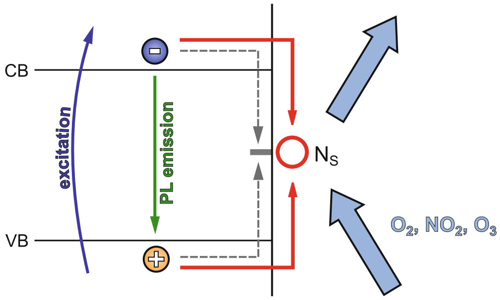

Fig. 12 Schematic band diagram of a NW in lateral direction. Non-radiative recombination via native surface defects is indicated by *gray dashed lines*. Physisorbed oxidizing gases are assumed to act as non-radiative recombination centers (density N_S), thus quenching the native PL response of the NW (recombination path indicated by *red solid lines*)

The removal of adsorbed hydrogen and the recovery of the initial intensity occur by oxygen-assisted water formation [67]. The increase of the response in the investigated temperature range (cf. Fig. 10) is caused by the temperature-dependent coverage of the Pt surface with hydrogen and water as known from field-effect gas sensors with a catalytic gate metal [68].

Following these considerations regarding the hydrogen response, the decreasing PL intensity of uncoated NWH ensembles upon exposure to oxygen and other oxidizing gases (cf. results of InGaN/GaN NWs in the following section) indicates an enhancement of non-radiative surface recombination. It is assumed that a molecular species in the gas ambient adsorbs on the NWH surface, thereby leading to an additional density of surface states N_S which increases with the partial pressure of this gas species (cf. schematics in Fig. 12). With the trapped electron the surface adsorbate forms a negatively charged Coulomb attractive center which easily captures a photo-generated hole from the NW bulk to complete the recombination process. Photo-generated electron–hole pairs that undergo this type of oxygen-induced recombination cannot contribute to the band recombination and the PL signal decreases.

The data presented in Fig. 10b (open symbols) for an NWH sample grown under slightly modified growth conditions that lead to a less pronounced lateral AlGaN-shell (cf. Fig. 7b) corroborate this model. Here, for both $T = 30°C$ and $T = 150°C$, the response to oxygen is enhanced due to increased tunneling to the NW surface and a stronger contribution of surface processes.

To sum up, the advances in MBE growth of III-N materials can be used to realize nanowire heterostructures in order to combine the large surface area of NWs with an improved temperature stability of the PL emission. Achievable detection limits of AlGaN/GaN NWH sensor structures below 5 ppm of H_2 and O_2 already at room temperature demonstrate the potential of this approach for the safety critical applications discussed above. By partial Pt coating, also selectivity between reducing gases (H_2) and oxidizing gases (O_2) can be achieved. The details of the gas response indicate a dominant role of surface recombination processes that are manipulated by adsorption of gas molecules. Therefore, PL measurements may also help to fundamentally investigate the adsorption processes and to extract molecule-specific properties.

4 InGaN/GaN Nanowire Heterostructures

Incorporation of In into GaN reduces the direct band gap of the material to an extent that depends on the In concentration [69]. Thus, taking the results of the previous section on GaN/AlGaN NWHs as a starting point, their replacement by InGaN/GaN NWHs is advantageous since commercial and inexpensive light sources can be used for the PL excitation. With InGaN NDs embedded in GaN NWs also the band gap of the barriers can be reduced so that excitation of barrier material and thus more efficient absorption of the excitation light become feasible.

InGaN material is characterized by strong alloy fluctuations leading to a strongly disordered potential landscape with deep localization centers [43, 70, 71]. While this is disadvantageous for many optoelectronic applications (e.g., in light emitting diodes or laser diodes) the field of opto-chemical sensors benefits from the resulting built-in carrier localization and temperature stability of the luminescence.

Incorporation of InGaN material in nanowire heterostructures has been demonstrated using GaN NWs grown on Si(111) substrates as templates [42, 43, 45, 48, 72–76]. For gas sensor applications, two types of InGaN/GaN NWHs, schematically shown in Fig. 13, have been used so far: Type A consists of a single GaN/InGaN heterostructure, i.e., a large section of InGaN (up to several 100 nm) on GaN NWs with an In content of approximately 34% that results in a PL peak emission energy of 2.25 eV at room temperature [76]. In type B, a ninefold superlattice structure with InGaN inclusions separated by GaN barriers has been used. For those, an In content of 28% and an emission energy of 2.4 eV were reported [48]. In both cases the heterostructure sections were grown by PAMBE on top of a GaN base part with a length of 400 nm. For InGaN growth the substrate temperature was significantly lowered while maintaining N-rich growth conditions. The lower growth temperatures are necessary to avoid the problem of InGaN decomposition but also lead to a widening of the NW diameters at the outer surface of the NWH [48].

Figure 14 shows TEM micrographs obtained from samples of type B. In this case the initial GaN NW is followed by a series of InGaN NDs with a thickness of 4 nm, separated by 7 nm thick GaN barrier layers and a 20 nm GaN cap layer. Details on the morphology and structural properties of these structures can be found in [48].

The reduced emission wavelength of InGaN NWHs comes along with a slightly weaker temperature stability (cf. Fig. 1) compared to GaN/AlGaN NDs or QDs which can be explained by smaller band offsets and the increased basal stacking fault density due to the lower substrate temperatures.

The fabrication of the prototypic opto-chemical sensor system with InGaN/GaN nanowires as transducer elements that was used to obtain the data presented in this

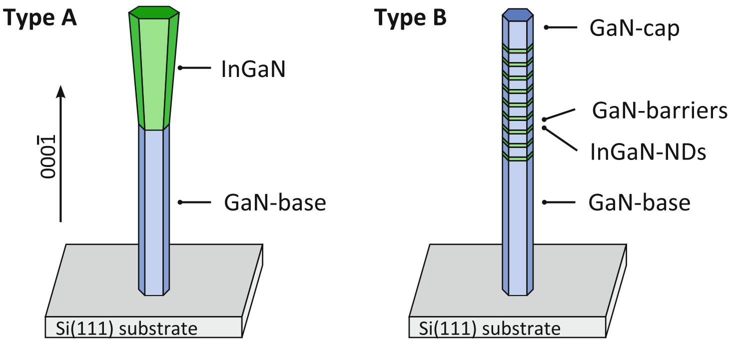

Fig. 13 Schematics of different types of InGaN/GaN NWHs used as chemical transducer structure for gas sensing applications. Both types are based on GaN NWs grown on Si(111) substrates followed by (*left*, type A) single heterostructures with several 100 nm long sections of InGaN or (*right*, type B) InGaN inclusions separated by GaN barriers

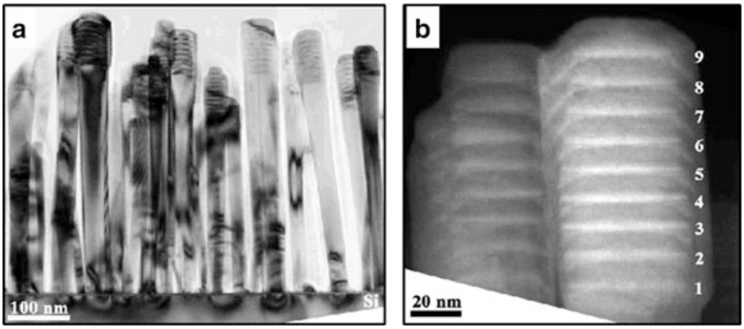

Fig. 14 (**a**) TEM micrograph showing the overall morphology of the GaN NWs with embedded InGaN/GaN heterostructures grown on Si(111) (**b**) STEM dark-field image clearly illustrating a nanodome shape of the facetted InGaN inclusions. Copyright IOP Publishing. Reproduced with permission from [48]. All rights reserved

section was described in [76]. The overall architecture is shown in Fig. 15. The InGaN/GaN NWH ensemble transducer element is mounted inside a gas-flow chamber (volume 3 cm^3) with the NWs facing the interior of the gas cell. An optically transparent sapphire window opposite to the transducer chip allows optical access. Excitation and detection of the PL signal were carried out using a UV power LED (optical power of 75 mW, peak emission wavelength 365 nm, and FWHM of 18 nm) and a photomultiplier (PMT) detector, respectively. Excitation and emission light were coupled into the chamber via separate branches of an optical Y-shaped fiber bundle. Suitable band pass filters were necessary on the excitation and detection side to separate the PL signal from tails of the excitation light. The opto-chemical transducers were mounted on microfabricated heater elements to allow experiments at different transducer temperatures.

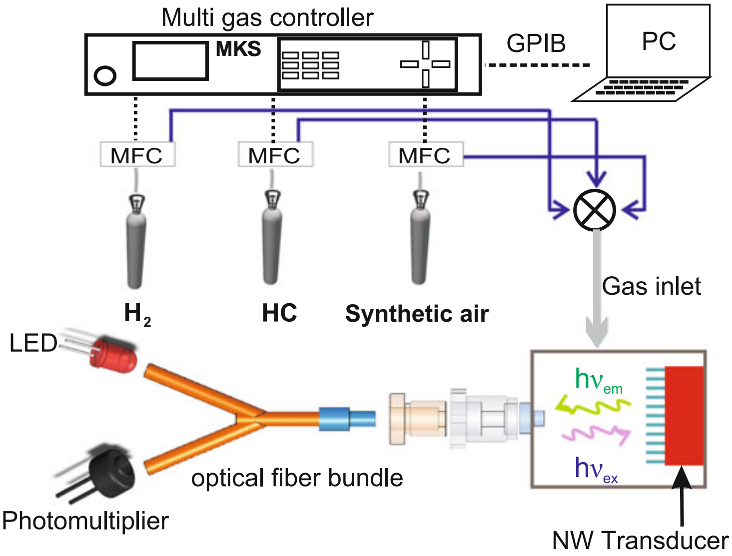

Fig. 15 Schematic of the experimental setup illustrating the opto-chemical sensor system and the gas mixing facility. Reprinted from [76], with permission from Elsevier

4.1 Detection of Hydrogen and Hydrocarbons

The hydrogen response of Pt-coated InGaN/GaN NWHs stands in analogy with the results presented in Sect. 3 and can be explained by the same model of an interfacial hydrogen dipole layer formation.

Figure 16a presents the transient output of the PMT amplifier of a sensor system using a Pt-coated NWH transducer of type A (cf. Fig. 13) upon exposure to different H_2 concentrations at a transducer temperature of 30°C as reported in [76]. From this data the gas response was extracted according to $R = (V_{gas} - V_0)/V_0$, i.e., as the relative change of the PMT output voltage as the NW transducer is exposed to target gases. As an unusual feature the sensor signal, i.e., the PMT output voltage, was found to scale logarithmically with the H_2 concentration as shown in Fig. 16c. The minimum detectable H_2 concentration was 10 ppm and 200 ppb at room temperature and 80°C, respectively (cf. Fig. 16b, c). Response and recovery time constants were in the order of 10 min.

For comparison, commercially available field-effect gas sensors (Schottky diode or MOSFET) exhibit H_2 detection limits in the range of a few hundred ppm when operated in this same temperature regime [77].

Much faster response and recovery times could be observed at moderately elevated transducer temperatures, i.e., about 2–3 min at 40°C and about 1 min at 80°C. Above 80°C the transducers' PL intensity sharply drops precluding measurement with the abovementioned demonstrator system above 120°C.

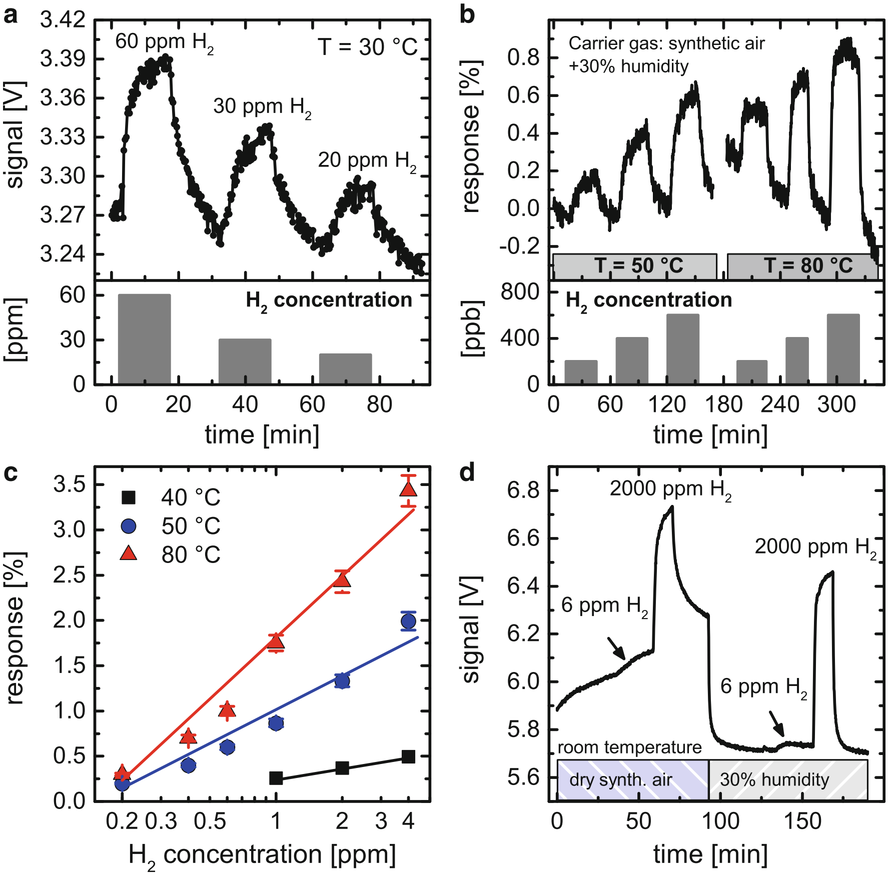

Fig. 16 Optical sensor response to (**a**) decreasing H_2 concentrations in dry synthetic air as carrier gas observed at a transducer temperature of 30°C and (**b**) low H_2 concentrations of 200 ppb in humidified (30%) synthetic air at 50 and 80°C. 200 ppb could be clearly detected at both temperatures with an rms noise voltage of 0.05%. The drift of the PL baseline signal is of purely thermal origin and arose due to an insufficient thermal stabilization of the sensor setup prior to the gas measurement. (**c**) Response as a function of H_2 concentration at different sensor operation temperatures. For a given temperature, the response increases logarithmically with increasing H_2 concentration. (**d**) Effect of humidity on the optical H_2 detection. Background humidity decreases the baseline signal and improves the time response of the H_2-sensor signal. Reprinted from [76], with permission from Elsevier

In [76] also humidity effects on the H_2 response were observed which disappeared when the transducer temperature was raised towards 100°C and beyond. The humidity reduces the sensor baseline signal and increases the speed of the gas response (cf. Fig. 16d), suggesting that the adsorption of water vapor leads to an enhanced surface recombination rate, possibly due to transfer of photoactivated charge carriers to redox levels of the adsorbed water layer according to recent results by Philipps et al. and Wallys et al. [62, 78].

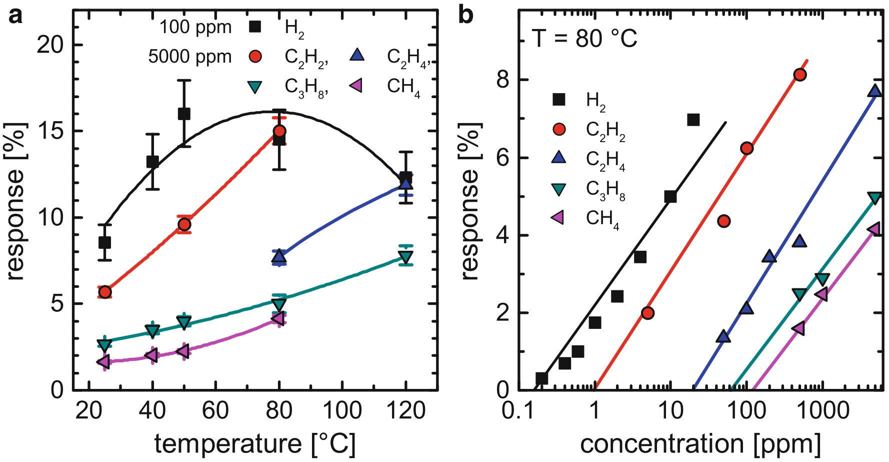

Fig. 17 (**a**) Temperature dependence of the gas response towards H_2 and different hydrocarbon gases and (**b**) variation of the gas response with gas concentration as measured at a transducer temperature of 80°C. In both cases, the carrier gas was synthetic air with 30% humidity. Reprinted from [76], with permission from Elsevier

In addition to a high sensitivity to H_2, Pt-coated InGaN/GaN opto-chemical transducers also exhibit a pronounced sensitivity to hydrocarbons (HC). The response to HCs in general is similar to that of H_2: The relative change in the PL intensity increases with increasing gas concentration and transducer temperature, whereas the time constants for response and recovery decrease with temperature. As a reason for this similarity the HC sensitivity is likely related to the primary sensitivity to H_2. H atoms tend to split off from hydrocarbon molecules on catalytic metal surfaces with a probability depending on the stability of the different molecules and the transducer temperature [79].

It was observed that the magnitude and the speed of the gas-response scale with the stability of the chemical bonds in the different hydrocarbon molecules [76]. In general, higher sensitivities and shorter response times were observed for unsaturated HCs from which it is easier to split off hydrogen atoms than from saturated HCs.

In Fig. 17 the results for H_2 and different HCs are summarized. Whereas an increasing temperature leads to a monotonous decrease in the response and recovery time constants in all cases, the situation regarding the absolute value of the gas response is more complex as shown in Fig. 17a. H_2, in particular, exhibits a pronounced maximum in the gas response around 80°C. Such a temperature behavior might originate from an interplay between two opposing trends with increasing temperature: enhanced dissociation and diffusion of H_2 and H atoms, on the one hand, and stronger surface recombination and desorption on the other.

Although the same arguments apply to all analyte species the data in Fig. 17a indicate that the temperature of maximum gas response, in general, lies beyond the

Table 1 Detector performance for H_2 and different hydrocarbon species operated at room temperature and 80°C. Reprinted from [76], with permission from Elsevier

Gas	Transducer temperature (°C)	Minimum detectable concentration
Hydrogen	RT	10 ppm
Hydrogen	80	200 ppb
Acetylene	80	5 ppm
Ethylene	80	20 ppm
Propane	80	80 ppm
Methane	80	150 ppm

maximum operation temperature of the GaN/InGaN transducers as for all HCs a monotonous increase with temperature was found. It is also noteworthy that the H_2 behavior sets itself apart from the results obtained from AlGaN/GaN NWHs where an increasing response was found up to 300°C. These differences might either be due to the different surface structure of InGaN material or the differences in excitation wavelength in the two experiments.

Figure 17b presents calibration curves derived from concentration-dependent gas sensing experiments at a temperature of 80°C which presents an optimum compromise between high gas response and a reasonably short response time.

The response for H_2 is much stronger than for all other investigated hydrocarbon species due to the much smaller energy barrier for breaking the H–H bond. Among the tested HCs the response is strongest for acetylene (C_2H_2) followed by ethylene (C_2H_4). Due to the triple C–C bond it is easier to extract atomic hydrogen from C_2H_2 than from C_2H_4 with a double C–C bond. As the extraction of H atoms from saturated hydrocarbons requires more energy the response is even smaller for propane (C_3H_8) and methane (CH_4). This trend is also reflected in the time constants with the longest response time of approximately ~30 min for methane. The extrapolation of the individual calibration curves towards $R = 0$ yield estimates for the minimum detectable concentrations of the individual target gases as listed in Table 1.

4.2 Detection of Oxidizing Gases

Similar to GaN/AlGaN NWHs described in Sect. 3, uncoated InGaN NWHs show luminescence quenching in contact with O_2 and an increase of the response as a function of the gas concentration as shown in Fig. 18.

These results were obtained from InGaN/GaN NWHs of type B (cf. Fig. 13) with 4 nm InGaN NDs separated by 7 nm barriers. Although in qualitative agreement with the results on AlGaN/GaN NWHs, the oxygen response of InGaN/GaN NWHs is significantly weaker.

Besides detection of O_2, room-temperature sensing of ozone (O_3) and nitrogen dioxide (NO_2) in humidified synthetic air as carrier gas has been demonstrated. The

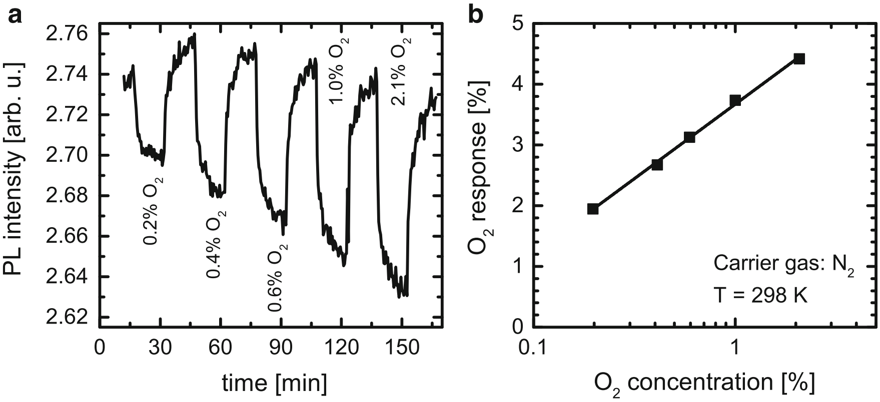

Fig. 18 (**a**) Transients of the PL intensity of InGaN/GaN NWHs for a sequence of pulses of different O_2 concentrations applied at room temperature and (**b**) extracted response as a function of O_2-concentration

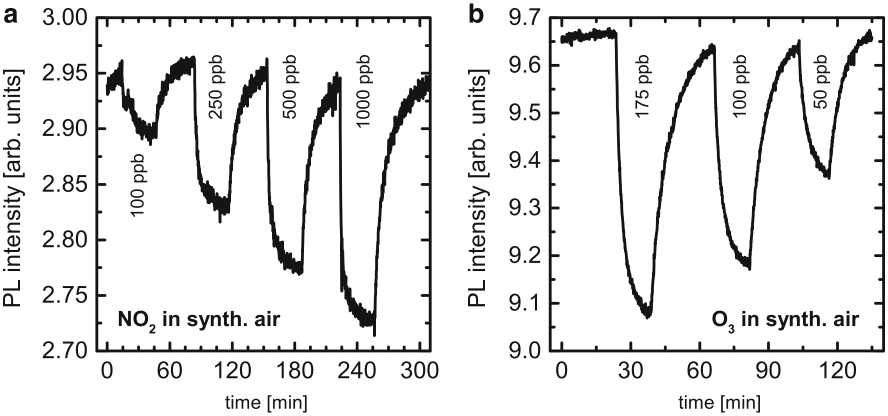

Fig. 19 Response of the PL intensity to a sequence of pulses of different concentrations applied at room temperature in case of (**a**) NO_2 and (**b**) O_3. Synthetic air with 30% humidity was used as background carrier gas

minimum detectable concentrations are 10 ppb for O_3 and 50 ppb for NO_2, i.e., much lower than in the case of O_2. Figure 19 shows the room-temperature response of the PL intensity to a sequence of NO_2 (a) and O_3 (b) pulses of different concentrations using synthetic air as carrier gas. For comparison, [31] reports an NO_2 response of SnO_2 nanobelts of 6–7% at a transducer temperature of 120°C and states that PL quenching by NO_2 is not efficient at temperatures lower than 80°C.

Considering the model for the O_2 response (cf. Sect. 3) and assuming electron trapping as the rate-limiting process in the surface recombination the superior detection efficiency of NO_2 and O_3 compared to the much more abundant O_2 might be explained by their strongly different electron affinities (cf. Table 2).

Table 2 Comparison of electron affinity and minimum detectable concentration of all three oxidizing gases analyzed

Analyte gas	Electron affinity (eV)	Minimum detectable concentration
O_2	0.451	400 ppm
NO_2	2.273	20 ppb
O_3	2.1028	5 ppb

While all three oxidizing gases exhibit a positive electron affinity, i.e., electron trapping at these molecules is energetically favorable, the values of NO_2 and O_3 are significantly higher than that of O_2, indicating a higher probability for electron trapping and thus for non-radiative surface recombination of photo-excited electron–hole pairs.

5 Summary/Outlook

Group III-nitride materials allow the synthesis of substrate-supported nanostructure ensembles such as semiconductor quantum dots and nanowires. Such nanostructures were successfully applied as opto-chemical transducers using the environmental dependence of their photoluminescence characteristics as a base for the realization of an optical readout technique. Here, large ensembles of nano-objects are probed in parallel which combines the superior sensitivity of nanoscale transducer structures with a minimal effort for sample processing and signal detection. Besides that, one of the main advantages of this approach is the possibility for a strict media separation of the active sensing element and the detection and signal processing units. For GaN/AlN QDs even a built-in separation of media was achieved using the transducer structure itself as a window between the gaseous and the ambient environment. A similar situation can be obtained for nanowires grown on transparent substrates such as sapphire or diamond. Furthermore, recent advances in growth techniques allowed the realization of complex heterostructure designs which offer control over the optical properties in order to optimize the transducer structure for specific application scenarios.

In recent years, this concept has been successfully applied in the field of optical gas sensors. In particular, the response to reducing (H_2, C_2H_2, C_2H_4, C_3H_6, CH_4) and oxidizing gases (O_2, NO_2, O_3) has been demonstrated with a sensitivity exceeding that of present technologies especially at moderate temperatures. Besides gas sensor applications, these structures can also be applied in liquid environment. Recently, GaN and InGaN nanowires as well as InGaN-quantum dots have been demonstrated to act as highly pH-sensitive devices with optical readout that bear unique advantages compared to presently used technologies [61, 62]. For example, by using conductive substrates or layers as a backside contact, the definition of an electrochemical working point to maximize sensitivity and to suppress electrochemical degradation is possible. In this context, this approach is suitable for imaging of local pH variations, e.g., the pH activity of living cells, thereby implying significant potential for biochemical and life science applications. This shows that the results discussed within this chapter are embedded in a broad and promising application platform for opto-chemical nanosensors based on group III-nitrides.

References

1. Li C, Zhang D, Liu X, Han S, Tang T, Han J, Zhou C (2003) In_2O_3 nanowires as chemical sensors. Appl Phys Lett 82:1613
2. Fan Z, Wang D, Chang P-C, Tseng W-Y, Lu JG (2004) ZnO nanowire field-effect transistor and oxygen sensing property. Appl Phys Lett 85:5923
3. Cui Y, Wei Q, Park H, Lieber CM (2001) Nanowire nanosensors for highly sensitive and selective detection of biological and chemical species. Science 293:1289
4. Zhou XT, Hu JQ, Li CP, Ma DDD, Lee CS, Lee ST (2003) Silicon nanowires as chemical sensors. Chem Phys Lett 369:220
5. Lim W, Wright JS, Gila BP, Johnson JL, Ural A, Anderson T, Ren F, Pearton SJ (2008) Room temperature hydrogen detection using Pd-coated GaN nanowires. Appl Phys Lett 93:072109
6. Prades JD, Hernandez-Ramirez F, Jimenez-Diaz R, Manzanares M, Andreu T, Cirera A, Romano-Rodriguez A, Morante JR (2008) The effects of electron–hole separation on the photoconductivity of individual metal oxide nanowires. Nanotechnology 19:465501
7. Baratto C, Comini E, Faglia G, Sberveglieri G (2012) The power of nanomaterial approaches in gas sensors. In: Fleischer M, Lehmann M (eds) Solid state gas sensors – industrial application. Springer, Berlin Heidelberg, pp 53–78
8. Sharma S, Madou M (2012) A new approach to gas sensing with nanotechnology. Philos Trans R Soc A 370:2448
9. Wang Y, Yeow JTW (2009) A review of carbon nanotubes-based gas sensors. J Sens 2009:493904
10. Stranski I, Krastanow L (1937) Zur Theorie der orientierten Ausscheidung von Ionenkristallen aufeinander. Monatsh Chem Verw Tl 71:351
11. Fan HJ, Werner P, Zacharias M (2006) Semiconductor nanowires: from self-organization to patterned growth. Small 2:700
12. Li S, Waag A (2012) GaN based nanorods for solid state lighting. J Appl Phys 111:071101
13. Eranna G, Joshi BC, Runthala DP, Gupta RP (2004) Oxide materials for development of integrated gas sensors – a comprehensive review. CRC Cr Rev Sol State 29:111
14. Comini E, Faglia G, Sberveglieri G (eds) (2009) Solid state gas sensing. Springer, USA
15. Lundström I (1981) Hydrogen sensitive mos-structures: part 1: principles and applications. Sensor Actuator 1:403
16. Schalwig J, Müller G, Eickhoff M, Ambacher O, Stutzmann M (2002) Gas sensitive GaN/AlGaN-heterostructures. Sensor Actuat B Chem 87:425
17. Schalwig J, Müller G, Karrer U, Eickhoff M, Ambacher O, Stutzmann M, Gorgens L, Dollinger G (2002) Hydrogen response mechanism of Pt-GaN Schottky diodes. Appl Phys Lett 80:1222
18. Chen RS, Lu CY, Chen KH, Chen LC (2009) Molecule-modulated photoconductivity and gain-amplified selective gas sensing in polar GaN nanowires. Appl Phys Lett 95:233119
19. Prades JD, Jimenez-Diaz R, Hernandez-Ramirez F, Barth S, Cirera A, Romano-Rodriguez A, Mathur S, Morante JR (2008) Ultralow power consumption gas sensors based on self-heated individual nanowires. Appl Phys Lett 93:123110
20. Comini E, Faglia G, Sberveglieri G, Pan Z, Wang ZL (2002) Stable and highly sensitive gas sensors based on semiconducting oxide nanobelts. Appl Phys Lett 81:1869

21. Wang HT, Kang BS, Ren F, Tien LC, Sadik PW, Norton DP, Pearton SJ, Lin J (2005) Hydrogen-selective sensing at room temperature with ZnO nanorods. Appl Phys Lett 86:243503
22. Johnson JL, Choi Y, Ural A, Lim W, Wright B, Gila JS, Ren F, Pearton S (2009) Growth and characterization of GaN nanowires for hydrogen sensors. J Electron Mater 38:490
23. Wright J, Lim W, Gila B, Pearton S, Johnson JL, Ural A, Ren F (2009) Hydrogen sensing with Pt-functionalized GaN nanowires. Sensor Actuat B Chem 140:196
24. Calarco R, Marso M, Richter T, Aykanat AI, Meijers R, Hart A v, Stoica T, Lüth H (2005) Size-dependent photoconductivity in MBE-grown GaN-nanowires. Nano Lett 5:981–984
25. Chen H-Y, Chen R-S, Chang F-C, Chen L-C, Chen K-H, Yang Y-J (2009) Size-dependent photoconductivity and dark conductivity of m-axial GaN nanowires with small critical diameter. Appl Phys Lett 95:143123
26. Butler MA (1984) Optical fiber hydrogen sensor. Appl Phys Lett 45:1007
27. Ando M (2006) Recent advances in optochemical sensors for the detection of H_2, O_2, O_3, CO, CO_2 and H_2O in air. TrAC Trend Anal Chem 25:937
28. Kamat PV (1993) Photochemistry on nonreactive and reactive (semiconductor) surfaces. Chem Rev 93:267
29. Sailor MJ, Lee EJ (1997) Surface chemistry of luminescent silicon nanocrystallites. Adv Mater 9:783
30. Lebedev MV (2002) Surface modification of III-V semiconductors: chemical processes and electronic properties. Prog Surf Sci 70:153
31. Faglia G, Baratto C, Sberveglieri G, Zha M, Zappettini A (2005) Adsorption effects of NO_2 at ppm level on visible photoluminescence response of SnO_2 nanobelts. Appl Phys Lett 86:011923
32. de la Mata M, Zhou X, Furtmayr F, Teubert J, Gradecak S, Eickhoff M, Fontcuberta i Morral A, Arbiol J (2013) A review of MBE grown 0D, 1D and 2D quantum structures in a nanowire. J Mater Chem C 1:4300
33. Arbiol J, de la Mata M, Eickhoff M, Fontcuberta i Morral A (2013) Bandgap engineering in a nanowire: self-assembled 0, 1 and 2D quantum structures. Mater Today 16:213, 10.1016/j.mattod.2013.06.006
34. Daudin B (2008) Polar and nonpolar GaN quantum dots. J Phys Cond Mat 20:473201
35. Calleja E, Sánchez-García MA, Sánchez FJ, Calle F, Naranjo FB, Munoz E, Jahn U, Ploog K (2000) Luminescence properties and defects in GaN nanocolumns grown by molecular beam epitaxy. Phys Rev B 62:16826
36. Furtmayr F, Vielemeyer M, Stutzmann M, Arbiol J, Estradé S, Peirò F, Morante JR, Eickhoff M (2008) Nucleation and growth of GaN nanorods on Si (111) surfaces by plasma-assisted molecular beam epitaxy – the influence of Si- and Mg-doping. J Appl Phys 104:034309
37. Arbiol J, Magen C, Becker P, Jacopin G, Chernikov A, Schafer S, Furtmayr F, Tchernycheva M, Rigutti L, Teubert J, Chatterjee S, Morante JR, Eickhoff M (2012) Self-assembled GaN quantum wires on GaN/AlN nanowire templates. Nanoscale 4:7517
38. Tchernycheva M, Sartel C, Cirlin G, Travers L, Patriarche G, Largeau L, Mauguin O, Harmand J–C, Dang LS, Renard J, Gayral B, Nevou L, Julien F (2008) GaN/AlN free-standing nanowires grown by molecular beam epitaxy. Phys Stat Sol (C) 5:1556
39. Renard J, Songmuang R, Bougerol C, Daudin B, Gayral B (2008) Exciton and biexciton luminescence from single GaN/AlN quantum dots in nanowires. Nano Lett 8:2092
40. Ristic J, Rivera C, Calleja E, Fernández-Garrido S, Povoloskyi M, Di Carlo A (2005) Carrier-confinement effects in nanocolumnar GaN/$Al_xGa_{1-x}N$ quantum disks grown by molecular-beam epitaxy. Phys Rev B 72:085330
41. Furtmayr F, Teubert J, Becker P, Conesa-Boj S, Morante JR, Chernikov A, Schäfer S, Chatterjee S, Arbiol J, Eickhoff M (2011) Carrier confinement in GaN/$Al_xGa_{1-x}N$ nanowire heterostructures ($0 < x \leq 1$). Phys Rev B 84:205303
42. Kikuchi A, Kawai M, Tada M, Kishino K (2004) InGaN/GaN multiple quantum disk nanocolumn light-emitting diodes grown on (111) Si substrate. Jpn J Appl Phys 43:L1524

43. Tourbot G, Bougerol C, Grenier A, Hertog MD, Sam-Giao D, Cooper D, Gilet P, Gayral B, Daudin B (2011) Structural and optical properties of InGaN/GaN nanowire heterostructures grown by PA-MBE. Nanotechnology 22:075601
44. Sekiguchi H, Kishino K, Kikuchi A (2010) Emission color control from blue to red with nanocolumn diameter of InGaN/GaN nanocolumn arrays grown on same substrate. Appl Phys Lett 96:231104
45. Guo W, Zhang M, Banerjee A, Bhattacharya P (2010) Catalyst-Free InGaN/GaN nanowire light emitting diodes grown on (001) silicon by molecular beam epitaxy. Nano Lett 10:3355
46. Limbach F, Gotschke T, Stoica T, Calarco R, Sutter E, Ciston J, Cusco R, Artus L, Kremling S, Höfling S, Worschech L, Grützmacher D (2011) Structural and optical properties of InGaN/GaN nanowire heterostructures grown by molecular beam epitaxy. J Appl Phys 109:014309
47. Albert S, Bengoechea-Encabo A, Lefebvre P, Barbagini F, Sanchez-Garcia MA, Calleja E, Jahn U, Trampert A (2012) Selective area growth and characterization of InGaN nano-disks implemented in GaN nanocolumns with different top morphologies. Appl Phys Lett 100:231906
48. Kehagias T, Dimitrakopulos GP, Becker P, Kioseoglou J, Furtmayr F, Koukoula T, Häeusler I, Chernikov A, Chatterjee S, Karakostas T, Solowan H-M, Schwarz UT, Eickhoff M, Komninou P (2013) Nanostructure and strain in InGaN/GaN superlattices grown in GaN nanowires. Nanotechnology 24:435702
49. Vurgaftman I, Meyer JR (2003) Band parameters for nitrogen-containing semiconductors. J Appl Phys 94:3675
50. Renard J, Kandaswamy PK, Monroy E, Gayral B (2009) Suppression of nonradiative processes in long-lived polar GaN/AlN quantum dots. Appl Phys Lett 95:131903
51. Gacevic Z, Das A, Teubert J, Kotsar Y, Kandaswamy PK, Kehagias T, Koukoula T, Komninou P, Monroy E (2011) Internal quantum efficiency of III-nitride quantum dot superlattices grown by plasma-assisted molecular-beam epitaxy. J Appl Phys 109:103501
52. Teubert J, Becker P, Furtmayr F, Eickhoff M (2011) GaN nanodiscs embedded in nanowires as optochemical transducers. Nanotechnology 22:275505
53. Weidemann O, Kandaswamy PK, Monroy E, Jegert G, Stutzmann M, Eickhoff M (2009) GaN quantum dots as optical transducers for chemical sensors. Appl Phys Lett 94:113108
54. Guillot F, Bellet-Amalric E, Monroy E, Tchernycheva M, Nevou L, Doyennette L, Julien FH, Dang LS, Remmele T, Albrecht M, Shibata T, Tanaka M (2006) Si-doped GaN/AlN quantum dot superlattices for optoelectronics at telecommunication wavelengths. J Appl Phys 100:044326
55. Lundström I, Armgarth M, Petersson L-G (1989) Physics with catalytic metal gate chemical sensors. CRC Cr Rev Sol State 15:201
56. Weidemann O, Hermann M, Steinhoff G, Wingbrant H, Lloyd-Spetz A, Stutzmann M, Eickhoff M (2003) Influence of surface oxides on hydrogen-sensitive Pd:GaN Schottky diodes. Appl Phys Lett 83:773
57. Miller DAB, Chemla DS, Damen TC, Gossard AC, Wiegmann W, Wood TH, Burrus CA (1984) Band-edge electroabsorption in quantum well structures: The quantum-confined Stark effect. Phys Rev Lett 53:2173
58. Miller DAB, Chemla DS, Damen TC, Gossard AC, Wiegmann W, Wood TH, Burrus CA (1985) Electric field dependence of optical absorption near the band gap of quantum-well structures. Phys Rev B 32:1043
59. Fry PW, Itskevich IE, Mowbray DJ, Skolnick MS, Finley JJ, Barker JA, O'Reilly EP, Wilson LR, Larkin IA, Maksym PA, Hopkinson M, Al-Khafaji M, David JPR, Cullis AG, Hill G, Clark JC (2000) Inverted electron–hole alignment in InAs-GaAs self-assembled quantum dots. Phys Rev Lett 84:733
60. Finley JJ, Sabathil M, Vogl P, Abstreiter G, Oulton R, Tartakovskii AI, Mowbray DJ, Skolnick MS, Liew SL, Cullis AG, Hopkinson M (2004) Quantum-confined Stark shifts of charged exciton complexes in quantum dots. Phys Rev B 70:201308

61. Teubert J, Koslowski S, Lippert S, Schäfer M, Wallys J, Dimitrakopulos G, Kehagias T, Komninou P, Das A, Monroy E, Eickhoff M (2013) InGaN/GaN quantum dots as optical probes for the electric field at the GaN/electrolyte interface. J Appl Phys 114:074313
62. Wallys J, Teubert J, Furtmayr F, Hofmann DM, Eickhoff M (2012) Bias-Enhanced optical pH response of group III-nitride nanowires. Nano Lett 12:6180
63. Ristic J, Sánchez-García M, Ulloa J, Calleja E, Sanchez-Páramo J, Calleja J, Jahn U, Trampert A, Ploog K (2002) AlGaN nanocolumns and AlGaN/GaN/AlGaN nanostructures grown by molecular beam epitaxy. Phys Stat Sol (B) 234(717)
64. Ristic J, Calleja E, Sánchez-Garcia MA, Ulloa JM, Sánchez-Páramo J, Calleja JM, Jahn U, Trampert A, Ploog KH (2003) Characterization of GaN quantum discs embedded in $Al_xGa_{1-x}N$ nanocolumns grown by molecular beam epitaxy. Phys Rev B 68:125305
65. Rivera C, Jahn U, Flissikowski T, Pau JL, Munoz E, Grahn HT (2007) Strain-confinement mechanism in mesoscopic quantum disks based on piezoelectric materials. Phys Rev B 75:045316
66. Pfüller C, Brandt O, Grosse F, Flissikowski T, Chèze C, Consonni V, Geelhaar L, Grahn HT, Riechert H (2010) Unpinning the Fermi level of GaN nanowires by ultraviolet radiation. Phys Rev B 82:045320
67. Lundström I, DiStefano T (1976) Hydrogen induced interfacial polarization at Pd-SiO_2 interfaces. Surf Sci 59:23
68. Lloyd Spetz A, Baranzahi A, Tobias P, Lundstr I (1997) High temperature sensors based on metal-insulator-silicon carbide devices. Phys Stat Sol (A) 162(493)
69. Ambacher O (1998) Growth and applications of group III-nitrides. J Phys D Appl Phys 31:2653
70. Bardoux R, Kaneta A, Funato M, Kawakami Y, Kikuchi A, Kishino K (2009) Positive binding energy of a biexciton confined in a localization center formed in a single $In_xGa_{1-x}N$/GaN quantum disk. Phys Rev B 79:155307
71. Lähnemann J, Brandt O, Pfüller C, Flissikowski T, Jahn U, Luna E, Hanke M, Knelangen M, Trampert A, Grahn HT (2011) Coexistence of quantum-confined Stark effect and localized states in an (In, Ga)N/GaN nanowire heterostructure. Phys Rev B 84:155303
72. Kim H-M, Cho Y-H, Lee H, Kim SI, Ryu SR, Kim DY, Kang TW, Chung KS (2004) High-brightness light emitting diodes using dislocation-free indium gallium nitride/gallium nitride multiquantum-well nanorod arrays. Nano Lett 4:1059
73. Armitage R, Tsubaki K (2010) Multicolour luminescence from InGaN quantum wells grown over GaN nanowire arrays by molecular-beam epitaxy. Nanotechnology 21:195202
74. Chang Y-L, Wang JL, Li F, Mi Z (2010) High efficiency green, yellow, and amber emission from InGaN/GaN dot-in-a-wire heterostructures on Si(111). Appl Phys Lett 96:013106
75. Jacopin G, Rigutti L, Largeau L, Fortuna F, Furtmayr F, Julien FH, Eickhoff M, Tchernycheva M (2011) Optical properties of wurtzite/zinc-blende heterostructures in GaN nanowires. J Appl Phys 110:064313
76. Paul S, Helwig A, Müller G, Furtmayr F, Teubert J, Eickhoff M (2012) Opto-chemical sensor system for the detection of H_2 and hydrocarbons based on InGaN/GaN nanowires. Sensor Actuat B Chem 173:120
77. Hübert T, Boon-Brett L, Black G, Banach U (2011) Hydrogen sensors – a review. Sensor Actuat B Chem 157:329
78. Philipps JM, Müntze GM, Hille P, Wallys J, Schörmann J, Teubert J, Hofmann DM, Eickhoff M (2013) Radical formation at the gallium nitride nanowire-electrolyte interface by photoactivated charge transfer. Nanotechnology 24:325701
79. Kreisl P, Helwig A, Friedberger A, Müller G, Obermeier E, Sotier S (2005) Detection of hydrocarbon species using silicon MOS capacitors operated in a non-stationary temperature pulse mode. Sensor Actuat B Chem 106:489

Index

C.-D. Kohl and T. Wagner (eds.), *Gas Sensing Fundamentals*,
Springer Series on Chemical Sensors and Biosensors (2014) 15: 339–342
DOI 10.1007/5346_2014, © Springer-Verlag Berlin Heidelberg 2014